FINAL REPORT

Investigating the Sensitivity of Emerging Geophysical Technologies to Immobile Porosity and Isolated DNAPL and Dissolved/Sorbed VOC Mass in Fractured Media

SERDP Project ER-2421

FEBRUARY 2020

Dr. Lee D. Slater
Frederick Day-Lewis
Kristina Keating
Beth Parker
Rutgers University-Newark

Distribution Statement A
This document has been cleared for public release

SERDP
DOD ▪ EPA ▪ DOE

Page Intentionally Left Blank

This report was prepared under contract to the Department of Defense Strategic Environmental Research and Development Program (SERDP). The publication of this report does not indicate endorsement by the Department of Defense, nor should the contents be construed as reflecting the official policy or position of the Department of Defense. Reference herein to any specific commercial product, process, or service by trade name, trademark, manufacturer, or otherwise, does not necessarily constitute or imply its endorsement, recommendation, or favoring by the Department of Defense.

Page Intentionally Left Blank

REPORT DOCUMENTATION PAGE

Form Approved
OMB No. 0704-0188

Public reporting burden for this collection of information is estimated to average 1 hour per response, including the time for reviewing instructions, searching existing data sources, gathering and maintaining the data needed, and completing and reviewing this collection of information. Send comments regarding this burden estimate or any other aspect of this collection of information, including suggestions for reducing this burden to Department of Defense, Washington Headquarters Services, Directorate for Information Operations and Reports (0704-0188), 1215 Jefferson Davis Highway, Suite 1204, Arlington, VA 22202-4302. Respondents should be aware that notwithstanding any other provision of law, no person shall be subject to any penalty for failing to comply with a collection of information if it does not display a currently valid OMB control number. **PLEASE DO NOT RETURN YOUR FORM TO THE ABOVE ADDRESS.**

1. REPORT DATE *(DD-MM-YYYY)*
02-12-20

2. REPORT TYPE
SERDP Final Report

3. DATES COVERED *(From - To)*
May 2014-May 2019

4. TITLE AND SUBTITLE

5a. CONTRACT NUMBER
14-C-0018

5b. GRANT NUMBER

5c. PROGRAM ELEMENT NUMBER

6. AUTHOR(S)

Dr. Lee D. Slater, Frederick Day-Lewis, Kristina Keating and Beth Parker

5d. PROJECT NUMBER
ER-2421

5e. TASK NUMBER
N/A

5f. WORK UNIT NUMBER
N/A

7. PERFORMING ORGANIZATION NAME(S) AND ADDRESS(ES)

Department of Earth & Environmental Sciences,
Rutgers University Newark, 101 Warren St,
Newark,
NJ 07102

8. PERFORMING ORGANIZATION REPORT NUMBER
ER-2421

9. SPONSORING / MONITORING AGENCY NAME(S) AND ADDRESS(ES)

10. SPONSOR/MONITOR'S ACRONYM(S) NUMBER(S) ER-2421

12. DISTRIBUTION / AVAILABILITY STATEMENT
DISTRIBUTION STATEMENT A. Approved for public release: distribution unlimited.

13. SUPPLEMENTARY NOTES
Prepared in cooperation with the United States Geological Survey Hydrogeophysics Branch and the G360 Center for Groundwater Research group at University of Guelph

14. ABSTRACT

The primary objectives of this research were to [1] determine the sensitivity of two emerging borehole geophysical technologies (nuclear magnetic resonance [NMR] and complex resistivity [CR]) to key pore geometric properties (primarily pore size distribution and permeability) controlling contaminant transport, [2] investigate the potential sensitivity of emerging geophysical methods to contaminant mass (as DNAPL and/or aqueous phase) isolated within the immobile porosity of fractured rock inaccessible to aqueous sampling techniques, and [3] to evaluate the predictive capabilities of these geophysical technologies with respect to quantifying immobile porosity and/or contaminant mass concentration. Laboratory and field datasets were acquired on three contaminated sedimentary fractured rock aquifers. Pore geometric parameters (e.g. pore size, permeability) controlling contaminant transport were predicted from the geophysical datasets. Contaminant mass distributions were inferred from analysis of multiple geophysical logs and a procedure for estimating a mass transfer rate coefficient from an electrical geophysical tracer test was demonstrated.

15. SUBJECT TERMS
Fractured rock, geophysics, mass transfer, back diffusion, nuclear magnetic resonance, complex resistivity

16. SECURITY CLASSIFICATION OF:			**17. LIMITATION OF ABSTRACT**	**18. NUMBER OF PAGES**	**19a. NAME OF RESPONSIBLE PERSON**
a. REPORT	**b. ABSTRACT**	**c. THIS PAGE**			Lee Slater
U	U	U	UU	285	**19b. TELEPHONE NUMBER** *(include area code)* 973-353-5109

Standard Form 298 (Rev. 8-98)
Prescribed by ANSI Std. Z39.18

Page Intentionally Left Blank

ACRONYM LIST

ATV	Acoustical televiewer
BET	Brunauer–Emmett–Teller
BOC	Bottom of casing
BFI	Bound fluid index, fraction of capillary bound fluid
COTS	Commercial off-the-shelf
CC	Complex conductivity
CR	Complex resistivity
CVOC	Chlorinated volatile organic compound
DCE	cis-dichloroethylene
DFN	Discrete Fracture Network
DNAPL	Dense non-aqueous phase liquid
EDL	Electric double layer
FFI	Free fluid index, fraction of free fluid within a sample
FRGT	Fractured Rock Geophysical Toolbox
HC	Hydrite Chemical Co.
HPFM	Heat pulse flow meter
MICP	Mercury Injection Capillary Pressure
MS	Magnetic susceptibility
NAPL	Non-aqueous phase liquid
NAWC	Naval Air Warfare Center
NMR	Nuclear Magnetic Resonance
OTV	Optical televiewer
SC	Fluid specific conductance
SCM	Site Conceptual Model
SSFL	Santa Susanna Field Laboratory
TCE	Trichloroethylene
TOC	Top of casing
VC	Vinyl chloride
VOC	Volatile organic compound

KEYWORDS

Fractured rock, geophysics, mass transfer, back diffusion, nuclear magnetic resonance, complex resistivity

ACKNOWLEDGEMENTS

Rutgers University Newark (RUN) contributions: Dr. Judy Robinson (now at Pacific Northwest National Laboratory) led on major laboratory physical and geophysical properties data acquisition activities. Dr. Samuel Falzone led the development, testing and data acquisition for the tracer tests on rock cores performed during the project extension. Robinson and Falzone both contributed significantly to the report writing, with Robinson leading initial efforts of the entire project team to compile a draft report. Undergraduate students Tonian Robinson (now at University of South Florida) and Yonesha Donaldson (now at University of Georgia) contributed extensively to laboratory physical and geophysical data acquisition.

University of Guelph G360 Institute for Groundwater Research contributions: Steven Chapman, MSc, P.Eng., Senior Hydrogeologist, took the lead project management role for G360 tasks including field work at the NAWC (NJ) site with USGS and Rutgers collaborations. Dr. Peeter Pehme contributed expertise with advanced borehole geophysical and hydrophysical logging in bedrock boreholes and supported the field logging efforts at the NAWC (NJ), SSFL (CA) and Hydrite (WI) sites. Dr. Jessica Meyer (now Assistant Professor at the University of Iowa) supported the field efforts at the Hydrite (WI) site and relevant data and knowledge transfer to project participants for lab samples. Amanda Pierce, MSc, P.Geo., Senior Hydrogeologist, provided on-site support to USGS borehole logging at SSFL (CA), core sample collection and site data and knowledge transfer. Carla Rose (former G360 Research Associate, now PhD Candidate in the Department of Earth and Environmental Sciences at the University of Ottawa) assisted with core physical property measurements and sample handling. Maria Gorecka (Senior Analytical Chemist and Laboratory Manager) performed contaminant analyses on core samples from the study sites.

U.S. Geological Survey (USGS) contributions: Carole Johnson led on fieldwork for collection of borehole geophysical data at the three study sites. Dr. Neil Terry led on a machine-learning analysis of borehole logs. Johnson contributed to report writing, and both Johnson and Terry contributed to manuscript drafts.

DISCLAIMER

Any opinions, findings and conclusions or recommendations expressed in this material are those of the author(s) and do not necessarily reflect the views of the U.S. Army Corps of Engineers, Humphreys Engineer Center Support Activity.

Contents

EXECUTIVE SUMMARY 1
1.0 Abstract 9
2.0 Objectives 10
3.0 Background 12
3.1 Emerging geophysical technologies 14
3.1.1 Nuclear magnetic resonance (NMR) 15
3.1.2 Complex resistivity (CR) 16
4.0 Theory of geophysical methods 17
4.1 Nuclear magnetic resonance (NMR) 17
4.1.1 NMR estimates of permeability 18
4.2 Complex resistivity (CR) 19
4.2.1 CR estimates of permeability 21
5.0 Study Sites 25
5.1 Santa Susana Field Laboratory (SSFL) 25
5.2 Hydrite Chemical Company (HC) 26
5.3 Naval Air Warfare Center (NAWC) 27
6.0 Methods 29
6.1 Technical Approach for acquisition of core samples 29
6.1.1 Hydrite 31
6.1.2 Santa Susana 31
6.1.3 NAWC 32
6.2 Quantification of variations in contaminant mass 33
6.3 Quantification of rock properties 34
6.3.1 Permeability 34
6.3.2 Submersible volumes 35
6.3.3 Sample saturation 35
6.3.4 Gravimetric porosity 36
6.3.5 X-ray diffraction (XRD) 36

6.3.6 Mercury injection capillary pressure (MICP) 36
6.3.7 Brunauer–Emmett–Teller (BET) Method 39
6.3.8 Ferrozine analysis 40
6.3.9 Magnetic susceptibility 40
6.4 Geophysical measurements on rock cores 41
6.4.1 Nuclear magnetic resonance (NMR) 41
6.4.2 Complex resistivity (CR) 42
6.4.3 Electrical Formation Factor F 44
6.4.4 Electrical Tracer Experiments 44
6.5 Modeling of transport and electrical measurements 52
6.5.1 Models of contaminant transport in fractured rock 53
6.5.2 Pore network modeling 54
6.6 Field-scale borehole data 56
6.6.1 Borehole Logging 56
6.6.2 Quantification of fracture network hydraulic properties and estimation of groundwater flow 62
6.6.3 Specialized geophysical logs NMR, IP, and MSUS 66
6.6.4 FACT 72
7.0 Results 74
7.1 Petrophysical relationships between laboratory geophysical measurements and rock properties 74
7.1.1 Porosity estimates 74
7.1.2 Pore scale relationships using geophysical measurements 74
7.1.3 Permeability relationships 76
7.2 Petrophysical relationships between geophysical measurements and contaminant mass .. 80
7.2.1 NAWC 80
7.2.2 Hydrite 81
7.2.3 SSFL 82
7.3 Electrical tracer experimental results 84
7.4 Pore scale modeling results 92
7.5 Assessment of distribution of contaminant mass relative to distribution of fractures 93
7.6 Evaluation of contaminant mass distribution relative to fractures at the study sites 95
8.0 Technology Limitations 99

9.0 Technology Transfer 101
10.0 Conclusions 103
11.0 Literature Cited 106
Appendix A.1: Borehole Logs 115
Hydrite MP24S 115
Hydrite MP25S 116
Santa Susana C3 117
Santa Susana C4 118
Santa Susana RD109 119
NAWC 94BR 120
Appendix A.2 Contaminant Mass 121
Appendix A.3: Rock core contaminant profiles 140
Appendix B.1: Complex resistivity (CR), Nuclear Magnetic Resonance (NMR) and physical property summary data 146
Appendix B.2: Nuclear magnetic resonance (NMR) T2 cutoff times 220
Appendix B.3: Mercury Injection Capillary Pressure (MICP) data 231
Appendix B.4: Laboratory data 251
Appendix C: Publications 267

Figure 2. 1: Project overview showing central tasks of the work performed. Cores were used to determine high resolution distribution of contaminant mass in relation to fractures. Immobile and mobile porosity, permeability and surface area, along with geophysical (NMR and CR) laboratory data, were acquired. Field-scale hydrological and geophysical properties were determined from borehole measurements using emerging technologies. The integrated dataset was used to determine the sensitivity of NMR and CR borehole measurements to contaminant mass in-situ. 11

Figure 3. 1: The DFN approach uses both rock core and core hole derived datasets to characterize contaminated sites on fractured sedimentary rock to result in an improved site conceptual model (adapted from Parker et al., 2012). The emerging NMR and CR geophysical technologies were considered an important advancement in the DFN approach and are embedded as ER 2421. An associated ESTCP project (ER201630) that leveraged ER2421 is also shown.. 13
Figure 3. 2: Nuclear magnetic resonance (NMR) and complex resistivity (CR) borehole logging tools are emerging technologies for sensing (1) pore geometric properties controlling contaminant mass transport/storage and (2) possibly contaminant mass itself. 14
Figure 3. 3: Overview of the basic principles of the nuclear magnetic resonance (NMR) and complex resistivity (CR) measurement highlighting the analogies between the two measurements. The NMR method exploits the quantum mechanics phenomenon of nuclear spin whereas the CR method is based on multiple electrical charge transport processes. The physical principles of the two methods are discussed in further detail in Section 4.0. 15

Figure 4. 1: Comparison of a) MICP intrusion and b) T2 distributions for three samples investigated in this project with varying pore size distributions..... 18
Figure 4. 2: Complex resistivity measurements represented in a) the frequency and b) time domains. In the frequency domain, the voltage magnitude and phase lag are recorded relative to the current waveform. In the time domain, a transient voltage decay is recorded following an abrupt termination of the current injection. 19
Figure 4. 3: Relationship between the dominant relaxation time a) τpc and grain/pore size with b) and without c) an applied electric field, E. Shown are three samples at sites Hydrite (HC), Santa Susana (SSFL) and NAWC. While a relaxation time was chosen for the NAWC sample based on Revil et al. (2013), other data suggest (see Figure 4.1) that the dominant grain/pore size is much smaller and would be measured at larger frequencies, out of the range of the PSIP used in this project..... 21

Figure 5. 1: a) Stratigraphic column of the Chatsworth Formation in the vicinity of C-3, C-4, and RD-109 and b) image of the interbedded sandstones and shale between Lower Burro Flats and Silvernale members (from Cilona et al., 2015)..... 26
Figure 5. 2: Conceptual geology of two boreholes sampled at Hydrite (modified from Ribiero et al. 2015). 27

Figure 5. 3: Cross-section at the NAWC site showing existing well and corehole configurations, stratigraphy, transmissivity estimated from packer testing and CVOC concentrations (adapted from Goode et al. (2014). Position of corehole 94BR from this study is also shown (later converted to a multi-level monitoring well). 28

Figure 6. 1: Source zone and plume evolution conceptual model (from Parker et al., 2012). 29
Figure 6. 2: Technical approach for collecting and subsampling continuous rock cores for contaminant mass distribution and contaminant pathways analysis. 30
Figure 6. 3: a) HQ triple tube rock coring at the NAWC site (corehole 94BR), b) field rock core subsampling, c) laboratory subcoring of rock core samples, and d) example of extracted core from borehole before field subsampling. 31
Figure 6. 4: VOC sample processing in the field: a) Trimming the core rind exposed to drilling fluids, b) crushing the sample using a hydraulic press and stainless steel crushing cells in a setup designed to minimize exposure time to air, c) sample transfer to pre-preserved (MeOH) vials, and d) 5 step process for decontamination of core crushing equipment applied between samples. 34
Figure 6. 5: Example of subsampled cores from the NAWC site with Styrofoam blocks marking positions of subsamples collected for VOC distribution or physical property analyses..... 34
Figure 6. 6: Low vacuum and high-pressure system used to saturate subcores in the laboratory. a) containment chamber constructed of fiberglass ballistic panels to withstand pressures up to 2800 psi. b) Low vacuum pump (one visible) and associated piping for saturation system at up to 2500 psi. 35
Figure 6. 7: A sample loaded into Bruker D8 Advance used for XRD measurements. 36
Figure 6. 8: Comparison of XRD spectra at HC within borehole MP24S. Individual sample responses were offset by 20 to better view stacking of spectra. 37
Figure 6. 9: Photograph of user performing MICP measurements with the Autopore IV..... 37
Figure 6. 10: Pore size diameter distributions from MICP with a sample from SSFL, HC and NAWC showing the variations in pore size between the three sites. The peak differential intrusion is representative of a dominant, interconnected pore diameter. The NAWC mudstone site is shown to have much smaller pores than HC and SSFL (sandstones)..... 38
Figure 6. 11: On-going BET data collection. Shown are two samples in the degas port and one sample where BET data are being collected. 39
Figure 6. 12: Preparation of acid digests for ferrozine analysis. 40
Figure 6. 13: Bartingston MS2K sensor measuring MS on a HC core. 40
Figure 6. 14: RoCA instrument used to collect all NMR data. 41
Figure 6. 15: Sample HC-MP24S-P001V data shown a) Raw T2 decay from echo times 200 and 1500 µs; b) Inverted T2 distributions corresponding to raw data in a); c) Fully saturated T2 distribution (also shown in red in b) compared to centrifuged T2 distribution. The T2 cutoff time distinguishes the mobile from immobile fractions of the pore space. Appendices B.1 and B.2 show data for all samples. 42
Figure 6. 16: a) Schematic of CR sample holder used for data collection. A geometric factor correction was necessary to account for the geometry of the sample holder b) Sample setup within a sample holder c) CR data collection in environmental chamber. 43

Figure 6. 17: Sample HC-MP24S-P001-1V data showing a) raw complex resistance and phase data b) real σ' and imaginary σ'' conductivity calculated after applying the geometric factor. Data for all samples can be found in Appendix B.1 and B.2. 44
Figure 6.18: (a) basic concept that complex resistivity senses the conductivity of both the mobile and immobile pore domains (and also surface conduction) whereas specific conductance just measures the conductivity of the pore fluid (b) conceptual representations of breakthrough curves of bulk conductivity and fluid conductivity with resulting hysteresis loop. 45
Figure 6. 19: From a plot (a) of bulk conductivity (σ_b) vs. fluid conductivity, σ_f, it is possible to infer the ratio, β, of immobile porosity, θ_{im}, to mobile porosity, θ_m. From a semi-log plot (b) of normalized bulk conductivity vs. time, t, it is possible to infer the rate coefficient, α, governing exchange between mobile and immobile porosities based on the slope, m, of the best-fit line. This approach was first presented and applied to experimental data in Briggs et al. (2014). 46
Figure 6. 20: The tracer experiment apparatus developed in this project (a), including the sample chamber (b) and schematic (c) developed to investigate the electrical signatures of mass transfer. 48
Figure 6. 21: Modelled hysteresis loops affected by data colocation issues (Modified from Briggs et al. 2014). 49
Figure 6. 22: An example of the colocation correction for (a) tracer flush and (b) tracer injection experiments (plotted over the first hour of the experiment). Also shown is (c) the resulting effect this correction has on the hysteresis curve, producing similar results as described in Briggs et al. (2014). Jumps in the data are due to the effect of bubbles on EC probe measurements. 50
Figure 6. 23: A comparison of the (a) uncorrected and (b) corrected complex resistivity breakthrough curves as measured using SIP and corrected from EC probes located in the influent and effluent chambers. Increased noise evident in the corrected flush curve is due to bubbles effecting the effluent EC probe. 51
Figure 6. 24: Schematic diagram illustrating our 6-step pore-network modeling approach to simulate the geoelectrical signature of solute transport through dual-domain geologic media.... 55
Figure 6. 25: a) Collection of standard logs in NAWC 94-BR – photo showing the lowering of the full-wave form sonic tool into the borehole and b) Collection of NMR in 94-BR – photo showing the NMR tool with fixed magnets being pushed through the steel casing into the open section of the borehole. 56
Figure 6. 26: 94BR interpretive notes: The most transmissive and vertically extensive fracture zone is apparent at ~20 m depth below TOC. Fracture zones are evident in caliper, ATV, OTV, and HPFM logs (not shown) at depths of about 38, 62, 88 and 130 ft (or about 12, 19, 27, and 40 m). Variations in lithology are indicated by minor changes in reflectivity, gamma, and normal resistivity. 61
Figure 6. 27: (a) Schematic of FLUTe T-profiling and example profile, (b) setup at NAWC 94BR. 63
Figure 6. 28: a) Photo showing SSFL borehole C4 with mobile logging system in the distance, b) NMR tool used for measuring water content in the formation surrounding the borehole, and c) NMR control unit and computer for viewing measurements and processing data for water-content, pore-size distribution, and hydraulic conductivity estimates. The NMR logging system

used for this investigation is lightweight and mobile relative to conventional NMR systems used in the oil industry. 67
Figure 6. 29: a) Calibration standards for magnetic susceptibility and the "wing" that is positioned on the tool with the calibration "pucks" at the specified distance from the tool. b) Magnetic susceptibility tool raised in the air at the Hydrite site for the zero value during the calibration process. All logs calibrated according to ASTM standards, manufacturer's instructions, and USGS protocols. 69
Figure 6. 30: 94-BR Nuclear magnetic resonance (NMR) logs showing transverse decay, mean log transverse decay (MLT2), pore-size distribution, water content: total, mobile, bound (immobile), and preliminary estimates of hydraulic conductivity using Schlumberger Doll Research (SDR) and sum of echoes (SOE) equations. NMR logs compare well with fracture locations in the OTV, ATV and caliper logs. 71
Figure 6. 31: (a) FACT schematic during downhole deployment with outer NAPL sensitive cover and FACT strip pressed up against the borehole wall and sealed in place by the blank FLUTe liner, and photos of NAWC 94BR deployment showing (b) the NAPL/FACT and cover prior to eversion downhole, (c) liner installation with NAPL/FACT, (d) liner removed after deployment time downhole and laid out for examination of the NAPL cover and removal of the FACT strip, (e) subsampling of the FACT strip, and (f) subsampled discrete (in 40 mL VOA vial) and composite (in 125 mL jar) FACT samples prior to methanol addition in the field. 73

Figure 7. 1: a) Comparison of MICP and gravimetric porosities (RMSE=1.56) b) Comparison of MICP and gravimetric porosities (RMSE=1.08). 74
Figure 7. 2: $Spor$ versus a) T2ml (RMSE=0.280) and b) $\sigma 1\ Hz$" (RMSE= 0.473). The RMSE values are calculated from the from a least linear regression fit of the data. This is shown as a solid black line. 75
Figure 7. 3: Λ versus a) T2ml (RMSE=1.17) and b) $\sigma 1\ Hz$" (RMSE= 1.08). NAWC cores do not correlate well with Hydrite and Santa Susana samples. 75
Figure 7. 4: Permeability predictions using geometric length scales a) Λ b) $Spor$. The dashed black lines represent one order above and below the 1:1 line. 76
Figure 7. 5: NMR SDR permeability equations and associated coefficients b and m: a) sandstone calibrated coefficients b) calibrated coefficients for entire SERDP dataset. 77
Figure 7. 6: NMR Timur-Coates (T-C) permeability equation and associated coefficients c and m: a) sandstone calibrated coefficients b) calibrated coefficient for entire SERP dataset. T2 cutoff values used based on before and after centrifuging data shown in Appendix B.2. Where no cutoff value was available, 33 ms was used. 77
Figure 7. 7: CR predicted permeability using geophysical Kozeny-Carmen equation incorporating $\sigma 1 Hz$" using a) predefined coefficients calibrated on sandstone samples (Equation 4.13) and b) coefficients solved through multiple linear regression. 78
Figure 7. 8: CR predicted permeability using geophysical Kozeny-Carmen equation incorporating mn using a) predefined coefficients calibrated on sandstone samples (Equation 4.14) and b) coefficients solved through multiple linear regression. 79

Figure 7. 9: CR predicted permeability using geophysical Katz and Thompson equation incorporating $\tau mean$. 79
Figure 7. 10: (a) Prediction of FACT from borehole logs vs. true FACT results, and (b) predicted TVOC from borehole logs vs. true TVOC from rock cores, based on multivariate linear regression with interaction between predictors..... 81
Figure 7. 11: Predicted TVOC from borehole logs vs. true TVOC from rock cores for Hydrite M25S, based on multivariate linear regression with interaction between predictors. 82
Figure 7. 12: Predicted TVOC from borehole logs vs. true TVOC from rock cores for SSFL RD109, based on multivariate linear regression with interaction between predictors. 82
Figure 7. 13: Predicted TVOC from borehole logs vs. true TVOC from rock cores for SSFL RD109, based on Gaussian process regression with interaction between predictors. 83
Figure 7. 14: The calibration curve used to correct SIP data during the mass transfer tracer tests. 84
Figure 7. 15: Breakthrough curves from the tracer flush (left column) and tracer injection (right column) tests for (a) HC-MP24S-P-006-1V, (b) HC-MP24S-P-007-2H, and (c) SS-C3-P-019.. 85
Figure 7. 16: Hysteresis loops for (a) HC-MP24S-P-006-1V, (b) HC-MP24S-P-007-2H, and (c) SS-C3-P-019. The tracer flush curve is collected from high to low σ_f and the tracer injection curve is collected from low to high σ_f. All hysteresis loops are plotted alongside Archie's Law, using the formation factor calculated during the initial phase of the tracer experiment for each sample. 86
Figure 7. 17: Data and graphical analysis of fluid and electrical data from borehole HC-MP24S-P-007-2H. Red lines indicate the predicted bulk:fluid relation for the formation factor estimated using different data sets collected during tracer injection and flushing. The distribution coefficient was estimated using hinge points 0, 2, and 3, and using 2, 3, and 0, giving two sets of estimates for mobile and immobile porosity..... 88
Figure 7. 18: Data and graphical analysis of fluid and electrical data from borehole HC-MP24S-P-006-1V. Red lines indicate the predicted bulk:fluid relation for the formation factor estimated using different data sets collected during tracer injection and flushing. The distribution coefficient was estimated using hinge points 0, 2, and 3, and using 2, 3, and 0, giving two sets of estimates for mobile and immobile porosity..... 89
Figure 7. 19: Data and graphical analysis of fluid and electrical data from borehole SS-C3-P-019. Red lines indicate the predicted bulk:fluid relation for the formation factor estimated using different data sets collected during tracer injection and flushing. The distribution coefficient was estimated using hinge points 0, 2, and 3, and using 2, 3, and 0, giving two sets of estimates for mobile and immobile porosity. 90
Figure 7. 20: An example of late time analysis of breakthrough curves for the purpose of estimating α. Fitting (a) σ_f and (b) σ_b at late times allows quantification of α. The sensitivity (also demonstrated in b) of the data to α (also demonstrated in b) is evident from modeled curve σ_b assuming α of different orders of magnitude. 91
Figure 7. 21: A schematic of the proposed changes to the experimental apparatus to eliminate uncertainties associated with flow irregularities and fluid mixture occurring in the influent and effluent chambers..... 92

Figure 7. 22: (a) Stochastic discrete fracture network calibrated to approximate the hydraulic properties of cores from the Hydrite site. (b) Local residence times within the fracture network, with residence time varying between the mobile domain and multiple immobile domains. (c) Simulated hysteretic bulk versus fluid conductivity relation. 94
Figure 7. 23: Example 1D diffusion simulations of matrix invasion off a fracture assuming a constant source for (a) sandstone type matrix (ϕm = 15%, τ = 0.10, R=1.5) representative of SSFL, and (b) mudstone type matrix (ϕm = 7.5%, τ = 0.05, R=20) representative of NAWC. Both linear and log concentration scales are shown. Although the matrix invasion distance is much lower for the mudstone, the total mass diffused may be higher due to the high sorption in the matrix which increases the storage capacity and maintains higher concentration gradients during the inward diffusion stage. 97
Figure 7. 24: WellCAD plot from Hydrite including simplified lithology logs, fracture distributions observed in the rock core, fractures interpreted from the Acoustic Televiewer (ATV) logging and contaminant distributions from the high-resolution rock core subsampling (provided as total VOCs). 98

Table 6. 1: Summary of saturation procedure 36
Table 6. 2: Borehole logging methods used in selected boreholes at Hydrite, Santa Susana, and NAWC 57
Table 6. 3: Location and orientation of fractures in borehole 94-BR at the NAWC site in New Jersey 58
Table 6. 4: Summary of NMR measurements in open-hole sections of boreholes 67

Table 7. 1: Regression results 81
Table 7. 2: Regression results 82
Table 7. 3: Regression results 83
Table 7. 4: Regression results 83
Table 7. 5: The flow rates (effluent and EC ports) and formation factors (calculated from the electrical tracer experiment and column (Section 6.4.3) experiment) of the samples analyzed during the electrical tracer experiment. 84
Table 7. 6: Results of graphical analysis for distribution coefficient and calculated mobile and immobile porosities 88
Table 7. 7: Hydraulic properties representing Hydrite cores and calibrated pore network model 92

EXECUTIVE SUMMARY

Introduction

Dense non-aqueous phase liquid (DNAPL) and dissolved/sorbed phase VOC contamination of fractured rock remains a long-term, persistent DoD problem. At most 'aged' sites where DNAPL releases occurred decades ago, contaminant mass now resides in the much lower permeability matrix blocks between fractures (immobile porosity). Fluid samples taken from wells primarily represent the mobile porosity produced by the fracture networks and therefore often fail to accurately quantify contaminant mass. For chlorinated solvents, contaminant storage can occur by several mechanisms, including: (1) NAPL accumulation in or on low-permeability layers or dead-end fractures, resulting in a long-term source for dissolved contamination; (2) sorption of dissolved contaminants on surfaces of grains or fractures; (3) diffusion of aqueous phase contaminants into low-permeability matrix blocks between fractures or in and from dead-end fractures. There is increasing recognition that the third mechanism, storage of dissolved contamination in low-permeability zones, is of principal importance.

Nearly all sedimentary rocks have substantial effective matrix porosity (2-20%) allowing large amounts of contaminant mass storage due to diffusion into the matrix, where sorption enhances the storage capacity, in the early decades of contamination, and out of the matrix in later decades or centuries. Although it is typical that nearly all groundwater flow occurs in the fracture network, at 'aged' contaminated sites most contaminant mass now resides in the much lower permeability matrix blocks between fractures. However, this mass can diffuse from the rock matrix back into the more permeable fractures, resulting in long term contaminant persistence even if source zones are depleted or remediated. Conventional approaches for investigating fractured rock are inadequate because they are biased toward answering questions most relevant to present-day groundwater quantity and water supply quality; hence, the rock matrix is ignored and most of the fractures with active flow and transport go unrecognized. For lack of rock core contaminant data, conventional studies commonly fail to characterize mass distribution in fractured porous rock. The performance of remediation is therefore critically dependent on development of methodologies that can quantify pore geometric properties controlling storage of contaminant mass in the rock matrix and also sense/monitor long-term changes in that mass. Furthermore, reducing the costs associated with such quantification is critically dependent on the development of approaches more efficient and less invasive than extensive coring and detailed rock core sampling for assessing the pore geometric properties and contaminant mass local to fractures.

This project explored relationships between two emerging geophysical technologies, complex resistivity (CR) and nuclear magnetic resonance (NMR) and the pore geometric properties (pore size distribution and permeability) controlling transport of contaminant mass. Secondly, it investigated relationships between the distribution of contaminant mass in the rock matrix and measurements acquired from a broad suite of geophysical logs under the assumption of a common control of the pore geometric properties of the rock mass. Thirdly, an innovative electrical geophysical approach to identifying signatures of mass transfer between relatively

mobile and immobile pore domains from coupled electrical geophysical and fluid electrical conductivity measurements during injection of a conductive tracer was explored.

Objectives

The primary objectives of this research were to [1] determine the sensitivity of two emerging borehole geophysical technologies (nuclear magnetic resonance [NMR] and complex resistivity [CR]) to key pore geometric properties (primarily pore size distribution and permeability) controlling contaminant transport, [2] investigate the potential sensitivity of geophysical logging methods (both emerging and established) to contaminant mass (as DNAPL and/or aqueous phase) isolated within the immobile porosity of fractured rock and inaccessible to aqueous sampling techniques, and [3] develop an electrical tracer test strategy for estimating the mass transfer coefficient and the mobile to immobile porosity ratio controlling back diffusion of contaminant mass. A secondary objective was to obtain better information at high spatial resolution on the distribution of contaminant mass within the immobile porosity of a fractured rock relative to primary fractures governing flow/transport. Sub-objectives included [1] determining quantitative relationships between NMR/CR parameters and pore size distribution, surface area and permeability of the rock matrix and assessing variations with site geology; [2] applying recently developed analytical and numerical models to estimate representative mass transfer rate coefficients from joint measurements of CR and fluid specific conductance.

Technical Approach

The technical approach involved an integration of field, laboratory, and numerical methods (Figure ES1). Field activities included acquisition of core samples, sampling of contaminant mass and borehole logging using a variety of geophysical and hydrophysical techniques. Laboratory activities included contaminant mass analysis distribution on core samples, quantification of rock properties, CR/NMR measurements and electrical tracer tests for estimating mass transfer coefficients. Rock properties measurements included pore size distributions from mercury porosimetry, specific surface area from gas adsorption and permeability from a combination of Darcy flow tests and pulse decay analysis (the latter for low permeability mudstones). The numerical methods focused on pore network modeling of electrical current flow and solute transport. Specific aspects of the technical approach included [1] fine-scale delineation of contaminant mass around fractures using a discrete fractured network (DFN) strategy, [2] fine-scale delineation of porosity, permeability and pore size distribution from core samples acquired as part of the DFN, [3] laboratory and borehole NMR and CR logging, and [4] development of first of a kind laboratory instrumentation whereby tracer experiments coupled to pore-network models are used to quantitatively link geophysical responses to contaminant mass transfer parameters. Laboratory measurements on cores and borehole logging data were acquired at three sites of DoD relevance: [1] the Naval Air Warfare Center (NAWC), West Trenton, NJ, [2] Santa Susana Field Laboratory (SSFL) in Southern California, and [3] Hydrite Chemical Company (HCC) in Wisconsin. The Santa Susana site is composed of sandstone with minor interbeds of shale and siltstone and occasional conglomerate of similar mineralogy. The sedimentary rocks at the Hydrite site are more heterogeneous, including sandstones and dolomite with variable grain size. The NAWC site is characterized by

alternating sequences of grey mudstones ranging from massive to thinly laminated, along with occasional thin black organic rich 'fissile' layers. Measurements at three contrasting sites permitted assessment of geophysical technology performance across a range of sedimentary rock geological settings.

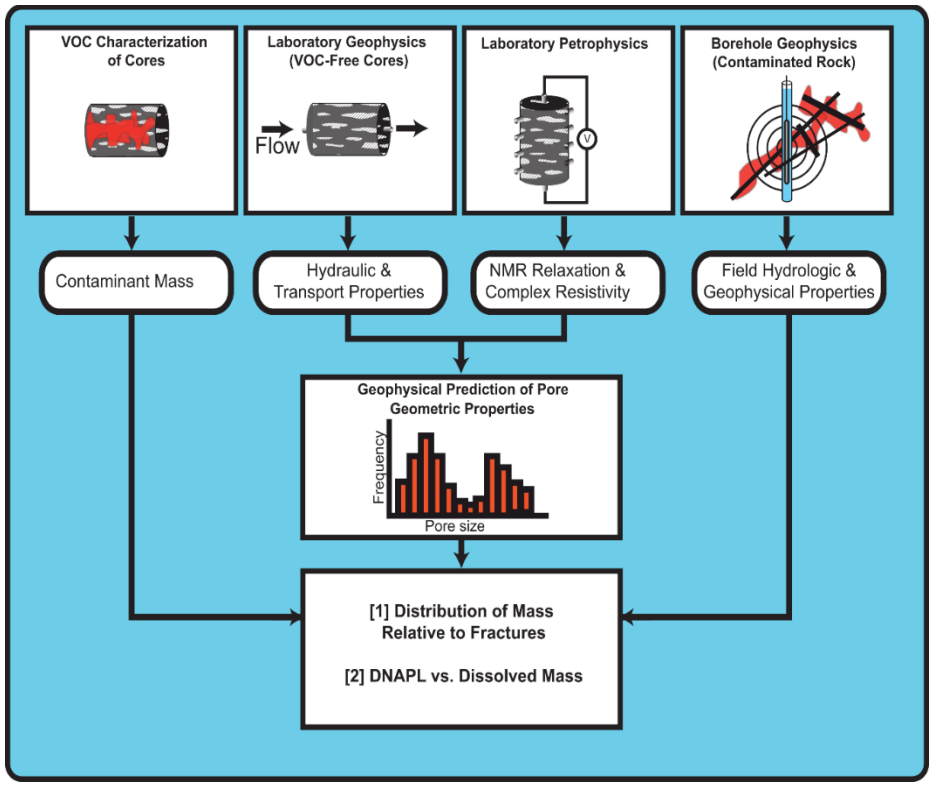

Figure ES1 Project overview showing central tasks of the work

Results and Discussion

A number of key findings regarding the role of, NMR, CR and geophysical technologies in general in support of remediation of contaminated sites resulted from this project. The exhaustive laboratory analysis of 75 cores from the three sites demonstrated that quantitative assessment of pore size and permeability is possible using NMR and CR. Both NMR- and CR-derived relaxation times were shown to be correlated with characteristic pore sizes derived from mercury porosimetry and surface area from gas adsorption. These correlations were strong for the sandstone-dominated cores from the SSFL and Hydrite sites. However, the mudstone cores from the NAWC site did not align well with the relationships obtained for the other two sites. One exception was the relationship between the NMR relaxation time and the pore volume normalized specific surface area (S_{por}), where a single strong relationship exists for all three sites. The NMR method contained sufficient sensitivity to the pore size distribution to allow estimates of the ratio of the immobile to mobile porosity of samples to be estimated. Both CR and NMR measurements provide a link to permeability through the definition of geophysical length scales that can be used in place of established geometric length scales in models of permeability prediction. An example for NMR measurements is shown in Figure ES2. Comparison of

geophysical predictions of permeability using recently proposed models with direct Darcy-test measures of permeability showed that both NMR and CR contain sufficient information on the pore geometry to permit order of magnitude estimates of permeability entirely from geophysical measurements. The joint use of NMR and CR data did not significantly improve permeability prediction relative to using the information extracted from a single measurement alone. However, none of the relationships were universal, highlighting the caution needed when applying such relationships outside of the lithology used for the calibration. Field-scale NMR logging highlighted the potential to extract information on variations in these pore geometric properties in situ along a borehole, albeit with lower resolution. CR measurements from an existing commercially available borehole logging tool did not have the sensitivity needed to reliably detect these variations in pore geometry in situ.

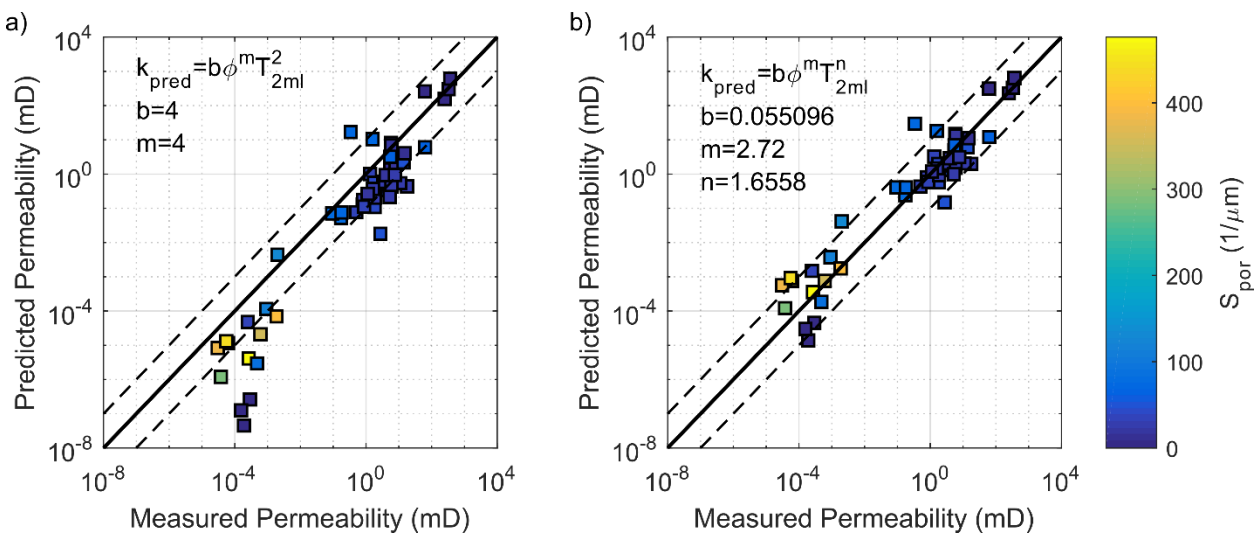

Figure ES2. Example NMR permeability prediction equations and associated coefficients a) coefficients established as representative of sandstones b) calibrated coefficients for entire SERDP dataset.

Statistical analysis of the NMR and CR logging signatures against contaminant mass distributions recorded in 6 boreholes from the three sites did not show a conclusive dependence of NMR or CR parameters on contaminant mass. Assessment of the sensitivity of the NMR and CR measurements to contaminant mass relied on comparison of the NMR and CR borehole logging data against TVOC measurements from cores. The contaminant mass analysis involved an extraction procedure performed in the field; it was not possible to reliably preserve contaminants in core in situ to allow for precision laboratory NMR and CR measurements on contaminated core. The logging data had the advantage that measurements were acquired on the in situ contaminants/rock matrix adjacent to the borehole wall. The effectiveness of the multivariate linear regression approach to the prediction of contaminant mass from geophysical logging data was shown to depend on the dataset used for the calibration. Results suggest that predictive models built with multivariate linear regression will be more likely to predict variations in contaminant mass distributions within a single borehole (Figure ES3) rather than between boreholes or across sites of varying lithology. However, the existing borehole logging

tools do not provide the precision data obtainable with the laboratory instrumentation. Therefore, the results of the contaminant mass sensitivity analysis relate to the information content extractable from currently available logging tools that do not represent the information ultimately obtainable from these emerging geophysical technologies as the logging tools improve.

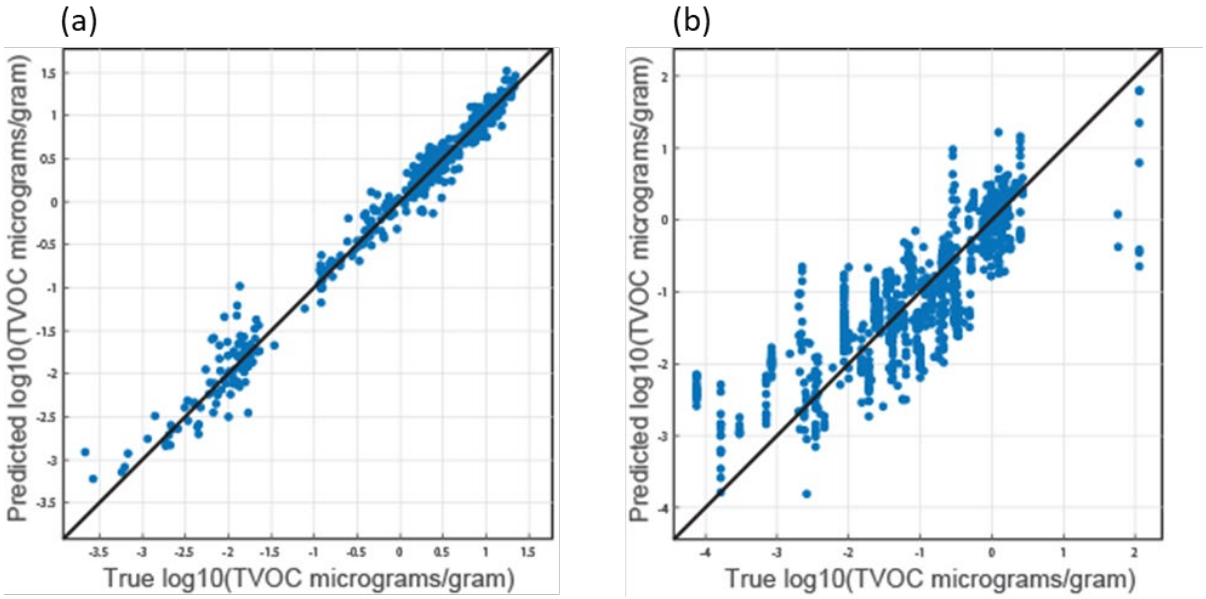

Figure ES3: Predicted TVOC from borehole geophysical logs vs. true TVOC from rock cores for based on multivariate linear regression with interaction between predictors (a) Hydrite M25S; (b) SSFL RD109

First of a kind electrical tracer experiments combined with pore-network modeling led to estimates of mass transfer coefficients and mobile/immobile porosity ratios from coupled simultaneous measurements of bulk electrical conductivity and fluid conductivity. Instrumentation based around a Hassler sleeve core holder encased in a pressure vessel was developed to perform tracer breakthrough tests on representative cores from the three field sites Figure ES4). Non-linearity in the relationship between bulk conductivity and fluid conductivity was identified, being diagnostic of a dual domain with mass transfer occurring between domains (Figure ES5). Extension of the approach to include measurements of the real and imaginary (polarization response) parts of the complex conductivity might allowing the modeling of mass transfer parameters to be improved by using the imaginary conductivity to account for the effects of surface conduction. The experiments revealed conclusive evidence for mass transfer occurring at a scale within the rock matrix, independent of a fracture network. Immobile/mobile porosity ratios were estimated through the application of a recent analytical model. This process may have significant implications for the fate and transport of contaminant mass, especially given the high surface area of the matrix porosity versus the fracture network.

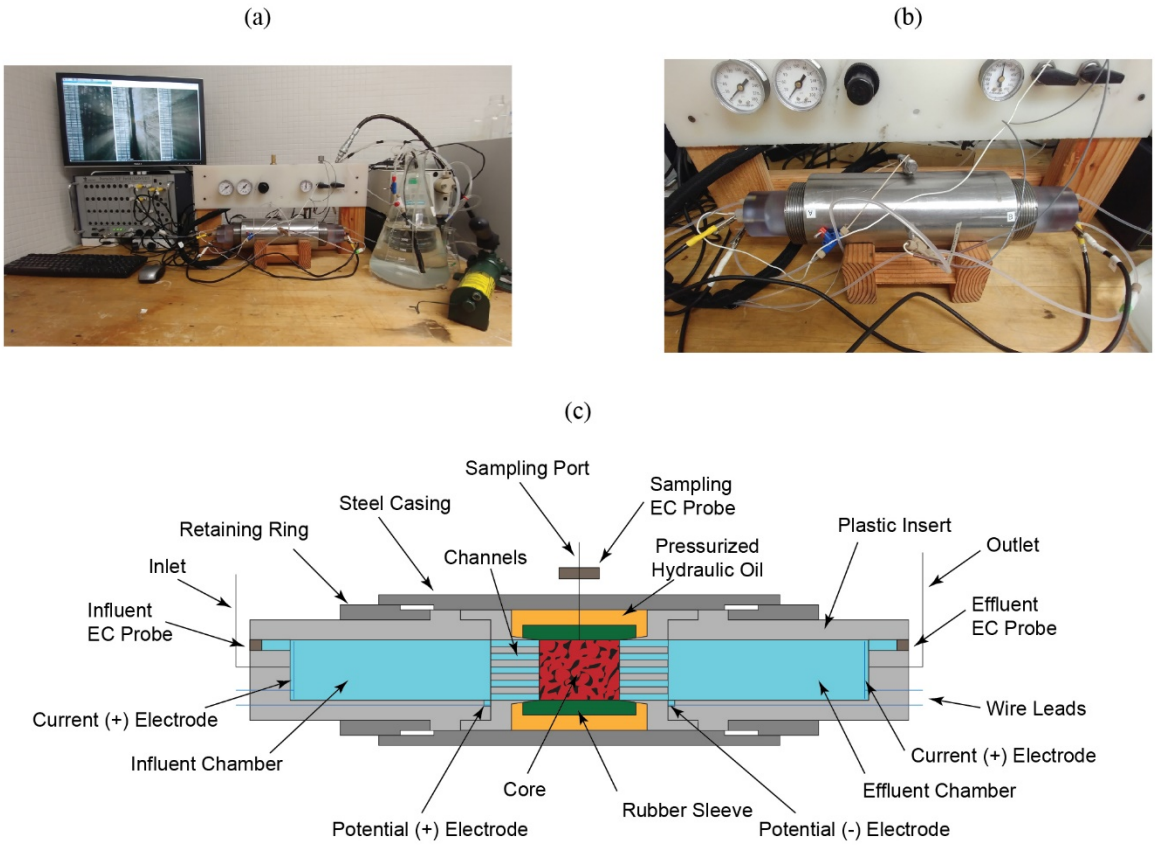

Figure ES4: Electrical tracer experiment apparatus (a), including the sample chamber (b) and schematic (c) developed to investigate the electrical signatures of mass transfer

Implications for Future Research and Benefits

Besides assessing the information content of the emerging NMR and CR geophysical technologies, this project also acquired a wealth of information on the distribution of physical properties, fracture zones and contaminant distributions at three high-profile chlorinated solvent sites. The Discrete Fracture Newark (DFN) approach was modified to incorporate information from NMR and CR measurements. This comprehensive approach that coupled coring/analysis with in-well measurements provided new insights into the distribution of contaminant mass in fractured rock settings at the three study sites, particularly around hydraulically active fracture zones. Distinct contrasts in contaminant mass distributions around fractures between the three sites were observed. Such extension of the DFN will benefit future efforts to develop conceptual site models for complex fractured rock sites.

Establishing robust relationships between geophysical logging datasets and contaminant mass would allow commercially available geophysical technologies to be employed for efficient monitoring of the effectiveness of multiple existing remedial technologies (e.g. bioremediation, thermal treatment, monitored natural attenuation (MNA), chemical addition) in reducing

contaminant mass in the rock matrix, particularly adjacent to hydraulically active fractures. Geophysical logs could be repeatedly run in a borehole at a fraction of the cost of conventional sampling methods that rely on direct quantification of mass from cores. Such geophysical monitoring data would provide early information to help predict the long-term performance of remedial technologies and aid in decision making e.g. with respect to discontinuation of a technology or implementation of an alternative. However, further research is needed to better constrain the value of machine learning methods for linking geophysical logging datasets to contaminant mass distributions via a common dependence on the pore geometric properties of the matrix.

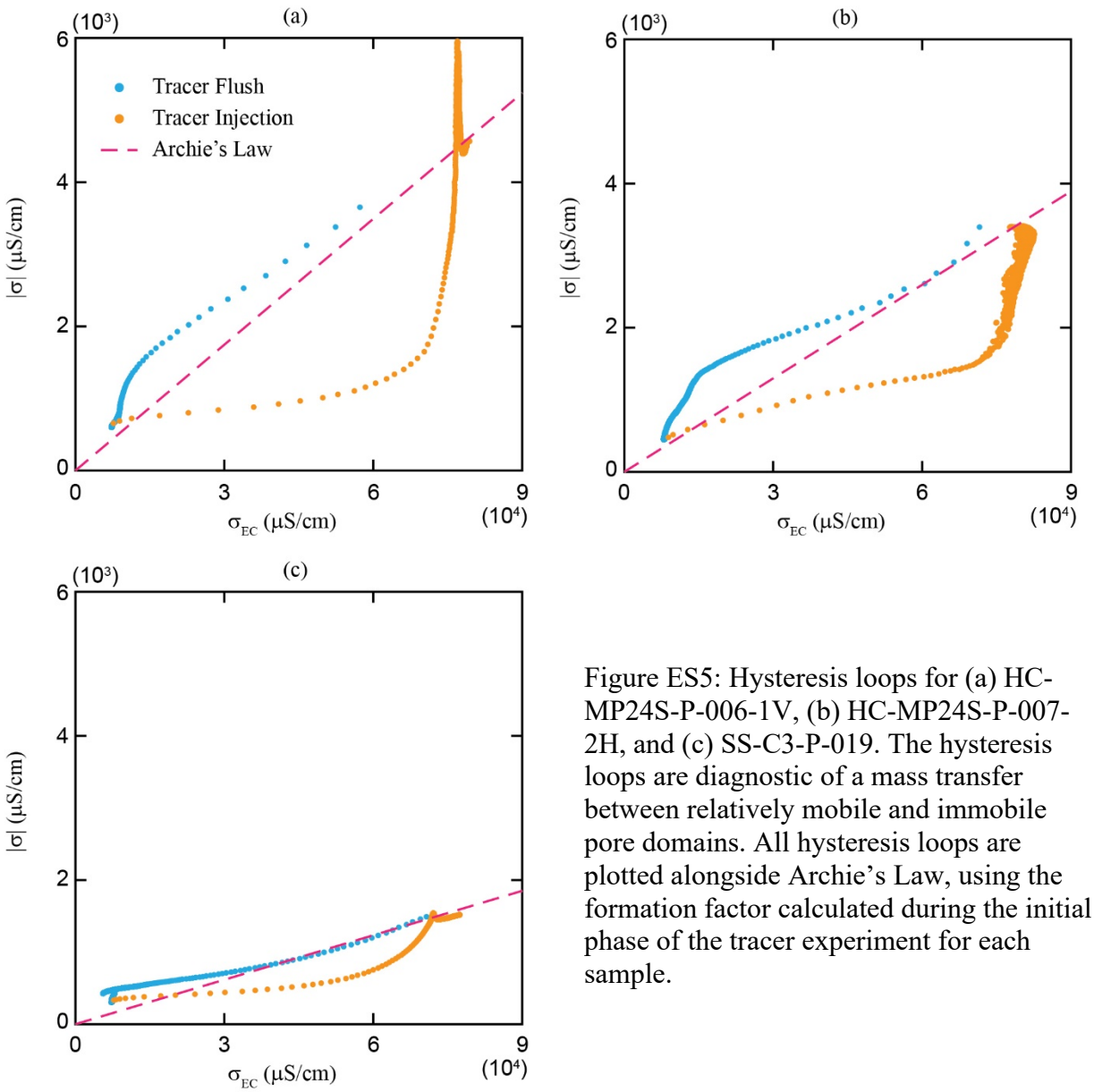

Figure ES5: Hysteresis loops for (a) HC-MP24S-P-006-1V, (b) HC-MP24S-P-007-2H, and (c) SS-C3-P-019. The hysteresis loops are diagnostic of a mass transfer between relatively mobile and immobile pore domains. All hysteresis loops are plotted alongside Archie's Law, using the formation factor calculated during the initial phase of the tracer experiment for each sample.

One of the most promising outcomes of this work is the possible estimation of mass transfer coefficients and the ratio of mobile to immobile porosity of the rock matrix from a relatively

simple tracer test involving simultaneous measurements of bulk fluid conductivity and specific conductance. Although only demonstrated in the laboratory, the measurement could be transferred to an in-borehole test with only a limited amount of technology development. The advantage of this measurement is its inherent scalability. Information on the scaling of mass transfer coefficients (e.g. from the matrix scale to larger scales that integrate across fracture zones) would be possible. Knowledge of the spatial variability in mass transfer coefficients could significantly advance understanding of long-term contaminant fate and the role of back diffusion at heterogeneous sites.

In total, results of this project support the adoption of two emerging geophysical technologies, NMR and CR, for the relatively rapid and cost-effective acquisition of information on the distribution of pore geometric properties controlling contaminant transfer at chlorinated solvent sites. These non-invasive borehole logging technologies provide information that cannot be readily obtained from the existing suite of geophysical logs that are in routine use at contaminated sites. The results of the project do not provide a compelling case for the direct detection of contaminant mass in situ. Future improvements in the sensitivity of borehole logging instrumentation (e.g. so that they have similar sensitivity to the laboratory measurements) may improve opportunities to detect contaminant mass with these measurements. However, results of this project suggest that these techniques should currently primary be focused on improving information on the spatial distribution of critical pore geometric properties controlling flow and transport such as the pore size distribution and permeability. In addition to providing valuable information on the likely distribution of contaminant mass, such high-resolution information could be invaluable for validating a variety of contaminant transport models.

1.0 Abstract

Introduction and Objectives: Dense non-aqueous phase liquid contamination of fractured rock remains a long-term, persistent Department of Defense problem. The diffusion of aqueous phase contaminants into low-permeability matrix blocks between fractures, or in and from dead-end fractures, limits the efficiency of fractured-aquifer remediation methods. Characterizing the physical properties of the rock containing the contaminant mass around fractures is critical for improving remediation operations in fractured rock settings. The primary objectives of this research were to [1] determine the sensitivity of two emerging borehole geophysical technologies (nuclear magnetic resonance [NMR] and complex resistivity [CR]) to key pore geometric properties (primarily pore size distribution and permeability) controlling contaminant transport, [2] investigate the potential sensitivity of emerging geophysical methods to contaminant mass (as DNAPL and/or aqueous phase) isolated within the immobile porosity of fractured rock inaccessible to aqueous sampling techniques, and [3] to evaluate the predictive capabilities of these geophysical technologies with respect to quantifying immobile porosity and/or contaminant mass concentration. A final objective was to investigate whether a mass transfer coefficient and the ratio of mobile to immobile porosity could be estimated for rock matrix from an electrical tracer test.

Technical Approach: The technical approach involved [1] fine-scale delineation of contaminant mass around fractures using a discrete fractured network (DFN) approach, [2] fine-scale delineation of porosity, permeability and pore size distribution from core samples acquired as part of the DFN, [3] laboratory and borehole NMR and CR logging, and [4] laboratory tracer experiments coupled to pore-scale modeling to quantitatively link geophysical responses to contaminant mass transfer parameters. Laboratory measurements on cores and borehole logging data were acquired at three sites of DoD relevance: [1] the Naval Air Warfare Center (NAWC), West Trenton, NJ, [2] Santa Susana Field Laboratory (SSFL) in Southern California, and [3] Hydrite Chemical Company (HCC) in Wisconsin. This permitted assessment of geophysical technology performance within a range of sedimentary rock geological settings.

Results: A number of key findings regarding the role of the NMR and CR technologies in support of remediation of contaminated sites resulted from this project. The exhaustive laboratory analysis of 75 cores from the three sites demonstrated that quantitative assessment of immobile versus mobile porosity and permeability is possible using b oth NMR and CR. NMR logging highlighted the potential to extract information on variations in these pore geometric properties in situ along a borehole, albeit with lower resolution. CR measurements from an existing commercially available borehole logging tool did not have the sensitivity to reliably detect these variations in pore geometry in situ. Statistical analysis of the NMR and CR logging signatures against contaminant mass distributions recorded in 6 boreholes from the three sites did not show a conclusive dependence of NMR or CR parameters on contaminant mass. However, preliminary laboratory tracer tests coupled to pore network modeling indicated the potential to quantitatively predict contaminant mass transfer parameters (rate coefficients and immobile to mobile porosity ratio) from simultaneous measurements of CR and fluid electrical conductivity.

Benefits: The unique, extensive database of core-scale and field scale physical, hydrogeological and aqueous geochemical data acquired on this project provided new information in support of recent conceptual models for the distribution of contaminant mass around hydraulically active fracture zones. Technology transfer efforts focused on disseminating key aspects of the work through novel spreadsheet tools and online videos generated by the project team. The geophysical technologies investigated here could ultimately be applied to assess the effectiveness of multiple existing remedial technologies (e.g. bioremediation, thermal treatment, monitored natural attenuation (MNA), chemical addition) in reducing contaminant mass in the rock matrix, particularly adjacent to hydraulically active fractures.

2.0 Objectives

The primary objectives of this research were to [1] determine the sensitivity of two emerging borehole geophysical technologies (nuclear magnetic resonance [NMR] and complex resistivity [CR]) to key pore geometric properties (primarily pore size distribution and permeability) controlling contaminant transport, [2] investigate the potential sensitivity of emerging geophysical methods to contaminant mass (as DNAPL and/or aqueous phase) isolated within the immobile porosity of fractured rock inaccessible to aqueous sampling techniques, and [3] to evaluate the predictive capabilities of these geophysical technologies with respect to quantifying immobile porosity and/or contaminant mass concentration (Figure 2.1). A secondary objective was to obtain better information at high spatial resolution on the distribution of contaminant mass within the immobile porosity of a fractured rock relative to primary fractures governing flow/transport.

Specific technical questions related to the primary objectives of this project included:

- What is the quantitative relationship between the geophysical signatures obtained from NMR and CR and pore size distribution of the rock matrix?
- What is the quantitative relationship between the geophysical signatures obtained from NMR and CR and matrix permeability?
- What is the sensitivity, if any, of NMR and CR geophysical signatures to the concentration of contaminant mass in the rock matrix?
- How does the information content acquired from the emerging borehole logging tools compare to the information content of the laboratory-based NMR and CR measurements acquired on rock cores?
- Can key mass transfer properties (rate coefficients, ratios of immobile to mobile porosity) be estimated from joint measurements of CR and fluid chemistry when coupled to recently developed analytical and numerical models?
- How do relationships between CR and NMR geophysical signatures and pore geometric properties vary between different fractured rock geologies (e.g. sandstone versus dolomite)?

Specific technical questions related to the secondary objectives of this project included:

- How is the contaminant mass within the matrix distributed around the primary fractures controlling groundwater flow?
- How is this fine-scale distribution of contaminant mass controlled by the matrix porosity?
- Could NMR and CR geophysical methods ultimately provide diagnostic temporal information on changes in distribution of contaminant mass, e.g., following implementation of a remedial strategy?

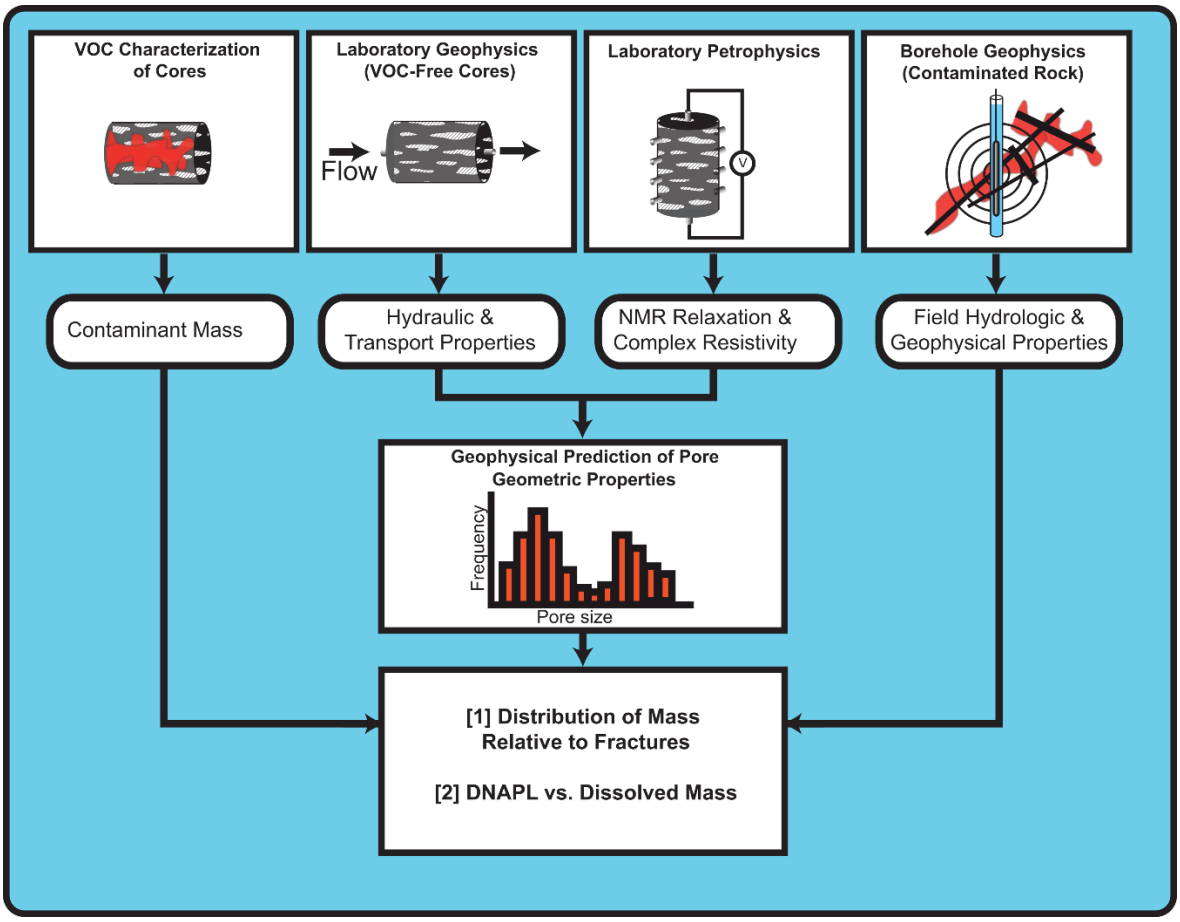

Figure 2. 1: Project overview showing central tasks of the work performed. Cores were used to determine high resolution distribution of contaminant mass in relation to fractures. Immobile and mobile porosity, permeability and surface area, along with geophysical (NMR and CR) laboratory data, were acquired. Field-scale hydrological and geophysical properties were determined from borehole measurements using emerging technologies. The integrated dataset was used to determine the sensitivity of NMR and CR borehole measurements to contaminant mass in-situ.

3.0 Background

DNAPL and dissolved/sorbed phase VOC contamination of fractured rock remains a long-term, persistent DoD problem (Leeson & Stroo, 2011). At most 'aged' sites where DNAPL releases occurred decades ago, contaminant mass now resides in the much lower permeability matrix blocks between fractures (immobile porosity). Fluid samples taken from wells primarily represent the mobile porosity produced by the fracture networks and therefore often fail to accurately quantify contaminant mass. For chlorinated solvents, contaminant storage can occur by several mechanisms, including: (1) NAPL accumulation in or on low-permeability layers or dead-end fractures, resulting in a long-term source for dissolved contamination; (2) sorption of dissolved contaminants on surfaces of grains or fractures; (3) diffusion of aqueous phase contaminants into low-permeability matrix blocks between fractures or in and from dead-end fractures. There is increasing recognition that the third mechanism, storage of dissolved contamination in low-permeability zones, is of principal importance (AFCEE, 2007).

This project was motivated by the opportunity to determine relationships in fractured rock between measurements obtained from complex resistivity (CR) and nuclear magnetic resonance (NMR), two emerging geophysical technologies, and (1) pore geometric properties (pore size distribution and permeability); (2) contaminant mass in the rock matrix. Establishing such relationships would allow these geophysical technologies to be employed for efficient monitoring of the effectiveness of multiple existing remedial technologies (e.g. bioremediation, thermal treatment, monitored natural attenuation (MNA), chemical addition) in reducing contaminant mass in the rock matrix, particularly adjacent to hydraulically active fractures. Geophysical logs could be repeatedly run in a borehole at a fraction of the cost of conventional sampling methods that rely on direct quantification of mass from cores. Such geophysical monitoring data could provide early information to help predict the long-term performance of remedial technologies and aid in decision making e.g. with respect to discontinuation of a technology or implementation of an alternative. The project was also motivated by the opportunity to determine new information on the fine-scale distribution of contaminant mass around fractures in four fractured rock sites of DoD concern.

This project made use of, and built upon, the comprehensive Discrete Fracture Network (DFN) approach (Parker et al., 2012) that has evolved for investigating sites in fractured rock, particularly fractured rock systems (Figure 3. 1). DFN research has resulted in the development of a general site conceptual model (SCM) for the formation and long-term evolution of source zones and plumes in fractured sedimentary rock. Nearly all sedimentary rocks have substantial effective matrix porosity (2-20%) allowing large amounts of contaminant mass storage due to diffusion into the matrix, where sorption enhances the storage capacity, in the early decades of contamination, and out of the matrix in later decades or centuries. Although it is typical that nearly all groundwater flow occurs in the fracture network, at 'aged' contaminated sites most contaminant mass now resides in the much lower permeability matrix blocks between fractures. However, this mass remains mobile as diffusion allows the migration of contaminants from the rock matrix back into the more permeable fractures, resulting in long term contaminant persistence even if source zones are depleted or remediated (Parker et al., 2010). Therefore, the DFN approach emphasizes using rock core for contaminant mass measurements to determine mass storage in the matrix (dissolved and sorbed phase) and its distribution with respect to fracture characteristics and the active groundwater flow system in the fracture network, and how this diffusion and other matrix

processes such as abiotic and/or biotic degradation influences downgradient concentrations with and without remediation. Conventional approaches for investigating fractured rock are inadequate because they are biased toward answering questions most relevant to present-day groundwater quantity and water supply quality; hence, the rock matrix is ignored and most of the fractures with active flow and transport go unrecognized. For lack of rock core contaminant data, conventional studies commonly fail to characterize mass distribution in fractured porous rock. The performance of remediation is therefore critically dependent on development of methodologies that can quantify pore geometric properties controlling storage of contaminant mass in the rock matrix and also sense/monitor long-term changes in that mass. Furthermore, reducing the costs associated with such quantification is critically dependent on the development of approaches more efficient and less invasive than extensive coring and detailed rock core sampling for assessing the pore geometric properties and contaminant mass local to fractures.

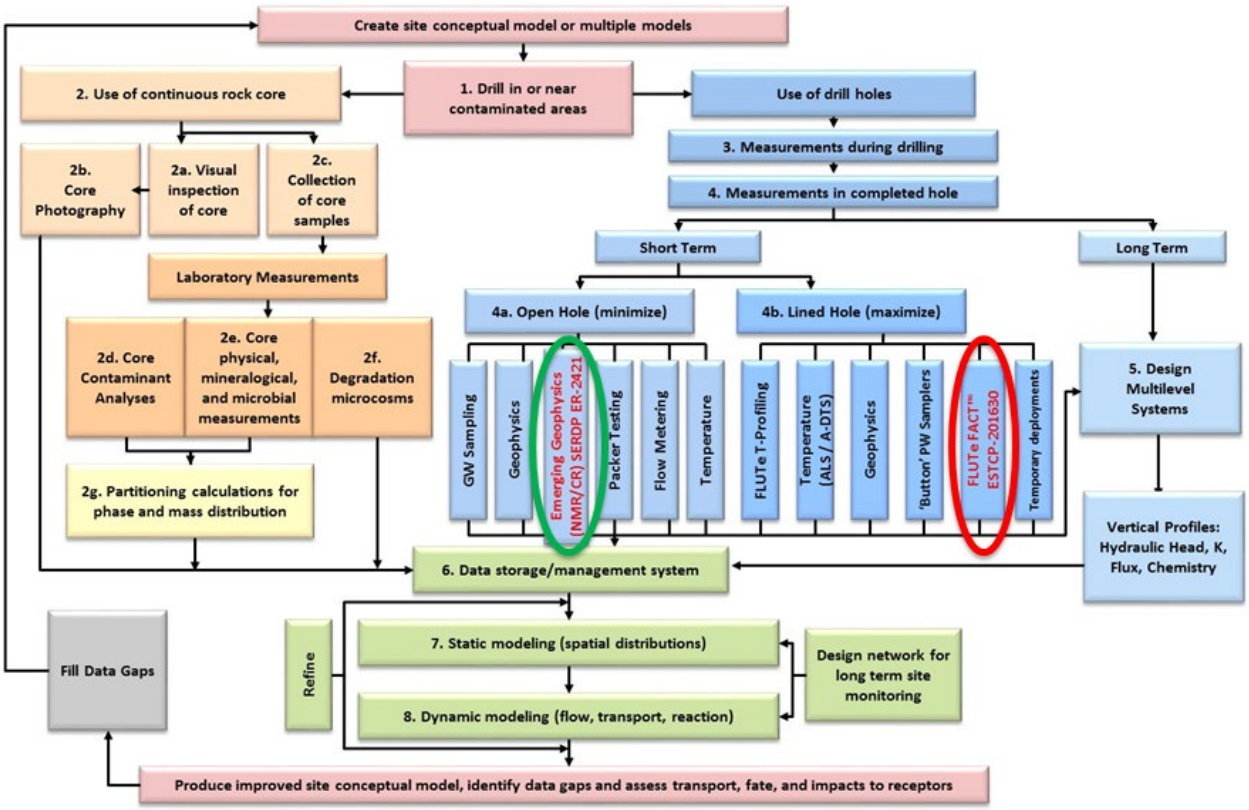

Figure 3. 1: The DFN approach uses both rock core and core hole derived datasets to characterize contaminated sites on fractured sedimentary rock to result in an improved site conceptual model (adapted from Parker et al., 2012). The emerging NMR and CR geophysical technologies were considered an important advancement in the DFN approach and are embedded as ER 2421. An associated ESTCP project (ER201630) that leveraged ER2421 is also shown.

Quantification of the pore geometric properties contaminant mass within the immobile pore space currently requires continuous coring using methods that minimize core disturbance and mechanical breaks and best preserves *insitu* conditions (e.g. triple tube coring methods), careful collection of many samples adjacent to fractures and from the matrix off fractures using a

methodology that accounts for the expected contaminant distribution based on contaminant type, time of contamination, and rock matrix properties, careful sample preparation procedures in the field, followed by rigorous extractions of the contaminant mass (ensuring methods provide complete extraction) (Dincutoiu et al., 2003, 2006) and analytical measurements utilizing methods capable of providing exceptionally low detection limits for the types of extraction performed (e.g. methanol extraction). Conventional methods are generally inappropriate for these measurements.

Such information can only be obtained once in time, i.e., as a single "snapshot," unless additional core is collected (usually impractical, expensive and subject to spatial variability issues). Quantification of pore geometric properties such as the immobile porosity in which contaminants resides traditionally requires labor intensive lab measurements on cores. Borehole geophysical logging is routinely employed to noninvasively obtain information on the physical and hydrogeological characteristics of the aquifer proximal to a borehole. Unlike coring, these methods can be repeated at minimal additional expense (assuming available boreholes) and are therefore well suited to long-term monitoring to evaluate temporal changes. The emerging NMR and CR technologies investigated in this project offer new opportunities to quantify pore size distributions/permeability, and potentially also the contaminant mass residing in the immobile pore space (Figure 3. 2).

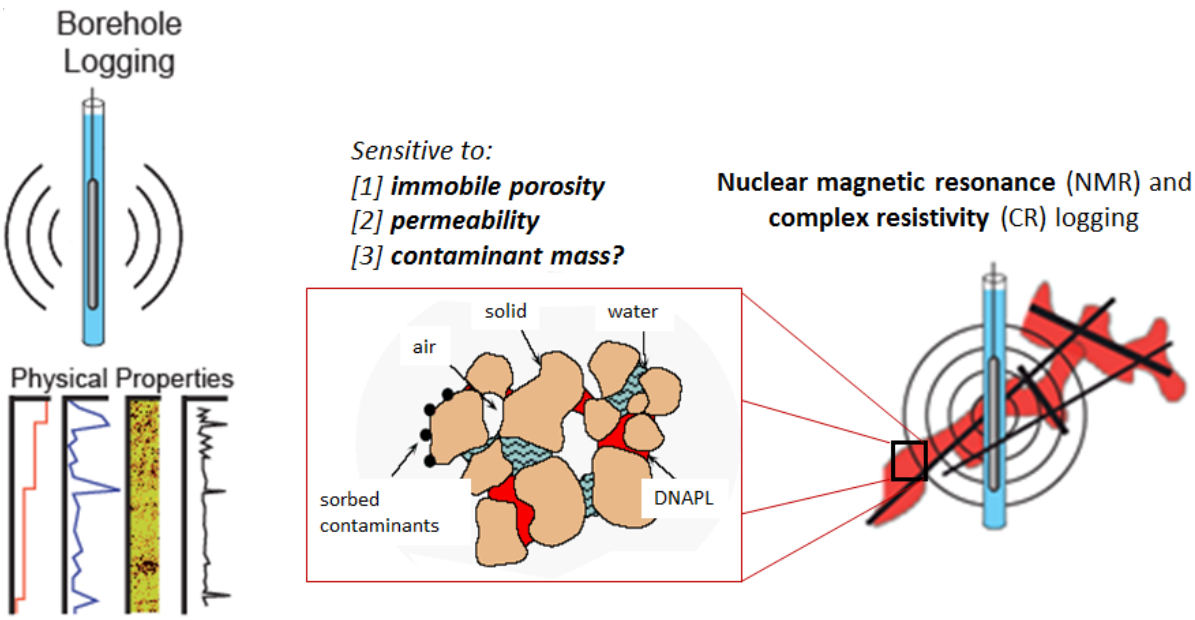

Figure 3. 2: Nuclear magnetic resonance (NMR) and complex resistivity (CR) borehole logging tools are emerging technologies for sensing (1) pore geometric properties controlling contaminant mass transport/storage and (2) possibly contaminant mass itself.

3.1 Emerging geophysical technologies

This project focused on the information content of two emerging geophysical technologies: Nuclear magnetic resonance (NMR) and complex resistivity (CR). Although NMR and CR are based on very different physics (Figure 3. 3), they share strong similarities in terms of how the measured parameters relate to physical properties of the pore space. Both methods measure a

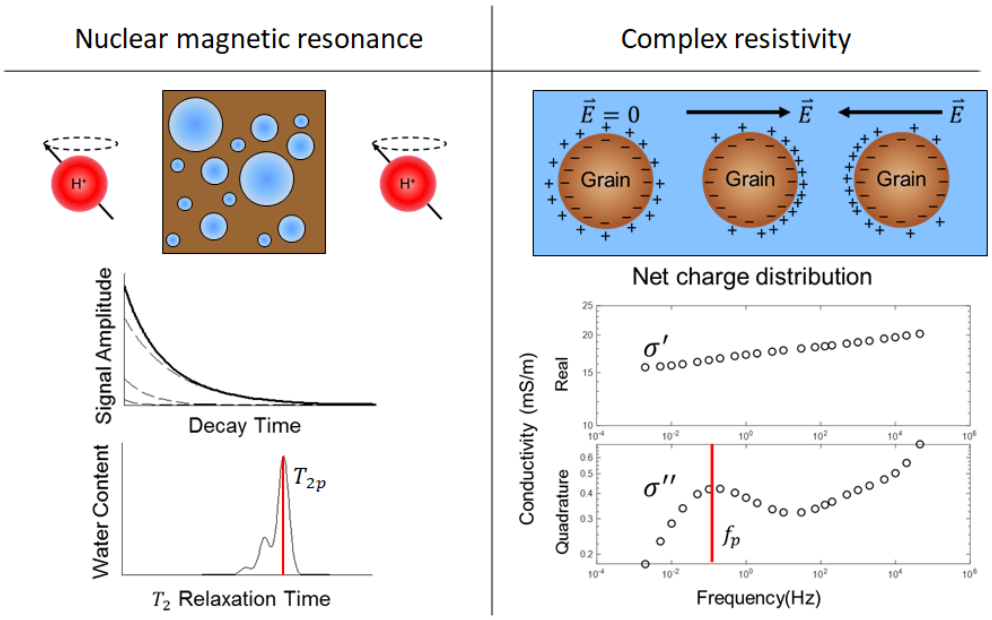

Figure 3. 3: Overview of the basic principles of the nuclear magnetic resonance (NMR) and complex resistivity (CR) measurement highlighting the analogies between the two measurements. The NMR method exploits the quantum mechanics phenomenon of nuclear spin whereas the CR method is based on multiple electrical charge transport processes. The physical principles of the two methods are discussed in further detail in Section 4.0.

signal intensity that is related to the total interfacial surface area in a rock. Both methods measure a distribution of relaxation times (expressed either in the time domain or the frequency domain) that is related to the distribution of pore or grain sizes within a rock. These similarities in the measurements provided were exploited in this project.

3.1.1 Nuclear magnetic resonance (NMR)

The NMR method has emerged as a geophysical technology unique in geophysics in that it is directly sensitive to the presence of hydrogen associated with water or hydrocarbons. NMR measurements can be collected in the field, using a borehole tool or a surface-based instrument (beyond the scope of this project), or in the laboratory. The borehole tool was developed for use in the petroleum industry to determine water and hydrocarbon content and estimate permeability and pore-size distributions in petroleum reservoirs (e.g. Kleinberg et al., 1992). This project capitalized on the recent development of an NMR borehole tool that can be used to collect measurements in near-surface boreholes (Walsh et al., 2010).

NMR measurements are already being utilized in the evaluation of petroleum reservoirs to determine porosity, to estimate the distribution of pore sizes and permeability, and to distinguish mobile fluid content from clay or capillary bound fluid content, (e.g. Allen et al., 2000; Kleinberg et al., 1992). NMR measurements have more recently been used to determine water content and estimate hydraulic conductivity in shallow aquifers (Knight et al., 2016). Recent advances in NMR data collection strategies have encouraged exploration of the sensitivity of NMR measurements to different fluid types (i.e., hydrocarbons from water as reported by Song, 2010). Such studies partially motivated the work performed under this project that focused on

evaluating the sensitivity of geophysical measurements to contaminant mass. The physical basis of the method is described later.

3.1.2 Complex resistivity (CR)

The CR method is unique in applied geophysics in that it has strong sensitivity to both the geometry of the pore space (like NMR) and the chemistry of the mineral-fluid interface (e.g. Knight et al., 2010). This method also provides information on the distribution of the pore sizes within a rock (e.g. Scott & Barker, 2003; Tong et al., 2006). Research on the CR method is also increasingly demonstrating its potential to detect and monitor geochemical and biogeochemical processes that alter both the physical and chemical properties of the mineral-fluid interface (Atekwana & Slater, 2009). Although findings from different research groups are the focus of ongoing scientific debate, the method has recently been shown to be sensitive to organic liquid concentrations, including DNAPL, particularly in the presence of clays (Personna et al., 2013; Roberts & Wildenschild, 2012; Ustra et al., 2012). The physical basis of the method is described later.

4.0 Theory of geophysical methods

4.1 Nuclear magnetic resonance (NMR)

The NMR relaxation phenomenon results from the fact that all nuclei with an odd number of protons or neutrons possess a nuclear spin angular momentum. In a static magnetic field, the nuclear spins of a fraction of the protons will align with the static field resulting in a total magnetization that is proportional to the number of protons in the sample. In the NMR experiment an oscillating radio frequency (RF) pulse tuned to perturb hydrogen spins, is applied to the sample for a short time. The frequency of the RF pulse is called the Larmor frequency, f_0, and is related to the strength of the static magnetic field, B_0, and the gyromagnetic ratio of hydrogen. The application of a series of RF pulses causes the nuclear spins to diverge from their equilibrium position; the return to equilibrium results in a measurable change in the bulk nuclear magnetization over time, t. For NMR measurements collected in the laboratory f0 ranges from 0.25 MHz to 900 MHz and is typically 2 MHz for rock core analyzers used for geophysical studies. For NMR borehole measurements f_0 ranges from 0.25 MHz to 2 MHz depending on instrument type and configuration. For a water-saturated geological material, the measurable signal, $I_{xy}(t)$, exhibits multi-exponential decay (e.g., Timur, 1969),

$$I_{xy}(t) = I_0 \sum_i f_i e^{-t/T_{2i}} \tag{4.1}$$

where the sum is taken over the pore environments in the measured volume. I_0, the initial signal magnitude, is proportional to the total number of hydrogen atoms (i.e., the water content) in the measured volume and can be used to estimate the porosity in a saturated sample and the water content in a partially saturated sample. F_i is the proportion of the measured signal that relaxes with a time of T_{2i}. The value of f_i is typically plotted versus T_{2i} to yield a distribution of NMR relaxation times (T_2-distributions; Figure 4. 1).

The value of T_{2i} is related to the physical and chemical properties of the pore. In a fully saturated pore, the inverse of T_{2i} is commonly assumed to be proportional to the radius of the ith pore r_i,

$$\frac{1}{T_{2i}} = \frac{\rho_{2i}}{r_i}, \tag{4.2}$$

where the constant of proportionality, ρ_{2i}, is called the surface relaxivity and is related to the paramagnetic content (e.g., unpaired electrons in iron(III)) on the surface of the pore (Foley et al., 1996; Keating & Knight, 2007). This equation allows the T2-distribution to represent the distribution of pore sizes in the measured volume. Figure 4. 1(a) shows an example of three T_2-distributions determined from water saturated sand with three different grain sizes along side their MICP pore size distributions (Figure 4. 1(b)) and demonstrates the sensitivity of the NMR measurement to the pore size distributions. The T_2-distribution can be used to determine the fraction of capillary bound fluid, termed the bound fluid index BFI and the fraction of free fluid within a sample termed the free fluid index FFI (Appendix B.2).

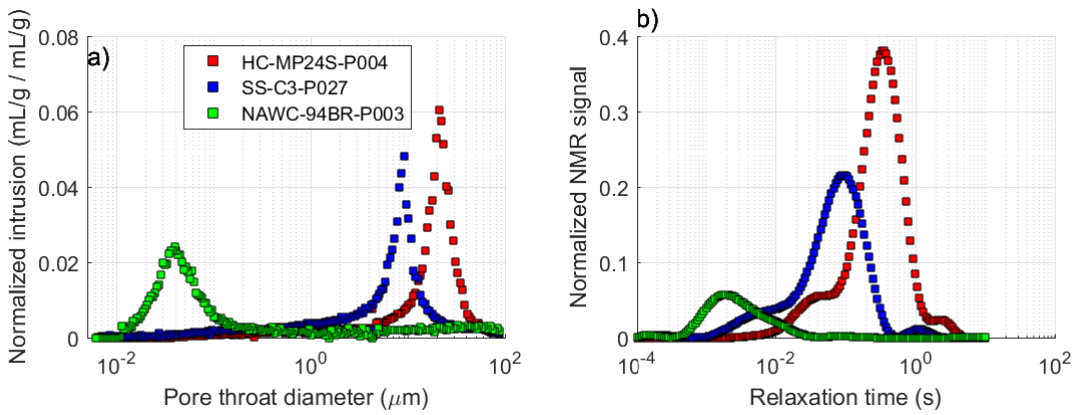

Figure 4. 1: Comparison of a) MICP intrusion and b) T2 distributions for three samples investigated in this project with varying pore size distributions.

The NMR relaxation time is often expressed with a single time, the mean log relaxation time, T_{2ML} (i.e. the weighted mean of the T2 distribution). If the surface relaxivity, ρ_2, is uniform throughout the pore-space, T_{2ML} can be used to determine the characteristic pore radius, i.e., S_{por}, of the measured volume,

$$\frac{1}{T_{2ML}} = \rho_2 S_{por}. \tag{4.3}$$

This equation assumes that there are no heterogeneities in the static magnetic field and that relaxation occurs in the "fast diffusion" regime where protons can move from the bulk fluid to the surface of a pore within the time scale of the measurement. Fast diffusion is valid as long as $\rho_2 r/D$ <<1 where D is the self-diffusion coefficient of water ($2.5\text{x}10^{-9}$ m^2/s for free water at 30°C) and r represents the average length traveled by a proton to reach the nearest surface (e.g., Keating & Knight, 2010). Since the assumption of fast diffusion has been found to hold in most geologic materials (Kleinberg, 2001), this relationship allows k to be estimated from NMR measurements via a Kozeny-Carman model (Kleinberg & Jackson, 2001; Yaramanci et al., 1999).

4.1.1 NMR estimates of permeability

The body of literature linking NMR relaxation measurements to k is extensive and is primarily focused on sediments of interest in petroleum reservoirs. The NMR-k models fall into two main categories: (1) Timur-Coates (T-C) models, which use the NMR determined porosity, ϕ_{NMR}, and the ratio of FFI to BFI to estimate k,

$$k \sim C\left(\frac{FFI}{BFI}\right)^a \phi_{NMR}^b, \tag{4.4}$$

and (2) Schlumberger Doll Research (SDR) models, which use ϕ_{NMR} and T_{2ML} to estimate k (Coates & Dumanior, 1974; Seevers & others, 1966; Timur, 1969),

$$k \sim C(T_{2ML})^a \phi_{NMR}^b. \tag{4.5}$$

In both cases, C, a, and b are empirically derived constants. As long as the models are properly calibrated for lithology, both T-C and SDR models have been found to yield comparable estimates of k, although SDR models are more commonly used (e.g., Allen et al., 2000) as a result of industry standards. In SDR models, the value of C depends on the lithology of the measured volume, a ranges from 1 to 5 and b ranges from 0 to 4. Numerous studies have attempted to determine universal estimates of C, a, and b with limited success (e.g., Borgia et al., 1996; Weller et al., 2010). The lack of a universal set of coefficients that describes k likely stems from two factors: (1) these models assume that k can be estimated from bulk properties of the system rather than the effective properties and (2) in samples where the effective properties are equal to the bulk properties, the models ignore the effect of ρ_2. For example, the determination of S_{por} from T_{2ML} assumes that ρ_2 is known or can be estimated; however, the value of ρ_2 depends on paramagnetic content and mineralogy and can vary over orders of magnitude (Keating & Knight, 2007).

4.2 Complex resistivity (CR)

Complex resistivity (CR) describes the combination of conduction and polarization properties of the subsurface. Conduction pathways determine how easily a rock conducts an electric current; the stored-charge response at low frequencies (below 1 kHz) is determined by diffusive polarization mechanisms associated with ions in the electrical double layer (EDL) forming at the mineral-fluid interface. Measurements can either be collected in the frequency or time domain (Figure 4. 2). Typically, an alternating (Figure 4. 2(a)) or direct (Figure 4. 2(b)) low frequency current is injected and the change in voltage at a receiving electrode(s) is measured along with the current phase lag ϕ (Figure 4. 2(a)) or the primary voltage time decay (Figure 4. 2(b)). CR measurements are therefore frequency (f) dependent.

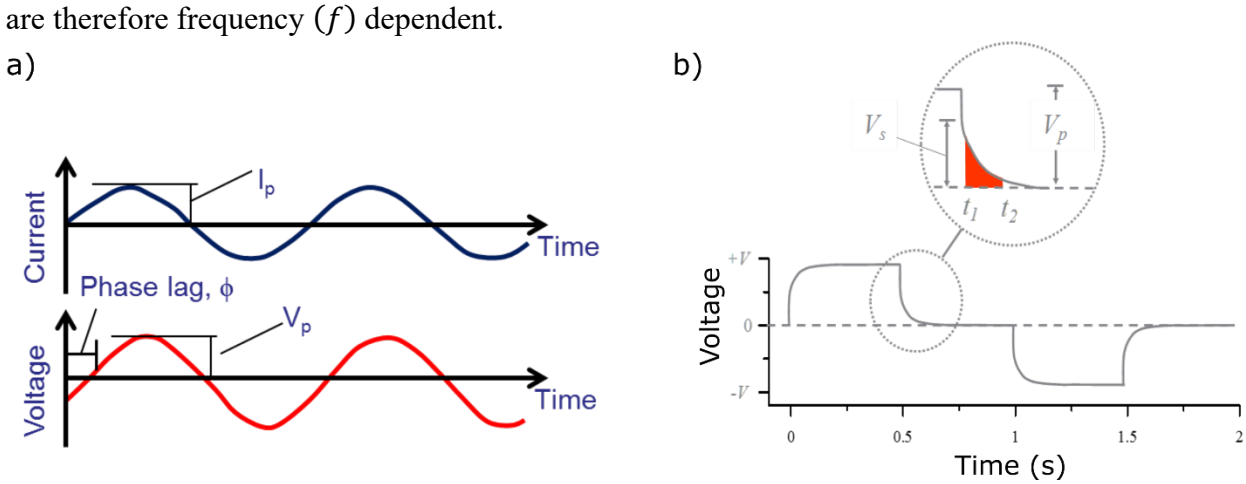

Figure 4. 2: Complex resistivity measurements represented in a) the frequency and b) time domains. In the frequency domain, the voltage magnitude and phase lag are recorded relative to the current waveform. In the time domain, a transient voltage decay is recorded following an abrupt termination of the current injection.

The complex conductivity σ^* ($\sigma^* = {}^{1}/_{\rho^*}$) is commonly represented by the real σ' and imaginary σ'' conductivity which represent the electrolytic and polarization components, respectively. The relationships between σ' and σ'' are,

$$\sigma^*(\omega) = \sigma'(\omega) + i\sigma''(\omega) \tag{4.6}$$

$$\phi = \tan^{-1}\left(\frac{\sigma''(\omega)}{\sigma'(\omega)}\right) \tag{4.7}$$

$$|\sigma^*(\omega)| = \sqrt{\left(\sigma'(\omega)\right)^2 + \left(\sigma''(\omega)\right)^2}, \tag{4.8}$$

CR measurements can be collected across a range of frequencies and, similar to NMR, a dominant relaxation time τ ($\tau = 1/(2\pi f)$) can be defined, which corresponds to a frequency at which the polarization is strongest. Schwarz, (1962) related τ to the particle radius, R for a colloidal suspension by,

$$\tau_{meas} = \frac{R^2}{2D_+}, \tag{4.9}$$

with D_+ related to the effective ionic mobility β_+^s , temperature T, the Boltzmann's constant k_b and the charge of counterions in the Stern layer q_+ by the Nernst-Einstein relationship $D_+ = k_b T \beta_+^s / |q_+|$. The form of equation 4.9 has been repeatedly used to relate polarization spectra to a dominant grain or pore size in porous media (Binley et al., 2005; Scott & Barker, 2003; Zisser et al., 2010). Analogous to the NMR method, short relaxation times τ correspond to small pores and large relaxation times correspond to large pores (Figure 4. 3).

A characteristic relaxation time is typically used to represent CR data which is associated with a characteristic frequency, f. Since different behaviors can be observed in the CR spectrum, the procedure to choose f can vary (Revil et al., 2015;Schwarz, 1962). Within our sample database, the σ'' spectra exhibited either a well-defined peak frequency f_p or a corner frequency f_c where σ'' rapidly decreased towards lower frequencies. If the σ'' spectrum contained a well-defined peak frequency, a parabola was fit to the five data points centered on this peak and used to estimate the apex, equal to f_p. If there was no clear peak, a spline was fit to the data points and f_c was chosen as the intersection of two linear fits to the data following the method of Revil et al. (2015). The time constant was then calculated from $\tau_{pc} = 1/2\pi\, f_{pc}$, where p or c indicates either peak or corner. Figure 4. 3 graphical shows τ_{pc} for samples at HC, SSFL and NAWC.

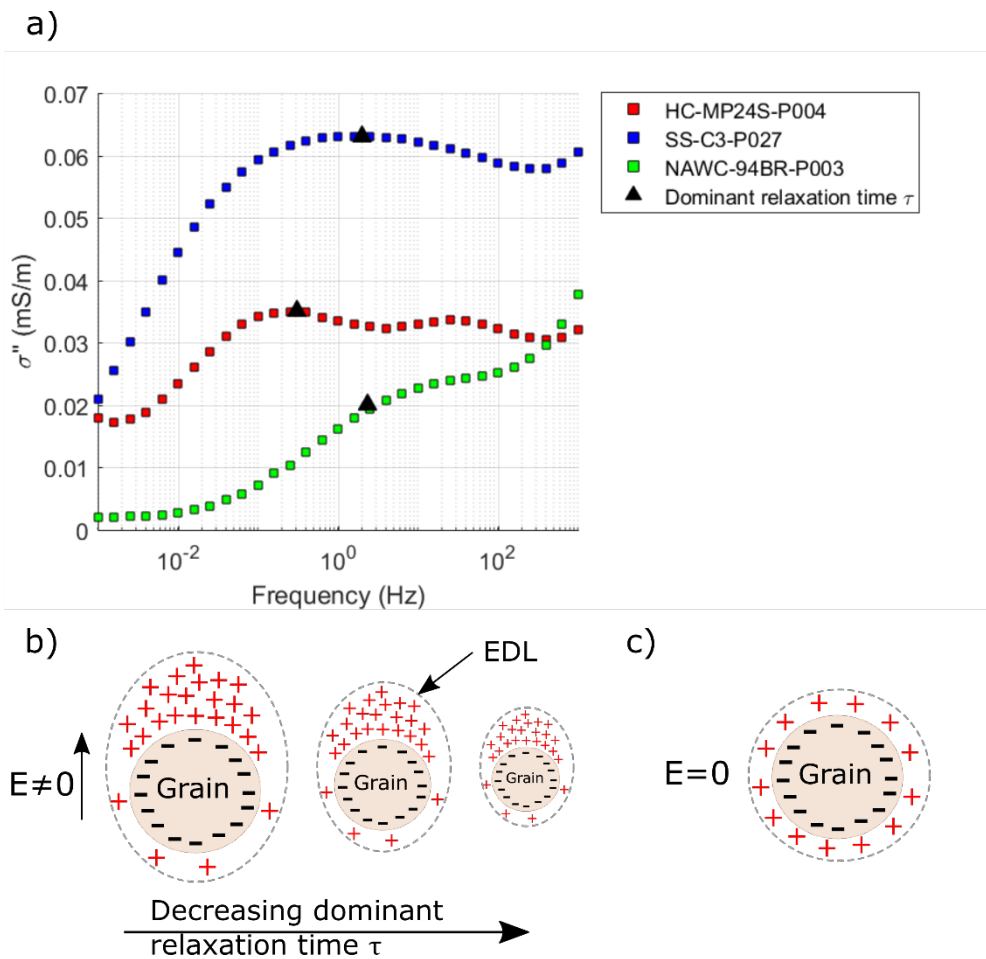

Figure 4. 3: Relationship between the dominant relaxation time a) τ_{pc} and grain/pore size with b) and without c) an applied electric field, E. Shown are three samples at sites Hydrite (HC), Santa Susana (SSFL) and NAWC. While a relaxation time was chosen for the NAWC sample based on Revil et al. (2013), other data suggest (see Figure 4.1) that the dominant grain/pore size is much smaller and would be measured at larger frequencies, out of the range of the PSIP used in this project.

Strong correlations exist between geometric length scales which control mass transfer and hydrogeological properties and CR measurements. The pore volume normalized specific surface area S_{por} has been strongly correlated with σ" in numerous studies. (e.g. Kruschwitz et al., 2016; Weller et al., 2010) . In addition, a strong correlation between τ and the pore radius (e.g. Revil et al., 2014) allows for a link with a dynamically interconnected pore diameter Λ, derived from the mercury injection capillary pressure (MICP) method.

4.2.1 CR estimates of permeability

Indirect estimation of permeability is built upon equations that utilize a representative length scale associated with a dominant pore-scale dimension controlling fluid flow (Carman, 1939) coupled with an electrical formation factor F describing the ratio between tortuosity and porosity

(Banavar and Johnson, 1987; Katz and Thompson, 1987, 1986). Pape et al. (1987) proposed one such equation that is referred to as the PaRiS model. This model uses the inverse of the pore volume normalized surface area S_{por} as the representative length scale, with fitting parameters calibrated against a database composed of a wide range of sandstone samples. Pape et al. (1987) proposed the following model,

$$k_{PaRiS} = \frac{475}{Spor^{3.1}F}, \tag{4.10}$$

where k_{PaRiS} is permeability predicted by the PaRiS model with originally presented units of Darcy (D) (1 D=9.869x10^{-13} m^2) and where S_{por} is in μm^{-1}.

Another equation proposed by Banavar and Johnson (1987) is based on the Katz and Thompson (KT) model (Katz and Thompson, 1987). A dynamically interconnected pore diameter Λ is derived from mercury injection capillary pressure (MICP) method and used as the representative length scale in permeability estimation. The KT permeability equation [Katz and Thompson 1986] is expressed as,

$$k_{KT} = \frac{{l_c}^2}{cF}, \tag{4.11}$$

where k_{KT} (m^2) is permeability predicted by the KT model and l_c (μm) is the equivalent pore diameter corresponding to the pressure at which the maximum incremental mercury intrusion occurs using MICP. The constant c is a scaling constant equal to 226. Katz and Thompson (1986) equated l_c to the inflection point on the MICP cumulative pore size distribution curve, considered to represent the threshold at which the pore space of a rock becomes hydraulically interconnected (i.e. sufficient fluid saturation for fluid flow). Johnson et al. (1986) reformulated this original model in terms of Λ (μm) and Banavar and Johnson (1987) related l_c to Λ by a scaling constant a. This reformulation results in,

$$k_{KT} = \frac{\Lambda^2}{8F}. \tag{4.12}$$

Modeling the pore network as a distribution of cylindrical pores of differing radii, Banavar and Johnson [1987] derived two scaling constants a to represent different sizes of pores and multiplied l_c by a to calculate Λ (i.e. $\Lambda = al_c$). Revil et al (2014) equated Equations 4.11 and 4.12 with c=226 (Equation 4.11) to derive a equal to 0.19.

The link between CR parameters and representative geometric length scales has encouraged efforts to develop permeability prediction equations based on CR measurements. These models rely on measurements of σ" or τ (Revil et al. 2015; Weller et al. 2015). However, unlike the true geometric length scales $1/S_{por}$ and Λ, σ'' and τ are dependent on the pore filling fluid chemistry (Niu et al., 2016; Revil and Skold, 2011; Weller and Slater, 2012) and the surface mineralogy (Abuseda et al., 2016; Kruschwitz et al., 2016; Revil, 2012). Weller et al. (2011) introduced the

concept of specific polarizability c_p, defined as the ratio of σ'' to S_{por}, to represent the control of the fluid chemistry and/or mineralogy on polarization magnitude. Similarly, Revil (2013) defined values of a diffusion coefficient D_+ to accommodate such factors in a mechanistic model describing the CR of soils and rocks (Revil et al., 2015).

Accounting for the fluid conductivity and /or mineralogy controls on CR measurements allows equivalent geophysical length scales to be defined to replace the classical length scale appearing in the geometric models. These representative geometric length scales are defined as $c_p/\ \sigma''$ and τD_+. They are coupled in permeability prediction equations with an electrical formation factor (F) to describe the porosity and tortuosity.

Based on 58 sandstones samples from 17 formations, Weller et al. (2015a) used multilinear regression to arrive at the following empirical equation,

$$k_{W2015a} = \frac{8.43}{\sigma''^{0.66} F^{5.35}}, \tag{4.13}$$

where k_{W2015a} is in mD and σ'' is in mS/m at a frequency of 1 Hz. Weller et al. (2015a) implicitly incorporated a single value of c_p in Equation 4.13, represented in the numerator. The value of c_p was previously found to be equal to $10\text{x}10^{-12}$ S for 114 samples (Weller et al., 2010), and $30\text{x}10^{-12}$ S and $3\text{x}10^{-12}$ S for sandstones from the Bahariya Formation with a high (greater than $100\text{x}10^{-6}$ SI) and low (less than $100\text{x}10^{-6}$ SI) magnetic susceptibility, respectively (Abuseda et al., 2016). Using the methylene blue (MB) method to determine S_{por}, Weller et al. (2015b) found c_p equal to $7.5\text{x}10^{-12}$ S for 60 samples saturated with a conductive fluid with a conductivity close to 100 mS/m.

Rather than relying on a single frequency measure of σ'', a Debye decomposition approach can be used to integrate over a range of frequencies to give a measure of the polarization strength that encompasses the frequency dependence of the CC response (Nordsiek and Weller, 2008). Weller et al. (2015a) also considered the normalized chargeability m_n obtained from a Debye decomposition where the equivalent predictive equation is,

$$k_{W2015b} = \frac{8.95}{m_n^{0.79} F^{5.38}}, \tag{4.14}$$

where k_{W2015b} (mD) is the permeability predicted using m_n (mS/m) from Weller et al. (2015a). Again, the numerator value of $8.69\text{x}10^{-7}$ implicitly incorporates a single value of c_p.

Revil et al. (2012) proposed that τ is related to Λ by,

$$\tau = \frac{\Lambda^2}{2D_+}. \tag{4.15}$$

with D_+ related to the effective ionic mobility β_+^s , temperature T, the Boltzmann's constant k_b and the charge of counterions in the Stern layer q_+ by the Nernst-Einstein relationship $D_+ = k_b T \beta_+^s / |q_+|$. Based on different β_+^s values for a shaly-sand (Vinegar and Waxman, 1984) and unconsolidated sand sediments (Koch et al., 2011), Revil (2013) and Revil el al. (2012) proposed two values of D_+: 1.3x10^{-9} m^2/s for clean sands and 3.8x10^{-12} m^2/s for clayey material.
This results in an alternative permeability prediction model based on the Katz and Thompson (KT) model (Katz and Thompson, 1987) proposed by Revil et al. (2012),

$$k_{KT} = \frac{\tau D_+}{4F}, \tag{4.16}$$

The application of Equation 4.12 for permeability prediction is thus inherently reliant on an accurate estimate of D_+.

5.0 Study Sites

We originally proposed to focus our research on multiple sites of DoD relevance that would permit an assessment of method performance across a range of geological settings from clastic to crystalline fractured rock spanning the east to west coasts of the United States. We obtained preliminary support for access to four sites that offered an extensive inventory of pre-existing data and samples, infrastructure and (in some cases) ongoing remediation activities that would support our research and output of deliverables. However, we intentionally left the door open for input from DoD staff regarding final site selection. The original proposed study sites were: [1] The former Naval Air Warfare Center (NAWC), West Trenton, NJ; [2] The Pease International Tradeport (the former Pease Air Force Base), Portsmouth, NH; [3] Edwards Air Force Base, located in Southern California; [4] The Santa Susana Field Laboratory (SSFL) in Southern California.

During the kick off meeting for the project held in late March, 2014, co-PI Parker presented a strong argument for switching out proposed work at Edwards Air Force Base for a different TCE-contaminated site in Wisconsin (Hydrite site) that her team had extensively studied over the last 10 years prior to the start of ER2421. Her reasons included: [1] Success of our project was critically dependent on comparison of geophysical data against hard data from cores, and there was an extensive inventory of data (including high resolution data on contaminant mass) at this site that we could access; [2] Working at Edwards would be logistically complicated, and the availability of critical supporting data was uncertain; [3] We could exploit the synergistic benefits of coupling to new drilling/coring activities at the Hydrite site planned for summer 2014 in order to make maximum use of data/project funds; [4] The geology of the Wisconsin site provides a good contrast to our other sites (see below) and maintains high relevance to DoD sites. Approval to make this switch was granted by program manager Dr. Andrea Leeson in early April 2014.

Ultimately, work was not conducted at the Pease International Tradesport as further discussion about the site revealed considerable uncertainty about whether contaminant mass actually remained at the site and whether boreholes could be located appropriately. Furthermore, difficulties we encountered (and ultimately overcame) with the physical properties measurements on very low permeability samples obtained from the NAWC mudstone site indicated that a similar campaign on cores from a crystalline rock site, where permeabilities could be as low or even lower, was unrealistic. Our project activities were instead intensified at the other three field sites. All three sites are characterized by high concentrations of VOCs in the dissolved/sorbed phase known to be persistent within the immobile porosity of the rock matrix and where long-term remedial actions (at one site) have proven ineffective. These sites are summarized below.

5.1 Santa Susana Field Laboratory (SSFL)

The Santa Susana Field Laboratory (SSFL), located north of Los Angeles in Ventura, County, California (CA), is a 2800-acre industrial site were TCE is the dominant contaminant utilized at many source areas across the site. Starting in 1997, co-PI Parker's research team has performed intensive site characterization efforts, including high resolution rock core sampling at 41 coreholes. The SSFL is underlain by a late Cretaceous turbidite sequence consisting of interbedded sandstone, siltstone and shale units, known as the Chatsworth Formation (Figure 5. 1). The Chatsworth Formation in this area has been uplifted and faulted resulting in a well-

connected fractured network consisting of bedding plane fractures dipping at approximately 30° and vertical fractures due to jointing. TCE entered the subsurface as a dense non-aqueous phase liquid (DNAPL) in the open fractures, where it dissolved and diffused into the water-saturated porous matrix blocks between fractures. Approximately 1.9 million litres of TCE was released, mainly in the 1950s and 1960s, at numerous rocket engine test stands and component testing laboratories at the site associated with historical DoE, NASA and Rocketdyne (now Boeing) operations. Nearly all the contaminant mass now resides in the porous rock matrix (mean porosity of 14%) with minimal to no DNAPL phase remaining. Fracture distributions and hydraulic properties have been well characterized using the DFN Approach (Parker et al., 2012). Sampling rock core for VOC analysis completed at 41 holes was done in phases of co-PI Parker's research endeavors at the site. The 3 coreholes included in this report include C-3 and RD-109. Corehole C-3 were part of the original source zone investigation work completed by Hurley (2003) in 2000 and RD-109 was part of continued source zone investigation work completed in 2013.

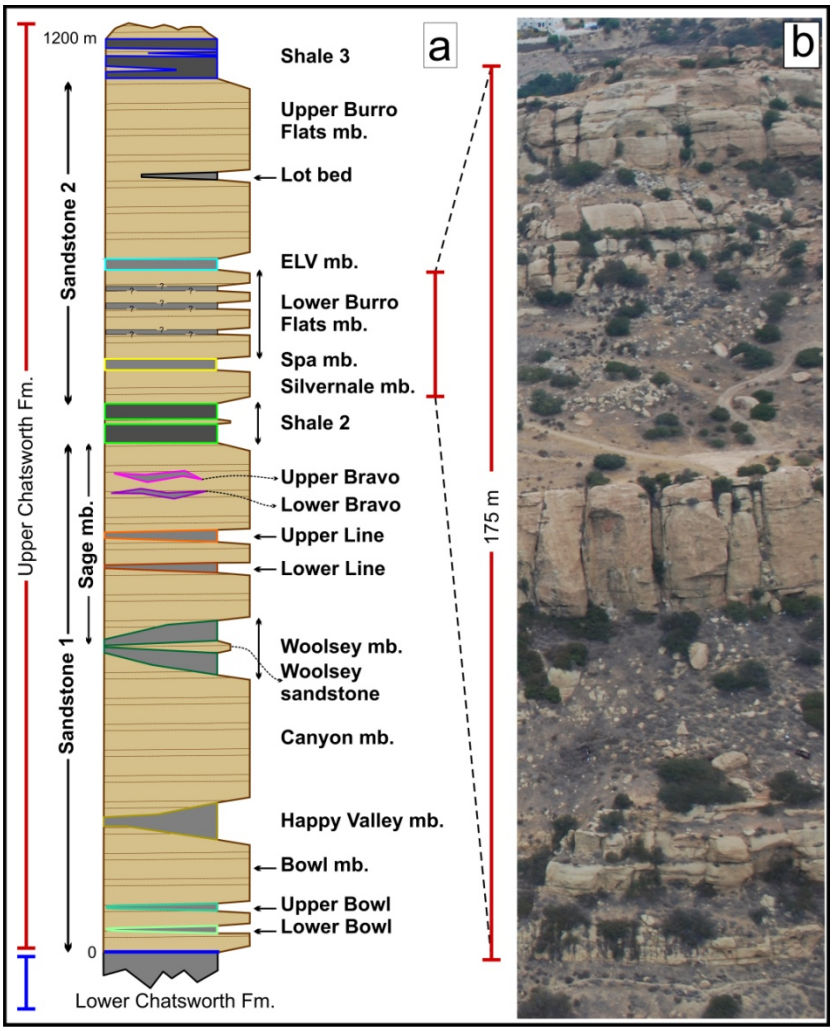

Figure 5. 1: a) Stratigraphic column of the Chatsworth Formation in the vicinity of C-3, C-4, and RD-109 and b) image of the interbedded sandstones and shale between Lower Burro Flats and Silvernale members (from Cilona et al., 2015).

5.2 Hydrite Chemical Company (HC)

A persistent DNAPL source zone and a 3 km long plume, both occurring in a fractured sandstone, at the Hydrite Chemical Co. site in southern Wisconsin (WI) have been a focus of research investigations by co-PI Parker and colleagues since 2003. Contaminants associated with the activities of the previous site owner, a chemical manufacturer/recycler, were released to the subsurface sometime prior to 1970. These releases contaminated the Quaternary unconsolidated sediments and a sequence of flat lying Cambrian to Ordovician aged siliciclastic and carbonate

rocks. The bedrock units at the site are important locally as water supply aquifers and throughout the mid-west United States for water supply and more recently for carbon sequestration. In contrast to the SSFL and NAWC sites, the contamination at the Hydrite site includes a broad mixture of chemicals including chlorinated solvents, Ketones, and BTEX compounds. DNAPL persists, occurring between about 46 and 56 m bgs in the Tunnel City Group fractured sandstone. In 2014, a transect of 5 coreholes arranged along a transect perpendicular to groundwater flow and just downgradient of the DNAPL source zone were drilled and comprehensively characterized using the DFN Approach (Parker et al., 2012). Two of these continuous cores and coreholes, MP-24S and MP-25S, were utilized for SERDP project measurements (Figure 5. 2).

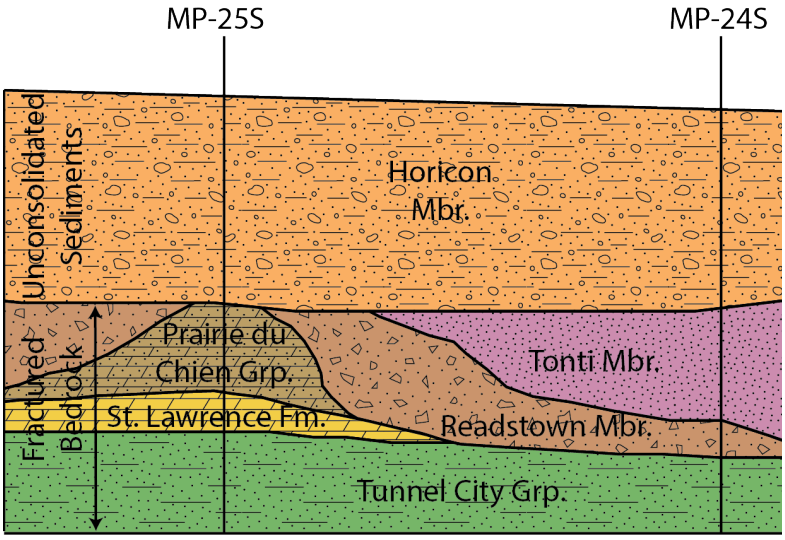

Figure 5. 2: Conceptual geology of two boreholes sampled at Hydrite (modified from Ribiero et al. 2015).

5.3 Naval Air Warfare Center (NAWC)

The Naval Air Warfare Center (NAWC), West Trenton, New Jersey (NJ), was used to test jet engines from the 1950's to 1994. The handling and disposal of TCE at the site resulted in contamination of the bedded, fractured mudstones of the Newark Basin (Lacombe & Burton, 2010). NAWC has been the subject of intensive study by the USGS Toxics Substances Hydrology Program (https://toxics.usgs.gov/investigations/fractured_rock/index.php) and several prior SERDP – ESTCP projects and thus has an extensive bibliography from the past studies (https://toxics.usgs.gov/bib/bib-NAWC.html). Current SERDP work (SERDP ER-1555) at NAWC has shown a complex spatial distribution of TCE and its degradation products, with TCE having been forced into small aperture fractures, as well as diffusing into the immobile, primary porosity of the rock matrix at this site (Goode et al., 2007; Goode et al., 2014). The rock matrix also has high sorption capacity for contaminants, particularly the black organic-rich fissile layers that tend to be highly fractured. Figure 5. 3 shows a cross-section of the dipping mudstone beds in the study area with position of the corehole (94BR) drilled as part of this study. General lithology of the mudstones is separated into three general strata: 1) gray mildly fractured thinly layered (laminated) strata, 2) light-gray weakly fractured massive strata, and 3) thin (<0.2 m) generally highly fractured (fissile) black organic carbon rich strata (Goode et al. (2014). The geologic setting at NAWC is similar to multiple other fractured rocks throughout the USA, including sedimentary basins along the east coast and central USA, where DoD (and DoE and EPA) are facing similar issues related to remediation of chlorinated solvents as DNAPL or dissolved and sorbed phases.

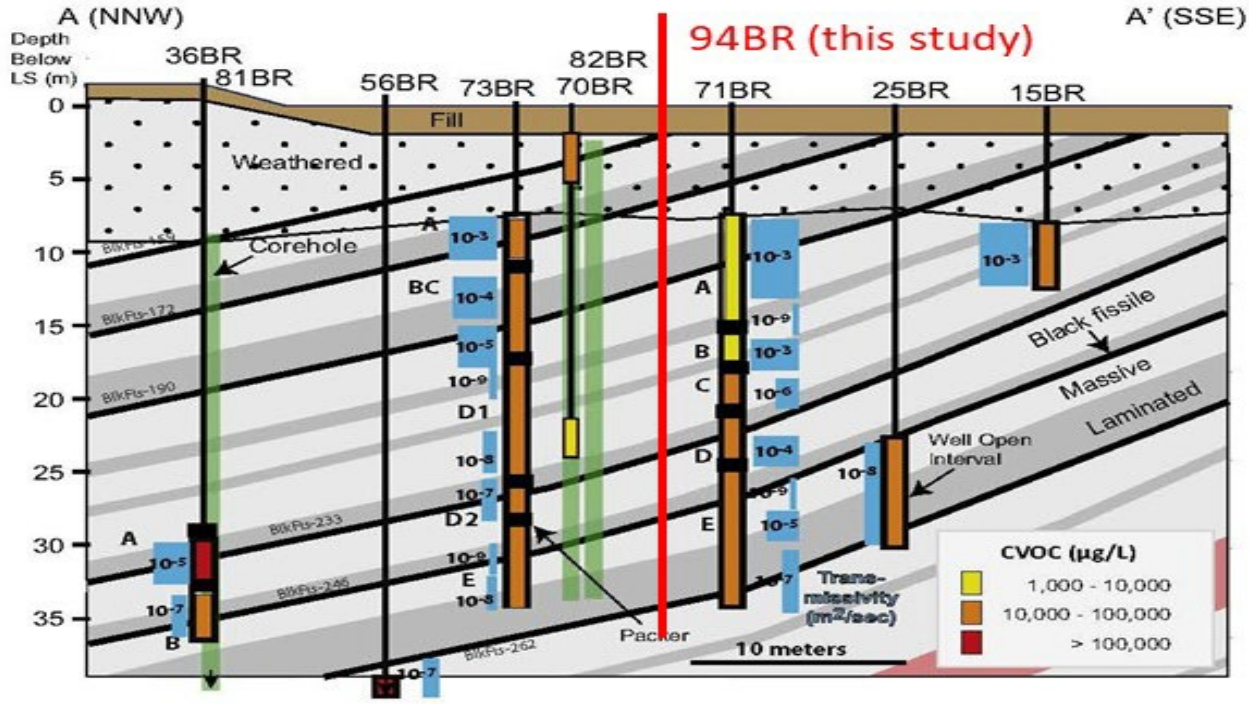

Figure 5. 3: Cross-section at the NAWC site showing existing well and corehole configurations, stratigraphy, transmissivity estimated from packer testing and CVOC concentrations (adapted from Goode et al. (2014). Position of corehole 94BR from this study is also shown (later converted to a multi-level monitoring well).

6.0 Methods

The methods included both field, laboratory, and numerical methods. Field methods included: acquisition of core samples for detailed characterization of lithology, rock matrix properties and contaminant mass distribution, and borehole logging using a variety of geophysical and hydrophysical techniques. Laboratory methods included: determination of contaminant mass distribution in core samples, laboratory quantification of rock properties and laboratory geophysical measurements. The numerical methods included pore scale modeling.

6.1 Technical Approach for acquisition of core samples

The coring and quantification of rock mass was led by the U. Guelph. Co-PI Parker and colleagues have pioneered the Discrete Fracture Network (DFN) approach (Parker et al., 2012) for investigating contaminated sites in fractured rock, particularly fractured sedimentary rock (e.g. sandstone, shale, dolostone), although the methods have also been successfully applied at fractured igneous and metamorphic rock sites as well. Nearly all sedimentary rocks have substantial effective matrix porosity (2-20%) which can serve as a large storage volume for contaminant mass as dissolved and sorbed phase. The process of diffusion transfers contaminant mass from the fractures into the matrix (where the storage capacity can be significantly enhanced by sorption) during the early decades of contamination. Although it is typical that nearly all groundwater flow occurs in the interconnected fracture network, at 'aged' contaminated sites where initial contaminant releases as dense-non-aqueous phase liquids (DNAPLs) occurred decades ago, most contaminant mass now resides in the much lower permeability matrix blocks between fractures as dissolved and sorbed phase. The DNAPL source zones at these sites have evolved, so that at many sites a substantial amount of the original DNAPL mass has become

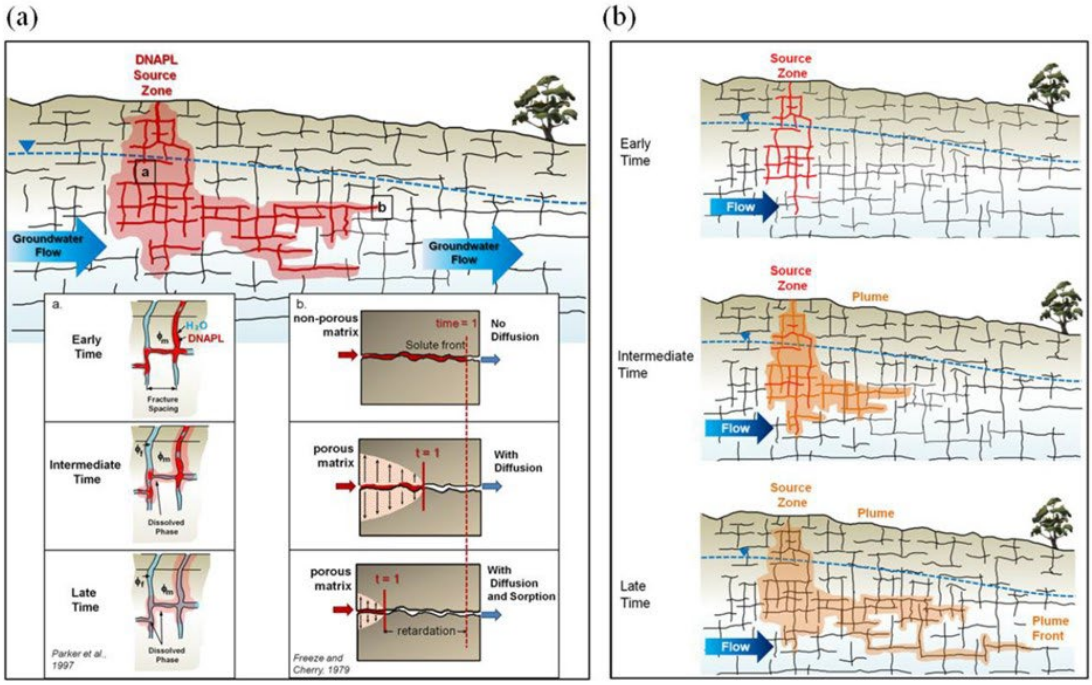

Figure 6. 1: Source zone and plume evolution conceptual model (from Parker et al., 2012).

depleted, or even complete disappearance of the DNAPL mass has occurred (Parker et al., 1994; Parker et al., 1997). Figure 6. 1 illustrates the conceptual model for source zone and plume evolution in fractured sedimentary rock (from Parker et al., 2012).However, this mass remains mobile as diffusion allows the migration of contaminants from the rock matrix back into the more permeable fractures, resulting in long term contaminant persistence even if source zones are depleted or remediated (Parker et al., 2010). The DFN approach (Figure 3. 1) emphasizes using rock core for contaminant mass measurements to determine mass storage in the matrix and its distribution with respect to fracture characteristics and contaminant transport pathways (Figure 6. 2).

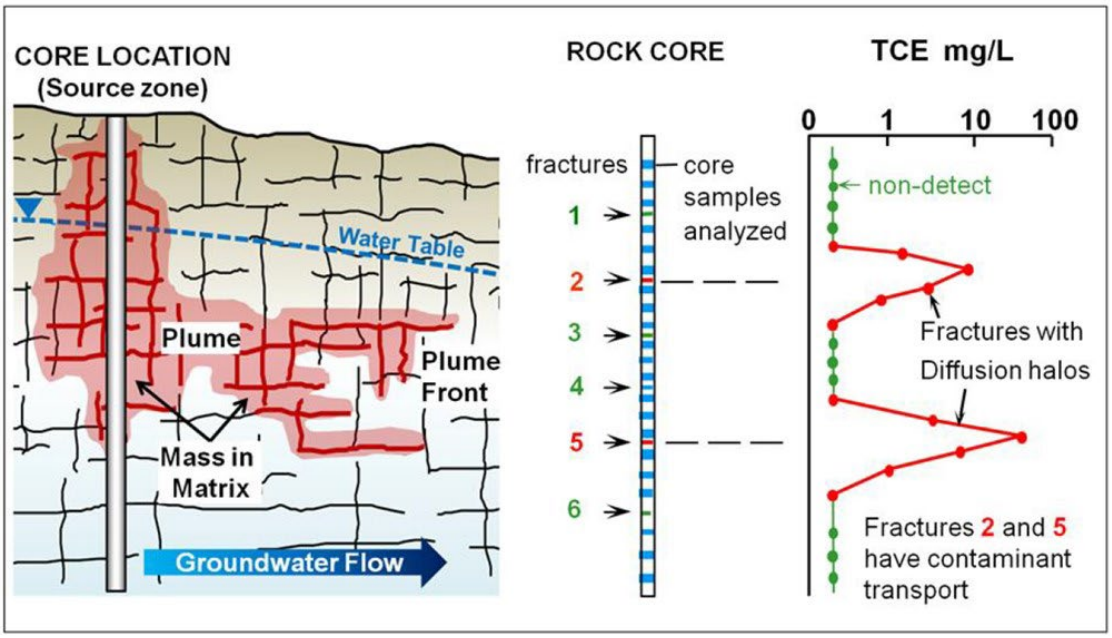

Figure 6. 2: Technical approach for collecting and subsampling continuous rock cores for contaminant mass distribution and contaminant pathways analysis.

Quantification of contaminant mass in the matrix was achieved at the SSFL, Hydrite, and NAWC sites by taking numerous, closely spaced samples from the continuous cores for laboratory analysis of contaminant concentrations. Sample locations were determined based on detailed visual inspection and logging of sedimentological properties and fractures observed in the core as well as knowledge of the contaminant type, release history, and expected diffusion parameters. Samples representative of distinct lithofacies were also collected for laboratory measurements of physical properties (e.g., porosity, permeability, organic carbon content, mineralogy, etc.). The sample methodology follows methods, templates and standard operating procedures (SOPs) for the field logging, sample collection and processing and laboratory analyses as developed and refined by Dr. Parker and colleagues over the past fifteen or more years and applied at many sites throughout the U.S., Canada and elsewhere (Figure 6. 3).

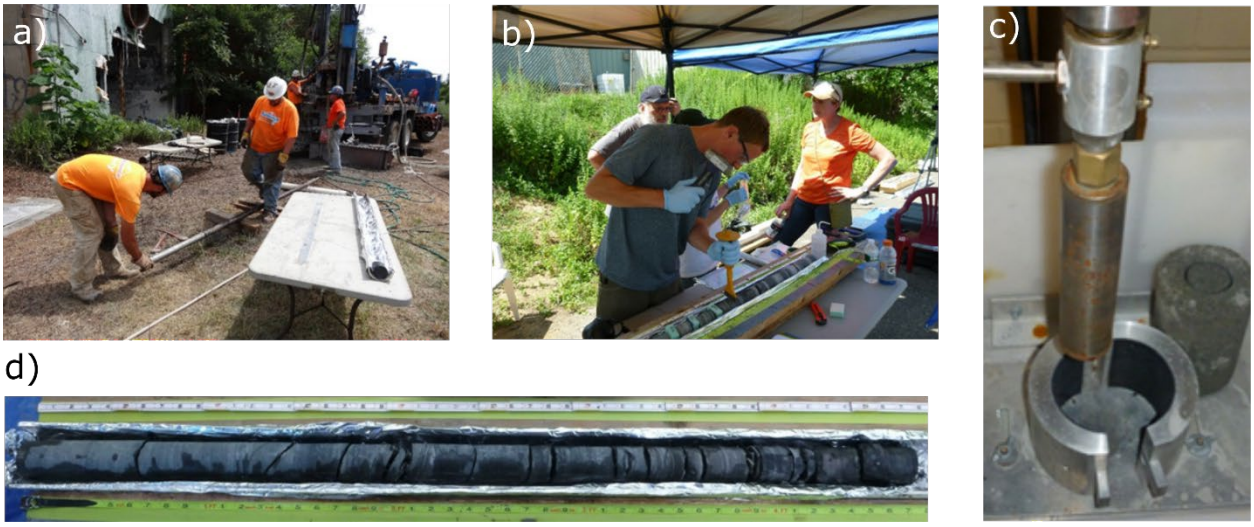

Figure 6. 3: a) HQ triple tube rock coring at the NAWC site (corehole 94BR), b) field rock core subsampling, c) laboratory subcoring of rock core samples, and d) example of extracted core from borehole before field subsampling.

6.1.1 Hydrite

Corehole MP-24S was drilled in mid July 2014 with coring/sampling following the procedure outlined above. The USGS team conducted borehole geophysics on this corehole in September 2014, including natural gamma and ATV logs. The MP-24S corehole is located about 50 m downgradient from a multi-component DNAPL source zone. Detailed core logging combined with the natural gamma log show a dominance of find grained, quartzose sandstone within the Tonti Member of the St. Peter Formation, fine grained sandstone with some thin intervals of clay in the Readstown Member of the St. Peter Formation, and very-fine- to fine-grained feldspathic and glauconitic subquartzose sandstone in the Tunnel City Group. Fracture picks derived from the ATV logs shows numerous fractures with varying dips throughout the members of the St. Peter Group and primarily low angle (bed parallel) fractures in the Tunnel City Group. A total of 110 rock core VOC samples were collected from the MP-24S corehole over a 25 m cored interval from about 30 to 55 m below ground surface (bgs) (average sample spacing of 0.23 m) and analyzed for 36 contaminants including ethanes, ethenes, ketones and petroleum hydrocarbon compounds. Parker et al. (2015) provides more details on the Hydrite site activities and results.

6.1.2 Santa Susana

Corehole RD-109 was drilled and sampled in December of 2013 at the former site of a small rocket engine testing facility and adjacent to a former large rocket engine test stand, as part of the continuing source zone characterization work at the site. The major contaminants of interest are TCE, a solvent used to clean equipment following tests, and its' main degradation product, cis-DCE. PCE occurs as an impurity in industrial-grade TCE, and the other ethenes are additional degradation products of TCE and PCE. The SSFL is underlain by the late Cretaceous Chatsworth

formation. This deep-sea turbidite deposit is composed primarily of sandstone with minor interbeds of shale and siltstone and, occasionally, conglomerate with similar mineralogy. The bedding under the SSFL dips 25° to 35° to the northwest (MWH, 2009). Mineralogy of the arkosic sandstone of the Chatsworth Formation is primarily comprised of quartz, plagioclase, feldspar and phyllosilicate minerals (biotite, chlorite) with lesser amounts of lithic fragments (MWH, 2009). The Chatsworth Formation contains a pervasive interconnected fracture network comprised of a systematic arrangement of bedding-parallel fractures and steeply dipping joints (i.e. bedding-perpendicular fractures) with highly variable orientations, densities, and apertures. A total of 115 rock core VOC samples were collected from the RD-109 corehole over a 38 m (125 ft) cored interval between 4.5 to 42.7 m (15 to 140 ft) bgs (average sample spacing of 0.33 m (1.1 ft), and analyzed for the target chlorinated ethenes according to the procedures outlined above.

6.1.3 NAWC

Corehole 94BR was drilled and sampled over a four-day period in August 2015 (one day to drill through overburden and set surface casing into top of rock at 35 ft bgs, followed by three days of continuous HQ3 wireline coring from 10.7 to 45.7 m (35 to 150 ft) bgs). The major contaminant of interest at NAWC is TCE released from industrial TCE DNAPL use at the facility over a period of decades (Lacombe, 2000) . However degradation in the formation is also occurring, so substantial amounts of degradation products (primarily cis-DCE, and VC to a lesser extent) are also observed in groundwater (and in rock core samples) from the site. As described earlier, NAWC is underlain by mudstones of the Lockatong Formation of Triassic age, of the Newark Basin. These mudstone beds dip to the NW and are comprised of alternating sequences of grey mudstones ranging from massive to thinly laminated, with occasional thin black organic rich 'fissile' layers (Figure 5. 2). Variable fracture frequency was observed in the 94BR cores, both bedding plane fractures and cross-cutting joints, with more intensive fracturing in some lithologies (e.g. the black fissile zones and laminated mudstones) versus others (e.g. the massive mudstones). Coring and rock core sampling at 94BR followed similar procedures as outlined above. A total of 213 rock core VOC samples were collected from the 35 m (115 ft) cored interval for an average sample spacing of 0.16 m (0.54 ft) and analyzed for TCE and degradation products according to the procedures outlined above. This high sample resolution was necessitated by a combination of high frequency of observed fractures in cores, combined with prior knowledge of high organic carbon content of the interbedded mudstone units (particularly the black organic rich fissile zones) and expected diffusion distances. Numerous physical property samples were also collected representative of each of the major lithologies. Following coring, the borehole was developed by pumping approximately five borehole volumes from the open hole with the pump intake at different levels, open hole fluid logging was performed by USGS, and then the hole was sealed with a blank FLUTe liner that including a NAPL cover (to detect free-phase DNAPL in the borehole, if present) and FACT (described later, and being tested rigorously as part of ESTCP Project ER-201630). Subsequent testing performed in this borehole, including geophysical logging and hydrophysical tests are described later.

6.2 Quantification of variations in contaminant mass

Rock core contaminant analyses was performed on small sections of rock collected along the entire length/depth of a core with an average 0.2 to 0.3 m spacing (tailored to the specific rock matrix type and variability, contaminant type and age, and fracture network conditions) to provide high resolution determination of the contaminant mass distributions. Rock samples collected from a core are processed and preserved in the field, either by crushing the rock samples and preserving them immediately in methanol, or sealing the intact sample "pucks" (i.e. 1-2-in long samples broken out from the core) in the field using a commercial grade vacuum sealer and mil-spec film foil bags to remove air and prevent volatile loss. Figure 6. 4 shows photos of core processing, and Figure 6. 5 shows an example of subsampled cores from the NAWC 94BR corehole. These samples were then crushed and preserved in methanol immediately upon arrival at the laboratory. Crushed or intact samples from the SSFL and NAWC sites were sent via overnight shipping to the U. Guelph for rigorous extraction and analysis of VOC mass using well-established methods and protocols that have received regulatory review and approval. The Hydrite samples were sent to the Stone Environmental laboratory in Montpelier, Vermont (now operating as Cascade Environmental) for extraction and analysis using the same methods/protocols developed by Dr. Parker and colleagues at the U. Guelph. The analytical methods utilize specialized techniques providing rigorous extraction of the contaminant mass from the crushed rock samples, using one of two techniques: 1) shake-flask method, where crushed rock samples are extracted in methanol with periodic shaking over a period of a few to several weeks utilizing time-series analyses of a subset of samples to verify extraction performance, or 2) microwave assisted extraction (MAE) which uses microwaving of the crushed rock samples in specialized containers providing rapid extraction of contaminant mass. Dincutoiu et al., (2003, 2006) and subsequent theses by Parker supervised or co-supervised students (e.g. Kusinski, 2012; Liu, 2005) describe evolution of these methods. Analytical protocols also utilize methods that provide exceptionally low method detection limits (MDLs) for the target contaminants (e.g. Gorecki et al., 2010). Conventional laboratory methods for extraction and analyses of crushed rock samples have been shown to provide incomplete extraction and generally have much higher MDLs due to need to dilute methanol extracts into water prior to analysis.

This rock core chemical analysis provides total contaminant mass concentrations on an analyte per wet mass of crushed rock basis, and these were converted via partitioning calculations using measured or estimated rock matrix parameters into dissolved and sorbed fractions as appropriate. (Sterling et al., 2005) provides an example of such partitioning calculations. In addition to the samples for defining the VOC mass distribution, representative samples from the different matrix types encountered were also retained, subjected to laboratory analyses for various parameters including bulk density, matrix porosity, and organic carbon content, and used in the partitioning calculations. Also a robust suite of QA/QC samples are collected for evaluating method performance, including several types of field and laboratory blanks (e.g. trip blanks, equipment blanks, methanol blanks, storage blanks) as well as field and laboratory duplicates and laboratory matrix spike samples.

Figure 6. 4: VOC sample processing in the field: a) Trimming the core rind exposed to drilling fluids, b) crushing the sample using a hydraulic press and stainless steel crushing cells in a setup designed to minimize exposure time to air, c) sample transfer to pre-preserved (MeOH) vials, and d) 5 step process for decontamination of core crushing equipment applied between samples.

Figure 6. 5: Example of subsampled cores from the NAWC site with Styrofoam blocks marking positions of subsamples collected for VOC distribution or physical property analyses.

6.3 Quantification of rock properties

6.3.1 Permeability

To measure permeability in the laboratory, dry air was used to yield an air permeability. Air permeability is usually a little larger than liquid permeability so a Klinkenberg correction (Klinkenberg, 1941) was applied to obtain an equivalent liquid permeability. U Guelph has instrumentation to obtain permeability to a minimum range of 0.01 mD, which was suitable for Hydrite and SSFL samples (0.04-367 mD). The NAWC samples required a lower permeability range than available at U Guelph; RN (RN) partnered with Colorado School of Mines (Dr. Manika Prasad) to use their Core Laboratories CMS300 Permeameter to measure permeability on NAWC samples (0.03-4.7µD).

6.3.2 Submersible volumes

Subcores tended to deviate from perfect cylindrical shape so submersible volumes were measured for each core to more accurately obtain the true volume of each sample needed to calculate gravimetric porosity. Subcores were first saturated (details following) and then fully submerged to obtain the mass of displacement. The same fluid was used for saturation and submersion.

6.3.3 Sample saturation

To saturate subcores, a suction of at least 10^{-2} mbar (more commonly 10^{-3} mbar) was applied. Air bubbles were minimized in the saturating fluids by boiling during preparation and fusing nitrogen gas into the samples for several minutes. The saturating fluid was then introduced into the containment vessels. High pressure was subsequently applied to the containment vessel containing the subcore and saturation fluid. The pressure applied and the duration of this application varied depending on the site characteristics (i.e. the tighter mudstone samples at NAWC required a different application than the sandstones at SSFL and HC), (Table 6. 1). HC and SSFL cores were saturated at U Guelph and Rutgers-Newark whereas NAWC cores were saturated at Rutgers-Newark.

In order to mimic in-situ conditions and collect electrical formation factor measurements, two saturating fluids were used for each sample. A low conductivity fluid (~665 µS/cm) represented a simulated groundwater with a 2:1 ratio of magnesium sulfate ($MgSO_4$) to calcium chloride ($CaCl_2$). A high conductivity fluid (required for formation factor measurements only) was a salt (NaCl) solution with a fluid specific conductance equal to 80 mS/cm.

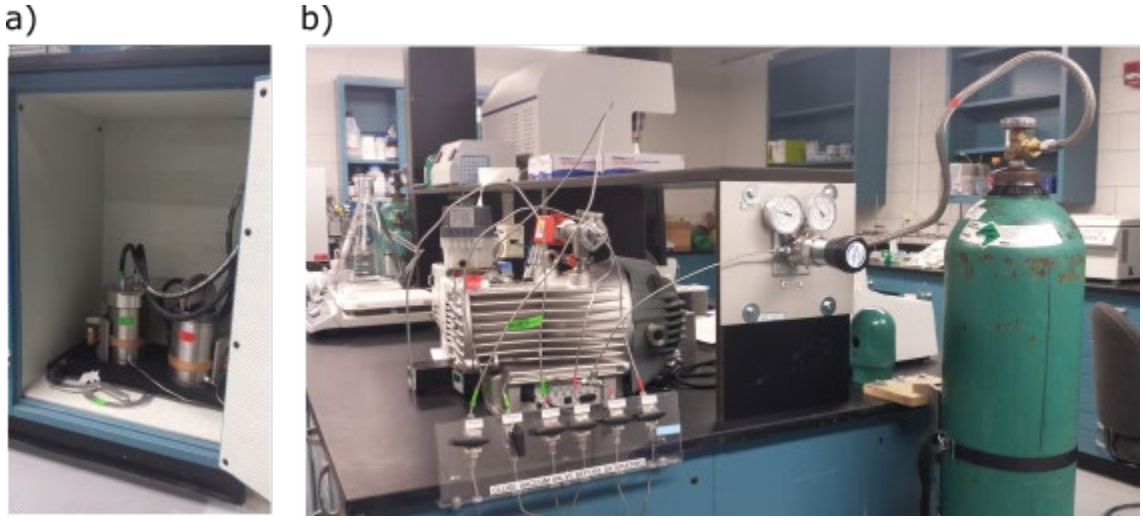

Figure 6. 6: Low vacuum and high-pressure system used to saturate subcores in the laboratory. a) containment chamber constructed of fiberglass ballistic panels to withstand pressures up to 2800 psi. b) Low vacuum pump (one visible) and associated piping for saturation system at up to 2500 psi.

6.3.4 Gravimetric porosity

Gravimetric porosity was measured by subtracting dry and saturated subcore mass and dividing by the submersible volume. At Rutgers-Newark, a low vacuum and high-pressure system was developed under this project and subsequently used to saturate cores (Figure 6. 6). The developed system consisted of the following components: [i] two vacuum pumps capable of at least 2.5×10^{-2} mbar suction; [ii] a containment chamber made from fiberglass ballistic panels (Figure 6. 6(a)), [iii] two containment vessels capable of withstanding pressures up to 2800 psi. U Guelph used a similar saturation system but only capable of saturating cores at pressures up to 500 psi. Consistency of gravimetric porosities were checked for the different saturating fluids and between the matching systems at U Guelph and Rutgers-Newark, where applicable.

Figure 6. 7: A sample loaded into Bruker D8 Advance used for XRD measurements.

Table 6. 1: Summary of saturation procedure

Site	Pressure (psi)	Duration
Hydrite (HC)	500	20 minutes
Santa Susana (SSFL)	500	20 minutes
Naval Air Warfare Center (NAWC)	> 2500	At least 4 days

6.3.5 X-ray diffraction (XRD)

X-ray diffraction (XRD) is used for mineral phase identification of crystalline material. XRD was used to validate the field geology logs and possibly identify clay content. The method requires samples to be finely grounded and about 2 grams was used within the instrument for a measurement. Rutgers-Newark owns a Bruker D8 Advance and the Eva suite of analysis software. Samples that were co-located to subcores were ground with a mortar and pestle. Several cores were subcored in both the horizontal and vertical directions; XRD was performed once for these co-located samples. X-ray spectra were collected every 0.02 degrees with 2θ ranging from 5-75 degrees (Figure 6. 7). We chose to identify a minimum number of phases where it a mineral phase was clearly present in the spectrum. A minimum of one and a maximum of three phases were selected for each sample. XRD spectra were compared across boreholes at each site by stacking measurements (Figure 6. 8). This was to validate changes in the phases identified, both in the field notes and XRD analysis.

6.3.6 Mercury injection capillary pressure (MICP)

The mercury injection capillary pressure (MICP) method is based on measuring the intrusion of mercury (a non-wetting fluid that must be forced into pores) into a porous structure at controlled pressures. The pressures are inversely proportional to the size of the pores (Washburn, 1921) which for measurements at numerous pressures over a wide range yields pore size distributions.

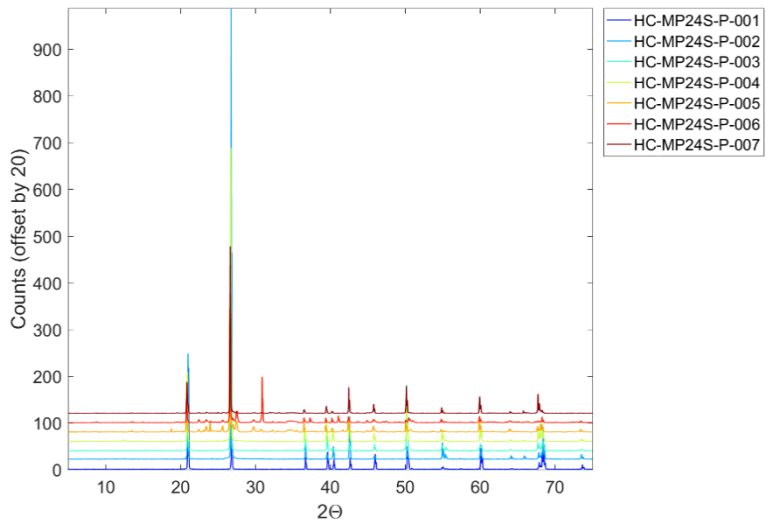

Figure 6. 8: Comparison of XRD spectra at HC within borehole MP24S. Individual sample responses were offset by 20 to better view stacking of spectra.

Rutgers-Newark owns a Micromeretics Autopore IV which capable of injection pressures up to 30,000 psi (Figure 6. 9). Synthesis of the data was performed in the Micromeretics proprietary software.

A pentrometer (a holder for the sample) is used for the measurement and measurements are performed on an empty pentrometer as a blank correction. Measurements collected using an empty pentrometer also allow for a more precise volumetric measurement. With the volume of the pentrometer known, an MICP estimate of porosity can be obtained in addition to pore size distributions (Appendix B.4).

Depending on the estimated porosity of the sample, a quick calculation may be performed to determine the sample mass necessary for optimal recommended instrument parameters. For HC and SSFL samples, gravimetric porosities were within range (i.e. > 10%) to run samples with a 5 cc pentrometer for optimal instrument parameters. Approximately 5 g of HC and SSFL samples was used in the 5 cc pentrometer. NAWC samples (many porosities < 10%) required duplicate and sometimes triplicate samples to achieve consistency since optimal pentrometer parameters (i.e. stem volume percentage) could not be obtained. MICP data for these samples needed to be collected in a 25 cc pentrometer and approximately 15-20 g of sample was used. A very fine scale of incremental pressures was used for data collection with at least 150 data points collected for each sample (Figure 6. 10).

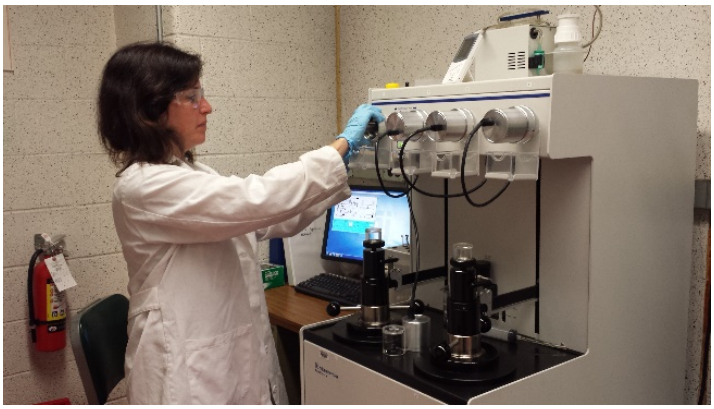

Figure 6. 9: Photograph of user performing MICP measurements with the Autopore IV.

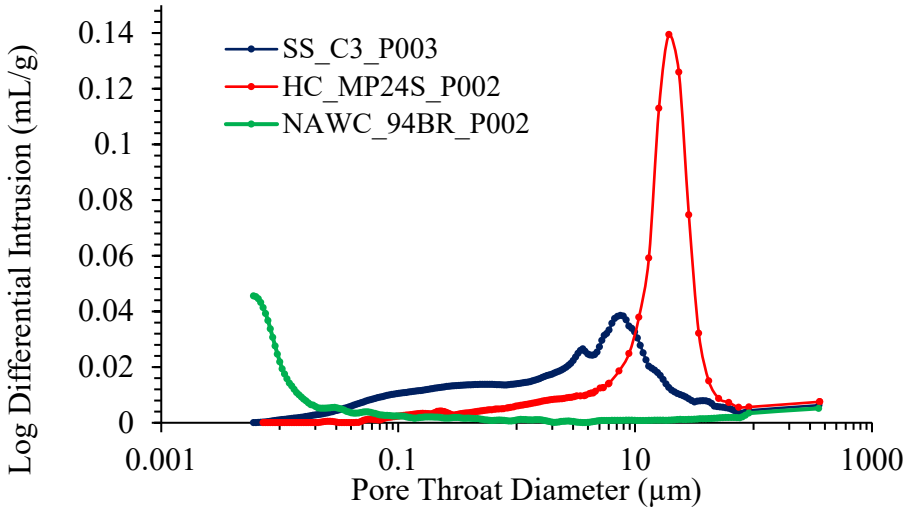

Figure 6. 10: Pore size diameter distributions from MICP with a sample from SSFL, HC and NAWC showing the variations in pore size between the three sites. The peak differential intrusion is representative of a dominant, interconnected pore diameter. The NAWC mudstone site is shown to have much smaller pores than HC and SSFL (sandstones).

MICP measures can be related to key hydrogeologic parameters. The maximum incremental intrusion pressure from MICP has been related to permeability (Katz & Thompson, 1986, 1987) as it represents a hydraulically interconnected pore diameter. Other MICP measures have also been related to permeability estimation, for example the pressure associated with 50% intrusion (Appendix B.4). The maximum incremental intrusion pressure corresponds to the peak log differential intrusion. Pressures *are* converted to pore size diameter *D* using the Washburn equation (Washburn, 1921)

$$D = \frac{-4\gamma cos\theta}{P}, \tag{6.1}$$

where γ is the surface tension of mercury and θ is the contact angle. See Appendix B.3 for MICP data.

6.3.7 Brunauer–Emmett–Teller (BET) Method

The Brunauer–Emmett–Teller (BET) method provides an estimate of the specific surface area by measuring gas absorption as a function of relative pressure (Brunauer, Emmett, & Teller, 1938). Rutgers-Newark owns a Micromeretics ASAP 2020 (Figure 6. 11) and all measurements were collected with this instrument. Approximately 3 to 5 grams of sample were used and data for at least 10 pressures were collected. The specific surface area was only computes when the correlation coefficient between the relative pressures and a measure of nitrogen gas absorption was at least 0.9999. In some cases, data points were removed to achieve this value. Specific surface areas were considered valid if the correlation coefficient criteria was satisfied and surface area was at least 1 m^2. For numerous (very tight) NAWC samples, these criteria could not be met and specific surface areas could not be measured. Appendix B.2 and/or B.4 provide summaries of the acquired BET data. From the BET surface area S_s and porosity ϕ, S_{por} can be calculated as,

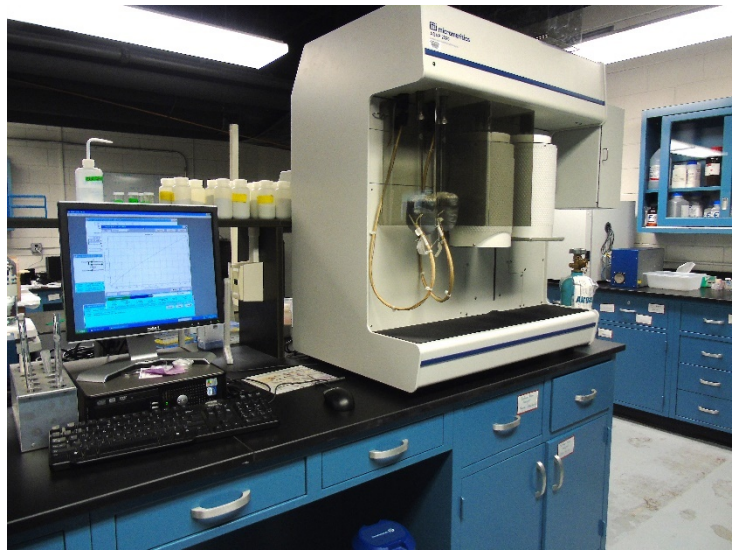

Figure 6. 11: On-going BET data collection. Shown are two samples in the degas port and one sample where BET data are being collected.

$$S_{por} = S_s \rho_s \frac{1-\phi}{\phi}, \tag{6.2}$$

where $\rho_s$is the density of the solids. S_{por} is an important parameter shown to be related to the pore size controlling fluid flow and therefore has been used as a parameter in predicting permeability (e.g. Pape et al., 1987).

6.3.8 Ferrozine analysis

Iron content was measured for samples using Ferrozine analysis (Stookey, 1970). In this method, an acid digest is prepared using a finely ground sample and then reacted with a ferrozine reagent (Figure 6. 12). This forms a chromatophor that is quantified at 562 nm in a spectrophotometer. Iron standards of a known concentration are prepared and an iron standard curve is generated. Sample measurements are compared to the iron standard curve.

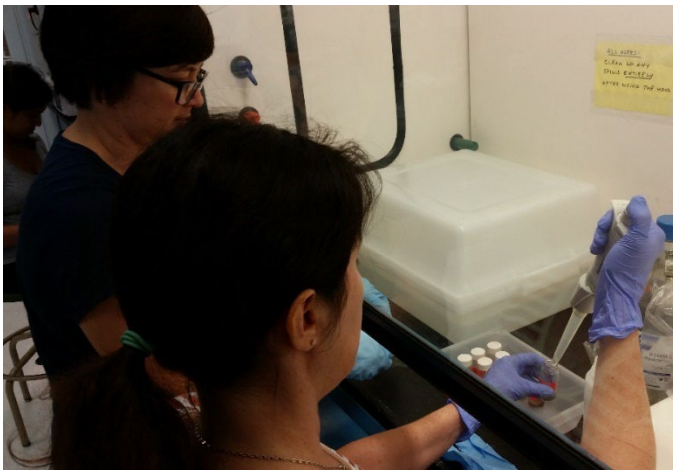

Figure 6. 12: Preparation of acid digests for ferrozine analysis.

An iron standard curve was prepared each time new field samples were measured; duplicate measurements were made in the spectrophotometer to ensure repeatability of measurements. Hydroxylamine hydrochloride was added to samples to reduce all Fe^{3+} to Fe^{2+} to measure total iron content. Fe^{3+} is calculated by subtracting the total iron content from the Fe^{2+} content.

6.3.9 Magnetic susceptibility

Magnetic susceptibility (MS) measures the degree of magnetization of a material in response to an applied magnetic field. Samples can either be diamagnetic, paramagnetic or ferromagnetic. Diamagnetic samples are characterized by negative susceptibilities and repel the applied magnetic field; paramagnetic samples are characterized by small positive susceptibilities; ferromagnetic samples are characterized by large positive magnetic susceptibilities. Generally, iron content is correlated with magnetic susceptibility.

Figure 6. 13: Bartingston MS2K sensor measuring MS on a HC core.

Measurements were primarily acquired with a Bartington MS2K handheld surface sensor which operates at a frequency of 0.93 kHz. As the volume measured by this sensor is not well constrained, it only gives a relative measure of magnetic susceptibility The top and bottom of dry and saturated (low conductivity solution) cores were measured (Figure 6. 13). Some measurements were also acquired using a Terraplus KT-20 owned by U Guelph, which can measure at frequencies of 10 kHz and 100 kHz. The MS was measured at these frequencies on dry cores for a top and side orientation. U. Guelph acquired the KT-20 during year 2 of the project, such that measurements were not collected on many of the HC and SSFL cores (Appendix B.4, Table 3).

6.4 Geophysical measurements on rock cores

6.4.1 Nuclear magnetic resonance (NMR)

Measurements were acquired on a RN owned 2 MHz NMR Rock Core Analyzer (RoCA) (Magritek) (Figure 6. 14). Saturated cores were wrapped in parafilm and fitted securely within the sample holder provided with the instrument. T2 Carr-Purcell-Meiboom-Gill (T2CPMG) (Carr & Purcell, 1954; Hahn, 1950; Meiboom & Gill, 1958) experiments were performed on each subcore after saturation with low and high conductivity solutions. Data were collected at echo times of 150, 200, 300, 400, 600, 800, 1000, 1200 and 1500 µs. The collection of data at long echo times allowed for a comparison of laboratory results with NMR borehole logging measurements. The multiple echo time data were also used to select the best smoothing coefficient in the multiexponential inversion of the T2 decays (described below). The number of stacks for all echo times was determined as the number of stacks necessary for a signal-to-noise ratio (SNR) equal to 200 for an echo time of 200 µs. To ensure thermal equilibrium, the time between stacks (i.e. the delay time) was set as a multiple of three of the time required for the NMR signal to decay to zero.

Figure 6. 14: RoCA instrument used to collect all NMR data.

To capture the NMR signal of immobile versus mobile water content, low and high conductivity saturated samples were centrifuged at 5000 rpm for 15-minute cycles until no liquid was extracted. T2CPMG experiments were then repeated.

Before inverting the multiexponential decays, the raw T2 decay data were corrected to remove the parafilm signal. A non-negative least square algorithm was used to fit the data to 160 logarithmically spaced T2 values, from 0.1 ms to 10 s. The inverted model was included a smoothness constraint that was selected by finding the minimum residual norm for a range of smoothing constraints and then comparing this value across echo times and also a given site and borehole. Based on this evaluation, a single value of the smoothness constraint was selected for a given site (Figure 6. 15).

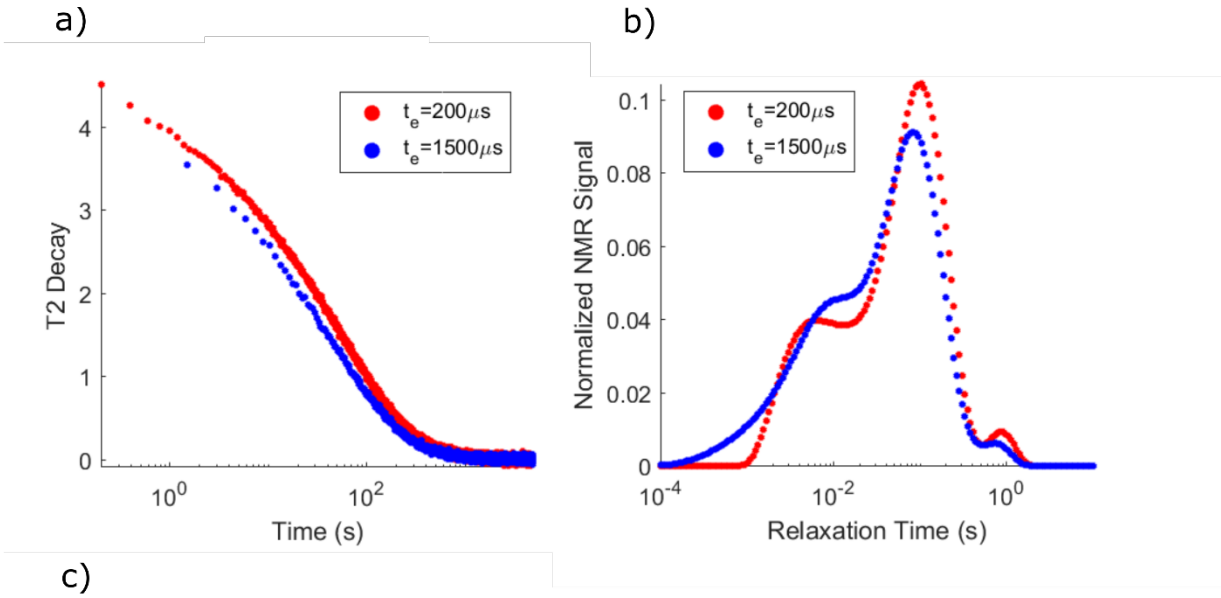

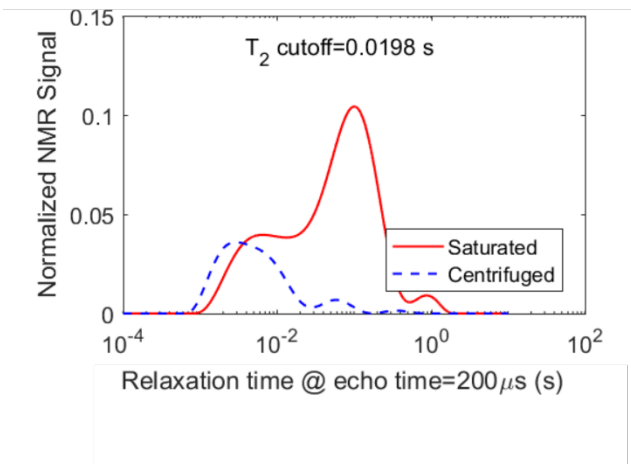

Figure 6. 15: Sample HC-MP24S-P001V data shown a) Raw T2 decay from echo times 200 and 1500 µs; b) Inverted T2 distributions corresponding to raw data in a); c) Fully saturated T2 distribution (also shown in red in b) compared to centrifuged T2 distribution. The T2 cutoff time distinguishes the mobile from immobile fractions of the pore space. Appendices B.1 and B.2 show data for all samples.

6.4.2 Complex resistivity (CR)

All complex resistivity (CR) measurements were acquired with a Portable Spectral Induced Polarization (PSIP) (Ontash & Ermac (O&E)) unit owned by RUN. The sample holder used (Figure 6. 16) consisted of two end caps filled with fluid with the rock core sample placed in the middle. Two silver (Ag) coiled current electrodes were used along with two silver-silver chloride (Ag/AgCl) potential electrodes.

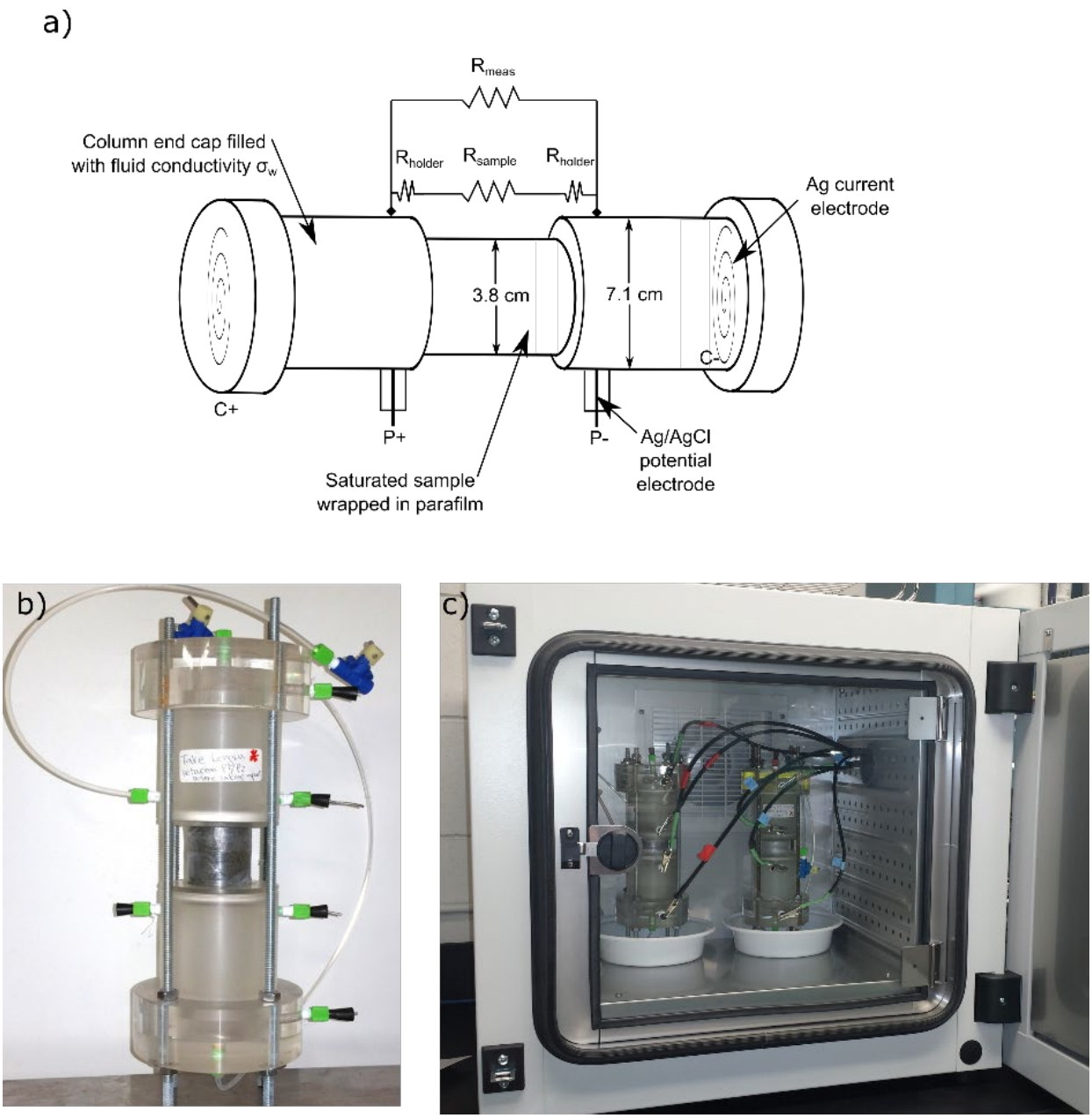

Figure 6. 16: a) Schematic of CR sample holder used for data collection. A geometric factor correction was necessary to account for the geometry of the sample holder b) Sample setup within a sample holder c) CR data collection in environmental chamber.

The sample holder was placed within an environmental chamber set to 25°C. In order to ensure equilibration of temperature and ion exchange processes between saturating pore fluid and mineral surface, measurements were collected twice daily until the difference between a previously collected measurement of both the resistance and phase was less than 2% (1 Hz was used to quantitatively compare successive measurements, but the entire spectrum was visually inspected for consistency). This took approximately one week following sample saturation. Measurements were recorded over a frequency range of 10^{-3} to 10^{3} Hz, with five measurements

per decade of frequency, for a total of 36 measurements (Figure 6. 17). Resistance data were converted to complex conductivity (the inverse of complex resistivity) using the geometric factor for the sample holder experimentally determined from measurements on water samples of precisely known complex conductivity.

6.4.3 Electrical Formation Factor F

The electrical formation factor F is a measure of the influence of pore structure on the bulk conductivity of a sample; it represents the reduction in fluid conductivity due to the porosity and tortuosity of a sample. Mathematically, F is defined as the ratio of the fluid conductivity σ_w to the bulk conductivity of the rock σ_b. At very high salinities, it can be assumed that surface conduction is low and σ_b is equal to σ'. Samples were saturated with a high salinity salt (NaCl) solution with a fluid specific conductance equal to 80 mS/cm. The same procedure used to collect low salinity CR data was used to collect high salinity CR data. The top and bottom fluid chamber conductivity σ_w (Figure 6. 17) was averaged when the CR data collection was complete and this averaged value was used to calculate F. The real conductivity σ' at 1 Hz was used in the calculation.

6.4.4 Electrical Tracer Experiments

A tracer experiment was used to investigate whether mass transfer between less-mobile and mobile pores/fractures could be quantified in rock cores using a recently proposed electrical methodology (Briggs et al., 2014). Whereas conventional fluid sampling is sensitive only to the mobile concentration, bulk electrical measurements are sensitive to both mobile and immobile concentration; thus a time-varying or hysteretic relation between bulk and fluid conductivity during ionic tracer breakthrough can develop as a signature of anomalous transport. The combination of tracer tests and geophysical monitoring has the potential to improve inference of dual-domain parameters (Briggs et al., 2014; Briggs et al., 2013; Day-

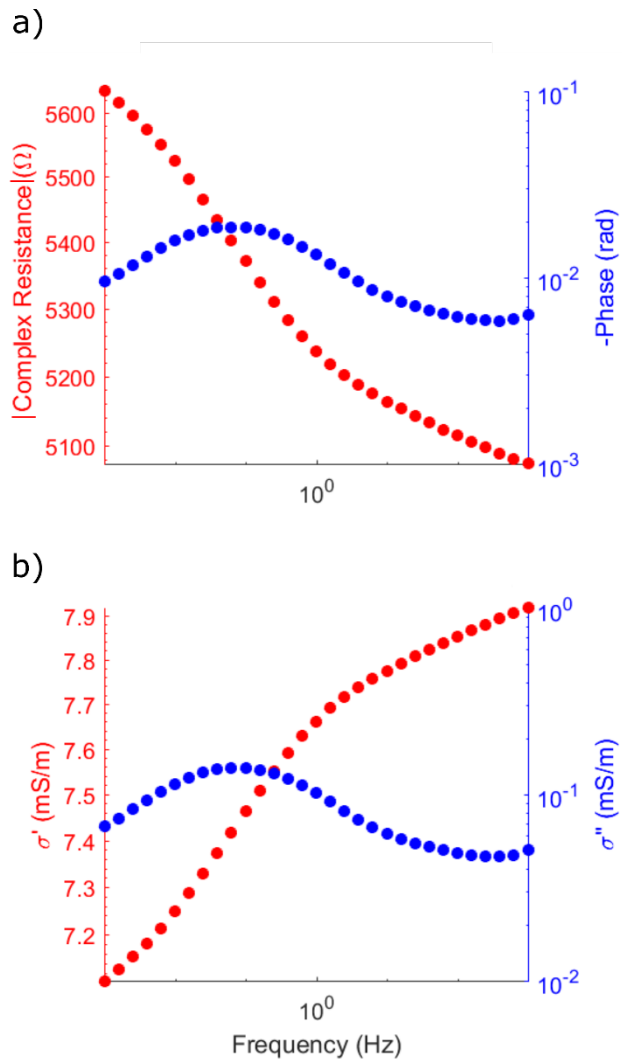

Figure 6. 17: Sample HC-MP24S-P001-1V data showing a) raw complex resistance and phase data b) real σ' and imaginary σ'' conductivity calculated after applying the geometric factor. Data for all samples can be found in Appendix B.1 and B.2.

Lewis & Singha, 2008) and characterization of contaminant storage and release in fractured rock. In this effort, we adapt and apply these experimental approaches to fractured-rock cores for the first time. The mathematical model for solute transport and its solution are presented in Section 6.5.

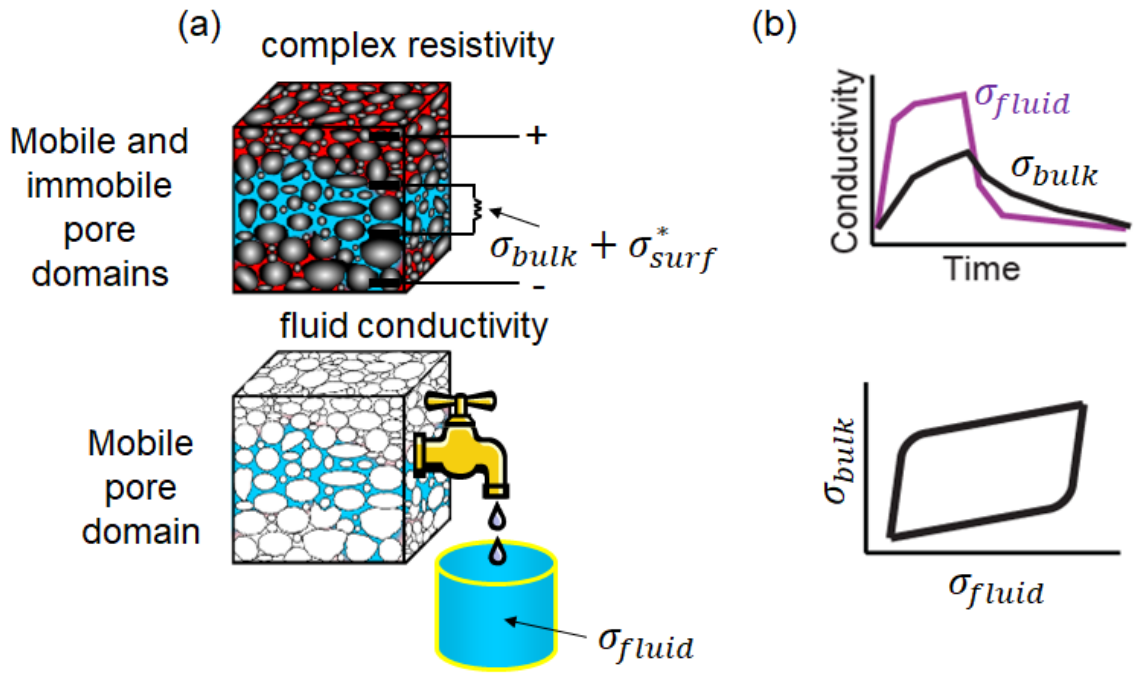

Figure 6.18: (a) basic concept that complex resistivity senses the conductivity of both the mobile and immobile pore domains (and also surface conduction) whereas specific conductance just measures the conductivity of the pore fluid (b) conceptual representations of breakthrough curves of bulk conductivity and fluid conductivity with resulting hysteresis loop.

Singha et al. (2007) developed a bicontinuum extension to Archie's Law (Archie, 1942) assuming (1) that mobile and immobile domains are filled with water of electrical conductivity σ_m and σ_{im}, respectively, and behave as conductors in parallel (i.e. with volume-weighted arithmetic averaging); and (2) surface conduction is negligible:

$$\sigma_e = (\theta_m + \theta_{im})^{m-1}(\theta_m\sigma_m + \theta_{im}\sigma_{im}), \tag{6.3}$$

where σ_e is effective bulk conductivity [μS/cm] and m [-] is Archie's cementation exponent, which is a function of pore connectivity and tortuosity. (In our notation the subscript 'm' indicates mobile, as in Equation 1, whereas the cementation exponent, m, is a variable, and thus italicized.) This petrophysical model has been used to qualitatively reproduce field data (Singha et al. 2007) and calibrate numerical and analytical models (Briggs et al., 2013, 2014). Figure 6. 18 shows a schematically simple, graphical approach to estimating dual-domain parameters from combined tracer and electrical measurements. Based on the shape of the hysteretic bulk/fluid conductivity relation (Figure 6. 19(a)), the ratio, β, of immobile:mobile porosity is easily obtained. Based on the change in bulk conductivity versus time, as the two domains approach

equilibrium, the rate coefficient, α, governing mobile/immobile exchange can be obtained (Figure 6. 18(b)).

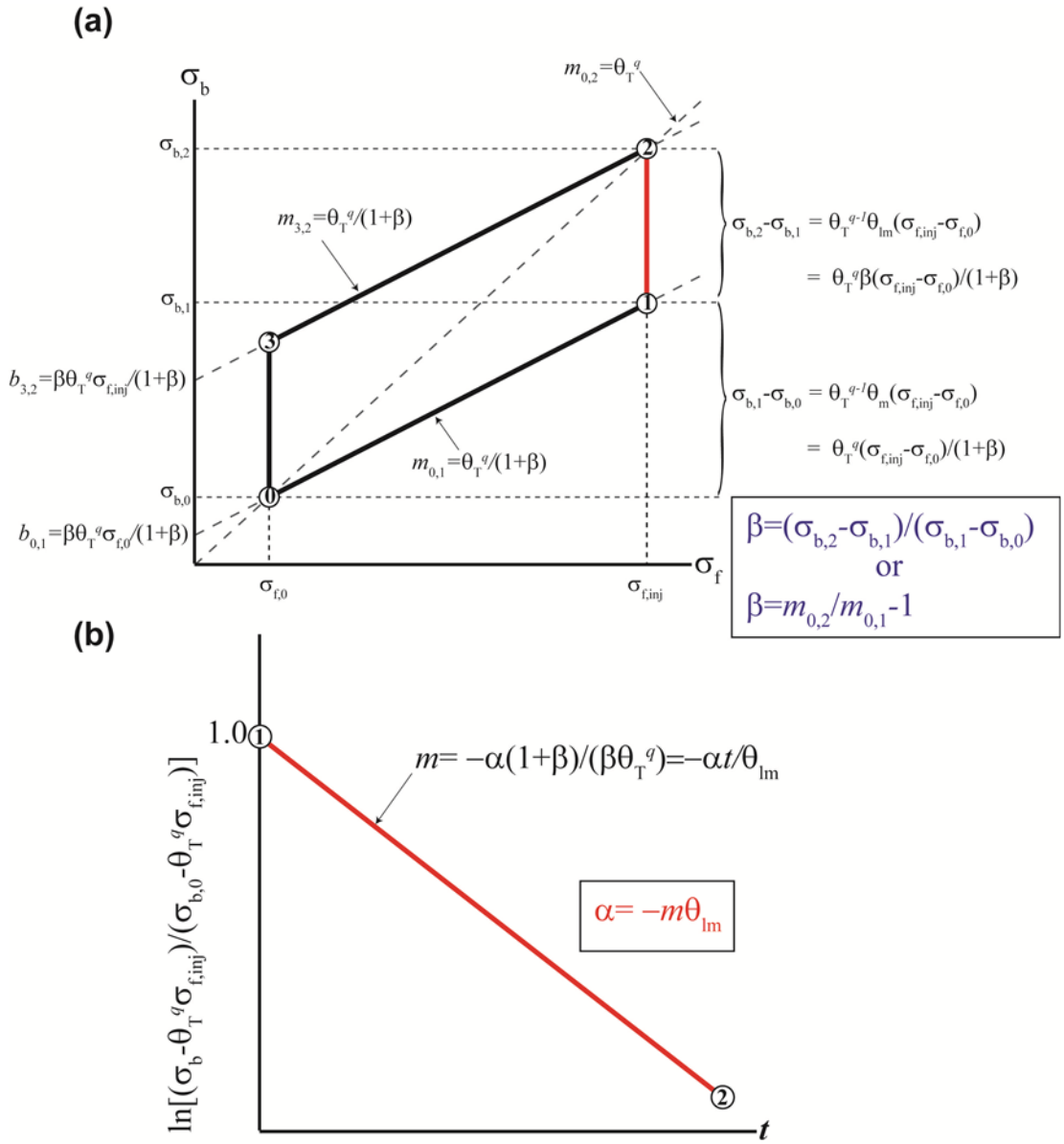

Figure 6. 19: From a plot (a) of bulk conductivity (σ_b) vs. fluid conductivity, σ_f, it is possible to infer the ratio, β, of immobile porosity, θ_{lm}, to mobile porosity, θ_m. From a semi-log plot (b) of normalized bulk conductivity vs. time, t, it is possible to infer the rate coefficient, α, governing exchange between mobile and immobile porosities based on the slope, m, of the best-fit line. This approach was first presented and applied to experimental data in Briggs et al. (2014).

While the methodology outlined in Briggs et al. (2014) is designed around measuring the σ_e, the design of this experiment expands on the previous methodology to measure the relationship between the complex conductivity and fluid conductivity σ_f during tracer breakthrough. Complex resistivity, $|\rho|$, measurements were acquired to determine $|\sigma|$ using the complex resistivity instrumentation described previously (see Section 6.4.2). σ_f measurements were

acquired using conductivity flow through cells. Data collected from these samples were then characterized using a dual-domain porosity model as defined in Singha et al. (2007) (Figure 6. 19).

Flow through chamber design: The tracer experiment is performed on rock cores using a flow through chamber custom-built for this project, outlined in Figure 6. 20, designed with the capability to simultaneously collect complex conductivity and σ_T measurements. The chamber is designed around a Hassler sleeve core holder. A polyurethane rubber tube with a wall thickness of 1.25 cm is used to isolate a core. The tube containing the core is then installed within a steel casing with an internal diameter of 8.25 cm and a wall thickness of 1.25 cm. Polycarbonate inserts are installed on either end of the tube to secure the core and tube within the chamber, and to form the end caps of the confining pressure volume around the tube. The confining pressure volume is filled with hydraulic oil (iso grade 32) and pressurized using a hand operated pressure generator. The inserts on either side of the core are designed to act as an influent and effluent chamber (2.5 cm x 12.5 cm), which also serve as the fluid chambers to house the current injection and potential electrodes for the complex resistivity measurements. A sampling tube, used for collecting fluid conductivity measurements of the core fluid, is imbedded in the polyurethane rubber tube halfway along the length of the core and is routed out of the steel casing to a flow through cell containing a fluid conductivity sensor. Additional fluid conductivity sensors are imbedded in the ends of the polycarbonate inserts to measure the fluid conductivities within the influent and effluent chambers during the course of the experiment.

Fluid conductivity measurements: Fluid conductivity is measured with flow through cells consisting of 1 cm offsets, and a cell geometric factor of ~1 cm^{-1} determined from a 1 cm electrode offset. Three cells are used to collect fluid conductivity measurements: one installed at the sampling port halfway along the length of the core and two imbedded within the influent and effluent chambers. Measurements on the conductivity cells (Microelectrodes, Inc.) are logged using conductivity circuits (Atlas Scientific) and a Raspberry Pi.

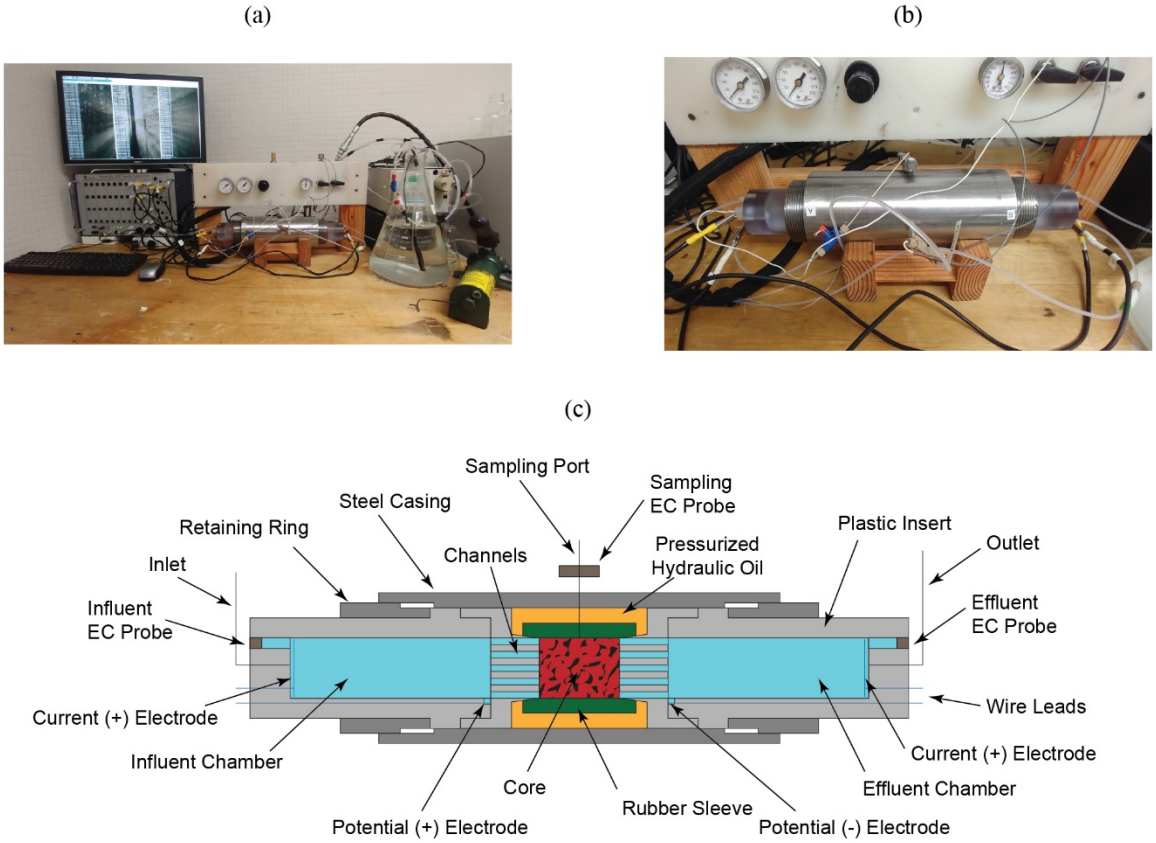

Figure 6. 20: The tracer experiment apparatus developed in this project (a), including the sample chamber (b) and schematic (c) developed to investigate the electrical signatures of mass transfer.

Complex resistivity measurements: Complex resistivity measurements are acquired using 1 cm^2 silver electrodes as potential electrodes installed 2.5 cm from the core surface on the wall of the influent and effluent chambers (Figure 6. 20). These electrodes are positioned at the bottom of the chambers in order to eliminate the possibility of interference from air bubbles, and are recessed 1 cm in order to assure that the electrodes were not in the current flow path. Current is applied to the chamber from circular silver electrodes, with a diameter of 2.5 cm. The $|\rho|$ response is measured at 1 Hz.

Sample preparation: Five cores were selected for analysis using the tracer experiment: SS-C3-P-019, SS-C3-P-022, HC-MP24S-P-007-2H, HC-MP24S-P-004-2H, and HC-MP24S-P-006-1V. Cores are originally saturated with a high conductivity solution referred to here as the saturating fluid (~80,000 µS/cm). Samples were saturated using the method described in Section 6.3.4. The saturating pressure (i.e. 2000 psi) used was higher than that used to originally saturate the cores Table 6. 1. This pressure was held for 3 days.

Experimental design: Following saturation, the cores are installed in the Hassler core holder and confining pressure is set to 3x the highest possible influent fluid pressure in order to eliminate external flow around the core (~300 psi). An HPLC (High-Performance Liquid Chromatography)

pump is used to inject the fluid into the flow through chamber at the desired influent fluid pressure. The saturating fluid is first injected into the chamber at pressures greater than atmospheric (up to ~100 psi) in order to obtain steady effluent and sampling port flow rates ideal for observing the non-linear relationship between $|\sigma|$ and σ_{EC} expected for samples exhibiting mass transfer associated with dual-domain porosities. This process takes between 2-3 weeks depending on the sample.

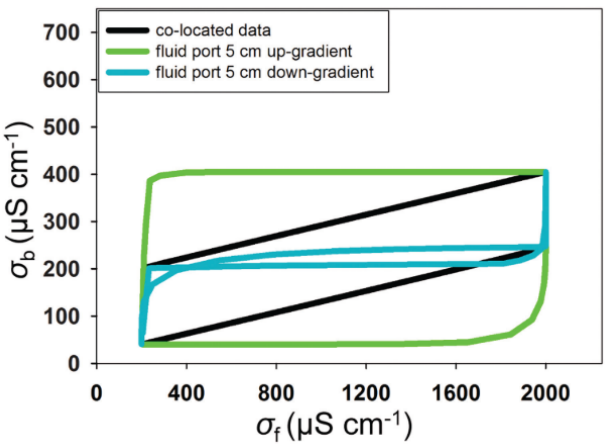

Figure 6. 21: Modelled hysteresis loops affected by data colocation issues (Modified from Briggs et al. 2014).

The tracer experiment is organized into three phases: the initial phase, the tracer flush phase, and the tracer injection phase. In between each phase, the fluid in the influent reservoir is drained and refilled with the injection fluid for the next phase. During the course of each phase, σ_T measurements were collected from the influent, effluent and sampling port using the EC probes, and ρ^* (i.e. $|\rho|$ and Φ) is collected using SIP. These measurements are collected at 8 second intervals. For the initial phase, the injection fluid used is the saturating fluid. The injection fluid is cycled through the cores for several hours to obtain baseline complex resistivity and fluid conductivity measurements. This process continues until all conductivities are determined to be stable for >1 hours. During the tracer flush phase, the injection fluid used is ~8,000 µS/cm. This fluid is injected into the cores over the course of 2-3 days. The tracer flush phase is terminated when the effluent σ_{EC} is stable and approximately equal to the injection fluid for at least 1 hour. During the tracer injection phase, the injection fluid used is the saturating fluid. This fluid is injected into the core over the course of 2-3 days. The tracer injection phase is terminated when the effluent σ_{EC} is stable and approximately equal to the injection fluid for at least 1 hour.

There are several sources of uncertainty that have to be addressed to assure accurate data interpretation. In most cases, post-processing strategies have been implemented to correct these issues. A thorough explanation of these uncertainties, and their associated corrections when possible, are described below.

Effect of co-location of data: Previous investigators have explained the effect of measuring the fluid conductivity at different locations to the complex electrical measurements during tracer injection tests (e.g. Briggs et al. 2014; Briggs et al. 2013). An example of this effect is outlined in Briggs et al. 2013 (Figure 6.4. 8). In this example, the measured hysteresis loop is obscured by the time period required for the different methods to respond to changing pore conductivities. The data collected from the apparatus used in this study had a similar issue, in which the SIP measurement was instantly sensitive to changes in the internal conductivity of the samples, while

the EC probe required an initial period of time before registering an associated response. In this scenario, the breakthrough curve associated with the EC probe would lag behind the breakthrough curve associated with the SIP measurements, resulting in data that resembles the blue loop plotted in Figure 6. 21.

A correction of this effect was implemented for the data in this study to numerically collocate the breakthrough curves, detailed in Figure 6. 22. This process involved interpreting the temporal offset exhibited by the EC breakthrough curve and subtracting it from the EC data (Figure 6. 22(a-b)). An example hysteresis loop from an example dataset is shown, alongside its corrected loop in Figure 6. 22(c). These datasets (both corrected and uncorrected) closely resemble the datasets in Figure 6. 21.

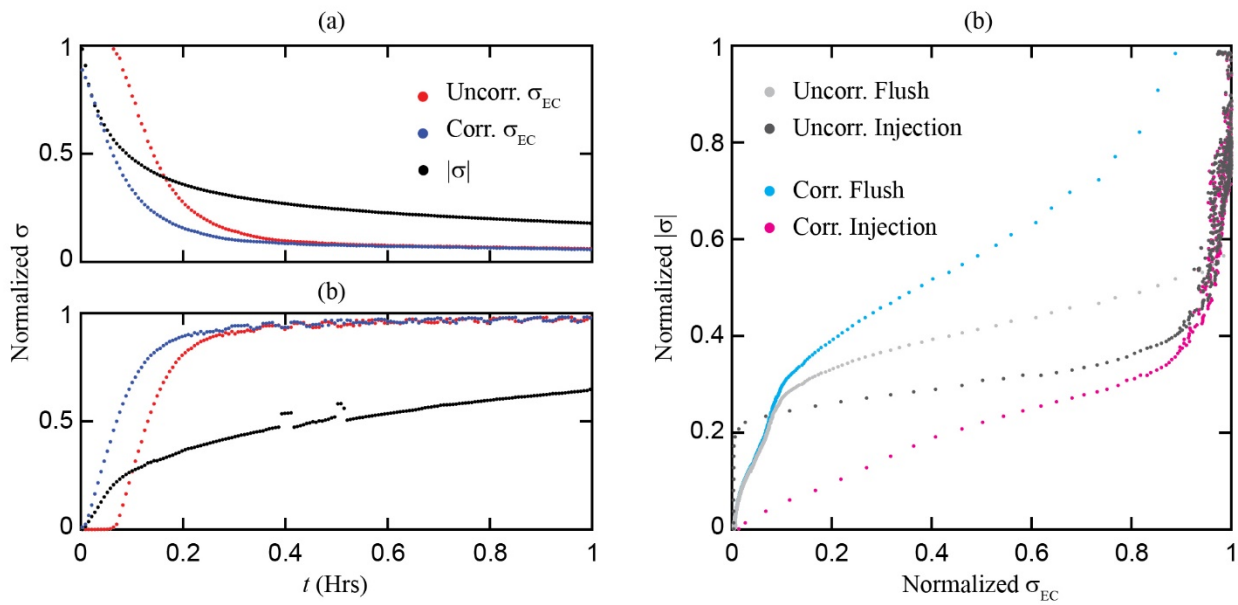

Figure 6. 22: An example of the colocation correction for (a) tracer flush and (b) tracer injection experiments (plotted over the first hour of the experiment). Also shown is (c) the resulting effect this correction has on the hysteresis curve, producing similar results as described in Briggs et al. (2014). Jumps in the data are due to the effect of bubbles on EC probe measurements.

Effect of variable fluid conductivity on SIP measurements: SIP sample holders for rock core analysis typically use a chamber of fluid on either side of a saturated core, which contain the current injection and potential electrodes (see Section 6.4.2). This configuration is used to assure 1D current flow through the sample core, and to assure that the entire volume of the core is measured, improving data quality. While these types of sample holders are ideal for obtaining

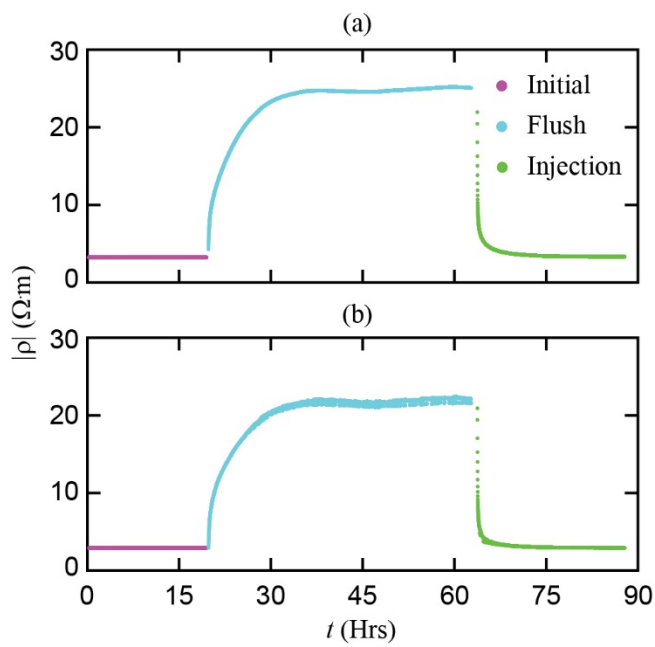

Figure 6. 23: A comparison of the (a) uncorrected and (b) corrected complex resistivity breakthrough curves as measured using SIP and corrected from EC probes located in the influent and effluent chambers. Increased noise evident in the corrected flush curve is due to bubbles effecting the effluent EC probe.

quality SIP data, for the purposes of the tracer injection experiment, the presence of the fluid reservoirs created data interpretation issues and uncertainty.

The modified version of this type of sample holder, as outlined in Figure 6. 20, increased the volume between the core and potential electrodes in order to support the Hassler Core holder tube, resulting in larger geometric factor corrections. Because the fluid chambers were additionally used as the influent and effluent chambers during tracer injection, the conductivity of the fluid within these chambers varied during the experiment. This variation in the conductivity made correcting for the geometric factor more difficult as the effect of changes in the conductivity of the reservoir fluid directly effects the geometric factor correction.

In order to account for this effect, the geometric factor was measured according to the procedure outlined in previously in section 6.4. The data associated with the geometric factor calculation for the apparatus used in the tracer experiment (Figure 6. 20) is shown in Figure 7. 14. This data is then used to calculate a fluid conductivity dependent geometric factor for each reservoir by,

$$R_{inf} = \rho_{inf} C_c \tag{6.4}$$

$$R_{eff} = \rho_{eff} C_c, \tag{6.5}$$

where, R_{inf} and R_{eff} are the influent and effluent corrections to the measured R, and C_c is the geometric factor of the sample holder excluding the effect of the core, which is defined as l/A. The total geometric factor, C_e, is therefore,

$$C_e = {}^{l}/_{A} + 2C_c, \tag{6.6}$$

assuming C_c is identical for both sides. After measuring C_e with the sample holder filled with a fluids of known conductivity, C_c can be calculated by taking into account the core dimensions (l and A) and the slope of the linear regression, m,

$$C_c = \frac{1}{2}\left(\frac{R_\rho}{\rho_f} - \frac{l}{A}\right) = \frac{1}{2}\left(m - \frac{l}{A}\right). \quad (6.7)$$

R_{inf} and R_{eff} can then be calculated using values of σ_{inf} and σ_{eff} measured from the influent and effluent chambers during the experiment.

During the tracer injection curve, the fluid conductivity in the influent and effluent reservoirs are monitored using separate EC probes mounted in the walls of each chamber (i.e. influent and effluent EC probes). These probes were logged at the same frequency as the SIP and EC probes, and used in equation 6.7 to determine the geometric factor for each SIP measurement collected during the tracer injection experiment. These factors were then used to calculate the fluid dependent geometric factor for correcting the complex resistivity data. A comparison of the corrected SIP datasets and their uncorrected equivalents are shown in Figure 6. 23. The effect of variations is evident in jumps between the end of one phase of the experiment and the beginning of the next (i.e. the points associated with the end of the initial phase and beginning of the flush phase). Correcting the SIP measurements in this way reduces this effect, resulting in more continuous datasets between phases.

Flow rate irregularities: Decreases and increases in flow rate through the fluid EC probe or through the rock core have the potential to increase and decrease the breakthrough associated with the cores, resulting in significant uncertainty. This effect was managed by using flow regulating valves to assure a constant flow through from both the effluent and sampling port. Because the run time of the experiment was a week, the flows had to be equilibrated for a long time prior to the tests, sometimes taking up to three weeks in advance depending on the sample. During the experiment, the flow rates (and ratio of flow rates) was monitored visually (i.e. counting bubbles over time) in order to determine detrimental changes in the flow rates.

Air bubbles: The presence of air within the system resulted from a number of sources, including failing fittings, seals, and imperfect saturation of test cores. Potentially the largest source of air was from chlorine gas production due to the presence of a DC offset inherent in the PSIP instrument. Generally this occurrence was not significant throughout the course of the experiment. Due to the low volume of the EC probes, however, any air bubbles passing through them resulted in anomalous spikes in the data. An example of these anomalies is inherent in the data shown in Figure 6. 22. While a despiking filter can effectively remove affected data, such a filter would remove a significant amount of data points. Despiking of the datasets was therefore not carried out as the presence of these spikes does not affect the ultimate data interpretation.

6.5 Modeling of transport and electrical measurements

In this work, pore-scale mechanistic modeling provides the link between hydrologic measurements, geophysical measurements, and the fundamental processes controlling contaminant storage and release in fractured rock. We use computer models, based on the work of Day-Lewis et al. (2017) and Briggs et al. (2015) to simulate flow, transport, and electrical geophysical measurements, and we use data-analysis methods first presented by Briggs et al. (2014). First we review field-scale approaches to simulating contaminant retention and release in

fractured rock. Second, we briefly introduce the theory and numerical modeling scheme to simulate hydrologic and geophysical measurements at the pore scale based on advection and diffusion and no a priori assumption of dual-domain behavior.

6.5.1 Models of contaminant transport in fractured rock

Computer models (e.g., MT3DMS by Zheng & Wang, 1999) describing field-scale contaminant transport in fractured rock commonly use a dual-porosity (also known as dual-domain or mobile/immobile) formulation (e.g. Feehley et al., 2000; Haggerty & Gorelick, 1995). In such models, the fractured-rock aquifer is conceptualized as comprising (1) the well-connected transmissive fractures (i.e., the mobile domain), in which advection and dispersion occur, and (2) the poorly connected or otherwise flow-obstructed pores and (or) dead-end fractures (i.e., the immobile domain or less-mobile domain). Exchange between the domains is commonly represented by diffusion. Here, for generality we use the multi-rate mass transfer (MRMT) formulation of (Harvey & Gorelick, 1995), in which the immobile domain is divided into N compartments. In the absence of sorption, one-dimensional (1D) transport is described by a system of $N+1$ partial differential equations:

$$\theta_{\mathrm{m}} \frac{\partial C_m}{\partial t} + \sum_{j=1}^{N} \theta_{\mathrm{im},j} \frac{\partial C_{im,f}}{\partial t} = \theta_{\mathrm{m}} D \frac{\partial^2 C_m}{\partial x^2} - \theta_{\mathrm{m}} \frac{\partial (C_m v)}{\partial x}, \tag{6.8}$$

$$\frac{\partial C_{im,f}}{\partial t} = \alpha_j \left(C_{\mathrm{m}} - C_{\mathrm{im},j}\right), j = 1, \dots, N \ , \tag{6.9}$$

where α_j is the rate coefficient for immobile compartment j; C_{m} is the mobile-domain concentration [M/L^3]; $C_{\mathrm{im},j}$ is the concentration in compartment j associated with rate j [M/L^3]; D is the molecular diffusion coefficient [L^2/T]; v is the pore water velocity [L/T]; θ_{m} is the mobile-domain porosity [-]; $\theta_{\mathrm{m},j}$ is the porosity comprising immobile compartment j; and t is time [T]. MRMT allows for residence in the immobile domain to occur over a broad range of spatial and temporal scales. For a single-rate mass-transfer (SRMT) formulation, Equation 6.9 reduces to one equation.

In fractured rock aquifers, conventional sampling draws fluid from the mobile domain and provides limited insight into total contaminant mass, which is largely stored in the rock matrix; this behavior is accounted for mathematically in Equation 6.8-9, with mobile concentration representing mass that would be sampled from fractures, and immobile concentration representing mass that would be in the rock matrix.

In analyzing tracer data (Section 6.4), we use an analytical solution to Equation 6.8-9, representing all diffusion as mass transfer, and effectively setting D_m=0; this approximation allows for a simple Laplace-domain solution (Day-Lewis et al., 2017):

$$\tilde{C}_{\mathrm{m}} = C_{\mathrm{inj}} \left[\frac{1}{s} - \frac{1}{s} exp(-T_{\mathrm{off}} s)\right] exp\left[\frac{-xs}{v}\left(1 + \sum_{i=1}^{N} \frac{\alpha_i \beta_i}{\alpha_i + s}\right)\right] H(x) + C_0 \ , \tag{6.10}$$

$$\tilde{C}_{\mathrm{im}} = \frac{\alpha_i \beta_i}{\alpha_i + s} \tilde{C}_{\mathrm{im}} + C_0 \ , \tag{6.11}$$

where $\tilde{C}_{\mathrm{m}}$ and $\tilde{C}_{\mathrm{im}}$ are the Laplace-transformed mobile- and immobile-domain concentrations, respectively; H(x) is the Heaviside function; v is average linear pore fluid velocity; T_{off} is the

time at which injection of tracer ends and flushing begins; N is the number of immobile compartments for the non-parametric distribution of rate coefficients; β_i is the distribution coefficient for immobile compartment i, given by $\theta_{\mathrm{im},i} / \theta_{\mathrm{m}}$; and C_0 is the initial concentration, equal in both domains and uniform within each immobile compartment; and s is the Laplace parameter.

6.5.2 Pore network modeling

We investigate the micro-scale geoelectrical signature of mass transfer using a pore-network model (PNM) with a pipe-lattice representation of the pore space. PNMs have been used extensively in studies of petrophysics (Bernabé et al., 2011; Bernabé & Revil, 1995; Jin & Sharma, 1991; Moysey & Liu, 2012; Suman & Knight, 1997) and solute-transport (e.g. Bijeljic & Blunt, 2007; De Arcangelis et al., 1986). Our approach to the electrical conduction problem amounts to solving a circuit problem (e.g. Greenberg & Brace, 1969), based on Ohm's Law and the architecture of the pipe network. For the transport problem, we solve for temporal moments of concentration rather than for concentration itself (Harvey & Gorelick, 1995), thereby reducing computational requirements and providing direct insight into mass transfer.

Our modeling approach is illustrated schematically in Figure 6. 24, briefly summarized here, and explained in detail Day-Lewis et al. (2017) and Briggs et al. (2015). In Step 1, we generate a regular two-dimensional (2D) pipe lattice. In Step 2, we solve the network flow problem for hydraulic head and calculate inter-pore flows according to the Hagen-Poiseuille Law. In Step 3, we solve a series of transport problems to calculate the advective-diffusive residence time for every pore and then assign pores to mobile or immobile domains based on a clustering algorithm. In Step 4, we solve a diffusive transport problem for each immobile region in the PNM to calculate the effective mass-transfer rate coefficient associated with each region; these rate coefficients are taken as the distribution of α_i in Equation 6.8-9. In Step 5, we solve Equation 6.8-9 using a semi-analytical model to simulate a column tracer experiment and produce mobile- and immobile-domain fluid-conductivity time series, which are used to calculate electrical conductances. In Step 6, we solve the electrical problem and calculate bulk conductivity through time, thereby producing the relation between bulk conductivity and fluid conductivity in the mobile domain.

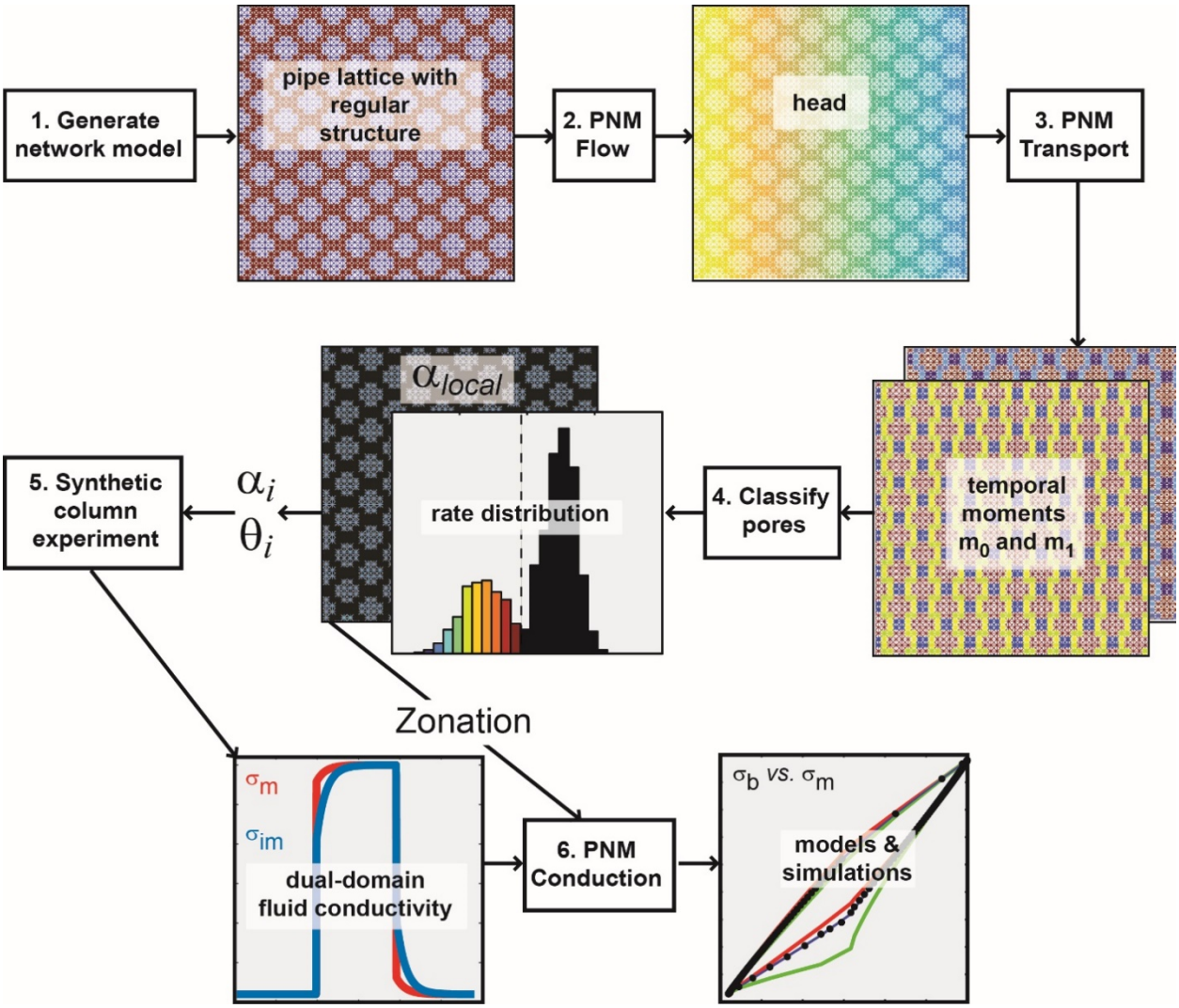

Figure 6. 24: Schematic diagram illustrating our 6-step pore-network modeling approach to simulate the geoelectrical signature of solute transport through dual-domain geologic media.

6.6 Field-scale borehole data

6.6.1 Borehole Logging

Borehole geophysical logs were collected at the Hydrite site, Santa Susana Field Laboratory (SSFL), and the former Naval Air Warfare Center (NAWC) (Figure 6. 25). Different suites of logs were collected as part of site characterization and the individual research initiatives at the three sites. Standard logs (as described in Johnson et al., 2011 and Day-Lewis et al., 2017) and specialized logs collected within each borehole are shown in Table 6. 2.

Figure 6. 25: a) Collection of standard logs in NAWC 94-BR – photo showing the lowering of the full-wave form sonic tool into the borehole and b) Collection of NMR in 94-BR – photo showing the NMR tool with fixed magnets being pushed through the steel casing into the open section of the borehole.

Table 6. 2: Borehole logging methods used in selected boreholes at Hydrite, Santa Susana, and NAWC

Methods	**Hydrite**		**SSFL**			**NAWC**
	MP 24S	**MP25S**	**RD-109**	**C3**	**C4**	**94-BR**
Gamma *	G	G	G	G	G	U
Mechanical caliper	-	-	-	-	-	U
Electromagnetic induction (EMI)	G	G	G	G	G	U
Acoustical televiewer (ATV)	G	G	G	G	G	U
Acoustic reflectivity	D	D	D	D	D	D
Acoustic caliper	D	D	D	D	D	D
Optical televiewer (OTV)	-	-	-	-	-	U
Deviation	G	G	G	G	G	U
Full-wave form sonic	G	G	G	G	G	U
Fluid temperature and conductivity	U	U	G	G	G-	U+
Heat-pulse flowmeter (FM)	-	-	-	-	-	U+
Temperature vector probe	G	G	G	G	G	-
Normal resistivity Spontaneous potential (SP) Single point resistance (SPR)	U	U	U	U	U	U
Induced polarization (IP)	U	U	U	U	U	U
Nuclear magnetic resonance (NMR)	U	U	U	U	U	U
Magnetic Susceptibility (MSUS)	U	U	U*	U*	U*	U

(G, Guelph; U, USGS Branch of Geophysics; D, derivative or computed log; * Collected by both; -, Not collected; + Collected under ambient and stressed conditions)

Borehole logs (ATV, OTV, and mechanical caliper) were used to identify the intersection depths and the orientation of the fractures and lithologic contacts. Borehole deviation logs were used to correct the orientations of structural features observed in the OTV and ATV image logs. The median value of the ATV acoustic reflectivity, which was computed for each 0.02-ft depth interval, provides a continuous log (in millivolts) that indicates the hardness of the rock at the borehole wall. Fracture locations are indicated by very low reflectivity values. The orientation of fracture locations were determined by visual inspection of the ATV and OTV logs. Fracture locations are shown on the composite plot as a structure log that shows fracture traces. Results are also provided in a table (Table 6. 3).

Table 6. 3: Location and orientation of fractures in borehole 94-BR at the NAWC site in New Jersey

Depth m	Depth ft	Dip Azimuth degree	Dip degree	Description of feature
11.44	37.53	108	6	bottom of casing
11.94	39.18	319	16	major joint or fracture
12.46	40.88	69	10	major joint or fracture
12.53	41.11	142	78	minor fracture
12.55	41.18	54	9	major joint or fracture
12.57	41.24	176	80	major joint or fracture
13.01	42.69	13	23	minor fracture
13.22	43.37	144	66	sealed fracture
13.92	45.67	294	12	major joint or fracture
14.03	46.03	332	17	major joint or fracture
14.19	46.56	323	35	minor fracture
14.66	48.10	151	64	minor fracture
15.1	49.54	144	69	minor fracture
15.31	50.23	128	70	minor fracture
15.62	51.25	142	70	minor fracture
15.75	51.68	308	20	major joint or fracture
15.89	52.14	147	62	minor fracture
16.09	52.79	302	12	minor fracture
16.25	53.32	314	19	minor fracture
18.14	59.52	330	24	minor fracture
18.86	61.88	345	20	major joint or fracture
19.26	63.19	6	23	minor fracture
19.92	65.36	6	24	minor fracture
20.39	66.90	180	29	minor fracture
20.44	67.06	157	74	minor fracture
20.83	68.34	5	11	minor fracture
20.94	68.70	8	24	major joint or fracture
21.18	69.49	303	18	minor fracture
22.01	72.21	356	14	sealed fracture
22.13	72.61	150	70	minor fracture
22.77	74.71	329	31	minor fracture
23.04	75.59	328	23	minor fracture
24.4	80.06	78	45	partial fracture
24.67	80.94	6	22	minor fracture
24.75	81.20	335	26	minor fracture
25.16	82.55	144	73	partial fracture
25.58	83.93	1	42	sealed fracture
25.8	84.65	359	18	minor fracture

26.5	86.95	192	76	minor fracture
26.52	87.01	3	19	minor fracture
26.66	87.47	356	28	major joint or fracture
27.41	89.93	270	62	minor fracture
27.93	91.64	13	21	minor fracture
28.27	92.75	251	62	partial fracture
30.75	100.89	255	85	sealed fracture
31.38	102.96	49	80	sealed fracture
31.39	102.99	23	15	sealed fracture
31.88	104.60	66	28	minor fracture
31.99	104.96	60	12	minor fracture
32.19	105.62	333	74	sealed fracture
33.03	108.37	337	22	sealed fracture
34.73	113.95	171	67	sealed fracture
35.03	114.93	25	15	major joint or fracture
35.07	115.06	159	67	sealed fracture
35.63	116.90	178	72	sealed fracture
35.77	117.36	4	16	major joint or fracture
35.98	118.05	20	18	major joint or fracture
36.85	120.90	328	23	major joint or fracture
37.83	124.12	144	69	partial fracture
39.08	128.22	149	72	sealed fracture
40.08	131.50	354	21	major joint or fracture
40.4	132.55	148	74	partial fracture
41.4	135.83	149	69	minor fracture
41.95	137.64	37	39	partial fracture
42.79	140.39	56	66	sealed fracture
43.47	142.63	223	31	partial fracture
43.58	142.99	54	48	partial fracture

The ATV, gamma, normal resistivity, electromagnetic induction, magnetic susceptibility, and full-waveform sonic logs were used to correlate lithologic units within each borehole and to identify the changes in lithology that might also be associated with changes in porosity and contaminant mass.

Single-hole heat-pulse flowmeter (HPFM) logs were collected under ambient and stressed conditions. Logs were collected during a tropical storm with periods of heavy rain, which complicated the HPFM logging with active recharge and changing ambient conditions. Single-hole HPFM testing can identify directional flow of water moving through the borehole in response to natural or imposed gradients. At NAWC 94-BR water was injected at the top of the well, and downflow was measured to identify out-flow zones. Minor intermittent ambient downflow was recorded at a maximum rate of 0.2 gal/min in 94-BR. Under a uniform injection

rate of 0.4 gal/min, two outflow zones were identified. The HPFM has a minimum measurement rate (0.015 gal/min) and a dynamic resolution (in an open hole) that limits the detection of hydraulically active zones to features that are within 1.5 orders of magnitude of the most transmissive feature in the borehole. The fluid differencing logs, which were used to compare the fluid electrical conductivity and temperature of logs collected under ambient conditions with logs collected under stressed conditions, were helpful for interpreting the HPFM results. HPFM methods provide a means to identify the most transmissive fractures in the boreholes. The temperature vector probe (TVP), which was used at Hydrite and SSFL, has a higher measurement resolution and can provide more detailed hydraulic characterizations along the borehole wall. An example composite log typical of the datasets acquired in this project is shown in Figure 6. 26.

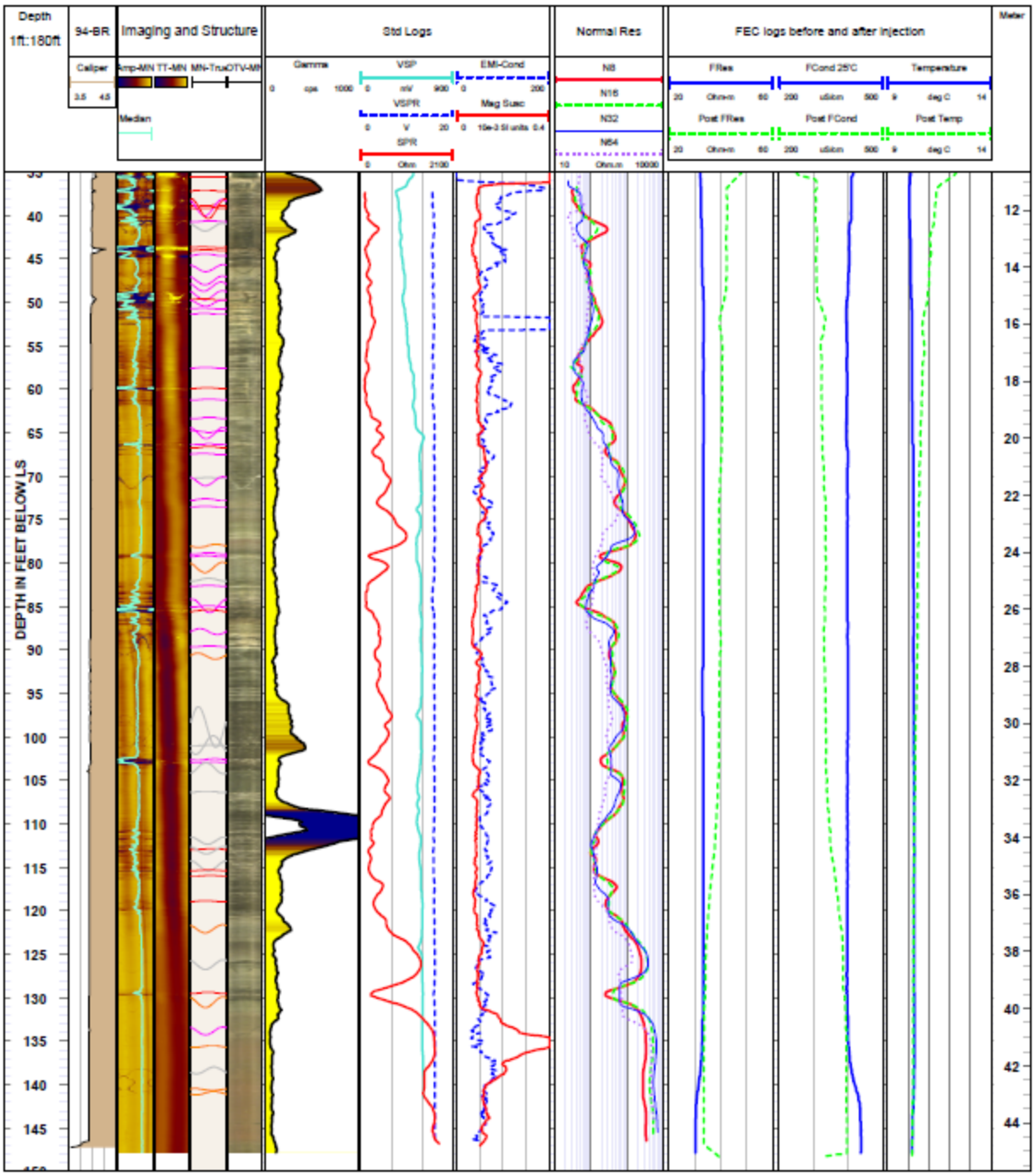

Figure 6. 26: 94BR interpretive notes: The most transmissive and vertically extensive fracture zone is apparent at ~20 m depth below TOC. Fracture zones are evident in caliper, ATV, OTV, and HPFM logs (not shown) at depths of about 38, 62, 88 and 130 ft (or about 12, 19, 27, and 40 m). Variations in lithology are indicated by minor changes in reflectivity, gamma, and normal resistivity.

6.6.2 Quantification of fracture network hydraulic properties and estimation of groundwater flow

The DFN Approach (Parker et al., 2012; Figure 3. 1) includes forced gradient methods for measuring the fracture network hydraulic properties such as transmissivity (T) profiling during installation of a blank FLUTe liner in boreholes (Keller et al., 2014; Quinn et al., 2015), and high resolution packer testing in open holes (Quinn et al., 2011, 2012, 2013, 2016), . The DFN Approach also includes methods for assessment of groundwater flow under natural gradient conditions using either high resolution temperature profiling in lined heated boreholes, referred to as the Active Line Source (ALS) method, described by (Pehme et al., 2007, 2010, 2013, 2014), or more recently through the application of Distributed Temperature Sensing (DTS) using fiber-optic cables deployed behind liners, described by Coleman et al., (2015). At Hydrite, T-profiling, ALS testing and packer testing were applied in boreholes used in this study, and at SSFL, T-profiling and packer testing were applied in boreholes used in this study; ALS testing was not done in these boreholes but has been completed in nearby boreholes. At NAWC, T-profiling (2 profiles on different dates) and ALS testing was performed at 94BR, but packer testing has not been performed to date. Each of these techniques is described in more detail below.

In addition to these hydraulic testing methods, other techniques were applied to assess the groundwater flow system in the boreholes, including measurement of depth-discrete hydraulic head profiles. These have included a new Reverse Head Profiling (RHP) method which was developed by FLUTe and tested at the NAWC site (Keller, 2017), and measurement of hydraulic head in multilevel systems (MLS) installed in the boreholes at all three study sites. Einarson (2006) describes the commercially available MLS. Meyer et al., 2016; Meyer et al., 2008, 2014) describes Westbay MLS application for hydraulic characterization and insights obtained at the Hydrite site. Different commercial MLS have been deployed in many boreholes at SSFL, but none in the specific boreholes used in this study to date. At NAWC, a Shallow Water FLUTe (SWF) MLS was installed in the 94BR borehole with 10 ports. The SWF is an updated and lower cost version of the Water FLUTe MLS described by Cherry et al. (2007), which is optimized for boreholes with shallower water table so that the ports have open tubes running to surface (water levels within suction limits so ports can be sampled with a peristaltic pump) instead of the regular gas drive pumping system employed by regular Water FLUTe MLS. In addition to hydraulic head profiles, the MLS have also been used for groundwater sampling, providing depth-discrete VOC concentrations that primarily target mobile groundwater in fractures.

Transmissivity Profiling using FLUTe Method: FLUTe Transmissivity profiling is a rapid method (a typical profile can be obtained in a few hours) that relies on the measurement of the driving head (i.e., the difference between the head inside the liner and the blended head in the open borehole) and the descent rate of a blank FLUTe liner as it is being installed in a borehole (Figure 6. 27). As the liner advances downhole, it seals the hole, and as each permeable feature is sealed off the liner descent velocity slows as the flow rate into the formation from the remaining open borehole decreases. Using these step changes in liner velocity, a continuous transmissivity of the borehole can be obtained. Keller et al. (2014) provides an overview of the method,

including comparisons to straddle packer testing results. Under ideal conditions, a FLUTe profile can identify all transmissive features in a borehole, however, non-idealities can often affect the quality of the T-profiling results; Quinn et al., (2016) discuss these non-idealities in detail. For example if the borehole has a very high transmissivity interval at depth, the liner descent velocity will be very large throughout the entire profile, and therefore can mask the identification of important features (e.g., the detection limit for identifying velocity changes increases as the liner descent velocity increases). The transmissivity profiling method is only available from FLUTe, using specialized equipment and FLUTe trained personnel: http://www.flut.com/TransmissivityProfiling/trans_method.html. Because of the expense of the mobilization of the FLUTe field crew it is most economical to conduct profiling on 2 or 3 holes in the same field episode, where the holes are spaced far enough apart to avoid interference with the profiling of each hole. The efficiency of the FLUTe field crew is enhanced through provision of local field support personnel to streamline the work (i.e. field support to pull the liner and retrieve the transducer below the liner when the profile is finished). In addition, it has been shown that the use of liners aid in borehole development every time a liner is pulled especially toward the bottom of the hole (i.e., the strong suction below the liner pulls fines into the hole).

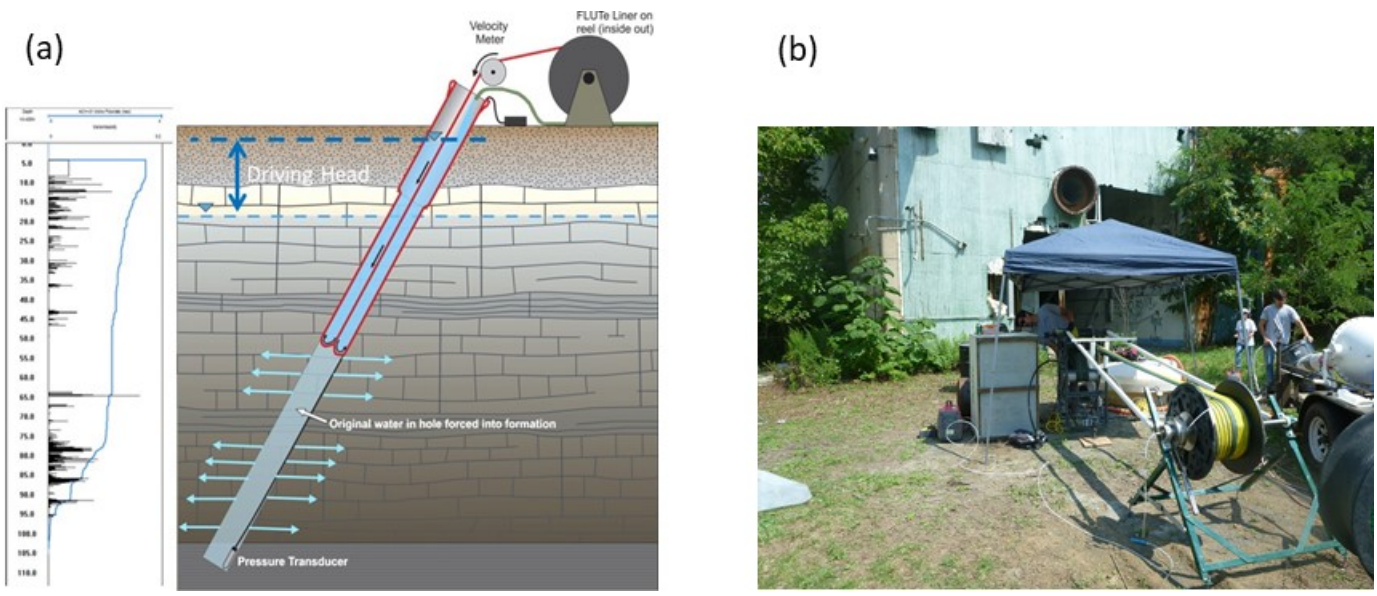

Figure 6. 27: (a) Schematic of FLUTe T-profiling and example profile, (b) setup at NAWC 94BR.

High Resolution Packer Testing: High resolution packer testing equipment and procedures developed at the University of Guelph are described in detail by Quinn et al. (2012). This method allows for different types of hydraulic tests to be conducted in each interval without removing or repositioning the packers by creating a temporary 2 in. (5.08 cm) well in each test interval using Solinst™ well casing (riser pipe) from the top packer to the ground surface. Transducers measure pressure inside the test interval and in the open hole above and below the test interval to monitor for short circuiting to the open hole. The range of hydraulic conductivity (K) which this equipment can accurately measure ranges from $7x10^{-10}$ to $2x10^{-2}$ m/s. Multiple pneumatic slug tests (both rising and falling head) are efficiently conducted over a large range of initial head displacements (0.1–1 m), and test procedures are designed to ensure effective development of the

test interval (i.e., dislodge sediment or drilling fines from the fractures) by first conducting a series of rising head tests (i.e., strong inward gradients pull fines into the test interval) before a series of falling head tests. A constant head (CH) step test is also conducted in all moderate to high permeable zones using a mini-packer lowered below the water level in the riser pipe and inflated to minimize casing storage effects; an adjustable check valve at the mini-packer is used to hold up the water in the injection line. Water is injected beginning at the lowest flow rate possible to cause a measurable change in head and then the flow rate is increased stepwise. Pumping tests (injection or withdrawal) can also be conducted in selective zones to obtain values for specific storage. Quinn et al (2015) show that when both FLUTe profiling and packer testing are used synergistically, more reliable T values can be obtained throughout the entire hole even when the liner profile is not ideal and less of the hole is tested using straddle packers (e.g., typically 50% of the hole is packer tested). The straddle packer method is able to measure T above the blended head, where the liner profile is unable to measure, and in the shallow portion just below the blended head, where the liner profile is least accurate (i.e., largest descent velocity). When the liner velocity is constant no measurable T is detected, however, representative sections can be tested with the straddle packer system to determine the actual T values (i.e. liner detection limit). These two methods used together result in a highly accurate T profile of the entire hole, which is necessary for determining hydraulic apertures, but less costly than testing the entire hole with straddle packers.

Active Line Source (ALS) and Distributed Temperature Sensing (DTS) Methods: The geophysical logging as well as the hydro-geophysical testing of the boreholes are in support of the broader investigation and to support the understanding flow through fracture network under "ambient" hydraulic conditions. The thermal tests involve the application of state of the art, evolving thermal technologies specifically active line source (ALS) testing (Pehme et al., 2010, 2013) and use of the thermal vector probe (TVP) (Pehme et al., 2014). This analysis of the results is undertaken to:

- identifying conduits for potential water movement (fractures) through the rock mass,
- improve understanding of ambient groundwater movement in the rock.

The phrase "*ambient groundwater movement*" above refers to groundwater flux that would occur as a result of normal hydraulic gradients (i.e due to variations in recharge, elevation and geology as well as regional pumping) but without artificially induced flow as part of the testing process or vertical cross-connected flow facilitated by the open borehole. Most forms of hydraulic testing (hydraulic packer tests, flow meter logging and FLUTe profiling) are "forced gradient" and involve hydraulically stressing the borehole (by pumping or injecting water) to create flow into or out of fractures. However, that flow may not be that that would typically occur naturally during contaminant distribution. In addition, during these forced gradient tests portions (if not all) of the borehole is open which can create a distorted perspective of groundwater flow by allowing flow between fractures that may not occur were the open hole not present (e.g. Pehme et al., 2010; Sterling et al., 2005).

Active line source (ALS) thermal testing (Pehme et al., 2013) is currently the only available technology that can be implemented in both contaminated and uncontaminated situations with the borehole lined so as to restrict cross-connected flow and provide interpretations of ambient groundwater flow at the time of testing. The test is based on heating the entire borehole followed by measuring high sensitivity temperature profiles during thermal recovery to identify narrow zones of preferentially accelerated cooling as being indicative of water movement through conduits (fractures) in the rock mass. This is a four-step process involving:

1. Sealing the borehole with a polyurethane covered nylon (FLUTe^{tm}) liner and allowing time for thermal stabilization
2. Collecting a background (passive) temperature log (data set)
3. Placing the borehole and the immediate vicinity into thermal disequilibrium by warming the length of the borehole with a line heater, (typically 5-6hrs at approximately 25.2W/m, typically raising the temperature by approximately 2C8). A temperature data set was collected as the heater was removed from the borehole.
4. Collecting three additional temperature data sets (at 1, 5.5 and approximately 19 hours after the end of heating).

Temperature logging was conducted with the "thermal vector probe" (TVP), which concurrently monitors four high sensitivity (0.001 C8 resolution) thermistors and three directional magnetometers so as measure temperature and the directional components of the thermal gradient (vertical and horizontal gradients, total magnitude, horizontal direction and inclination). Readings are collected at 2 samples per second (hertz) and low logging speeds so as to provide a nominal data density of 0.005m.

The following definitions apply within this document:
Passive Temperature Log: A temperature log collected within a borehole that has been allowed to thermally stabilize over many days or weeks. The passive log is considered to represent the ambient background thermal stratigraphy of the rock around the borehole. These data are collected slowly (~0.7m/min) to maximize spatial resolution.
Active Temperature Log: A log collected immediately after heating the borehole with an ALS heater (see definition below) with an RBR duo sensor attached to the bottom of the heater cable. These data tend to be irregular as the probe moves around the borehole as well as deterioration in data quality by increasing logging speed (these data were collected at ~2 m/min). The background temperature of an active log is expected to decrease towards the top of the borehole due to the increasing length of cooling time while the data are collected. Local variations in the active log result from changes in the thermal conductivity of the formation, advection of thermal energy by water moving past the borehole and the aforementioned geometric variations.
Thermal Recovery Log: A temperature log collected shortly (hours) after the ALS heater has been turned off. These data are a measurement of the temperature of the borehole fluid during the thermal recovery process as the heat dissipates and the rock gradually cools towards ambient temperatures. The rate at which the borehole fluid cools is a function of the thermal conductivity of the surrounding rock and of the water movement around the borehole. These logs tend to be

considerably more uniform than active logs and do not suffer from the high noise levels described above. These data are preferably collected at a rate of less than 1 m/min. Multiple cooling logs were collected in each hole; typically, the first (TR1) starts at least a half hour after the heater is turned off, the second (TR2) at a time interval after the heater has been turned off that is approximately the same as the duration of heating, and the third (TR3) the following morning. Logs used to calculate thermal conductivity must be collected after the borehole is allowed to cool longer than it was heated.

Active Line Source (ALS) Heater: a continuous wire heater that extends from surface to approximately the bottom of the everted liner. The heater was powered at 240 volts yielding ~25W/m for approximately 5.5 hours of heating.

Cooling Log: a presentation of the thermal recovery data intended to highlight narrow zones of preferential cooling. The temperature measured at each depth is subtracted from a smoothed version of the maximum observed over a 1m window (above and below). Consistent peaks in the cooling logs in two or more of the data sets collected during thermal recovery are identified as being indicative of preferential cooling due to water movement, with the size of the peak used as a qualitative indicator of relative groundwater flux.

6.6.3 Specialized geophysical logs NMR, IP, and MSUS

Specialized logs, including nuclear magnetic resonance (NMR), induced polarization (IP), and magnetic susceptibility (MSUS), were collected as part of this investigation in six boreholes (Table 6. 4). NMR, IP, and MSUS logs were collected at Hydrite in MP-24S and MP-25S during September 8-13, 2014 and in SSFL boreholes RD-109, C3, and C4 from January 12-22, 2015. The complete suite of standard geophysical logs and NMR, IP, and MSUS logs were collected in NAWC 94-BR borehole October 26-30, 2015.

Nuclear magnetic resonance (NMR) logs were collected in six boreholes at the three sites (Table 6. 4). NMR measurements were made with dual-frequency measurements in the open sections of the boreholes using Javelin tools manufactured by Vista Clara Incorporated (Figure 6. 28). The photos highlight that the NMR logging system and the tools used in this investigation are light weight, small diameter, short in length, and easily managed relative to NMR logging systems designed for oil field applications. With the Javelin borehole tools the measurement is imaging outside the borehole and ideally outside of the zone disturbed by drilling.

Table 6. 4: Summary of NMR measurements in open-hole sections of boreholes

Site and Well	Tool used	Radial depth of investigation (mm)	Recovery Time (Tr) (s)	Stacks for Full Time	Stacks for Early Time	No. of 0.5-m Measure-ments	Echo spacing Te (ms)
NAWC 94-BR	JP238	~146	6	30	180	68	1.5
	JP238	~146	4	60	360	16*	1.5
Hydrite MP24S	JP238	~146	6	30	180	41	1.5
Hydrite MP25S	JP238	~146	6	30	180	51	1.5
SSFL C3	JP350	~190	5	20	120	105	1.5
SSFL C4	JP350	~190	5	30	180	201	1.5
SSFL RD109	JP350	~190	5	30	180	58	1.5

[JP238 and JP350 indicate Javelin System 2.38-in and 3.5-in diameter tools manufactured by Vista Clara Inc.; *non-continuous log, measurements collected at core sample locations]

For each 0.5-m depth interval, 20 to 60 measurements were collected and stacked for each frequency. In the NMR measurement, the total water content is directly proportional to the strength of the magnetic field in the transverse (T_2) plane, and the timing of the T_2 decay is related to the pore-size distribution (Walsh et al, 2013). The echo spacing time was 1.5 milliseconds for both tools. This factor limits the earlies decay that can be measured with this equipment. Early-time decays are indicative of small pore sizes where water is bound, and long decay times are indicative of larger pores (and fractures) where water is mobile. NMR measurements were analyzed to determine the total water content and the mobile and immobile

Figure 6. 28: a) Photo showing SSFL borehole C4 with mobile logging system in the distance, b) NMR tool used for measuring water content in the formation surrounding the borehole, and c) NMR control unit and computer for viewing measurements and processing data for water-content, pore-size distribution, and hydraulic conductivity estimates. The NMR logging system used for this investigation is lightweight and mobile relative to conventional NMR systems used in the oil industry.

fraction. The results indicate the NMR water content values ranged from 0.01 to 0.50 and were generally under 0.10 for each 0.5-m interval.

For each depth interval the total, mobile, and immobile water fractions were determined using empirically derived cut-off values of relaxation times. The total water content includes the mobile and immobile fractions of water. The mobile fraction, which is the fraction that decays after the 33 ms cut off, is the mobile fraction and represents the effective porosity. The immobile fraction, which includes the clay and capillary fractions that decay in earlier than the 33-ms cut off, represent bound water. The clay-fraction cut off was set at a relaxation time of 3 ms. The output from the interpretation program included comma separated data files for the T_2 decay and the water content, which were imported into the composite of well logs for direct comparison with the gamma, EMI, and drilling logs.

In addition, estimates of hydraulic conductivity were made using the Schlumberger-Doll Research (SDR) equation and the sum of echoes (SOE) equation (Beroozmand et al., 2015). The estimates of hydraulic conductivity were determined using empirical equations with default values from the literature, and are considered to be relative estimates of hydraulic conductivity. The SDR equation uses the measured values of total porosity, (ϕ) and the mean log T_2 (MLT_2). In addition, it uses empirically derived values for parameters C, m, and n.

$$K_{SDR} = C\ \phi^m\ MLT_2^n, \tag{6.12}$$

where C is a constant (C) that was set to the default parameter of 8900. For unconsolidated sands, m is generally about 1, and n fixed at 2. Hydraulic conductivity (K) is in meters per day (m/d).
The K_{SOE} equation uses the summed amplitudes of the echoes (SE) in the T_2 decay for each depth interval,

$$K_{SOE} = C * \sum SE^2, \tag{6.13}$$

where *C* is an empirically derived constant set to 4200, and SE is the measured sum of echoes. Hydraulic conductivity (*K*) is in meters per day (m/d).

A comparison of the results of both estimates of K show the K_{SDR} equation is more subject to variations caused by noise and variations in the mean log T_2 value than with the K_{SOE} estimate. Thus the K*soe* is less sensitive to noise but the K*sdr* is able to show small variations caused by small pore-sizes as reflected by early time decay. Fracture permeability cannot be estimated using NMR, and the K estimates determined for the matrix are considered relative estimates of K.

Induced polarization (IP) logs were collected with a time domain QL40-ELOG/IP tool manufactured by Mount Sopris Instruments. IP is a measure of the ability of an earth material to hold an electrical charge. IP is a physical property determined by injecting a current into the fluid in the borehole causing some of the earth materials to get polarized. Current charge accumulates over a charging period and then when the current is turned off the tool monitors the residual

current as it decays to background. Normal resistivity data were collected on the downward logging pass, and induced polarization data were collected going up the borehole using different time intervals of charging and monitoring times (100, 250, or 500 milliseconds). The time-domain IP tool cycles a square-wave current on and off, and the tool measures the remnant decay for the 16- and 64-in electrode spacings. In the composite plots (Figure 6. 29) the IP data are shown as a shaded amplitude image that shows the decay voltage after the positive charge injection period and during the release period as the tool monitors decay. Chargeability (Ma) is computed from the decay curves, and is shown as continuous plots at 0.2-ft depth intervals in units of milliseconds. In general the IP chargeability values near the top of the well are less reliable than deeper in the borehole, as there is the electrode that is approximately 8 m (26 ft) above the top of the tool that must be submerged in the water and below the casing to provide accurate readings. Zones of mineralization, including sulfides and ferrous minerals, and clay units exhibit IP effects with increased chargeability. The logs in 94-BR exhibit noise that could not be removed from the data, however the full time plot of the IP data appears to be correlated with rock types.

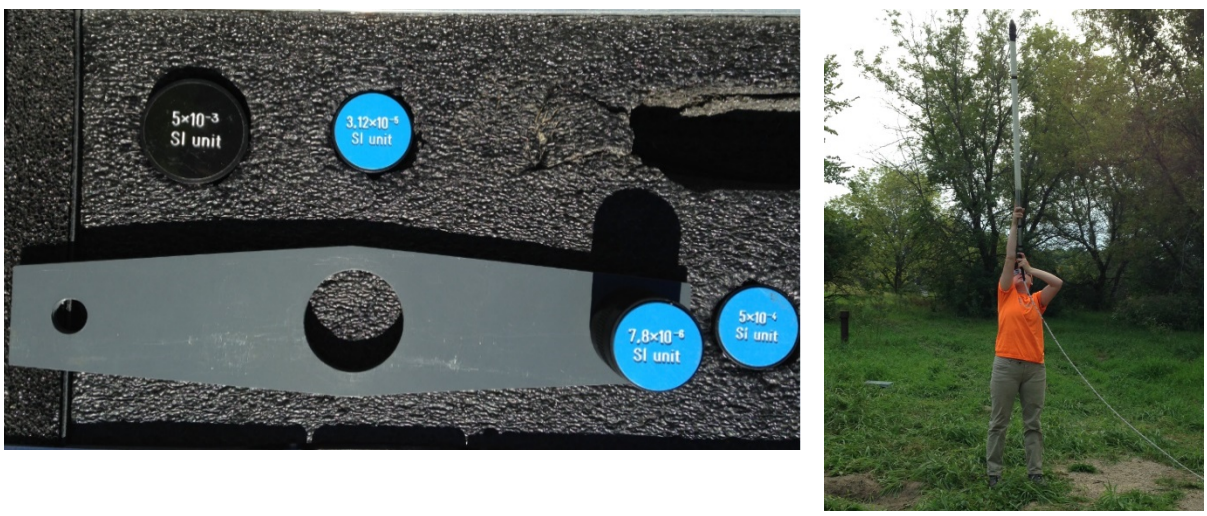

Figure 6. 29: a) Calibration standards for magnetic susceptibility and the "wing" that is positioned on the tool with the calibration "pucks" at the specified distance from the tool. b) Magnetic susceptibility tool raised in the air at the Hydrite site for the zero value during the calibration process. All logs calibrated according to ASTM standards, manufacturer's instructions, and USGS protocols.

Magnetic susceptibility logs were collected with HM453S, which is manufactured by W&R Instruments and integrated with the Mount Sopris Instruments logging system. The MSUS logs were calibrated in the field with manufacture's specifications and calibration standards (Figure 6. 29 (a)). In general, the tool was allowed to thermally equilibrate in the borehole, and then it was pulled out of the well, held vertically in the air, and a zero measurement was collected in the air (Figure 6. 29 (b)). Measurements were also taken with each of the calibration "pucks" that are threaded onto the calibration wing that is slipped onto the tool. The logs were calibrated using two points that were closest to site conditions, which were air and the lowest magnetic susceptibility standard. Units of magnetic susceptibility are in of 10 E-3 SI units.

In general the magnetic susceptibility tools are electromagnetic induction systems with transmitter and receiver coils spaced about 25 to 100 cm apart. A bucking coil is used to compensate for the primary field, and the tool measures the in-phase and quadrature components of the secondary field. Some tools report both the quadrature that is proportional to the conductivity, and the in-phase component that is proportional to the magnetic susceptibility. The HM453S used for this investigation has coils spaced at 50 centimeters apart and is tuned to a low frequency to optimize the magnetic susceptibility and sensitivity. HM453S measures and reports the MSUS over a range of 7.0 E-6 to 0.07 SI units at a depth increment of 0.1 ft. Variations in MSUS are typically indicative of change in lithology and can be an indicator of bioremediation. Zones of high MSUS are not ideal for NMR measurements, and can cause a reduction in the signal strength, a down-shift in T_2 time and amplitude. The MSUS log can therefore be used to provide some quality control of borehole NMR measurements. There appeared to be no zones in 94-BR exhibiting high MSUS that would adversely impact the NMR.

The estimated proportions of water content from NMR logs are shown in Figure 6. 30 along with the distributions of the transverse decay (T_2 decay) and pore-sizes. Variations in water content appear to coincide with the presence and absence of fractures in the image logs in 94-BR. NMR logs collected in MP-24S and MP-25S at Hydrite show changes in the water content appear to coincide with major changes in the lithology.

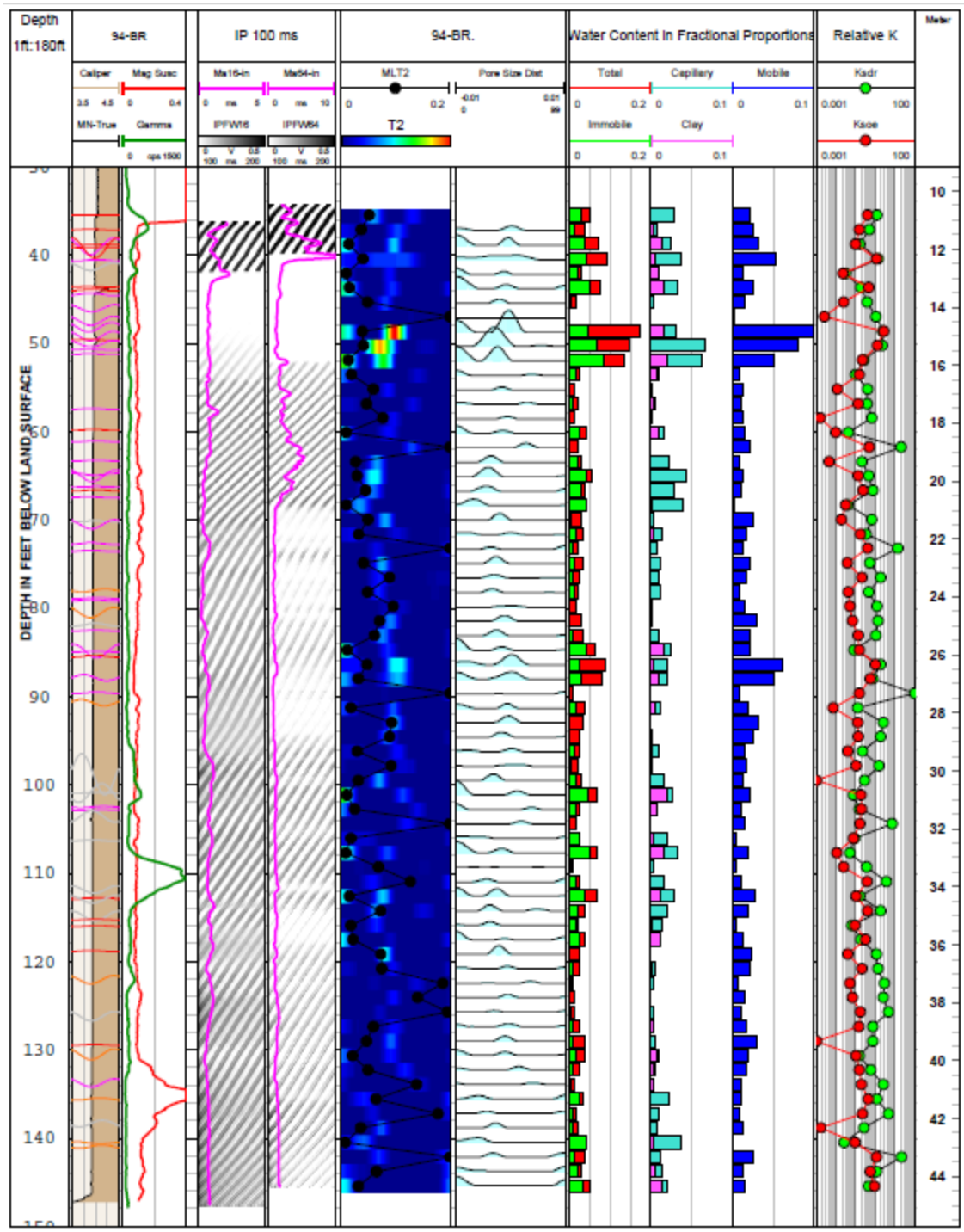

Figure 6. 30: 94-BR Nuclear magnetic resonance (NMR) logs showing transverse decay, mean log transverse decay (MLT2), pore-size distribution, water content: total, mobile, bound (immobile), and preliminary estimates of hydraulic conductivity using Schlumberger Doll Research (SDR) and sum of echoes (SOE) equations. NMR logs compare well with fracture locations in the OTV, ATV and caliper logs.

6.6.4 FACT

The FLUTe Activated Carbon Technique (FACT) is a new method developed by FLUTe (www.flut.com/FACTFLUTe/fact_method.html) to generate vertical profiles of ground water contamination in both fractures and rock matrix porosity of fractured rock formations (Figure 6. 31). The method uses an everting flexible liner (www.flut.com/BlankLiners/blank_methods.html) to emplace and isolate a strip of activated carbon felt against a borehole wall while sealing the entire borehole. The activated carbon felt adsorbs contaminants transported by advection in groundwater in fractures (secondary porosity) and from the rock matrix (primary porosity) transported primarily by diffusion. The felt strip is attached to a NAPL sensitive cover (www.flut.com/NAPLFLUTe/napl_method.html) over the liner that has dye strips that produce visible stains when in contact with various NAPLs including chlorinated solvents. Combined the NAPL cover and FACT strip are referred to as the NAPL/FACT. Following a sufficient exposure time after deployment in a borehole (generally 1-2 weeks is recommended) the FACT is recovered by inversion of the sealing liner, followed by removal of the FACT strip and then sampling of the carbon felt at any desired length for analysis depending on the spatial resolution desired. The FACT samples then undergo solvent extraction (e.g. methanol, pentane) and analysis using methods similar to the rock core samples. The result is a relative distribution with depth (profile) of the mass of contaminants per mass of (dry) activated carbon felt that ideally is a function of mass transported by advection in permeable zones (fractures), and by diffusion (wicking) from the rock matrix in unfractured intervals. When combined with the NAPL cover, the FACT provides a means of profiling aqueous phase, vapor phase (when deployed above the water table) and NAPL in-situ focused on both fractures and in the rock matrix.

Early results of FACT trials in Denmark are provided by the thesis of Beyer (2012) and in a fractured limestone aquifer by Broholm et al., (2016). Two FACT deployments were conducted at the NAWC 94BR borehole. The first NAPL/FACT was deployed the day after the borehole was drilled and developed and left downhole for 16 days, followed by removal and sampling at 0.5 to 1.0 ft spacing with discrete 0.2 ft subsamples. The second NAPL/FACT was deployed three weeks after the first was removed, with the hole sealed by a blank liner in the interim, and left in place for 17 days, followed by removal and sampling continuously in 0.5 ft increments (discrete samples) with the felt strip cut lengthwise, and the adjacent strip sampled in longer 2.0 ft increments (composite samples). A paper nearly ready for submission (Keller et al., in prep) describes these FACT trial at 94BR at the NAWC site in detail, including discussion of factors that can influence the FACT results such as cross-connection of dissolved contamination (and possibly DNAPL) in the open borehole during drilling and prior to deployment of the liner with the NAPL/FACT, and shows comparisons of FACT profiles with the rock core VOC profile and subsequent groundwater sampling with the SWF MLS. A new ESTCP project ER-201630 (www.serdp-estcp.org/Program-Areas/Environmental-Restoration/Contaminated-Groundwater/Persistent-Contamination/ER-201630) is evaluating FACT in more detail, which will include additional trials at the NAWC site as well as at another site with different geology and contaminant conditions, along with different drilling techniques and deployment conditions.

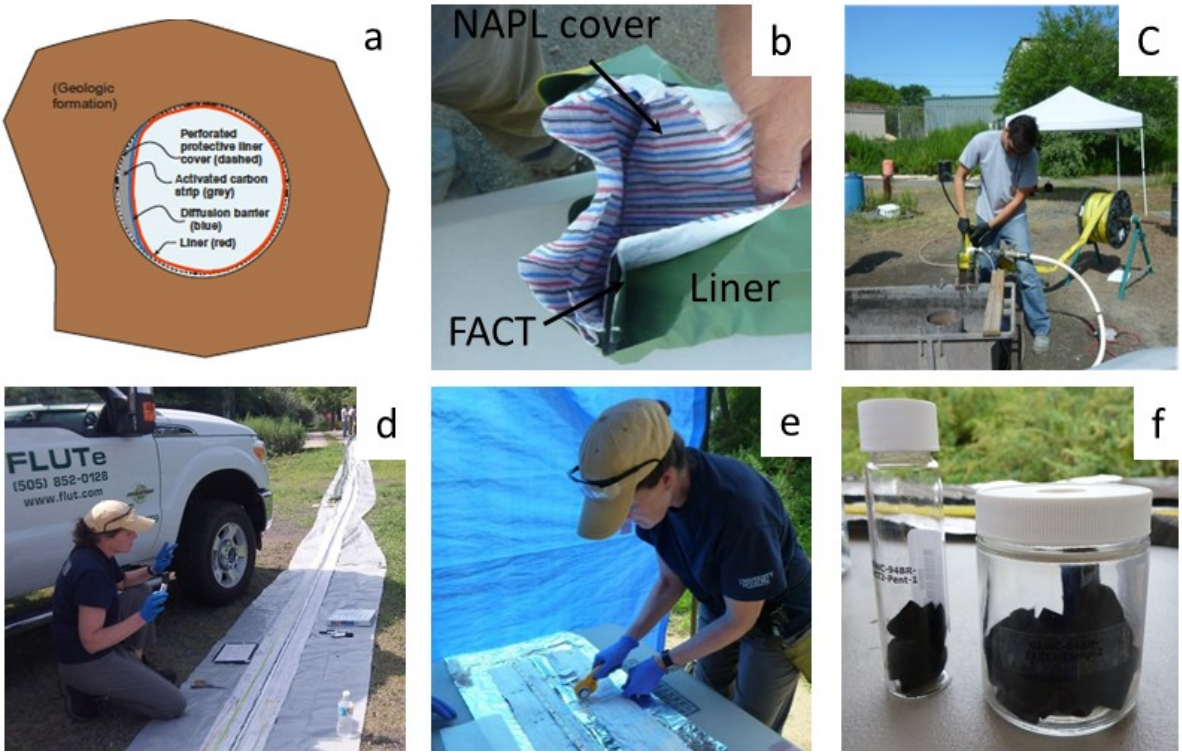

Figure 6. 31: (a) FACT schematic during downhole deployment with outer NAPL sensitive cover and FACT strip pressed up against the borehole wall and sealed in place by the blank FLUTe liner, and photos of NAWC 94BR deployment showing (b) the NAPL/FACT and cover prior to eversion downhole, (c) liner installation with NAPL/FACT, (d) liner removed after deployment time downhole and laid out for examination of the NAPL cover and removal of the FACT strip, (e) subsampling of the FACT strip, and (f) subsampled discrete (in 40 mL VOA vial) and composite (in 125 mL jar) FACT samples prior to methanol addition in the field.

7.0 Results

7.1 Petrophysical relationships between laboratory geophysical measurements and rock properties

7.1.1 Porosity estimates

Porosity estimations can be obtained from MICP and NMR measurements. We compare these estimates to direct measurements of gravimetric porosity. Both methods provide a reasonable prediction of sample porosity (Figure 7. 1). Figure 7. 1(a) demonstrates the ability of MICP to estimate porosities (RMSE=1.56) even with the differences between these sample volumes. Figure 7. 1(b) demonstrates the ability of NMR to better predict porosities than MICP (RMSE=1.08) when gravimetric measurements are the standard. In Figure 7. 1(b), overestimations of NMR porosity are attributed to a small amount of fluid trapped beneath parafilm (necessary to maintain the moisture content in the cores).

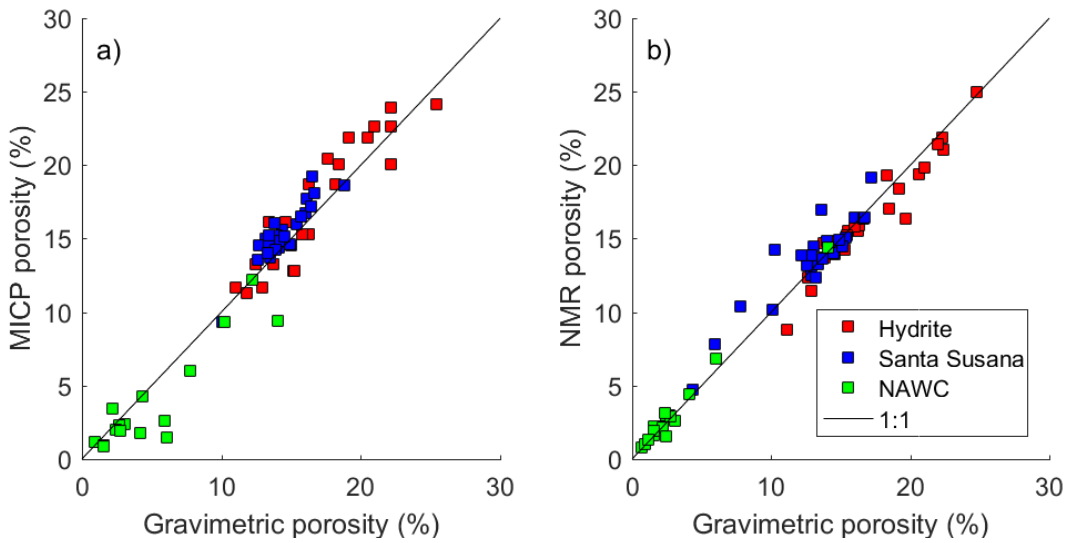

Figure 7. 1: a) Comparison of MICP and gravimetric porosities (RMSE=1.56) b) Comparison of MICP and gravimetric porosities (RMSE=1.08).

7.1.2 Pore scale relationships using geophysical measurements

A strong relationship is anticipated between geophysical measurements and physical rock properties (refer to Section 4). Figure 7. 2 shows the relationship between S_{por}, T_{2ml} and imaginary conductivity at 1 Hz $\sigma''_{1\,Hz}$. Both T_{2ml} and $\sigma''_{1\,Hz}$ are reasonably correlated with S_{por}, however unlike T_{2ml}, $\sigma''_{1\,Hz}$ is affected by fluid chemistry and/or minerology (see Section 4.2.1) and the correlation is less robust (RMSE of 0.473 versus 0.280). Another geometric length scale used in permeability prediction is Λ (see Section 4). In Figure 7. 3, Λ is plotted against T_{2ml} *and* $\sigma''_{1\,Hz}$. The correlations of T_{2ml} and $\sigma''_{1\,Hz}$ versus Λ are less robust than S_{por} (Figure 7. 2), and the NAWC cores are obvious outliers. As seen in Appendix B.3, this poor correlation can be attributed to Λ (represented by l_c, r_{50} and r_{70}) not best representing the hydraulically

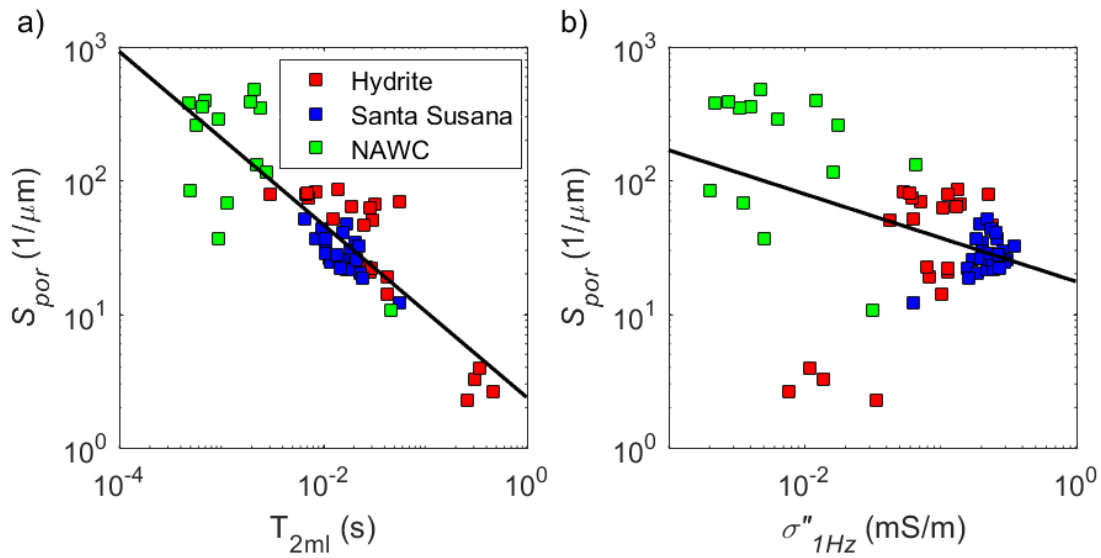

Figure 7. 2: S_{por} versus a) T2ml (RMSE=0.280) and b) $\sigma''_{1\,Hz}$ (RMSE= 0.473). The RMSE values are calculated from the from a least linear regression fit of the data. This is shown as a solid black line.

interconnected pore throat diameter. Many of the NAWC cumulative intrusions differ from SSFL and HC samples by showing a slower initial progression of intrusion which increases near the 30,000 psi limit of the instrument. While SSFL and HC samples in Appendix B.3 reach full intrusion (demonstrated with the cumulative intrusion reaching a constant maximum value), many NAWC samples have not (demonstrated by the increasing cumulative intrusion at the smallest pore diameters). While these smaller pore throats represent a small portion of the overall porosity (note the robust correlation in Figure 7. 1(a)), the effect on Λ is more significant.

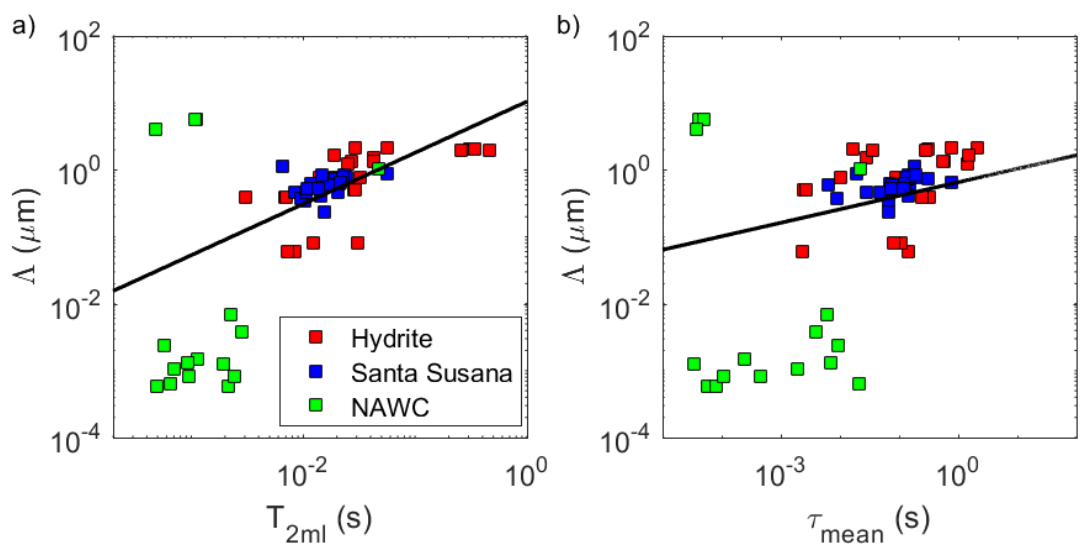

Figure 7. 3: Λ versus a) T2ml (RMSE=1.17) and b) $\sigma''_{1\,Hz}$ (RMSE= 1.08). NAWC cores do not correlate well with Hydrite and Santa Susana samples.

7.1.3 Permeability relationships

Using geometric length scales S_{por} and Λ to predict permeability (Figure 7. 4) shows that most HC and SSFL samples are within one order of magnitude of measured permeabilities. The permeability prediction appears less robust with Λ (Figure 7. 4(a)) than with S_{por} (Figure 7. 4(b)), in part due to MICP predictions of Λ as noted in Section 7.1.2. Note, S_{por} could not be acquired for all NAWC samples (refer to Appendix B.4, Table 2) and these are eliminated from Figure 7. 4(b).

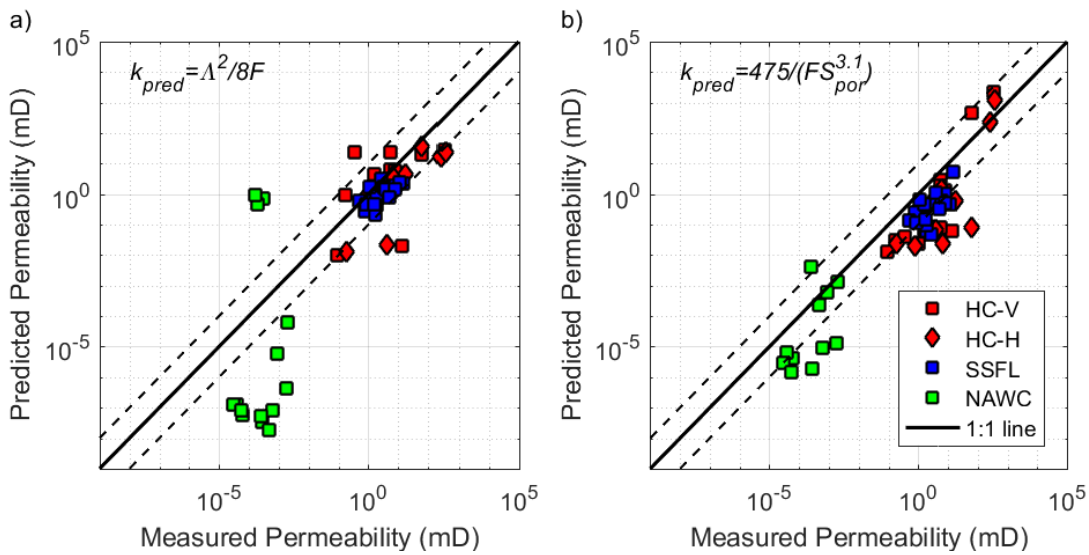

Figure 7. 4: Permeability predictions using geometric length scales a) Λ b) S_{por}. The dashed black lines represent one order above and below the 1:1 line.

Permeability equations using NMR and CR geometric length scales reveal that geophysical parameters have the capability to estimate permeability as well as equations using geometric length scales. Figure 7. 5 uses the NMR SDR equation (Section 4.1.1). Using pre-calibrated coefficients, permeability is predicted within one order of magnitude for most samples with the exception of the NAWC samples (Figure 7. 5(a)), not surprising given the coefficients were calibrated in a sandstone lithology. Figure 7. 5(b) shows that a multiple linear least squares regression can adequately fit all samples. This shows that with further study, it may be possible to find a universal equation.

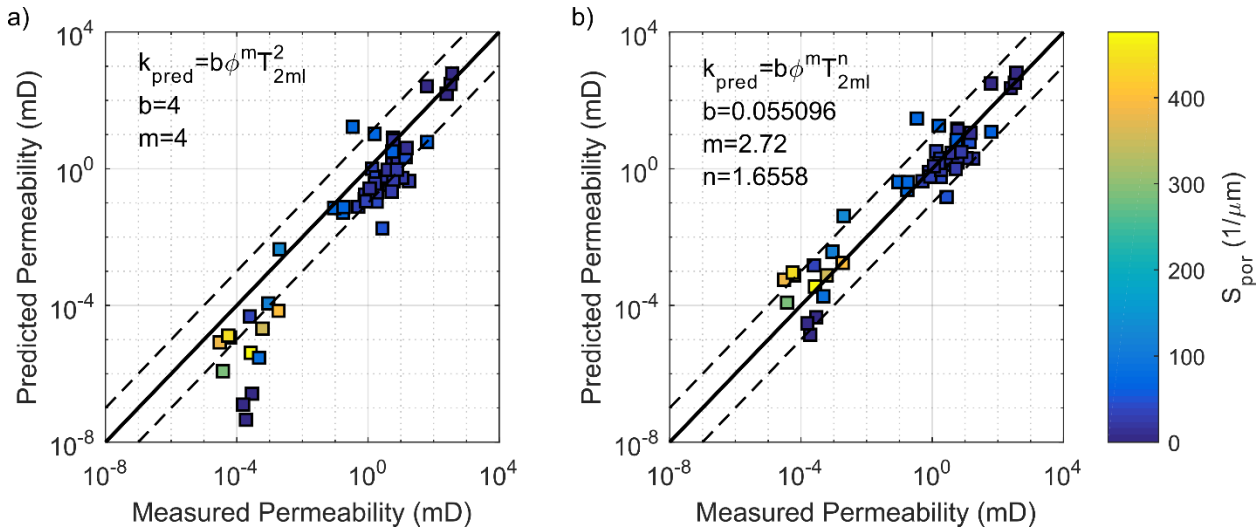

Figure 7. 5: NMR SDR permeability equations and associated coefficients b and m: a) sandstone calibrated coefficients b) calibrated coefficients for entire SERDP dataset.

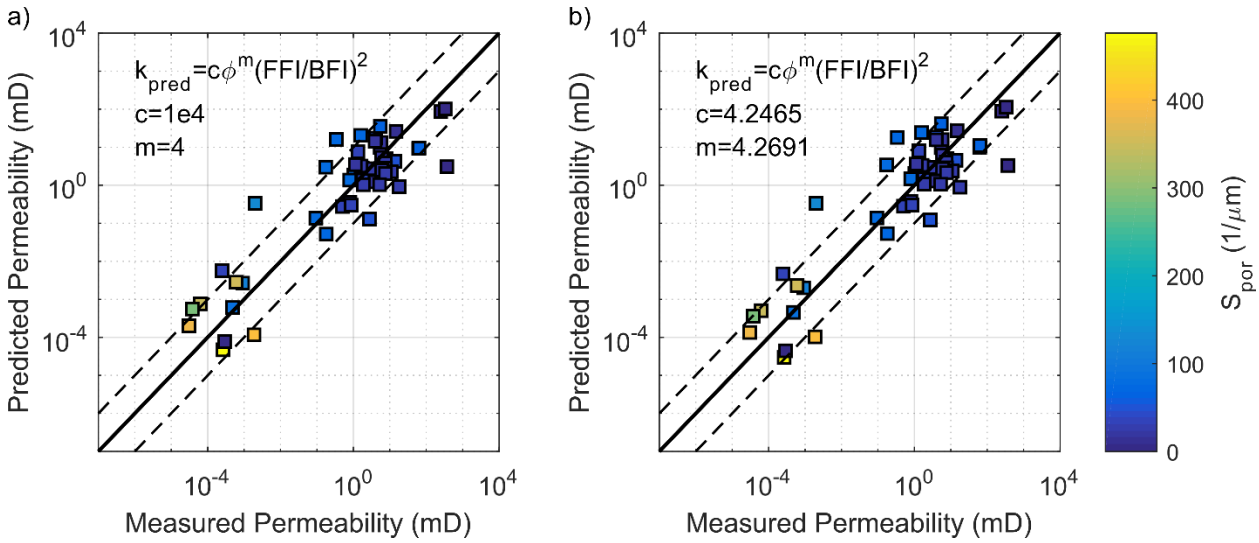

Figure 7. 6: NMR Timur-Coates (T-C) permeability equation and associated coefficients c and m: a) sandstone calibrated coefficients b) calibrated coefficient for entire SERP dataset. T2 cutoff values used based on before and after centrifuging data shown in Appendix B.2. Where no cutoff value was available, 33 ms was used.

In the NMR T-C equation (Section 4.1.1), pre-calibrated coefficients estimate permeability for all but 7 samples within one order of magnitude of measured values (Figure 7. 6(a)). Performing a multilinear least squares regression improves the permeability prediction slightly (Figure 7. 6(b)). The FFI/BFI values used are from the T2 cutoff values shown in Appendix 2 and

Appendix 4, Table 4). Any sample with T2 cutoff values not available, a cutoff time of 33 ms was used; this could add misfit to the plots shown in Figure 7. 6.

Permeability predicted from CR geophysical length scales σ'' (at 1 Hz) and F is shown in Figure 7. 7. Using predetermined coefficients (Section 4.2.1, Equation 4.13), permeability is not well predicted (Figure 7. 7(a)). NAWC cores with a high S_{por} are underpredicted and several sandstone cores (with a high S_{por} relative to other sandstones) are also not well predicted. Using the general form of the equation and performing a multilinear least squares regression yields well-predicted NAWC cores, however, several high S_{por} samples are again not predicted within one order of magnitude (Figure 7. 7(b)). Similar observations can be seen in Figure 7. 8 where using predetermined coefficients does not predict permeability well (Figure 7. 8(a)) (Section 4.2.1, Equation 4.14) and with a multilinear regression to determine coefficients in the generalized equation, permeability is not well predicted with several high S_{por} (relative to other sandstones) (Figure 7. 8(b)). Future work needs to focus on accounting for the variations in fluid chemistry and minerology to successfully calibrate these parameters with permeability.

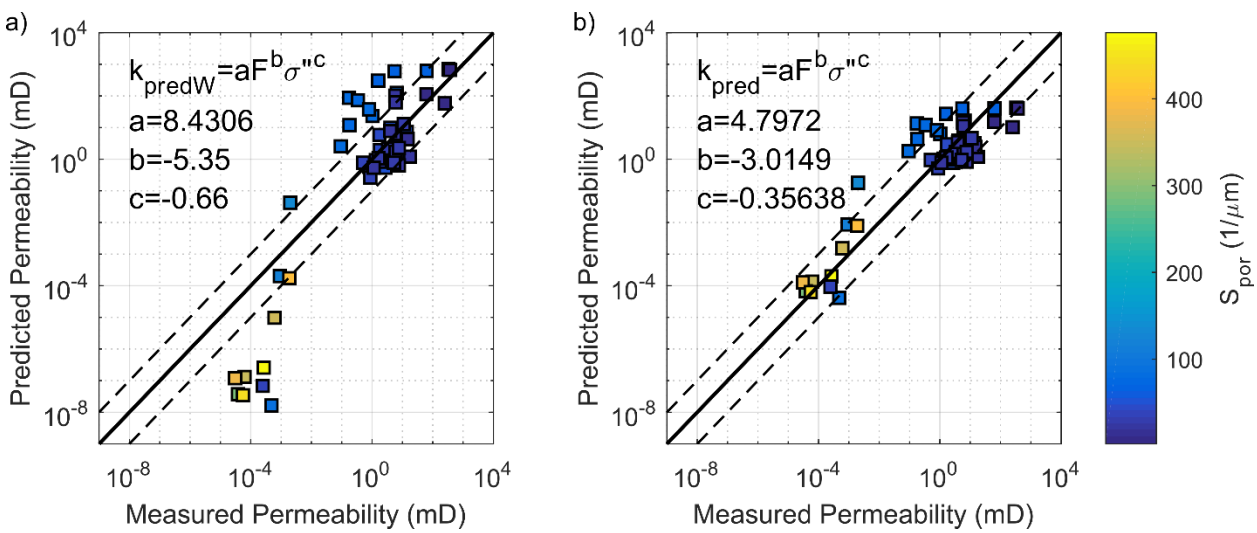

Figure 7. 7: CR predicted permeability using geophysical Kozeny-Carmen equation incorporating σ''_{1Hz} using a) predefined coefficients calibrated on sandstone samples (Equation 4.13) and b) coefficients solved through multiple linear regression.

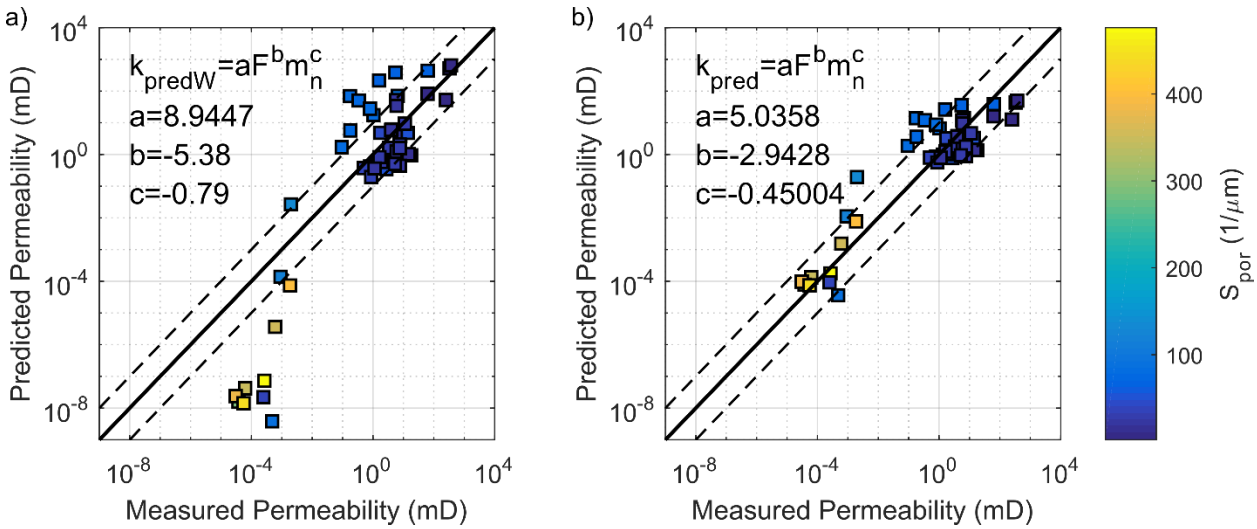

Figure 7. 8: CR predicted permeability using geophysical Kozeny-Carmen equation incorporating m_n using a) predefined coefficients calibrated on sandstone samples (Equation 4.14) and b) coefficients solved through multiple linear regression.

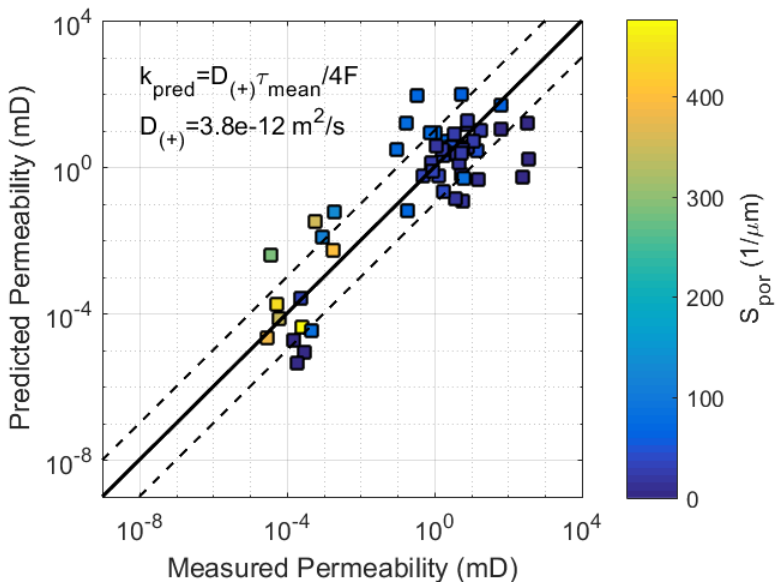

Figure 7. 9: CR predicted permeability using geophysical Katz and Thompson equation incorporating τ_{mean}.

As shown in Section 4.2 (and Figure 4. 3(a)), selecting τ_{pc}, in particular for the NAWC samples can be challenging, subjective and/or a defined peak may not exist for a given sample. Given this, we use the entire frequency spectrum and use τ_{mean} in Equation 4.16 to estimate permeability. We used D_+equal to 3.8x10^{-12} m^2/s as this best represents our sample database. Figure 7. 9 shows numerous outliers in predicting permeability within one order of magnitude of measured values.

Geophysical parameters are well-correlated with rock properties S_{por} and Λ and as such can predict permeability as well or better than using these rock properties.

7.2 Petrophysical relationships between geophysical measurements and contaminant mass

Geophysical inference of contaminant mass would represent a game-changing advance in the science and industry of environmental remediation; however, geophysical measurements are not sufficiently sensitive to detect low-level (ppm or ppb) concentrations of dissolved contamination even in controlled settings. In field applications, geophysical measurements are further limited by noise, measurement errors, and resolution. Nevertheless, we investigate whether site-specific relationships exist between geophysical measurements and contaminant mass, as (1) TVOC determined by analysis of rock cores (Section 6.2) and (2) FACT (Section 6.6.4). We stress that any relationships identified are indirect and based on sensitivity to lithology (e.g., the presence of organic carbon) rather than direct sensitivity to contaminant mass. For example, at the NAWC site, natural gamma logs have been used successfully to characterize (1) black, carbon-rich laminated mudstone, (2) dark-gray laminated mudstone, (3) light-gray massive mudstone, and (4) red massive mudstone, with the TCE concentrations highest in the black, carbon- and clay-rich laminated mudstones (Lacombe & Burton, 2010). Discrimination of lithology may be improved relative to discrimination based only on gamma logs by consideration of other logs sensitive to porosity (e.g., NMR), fracturing (e.g., ATV), or carbon content (e.g., color from OTV).

In the following sections, we present the results of various regression approaches, applied to data from NAWC (Section 7.2.1), Hydrite (Section 7.2.2) and SSFL (Section 7.2.3). We considered standard multivariate linear regression, regression trees, Gaussian process regression models, and support vector machines. These regression approaches were applied using the available of borehole logs as predictors, and the TVOC and FACT results as responses. To mitigate problems of overfitting, 5-fold cross validation was performed, and the predicted R^2 for cross validation is reported. To enable straightforward comparison between prediction of TVOC from rock core and from FACT where both datasets are available, we present results for the same regression approach. Regression modeling was performed in MATLAB.

7.2.1 NAWC

The suite of geophysical logs available from NAWC borehole 94BR include fluid temperature (before and after injections), fluid resistivity (before and after injections), normal resistivity (8-, 16-, 32- and 64 inches), spontaneous potential, single-point resistance (as voltage and resistance), natural gamma, EMI, ATV median acoustic reflectivity, OTV median, total NMR porosity, NMR clay fraction, NMR capillary fraction, NMR immobile fraction, NMR mobile fraction, magnetic susceptibility, and NMR mean log(T2). Induced polarization data from the NAWC site were considered noisy and unusable for this analysis. Regression results are summarized in Table 7. 1 and Figure 7. 10. The suite of logs are able to more accurately predict the FACT results than the TVOC results from rock cores. We interpret this finding to indicate that the FACT results more closely approximate the support volume of the log measurements; however, additional work is required to confirm this interpretation.

Table 7. 1: Regression results

	TVOC rock core (μg/g)	FACT (μg/g)
R^2	0.60	0.83
Root mean squared error	1.0	0.29
Mean squared error	1.0	0.09
Mean absolute error	0.74	0.22

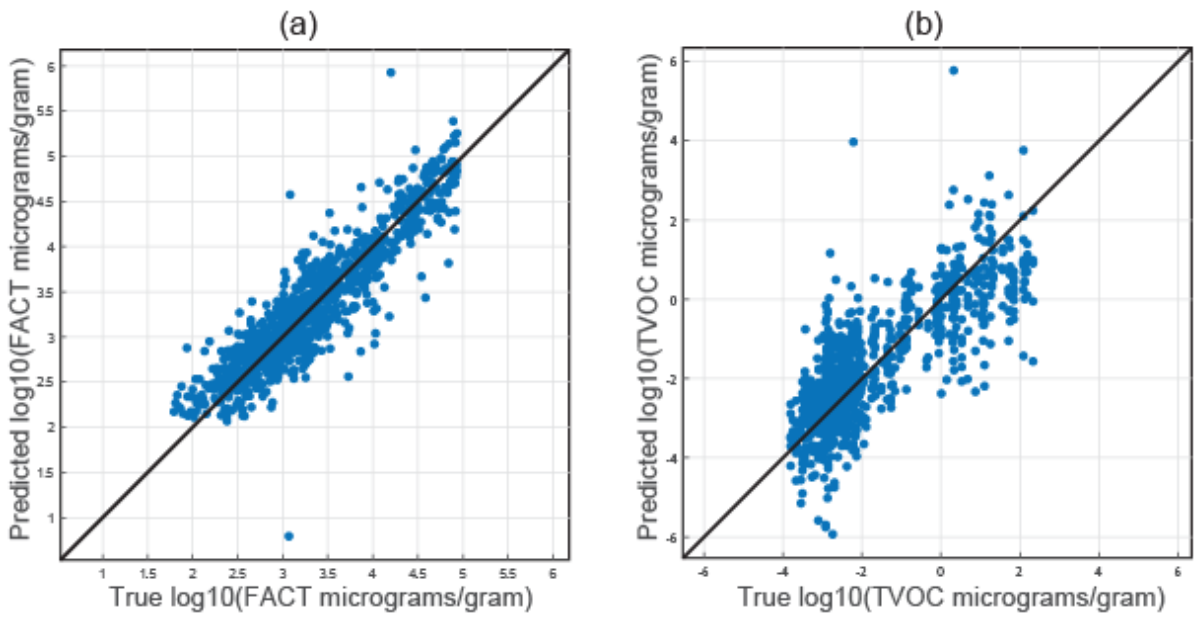

Figure 7. 10: (a) Prediction of FACT from borehole logs vs. true FACT results, and (b) predicted TVOC from borehole logs vs. true TVOC from rock cores, based on multivariate linear regression with interaction between predictors.

7.2.2 Hydrite

The suite of geophysical logs available from Hydrite borehole MP25S includes induced polarization, normal resistivity (8-, 16-, 32- and 64 inches), spontaneous potential, single-point resistance, natural gamma, EMI, ATV median acoustic reflectivity, OTV median, total NMR porosity, NMR clay fraction, NMR capillary fraction, NMR immobile fraction, NMR mobile fraction, magnetic susceptibility, and NMR mean log(T2). Regression results are summarized in Table 7. 2 and Figure 7. 11. No FACT data were available from Hydrite. Compared to the results from NAWC, a stronger relationship between TVOC and the geophysical logs was found for Hydrite.

Table 7. 2: Regression results

	TVOC rock core (μg/g)
R^2	0.98
Root mean squared error	0.16
Mean squared error	0.03
Mean absolute error	0.11

7.2.3 SSFL

The suite of geophysical logs available from SSFL borehole RD109 includes normal resistivity (8-, 16-, 32- and 64 inches), spontaneous potential, single-point resistance, natural gamma, EMI, ATV median acoustic reflectivity, total NMR porosity, NMR clay fraction, NMR capillary fraction, NMR immobile fraction, NMR mobile fraction, magnetic susceptibility, and NMR mean log(T2). Noisy data over sections of the holes resulted in non-physical data values for a number of logs; thus we focused our regression modeling on the following logs, which were less noisy: ATV median acoustic reflectivity, gamma, EMI, magnetic susceptibility, mean log(T2), total porosity, immobile porosity, and capillary fraction. Regression results are summarized in Table 7. 3 and Figure 7. 12. No FACT data were available from Hydrite. Compared to the results from NAWC and Hydrite, a weaker relationship between TVOC and the geophysical logs was found for SSFL based on linear regression; however, a Gaussian process regression model with a quadratic kernel (Table 7. 4, Figure 7. 13) enabled improvement on the predictive capability of the geophysical logs for this dataset.

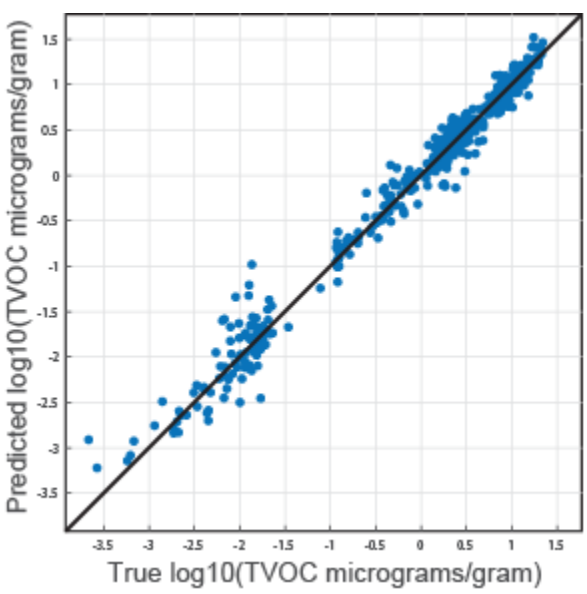

Figure 7. 11: Predicted TVOC from borehole logs vs. true TVOC from rock cores for Hydrite M25S, based on multivariate linear regression with interaction between predictors.

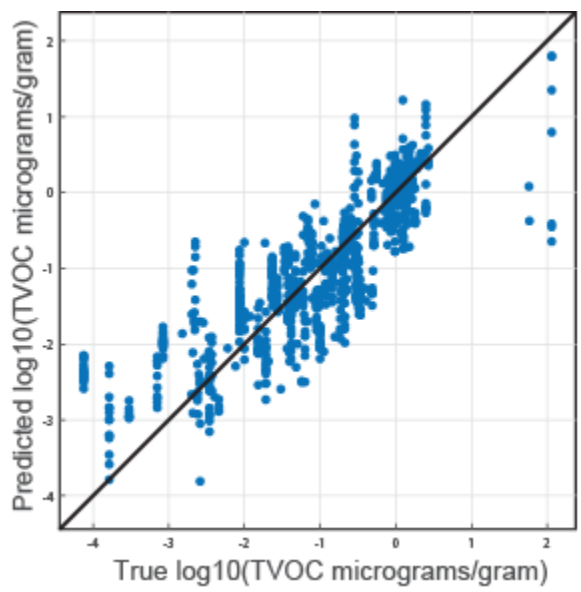

Figure 7. 12: Predicted TVOC from borehole logs vs. true TVOC from rock cores for SSFL RD109, based on multivariate linear regression with interaction between predictors.

Table 7. 3: Regression results

	TVOC rock core (µg/g)
R^2	0.75
Root mean squared error	0.62
Mean squared error	0.38
Mean absolute error	0.47

Table 7. 4: Regression results

	TVOC rock core (µg/g)
R^2	0.94
Root mean squared error	0.30
Mean squared error	0.09
Mean absolute error	0.15

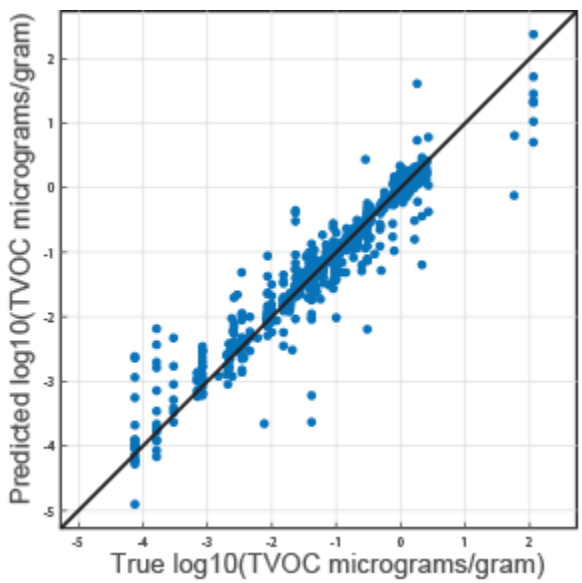

Figure 7. 13: Predicted TVOC from borehole logs vs. true TVOC from rock cores for SSFL RD109, based on Gaussian process regression with interaction between predictors.

7.3 Electrical tracer experimental results

The geometric factor for the sample holder determined using a calibration curve consisting of 4 fluid resistivities (i.e. 11.36-34.01 Ωm) and a tube length of 4.13 cm. Resistance was measured at 1 Hz for all fluids and varied between 1608 and 4667 Ω., shown in Figure 7. 14. The geometric factor specific to each side of the sample holder was calculated from the linear regression of this data to be 51.33 m^{-1}. This correction was applied to each SIP measurement using Equation 6.7 and the corresponding ρ_f calculated from σ_{EC} measured from the influent and effluent EC probes. Correcting the SIP data using the EC probe data resulted in some artifacts such as bubble spikes and lag artifacts (see Section 6.4). All relevant corrections were applied to the data to correct these artifacts as described in Section 6.4.

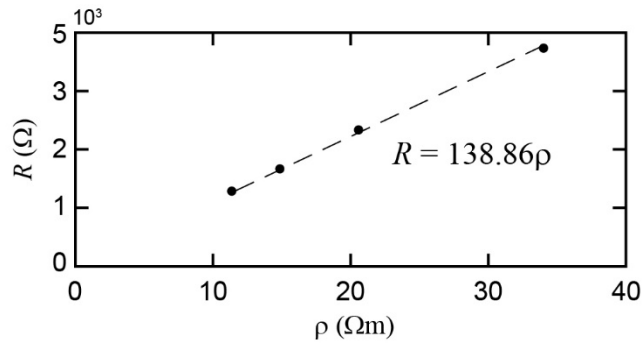

Figure 7. 14: The calibration curve used to correct SIP data during the mass transfer tracer tests.

A confining pressure of ~300 psi was used for all samples. All samples were unaffected by this pressure except for SS-C3-P-022. This sample suffered significant structural damage following the application of confining pressure and no data was collected. Data from all other samples were collected using <100 psi fluid injection in order to obtain steady flow rates. Establishing a steady flow rate for the effluent and sampling ports of the sample chamber took between 2 and 3 weeks for the samples analyzed in this study. An acceptable flow rate was not established for sample HC-MP24S-P-004-2H. Due to this, no tracer injection or flush data was obtained for this sample. For the remaining samples, steady flow rates were obtained that varied between 0.364-0.804 mL/min for the effluent and 0.092-0.253 mL/min for the sampling port. All flow rates are tabulated in Table 7. 5.

Table 7. 5: The flow rates (effluent and EC ports) and formation factors (calculated from the electrical tracer experiment and column (Section 6.4.3) experiment) of the samples analyzed during the electrical tracer experiment.

	Flow Rate ($mL \cdot min^{-1}$)		Formation Factor	
Sample ID	*Effluent*	*EC Port*	*Tracer*	*Column*
HC-MP24S-P-006-1V	0.80	0.25	17.185	17.451
HC-MP24S-P-007-2H	0.64	0.32	23.122	16.543
SS-C3-P-019	0.36	0.09	48.654	47.774

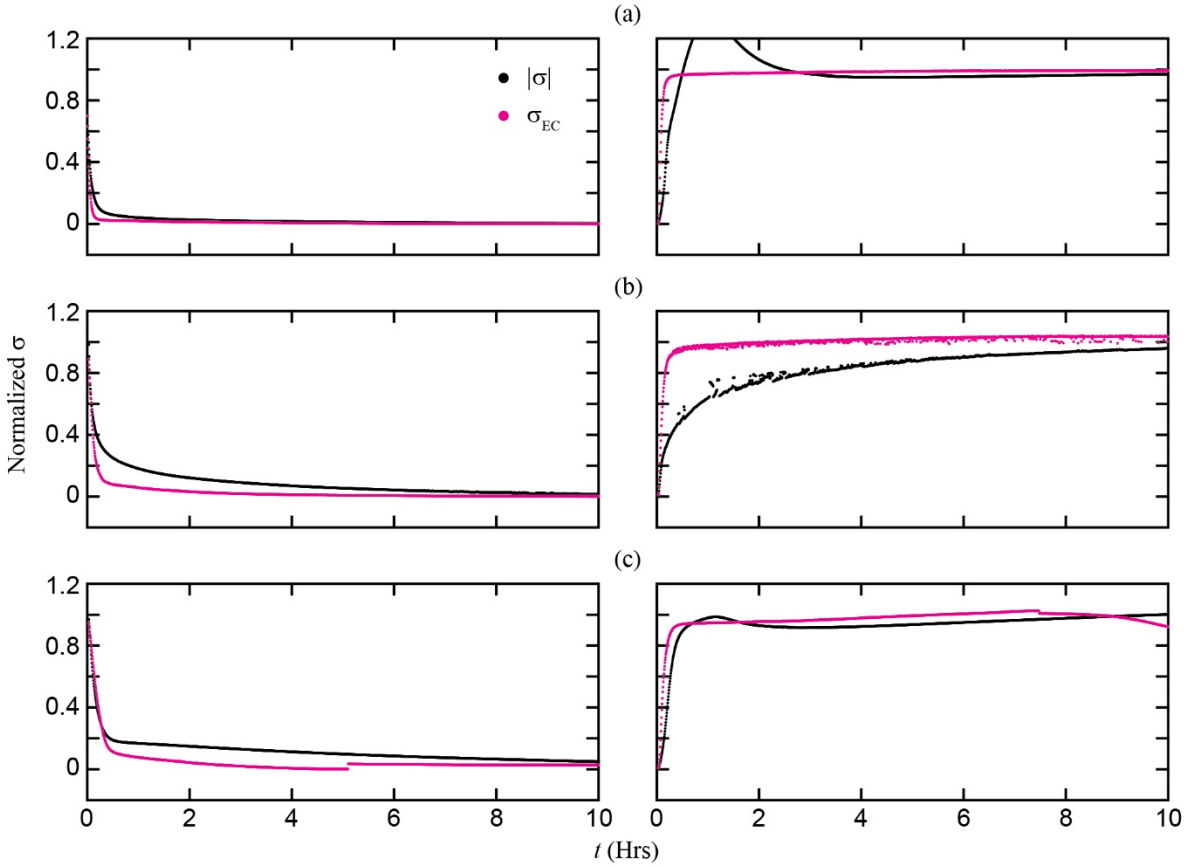

Figure 7. 15: Breakthrough curves from the tracer flush (left column) and tracer injection (right column) tests for (a) HC-MP24S-P-006-1V, (b) HC-MP24S-P-007-2H, and (c) SS-C3-P-019.

After establishing a steady flow rate, initial measurements were collected under flow with the saturating fluid (i.e. ~80,000 μS/cm). All samples exhibited constant σ_{EC} and $|\sigma|$ over a period of 1 hour. Following this period, the tracer flush test was started. Tracer flush and injection tests ran between 24-48 hours each, and were terminated after the effluent EC probe readings matched the influent EC probe readings. The one exception was the tracer injection test for sample HC-MP24S-P-007-2H, which stopped logging EC data before this criterion was reached due to a computer malfunction. SIP data were corrected using the method described in Section 6.4, with the geometric factor determined from the regression shown in Figure 7. 14. All breakthrough curves were corrected for collocation issues using the methods discussed in Section 6.4, and are shown in Figure 7. 15. Both σ_{EC} and $|\sigma|$ exhibited the expected breakthrough curves, with their conductivities decaying from the higher (~80,000 μS/cm) to lower (~8,000 μS/cm) fluid conductivity during the tracer flush test, and reverse during the tracer injection test. The conductivity measured by the influent EC probe was constant during the tracer flush and injection test, and was close to the injecting fluid. The conductivity measured by the effluent EC probe also exhibited a breakthrough curve, lagging behind the conductivities measured by the EC sampling probe and SIP. Bubble events affected the sampling and effluent EC probes in all the datasets. These were most significant in the HC-MP24S-P-006-1V and SS-C3-P-019 tracer

injection curves. The interpretation of data collected from sample HC-MP24S-P-006-1V was not adversely affected by these artifacts, and no correction was applied. Bubble artifacts significantly impacted data from the EC sampling probe, collected during the SS-C3-P-019 tracer injection phase. Impacted data were removed from the dataset using the approach defined in Section 6.4. before fitting the hysteresis curve. For all experiments, accept the tracer flush test for SS-C3-P-019, the breakthrough curves for $|\sigma|$ lagged behind σ_{EC}.

The corrected $|\sigma|$-σ_{EC} hysteresis loops are shown in Figure 7. 16 alongside Archie's Law as calculated using the formation factor determined from the initial phase of the tracer experiment. All datasets indicate some degree of hysteresis between $|\sigma|$ and σ_{EC}, with clearly defined hinge points (i.e. points 1 and 3 as defined in Figure 6. 18). The loops also clearly resemble the

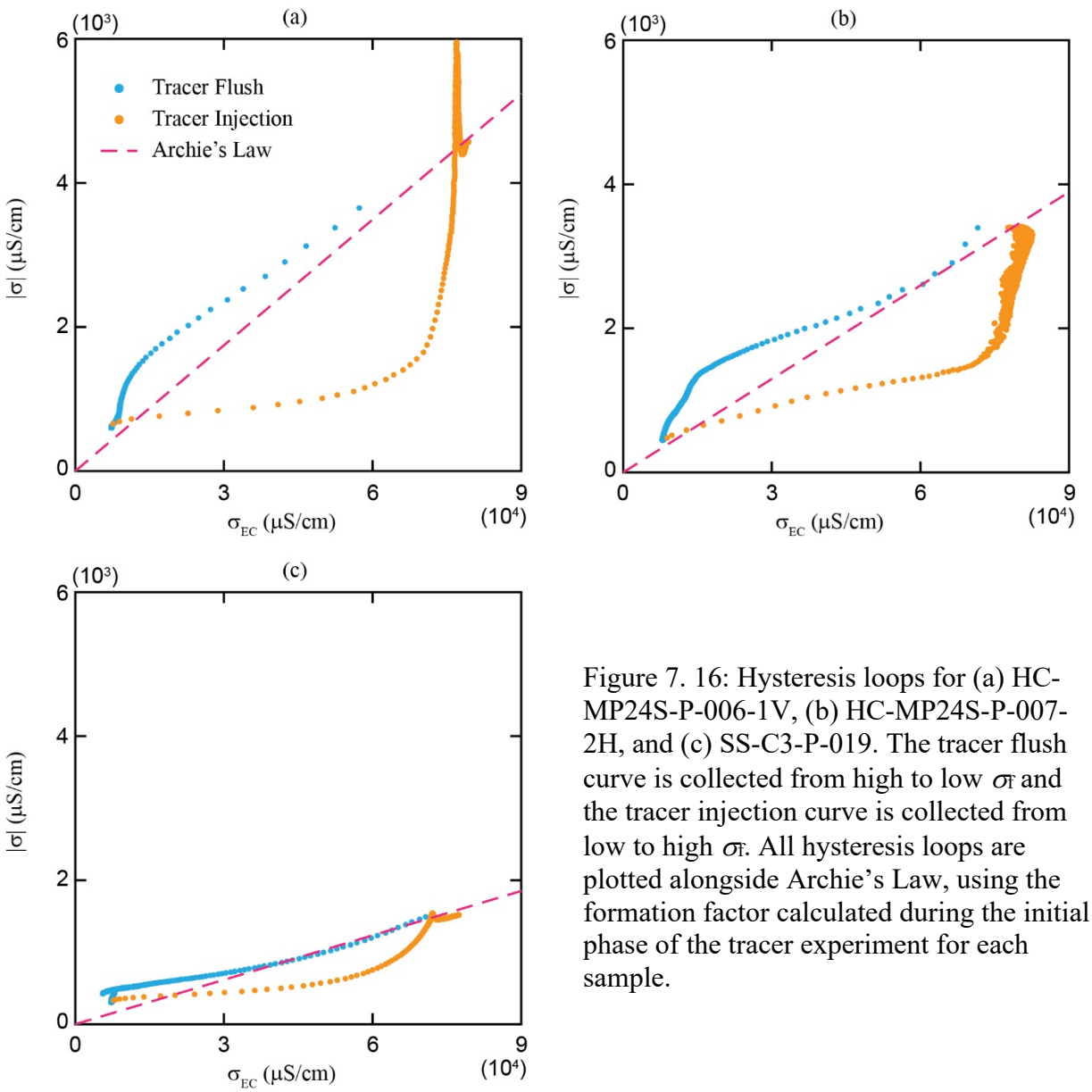

Figure 7. 16: Hysteresis loops for (a) HC-MP24S-P-006-1V, (b) HC-MP24S-P-007-2H, and (c) SS-C3-P-019. The tracer flush curve is collected from high to low σ_T and the tracer injection curve is collected from low to high σ_T. All hysteresis loops are plotted alongside Archie's Law, using the formation factor calculated during the initial phase of the tracer experiment for each sample.

example of co-located hysteresis data in Figure 6. 20. Sample SS-C3-P-019 exhibited the least hysteresis, while the degrees of hysteresis for HC-MP24S-P-006-1V and HC-MP24S-P-007-2H was similar. Samples SS-C3-P-019 and HC-MP24S-P-006-1V exhibited non-parallel tracer injection and flush phase curves, while the curve exhibited by HC-MP24S-P-007-2H was noticeably more parallel. Data artifacts evident in the breakthrough curves (Figure 7. 15) are also apparent in the hysteresis loops, most notably at the end of each phase (i.e. points 0 and 2 from Figure 6. 18).

The breakthrough curves shown in Figure 7.3.2 exhibited the expected behavior for dual domain porosity samples, in which the measured bulk electrical conductivity (in the case of this experiment $|\sigma|$) lags behind the directly sampled σ_T due to the added dependence of the bulk electrical conductivity on the immobile domain fluids. Due to this, plotting the $|\sigma|$-σ_T curves for all samples (Figure 7.3.3) results in characteristic hysteresis loops, similar to those observed in previous studies focusing on unconsolidated (Briggs et al. 2013; Briggs et al. 2014; Singha et al. 2007). In addition to observing hysteresis, the curves plotted in Figure 7.3.3 do not exhibit the averaging effects of low flow media reported previously (see Briggs et al. 2014). All samples have clearly defined hinge points, indicating that the approach of using elevated pressures to inject tracer fluids through the cores was successful in overcoming any averaging effects caused by low flow rates. These results confirm the ability of the approach outlined in this study to characterize mass transfer parameters in rock cores.

Following the approach outlined in Briggs et al. (2014) and explained schematically in Figure 6. 19, we analyzed the experimental hysteresis loops graphically to determine β, the ratio of immobile to mobile porosity (Figure 7. 17-19). This analysis involves identification of four hinge points on the hysteresis loops; these hinge points define a quadrilateral. If the mobile and immobile domains behave as conductors in parallel, the loops appear symmetric around a line corresponding to the equilibrium, single-phase Archie's Law, as defined by the formation factor (as in Figure 7. 17). Under parallel conduction, the analysis for β could be performed using hinge points 0, 1, and 2 or 2, 3, and 0, with approximately equivalent results. Here, we see evidence of non-parallel conduction, as evidenced by asymmetric hysteresis loops, which is consistent with theoretical findings for realistic immobile regions (Day-Lewis et al., 2017); thus, we report two sets of values for β, θ_m and θ_{im}. Porosity was independently measured gravimetrically. Given the β estimated graphically and porosity, θ, determined gravimetrically, the immobile and mobile porosities are calculated as:

$$\theta_{\mathrm{im}} = \frac{\beta\theta}{1+\beta} \quad \text{and} \quad \theta_{\mathrm{m}} = \frac{\theta}{1+\beta}\,. \tag{7.1}$$

The results of graphical analyses for β are reported in Table 7. 6 along with calculated values for θ_{m} and θ_{im}. Values of α were calculated by forward modelling the decay curves (Figure 7. 20) using the derivative of Equation 6.3:

$$\frac{\partial \sigma_b}{\partial t} = (\theta_m + \theta_{im})^{q-1} \left\{ \begin{array}{c} \theta_m(abe^{bt} + cde^{dt}) + \\ \alpha \left[ae^{bt} + ce^{dt} - \left(\frac{\sigma_b/(\theta_m - \theta_{im})^{q-1} - \theta_m(ae^{bt} + ce^{dt})}{\theta_{im}} \right) \right] \end{array} \right\} \tag{7.2}$$

Modelling results were optimized to the late time data points from the flush breakthrough curves (i.e. left column of Figure 7. 15), α values for all three cores are shown in Table 7. 6.

Table 7. 6: Results of graphical analysis for distribution coefficient and calculated mobile and immobile porosities.

	α (Day^{-1})	β	θ_m	θ_{im}
HC-MP24S-P-007-2H	1.41	1.74, 2.18	0.08, 0.07	0.14, 0.15
HC-MP24S-P-006-1V	1.31	3.79, 6.43	0.03, 0.05	0.19, 0.17
SS-C3-P-019	21.1	2.76, 6.40	0.04, 0.02	0.11, 0.13

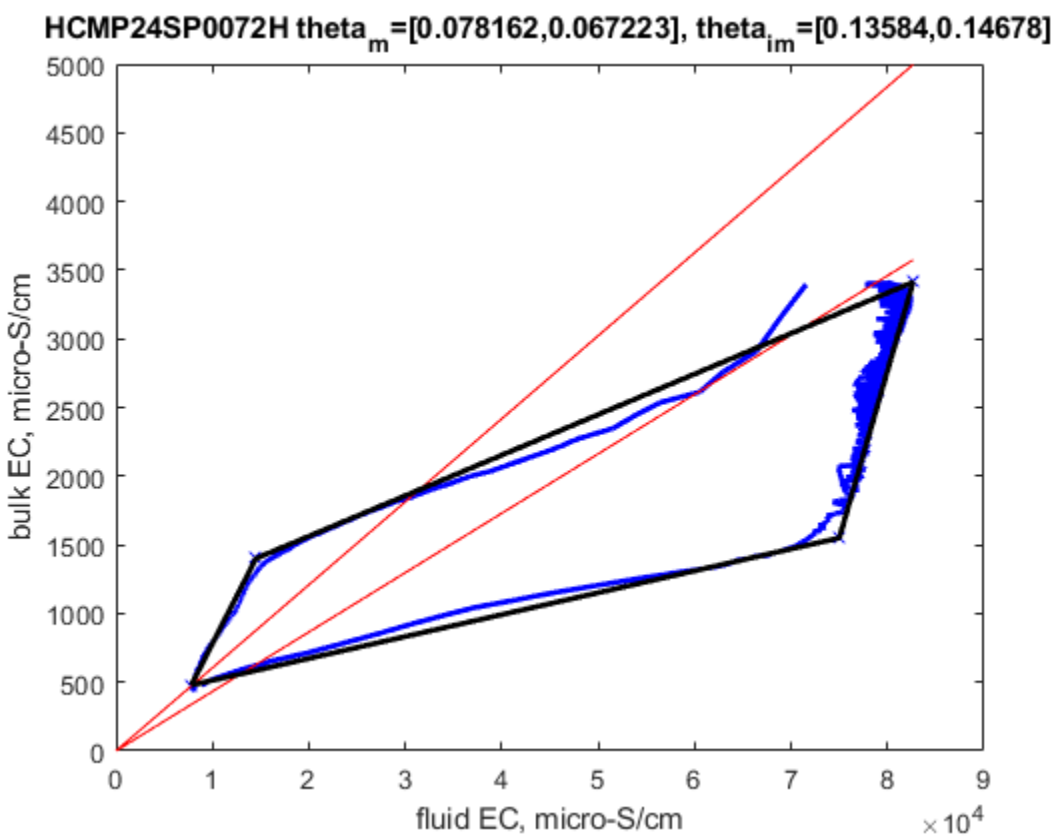

Figure 7. 17: Data and graphical analysis of fluid and electrical data from borehole HC-MP24S-P-007-2H. Red lines indicate the predicted bulk:fluid relation for the formation factor estimated using different data sets collected during tracer injection and flushing. The distribution coefficient was estimated using hinge points 0, 2, and 3, and using 2, 3, and 0, giving two sets of estimates for mobile and immobile porosity.

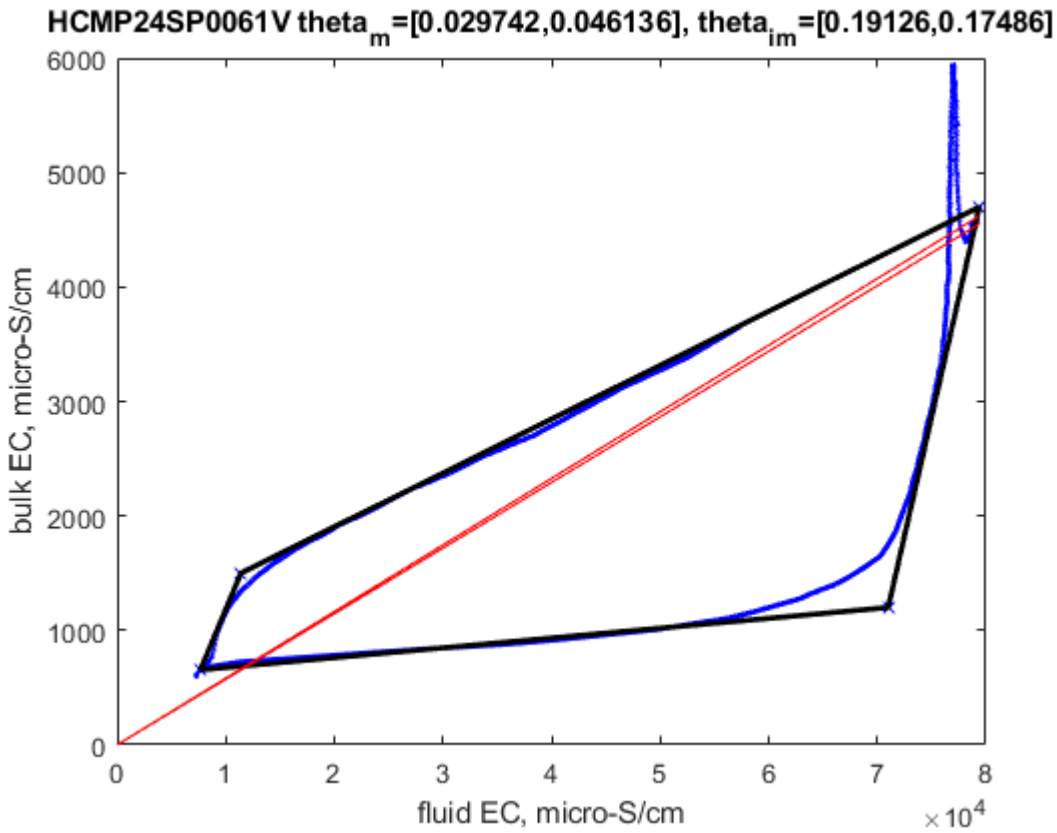

Figure 7. 18: Data and graphical analysis of fluid and electrical data from borehole HC-MP24S-P-006-1V. Red lines indicate the predicted bulk:fluid relation for the formation factor estimated using different data sets collected during tracer injection and flushing. The distribution coefficient was estimated using hinge points 0, 2, and 3, and using 2, 3, and 0, giving two sets of estimates for mobile and immobile porosity.

Transport implications: Mass transfer is known to occur at multiple scales, due to the many scenarios in which solute can diffuse between mobile and immobile porosities. Some examples of these scenarios may be the diffusion of solute between the rock matrix and a fracture network, to and from a low permeability zone (LPZ), or between geological contacts with varying flow characteristics (e.g. Parker et al. 2012). The samples collected in this study are relatively small volumes and so are susceptible only to mass transfer occurring at the pore scale. The likelihood of prominent longitudinal (oriented along the flow field axis) fractures is also low due to the volume and random sampling of the cores, indicating that the hysteresis observed in Figure 7. 16 is due to mass transfer occurring exclusively within the rock matrix. This observation introduces a significant amount of uncertainty into conventional transport prediction models due to the complexity of transport and storage of solute within matrix porosity within the subsurface. Values of α are similar for the Hydrite Chemical cores, while the Santa Susanna core, which represents a more heterogeneous geologic material than the Hydrite Chemical cores, was higher by a factor of ~10.

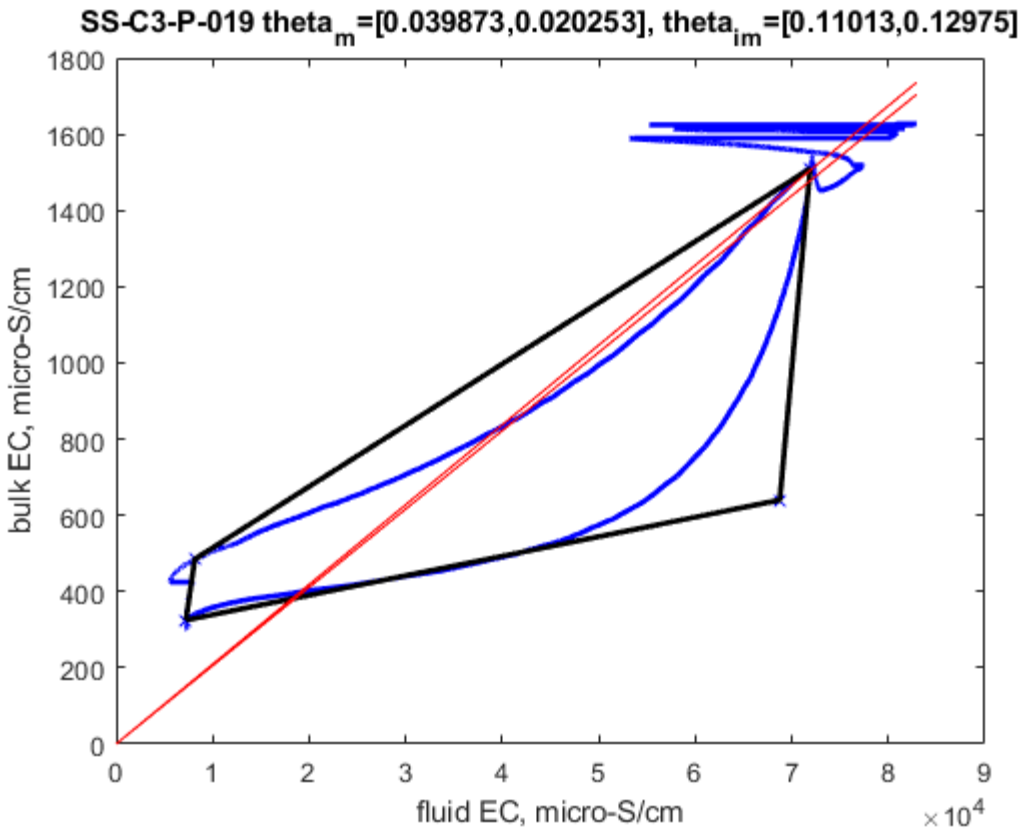

Figure 7. 19: Data and graphical analysis of fluid and electrical data from borehole SS-C3-P-019. Red lines indicate the predicted bulk:fluid relation for the formation factor estimated using different data sets collected during tracer injection and flushing. The distribution coefficient was estimated using hinge points 0, 2, and 3, and using 2, 3, and 0, giving two sets of estimates for mobile and immobile porosity.

Future modifications to the apparatus: Many of the sources of uncertainty discussed above are due to two issues with the apparatus: (1) fluid mixtures in the influent and effluent chambers during the course of the experiment and (2) flow irregularities due to different flow pathways through the sample (i.e. the effluent and sample port). These issues are inherent in the strategies used for obtaining complex measurements from rock cores, and the approach outlined in Briggs et al. (2014) for investigating mass transfer. The apparatus in this experiment designed to be consistent with these methods; however a redesign of the conventional complex and mass transfer apparatuses could eliminate many of the data interpretation issues associated with these uncertainties. A hypothetical redesign of the flow through apparatus is shown in Figure 7. 17. By reducing the volume of the influent and effluent chambers, fluid mixture is diminished and more easily correctible. This could be accomplished by using a conductive resin rather than water for the SIP measurement. This modification would also eliminate the need for the sampling port at the side of the core, making the hassler core holder less prone to sealing issues. The fluid EC data could be collected from a cell along the effluent tube instead, also eliminating many of the fluid flow issues that were encountered during this experiment. This approach may also better

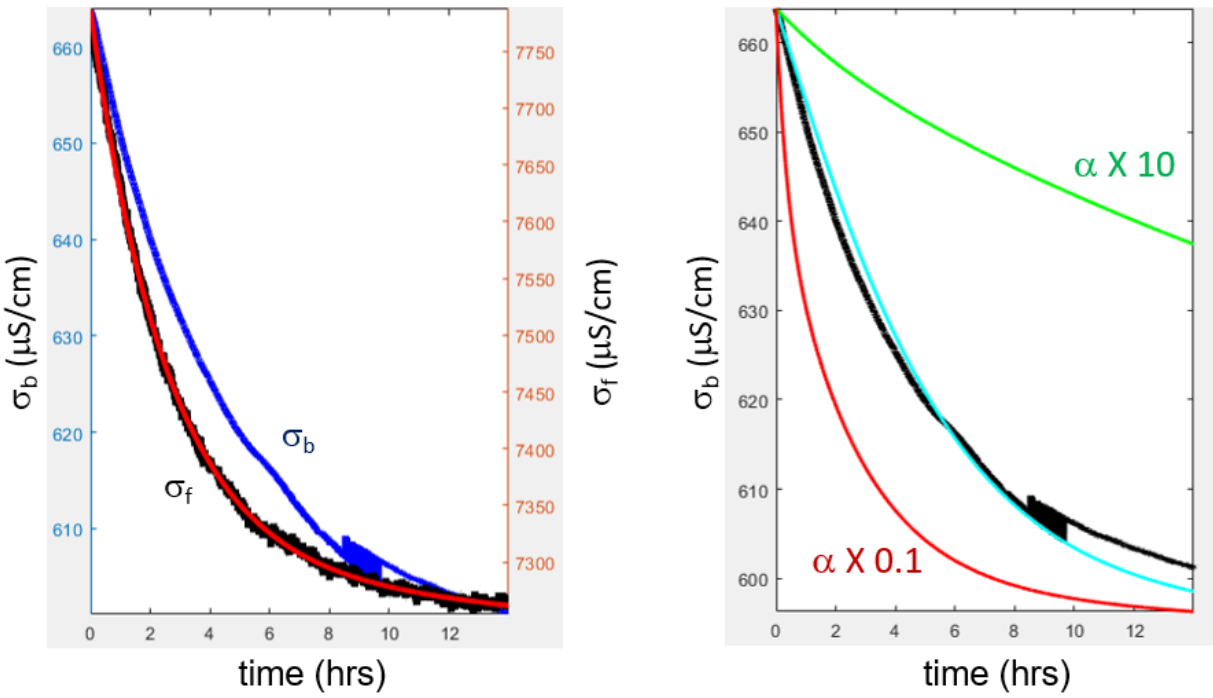

Figure 7. 20: An example of late time analysis of breakthrough curves for the purpose of estimating α. Fitting (a) σ_f and (b) σ_b at late times allows quantification of α. The sensitivity (also demonstrated in b) of the data to α (also demonstrated in b) is evident from modeled curve σ_b assuming α of different orders of magnitude.

promote a 1D flow field through the core, and lead to more relatable values of $|\sigma|$ and σ_f as both of these parameters in the redesigned apparatus would be sampling from a similar volume. In this configuration, $|\sigma|$ would be measuring the entire core, and σ_f would be sampling fluids that have traveled through the length of the core. Correcting for the co-location issue would also be simplified, as it could be easily calculated using the total porosity and flow rate used for the experiment. While there are many column design issues to consider when collecting complex data, these modifications are feasible as the use of gel in SIP sample holders has been implemented in the past.

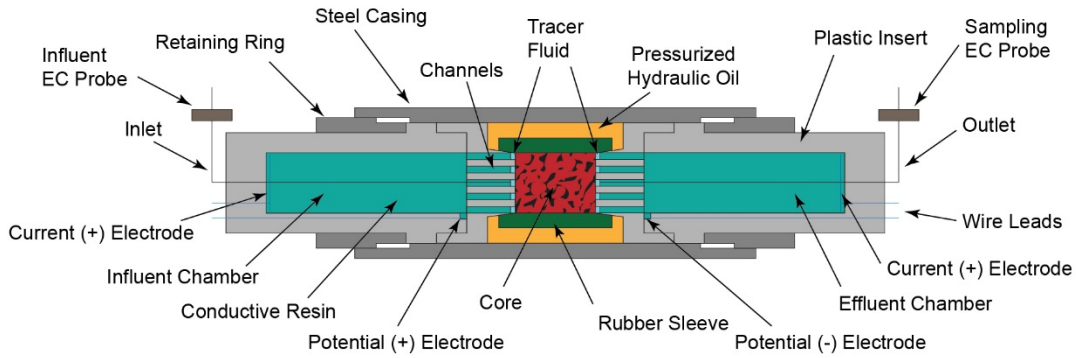

Figure 7. 21: A schematic of the proposed changes to the experimental apparatus to eliminate uncertainties associated with flow irregularities and fluid mixture occurring in the influent and effluent chambers.

7.4 Pore scale modeling results

Numerical pore-scale models were also developed to explore the possible interaction between fractures and rock matrix that could not be explore experimentally using laboratory measurements on rock core. These numerical experiments were done using the USGS codes discussed in Section 6.5. Flow, solute transport, and electrical conduction were simulated for two-dimensional pipe-lattice networks incorporating fractures based on the total porosity, centrifuge-estimated immobile/total porosity, permeability, and formation factors identified experimentally. Here, we present results for a model that approximates the properties of core samples (Table 7. 7) from the Hydrite boreholes.

Table 7. 7: Hydraulic properties representing Hydrite cores and calibrated pore network model

	Target	*Pore network model*
Porosity	0.22	0.23
Immobile porosity	0.12	0.15
Mobile porosity	0.10	0.08
Hydraulic conductivity	1.5×10^{-6} cm/s	6.4×10^{-6} cm/s
Immobile/total porosity	0.55	0.56

Once calibrated, we use the pore network model (Figure 7. 22(a)) to identify mobile (here conceptualized as fractures) and immobile domains and to calculate the residence times in the latter (Figure 7. 22(b)), which are taken as the reciprocals of the rate coefficients, α, in Section 6.5; these rates, along with the parameters of the tracer experiment (e.g., flow rate, core length) and physical properties calculated by the model (i.e., permeability, mobile porosity, immobile porosity) are used as input to the one-dimensional analytical model (Section 6.4.4) to simulate the hysteretic relation between bulk and fluid conductivity that occurs during tracer breakthrough and flushing (Figure 7. 22(c)). This model result can then be compared to the results from the laboratory combined tracer/electrical experiments. The developed pore network model opens the

door to further improve understanding of dual domain mass transfer processes in rocks characterized by discrete fracture networks such as shown in Figure 7. 22.

7.5 Assessment of distribution of contaminant mass relative to distribution of fractures

The conceptual model for contamination by dense non-aqueous phase liquids (DNAPLs) at sites situated on fractured sedimentary rock (Figure 6. 1, from Parker et al., 2012) has matrix diffusion and other processes playing a key role on source zone evolution (Figure 6. 1(a) inset, LHS) and plume transport (Figure 6. 1(a) inset, RHS). At early time DNAPL releases occur and the DNAPL is largely constrained to fractures and may penetrate deep below the water table depending on release conditions and capillary forces and the DNAPL achieves a stable positon in a relatively short period of time (early time stage, Figure 6. 1(b)). Then over many years to decades (intermediate time stage, Figure 6. 1(b)) the source zone evolves where DNAPL becomes depleted due to dissolution in groundwater flowing in fractures and diffusive-driven mass transfer between fractures and the rock matrix in both the source zone and plume that forms downgradient. Parker et al., (1994 and Parker et al., (1997) examine diffusion effects on DNAPL source evolution and DNAPL disappearance, and VanderKwaak & Sudicky (1996) expanded the analysis to include dissolution in groundwater flowing in the fractures in addition to diffusion. The bulk fracture porosity of these systems is generally small (ϕ_f = 0.01 to 0.0001%) and nearly all groundwater flow occurs through the interconnected fracture network. In contrast the rock matrix generally has much larger porosity (typically ϕ_m = 2 to 20% in sedimentary rock) and constitutes the bulk of the contaminant mass storage capacity in the system. The storage capacity in the matrix may be further enhanced by organic carbon dominated sorption in the rock matrix. At later times, which may be after several years to a few decades, most of all of the DNAPL may become depleted (late time stage, Figure 6. 1(b)), nearly all contaminant mass occurs in the rock matrix, and plumes are strongly attenuated by diffusion and other processes. Source inputs may also decline over time as the source evolves, and contamination in the matrix may be subject to

degradation by abiotic and/or biological degradation processes (e.g. Lima et al., 2012; Schaefer et al., 2013). This seems to be the case at the SSFL and NAWC sites at locations investigated in this study, which show little or no remnant DNAPL at this time. Goode et al.,(2014b) indicates that remnant DNAPL was previously observed in one borehole at the NAWC site. In contrast substantial DNAPL persists at the Hydrite site, likely due to the large volumes of multicomponent DNAPL releases that have occurred over longer time periods that basically "swamped" the storage capacity of the bedrock matrix. Regardless, detailed profiles at all sites

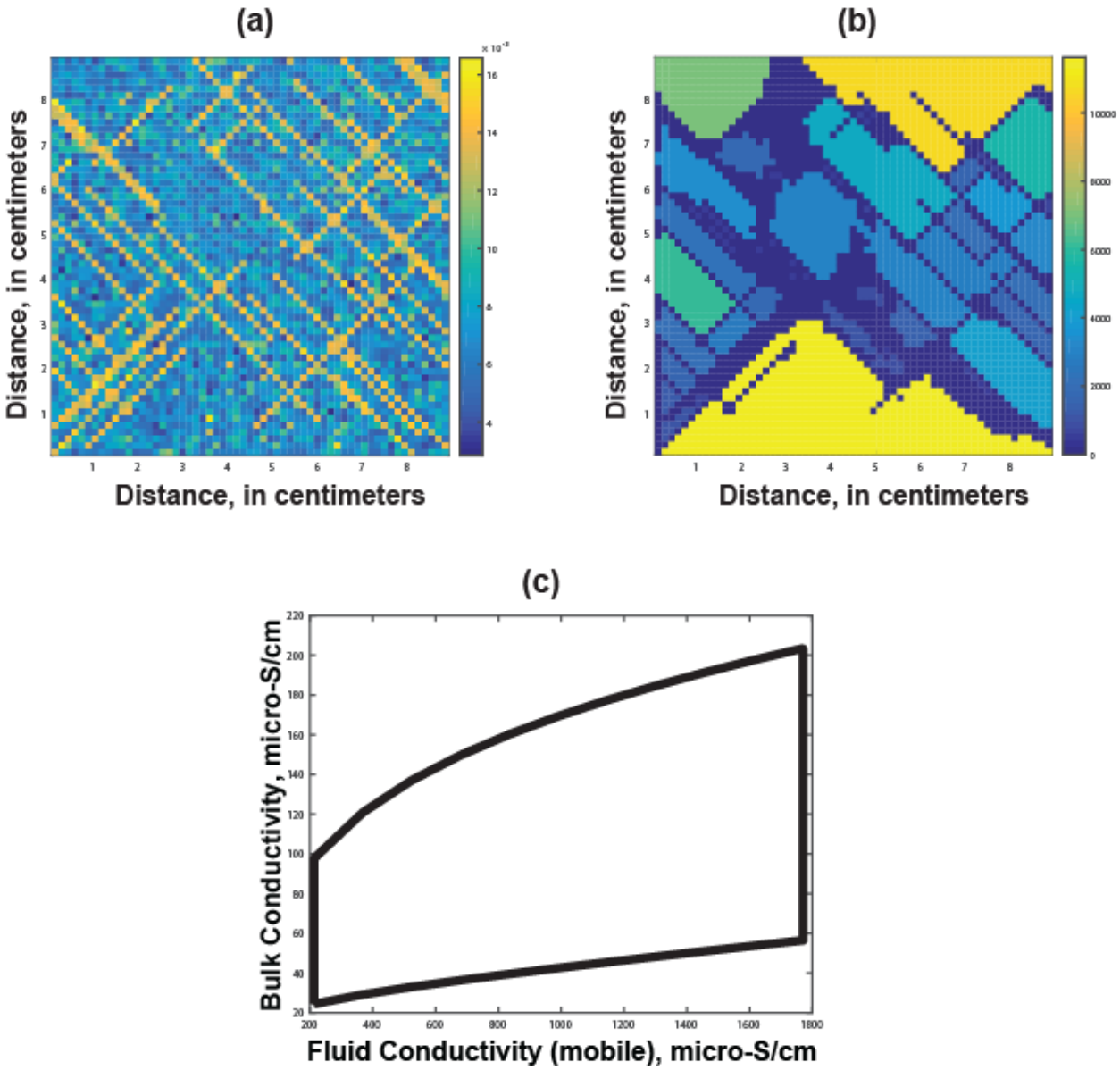

Figure 7. 22: (a) Stochastic discrete fracture network calibrated to approximate the hydraulic properties of cores from the Hydrite site. (b) Local residence times within the fracture network, with residence time varying between the mobile domain and multiple immobile domains. (c) Simulated hysteretic bulk versus fluid conductivity relation.

from high resolution core sub-sampling confirm the presence of substantial mass in the bedrock matrix as a result of diffusive driven mass transfer. The challenge at these sites is assessment of the contaminant mass distribution, in order to understand matrix diffusion effects on plume transport and fate, risk assessment and remedial decision making.

The contaminant mass distribution relative to fractures is spatially and temporally variable, dependent on the rock matrix and contaminant properties and contaminant concentration history in the fracture. For example, Figure 7. 23 shows 1-D diffusion profiles into a rock matrix using an analytical solution assuming a constant concentration in the fracture for two different rock matrix conditions, one representing a 'sandstone' type material with relatively high matrix porosity (and consequently a higher tortuosity factor) and low sorption (consistent with SSFL and Hydrite) and the other a 'mudstone' type material with lower matrix porosity (and consequently lower tortuosity factor) and high sorption. The extent of matrix invasion off a fracture varies, with potential for much higher invasion distances in the sandstone matrix versus mudstone matrix, although the total mass diffused may be larger for the latter since the greater sorption increases the matrix storage capacity and allows higher concentration gradients for inward diffusion to be maintained. The fracture – matrix surface area is also key to how plumes evolve and matrix diffusion effects, which depends on distributions of fractures (spacing, lengths, connectivity, apertures) and flow system conditions in the fracture network. Groundwater sampling focuses primarily on the mobile groundwater in fractures and misses the bulk of the contaminant mass stored in the rock matrix and is also vulnerable to bias from cross-connection effects (e.g. Sterling et al., 2005). High resolution rock core sampling, focused on sample collection both adjacent to fractures and from the rock matrix between fractures, with the sampling scheme tailored to the fracture network and contaminant properties and expected matrix invasion distances, provides the most robust measure of the contaminant distribution relative to fractures, but is costly given the need for collection of continuous rock cores, requirements for a field crew with specialized equipment to conduct the rock core sampling and sample processing (i.e. crushing and field preservation in suitable solvent for extraction), sample shipping to a laboratory, and for specialized laboratory extraction of the contaminant mass and analyses of the many samples needed to adequately define the mass distribution. Therefore a critical question is whether the new geophysical tools being investigated in this study offer potential to assess the contaminant mass distribution relative to fractures.

7.6 Evaluation of contaminant mass distribution relative to fractures at the study sites

Figure 7. 24 shows an example WellCAD plot from Hydrite including simplified lithology logs, fracture distributions observed in the rock core, fractures interpreted from the Acoustic Televiewer (ATV) logging and contaminant distributions from the high-resolution rock core subsampling (provided as total VOCs) (refer to Appendix A.3 for all three sites). In general, it is expected that core logs will over-represent the *in situ* fracture intensity due to logging of mechanical breaks, whereas interpretation of ATV logs is expected to under-represent the *insitu* fracture density due to instrument resolution limits. Judgement calls are made by the field geologist in identifying core breaks suspected of being mechanical breaks versus actual fractures. Rock core collection at all three sites utilized triple-tube coring methods (HQ3), which was

intended to minimize mechanical breaks in the core. Interpretation of ATV logs is also subjective and depends on the experience of the geophysicist doing the interpretations, as well as the rock type, drilling method and borehole wall quality, borehole diameter, etc. but it is unlikely that fractures with apertures much smaller than 1 mm would be picked up via ATV. Also little information is obtained from logging of fractures in core and via ATV logs on whether groundwater flow is occurring in the fractures and at what rates under ambient conditions. Other hydrophysical tests described elsewhere in the report provide more insights.

Besides the high resolution rock core contaminant data which was collected at all three sites, data from a new technology developed by FLUTe, referred to as the FLUTe Activated Carbon Technique (FACT) also provides contaminant data from fractured rock boreholes. The FACT is essentially a carbon strip pressed up against the borehole wall for a relatively short time interval (typically two weeks) and provides an integrated measure of contaminant mass that is up taken by the FACT during the deployment period, both from diffusion out of the rock matrix and from advection in fractures. The degree to which cross-connection effects (e.g. during drilling and while the borehole is open) influences the FACT is unknown and likely strongly dependent on site conditions, drilling method, and FACT deployment conditions. FACT is being evaluated in more detail in ESTCP Project ER-201630 "Evaluation of FLUTe FACT as a Screening Technology for VOC Distribution in Fractured Rock Boreholes" which will include further assessment of the 94BR dataset as well as additional datasets from NAWC and other site(s). Also the FACT only provides a relative measure of contaminant mass flux to the carbon strip during the deployment period, and it is currently unknown whether this can be related with certainty to actual contaminant concentrations and/or mass distribution.

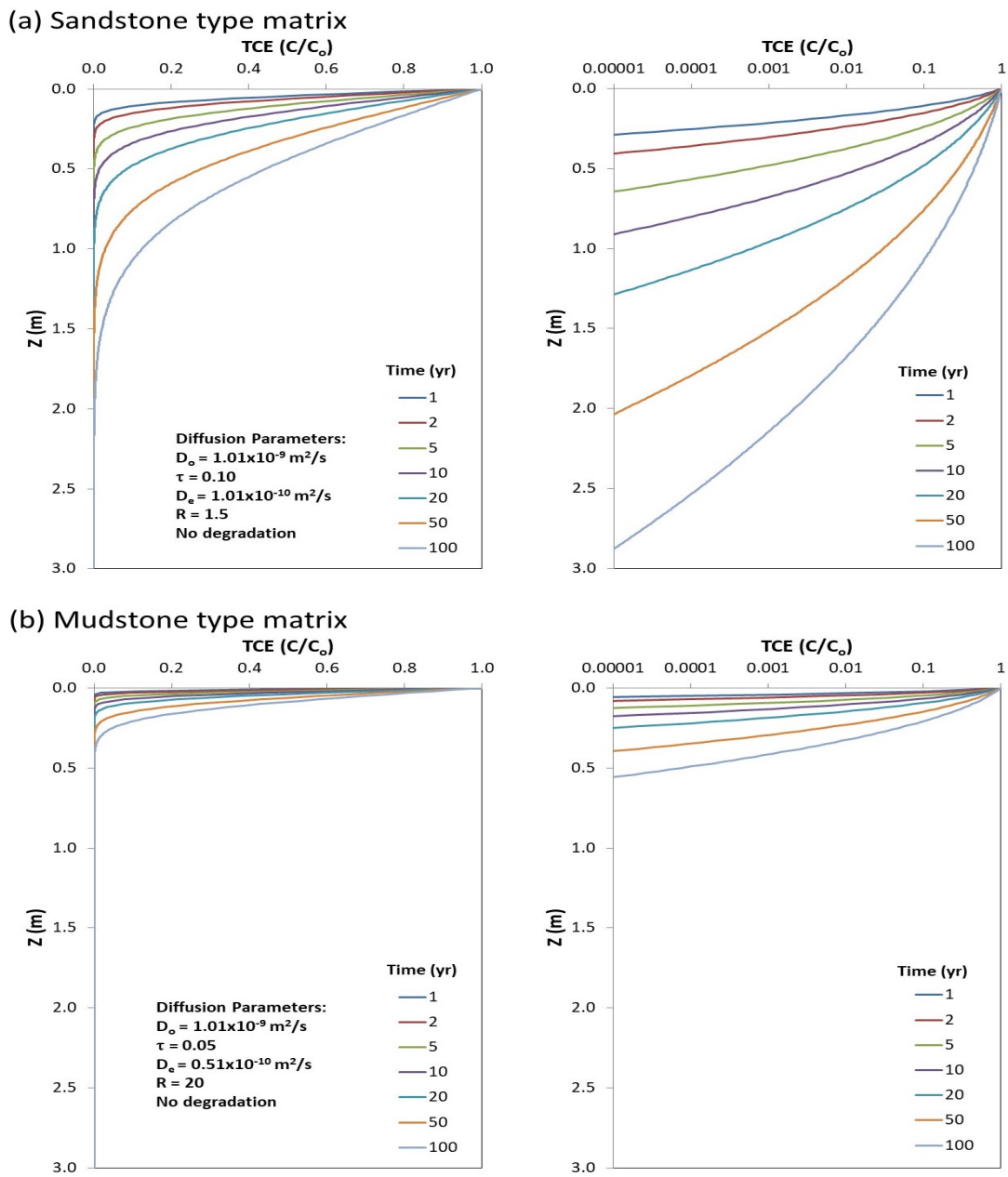

Figure 7. 23: Example 1D diffusion simulations of matrix invasion off a fracture assuming a constant source for (a) sandstone type matrix (ϕm = 15%, τ = 0.10, R=1.5) representative of SSFL, and (b) mudstone type matrix (ϕm = 7.5%, τ = 0.05, R=20) representative of NAWC. Both linear and log concentration scales are shown. Although the matrix invasion distance is much lower for the mudstone, the total mass diffused may be higher due to the high sorption in the matrix which increases the storage capacity and maintains higher concentration gradients during the inward diffusion stage.

The rock core contaminant profiles at all three sites show much contaminant mass in the rock matrix, both associated with fractures and in the matrix off fractures (Appendix A.3).

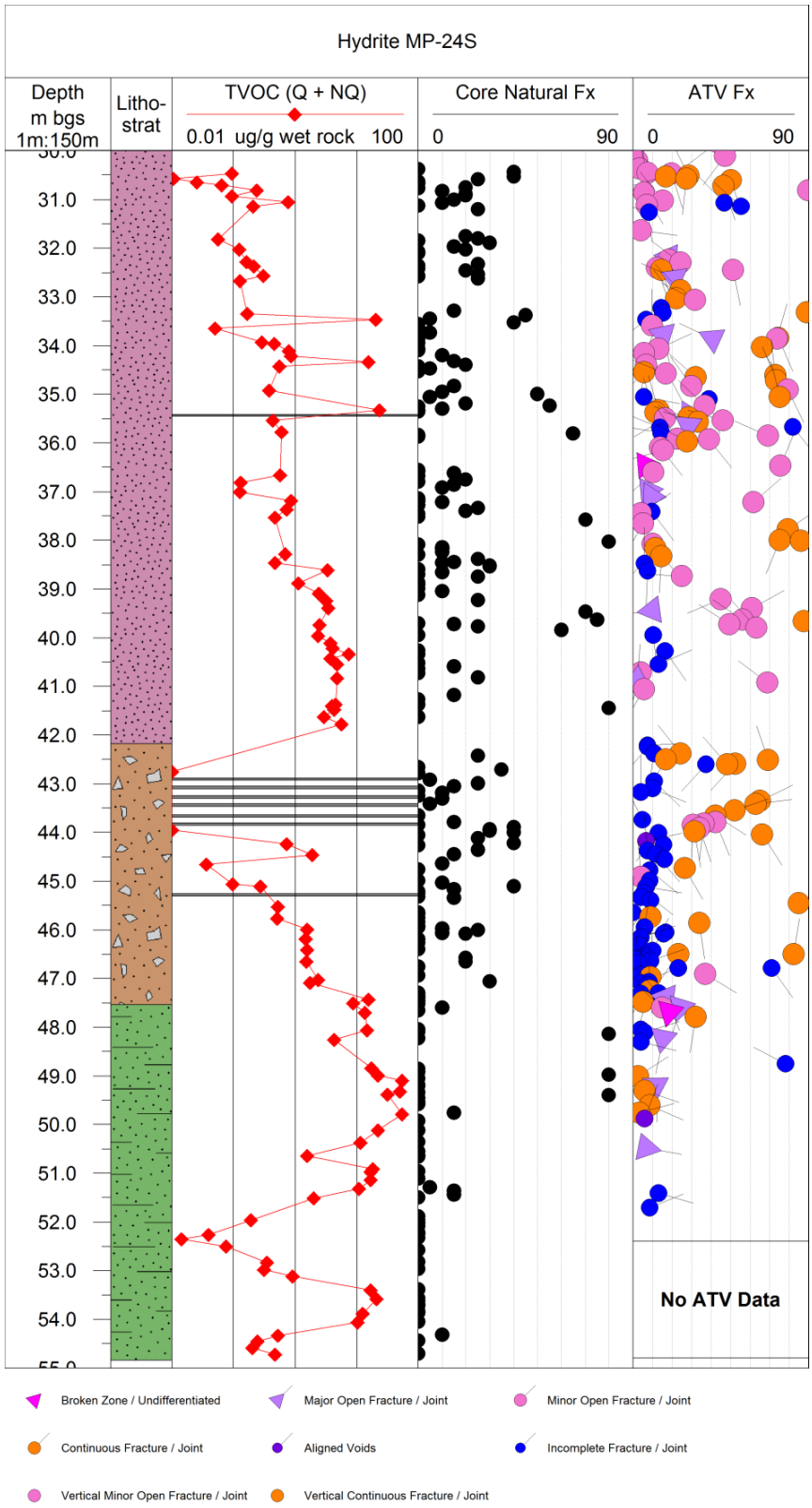

Figure 7. 24: WellCAD plot from Hydrite including simplified lithology logs, fracture distributions observed in the rock core, fractures interpreted from the Acoustic Televiewer (ATV) logging and contaminant distributions from the high-resolution rock core subsampling (provided as total VOCs).

8.0 Technology Limitations

This section is a direct response to the following comment received on the May 2017 Interim Progress Review (IPR) presentation: "*In the Final Report please include a description of conditions under which technology may have difficulty functioning (i.e. certain minerals etc.)*"

The primary limitation of the geophysical technologies investigated in this project is that they only provide proxy measurements of the physical and chemical properties of interest. These measurements must always be interpreted within the context of any direct supporting observations available. Physics-based relationships between the geophysical measurement (e.g. the imaginary part of the complex conductivity) and the subsurface property of interest (e.g. the permeability) exist but can only be defined on simple geometrical representations of porous media that inevitably do not represent the complexity of the subsurface. Consequently, empirically-derived relationships (based on extensive observations) are employed to implement the technologies in practice. This project has highlighted limitations of this approach. For example, previously derived relationships relating complex resistivity measurements to permeability were applicable to two sites (the sandstone dominated SSFL and the sandstone/dolomite Hydrite site) but were inapplicable to the mudstone site (NAWC). This in part may be the result of the small pore sizes in these fine-grained rocks being beyond the detection range of the complex resistivity method. The NMR permeability prediction equations performed quite well across all three sites. The better performance of NMR over CR in this respect may reflect the better sensitivity of NMR to small pore sizes relative to the CR methodology.

Mineralogical variability also likely limits the transferability of empirical relationships between geophysical measurements (NMR and CR) and pore geometric properties across the sites. In this study, XRD analysis highlighted the mineralogical complexity of the NAWC site relative to the SSFL site. Both the NMR and CR permeability prediction equations include parameters that capture the dependence of these measurements on the mineral surface chemistry (rather than the pore geometry). These parameters have been investigated and do show sensitivity to mineralogical variation. For example, the surface relaxivity appearing in the NMR equations is highly sensitive to the presence of iron minerals (Keating and Knight, 2007). It is well known that large iron mineral concentrations can cause NMR predictions of permeability based on published models to perform poorly. The complex resistivity measurements are also very sensitive to the presence of electronically conductive minerals (e.g. iron sulfide), which complicates the interpretation of the measurements in terms of geometric properties of the pore space. The presence of electronically conductive minerals at concentrations greater than about 0.5% will modify the CR response. Further work is needed to constrain the dependence of NMR and CR model parameters to mineralogy and how this causes uncertainty in the prediction of pore-geometric parameters.

A second general fundamental limitation of geophysical technologies relates to the resolution limitations when investigating contaminated fractured rock formations. The resolution of

borehole geophysical tools varies between technologies. A high resolution Acoustic Televiewer Viewer (ATV) may image fractures daylighting at the borehole wall with a resolution of 1-2 mm. However, geophysical technologies that image beyond the borehole wall, as needed to assess contaminant mass in the rock matrix between fractures, offer vertical resolution on the order of 10s of centimeters at the very best. No proven geophysical technologies currently exist to inform on fracture distributions in formations characterized by micro-fractures e.g. in crystalline rock. However, geophysical technologies that sense beyond the borehole wall are well suited to providing information on fractured formations characterized by bedding plane features and joints. For example, at the NAWC site, most of the contaminant transport is associated with highly fractured coal seam units (approximately 30-60 cm thick) and the contaminant mass has diffused into the rock matrix around these fractured zones. This makes for a realistic application of geophysical logging technologies to inform on matrix properties adjacent to such fractured zones.

This project specifically focused on estimating pore geometric properties of the rock mass controlling mass transfer and the possibility of estimating contaminant mass directly from geophysical logging datasets. CR and NMR remain the two geophysical technologies with the highest likelihood of providing non-invasive estimates of the pore size distribution and permeability. Given the unique aspects of both measurements with respect to the pore geometry, no other geophysical logging technology is likely to perform better for this purpose. However, the performance of these tools for the purpose of estimating pore size distribution and permeability might be improved through better integration of geophysical datasets that can constrain variations in the rock mineralogy as it is clear that the uncertainty in the CR and NMR predictions of pore geometric properties is largely associated with mineralogical variability. Assumed “constants” in the CR and NMR permeability equations depend on mineralogy. Integration of technologies that can constrain variations in mineralogy (e.g. spectral gamma loggers in addition to magnetic susceptibility tools) provide a possible path forward to improved technology performance.

A fundamental limitation of geophysics is that no technology exists to directly quantify the contaminant mass at the typical concentrations found at DoD sites. This project explored whether multi-variate linear regression could be used to identity relationships between a suite of commercially available geophysical logs and contaminant mass recorded in cores recovered from the boreholes. Although some success with building predictive equations within a single well was achieved, the regression equations did not transfer well between wells or sites. Lithological (and once again mineralogical) variations between wells and sites are likely to explain this limited success. One opportunity to improve on this performance is through the application of more powerful machine learning-based techniques for extracting non-linear relationships from large datasets. Such an approach might lead to better predictive relationships that can better compensate for lithological variations between sites.

Laboratory measurements on electrical signatures of mass transfer highlight an opportunity to develop new borehole geophysical instrumentation whereby electrical measurements are

acquired during injection of an electrically conductive tracer (in very conductive groundwater a dilute, resistive tracer could be used). Demonstration of the performance of such a borehole tool is currently in progress (ESTP project ER201732, R. Iery, NAVFAC-EXWC, PI). This tool has the potential to provide in situ estimates of mobile-immobile porosity ratios and mass transfer coefficients over multiple scales. The tool could be used to examine scale-dependent behavior of mass transfer as it can be configured to measure a range of rock volumes beyond the borehole wall. There is also the possibility to upscale these measurements further by imaging between boreholes.

9.0 Technology Transfer

Technology transfer was implemented through numerous avenues. Findings of this research provided content utilized in dedicated technology transfer activities on ESTCP ER201567-T2 (Slater, PI) that was running at the same time as this grant. Activities under ER201567-T2 included the development of short tutorial videos on different geophysical technologies. One of these videos specifically focused on the borehole NMR logging method that relied heavily on efforts conducted under this SERDP project [https://doi.org/10.5066/F73J3BW0].

Material from this project was used in a number of technology transfer efforts addressing the challenges of characterization of contaminated fractured rock aquifers. Examples include:
[1] Development of an invited paper that followed participation in a special session a special technology transfer focused session at the *May 2016 Chlorinated Conference* (under ER201567-T2) This review paper provided an overview of geophysical technologies appropriate for characterization and monitoring at fractured-rock sites and was published in the Journal of Environmental Management (Day-Lewis, Slater, et al., 2017)
[2] Presentations on the technologies at national conferences/workshops that specifically target site remediation professionals. This included the keynote presentation at the *2017 NGWA Conference on Fractured Rock and Groundwater* given by PI Slater.
[3] Presentations on the technologies at international conferences/workshops that specifically target site remediation professionals. This included a keynote presentation at the 2017 '*Novel Methods for Subsurface Characterization and Monitoring (Novcare): From theory to practice*' meeting in Dresden (Germany) given by PI Slater.
[4] Contributions to material presented in "*Introduction to Geophysical Methods for Fractured Rock*," a USGS-led 2-day workshop on fractured-rock for EPA Region 3 staff (May 24-25, 2017) given by co-PI Day-Lewis; an additional workshop is planned for EPA Region 4 in September, 2019.
[5] Contribution of fractured-rock case-study material to Navy RITS seminars presented at six locations, in coordination with ER-201579 and ER201567-T2 (3 presentations by PI Slater and co-PI Day-Lewis).
[6] Contributions of background and fractured-rock case-study material to the Environmental Restoration Wiki pages on geophysics developed by PI Slater and co-PI Day-Lewis: http://www.environmentalrestoration.wiki/index.php?title=Main_Page

[7] Contribution of material to the US Navy Fact Sheet " *Geophysical Methods for Characterization and Monitoring at Groundwater Remediation Sites*," developed in coordination with ER201567-T2.
[8] A Learning Lab for the Battelle Conference on Remediation of Chlorinated and Recalcitrant Compounds, on "*Using the Fractured Rock Geophysical Toolbox - Method Selection Tool*," led by co-PI Day-Lewis. The FRGT-MST was developed under ESTCP-201118.
[9] An invited platform presentation at the 2018 Battelle Conference on Remediation of Chlorinated and Recalcitrant Compounds, "*State-of-the-Practice in Geophysical Site Characterization and Monitoring*", delivered by co-PI Day-Lewis.

10.0 Conclusions

Findings from this basic research project provide solid insights into the potential of nuclear magnetic resonance (NMR) and complex resistivity (CR), two emerging geophysical technologies, for improving the characterization of sedimentary rock aquifers impacted by chlorinated solvent contamination. The center of the project effort was a methodical, exhaustive set of precise measurements of the physical properties of the rock mass controlling matrix diffusion coupled with state-of-the-art laboratory NMR and CR measurements performed on the same cores. This laboratory effort was supplemented by borehole NMR and CR logging using recently developed commercial technologies that have yet to enter mainstream use in the environmental site management sector.

The most compelling results of the project relate to the laboratory-scale characterization of the fundamental physical properties (pore size distribution and permeability) controlling contaminant transport and mass transfer between mobile pore domains (including fractures) and immobile pore domains (the rock matrix adjacent to fractures). Both NMR- and CR-derived relaxation times were shown to be correlated with characteristic pore sizes derived from mercury porosimetry and surface area from gas adsorption. These correlations were strong for the sandstone-dominated cores from the SSFL and Hydrite sites; the mudstone cores from the NAWC site did not align well with the relationships obtained for the other two sites. One exception was the relationship between the NMR relaxation time and the pore volume normalized specific surface area (S_{por}), where a single strong relationship exists for all three sites. The NMR method contained sufficient sensitivity to the pore size distribution to allow estimates of the ratio of the immobile to mobile porosity of samples to be estimated. Both CR and NMR measurements provide a link to permeability through the definition of geophysical length scales that can be used in place of established geometric length scales in models of permeability prediction. Comparison of geophysical predictions of permeability using recently proposed models with direct Darcy-test measures of permeability showed that both NMR and CR contain sufficient information on the pore geometry to permit order of magnitude estimates of permeability entirely from geophysical measurements. The joint use of NMR and CR data did not significantly improve permeability prediction relative to using the information extracted from a single measurement alone.

Assessment of the sensitivity of the NMR and CR measurements to contaminant mass relied on comparison of the NMR and CR borehole logging data against TVOC measurements from cores. The contaminant mass analysis involved an extraction procedure performed in the field; it was not possible to reliably preserve contaminants in core in situ to allow for precision laboratory NMR and CR measurements on contaminated core. The logging data had the advantage that measurements were acquired on the in situ contaminants/rock matrix adjacent to the borehole wall. A machine learning approach was performed to demonstrate that information from a large number of rapidly acquired borehole geophysical logs could be used to predict contaminant mass distributions along a borehole. The effectiveness of the approach was shown to depend on the dataset used for the calibration. Results suggest that predictive models built via machine learning will be more likely to predict variations in contaminant mass distributions within a single

borehole rather than between boreholes or across sites. However, the existing borehole logging tools do not provide the precision data obtainable with the laboratory instrumentation. Therefore, the results of the contaminant mass sensitivity analysis relate to the information content extractable from currently available logging tools that do not represent the information ultimately obtainable from these emerging geophysical technologies at the logging tools improve.

Besides assessing the information content of the emerging NMR and CR geophysical technologies, this project also acquired a wealth of information on the distribution of physical properties, fracture zones and contaminant distributions at three high-profile chlorinated solvent sites. The Discrete Fracture Newark (DFN) approach (Parker et al., 2012) was modified to incorporate the information obtainable from the NMR and CR measurements. This comprehensive approach that coupled coring/analysis with-in well measurements provided new insights into the distribution of contaminant mass around transmissive fracture zones at the three study sites. Distinct contrasts in contaminant mass distributions around fractures between the three sites were observed.

In an extension to the project, preliminary electrical tracer experiments coupled with pore-scale modeling of dual domain mass transfer demonstrated the opportunity that exists to build upon recent theoretical developments to estimate mass transfer coefficients and mobile/immobile porosity ratios from coupled measurements of bulk electrical conductivity and fluid conductivity. First of-a-kind instrumentation based around a Hassler sleeve encased in pressure vessel was developed to perform tracer breakthrough tests on representative cores from the three sites. The instrumentation proved challenging to perfect such that accurate measurements were only reliably acquired on five cores (rather than the 20 originally planned). Non-linearity in the relationship between bulk conductivity and fluid conductivity was identified, being diagnostic of a dual domain with mass transfer occurring between domains. Extension of the approach to include measurements of the real and imaginary (polarization response) parts of the complex conductivity might allowing the modeling of mass transfer parameters to be improved by using the imaginary conductivity to account for the effects of surface conduction. The experiments revealed for the first time mass transfer occurring within the rock matrix, independent of a fracture network. Mass transfer rate coefficients and immobile/mobile porosity ratios were estimated through the application of a recent analytical model. This process may have a significant effect on the fate and transport of contaminant mass, due to the significant surface area of the matrix porosity versus the fracture network.

In summary, results of this project support the adoption of two emerging geophysical technologies, NMR and CR, for the relatively rapid and cost-effective acquisition of information on the distribution of pore geometric properties controlling contaminant transfer at chlorinated solvent sites. These non-invasive borehole logging technologies provide information that cannot be readily obtained from the existing suite of geophysical logs that are in routine use at contaminated sites. The results of the project do not provide a compelling case for the direct detection of contaminant mass in situ. Future improvements in the sensitivity of borehole logging instrumentation (e.g. so that they have similar sensitivity to the laboratory measurements) may

improve opportunities to detect contaminant mass with these measurements. However, results of this project suggest that these measurements should currently primary be directed towards critical pore geometric properties controlling flow and transport such as the pore size distribution and permeability. In addition to providing valuable information on the likely distribution of contaminant mass, such high-resolution information could be invaluable for validating a variety of contaminant transport models.

Finally, this project also resulted in the creation of a unique database of physical properties and geophysical attributes obtained on 75 cores from three fieldsites that are distinguished by distinctly different geological characteristics. The database of measurements has been summarized in comprehensive set of appendices that are accessible to future investigators.

11.0 Literature Cited

Abuseda, H., Weller, A., Sattler, C., & Debschütz, W. (2016). Petrographical and petrophysical investigations of upper cretaceous sandstones of the South West Sennan field , Western Desert , Egypt. *Arab Journal of Geosciences*, *9*(212), 1–18. https://doi.org/10.1007/s12517-015-2156-1

Allen, D., Flaum, C., Ramakrishnan, T. S., Bedford, J., Castelijns, K., Fairhurst, D., … others. (2000). Trends in NMR logging. *Oilfield Review*, *12*(3), 2–19.

Archie, G. E. (1942). The Electrical Resistivity Log as an Aid in Determining Some Reservoir Characteristics. *Petroleum Transactions of AIME*, *146*, 54–62.

Atekwana, E., & Slater, L. D. (2009). Biogeophysics : a New Frontier in Earth Science Research. *Reviews of Geophysics*, 1–30. https://doi.org/10.1029/2009RG000285.1.INTRODUCTION

Banavar, J. R., & Johnson, D. L. (1987). Characteristic pore sizes and transport in porous media. *Physical Review B*, *35*(13), 7283–7286. https://doi.org/10.1103/PhysRevB.35.7283

Bernabé, Y., & Revil, A. (1995). Pore-scale heterogeneity, energy dissipation and the transport properties of rocks. *Geophysical Research Letters*, *22*(12), 1529–1532.

Bernabé, Y., Zamora, M., Li, M., Maineult, A., & Tang, Y. B. (2011). Pore connectivity, permeability, and electrical formation factor: a new model and comparison to experimental data. *Journal of Geophysical Research: Solid Earth*, *116*(B11).

Beyer, M. (2012). *DNAPL Characterization in Clayey Till and Chalk by FACT (FLUTe Activated Carbon Technique)*. Technical University of Denmark.

Bijeljic, B., & Blunt, M. J. (2007). Pore-scale modeling of transverse dispersion in porous media. *Water Resources Research*, *43*(12).

Binley, A., Slater, L. D., Fukes, M., & Cassiani, G. (2005). Relationship between spectral induced polarization and hydraulic properties of saturated and unsaturated sandstone. *Water Resources Research*, *41*(12), n/a-n/a. https://doi.org/10.1029/2005WR004202

Borgia, G. C., Bortolotti, V., Brancolini, A., Brown, R. J. S., & Fantazzini, P. (1996). Developments in core analysis by NMR measurements. *Magnetic Resonance Imaging*, *14*(7–8), 751–760.

Briggs, M. A., Day-Lewis, F. D., Ong, J. B., Harvey, J. W., & Lane, J. W. (2014). Dual-domain mass-transfer parameters from electrical hysteresis: Theory and analytical approach applied to laboratory, synthetic streambed, and groundwater experiments. *Water Resources Research*, *50*(10), 8281–8299. https://doi.org/doi:10.1002/2014WR015880

Briggs, M. a., Day-Lewis, F. D., Ong, J. B. T., Curtis, G. P., & Lane, J. W. (2013). Simultaneous estimation of local-scale and flow path-scale dual-domain mass transfer parameters using geoelectrical monitoring. *Water Resources Research*, *49*(9), 5615–5630. https://doi.org/10.1002/wrcr.20397

Briggs, M. A., Day-Lewis, F. D., Zarnetske, J. P., & Harvey, J. W. (2015). A physical explanation for the development of redox microzones in hyporheic flow. *Geophysical Research Letters*, *42*(11), 4402–4410.

Broholm, M. M., Janniche, G. S., Mosthaf, K., Fjordbøge, A. S., Binning, P. J., Christensen, A. G., … others. (2016). Characterization of chlorinated solvent contamination in limestone using innovative FLUTe{®} technologies in combination with other methods in a line of evidence approach. *Journal of Contaminant Hydrology*, *189*, 68–85.

Brunauer, S., Emmett, P. H., & Teller, E. (1938). Adsorption of gases in multimolecular layers. *Journal of the American Chemical Society*, *60*(2), 309–319.

Carman, P. C. (1939). Permeability of saturated sands, soils and clays. *The Journal of Agricultural Science*, *29*, 262. https://doi.org/10.1017/S0021859600051789

Carr, H. Y., & Purcell, E. M. (1954). Effects of diffusion on free precession in nuclear magnetic resonance experiments. *Physical Review*, *94*(3), 630.

Cherry, J. A., Parker, B. L., & Keller, C. (2007). A New Depth-Discrete Multilevel Monitoring Approach for Fractured Rock. *Groundwater Monitoring & Remediation*, *27*(2), 57–70.

Cilona, A., Aydin, A., & Johnson, N. M. (2015). Permeability of a fault zone crosscutting a sequence of sandstones and shales and its influence on hydraulic head distribution in the Chatsworth Formation, California, USA. *Hydrogeology Journal*, *23*(2), 405–419.

Coates, G. R., & Dumanior. (1974). A New Approach to Improved Log Derived Permeability. *The LogAnalyst*, *15*(1).

Coleman, T. I., Parker, B. L., Maldaner, C. H., & Mondanos, M. J. (2015). Groundwater flow characterization in a fractured bedrock aquifer using active DTS tests in sealed boreholes. *Journal of Hydrology*, *528*, 449–462.

Day-Lewis, F. D., Linde, N., Haggerty, R., Singha, K., & Briggs, M. A. (2017). Pore-Network Modeling of the Electrical Signature of Solute Transport in Dual-Domain Media. *Geophysical Research Letters*. https://doi.org/10.1002/2017GL073326

Day-Lewis, F. D., & Singha, K. (2008). Geoelectrical inference of mass transfer parameters using temporal moments. *Water Resources Research*, *44*, W05201. https://doi.org/10.1029/2007WR006750

Day-Lewis, F. D., Slater, L. D., Robinson, J., Johnson, C. D., Terry, N., & Werkema, D. (2017). An overview of geophysical technologies appropriate for characterization and monitoring at fractured-rock sites. *Journal of Environmental Management*.

De Arcangelis, L., Koplik, J., Redner, S., & Wilkinson, D. (1986). Hydrodynamic dispersion in network models of porous media. *Physical Review Letters*, *57*(8), 996.

Dincutoiu, I., Górecki, T., & Parker, B. L. (2003). A novel technique for rapid extraction of volatile organohalogen compounds from low permeability media. *Environmental Science & Technology*, *37*(17), 3978–3984.

Dincutoiu, I., Górecki, T., & Parker, B. L. (2006). Microwave-assisted extraction of trichloroethylene from clay samples. *International Journal of Environmental and Analytical Chemistry*, *86*(15), 1113–1125.

Einarson, M. D. (2006). Multilevel ground-water monitoring. *Practical Handbook of*

Environmental Site Characterization and Ground-Water Monitoring, *11*, 808–845.

Feehley, C. E., Zheng, C., & Molz, F. J. (2000). A dual-domain mass transfer approach for modeling solute transport in heterogeneous aquifers: Application to the Macrodispersion Experiment (MADE) site. *Water Resources Research*, *36*(9), 2501–2515.

Foley, I., Farooqui, S. A., & Kleinberg, R. L. (1996). Effect of paramagnetic ions on NMR relaxation of fluids at solid surfaces. *Journal of Magnetic Resonance, Series A*, *123*(1), 95–104.

Goode, D. J., Imbrigiotta, T. E., & Lacombe, P. J. (2014a). High-resolution delineation of chlorinated volatile organic compounds in a dipping, fractured mudstone: Depth- and strata-dependent spatial variability from rock-core sampling. *Journal of Contaminant Hydrology*. https://doi.org/10.1016/j.jconhyd.2014.10.005

Goode, D. J., Imbrigiotta, T. E., & Lacombe, P. J. (2014b). High-resolution delineation of chlorinated volatile organic compounds in a dipping, fractured mudstone: Depth- and strata-dependent spatial variability from rock-core sampling. *Journal of Contaminant Hydrology*, *171*, 1–11. https://doi.org/10.1016/j.jconhyd.2014.10.005

Goode, D. J., Tiedeman, C. R., Lacombe, P. J., Imbrigiotta, T. E., Shapiro, A. M., & Chapelle, F. H. (2007). Contamination in Fractured-Rock Aquifers—Research at the former Naval Air Warfare Center, West Trenton, New Jersey. *USGS Fact Sheet 2007-3074*, http://pubs.usgs.gov/fs/2007/3074/.

Greenberg, R. J., & Brace, W. F. (1969). Archie's law for rocks modeled by simple networks. *Journal of Geophysical Research*, *74*(8), 2099–2102.

Haggerty, R., & Gorelick, S. M. (1995). Multiple-rate mass transfer for modeling diffusion and surface reactions in media with pore-scale heterogeneity. *Water Resources Research*, *31*(10), 2383–2400.

Hahn, E. L. (1950). Spin echoes. *Physical Review*, *80*(4), 580.

Harvey, C. F., & Gorelick, S. M. (1995). Temporal moment-generating equations: Modeling transport and mass transfer in heterogeneous aquifers. *Water Resources Research*, *31*(8), 1895–1911.

Hurley, J. C. (2003). *Rock Core Investigation of DNAPL Penetration and Persistence in Fractured Sandstone*. University of Waterloo [Department of Earth Sciences].

Jin, M., & Sharma, M. M. (1991). A model for electrochemical and electrokinetic coupling in inhomogeneous porous media. *Journal of Colloid and Interface Science*, *142*(1), 61–73.

Johnson, C. D., Mondazzi, R. A., & Joesten, P. K. (2009). *Borehole Geophysical Investigation of a Formerly Used Defense Site , Machiasport , Maine, 2003-2006: U.S. Geological Survey Scientific Investigations Report 2009-5120*. Retrieved from http://pubs.usgs.gov/sir/2009/5120/

Johnson, D. L., Koplik, J., & Schwartz, L. M. (1986). New pore-size parameter characterizing transport in porous media. *Physical Review Letters*, *57*(20), 2564–2567. https://doi.org/10.1103/PhysRevLett.57.2564

Katz, A. J., & Thompson, A. H. (1986). Quantitative prediction of permeability in porous rock. *Physical Review B*, *34*(11), 8179–8181. https://doi.org/10.1103/PhysRevB.34.8179

Katz, A. J., & Thompson, A. H. (1987). Prediction of rock electrical conductivity from mercury injection measurements. *Journal of Geophysical Research*, *92*(B1), 599. https://doi.org/10.1029/JB092iB01p00599

Keating, K., & Knight, R. (2007). A laboratory study to determine the effect of iron oxides on proton NMR measurements. *Geophysics*, *72*(1), E27. https://doi.org/10.1190/1.2399445

Keating, K., & Knight, R. (2010). A laboratory study of the effect of Fe (II)-bearing minerals on nuclear magnetic resonance (NMR) relaxation measurements. *Geophysics*.

Keller, C. (2017). A New Rapid Method for Measuring the Vertical Head Profile. *Groundwater*, *55*(2), 244–254.

Keller, C., Chapman, S., Pitkin, S., & Parker, B. (2017). New method for a continuous vertical profile of contamination in fractured rock, In Preparation. *Groundwater Monitoring & Remediation*.

Keller, C. E., Cherry, J. A., & Parker, B. L. (2014). New method for continuous transmissivity profiling in fractured rock. *Groundwater*, *52*(3), 352–367.

Kleinberg, R. L., & Jackson, J. A. (2001). An introduction to the history of NMR well logging. *Concepts in Magnetic Resonance*, *13*(6), 340–342.

Kleinberg, R. L., Sezginer, A., Griffin, D. D., & Fukuhara, M. (1992). Novel NMR apparatus for investigating an external sample. *Journal of Magnetic Resonance (1969)*, *97*(3), 466–485.

Klinkenberg, L. J. (1941). The Permeability of Porous Media to Liquids and Gases. *Drill & Prod. Prac.*, *200*.

Knight, R., Nolte, L. J. P., Slater, L., Atekwana, E., Endres, A., Geller, J., … Straley, C. (2010). GEOPHYSICS AT THE INTERFACE : RESPONSE OF GEOPHYSICAL PROPERTIES TO SOLID - FLUID , FLUID - FLUID , AND SOLID - SOLID INTERFACES. *Reviews of Geophysics*, *48*(RG4002). https://doi.org/10.1029/2007RG000242.1.INTRODUCTION

Knight, R., Walsh, D. O., Butler, J. J., Grunewald, E., Liu, G., Parsekian, A. D., … Barrows, M. (2016). NMR Logging to Estimate Hydraulic Conductivity in Unconsolidated Aquifers. *Groundwater*, *54*(1), 104–114. https://doi.org/10.1111/gwat.12324

Koch, K., Kemna, a., Irving, J., & Holliger, K. (2011). Impact of changes in grain size and pore space on the hydraulic conductivity and spectral induced polarization response of sand. *Hydrology and Earth System Sciences*, *15*(6), 1785–1794. https://doi.org/10.5194/hess-15-1785-2011

Kruschwitz, S., Prinz, C., & Zimathies, A. (2016). Study into the correlation of dominant pore throat size and SIP relaxation frequency. *Journal of Applied Geophysics*. https://doi.org/10.1016/j.jappgeo.2016.07.007

Kusinski, M. (2012). *Application of Microwave-Assisted Technologies for the Analysis of Chlorinated Solvents in Rock Samples*. University of Waterloo.

Lacombe, P. J. (2000). *Hydrogeologic framework, water levels, and trichloroethylene contamination, Naval Air Warfare Center, West Trenton, New Jersey, 1993-97*.

Lacombe, P. J., & Burton, W. C. (2010). Hydrogeologic Framework of Fractured Sedimentary Rock , Newark Basin , New Jersey. *Groundwater Monitoring and Remediation*, (2), 35–45. https://doi.org/10.1111/j1745

Leeson, A., & Stroo, H. (2011). *SERDP and ESTCP workshop on investment strategies to optimize research and demonstration impacts in support of DoD restoration goals*.

Lima, G., Parker, B., & Meyer, J. (2012). Dechlorinating microorganisms in a sedimentary rock matrix contaminated with a mixture of VOCs. *Environmental Science & Technology*, *46*(11), 5756–5763.

Liu, Y. (2005). *Microwave Assisted Rapid Extraction of VOCs from Low Permeability Media*. University of Waterloo.

Meiboom, S., & Gill, D. (1958). Modified spin-echo method for measuring nuclear relaxation times. *Review of Scientific Instruments*, *29*(8), 688–691.

Meyer, J. R., Parker, B. L., Arnaud, E., & Runkel, A. C. (2016). Combining high resolution vertical gradients and sequence stratigraphy to delineate hydrogeologic units for a contaminated sedimentary rock aquifer system. *Journal of Hydrology*, *534*, 505–523.

Meyer, J. R., Parker, B. L., & Cherry, J. A. (2008). Detailed hydraulic head profiles as essential data for defining hydrogeologic units in layered fractured sedimentary rock. *Environmental Geology*, *56*(1), 27–44.

Meyer, J. R., Parker, B. L., & Cherry, J. A. (2014). Characteristics of high resolution hydraulic head profiles and vertical gradients in fractured sedimentary rocks. *Journal of Hydrology*, *517*, 493–507.

Moysey, S. M. J., & Liu, Z. (2012). Can the Onset of Macropore Flow be Detected using Electrical Resistivity Measurements? *Soil Science Society of America Journal*, *76*(1), 10–17.

Niu, Q., Revil, A., & Saidian, M. (2016). Salinity dependence of the complex surface conductivity of the Portland sandstone. *Geophysics*, *81*(2), D125–D140. https://doi.org/10.1190/geo2015-0426.1

Nordsiek, S., & Weller, A. (2008). A new approach to fitting induced-polarization spectra. *Geophysics*, *73*(6), F235. https://doi.org/10.1190/1.2987412

Pape, H., Riepe, L., & Schopper, J. (1987). Theory of self-similar network structures in sedimentary and igneous rocks and their investigation with microscopical and physical method. *Journal of Microscopy*, *148*(June), 121–147.

Parker, B. L., Chapman, S. W., & Cherry, J. A. (2010). Plume Persistence in Fractured Sedimentary Rock After Source Zone Removal. *Groundwater*, *48*(6), 799–803. https://doi.org/10.1111/j.1745-6584.2010.00755.x

Parker, B. L., Cherry, J. A., & Chapman, S. W. (2012). Discrete Fracture Network Approach for

Studying Contamination in Fractured Rock. *AQUA Mundi*, *3*(2), 101–116. https://doi.org/10.4409/Am-052-12-0046

Parker, B. L., Cherry, J. A., Meyer, J. R., & Casado, P. (2015). *University Consortium for Field Focused Groundwater Contamination Research, Year 2014 Progress Report, Hydrite Chemical Co. Cottage Grove, WI.*

Parker, B. L., Gillham, R. W., & Cherry, J. A. (1994). Diffusive Disappearance of Immiscible-Phase Organic Liquids in Fractured Geologic Media. *Ground Water*, *32*(5), 805–820.

Parker, B. L., McWhorter, D. B., & Cherry, J. A. (1997). Diffusive Loss of Non-Aqueous Phase Organic Solvents from Idealized Fracture Networks in Geologic Media. *Groundwater*, *35*(6), 1077–1088.

Pehme, P. E., Chapman, S. W., Parker, B. L., & Cherry, J. A. (2014). Temporary Sensor Deployments: a Method for Improved Insight into Hydraulic Variations and Design of Permanent Multilevel Installations. In *International Discrete Fracture Network Engineering Conference* (Vol. 239).

Pehme, P. E., Greenhouse, J. P., & Parker, B. L. (2007). The active line source temperature logging technique and its application in fractured rock hydrogeology. *Journal of Environmental & Engineering Geophysics*, *12*(4), 307–322.

Pehme, P. E., Parker, B. L., Cherry, J. A., & Greenhouse, J. P. (2010). Improved resolution of ambient flow through fractured rock with temperature logs. *Groundwater*, *48*(2), 191–205.

Pehme, P. E., Parker, B. L., Cherry, J. a., Molson, J. W., & Greenhouse, J. P. (2013). Enhanced detection of hydraulically active fractures by temperature profiling in lined heated bedrock boreholes. *Journal of Hydrology*, *484*, 1–15. https://doi.org/10.1016/j.jhydrol.2012.12.048

Pehme, P. E., Parker, B. L., Cherry, J. A., Molson, J. W., & Greenhouse, J. P. (2013). Enhanced detection of hydraulically active fractures by temperature profiling in lined heated bedrock boreholes. *Journal of Hydrology*, *484*, 1–15.

Personna, Y. R., Slater, L., Ntarlagiannis, D., Werkema, D., & Szabo, Z. (2013). Electrical signatures of ethanol--liquid mixtures: Implications for monitoring biofuels migration in the subsurface. *Journal of Contaminant Hydrology*, *144*(1), 99–107.

Quinn, P., Cherry, J. A., & Parker, B. L. (2012). Hydraulic testing using a versatile straddle packer system for improved transmissivity estimation in fractured-rock boreholes. *Hydrogeology Journal*, *20*(8), 1529–1547.

Quinn, P., Cherry, J. A., & Parker, B. L. (2015). Combined use of straddle packer testing and FLUTe profiling for hydraulic testing in fractured rock boreholes. *Journal of Hydrology*, *524*, 439–454.

Quinn, P. M., Cherry, J. A., & Parker, B. L. (2016). Depth-discrete specific storage in fractured sedimentary rock using steady-state and transient single-hole hydraulic tests. *Journal of Hydrology*, *542*, 756–771.

Quinn, P. M., Parker, B. L., & Cherry, J. A. (2011). Using constant head step tests to determine hydraulic apertures in fractured rock. *Journal of Contaminant Hydrology*, *126*(1), 85–99.

Revil, A. (2012). Spectral induced polarization of shaly sands: Influence of the electrical double layer. *Water Resources Research*, *48*(2), W02517. https://doi.org/10.1029/2011WR011260

Revil, A. (2013). Effective conductivity and permittivity of unsaturated porous materials in the frequency range 1 mHz-1GHz. *Water Resources Research*, *49*(1), 306–327. https://doi.org/10.1029/2012WR012700

Revil, A., Binley, A., Mejus, L., & Kessouri, P. (2015). Predicting permeability from the characteristic relaxation time and intrinsic formation factor of complex conductivity spectra. *Water Resources Research*, *51*, 1–29. https://doi.org/10.1002/ 2015WR017074

Revil, A., Koch, K., & Holliger, K. (2012). Is it the grain size or the characteristic pore size that controls the induced polarization relaxation time of clean sands and sandstones? *Water Resources Research*, *48*, W05602. https://doi.org/10.1029/2011WR011561

Revil, A., & Skold, M. (2011). Salinity dependence of spectral induced polarization in sands and sandstones. *Geophysical Journal International*, *187*(2), 813–824. https://doi.org/10.1111/j.1365-246X.2011.05181.x

Revil, a., Florsch, N., & Camerlynck, C. (2014). Spectral induced polarization porosimetry. *Geophysical Journal International*, *198*(2), 1016–1033. https://doi.org/10.1093/gji/ggu180

Ribiero, L. A. F. ., Meyer, J. R., & Parker, B. L. (2015). Fracture network and groundwater flux characterization using a suite of high resolution methods in a sedimentary bedrock aquifer. In *Canadian Hydrogeology, IAH-CNC Conference, October 27-30, Waterloo, Ontario*.

Roberts, J. J., & Wildenschild, D. (2012). Electrical properties of sand--clay mixtures containing trichloroethylene and ethanol. *Journal of Environmental & Engineering Geophysics*.

Sale, T. C., Illangasekare, T., Zimbron, J., Rodriguez, D., Wilkins, B., & Marinelli, F. (2007). AFCEE source zone initiative. *Report Prepared for the Air Force Center for Environmental Excellence by Colorado State University and Colorado School of Mines*.

Schaefer, C. E., Towne, R. M., Lippincott, D. R., Lazouskaya, V., Fischer, T. B., Bishop, M. E., & Dong, H. (2013). Coupled diffusion and abiotic reaction of trichlorethene in minimally disturbed rock matrices. *Environmental Science & Technology*, *47*(9), 4291–4298.

Schwarz, G. (1962). A theory of the low-frequency dielectric dispersion of colloidal particles in electrolyte solution. *The Journal of Physical Chemistry*, *66*(12), 2636–2642. https://doi.org/10.1021/j100818a067

Scott, J. B. T., & Barker, R. D. (2003). Determining pore-throat size in Permo-Triassic sandstones from low-frequency electrical spectroscopy. *Geophysical Research Letters*, *30*(9), 1450. https://doi.org/10.1029/2003GL016951

Seevers, D. O., & others. (1966). A nuclear magnetic method for determining the permeability of sandstones. In *SPWLA 7th Annual Logging Symposium*.

Singha, K., Day-Lewis, F. D., & Lane, J. W. (2007). Geoelectrical Evidence of Bicontinuum Transport in Groundwater. *Geophysical Research Letters*, *34*, L12401. https://doi.org/10.1029/2007GL030019.)

Song, Y.-Q. (2010). Recent Progress of Nuclear Magnetic Resonance Applications in Sandstones and Carbonate Rocks. *Vadose Zone Journal*, *9*(4), 828. https://doi.org/10.2136/vzj2009.0171

Sterling, S. N., Parker, B. L., Cherry, J. A., Williams, J. H., Lane, J. W., & Haeni, F. P. (2005). Vertical cross contamination of trichloroethylene in a borehole in fractured sandstone. *Groundwater*, *43*(4), 557–573.

Stookey, L. L. (1970). Ferrozine-A New Spectrophotometric Reagent for Iron. *Analytical Chemistry*, *42*(7), 779–781.

Suman, R. J., & Knight, R. J. (1997). Effects of pore structure and wettability on the electrical resistivity of partially saturated rocks—A network study. *Geophysics*, *62*(4), 1151–1162.

T.Gorecki, Parker, B. L., Gorecka, M., & Liu, Y. (2010). Determination of trichloroethylene in rock samples using microwave-assisted extraction and cool on-column injection. In *North American Environmental Field Conference and Exposition, Tampa, FL, January 12-14*.

Timur, A. (1969). Pulsed Nuclear Magnetic Resonance Studies of Porosity, Movable Fluid, and Permeability of Sandstones. *Journal of Petroleum TechnologyJournal of Petroleum Technology*, 775–786.

Tong, M., Li, L., Wang, W., & Jiang, Y. (2006). Determining capillary-pressure curve , pore-size distribution , and permeability from induced polarization of shaley sand. *Geophysics*, *71*(3), N33–N40.

Ustra, A., Slater, L., Ntarlagiannis, D., & Elis, V. (2012). Spectral induced polarization (SIP) signatures of clayey soils containing toluene. *Near Surface Geophysics*, *10*(6), 503–515.

VanderKwaak, J. E., & Sudicky, E. A. (1996). Dissolution of non-aqueous-phase liquids and aqueous-phase contaminant transport in discretely-fractured porous media. *Journal of Contaminant Hydrology*, *23*(1–2), 45–68.

Vinegar, H., & Waxman, M. (1984). Induced polarization of shaly sands. *Geophysics*, *49*(8), 1267–1287.

Walsh, D. O., Grunewald, E., Turner, P., & Frid, I. (2010). Javelin: A slimhole and microhole NMR logging tool. *FastTimes*, *15*(3), 67–72.

Washburn, E. (1921). The Dynamics of Capillary Flow. *The Physical Review*, *XVII*(3), 273–283.

Weller, A., Breede, K., Slater, L., & Nordsiek, S. (2011). Effect of changing water salinity on complex conductivity spectra of sandstones. *Geophysics*, *76*(5), F315–F327.

Weller, A., Nordsiek, S., & Debschütz, W. (2010). Estimating permeability of sandstone samples by nuclear magnetic resonance and spectral-induced polarization. *Geophysics*, *75*(6), E215. https://doi.org/10.1190/1.3507304

Weller, A., & Slater, L. (2012). Salinity dependence of complex conductivity of unconsolidated and consolidated materials: Comparisons with electrical double layer models. *Geophysics*, *77*(5), D185. https://doi.org/10.1190/geo2012-0030.1

Weller, A., Slater, L., Binley, A., Nordsiek, S., & Xu, S. (2015). Permeability prediction based

on induced polarization : Insights from measurements on sandstone and unconsolidated samples spanning a wide permeability range. *Geophysics*, *80*(2), D161–D173.

Weller, A., Slater, L., Huisman, J. A., Esser, O., & Haegel, F. (2015). On the specific polarizability of sands and sand-clay mixtures. *Geophysics*, *80*(3), A57–A61.

Weller, A., Slater, L., Nordsiek, S., & Ntarlagiannis, D. (2010). On the estimation of specific surface per unit pore volume from induced polarization: A robust empirical relation fits multiple data sets. *Geophysics*, *75*(4), WA105-WA112. https://doi.org/10.1190/1.3471577

Yaramanci, U., Lange, G., & Knödel, K. (1999). Surface NMR within a geophysical study of an aquifer at Haldensleben (Germany). *Geophysical Prospecting*, *47*(6), 923–943.

Zheng, C., & Wang, P. P. (1999). *MT3DMS: a modular three-dimensional multispecies transport model for simulation of advection, dispersion, and chemical reactions of contaminants in groundwater systems; documentation and user's guide*.

Zisser, N., Kemna, a., & Nover, G. (2010). Dependence of spectral-induced polarization response of sandstone on temperature and its relevance to permeability estimation. *Journal of Geophysical Research: Solid Earth*, *115*(9), 1–15. https://doi.org/10.1029/2010JB007526

Appendix A.1: Borehole Logs

Hydrite MP24S

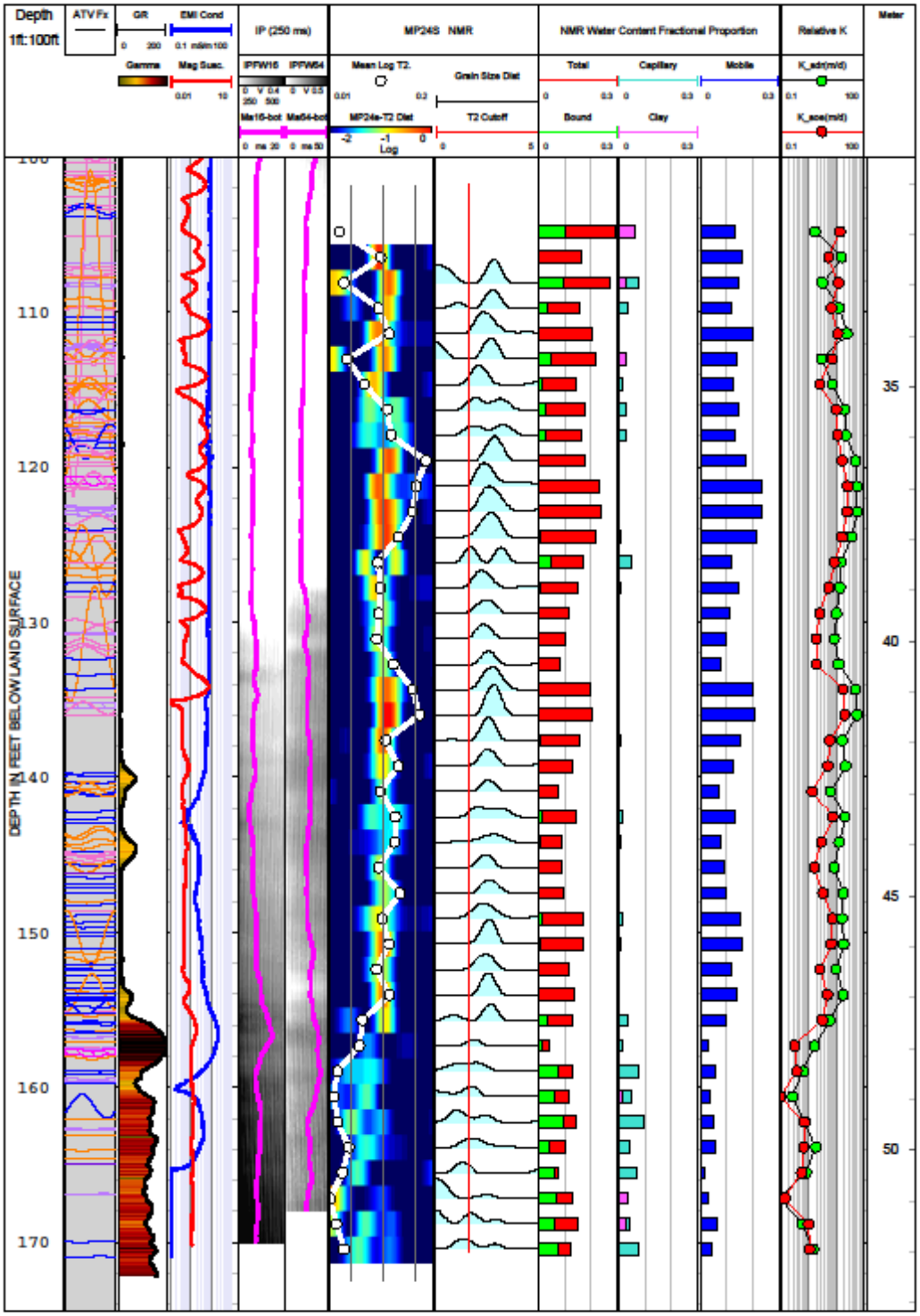

Page 1

Hydrite MP25S

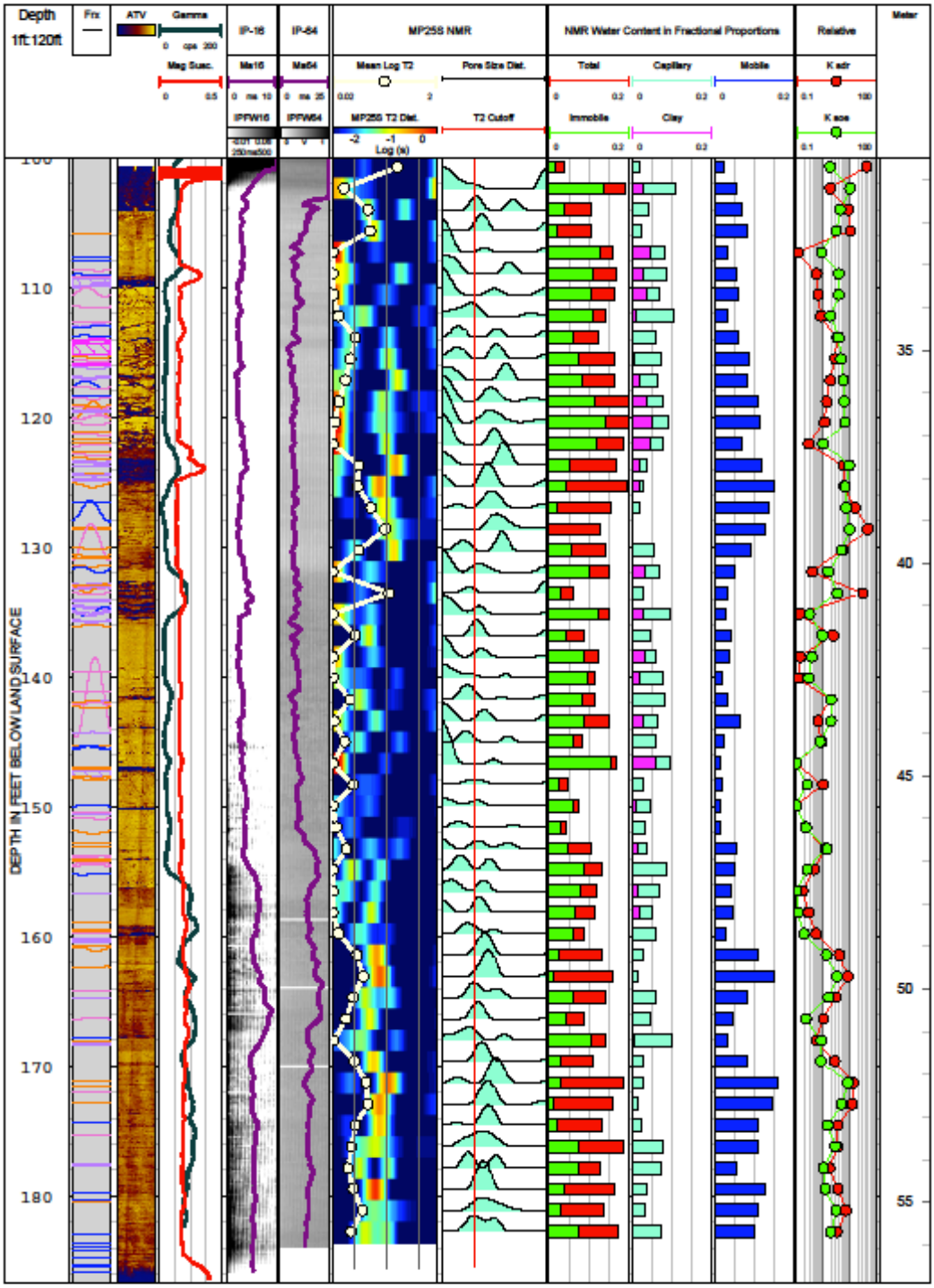

Page 1

Santa Susana C3

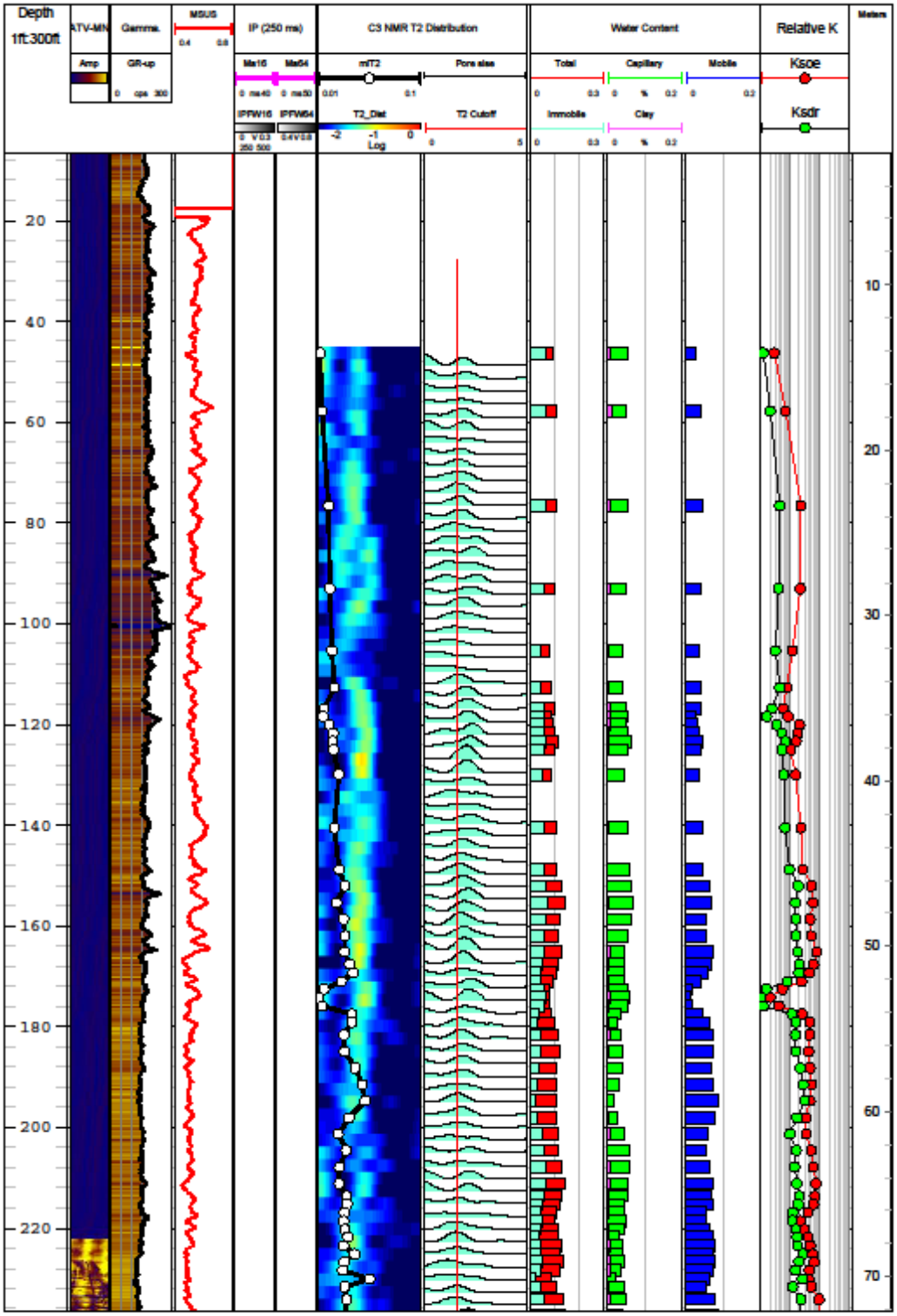

Page 1

Santa Susana C4

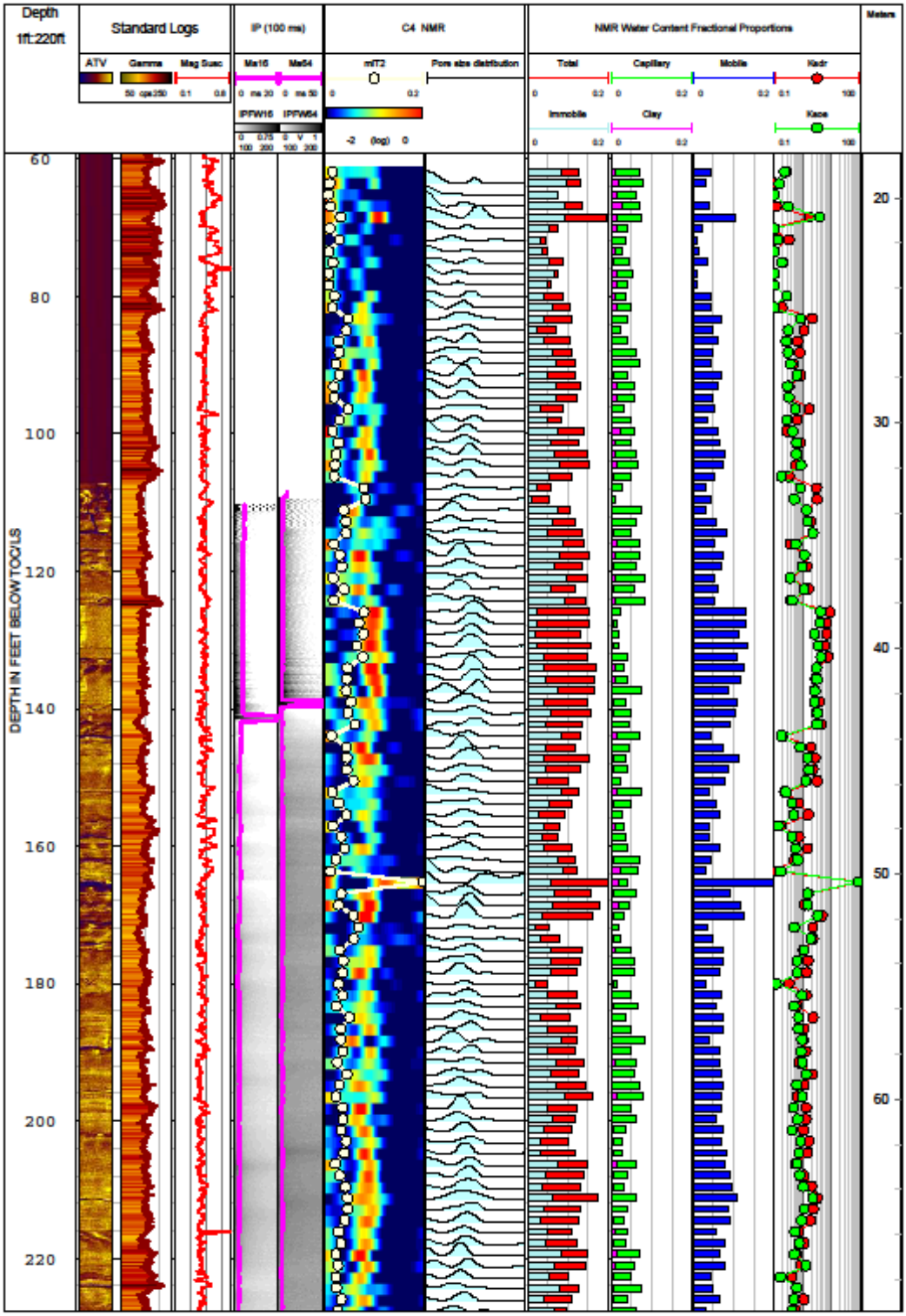

Page 1

Santa Susana RD109

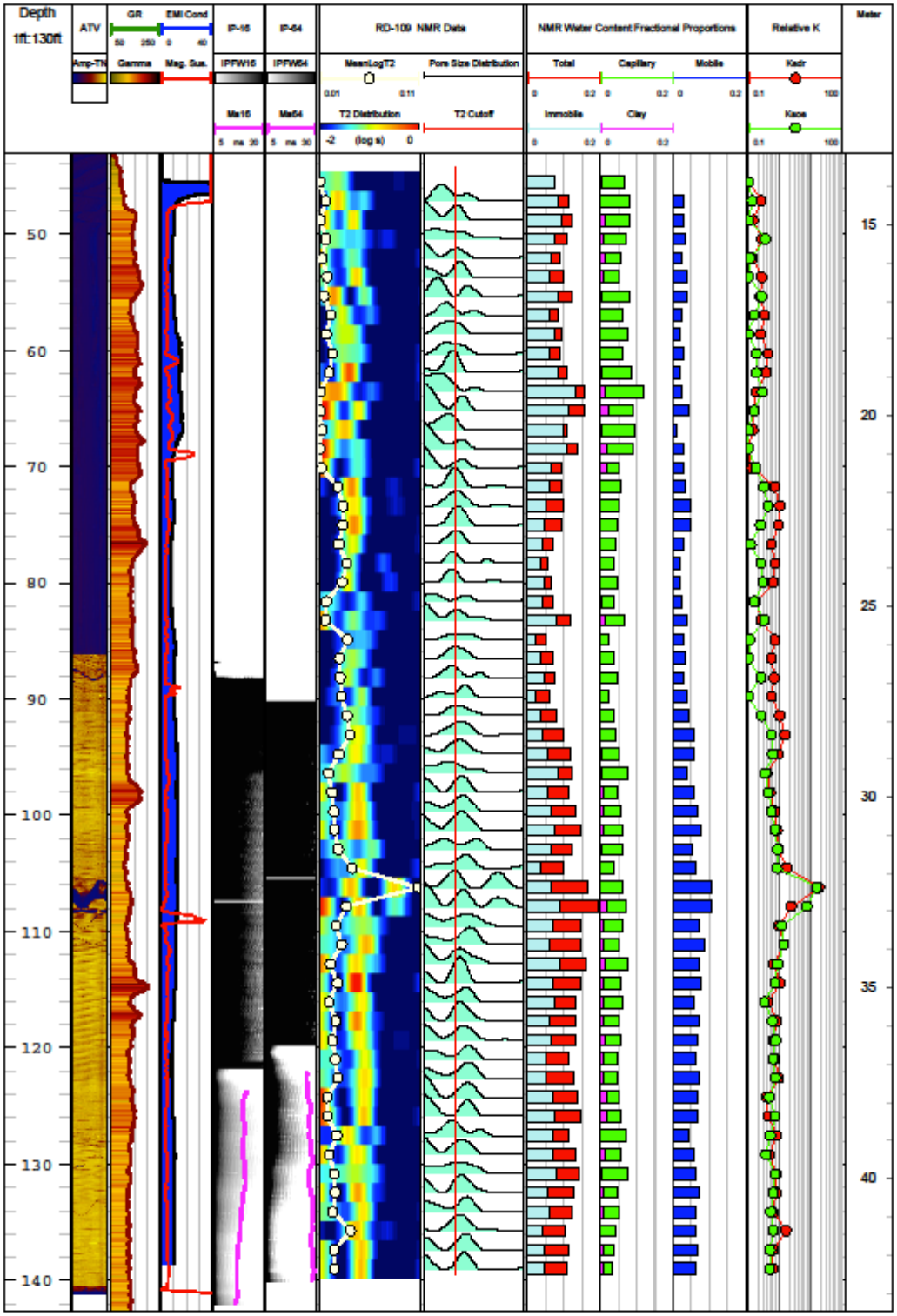

Page 1

NAWC 94BR

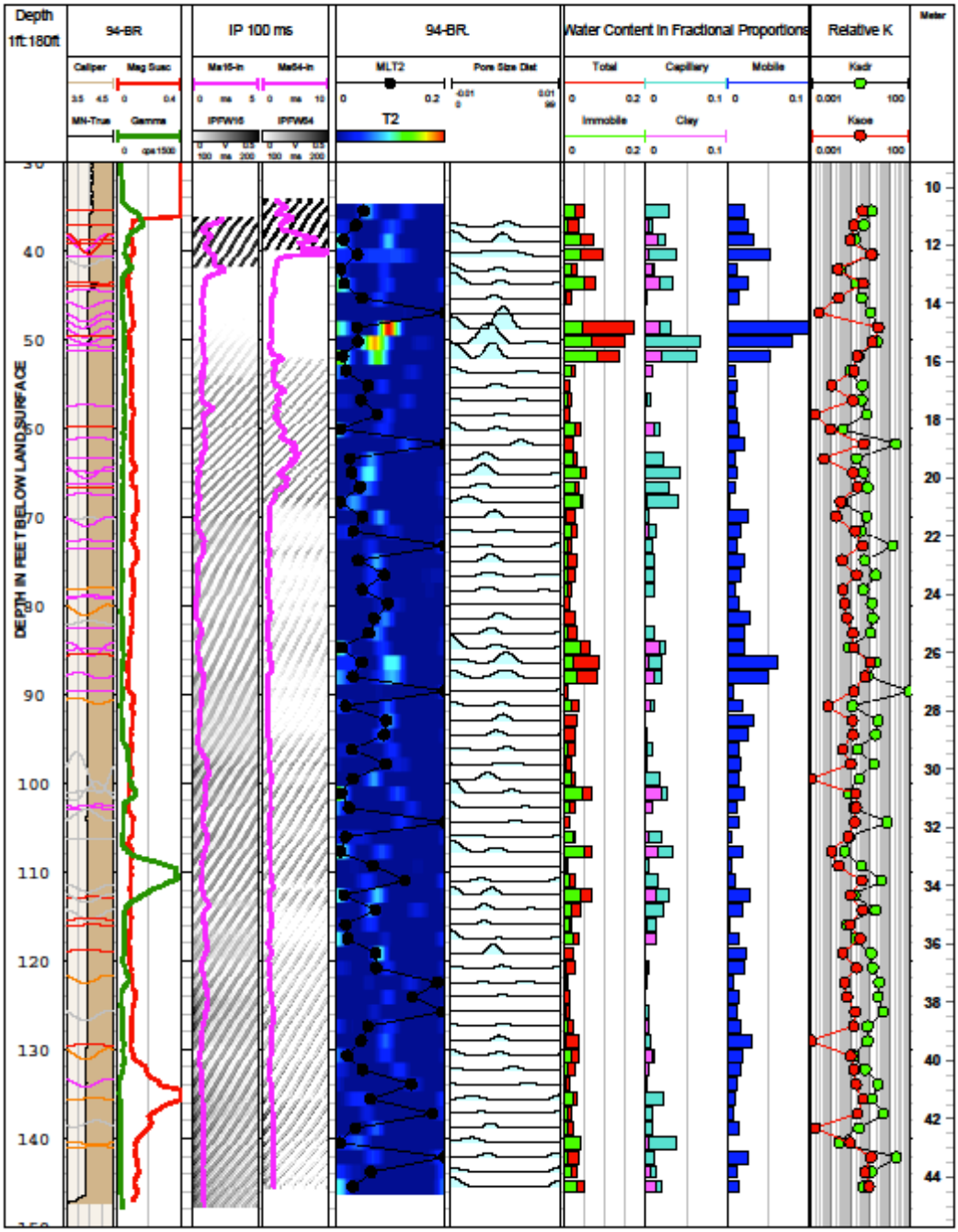

Page 1

Appendix A.2 Contaminant Mass

Hydrite MP25S		Hydrite MP24S	
MidPoint Depth (ft bgs)	TVOC (ug/g wet rock)	MidPoint Depth (ft bgs)	TVOC (ug/g wet rock)
103.29	0.00E+00	99.93	9.45E-02
103.64	0.00E+00	100.29	1.06E-02
103.9	0.00E+00	100.53	2.50E-02
104.39	0.00E+00	100.72	6.50E-02
105.17	0.00E+00	101.06	2.38E-01
105.85	0.00E+00	101.5	9.36E-02
106.34	0.00E+00	101.88	7.71E-01
107.03	0.00E+00	102.17	2.07E-01
108.02	0.00E+00	104.37	5.67E-02
108.74	0.00E+00	105.05	1.22E-01
108.81	0.00E+00	105.92	1.64E-01
109.09	0.00E+00	106.22	2.16E-01
110.2	0.00E+00	106.82	3.02E-01
110.56	0.00E+00	107.19	1.26E-01
111.09	0.00E+00	109.4	1.67E-01
111.35	1.89E-02	109.79	2.06E+01
111.57	1.17E-02	110.36	5.08E-02
112.22	1.76E-02	111.1	2.85E-01
112.87	0.00E+00	111.44	4.65E-01
113.25	0.00E+00	111.9	7.89E-01
115.15	2.40E-02	112.25	8.52E-01
116.2	0.00E+00	112.66	1.57E+01
116.85	2.21E-02	112.93	5.61E-01
118.45	0.00E+00	114.58	3.77E-01
119.17	0.00E+00	115.9	2.38E+01
120.19	0.00E+00	116.23	0.00E+00
121.17	1.91E-02	116.59	4.38E-01
122.48	0.00E+00	117.36	6.06E-01
123.22	0.00E+00	120.27	5.73E-01
124.25	0.00E+00	120.78	1.31E-01
125.17	0.00E+00	121.4	1.27E-01
125.7	0.00E+00	121.98	5.17E-01
127.05	0.00E+00	122.58	7.25E-01
127.38	0.00E+00	123.15	4.66E-01
127.75	0.00E+00	125.57	6.87E-01
130.3	0.00E+00	126.16	4.76E-01
132.65	0.00E+00	126.67	3.40E+00

133.72	0.00E+00	127.54	1.12E+00
Hydrite MP25S		**Hydrite MP24S**	
MidPoint Depth (ft bgs)	**TVOC (ug/g wet rock)**	**MidPoint Depth (ft bgs)**	**TVOC (ug/g wet rock)**
134.1	0.00E+00	128.23	2.41E+00
135.29	0.00E+00	128.75	3.20E+00
135.43	0.00E+00	129.23	3.49E+00
135.82	0.00E+00	130.36	2.46E+00
136.25	0.00E+00	131.11	2.38E+00
139.32	0.00E+00	131.61	3.76E+00
141.35	8.85E-01	131.95	4.12E+00
141.75	3.39E+00	132.34	7.40E+00
143.25	1.67E+00	132.64	3.73E+00
144.35	1.18E+00	133	4.86E+00
145.7	2.90E+00	133.96	4.84E+00
147.41	2.38E+00	135.74	4.57E+00
147.71	2.15E+00	135.81	4.02E+00
148.06	3.53E+00	136.05	4.30E+00
149.09	2.61E+00	136.55	2.98E+00
150.41	3.48E+00	137.05	5.64E+00
150.7	2.66E+00	140.25	1.01E-02
151.92	1.97E+00	140.75	0.00E+00
153.55	1.97E+00	141.3	0.00E+00
156.07	2.03E+01	141.95	0.00E+00
156.58	7.46E+00	142.5	0.00E+00
156.76	7.05E+00	143.25	0.00E+00
157.49	2.47E+00	143.75	0.00E+00
158.43	4.34E-01	144.2	8.98E-03
159.15	7.78E-01	145.15	7.28E-01
159.52	1.77E+00	145.89	1.92E+00
159.78	1.19E+01	146.5	3.60E-02
160.19	1.20E+01	147.85	9.73E-02
160.68	1.03E+01	148	2.70E-01
160.98	9.02E+00	148.55	0.00E+00
161.43	7.35E+00	149.35	5.31E-01
162.12	1.14E+00	150.15	5.08E-01
162.54	2.54E-01	150.88	1.56E+00
162.8	6.39E+00	151.54	1.48E+00
162.9	4.83E-01	152.25	1.56E+00
164.1	9.31E+00	153.07	1.52E+00
165.04	7.10E+00	154.3	2.37E+00
165.45	6.50E+00	154.5	1.75E+00

165.75	9.78E+00	155.6	1.56E+01
Hydrite MP25S		**Hydrite MP24S**	
MidPoint Depth (ft bgs)	**TVOC (ug/g wet rock)**	**MidPoint Depth (ft bgs)**	**TVOC (ug/g wet rock)**
166.21	9.32E+00	155.85	8.84E+00
167	6.36E+00	156.5	1.35E+01
167.67	6.02E+00	157.7	1.46E+01
168.5	1.69E+01	158.3	4.35E+00
168.65	1.41E+01	160.24	1.74E+01
170.12	3.67E+00	160.75	2.22E+01
170.45	1.71E+00	161.05	5.51E+01
170.9	1.83E+00	161.8	5.10E+01
171.58	2.12E+00	162	3.20E+01
172.11	2.52E+00	163.35	5.42E+01
172.98	4.78E-01	164.41	2.20E+01
174.41	3.60E-01	165.25	1.16E+01
174.95	1.30E-01	166.15	1.56E+00
175.75	1.17E-01	167.05	1.81E+01
176.45	1.29E-01	167.21	1.71E+01
177.02	2.01E-01	167.75	1.70E+01
177.35	2.06E-01	168.35	1.10E+01
177.75	5.35E-01	169	2.00E+00
179.05	7.92E+00	170.48	1.90E-01
180	8.30E+00	171.44	3.90E-02
180.81	1.08E+01	171.75	1.42E-02
181.1	8.35E+00	172.25	7.50E-02
181.4	1.39E+01	173.35	3.50E-01
182	2.31E+01	173.8	3.15E-01
182.65	1.14E+01	174.25	9.02E-01
183.04	1.45E+01	175.2	1.71E+01
183.78	8.16E+00	175.8	2.13E+01
184.35	5.86E+00	176.75	1.24E+01
185.06	1.89E+00	177.35	1.02E+01
185.83	4.13E-01	178.24	5.26E-01
186.47	3.02E-01	178.66	2.46E-01
187.65	9.85E-02	179.1	2.01E-01
187.95	3.77E-01	179.55	4.72E-01
188.28	5.26E-02		
188.65	2.19E-01		
189.05	1.47E-01		
189.35	1.34E-01		

Santa Susana

SSFL - C3		SSFL -C4		SSFL -RD109	
MidPoint Depth (ft bgs)	TVOC (ug/g wet rock)	MidPoint Depth (ft bgs)	TVOC (ug/g wet rock)	MidPoint Depth (ft bgs)	TVOC (ug/g wet rock)
8.38	1.60E-02	8.27	6.73E-04	15.05	3.00E-03
10.52	9.17E-04	8.92	3.76E-03	15.65	5.59E-03
13.04	2.47E-03	9.92	2.32E-02	16.95	2.56E-03
14.46	5.20E-03	10.08	8.80E-03	17.55	9.31E-04
15.25	4.59E-03	10.08	9.35E-03	21.95	8.89E-04
15.96	1.03E-03	11.54	6.47E-03	23.65	6.56E-04
16.58	1.12E-01	12.04	1.49E-03	24.05	2.51E-03
16.71	1.15E-02	12.13	2.21E-03	25.25	9.33E-03
21.17	1.15E-03	13.13	2.97E-03	25.85	1.51E-02
21.17	8.15E-04	13.25	6.23E-03	26.05	1.08E-02
23.50	8.88E-04	15.46	2.50E-03	28.45	8.48E-03
24.17	1.62E-01	15.46	1.92E-03	28.75	6.67E-03
26.08	4.20E-04	18.08	8.78E-03	30.55	2.50E-03
26.92	4.89E-04	19.21	1.13E-02	31.3	2.55E-03
28.00	2.68E-02	19.92	1.99E-02	31.4	9.89E-04
29.08	7.73E-04	19.92	5.13E-03	33.05	4.50E-04
29.92	3.69E-02	20.33	1.50E-02	40.65	1.95E-03
30.92	2.94E-03	20.71	6.46E-03	41.45	4.48E-04
31.67	1.38E-03	21.96	2.16E-02	43.65	2.84E-04
32.92	7.88E-04	22.79	7.40E-03	45.75	2.63E-03
34.58	9.58E-04	24.46	2.69E-02	46.45	2.42E-03
35.42	2.37E-03	25.71	9.30E-03	47.05	3.50E-03
36.33	3.65E-02	26.50	1.72E-02	49.35	3.50E-03
38.08	2.04E-03	27.21	4.09E-03	49.7	4.64E-03
39.33	2.21E-03	28.25	1.93E-02	51.35	3.76E-03
40.58	1.76E-03	29.50	5.52E-03	51.65	2.04E-03
41.17	4.15E-03	31.08	1.90E-02	52.25	2.27E-03
42.08	2.47E-03	31.58	7.86E-02	52.65	2.21E-03
43.08	2.01E-03	32.58	2.92E-02	53.25	8.49E-04
43.17	2.39E-03	34.58	3.48E-02	56.25	1.94E-02
43.92	1.86E-01	34.88	1.85E-02	56.65	2.78E-02
44.08	9.31E-03	36.50	5.91E-02	57.55	2.30E-02
45.71	1.49E-02	37.33	2.19E-02	58.25	6.41E-02
47.25	4.11E-03	37.33	2.33E-02	59.65	4.77E-02
48.08	1.84E-03	38.45	7.62E-03	60.5	3.85E-02
49.13	3.65E-03	39.42	2.36E-02	60.75	1.06E-01
49.13	1.24E-03	39.75	1.61E-01	62.4	2.52E-01

50.50	4.44E-03	42.21	2.56E-01	62.85	7.46E-02
SSFL - C3		**SSFL -C4**		**SSFL -RD109**	
MidPoint Depth (ft bgs)	**TVOC (ug/g wet rock)**	**MidPoint Depth (ft bgs)**	**TVOC (ug/g wet rock)**	**MidPoint Depth (ft bgs)**	**TVOC (ug/g wet rock)**
51.25	1.43E-03	44.08	1.00E-02	63.75	7.87E-02
52.42	1.04E-02	46.92	8.21E-03	67.85	3.02E-01
53.50	2.33E-03	47.92	2.21E-02	68.4	3.43E-01
54.17	1.07E-02	48.50	9.06E-02	68.65	1.13E-01
55.58	2.30E-03	49.92	1.41E+00	70.55	9.64E-02
56.96	3.75E-03	51.25	5.33E-02	70.95	2.81E-02
57.58	2.95E-03	51.96	4.56E-01	71.45	4.56E-01
59.75	2.68E-03	52.50	2.71E-02	78.95	2.12E-01
60.88	4.36E-03	54.08	3.94E-01	79.45	2.52E-01
61.58	2.62E-03	54.88	2.50E-01	79.65	2.66E-01
63.08	4.03E-03	55.42	3.42E-01	81.45	3.30E-01
64.25	2.87E-03	56.75	4.32E+00	82.15	4.95E-01
64.92	2.72E-03	60.54	6.27E-01	82.95	3.08E-01
66.46	4.37E-03	61.46	1.01E-01	85.25	2.53E+00
67.75	2.53E-03	61.46	5.26E-02	85.55	8.60E-01
68.50	2.69E-03	62.08	4.28E-03	86.05	7.63E-01
69.21	1.85E-02	63.63	1.32E-02	91.05	1.45E+00
70.75	1.69E-02	64.33	3.37E+00	92.55	1.26E+00
70.96	1.76E-02	65.21	4.72E-02	94.05	8.06E-01
73.08	2.74E-03	65.63	8.20E-01	95.35	5.67E-01
73.08	3.01E-03	67.08	4.57E+00	97.95	1.67E+00
73.83	3.80E-03	67.08	1.64E+00	99.45	1.26E+00
77.08	5.23E-03	68.46	4.04E+00	102.25	1.39E+00
79.08	7.52E-03	69.79	7.40E-04	102.85	9.33E-01
79.08	2.66E-03	69.96	2.02E+01	103.05	1.10E+00
80.75	8.27E-03	70.38	4.07E-03	103.45	1.11E+00
80.92	3.14E-03	71.46	5.85E-01	104.05	2.17E+00
84.08	8.76E-03	72.58	5.93E-01	105.45	1.54E+00
86.08	2.90E-03	73.42	4.25E-03	106.75	1.26E+00
87.25	6.45E-03	74.46	6.12E-01	107.45	3.23E-01
87.42	1.05E-02	75.38	4.76E-03	108.4	2.89E-01
88.25	9.92E-03	78.92	3.05E-02	109.15	1.17E+02
89.58	1.02E-03	79.88	1.21E-04	110.35	1.83E+00
92.50	3.03E-03	80.54	9.31E-01	112.05	9.90E-01
93.75	9.13E-04	81.25	2.21E-02	111.35	1.16E+00
94.54	2.79E-03	82.46	2.76E-02	111.75	2.73E+00
95.42	1.04E-03	82.46	2.93E-02	116.05	2.37E-02
97.08	3.84E-03	83.08	9.45E-03	117.55	8.80E-03

98.13	2.80E-03	83.88	2.26E-02	119.05	1.54E-02
SSFL - C3		**SSFL -C4**		**SSFL -RD109**	
MidPoint Depth (ft bgs)	**TVOC (ug/g wet rock)**	**MidPoint Depth (ft bgs)**	**TVOC (ug/g wet rock)**	**MidPoint Depth (ft bgs)**	**TVOC (ug/g wet rock)**
100.92	3.59E-03	89.08	4.20E-02	122.55	1.01E-01
101.88	6.52E-03	91.29	6.52E-01	124.05	2.15E-01
102.88	0.00E+00	92.29	6.83E-02	127.05	7.74E-02
102.88	2.88E-03	93.21	1.41E-01	126.45	1.87E-01
106.50	1.00E-02	94.63	6.32E-01	126.95	4.01E-02
106.67	8.64E-03	94.63	5.37E-01	127.45	3.46E-03
107.54	2.75E-01	96.08	7.46E-02	128.25	8.74E-03
108.33	4.59E-03	97.50	8.00E-02	131.85	9.12E-02
109.25	1.96E-03	98.58	7.24E-02	132.35	4.65E-02
111.63	8.68E-03	99.42	7.13E-02	133.35	4.21E-02
112.46	9.52E-03	100.54	1.29E+01	136.05	1.66E-04
113.83	1.63E-01	101.13	1.26E-01	137.55	1.03E-04
114.00	1.07E-01	102.17	4.54E-02	139.05	7.13E-05
114.92	2.25E-02	103.58	1.56E-01	17.55	6.12E-04
115.79	1.82E-02	104.63	1.08E-01	40.65	3.51E-04
116.67	5.41E+00	105.46	1.25E-01	57.55	1.01E-02
116.96	8.05E-02	105.46	1.32E-01	71.45	3.48E-01
117.54	2.29E-02	106.08	7.16E-02	99.45	1.10E+00
118.46	2.02E-03	107.04	2.36E-02	127.05	5.78E-02
122.54	4.78E-02	108.33	7.54E-02	139.05	7.37E-05
123.54	1.01E-01	109.63	1.30E-01	15.75	7.17E-04
124.38	1.23E-01	110.29	1.36E-01	20.35	9.51E-04
125.54	9.65E-03	111.04	2.05E-01	44.75	4.67E-04
126.38	5.77E-03	112.17	1.74E-01	48.35	7.14E-04
126.96	1.37E-02	112.83	1.63E+00	50.25	3.03E-04
126.96	6.53E-04	116.21	1.20E+01	61.35	3.44E-02
127.96	2.16E-03	116.33	9.55E+00	65.75	1.47E-01
132.08	9.76E-03	117.46	1.48E+01	68.95	6.04E-02
132.25	7.91E-04	118.38	1.48E-01	72.05	1.19E-01
133.79	7.32E-03	118.96	4.08E-01	73.05	6.98E-02
136.54	2.06E-02	120.83	3.24E-02	74.05	2.03E-01
136.67	1.28E-03	121.46	3.11E-01	76.55	7.98E-02
137.92	4.10E-02	122.33	3.20E+00	87.2	5.20E-01
137.92	3.86E-02	123.08	2.28E+00	88.15	8.68E-01
138.08	5.89E-01	123.75	1.18E-01	95.45	4.84E-01
140.21	2.52E-01	123.75	1.16E-01	96.45	1.04E+00
140.38	5.35E-02	124.58	1.44E-01	76.55	3.82E-02
141.17	4.66E-03	126.08	7.83E-02		

141.75	2.26E-02	127.92	2.26E-02
SSFL - C3		**SSFL -C4**	
MidPoint Depth (ft bgs)	**TVOC (ug/g wet rock)**	**MidPoint Depth (ft bgs)**	**TVOC (ug/g wet rock)**
145.92	1.20E-01	129.58	9.09E-03
146.63	8.68E-01	130.75	5.08E-03
147.25	4.36E-02	131.54	5.59E-03
148.67	0.00E+00	132.13	8.21E-03
148.67	0.00E+00	133.08	6.20E-03
150.88	6.95E-01	134.08	3.06E-04
152.25	6.05E-02	134.08	9.68E-04
153.92	1.53E+00	136.92	8.61E-04
154.92	1.57E-01	137.96	4.45E-03
155.38	1.20E-01	138.71	9.73E-04
156.50	0.00E+00	139.88	7.69E-02
158.42	1.29E-01	140.54	2.46E-01
159.50	1.51E-01	140.54	2.30E-01
160.38	3.32E+00	140.63	3.89E-01
160.38	2.90E+00	140.63	3.57E-01
161.83	0.00E+00	141.58	1.68E-03
162.88	0.00E+00	142.17	4.22E-01
164.13	2.70E-02	142.92	6.97E-04
164.92	0.00E+00	143.75	5.09E-03
166.46	0.00E+00	146.92	5.14E-04
167.29	0.00E+00	147.92	7.43E-03
168.54	1.22E-01	148.92	5.81E-04
169.29	0.00E+00	150.50	5.38E-03
170.63	0.00E+00	150.92	7.48E-04
170.71	1.03E-01	151.67	5.68E-04
171.71	3.61E+00	152.50	4.33E-03
172.46	5.07E-02	153.71	3.44E-03
173.21	1.79E-02	154.50	6.82E-04
175.29	1.41E-01	155.75	2.49E-01
176.96	0.00E+00	155.92	2.74E-01
177.54	1.62E-01	157.29	1.24E-02
178.38	2.22E-01	157.42	2.18E-04
180.38	2.18E-01	158.25	3.81E-03
180.38	1.90E-01	158.25	1.85E-04
180.96	2.74E-01	158.50	1.08E-02
182.04	2.30E-01	160.42	2.84E-02
184.08	3.50E-01	160.58	5.40E-03
186.46	1.79E-01	161.42	9.09E-03

187.46	2.95E-01	162.29	5.47E-03
SSFL - C3		**SSFL -C4**	
MidPoint Depth (ft bgs)	**TVOC (ug/g wet rock)**	**MidPoint Depth (ft bgs)**	**TVOC (ug/g wet rock)**
189.38	0.00E+00	163.88	7.95E-03
191.67	2.69E-01	165.67	3.02E-02
194.21	1.33E-01	166.46	5.44E-02
194.92	1.44E-01	167.17	2.58E-02
197.21	1.87E-01	168.08	3.50E-04
199.17	2.05E-01	168.08	1.54E-04
200.92	0.00E+00	168.79	2.66E-01
201.92	0.00E+00	169.54	2.56E-01
203.08	5.37E-02	171.21	3.60E-04
204.42	7.86E-02	171.79	1.12E-02
206.33	9.54E-03	172.46	1.44E-01
206.54	0.00E+00	173.67	1.11E-02
208.08	0.00E+00	173.67	1.18E-02
208.58	0.00E+00	174.50	2.30E-02
209.96	2.03E-02	175.67	6.67E-03
209.96	9.59E-03	177.33	2.34E-02
210.58	0.00E+00	178.33	3.35E-04
210.58	1.09E-01	179.25	3.09E-04
211.92	8.94E-02	179.71	2.24E-02
213.92	1.07E-01	180.46	3.67E+00
215.83	2.33E-02	180.46	4.24E+00
217.25	3.42E-01	181.04	3.16E-02
218.08	2.45E-02	183.08	2.39E-04
219.08	7.50E-02	186.13	1.65E-04
220.54	4.79E-02	186.29	3.50E-04
221.29	0.00E+00	187.21	4.58E-03
222.63	0.00E+00	188.38	5.43E-04
223.63	6.01E-02	189.04	1.84E-04
226.00	0.00E+00	190.63	2.16E-04
227.83	0.00E+00	191.63	2.44E-04
228.00	0.00E+00	192.46	3.09E-04
229.04	0.00E+00	194.13	3.13E-04
229.71	5.61E-02	195.63	8.78E-05
231.42	1.62E-03	196.63	1.12E-04
232.83	5.20E-02	197.29	1.96E-04
234.58	0.00E+00	198.21	5.48E-03
234.58	0.00E+00	202.00	6.82E-03
235.88	8.13E-02	204.00	6.02E-03

235.88	5.96E-02	206.88	1.57E-04
SSFL - C3		**SSFL -C4**	
MidPoint Depth (ft bgs)	**TVOC (ug/g wet rock)**	**MidPoint Depth (ft bgs)**	**TVOC (ug/g wet rock)**
237.58	1.10E-01	208.13	2.84E-04
238.58	0.00E+00	208.13	5.60E-04
239.42	1.09E-01	208.25	4.44E-03
240.83	1.30E-01	209.38	1.74E+00
241.63	1.70E-01	212.29	3.03E-04
242.92	1.20E-01	213.21	2.32E-04
244.75	0.00E+00	213.92	5.52E-04
245.75	1.20E-01	214.79	3.31E-04
247.17	0.00E+00	217.04	2.58E-04
248.29	0.00E+00	219.08	1.72E-04
249.92	1.92E-01	221.33	2.42E-04
250.33	0.00E+00	221.46	2.69E-04
251.75	0.00E+00	221.46	1.66E-04
253.92	0.00E+00	222.58	2.54E-04
254.92	0.00E+00	223.38	2.30E-04
256.13	1.80E-02	224.38	1.43E-04
257.75	9.50E-03	225.54	1.51E-04
258.58	0.00E+00	226.54	2.74E-04
258.75	2.90E-04	227.00	1.59E-04
261.13	0.00E+00	227.00	3.97E-04
263.83	8.61E-04	228.00	1.29E-04
263.83	0.00E+00	229.25	4.94E-02
264.50	0.00E+00	230.04	8.14E-04
266.79	7.24E-03	232.08	1.02E-02
267.63	3.02E-02	232.46	3.50E-04
270.58	5.50E-03	233.92	2.96E-04
271.46	3.79E-03	234.54	7.13E-05
272.79	1.17E-02	235.92	3.40E-04
272.79	0.00E+00	235.92	2.74E-02
274.29	0.00E+00	236.83	2.19E-02
276.33	2.26E-02	237.79	1.25E-02
277.04	1.56E-02	238.42	8.03E-02
279.50	0.00E+00	239.17	2.40E-03
280.54	2.00E-02	241.00	2.47E-04
282.00	9.37E-03	242.21	3.26E-03
282.67	7.52E-04	243.29	5.70E-04
284.00	6.24E-02	244.08	2.83E-04
285.29	3.79E-03	245.63	6.35E-03

286.29	1.68E-03	246.63	3.69E-03
SSFL - C3		**SSFL -C4**	
MidPoint Depth (ft bgs)	**TVOC (ug/g wet rock)**	**MidPoint Depth (ft bgs)**	**TVOC (ug/g wet rock)**
287.13	3.27E-02	247.38	2.93E-02
288.04	6.93E-04	248.42	4.18E-02
289.21	7.43E-03	249.38	1.70E-01
291.29	4.26E-02	251.08	1.56E-01
292.71	5.04E-02	251.83	1.87E-02
294.08	3.71E-04	253.21	1.11E-02
294.88	3.43E-02	253.88	6.58E-03
295.63	3.98E-02	254.54	2.81E-02
296.63	5.22E-02	255.58	5.91E-04
297.21	3.91E-02	255.58	6.94E-04
298.04	5.33E-02	256.46	2.30E-04
298.96	4.48E-02	257.08	3.51E-04
300.96	1.34E-02	258.13	2.69E-04
301.46	8.10E-04	260.33	2.35E-04
301.46	3.74E-02	261.38	2.66E-04
301.50	9.74E-04	262.00	2.96E-04
301.50	6.98E-03	263.46	2.93E-04
302.38	4.80E-02	265.63	3.71E-04
303.33	2.85E-02	266.29	4.53E-03
304.29	6.23E-02	266.29	7.97E-03
304.29	5.27E-02	267.04	3.26E-04
306.54	9.02E-02	268.04	2.99E-04
307.54	6.50E-02	270.75	2.14E-04
308.17	5.31E-04	272.92	2.15E-04
308.38	7.12E-03	276.17	1.57E-04
311.71	4.97E-02	278.08	4.29E-04
312.79	9.72E-02	278.08	4.58E-04
313.42	1.14E-02	282.25	2.49E-03
314.04	6.35E-02	283.17	2.65E-04
316.88	5.31E-02	285.75	2.26E-04
317.54	2.34E-04	288.00	7.10E-03
318.46	6.08E-04	290.46	6.80E-03
319.21	2.36E-04	291.17	5.24E-05
320.88	1.30E-03	292.67	1.14E-04
320.88	1.66E-04	292.83	1.04E-04
321.92	4.19E-04	295.96	3.91E-04
322.92	9.94E-05	295.96	3.12E-04
324.21	2.54E-04	298.83	3.95E-04

326.83	5.27E-04	300.63	2.48E-04
SSFL - C3		**SSFL -C4**	
MidPoint Depth (ft bgs)	**TVOC (ug/g wet rock)**	**MidPoint Depth (ft bgs)**	**TVOC (ug/g wet rock)**
327.46	6.41E-04	301.92	2.31E-04
328.08	1.15E-04	305.08	3.84E-03
328.92	9.99E-03	309.88	7.77E-04
329.42	2.05E-04	310.08	7.01E-04
331.00	3.75E-02	315.17	6.06E-04
331.67	1.62E-02	315.88	1.25E-02
332.79	4.51E-02	321.25	3.06E-02
333.42	6.12E-02	325.42	8.24E-04
335.46	3.44E-02	325.42	8.17E-03
336.67	9.56E-03	326.58	6.00E-05
337.29	5.93E-03	326.71	8.73E-05
338.63	8.85E-03	327.21	1.19E-04
340.92	8.85E-05	328.79	1.21E-04
341.13	2.65E-02	329.21	7.62E-05
341.71	1.16E-02	331.29	4.69E-05
342.21	1.44E-02	332.38	1.47E-04
343.21	5.14E-04	333.38	1.52E-04
343.21	1.28E-03	334.46	1.17E-04
346.96	4.19E-04	336.13	4.50E-03
347.96	1.40E-02	336.67	1.70E-02
348.54	5.78E-02	336.88	1.20E-02
350.63	7.64E-05	338.42	6.42E-04
352.21	2.11E-02	339.54	4.83E-05
353.04	3.90E-04	340.42	1.60E-03
353.79	1.57E-03	340.58	4.30E-03
355.29	1.87E-02	342.38	5.19E-03
355.46	4.80E-02	343.79	1.16E-02
356.17	9.36E-04	344.04	3.25E-04
356.79	6.63E-04	344.04	7.29E-03
357.50	9.17E-03	344.54	7.57E-03
358.46	6.19E-04	346.50	6.89E-03
362.38	8.18E-04	346.63	6.94E-03
362.71	7.58E-04	347.13	5.37E-03
363.46	1.72E-02	347.83	2.17E-02
364.88	2.94E-02	349.46	5.56E-04
366.71	9.58E-02	350.46	5.44E-04
367.71	1.61E-01	351.21	4.21E-05
367.71	9.78E-02	351.88	3.76E-03

368.58	1.99E-02	352.71	5.94E-05
SSFL - C3		**SSFL -C4**	
MidPoint Depth (ft bgs)	**TVOC (ug/g wet rock)**	**MidPoint Depth (ft bgs)**	**TVOC (ug/g wet rock)**
369.58	4.63E-02	352.71	8.24E-05
370.88	6.33E-02	353.71	3.51E-04
371.88	3.71E-02	355.38	1.00E+00
372.88	5.92E-02	355.38	7.28E-01
374.13	5.21E-02	355.96	8.91E-05
376.04	4.45E-02	356.88	5.35E-05
376.79	6.98E-02	358.17	4.03E-05
376.79	6.33E-02	358.63	5.35E-03
377.54	6.99E-02	359.63	4.51E-05
378.25	5.11E-02	360.13	3.86E-05
379.25	6.45E-02	360.83	4.97E-05
381.33	7.22E-02	362.13	6.45E-05
382.38	6.39E-03	366.96	5.66E-05
383.33	1.90E-01	369.00	4.62E-05
384.21	1.50E-04	372.17	3.69E-05
386.08	2.35E-03	374.08	3.16E-05
386.88	7.11E-02	375.13	3.44E-05
388.54	8.43E-02	376.38	6.86E-03
389.21	1.15E-01	378.67	5.05E-05
391.88	3.19E-04	380.13	5.18E-05
392.96	4.69E-02	380.63	5.09E-05
394.08	1.09E-01	382.13	5.56E-05
394.79	1.55E-01	382.13	4.84E-05
395.92	5.76E-02	383.00	6.68E-03
396.08	1.01E-01	383.63	5.94E-03
397.33	1.25E-01	384.63	3.33E-03
398.00	9.11E-02	385.79	4.09E-05
399.04	2.97E-03	387.83	6.81E-03
399.04	8.27E-04	389.08	4.00E-05
400.67	6.14E-02	389.21	3.31E-05
401.21	5.82E-02	389.88	6.51E-05
402.04	1.56E-01	390.04	2.89E-03
403.46	1.55E-02	392.75	3.78E-05
404.33	1.24E-04	392.75	6.82E-05
407.08	5.66E-05	394.17	1.02E-02
409.04	4.49E-04	396.04	7.43E-03
411.21	0.00E+00	396.13	2.43E-02
412.88	4.36E-05	397.79	3.01E-03

413.63	1.08E-02	398.79	1.86E-02
SSFL - C3		**SSFL -C4**	
MidPoint Depth (ft bgs)	**TVOC (ug/g wet rock)**	**MidPoint Depth (ft bgs)**	**TVOC (ug/g wet rock)**
414.29	2.46E-03	399.46	4.90E-05
415.54	4.95E-04		
416.54	1.75E-02		
417.46	1.54E-01		
418.38	1.36E-01		
419.71	1.47E-01		
421.17	1.48E-01		
422.83	1.68E-01		
423.58	1.02E-01		
424.58	5.93E-05		
426.38	3.79E-04		
426.38	1.41E-04		
427.46	6.15E-04		
428.08	1.73E-04		
428.63	5.35E-04		
429.63	3.43E-04		
430.92	2.89E-01		
431.54	5.65E-03		
431.54	1.11E-04		
432.54	2.05E-04		
437.04	3.49E-02		
439.17	6.92E-02		
441.00	1.21E-01		
441.92	1.42E-01		
443.08	1.53E-01		
443.71	8.74E-02		
444.63	1.94E-04		
446.42	6.68E-01		
447.92	1.09E+00		
448.54	8.75E-02		
450.08	2.54E+00		
451.50	2.37E-02		
453.42	1.57E-01		
454.71	9.06E-02		

NAWC 94BR	
MidPoint Depth (ft bgs)	TVOC (ug/g wet rock)
35.65	6.49E+00
36.15	2.66E+00
36.75	2.38E+01
37.35	1.26E+01
37.95	3.17E+01
38.65	2.40E+01
39.15	5.04E-01
39.55	2.12E+00
40.35	3.39E-03
40.95	4.99E+00
41.65	3.19E-02
41.9	1.36E-03
42.15	5.38E-02
42.85	7.82E-03
43.05	5.03E-03
43.45	4.86E+00
43.7	2.25E-03
44.15	5.33E+01
45.55	1.20E-03
45.55	1.39E-03
46.3	5.43E-02
46.7	5.28E-04
47.55	1.97E-03
48.45	8.95E-01
49.05	2.79E-01
49.35	2.52E+00
49.45	1.53E-01
49.8	1.37E-01
50.25	2.21E+00
50.75	3.03E-03
51.05	1.89E-03
51.15	2.27E-02
51.45	1.37E-01
52.35	6.97E-04
52.65	5.60E-04
52.95	3.57E-04
53.25	3.72E-04
53.85	3.80E-03
54.75	2.98E-03

NAWC 94BR	
MidPoint Depth (ft bgs)	TVOC (ug/g wet rock)
55.45	3.17E-03
55.45	4.81E-03
55.7	7.52E-03
56.05	1.66E-03
56.4	6.87E-03
56.7	4.13E-03
57.1	3.40E-03
57.35	1.84E-04
58.35	1.01E-03
58.65	2.95E-04
59.35	1.15E-02
60.25	9.22E-03
60.55	2.98E-03
60.7	2.85E-03
60.9	1.08E-02
61.25	7.43E-03
62.15	1.38E-03
62.35	3.50E-03
62.5	7.04E-02
62.75	2.01E-02
64.15	9.45E-03
64.45	2.20E-03
64.8	1.81E-02
65.55	1.36E+00
65.55	9.48E-01
65.75	1.11E+01
66	6.12E-02
66.3	1.40E-03
66.6	1.31E+01
67.05	1.52E-03
67.3	2.82E-03
68.25	1.08E-03
68.65	3.45E+00
69.25	1.73E-03
70.4	1.26E+02
70.85	7.55E-03
71.55	4.44E-02
71.8	8.18E-03
72.6	8.26E-01

NAWC 94BR	
MidPoint Depth (ft bgs)	TVOC (ug/g wet rock)
72.9	4.93E-03
72.95	7.63E-01
73.2	9.51E-02
74.45	1.15E-01
74.85	1.99E-01
74.85	4.43E-01
75.1	2.36E-03
75.2	5.61E-02
75.5	9.81E-04
76.2	8.17E-04
76.6	4.09E-03
76.9	2.45E-03
77.45	9.08E-01
78.5	9.20E+00
78.8	7.17E+00
79.05	7.50E-01
79.675	1.28E+01
80.3	2.65E-03
80.6	4.85E-01
81.28	2.21E+00
81.95	2.20E+00
82.3	3.95E-03
82.5	1.36E+00
82.7	1.82E-01
83.5	7.21E+01
84.15	1.59E+02
84.5	2.43E+01
84.5	1.73E+01
85.35	2.00E+01
85.875	3.78E+01
86.2	3.53E+01
86.3	1.68E+00
86.85	2.16E+00
87.65	2.04E+00
88.3	3.07E+00
88.5	7.54E+00
88.6	3.46E+00
89.275	8.37E-01
90.325	1.44E+00

NAWC 94BR	
MidPoint Depth (ft bgs)	TVOC (ug/g wet rock)
90.9	1.38E-03
91.275	1.25E-03
92.4	1.44E-03
92.7	9.62E-04
92.95	2.21E-03
93.25	8.32E-04
94.3	6.42E-04
94.5	4.97E-04
94.5	4.21E-04
94.8	1.88E-03
95.55	3.80E-04
95.9	1.62E-03
96.6	1.20E+01
97.55	2.14E+01
97.95	1.35E+02
98.8	5.83E+01
99.5	4.67E-02
101.2	2.17E-02
101.85	3.81E-03
102.55	2.30E-03
102.75	1.44E-03
105.65	3.57E-03
106.05	3.13E-03
106.35	2.91E-03
106.65	6.15E-03
107.05	1.09E-03
107.65	3.08E-03
108.15	2.74E-03
109.1	8.39E-03
109.1	7.37E-03
109.35	1.32E-02
109.7	4.73E-04
110.55	1.05E-03
111.1	1.39E-03
111.35	6.03E-03
111.85	5.68E-03
112.45	1.85E+01
112.8	7.69E+00
113.3	2.58E+00

NAWC 94BR	
MidPoint Depth (ft bgs)	TVOC (ug/g wet rock)
113.65	4.43E-03
114.3	8.68E-03
114.65	1.68E-03
115.575	4.29E-03
115.95	1.31E-03
116.75	4.49E-03
117.35	5.43E-04
118	8.27E-04
118.2	1.24E-03
118.75	1.23E-03
119.175	4.67E-03
119.175	8.09E-04
119.475	1.67E-03
120.95	3.65E-04
121.65	1.61E-04
122.05	4.03E-04
122.375	1.91E-03
122.85	2.21E-04
124.75	3.20E-04
125.45	7.11E-03
126.15	5.18E-04
126.65	6.70E-04
127	7.68E-04
128.3	1.15E-03
128.7	5.47E-03
129.075	2.20E+02
129.55	1.41E-03
130.45	8.11E-04
131.65	4.52E-03
132.05	1.32E-03
133.45	6.27E-03
134.45	1.40E-03
134.45	1.54E-03
134.8	2.07E-03
135.4	5.12E-03
136.05	2.07E-03
136.85	1.45E-03
137.15	1.32E-03
137.65	8.98E-04

NAWC 94BR	
MidPoint Depth (ft bgs)	**TVOC (ug/g wet rock)**
137.65	1.07E-03
138.15	9.34E-04
138.65	9.05E-03
139.2	1.25E-01
140.725	1.05E+00
141.05	2.78E-03
141.25	1.95E-03
141.65	1.17E-03
143	2.53E-03
143.45	1.87E-03
144.15	1.28E-03
144.85	1.08E-03
146.3	3.24E-03
146.7	2.51E-03
147.55	1.97E-03
147.55	1.13E-03
148.55	2.53E-03
149.25	5.77E-04

Appendix A.3: Rock core contaminant profiles

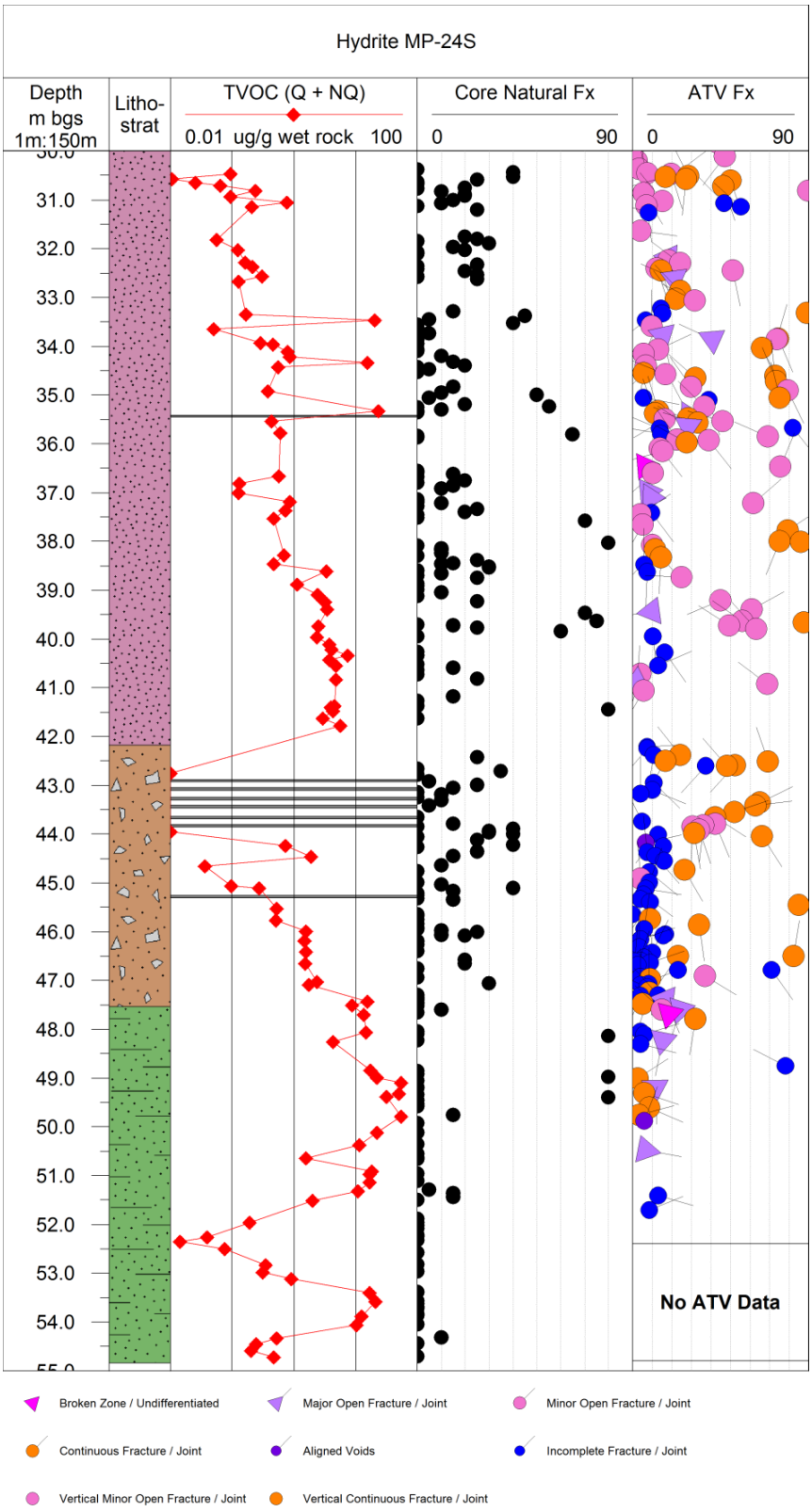

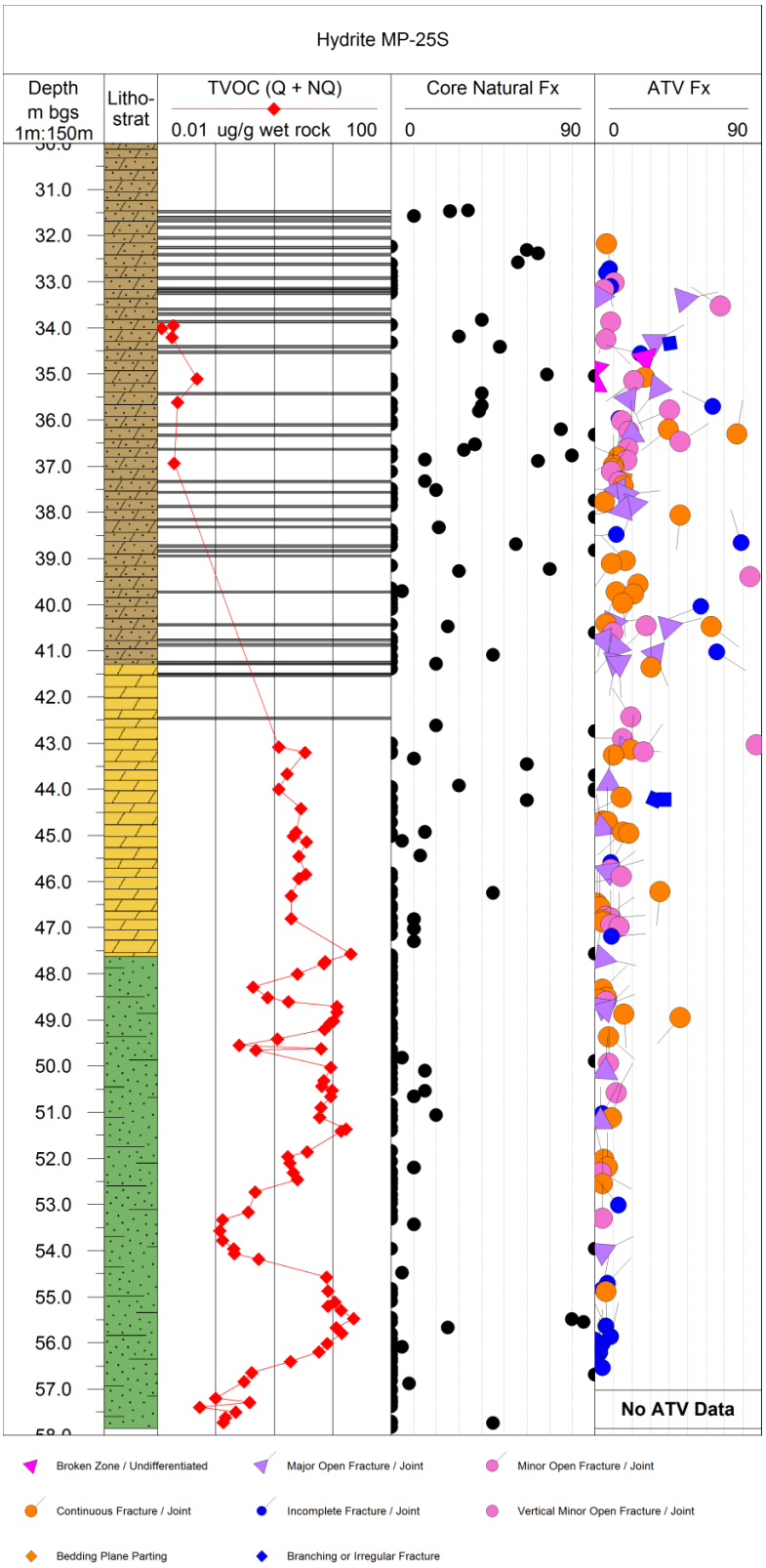
Hydrite MP-25S
Depth m bgs 1m:150m
Litho-strat
TVOC (Q + NQ)
0.01 ug/g wet rock 100
Core Natural Fx
0 90
ATV Fx
0 90
31.0
32.0
33.0
34.0
35.0
36.0
37.0
38.0
39.0
40.0
41.0
42.0
43.0
44.0
45.0
46.0
47.0
48.0
49.0
50.0
51.0
52.0
53.0
54.0
55.0
56.0
57.0
No ATV Data
Broken Zone / Undifferentiated
Major Open Fracture / Joint
Minor Open Fracture / Joint
Continuous Fracture / Joint
Incomplete Fracture / Joint
Vertical Minor Open Fracture / Joint
Bedding Plane Parting
Branching or Irregular Fracture

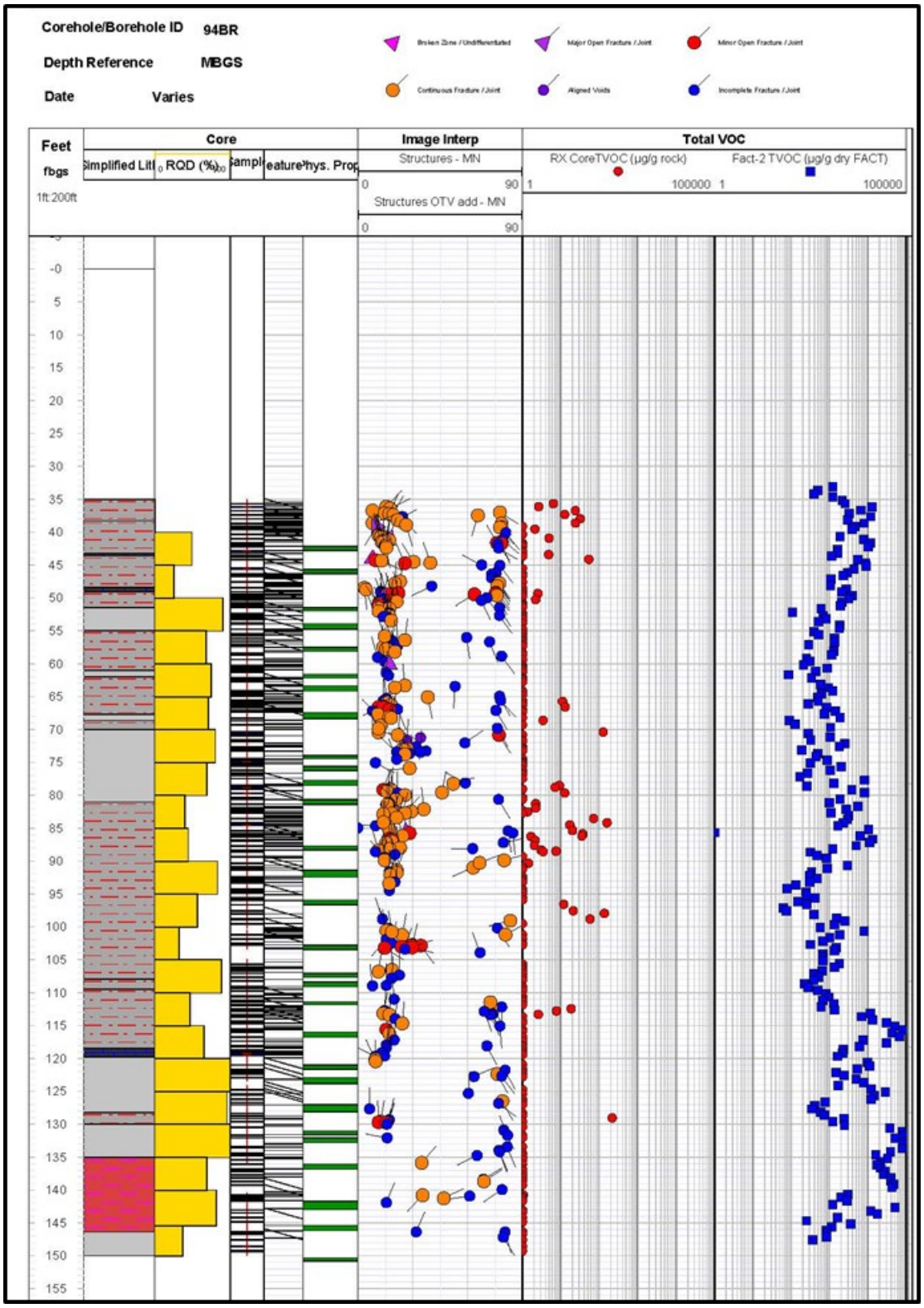
Corehole/Borehole ID 94BR
Depth Reference MBGS
Date Varies
Broken Zone / Undifferentiated
Major Open Fracture / Joint
Minor Open Fracture / Joint
Continuous Fracture / Joint
Aligned Voids
Incomplete Fracture / Joint
Feet
fbgs
1ft:200ft
Core
Simplified Litl
RQD (%)
Sampl
eature
hys. Prop
Image Interp
Structures - MN
0
90
Structures OTV add - MN
0
90
Total VOC
RX CoreTVOC (µg/g rock)
1
100000
Fact-2 TVOC (µg/g dry FACT)
1
100000
-0
5
10
15
20
25
30
35
40
45
50
55
60
65
70
75
80
85
90
95
100
105
110
115
120
125
130
135
140
145
150
155

FIELD SITE: Santa Suzanna Field Laboratory **DRILLING DATE:**

BORE HOLE: C-3 **LOGGING DATE:**

DEPTH REFERENCE:	Grnd	**CASING HEIGHT:**	0 m	**NOTES:**
DEPTH DRILLED:	455' bgs	**CASING DEPTH:**	6 m	N
DEPTH LOGGED:	-	**WATER LEVEL (original):**	-	E
BORE HOLE DIAMETER:		**WATER LEVEL (logging):**	67.22 m TOC	
SURFACE ELEVATION:	1839.5 ft			

MAJOR LITHOLOGY
- Sandstone
- Siltstone
- Shale
- Sand
- Interbedded
- Unknown

STRATIGRAPHY
- Sage Member
- Lower Line Bed

FRACTURES
- Mechanical
- Open
- OpenStained
- Closed
- ClosedStained
- No Data Given

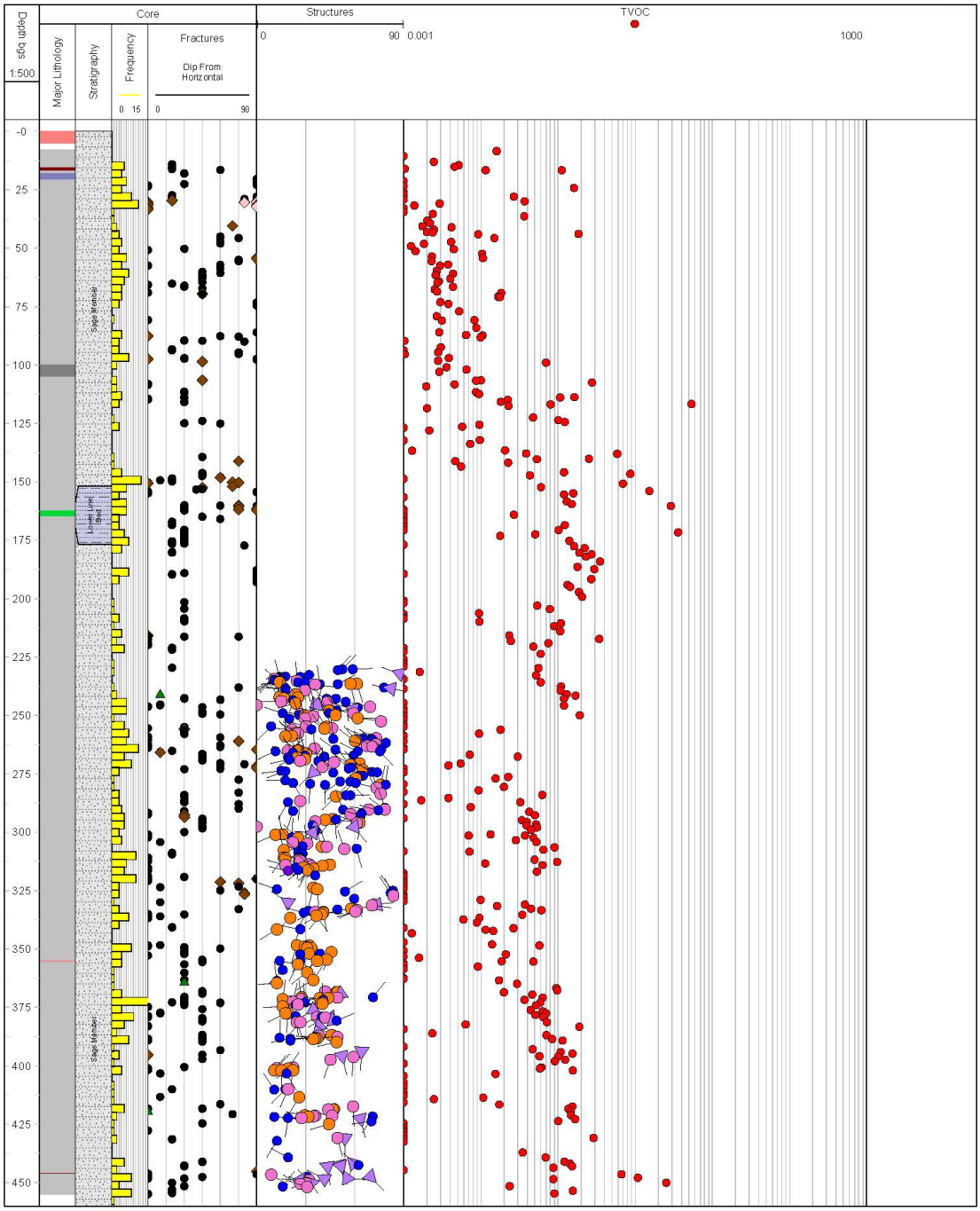

FIELD SITE: Santa Suzanna Field Laboratory **DRILLING DATE:**

BORE HOLE: C-4 **LOGGING DATE:**

DEPTH REFERENCE:	1819.7 ft	**CASING HEIGHT:**	0.71 m	**NOTES:**
DEPTH DRILLED:	121.9 m	**CASING DEPTH:**	5.38 m	
DEPTH LOGGED:	-	**WATER LEVEL (original):**	-	
BORE HOLE DIAMETER:		**WATER LEVEL (logging):**	34.21 m TOC	
SURFACE ELEVATION:	1817.37 ft			

MAJOR LITHOLOGY	STRATIGRAPHY	FRACTURES
Sandstone	Bowl Member	Open
Interbedded	Upper Bowl Bed	OpenStained
Silty Sand	Lower Bowl Bed	Closed
Unknown	Lower Chatsworth A	ClosedStained
	Lower Chatsworth B	No Data Given
	Lower Chatsworth C	
	Shale Bed A	
	Shale Bed B	

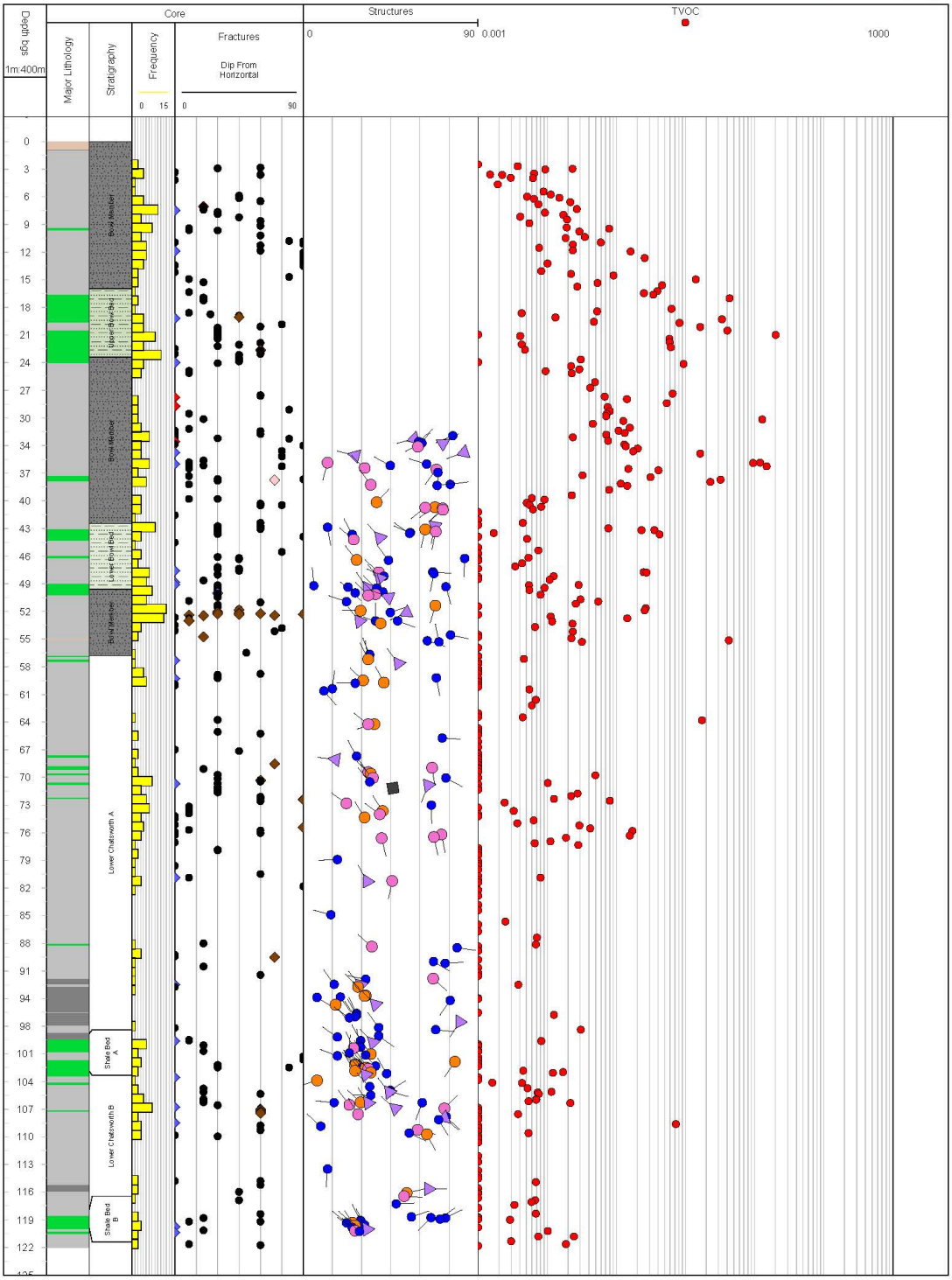

FIELD SITE: Santa Suzanna Field Laboratory **DRILLING DATE:** 16/12/2013

BORE HOLE: **RD-109** **LOGGING DATE:** 17/11/16

DEPTH REFERENCE:	TOC,Gnd	**CASING HEIGHT:**	0.91 m	**NOTES:**	N 267657.28
DEPTH DRILLED:		**CASING DEPTH:**	14.00 m		E 1795087.84
DEPTH LOGGED:		**WATER LEVEL (original):**	-		
BORE HOLE DIAMETER:		**WATER LEVEL (logging):**	27.661 m TOC		
SURFACE ELEVATION:	1885.67 ft				

MAJOR LITHOLOGY
- Sandstone
- Interbedded
- Siltstone
- No Recovery

STRATIGRAPHY
- Canyon Member

FRACTURES
- Mechanical
- OpenSeries
- OpenStained
- Open
- Closed

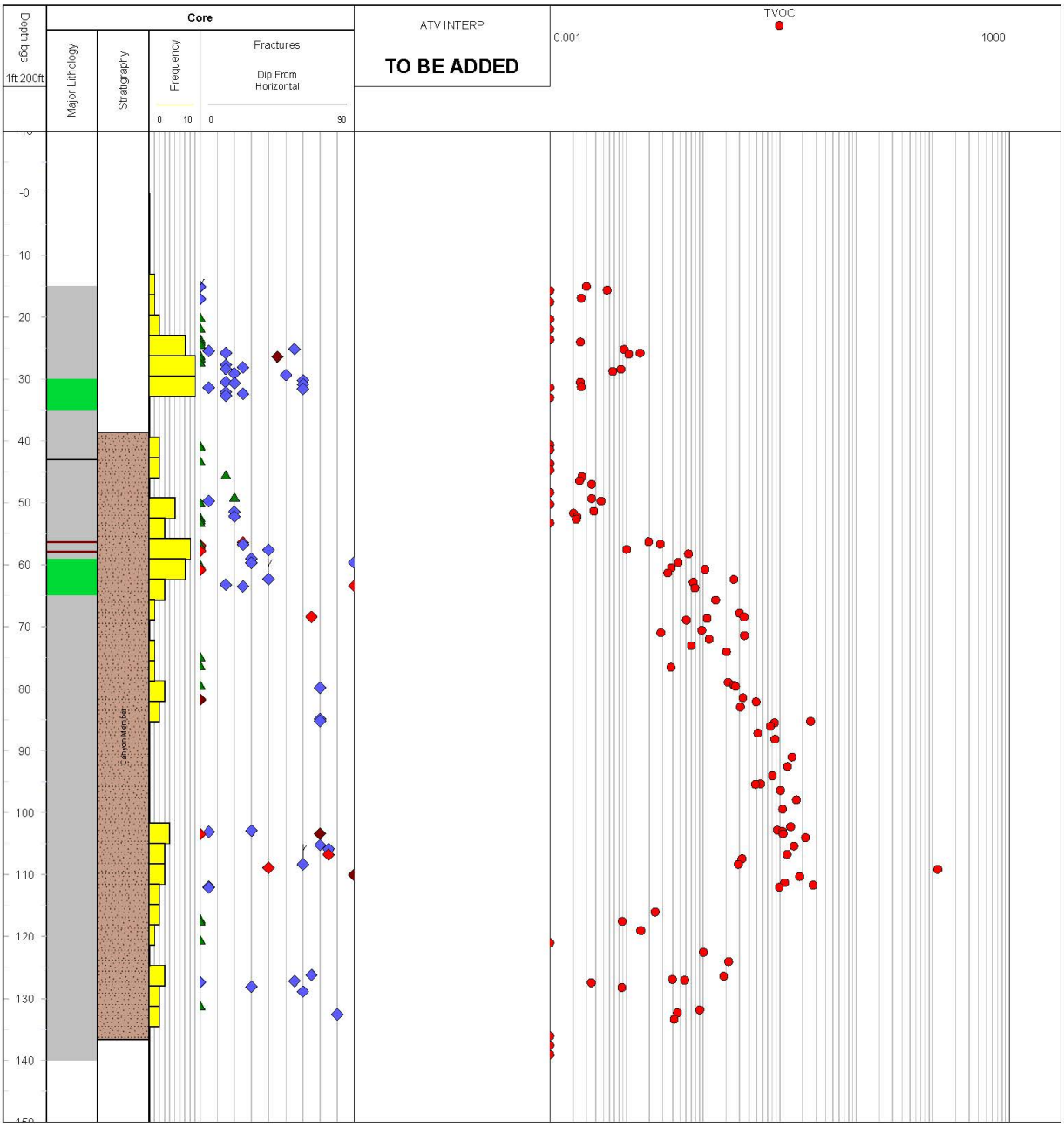

Appendix B.1: Complex resistivity (CR), Nuclear Magnetic Resonance (NMR) and physical property summary data

Each page in Appendix B.1 contains a data summary for each sample. The page is partitioned into a figure (top) and a table (bottom). The figure contains 4 subfigures:

(A) Complex resistivity (CR) raw data are shown as collected by the PSIP instrument as complex resistance (Ω) and -Phase (mrad) versus frequency (Hz).

(B) Using the CR data shown in (A) and knowing the geometric factor of the sample holder, complex resistivity can be calculated. The inverse of complex resistivity is complex conductivity. The phase angle can be used to separate out conduction (the real σ' conductivity component) and polarization (the imaginary conductivity σ" component).

(C) NMR CPMG raw data as collected from the RockCore instrument as T2 decay versus time. NMR decays are shown for two echo times: 200 and 1500 µs. Laboratory studies typically use shorter echo times and a higher signal-to-noise ratio (SNR): 1) to capture the entire spectrum of the decay curve and 2) longer data acquisition is less of an issue for laboratory data collection. Since NMR borehole logging data were acquired using an echo spacing of 1500 µs, we provide this data for direct comparison with the borehole logs.

(D) NMR T2 distributions are shown for 200 and 1500 µs echo times.

The table for each sample contains physical properties, electrical/CR measures and NMR measures. Sections 4.0, 6.3 and 6.4 provide more information regarding these properties. As a result of the small pore sizes, NAWC samples proved more challenging in terms of data collection than the SSFL and Hydrite samples. Regarding physical property data:

- Where permeability measurements could not be collected for a sample, it is reported as zero (0). NAWC samples in particular split easily along bedding planes which made samples unusable for the permeability sample holder.
- If the electrical formation factor (F) is blank, high salinity measurements could not be collected for a particular sample. In particular, NAWC samples that split easily along bedding planes made samples unusable for the sample holder.
- Where no peak could be defined in the CR raw data (A from above), the peak CR relaxation time (τ_{peak}) is reported as NaN.
- For very tight samples, BET data could not be obtained where the surface area was greater than 1 m^2. To calculate S_{por}, specific surface area from BET is required. For samples where BET data could not be acquired, S_{por} is reported as NaN.

B.1 Figure 1: HC-MP24S-P-001-1V

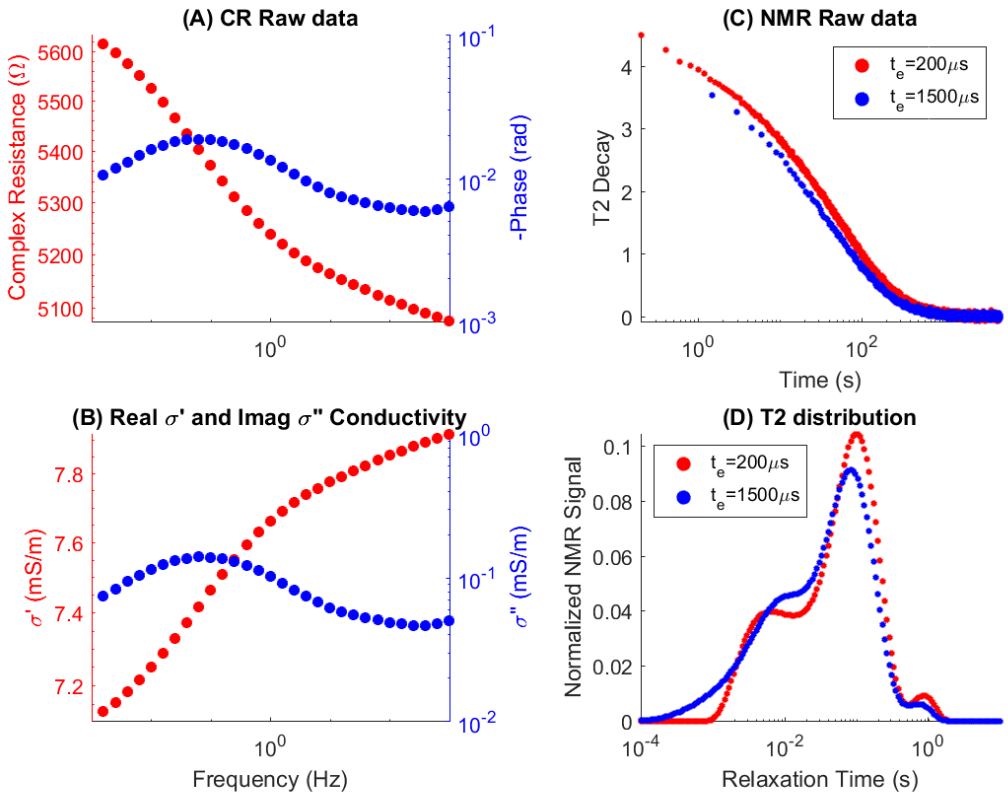

B.1 Table 1: HC-MP24S-P-001-1V Depth below ground surface=34.04 m

Physical properties

Permeability (mD): 5.44

Gravimetric Porosity (%): 11.8

Surface area normalized by pore volume (S_{por}) (μm^{-1}): 14.05

Electrical / CR measures

Electrical Formation Factor (F) (unitless): 44.05

Imaginary Conductivity at 1Hz (σ''_{1Hz}) (mS/m): 0.102

Peak relaxation time (τ_{peak}) (s): 2.15

NMR measures

Mean relaxation time echo time=200μs (T_{2ml}@t_e=200μs) (s): 4.22e-02

Peak relaxation time echo time=200μs (T_{2peak}@t_e=200μs) (s): 1.00e-01

Mean relaxation time echo time=1500μs (T_{2ml}@t_e=1500μs) (s): 3.00e-02

Peak relaxation time echo time=1500μs (T_{2peak}@t_e=1500μs) (s): 8.32e-02

B.1 Figure 2: HC-MP24S-P-002-1V

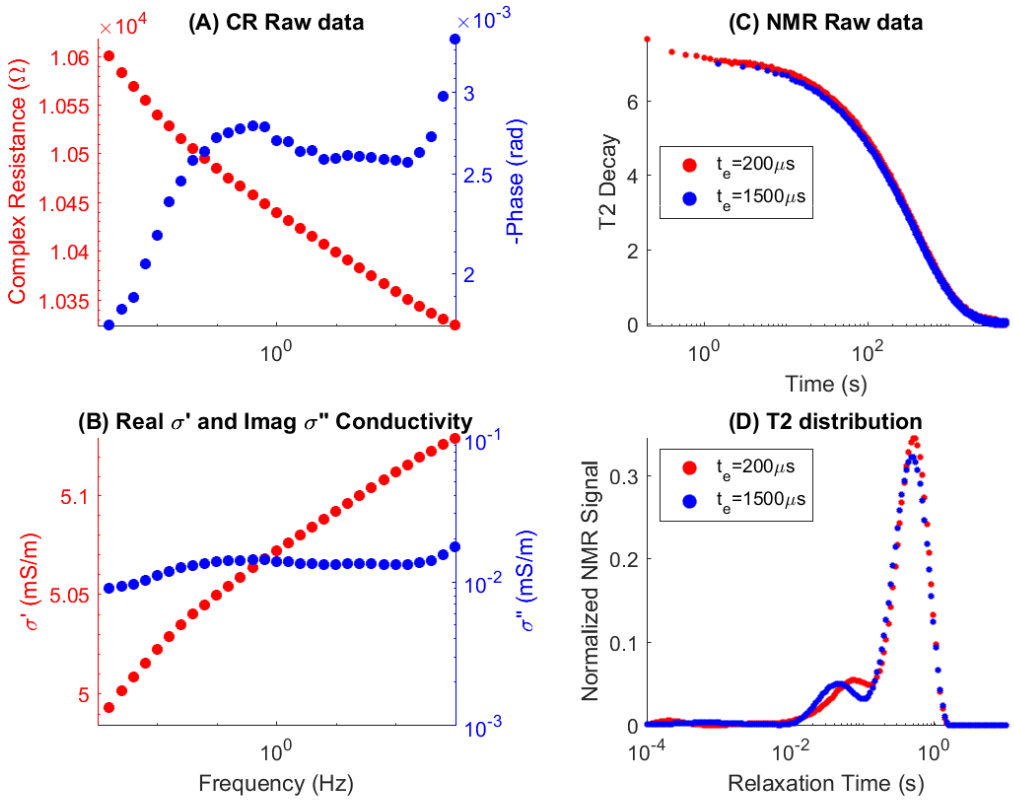

B.1 Table 2: HC-MP24S-P-002-1V Depth below ground surface=42.09 m

Physical properties

Permeability (mD): 62

Gravimetric Porosity (%): 16.2

Surface area normalized by pore volume (S_{por}) (μm^{-1}): 3.23

Electrical / CR measures

Electrical Formation Factor (F) (unitless): 26.41

Imaginary Conductivity at 1Hz (σ''_{1Hz}) (mS/m): 0.0136

Peak relaxation time (τ_{peak}) (s): 0.518

NMR measures

Mean relaxation time echo time=200μs (T_{2ml}@t_e=200μs) (s): 3.07e-01

Peak relaxation time echo time=200μs (T_{2peak}@t_e=200μs) (s): 5.25e-01

Mean relaxation time echo time=1500μs (T_{2ml}@t_e=1500μs) (s): 2.97e-01

Peak relaxation time echo time=1500μs (T_{2peak}@t_e=1500μs) (s): 5.01e-01

B.1 Figure 3: HC-MP24S-P-002-2H

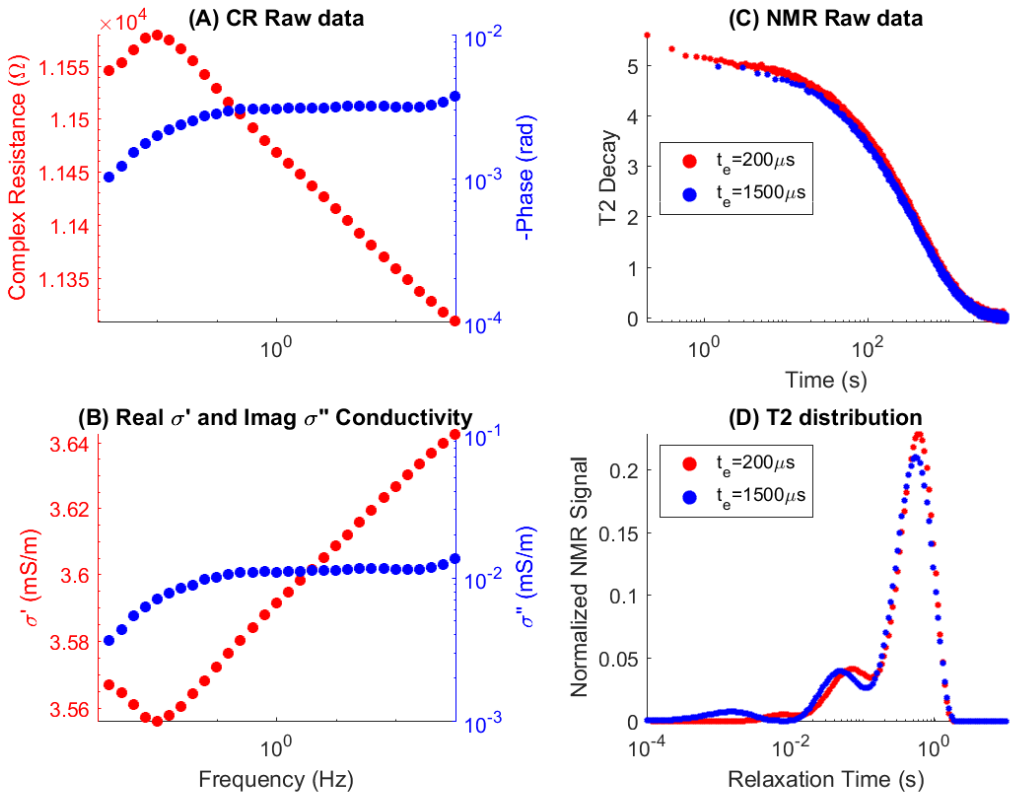

B.1 Table 3: HC-MP24S-P-002-2H Depth below ground surface=42.09 m

Physical properties

Permeability (mD): 249

Gravimetric Porosity (%): 13.5

Surface area normalized by pore volume (S_{por}) (μm^{-1}): 3.923

Electrical / CR measures

Electrical Formation Factor (F) (unitless): 30.76

Imaginary Conductivity at 1Hz (σ''_{1Hz}) (mS/m): 0.0109

Peak relaxation time (τ_{peak}) (s): 0.652

NMR measures

Mean relaxation time echo time=200μs (T_{2ml}@t_e=200μs) (s): 3.43e-01

Peak relaxation time echo time=200μs (T_{2peak}@t_e=200μs) (s): 6.03e-01

Mean relaxation time echo time=1500μs (T_{2ml}@t_e=1500μs) (s): 2.77e-01

Peak relaxation time echo time=1500μs (T_{2peak}@t_e=1500μs) (s): 5.50e-01

B.1 Figure 4: HC-MP24S-P-003-1V

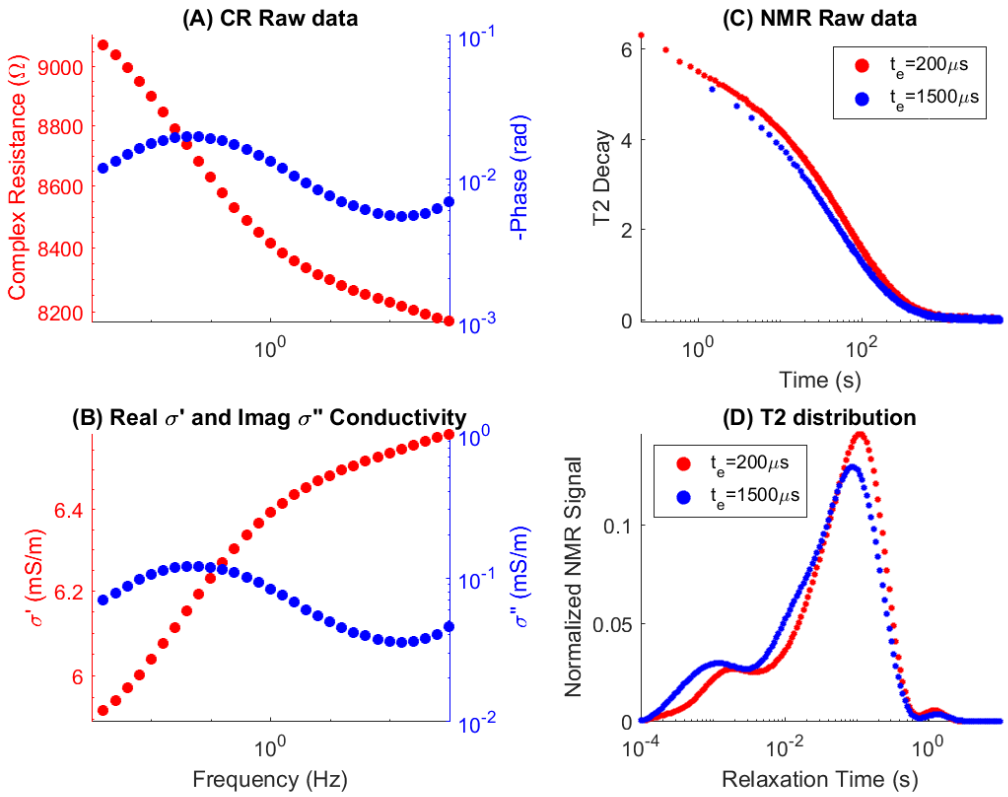

B.1 Table 4: HC-MP24S-P-003-1V Depth below ground surface=44.87 m

Physical properties

Permeability (mD): 7.92

Gravimetric Porosity (%): 12.9

Surface area normalized by pore volume (S_{por}) (μm^{-1}): 19.08

Electrical / CR measures

Electrical Formation Factor (F) (unitless): 38.11

Imaginary Conductivity at 1Hz (σ''_{1Hz}) (mS/m): 0.0832

Peak relaxation time (τ_{peak}) (s): 3.46

NMR measures

Mean relaxation time echo time=200μs (T_{2ml}@t_e=200μs) (s): 4.22e-02

Peak relaxation time echo time=200μs (T_{2peak}@t_e=200μs) (s): 1.10e-01

Mean relaxation time echo time=1500μs (T_{2ml}@t_e=1500μs) (s): 2.80e-02

Peak relaxation time echo time=1500μs (T_{2peak}@t_e=1500μs) (s): 8.71e-02

B.1 Figure 5: HC-MP24S-P-003-2H

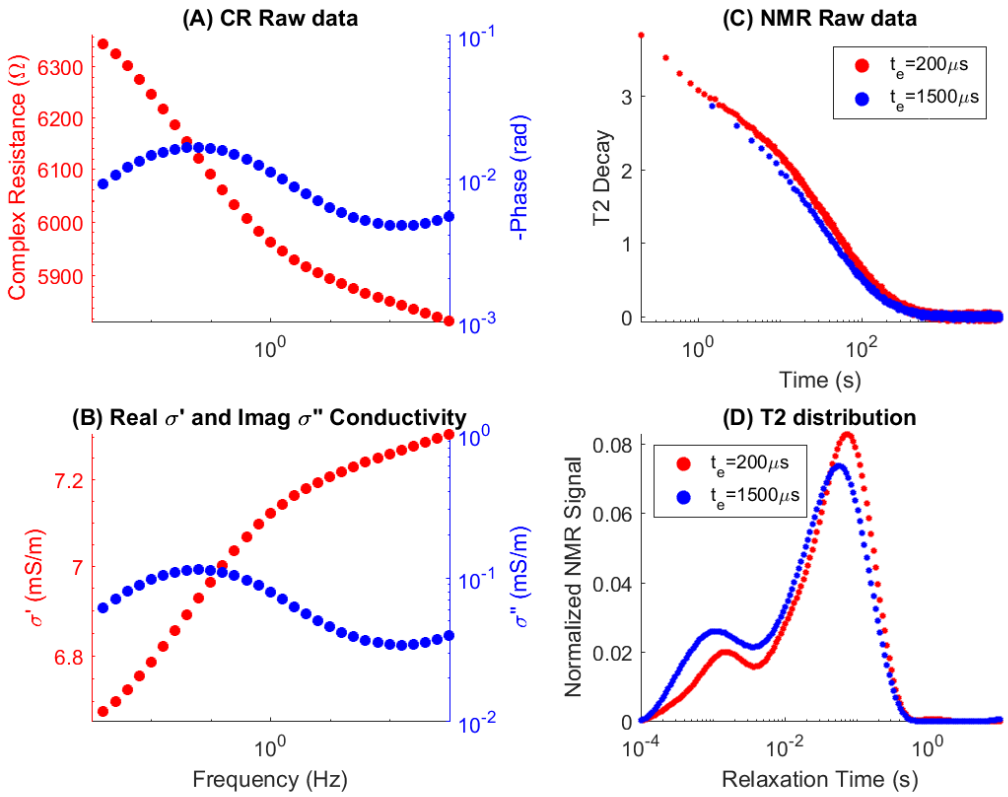

B.1 Table 5: HC-MP24S-P-003-2H Depth below ground surface=44.87 m

Physical properties

Permeability (mD): 17.9

Gravimetric Porosity (%): 11.1

Surface area normalized by pore volume (S_{por}) (μm^{-1}): 22.67

Electrical / CR measures

Electrical Formation Factor (F) (unitless): 49.8

Imaginary Conductivity at 1Hz (σ''_{1Hz}) (mS/m): 0.0788

Peak relaxation time (τ_{peak}) (s): 2.15

NMR measures

Mean relaxation time echo time=200μs (T_{2ml}@t_e=200μs) (s): 2.68e-02

Peak relaxation time echo time=200μs (T_{2peak}@t_e=200μs) (s): 7.24e-02

Mean relaxation time echo time=1500μs (T_{2ml}@t_e=1500μs) (s): 1.68e-02

Peak relaxation time echo time=1500μs (T_{2peak}@t_e=1500μs) (s): 5.75e-02

B.1 Figure 6: HC-MP24S-P-004-1V

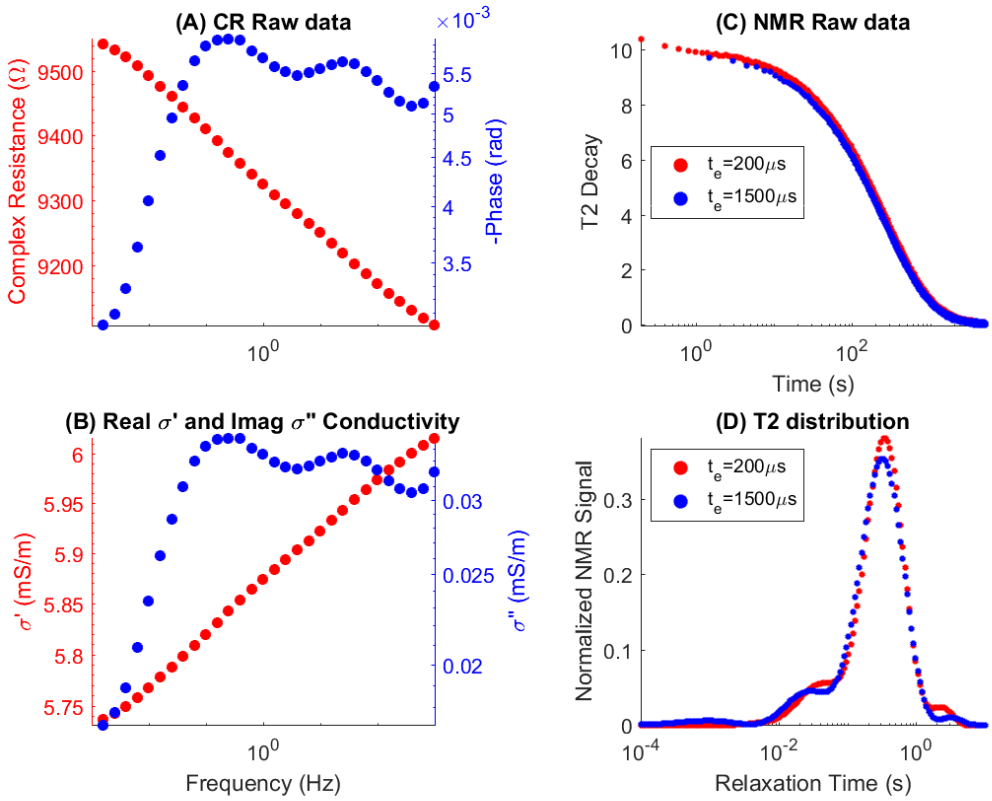

B.1 Table 6: HC-MP24S-P-004-1V Depth below ground surface=46.86 m

Physical properties

Permeability (mD): 330

Gravimetric Porosity (%): 18.3

Surface area normalized by pore volume (S_{por}) (μm^{-1}): 2.281

Electrical / CR measures

Electrical Formation Factor (F) (unitless): 16.82

Imaginary Conductivity at 1Hz (σ''_{1Hz}) (mS/m): 0.0335

Peak relaxation time (τ_{peak}) (s): 0.518

NMR measures

Mean relaxation time echo time=200μs (T_{2ml}@t_e=200μs) (s): 2.59e-01

Peak relaxation time echo time=200μs (T_{2peak}@t_e=200μs) (s): 3.47e-01

Mean relaxation time echo time=1500μs (T_{2ml}@t_e=1500μs) (s): 2.20e-01

Peak relaxation time echo time=1500μs (T_{2peak}@t_e=1500μs) (s): 3.16e-01

B.1 Figure 7: HC-MP24S-P-004-2H

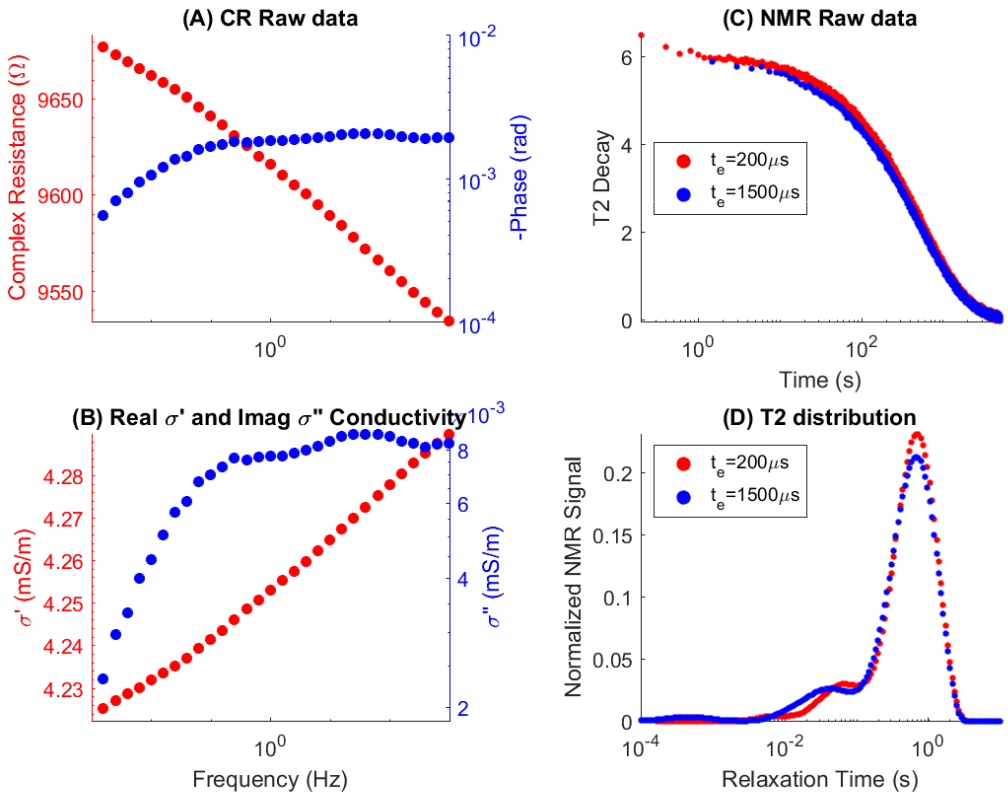

B.1 Table 7: HC-MP24S-P-004-2H Depth below ground surface=46.86 m

Physical properties

Permeability (mD): 367

Gravimetric Porosity (%): 16.3

Surface area normalized by pore volume (S_{por}) (μm^{-1}): 2.627

Electrical / CR measures

Electrical Formation Factor (F) (unitless): 20.36

Imaginary Conductivity at 1Hz (σ''_{1Hz}) (mS/m): 0.0077

Peak relaxation time (τ_{peak}) (s): 0.00461 0.733

NMR measures

Mean relaxation time echo time=200μs (T_{2ml}@t_e=200μs) (s): 4.66e-01

Peak relaxation time echo time=200μs (T_{2peak}@t_e=200μs) (s): 6.92e-01

Mean relaxation time echo time=1500μs (T_{2ml}@t_e=1500μs) (s): 3.89e-01

Peak relaxation time echo time=1500μs (T_{2peak}@t_e=1500μs) (s): 6.92e-01

B.1 Figure 8: HC-MP24S-P-005-1V

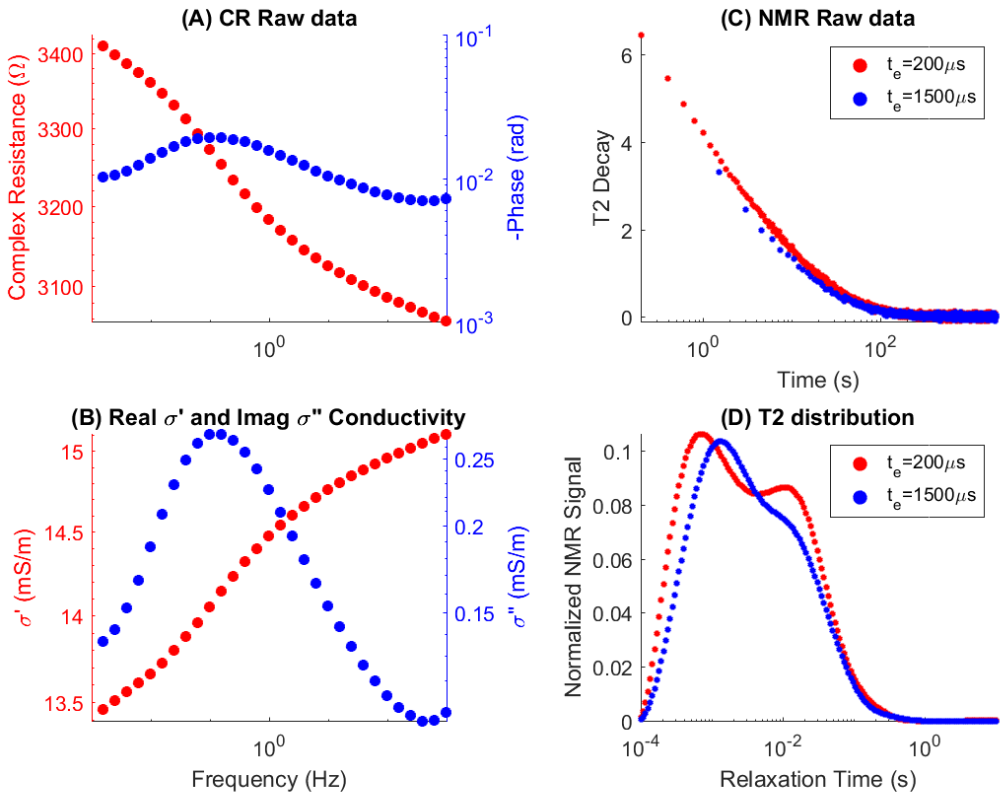

B.1 Table 8: HC-MP24S-P-005-1V Depth below ground surface=47.9 m

Physical properties

Permeability (mD): 0.174

Gravimetric Porosity (%): 19.3

Surface area normalized by pore volume (S_{por}) (μm^{-1}): 78.45

Electrical / CR measures

Electrical Formation Factor (F) (unitless): 19.62

Imaginary Conductivity at 1Hz (σ''_{1Hz}) (mS/m): 0.226

Peak relaxation time (τ_{peak}) (s): 1.34

NMR measures

Mean relaxation time echo time=200μs (T_{2ml}@t_e=200μs) (s): 3.05e-03

Peak relaxation time echo time=200μs (T_{2peak}@t_e=200μs) (s): 7.24e-04

Mean relaxation time echo time=1500μs (T_{2ml}@t_e=1500μs) (s): 3.32e-03

Peak relaxation time echo time=1500μs (T_{2peak}@t_e=1500μs) (s): 1.32e-03

B.1 Figure 9: HC-MP24S-P-006-1V

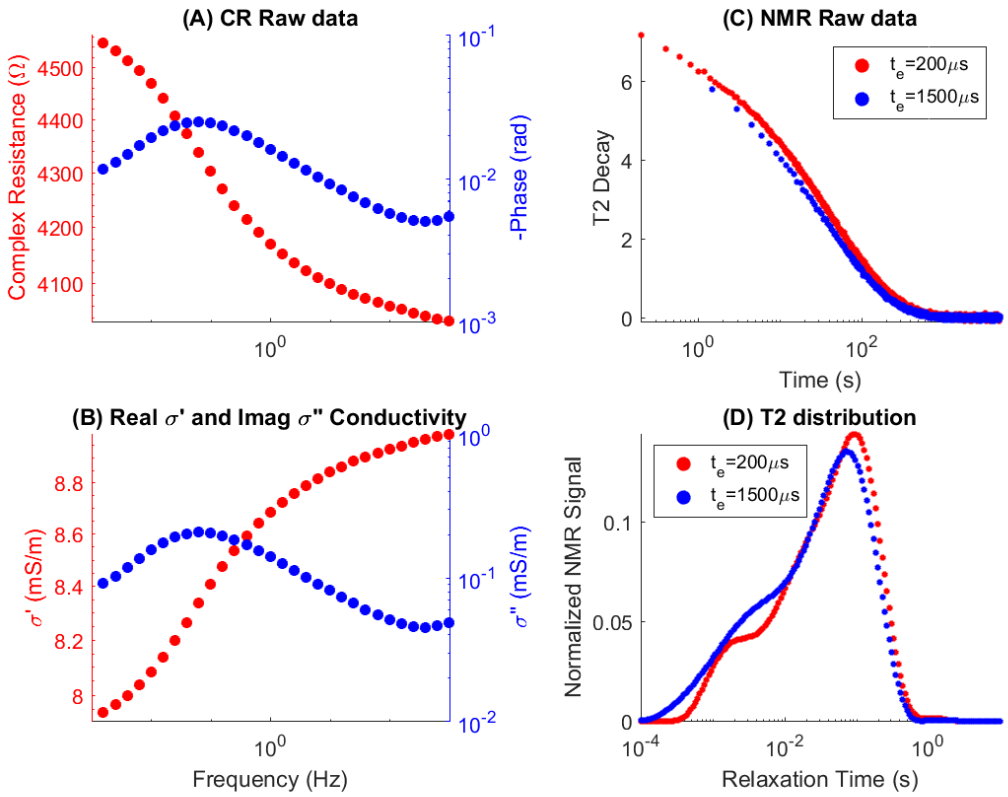

B.1 Table 9: HC-MP24S-P-006-1V Depth below ground surface=52.7 m

Physical properties

Permeability (mD): 1.58

Gravimetric Porosity (%): 22.4

Surface area normalized by pore volume (S_{por}) (μm^{-1}): 67.21

Electrical / CR measures

Electrical Formation Factor (F) (unitless): 16.51

Imaginary Conductivity at 1Hz (σ''_{1Hz}) (mS/m): 0.138

Peak relaxation time (τ_{peak}) (s): 2.15

NMR measures

Mean relaxation time echo time=200μs (T_{2ml}@t_e=200μs) (s): 3.23e-02

Peak relaxation time echo time=200μs (T_{2peak}@t_e=200μs) (s): 9.55e-02

Mean relaxation time echo time=1500μs (T_{2ml}@t_e=1500μs) (s): 2.33e-02

Peak relaxation time echo time=1500μs (T_{2peak}@t_e=1500μs) (s): 7.59e-02

B.1 Figure 10: HC-MP24S-P-006-2H

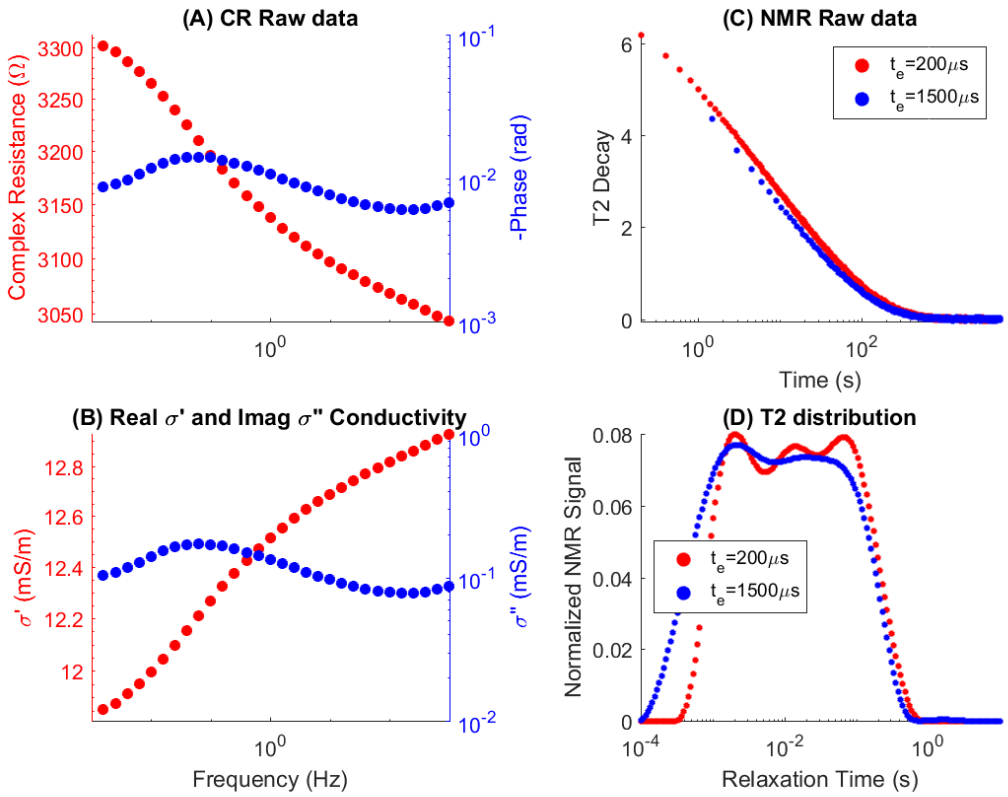

B.1 Table 10: HC-MP24S-P-006-2H Depth below ground surface=52.7 m

Physical properties

Permeability (mD): 6.51

Gravimetric Porosity (%): 18.5

Surface area normalized by pore volume (S_{por}) (μm^{-1}): 86.03

Electrical / CR measures

Electrical Formation Factor (F) (unitless): 19.61

Imaginary Conductivity at 1Hz (σ''_{1Hz}) (mS/m): 0.133

Peak relaxation time (τ_{peak}) (s): 2.15

NMR measures

Mean relaxation time echo time=200μs (T_{2ml}@t_e=200μs) (s): 1.38e-02

Peak relaxation time echo time=200μs (T_{2peak}@t_e=200μs) (s): 2.09e-03

Mean relaxation time echo time=1500μs (T_{2ml}@t_e=1500μs) (s): 8.48e-03

Peak relaxation time echo time=1500μs (T_{2peak}@t_e=1500μs) (s): 2.19e-03

B.1 Figure 11: HC-MP24S-P-007-1V

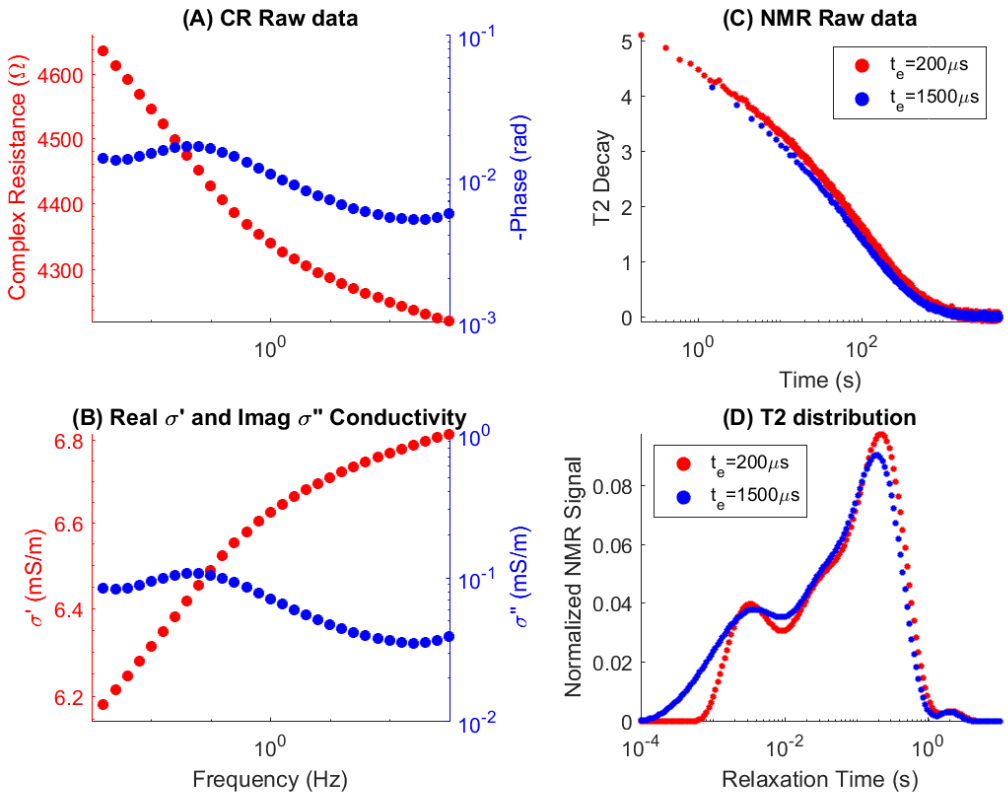

B.1 Table 11: HC-MP24S-P-007-1V Depth below ground surface=54.19 m

Physical properties

Permeability (mD): 0.341

Gravimetric Porosity (%): 19.2

Surface area normalized by pore volume (S_{por}) (μm^{-1}): 69.08

Electrical / CR measures

Electrical Formation Factor (F) (unitless): 23.4

Imaginary Conductivity at 1Hz (σ''_{1Hz}) (mS/m): 0.0709

Peak relaxation time (τ_{peak}) (s): 3.46

NMR measures

Mean relaxation time echo time=200μs (T_{2ml}@t_e=200μs) (s): 5.58e-02

Peak relaxation time echo time=200μs (T_{2peak}@t_e=200μs) (s): 2.19e-01

Mean relaxation time echo time=1500μs (T_{2ml}@t_e=1500μs) (s): 3.61e-02

Peak relaxation time echo time=1500μs (T_{2peak}@t_e=1500μs) (s): 1.91e-01

B.1 Figure 12: HC-MP24S-P-007-2H

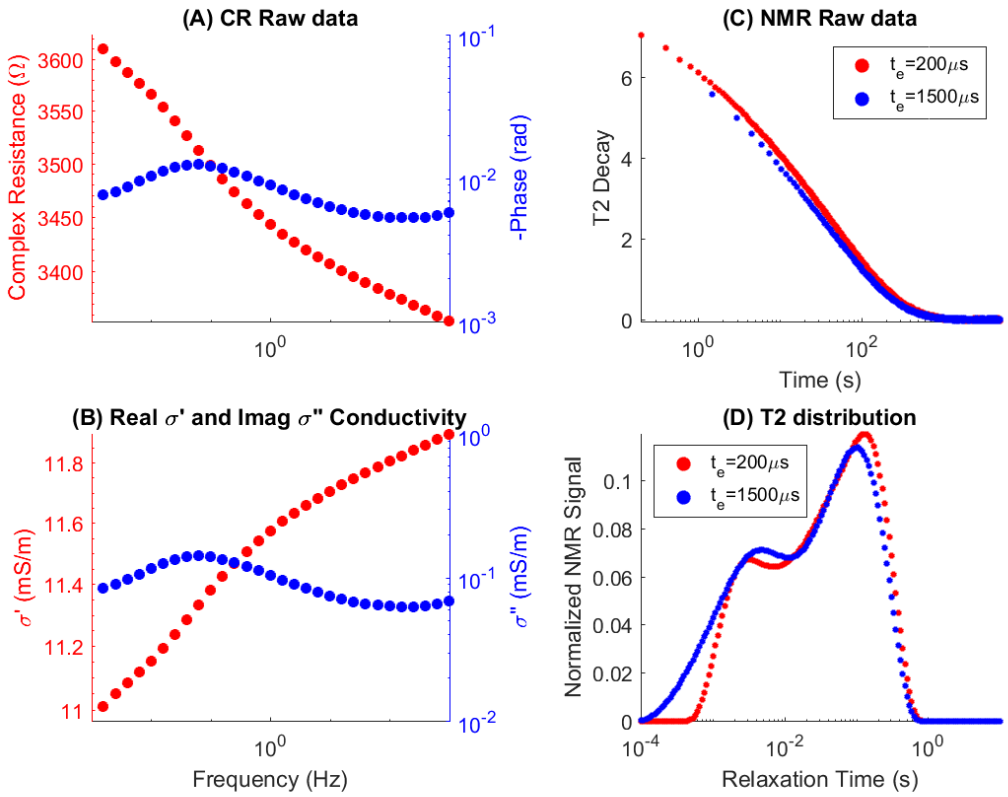

B.1 Table 12: HC-MP24S-P-007-2H Depth below ground surface=54.19 m

Physical properties

Permeability (mD): 63.1

Gravimetric Porosity (%): 20.6

Surface area normalized by pore volume (S_{por}) (μm^{-1}): 62.95

Electrical / CR measures

Electrical Formation Factor (F) (unitless): 14.97

Imaginary Conductivity at 1Hz (σ''_{1Hz}) (mS/m): 0.103

Peak relaxation time (τ_{peak}) (s): 2.15

NMR measures

Mean relaxation time echo time=200μs (T_{2ml}@t_e=200μs) (s): 2.90e-02

Peak relaxation time echo time=200μs (T_{2peak}@t_e=200μs) (s): 1.26e-01

Mean relaxation time echo time=1500μs (T_{2ml}@t_e=1500μs) (s): 1.96e-02

Peak relaxation time echo time=1500μs (T_{2peak}@t_e=1500μs) (s): 1.00e-01

B.1 Figure 13: HC-MP25S-P-001-1V

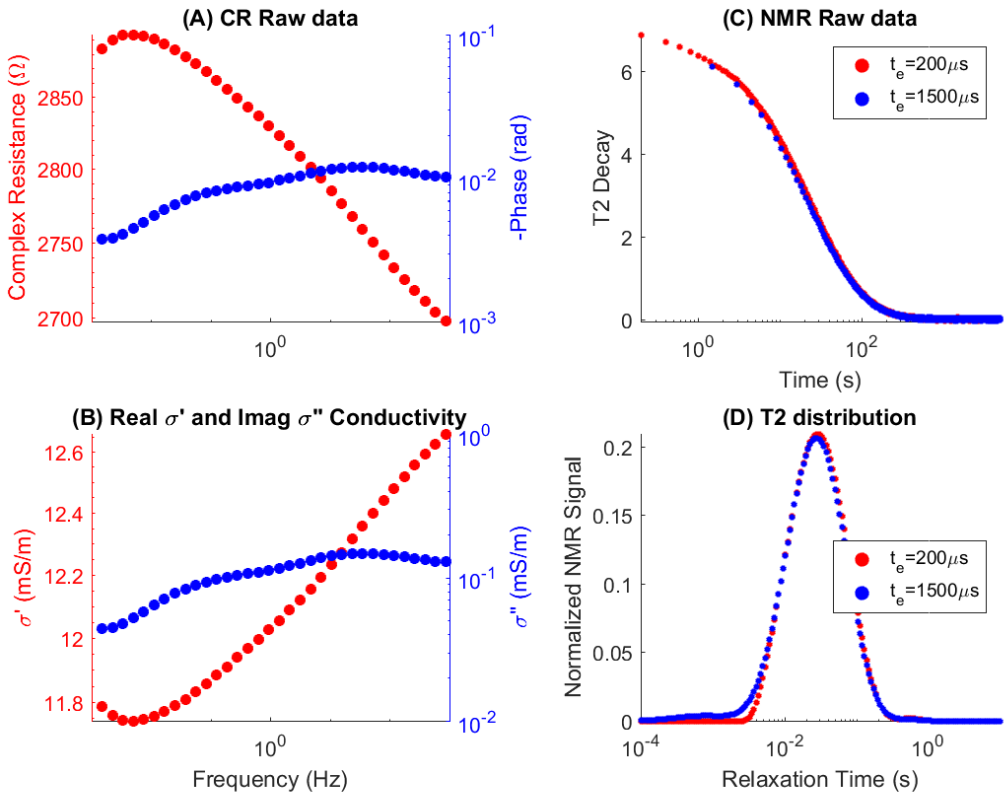

B.1 Table 13: HC-MP25S-P-001-1V Depth below ground surface=40.26 m

Physical properties

Permeability (mD): 5.79

Gravimetric Porosity (%): 22.3

Surface area normalized by pore volume (S_{por}) (μm^{-1}): 20.55

Electrical / CR measures

Electrical Formation Factor (F) (unitless): 20.8

Imaginary Conductivity at 1Hz (σ''_{1Hz}) (mS/m): 0.112

Peak relaxation time (τ_{peak}) (s): 0.00461 1.5

NMR measures

Mean relaxation time echo time=200μs (T_{2ml}@t_e=200μs) (s): 2.87e-02

Peak relaxation time echo time=200μs (T_{2peak}@t_e=200μs) (s): 2.88e-02

Mean relaxation time echo time=1500μs (T_{2ml}@t_e=1500μs) (s): 2.53e-02

Peak relaxation time echo time=1500μs (T_{2peak}@t_e=1500μs) (s): 2.75e-02

B.1 Figure 14: HC-MP25S-P-001-2H

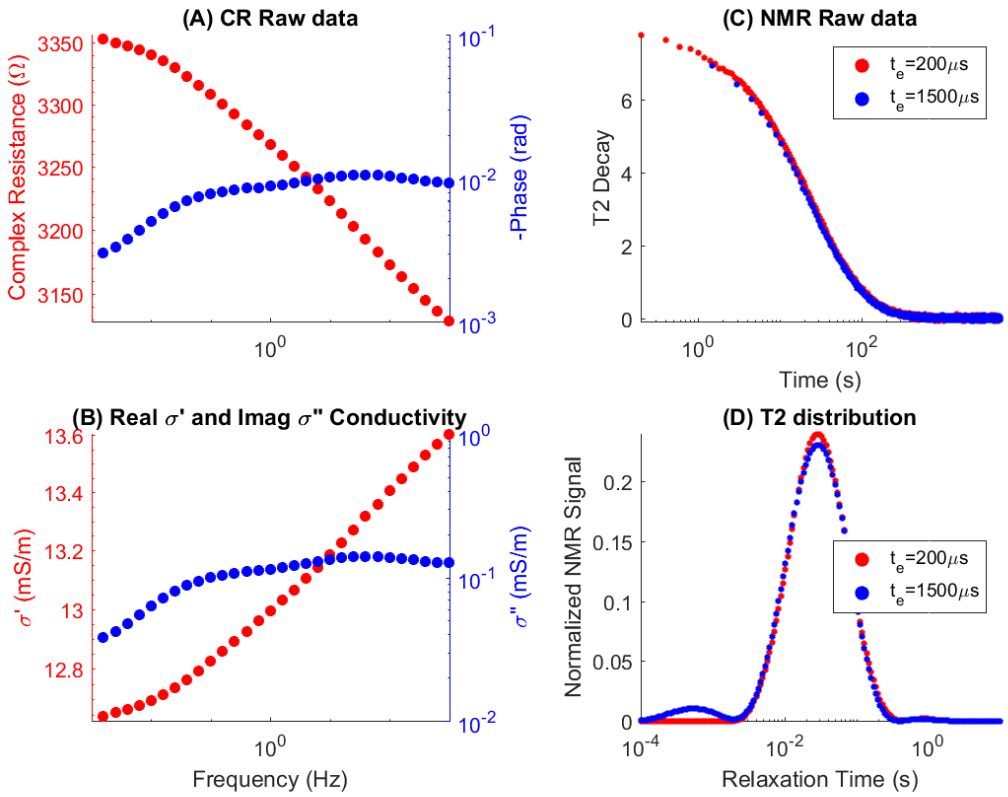

B.1 Table 14: HC-MP25S-P-001-2H Depth below ground surface=40.26 m

Physical properties

Permeability (mD): 5.95

Gravimetric Porosity (%): 21.1

Surface area normalized by pore volume (S_{por}) (μm^{-1}): 22.22

Electrical / CR measures

Electrical Formation Factor (F) (unitless): 22.7

Imaginary Conductivity at 1Hz (σ''_{1Hz}) (mS/m): 0.114

Peak relaxation time (τ_{peak}) (s): 0.00287 1.15

NMR measures

Mean relaxation time echo time=200μs (T_{2ml}@t_e=200μs) (s): 2.94e-02

Peak relaxation time echo time=200μs (T_{2peak}@t_e=200μs) (s): 2.88e-02

Mean relaxation time echo time=1500μs (T_{2ml}@t_e=1500μs) (s): 2.51e-02

Peak relaxation time echo time=1500μs (T_{2peak}@t_e=1500μs) (s): 2.88e-02

B.1 Figure 15: HC-MP25S-P-002-1V

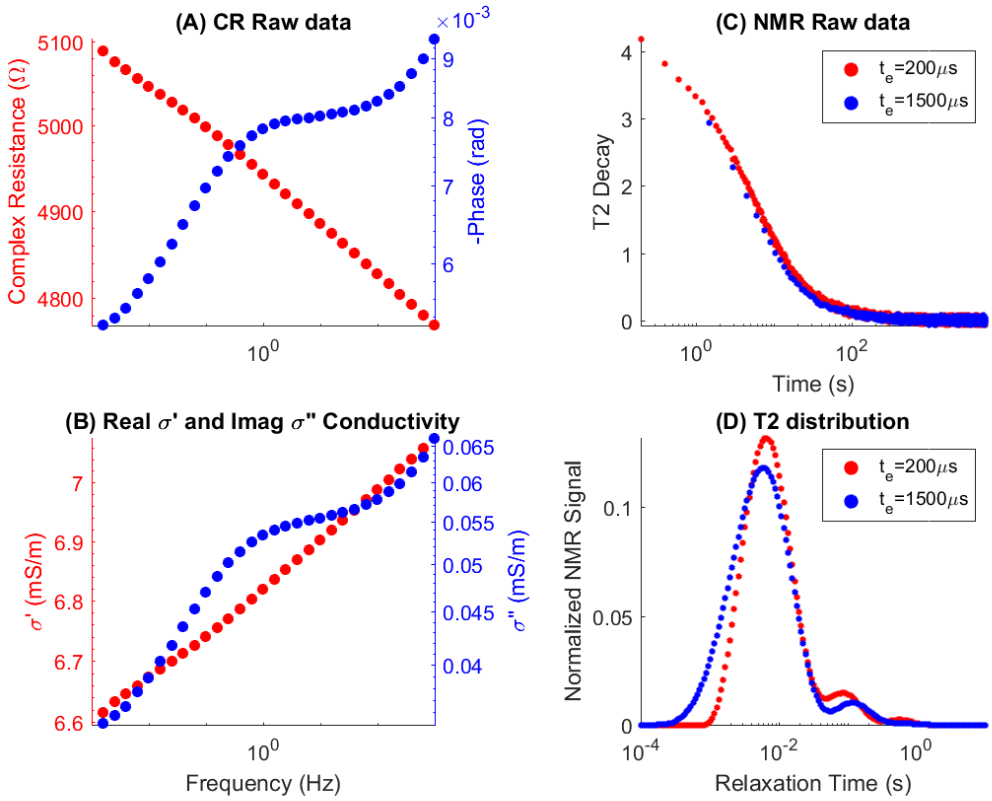

B.1 Table 15: HC-MP25S-P-002-1V Depth below ground surface=41.99 m

Physical properties

Permeability (mD): 0.0933

Gravimetric Porosity (%): 12.6

Surface area normalized by pore volume (S_{por}) (μm^{-1}): 81.58

Electrical / CR measures

Electrical Formation Factor (F) (unitless): 45.4

Imaginary Conductivity at 1Hz (σ''_{1Hz}) (mS/m): 0.0534

Peak relaxation time (τ_{peak}) (s): 0.228

NMR measures

Mean relaxation time echo time=200μs (T_{2ml}@t_e=200μs) (s): 8.40e-03

Peak relaxation time echo time=200μs (T_{2peak}@t_e=200μs) (s): 6.61e-03

Mean relaxation time echo time=1500μs (T_{2ml}@t_e=1500μs) (s): 6.00e-03

Peak relaxation time echo time=1500μs (T_{2peak}@t_e=1500μs) (s): 6.03e-03

B.1 Figure 16: HC-MP25S-P-002-2H

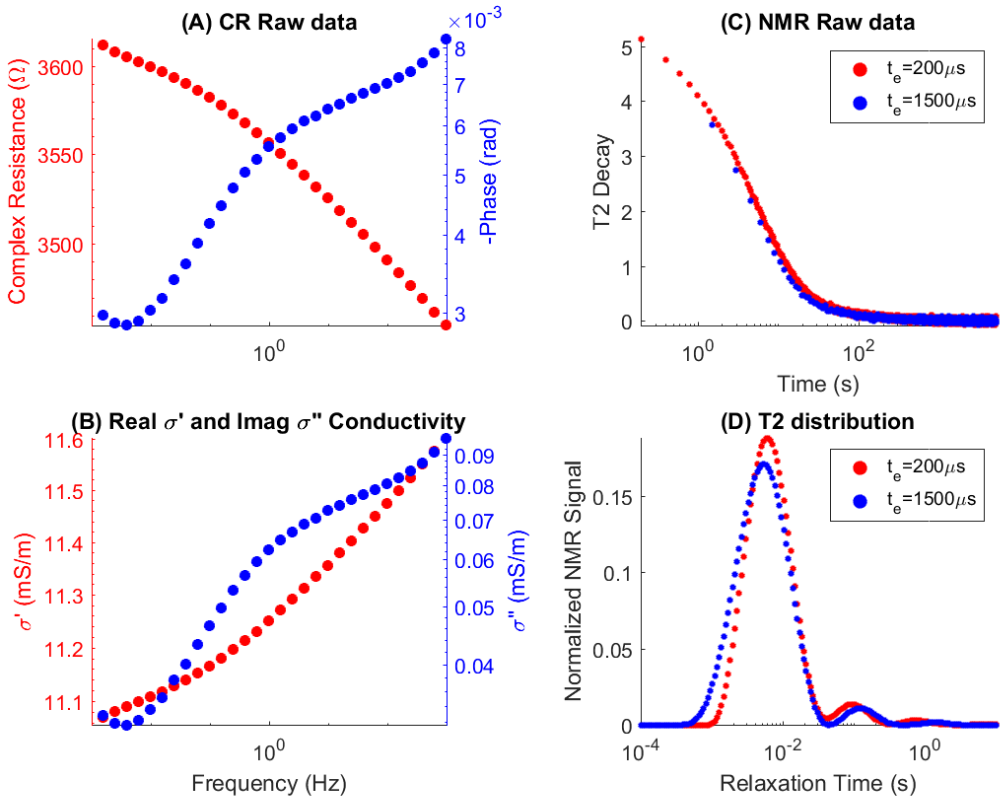

B.1 Table 16: HC-MP25S-P-002-2H Depth below ground surface=41.99 m

Physical properties

Permeability (mD): 0.18

Gravimetric Porosity (%): 13.8

Surface area normalized by pore volume (S_{por}) (μm^{-1}): 73.55

Electrical / CR measures

Electrical Formation Factor (F) (unitless): 33.37

Imaginary Conductivity at 1Hz (σ''_{1Hz}) (mS/m): 0.0623

Peak relaxation time (τ_{peak}) (s): 0.217

NMR measures

Mean relaxation time echo time=200μs (T_{2ml}@t_e=200μs) (s): 7.23e-03

Peak relaxation time echo time=200μs (T_{2peak}@t_e=200μs) (s): 6.03e-03

Mean relaxation time echo time=1500μs (T_{2ml}@t_e=1500μs) (s): 5.65e-03

Peak relaxation time echo time=1500μs (T_{2peak}@t_e=1500μs) (s): 5.25e-03

B.1 Figure 17: HC-MP25S-P-003-1V

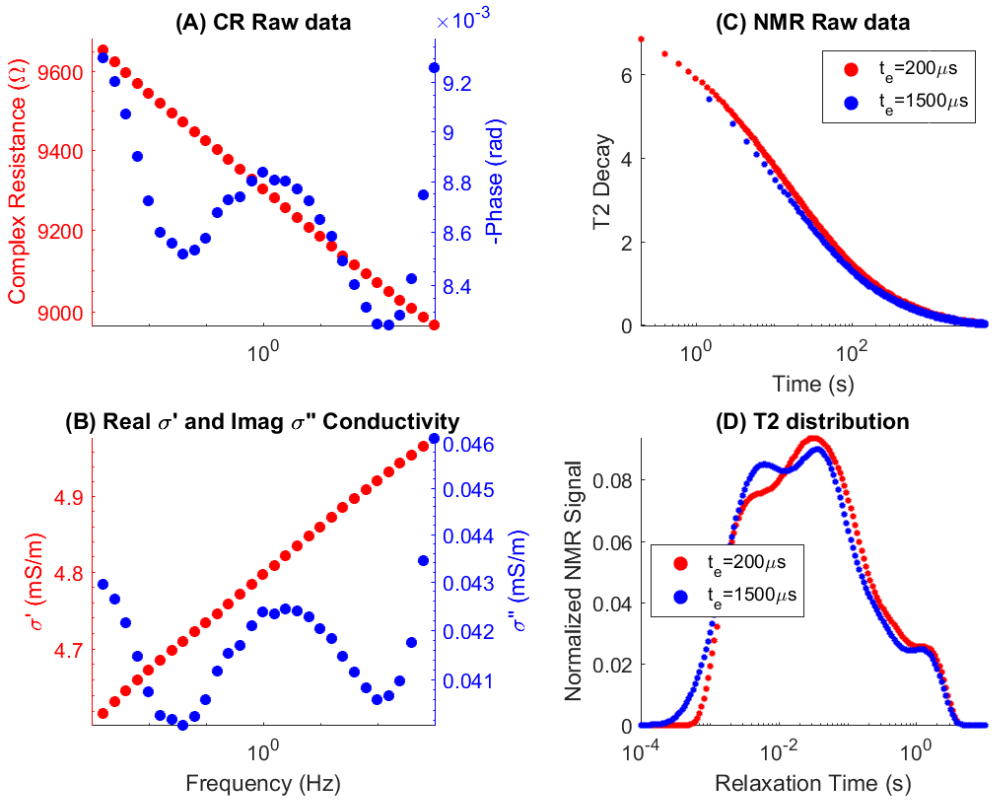

B.1 Table 17: HC-MP25S-P-003-1V Depth below ground surface=47.47 m

Physical properties

Permeability (mD): 13.9

Gravimetric Porosity (%): 15.6

Surface area normalized by pore volume (S_{por}) (μm^{-1}): 50.84

Electrical / CR measures

Electrical Formation Factor (F) (unitless): 38.45

Imaginary Conductivity at 1Hz (σ''_{1Hz}) (mS/m): 0.0424

Peak relaxation time (τ_{peak}) (s): 0.0784

NMR measures

Mean relaxation time echo time=200μs (T_{2ml}@t_e=200μs) (s): 3.03e-02

Peak relaxation time echo time=200μs (T_{2peak}@t_e=200μs) (s): 3.31e-02

Mean relaxation time echo time=1500μs (T_{2ml}@t_e=1500μs) (s): 2.38e-02

Peak relaxation time echo time=1500μs (T_{2peak}@t_e=1500μs) (s): 3.63e-02

B.1 Figure 18: HC-MP25S-P-003-2H

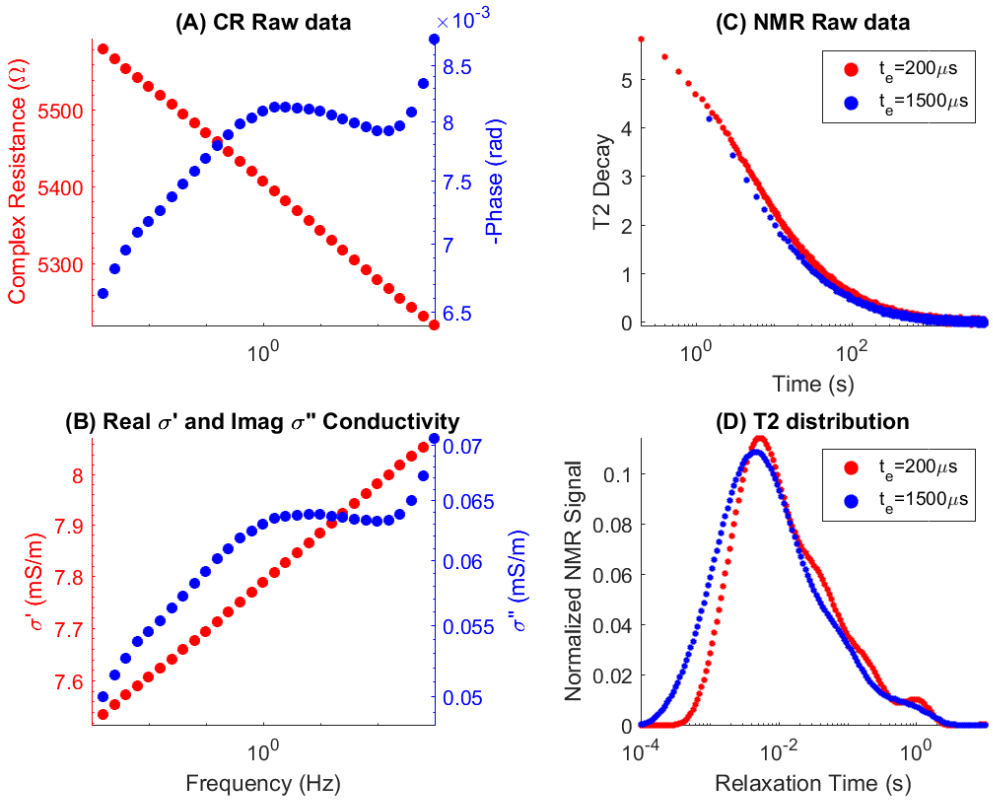

B.1 Table 18: HC-MP25S-P-003-2H Depth below ground surface=47.47 m

Physical properties

Permeability (mD): 4.07

Gravimetric Porosity (%): 15.3

Surface area normalized by pore volume (S_{por}) (μm^{-1}): 52.08

Electrical / CR measures

Electrical Formation Factor (F) (unitless): 34.57

Imaginary Conductivity at 1Hz (σ''_{1Hz}) (mS/m): 0.063

Peak relaxation time (τ_{peak}) (s): 0.221

NMR measures

Mean relaxation time echo time=200μs (T_{2ml}@t_e=200μs) (s): 1.24e-02

Peak relaxation time echo time=200μs (T_{2peak}@t_e=200μs) (s): 5.25e-03

Mean relaxation time echo time=1500μs (T_{2ml}@t_e=1500μs) (s): 7.85e-03

Peak relaxation time echo time=1500μs (T_{2peak}@t_e=1500μs) (s): 4.57e-03

B.1 Figure 19: HC-MP25S-P-004-1V

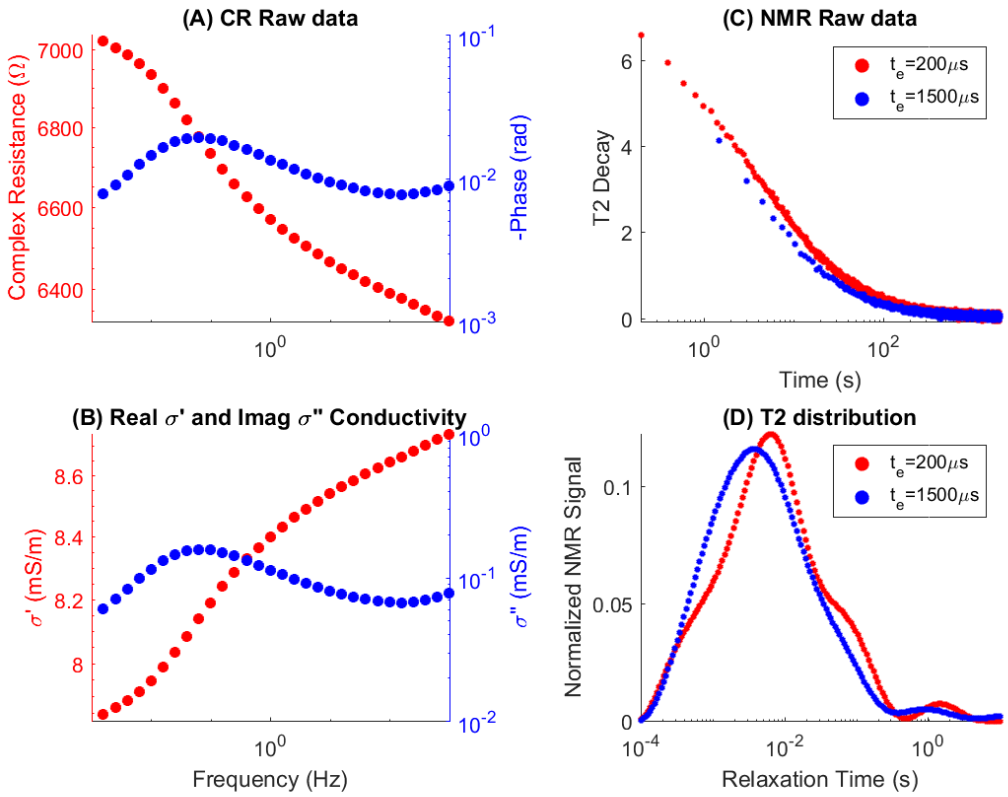

B.1 Table 19: HC-MP25S-P-004-1V Depth below ground surface=51.56 m

Physical properties

Permeability (mD): 1.03

Gravimetric Porosity (%): 16.3

Surface area normalized by pore volume (S_{por}) (μm^{-1}): 78.75

Electrical / CR measures

Electrical Formation Factor (F) (unitless): 27.38

Imaginary Conductivity at 1Hz (σ''_{1Hz}) (mS/m): 0.112

Peak relaxation time (τ_{peak}) (s): 2.15

NMR measures

Mean relaxation time echo time=200μs (T_{2ml}@t_e=200μs) (s): 6.84e-03

Peak relaxation time echo time=200μs (T_{2peak}@t_e=200μs) (s): 6.31e-03

Mean relaxation time echo time=1500μs (T_{2ml}@t_e=1500μs) (s): 5.03e-03

Peak relaxation time echo time=1500μs (T_{2peak}@t_e=1500μs) (s): 3.80e-03

B.1 Figure 20: HC-MP25S-P-004-2H

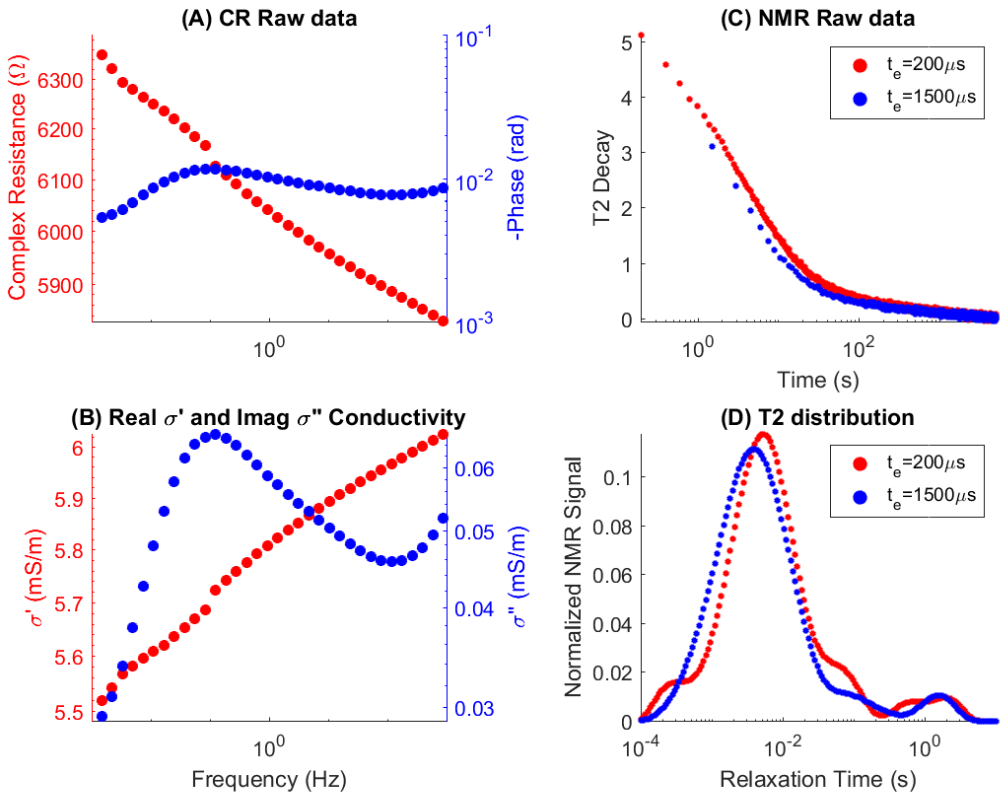

B.1 Table 20: HC-MP25S-P-004-2H Depth below ground surface=51.56 m

Physical properties

Permeability (mD): 0.793

Gravimetric Porosity (%): 16

Surface area normalized by pore volume (S_{por}) (μm^{-1}): 81.35

Electrical / CR measures

Electrical Formation Factor (F) (unitless): 27.13

Imaginary Conductivity at 1Hz (σ''_{1Hz}) (mS/m): 0.0586

Peak relaxation time (τ_{peak}) (s): 1.34

NMR measures

Mean relaxation time echo time=200μs (T_{2ml}@t_e=200μs) (s): 7.01e-03

Peak relaxation time echo time=200μs (T_{2peak}@t_e=200μs) (s): 5.25e-03

Mean relaxation time echo time=1500μs (T_{2ml}@t_e=1500μs) (s): 5.34e-03

Peak relaxation time echo time=1500μs (T_{2peak}@t_e=1500μs) (s): 3.80e-03

B.1 Figure 21: HC-MP25S-P-005-1V

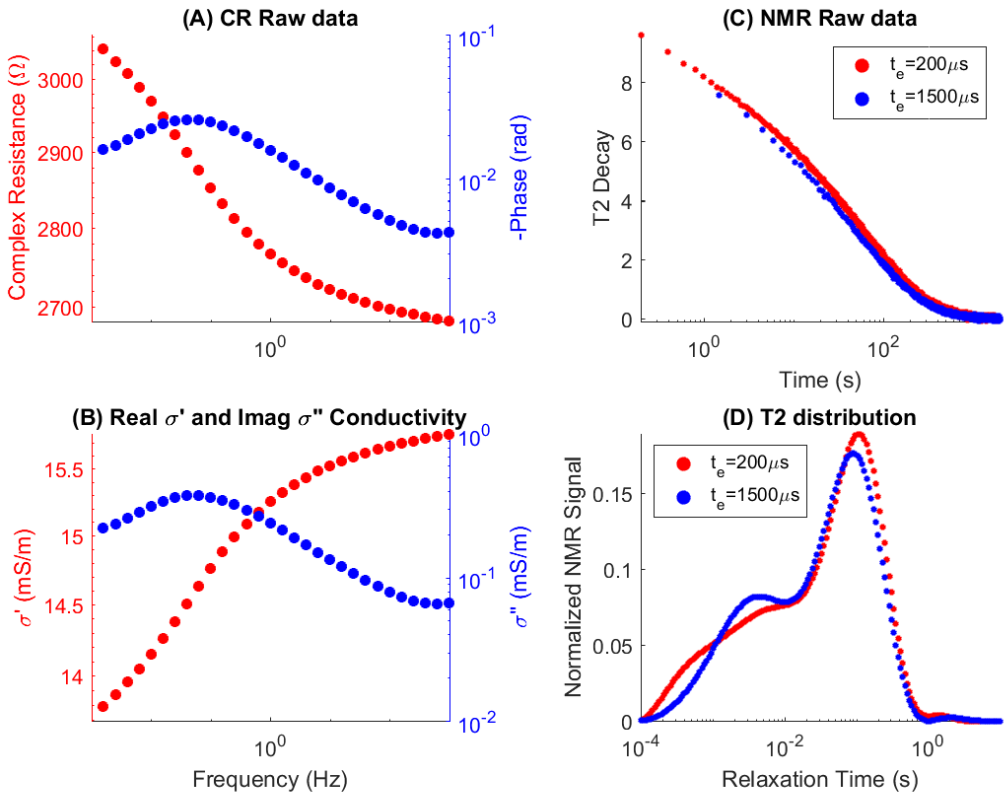

B.1 Table 21: HC-MP25S-P-005-1V Depth below ground surface=53.07 m

Physical properties

Permeability (mD): 6.53

Gravimetric Porosity (%): 24.3

Surface area normalized by pore volume (S_{por}) (μm^{-1}): 46.67

Electrical / CR measures

Electrical Formation Factor (F) (unitless):

Imaginary Conductivity at 1Hz (σ''_{1Hz}) (mS/m): 0.238

Peak relaxation time (τ_{peak}) (s): 3.46

NMR measures

Mean relaxation time echo time=200μs (T_{2ml}@t_e=200μs) (s): 2.50e-02

Peak relaxation time echo time=200μs (T_{2peak}@t_e=200μs) (s): 1.10e-01

Mean relaxation time echo time=1500μs (T_{2ml}@t_e=1500μs) (s): 2.48e-02

Peak relaxation time echo time=1500μs (T_{2peak}@t_e=1500μs) (s): 9.12e-02

B.1 Figure 22: HC-MP25S-P-006-1V

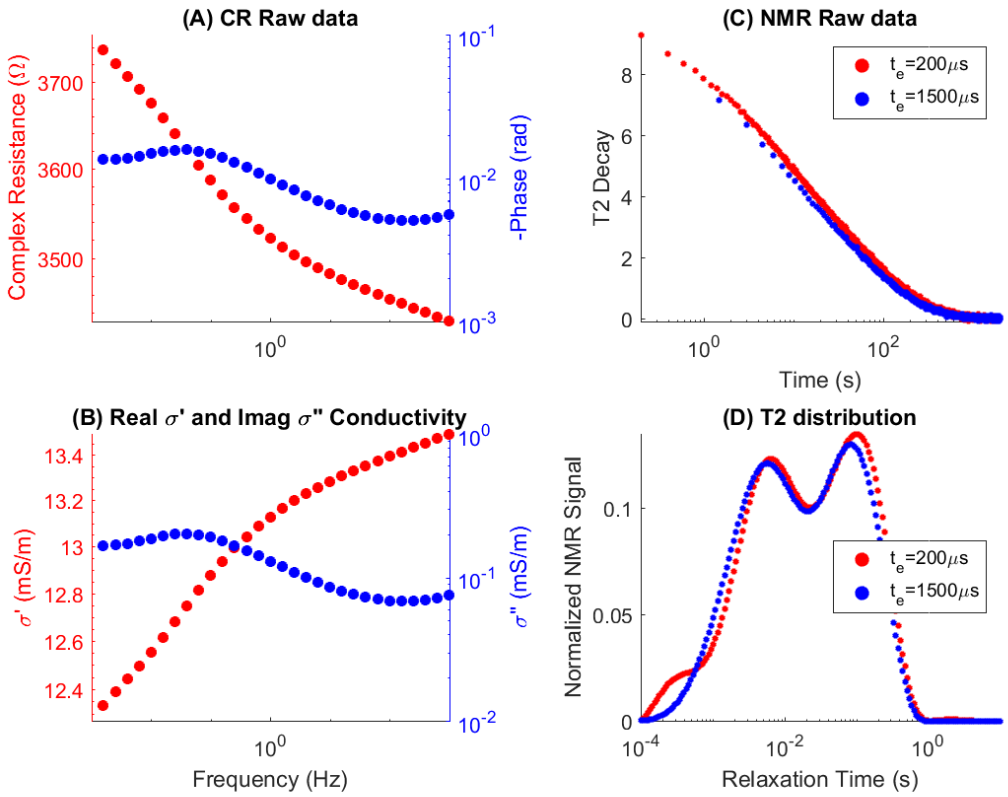

B.1 Table 22: HC-MP25S-P-006-1V Depth below ground surface=54.35 m

Physical properties

Permeability (mD): 5.5

Gravimetric Porosity (%): 21.6

Surface area normalized by pore volume (S_{por}) (μm^{-1}): 64.21

Electrical / CR measures

Electrical Formation Factor (F) (unitless): 14.64

Imaginary Conductivity at 1Hz (σ''_{1Hz}) (mS/m): 0.13

Peak relaxation time (τ_{peak}) (s): 5.49

NMR measures

Mean relaxation time echo time=200μs (T_{2ml}@t_e=200μs) (s): 1.92e-02

Peak relaxation time echo time=200μs (T_{2peak}@t_e=200μs) (s): 1.00e-01

Mean relaxation time echo time=1500μs (T_{2ml}@t_e=1500μs) (s): 1.77e-02

Peak relaxation time echo time=1500μs (T_{2peak}@t_e=1500μs) (s): 8.32e-02

B.1 Figure 23: SS-C3-CI-100.0

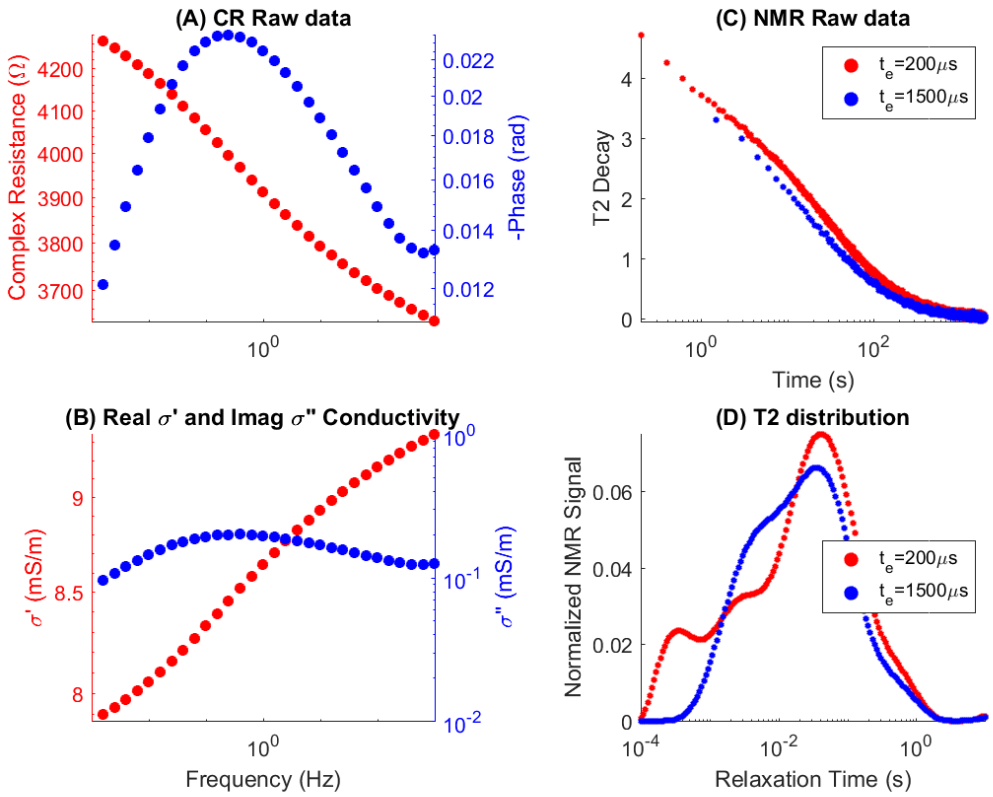

B.1 Table 23: SS-C3-CI-100.0 Depth below ground surface=30.53 m

Physical properties

Permeability (mD): 1.91

Gravimetric Porosity (%): 14.1

Surface area normalized by pore volume (S_{por}) (μm^{-1}): 47.05

Electrical / CR measures

Electrical Formation Factor (F) (unitless): 50.08

Imaginary Conductivity at 1Hz (σ''_{1Hz}) (mS/m): 0.195

Peak relaxation time (τ_{peak}) (s): 0.518

NMR measures

Mean relaxation time echo time=200μs (T_{2ml}@t_e=200μs) (s): 1.71e-02

Peak relaxation time echo time=200μs (T_{2peak}@t_e=200μs) (s): 4.17e-02

Mean relaxation time echo time=1500μs (T_{2ml}@t_e=1500μs) (s): 2.05e-02

Peak relaxation time echo time=1500μs (T_{2peak}@t_e=1500μs) (s): 3.63e-02

B.1 Figure 24: SS-C3-CI-118.6

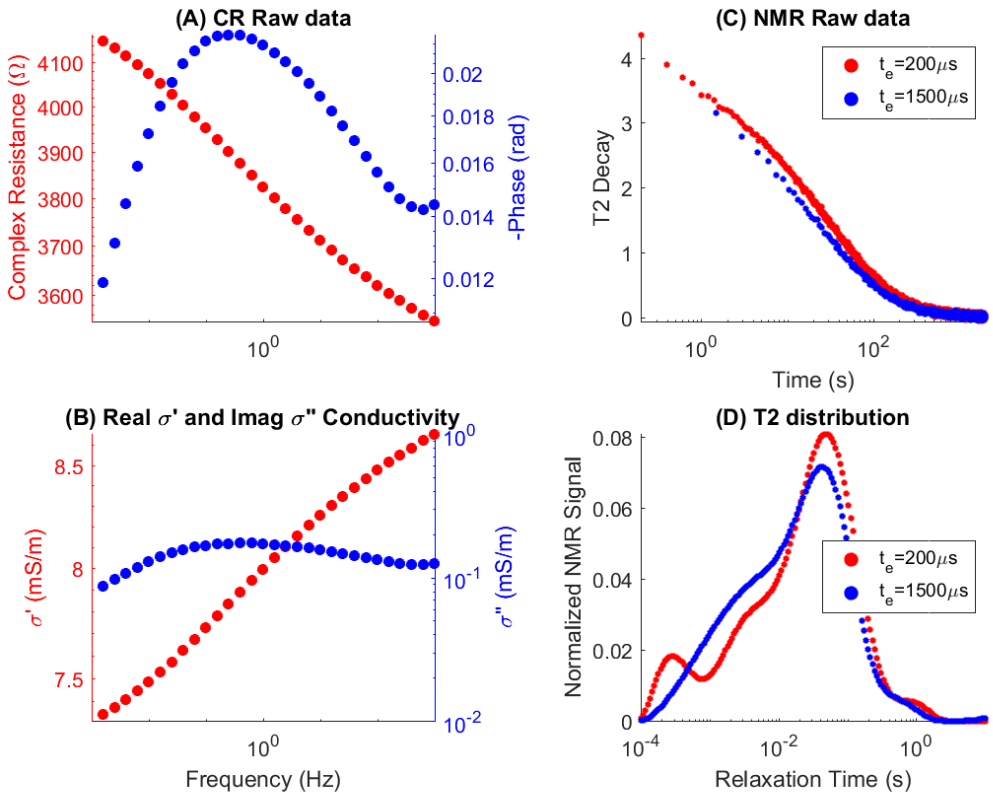

B.1 Table 24: SS-C3-CI-118.6 Depth below ground surface=36.2 m

Physical properties

Permeability (mD): 7.49

Gravimetric Porosity (%): 14.9

Surface area normalized by pore volume (S_{por}) (μm^{-1}): 25.69

Electrical / CR measures

Electrical Formation Factor (F) (unitless): 38.94

Imaginary Conductivity at 1Hz (σ''_{1Hz}) (mS/m): 0.171

Peak relaxation time (τ_{peak}) (s): 0.323

NMR measures

Mean relaxation time echo time=200μs (T_{2ml}@t_e=200μs) (s): 1.88e-02

Peak relaxation time echo time=200μs (T_{2peak}@t_e=200μs) (s): 4.79e-02

Mean relaxation time echo time=1500μs (T_{2ml}@t_e=1500μs) (s): 1.57e-02

Peak relaxation time echo time=1500μs (T_{2peak}@t_e=1500μs) (s): 4.37e-02

B.1 Figure 25: SS-C3-CI-139.7

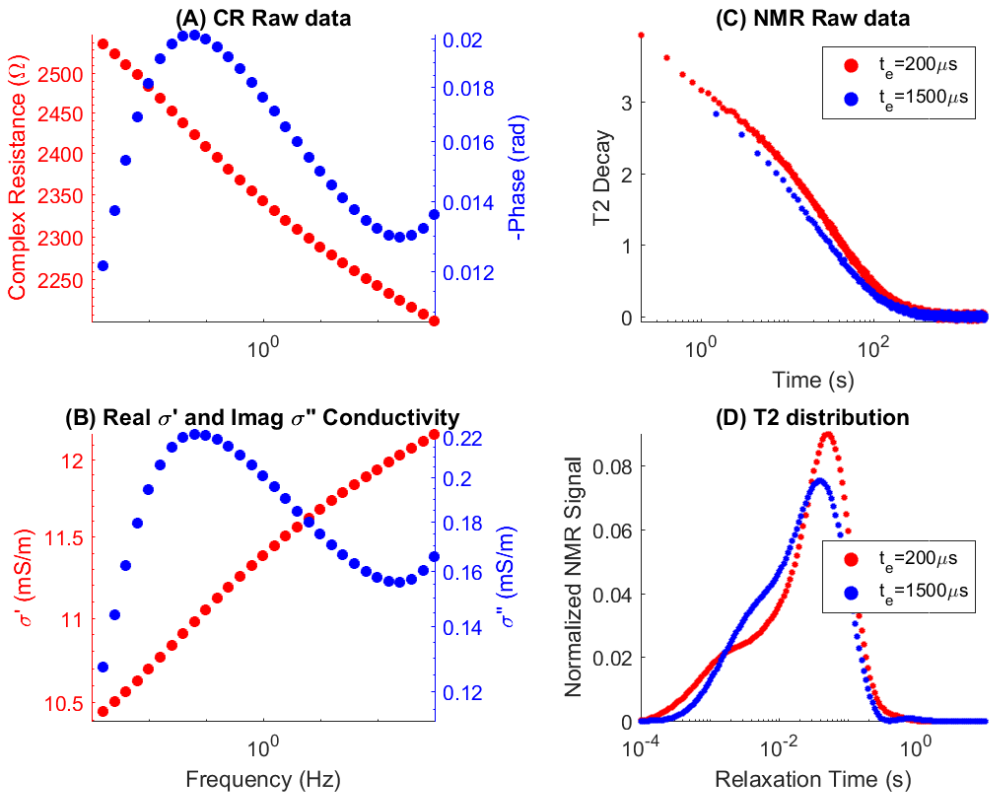

B.1 Table 25: SS-C3-CI-139.7 Depth below ground surface=42.63 m

Physical properties

Permeability (mD): 1.33

Gravimetric Porosity (%): 15.6

Surface area normalized by pore volume (S_{por}) (μm^{-1}): 34.48

Electrical / CR measures

Electrical Formation Factor (F) (unitless): 46.51

Imaginary Conductivity at 1Hz (σ''_{1Hz}) (mS/m): 0.201

Peak relaxation time (τ_{peak}) (s): 2.15

NMR measures

Mean relaxation time echo time=200μs (T_{2ml}@t_e=200μs) (s): 2.06e-02

Peak relaxation time echo time=200μs (T_{2peak}@t_e=200μs) (s): 5.25e-02

Mean relaxation time echo time=1500μs (T_{2ml}@t_e=1500μs) (s): 1.79e-02

Peak relaxation time echo time=1500μs (T_{2peak}@t_e=1500μs) (s): 3.98e-02

B.1 Figure 26: SS-C3-P-015

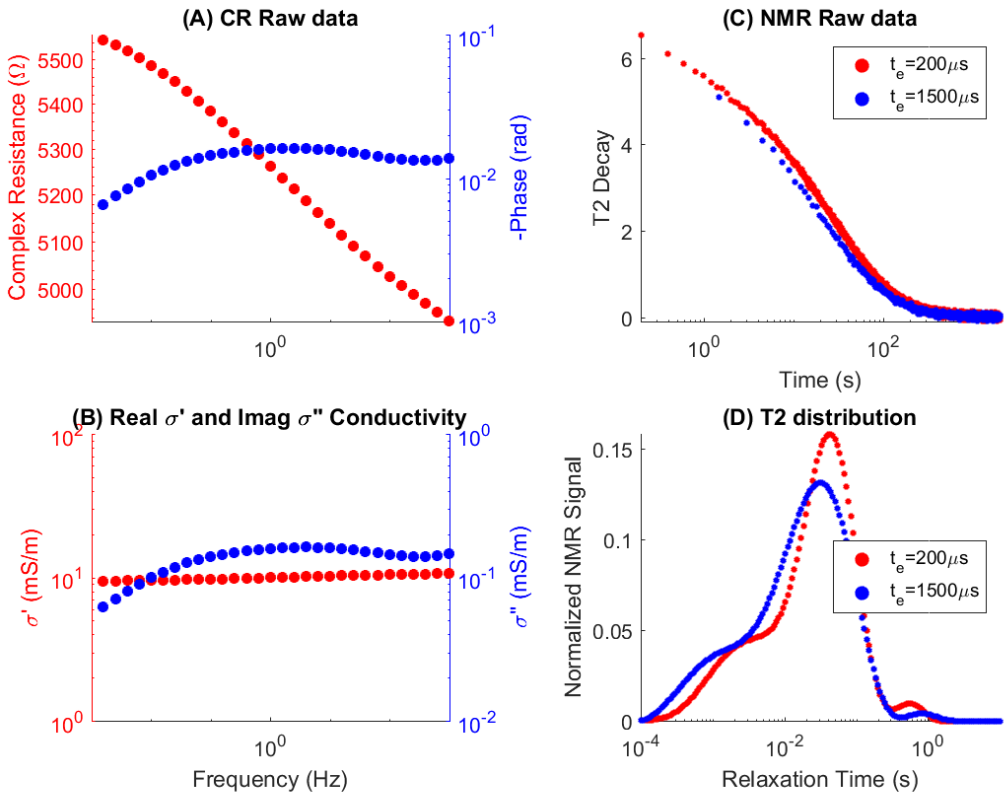

B.1 Table 26: SS-C3-P-015 Depth below ground surface=56.98 m

Physical properties

Permeability (mD): 4.61

Gravimetric Porosity (%): 13.1

Surface area normalized by pore volume (S_{por}) (μm^{-1}): 22.15

Electrical / CR measures

Electrical Formation Factor (F) (unitless): 50.98

Imaginary Conductivity at 1Hz (σ''_{1Hz}) (mS/m): 0.159

Peak relaxation time (τ_{peak}) (s): 0.0489

NMR measures

Mean relaxation time echo time=200μs (T_{2ml}@t_e=200μs) (s): 2.08e-02

Peak relaxation time echo time=200μs (T_{2peak}@t_e=200μs) (s): 4.17e-02

Mean relaxation time echo time=1500μs (T_{2ml}@t_e=1500μs) (s): 1.46e-02

Peak relaxation time echo time=1500μs (T_{2peak}@t_e=1500μs) (s): 3.16e-02

B.1 Figure 27: SS-C3-P-017

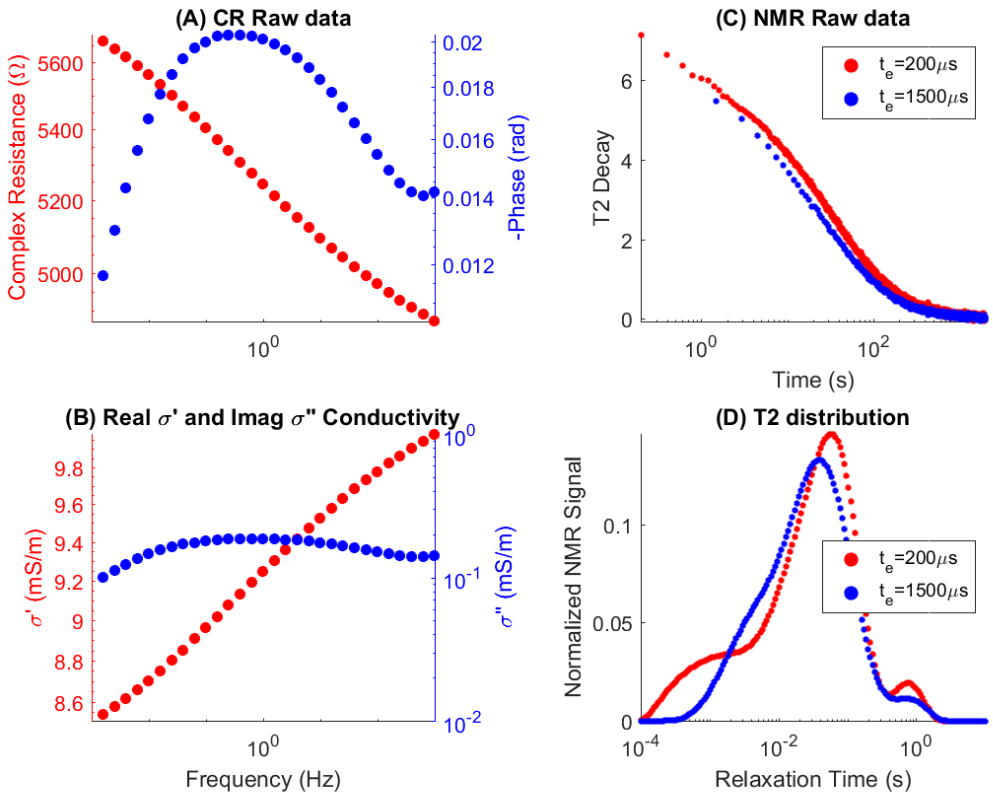

B.1 Table 27: SS-C3-P-017 Depth below ground surface=63.13 m

Physical properties

Permeability (mD): 6.56

Gravimetric Porosity (%): 16

Surface area normalized by pore volume (S_{por}) (μm^{-1}): 20.34

Electrical / CR measures

Electrical Formation Factor (F) (unitless):

Imaginary Conductivity at 1Hz (σ''_{1Hz}) (mS/m): 0.186

Peak relaxation time (τ_{peak}) (s): 0.201

NMR measures

Mean relaxation time echo time=200μs (T_{2ml}@t_e=200μs) (s): 2.32e-02

Peak relaxation time echo time=200μs (T_{2peak}@t_e=200μs) (s): 5.75e-02

Mean relaxation time echo time=1500μs (T_{2ml}@t_e=1500μs) (s): 2.51e-02

Peak relaxation time echo time=1500μs (T_{2peak}@t_e=1500μs) (s): 3.80e-02

B.1 Figure 28: SS-C3-P-021

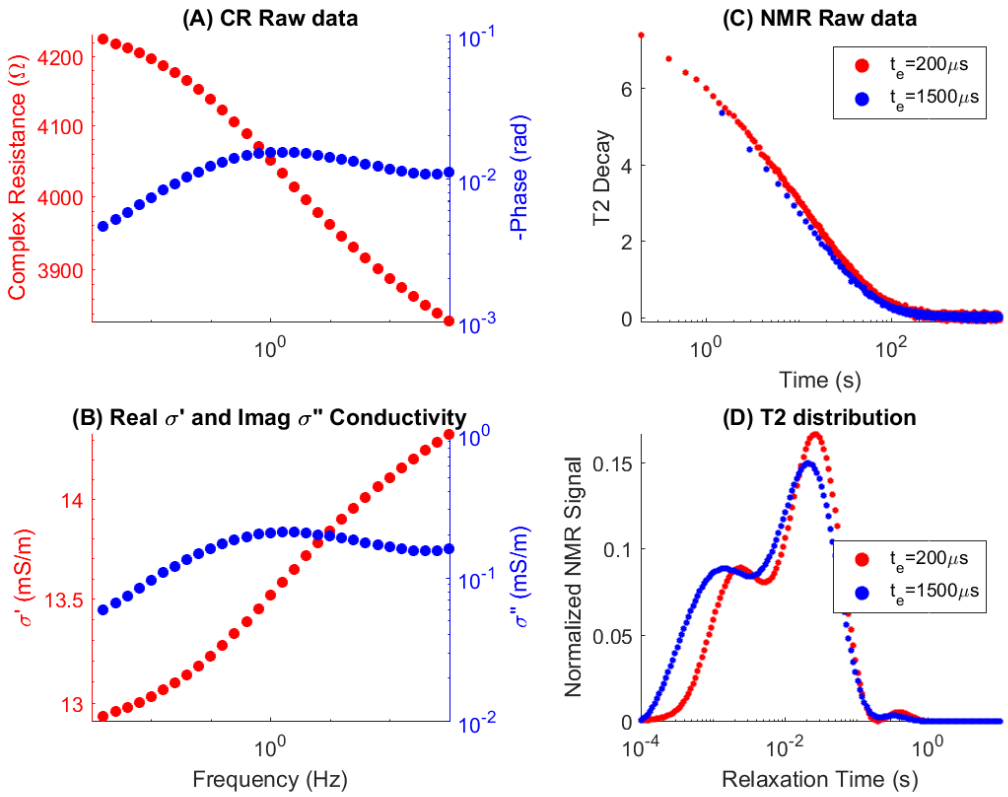

B.1 Table 28: SS-C3-P-021 Depth below ground surface=77.37 m

Physical properties

Permeability (mD): 0.804

Gravimetric Porosity (%): 14.2

Surface area normalized by pore volume (S_{por}) (μm^{-1}): 29.4

Electrical / CR measures

Electrical Formation Factor (F) (unitless): 50.83

Imaginary Conductivity at 1Hz (σ''_{1Hz}) (mS/m): 0.204

Peak relaxation time (τ_{peak}) (s): 0.0784

NMR measures

Mean relaxation time echo time=200μs (T_{2ml}@t_e=200μs) (s): 1.04e-02

Peak relaxation time echo time=200μs (T_{2peak}@t_e=200μs) (s): 2.63e-02

Mean relaxation time echo time=1500μs (T_{2ml}@t_e=1500μs) (s): 6.45e-03

Peak relaxation time echo time=1500μs (T_{2peak}@t_e=1500μs) (s): 2.19e-02

B.1 Figure 29: SS-C3-P-022

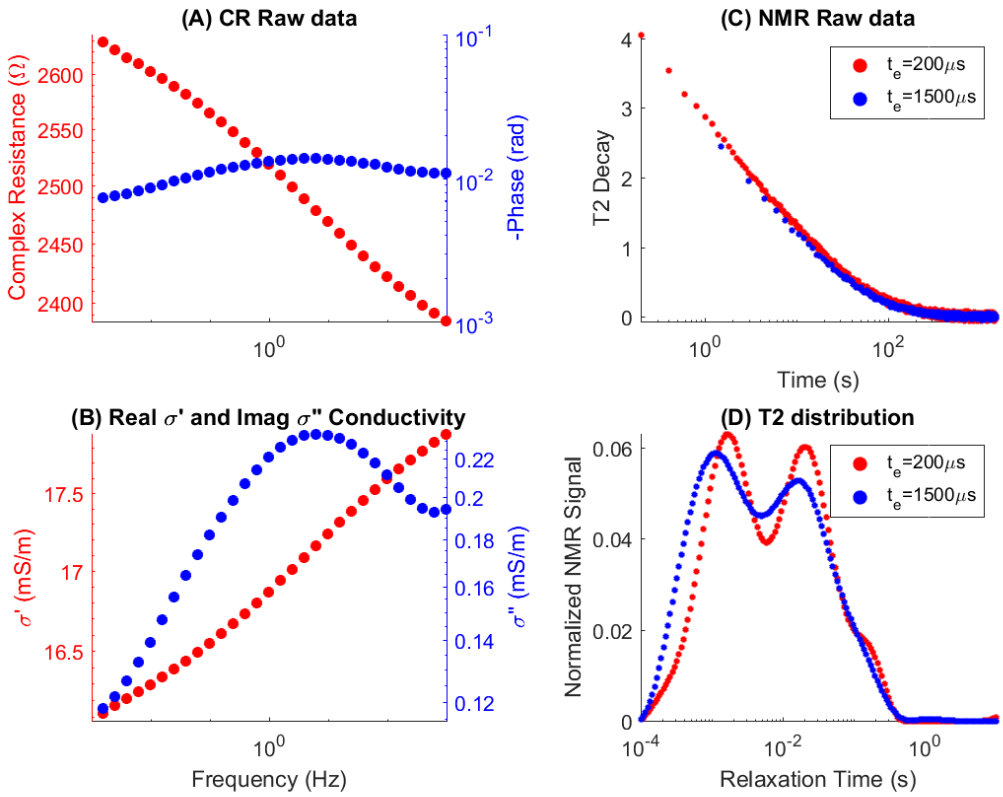

B.1 Table 29: SS-C3-P-022 Depth below ground surface=78.44 m

Physical properties

Permeability (mD): 2.75

Gravimetric Porosity (%): 10.1

Surface area normalized by pore volume (S_{por}) (μm^{-1}): 51.19

Electrical / CR measures

Electrical Formation Factor (F) (unitless): 50.93

Imaginary Conductivity at 1Hz (σ''_{1Hz}) (mS/m): 0.221

Peak relaxation time (τ_{peak}) (s): 0.019

NMR measures

Mean relaxation time echo time=200μs (T_{2ml}@t_e=200μs) (s): 6.58e-03

Peak relaxation time echo time=200μs (T_{2peak}@t_e=200μs) (s): 1.66e-03

Mean relaxation time echo time=1500μs (T_{2ml}@t_e=1500μs) (s): 4.82e-03

Peak relaxation time echo time=1500μs (T_{2peak}@t_e=1500μs) (s): 1.15e-03

B.1 Figure 30: SS-C3-P-023

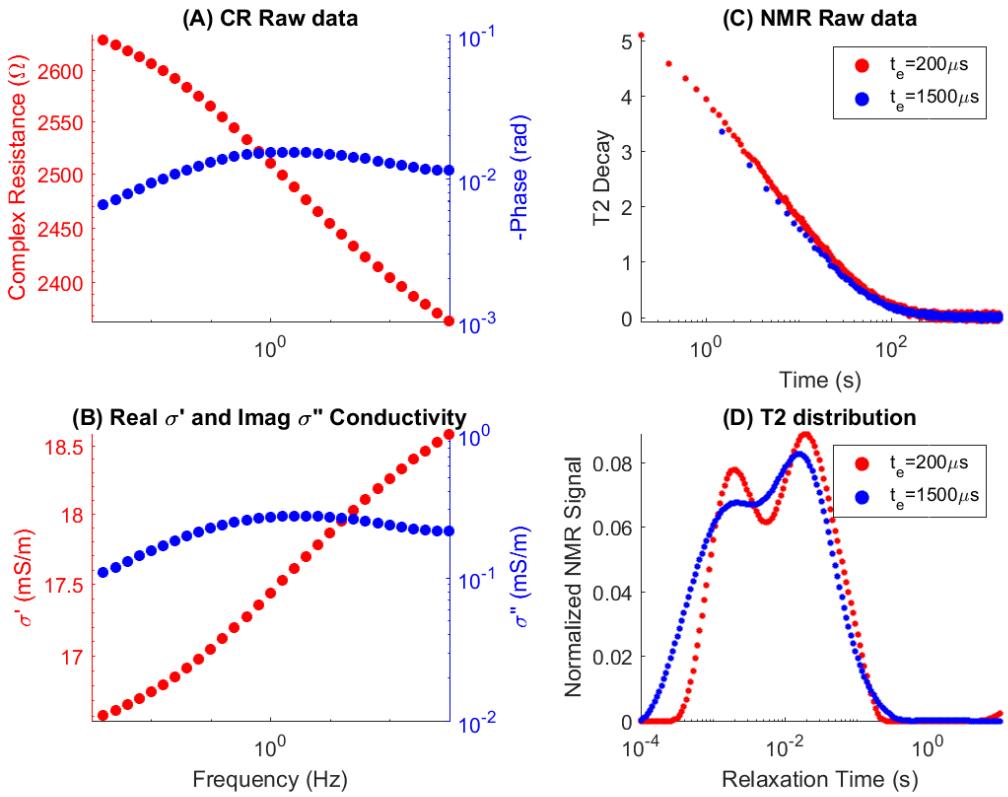

B.1 Table 30: SS-C3-P-023 Depth below ground surface=87.64 m

Physical properties

Permeability (mD): 0.503

Gravimetric Porosity (%): 12.9

Surface area normalized by pore volume (S_{por}) (μm^{-1}): 36.92

Electrical / CR measures

Electrical Formation Factor (F) (unitless): 46.57

Imaginary Conductivity at 1Hz (σ''_{1Hz}) (mS/m): 0.263

Peak relaxation time (τ_{peak}) (s): 0.0489

NMR measures

Mean relaxation time echo time=200μs (T_{2ml}@t_e=200μs) (s): 8.35e-03

Peak relaxation time echo time=200μs (T_{2peak}@t_e=200μs) (s): 2.00e-02

Mean relaxation time echo time=1500μs (T_{2ml}@t_e=1500μs) (s): 5.81e-03

Peak relaxation time echo time=1500μs (T_{2peak}@t_e=1500μs) (s): 1.58e-02

B.1 Figure 31: SS-C3-P-024

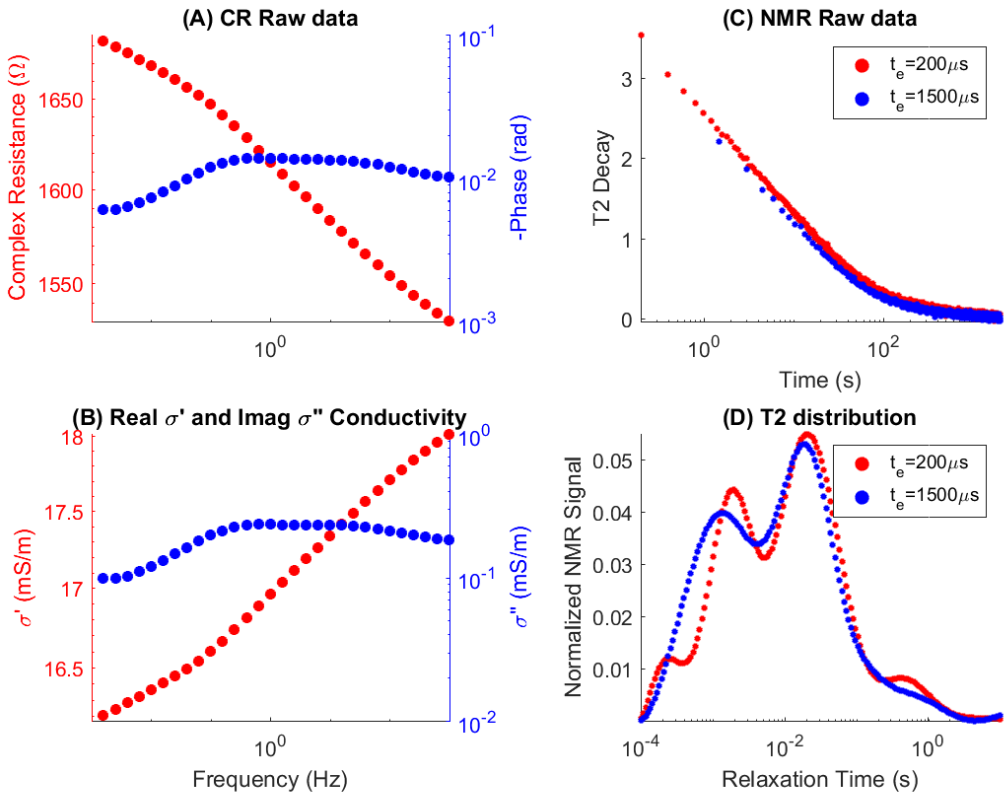

B.1 Table 31: SS-C3-P-024 Depth below ground surface=90.5 m

Physical properties

Permeability (mD): 1.83

Gravimetric Porosity (%): 13.1

Surface area normalized by pore volume (S_{por}) (μm^{-1}): 43.57

Electrical / CR measures

Electrical Formation Factor (F) (unitless): 39.73

Imaginary Conductivity at 1Hz (σ''_{1Hz}) (mS/m): 0.234

Peak relaxation time (τ_{peak}) (s): 0.126

NMR measures

Mean relaxation time echo time=200μs (T_{2ml}@t_e=200μs) (s): 9.62e-03

Peak relaxation time echo time=200μs (T_{2peak}@t_e=200μs) (s): 2.09e-02

Mean relaxation time echo time=1500μs (T_{2ml}@t_e=1500μs) (s): 7.43e-03

Peak relaxation time echo time=1500μs (T_{2peak}@t_e=1500μs) (s): 1.91e-02

B.1 Figure 32: SS-C3-P-027

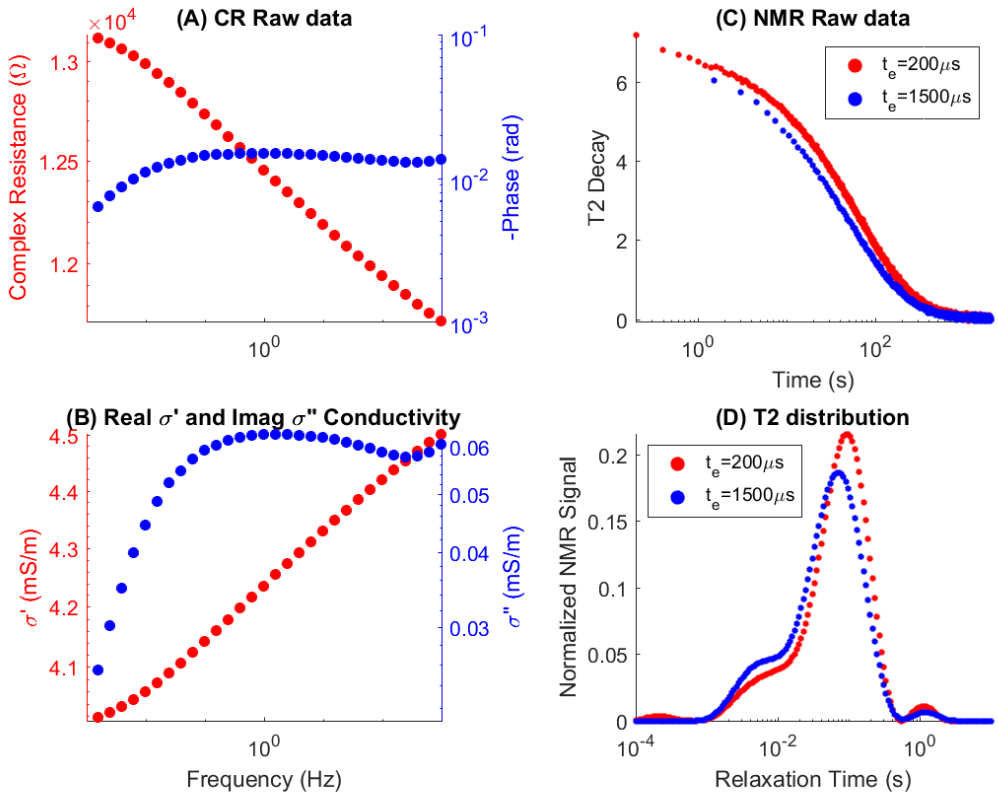

B.1 Table 32: SS-C3-P-027 Depth below ground surface=103.4 m

Physical properties

Permeability (mD): 14.9

Gravimetric Porosity (%): 13.3

Surface area normalized by pore volume (S_{por}) (μm^{-1}): 12.05

Electrical / CR measures

Electrical Formation Factor (F) (unitless): 40.25

Imaginary Conductivity at 1Hz (σ''_{1Hz}) (mS/m): 0.063

Peak relaxation time (τ_{peak}) (s): 0.0784

NMR measures

Mean relaxation time echo time=200μs (T_{2ml}@t_e=200μs) (s): 5.68e-02

Peak relaxation time echo time=200μs (T_{2peak}@t_e=200μs) (s): 9.55e-02

Mean relaxation time echo time=1500μs (T_{2ml}@t_e=1500μs) (s): 4.44e-02

Peak relaxation time echo time=1500μs (T_{2peak}@t_e=1500μs) (s): 6.92e-02

B.1 Figure 33: SS-C3-P-037

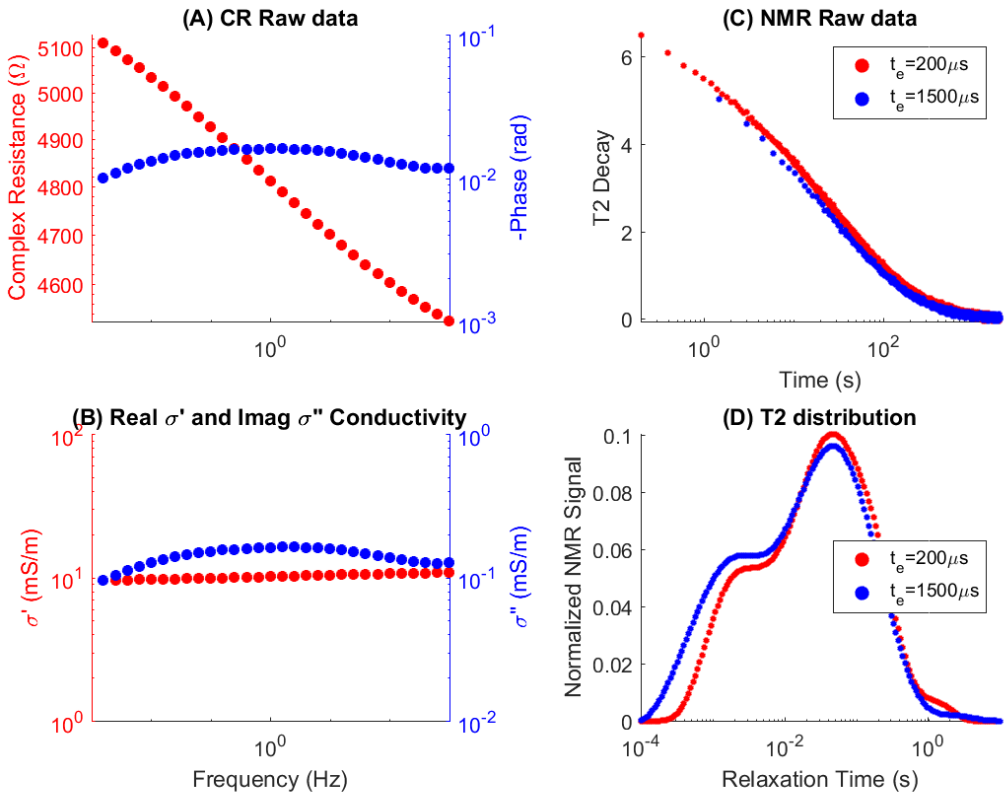

B.1 Table 33: SS-C3-P-037 Depth below ground surface=126.6 m

Physical properties

Permeability (mD): 7.64

Gravimetric Porosity (%): 13.7

Surface area normalized by pore volume (S_{por}) (μm^{-1}): 18.7

Electrical / CR measures

Electrical Formation Factor (F) (unitless): 51.35

Imaginary Conductivity at 1Hz (σ''_{1Hz}) (mS/m): 0.162

Peak relaxation time (τ_{peak}) (s): 0.0784

NMR measures

Mean relaxation time echo time=200μs (T_{2ml}@t_e=200μs) (s): 2.46e-02

Peak relaxation time echo time=200μs (T_{2peak}@t_e=200μs) (s): 4.79e-02

Mean relaxation time echo time=1500μs (T_{2ml}@t_e=1500μs) (s): 1.62e-02

Peak relaxation time echo time=1500μs (T_{2peak}@t_e=1500μs) (s): 4.79e-02

B.1 Figure 34: SS-C3-P-038

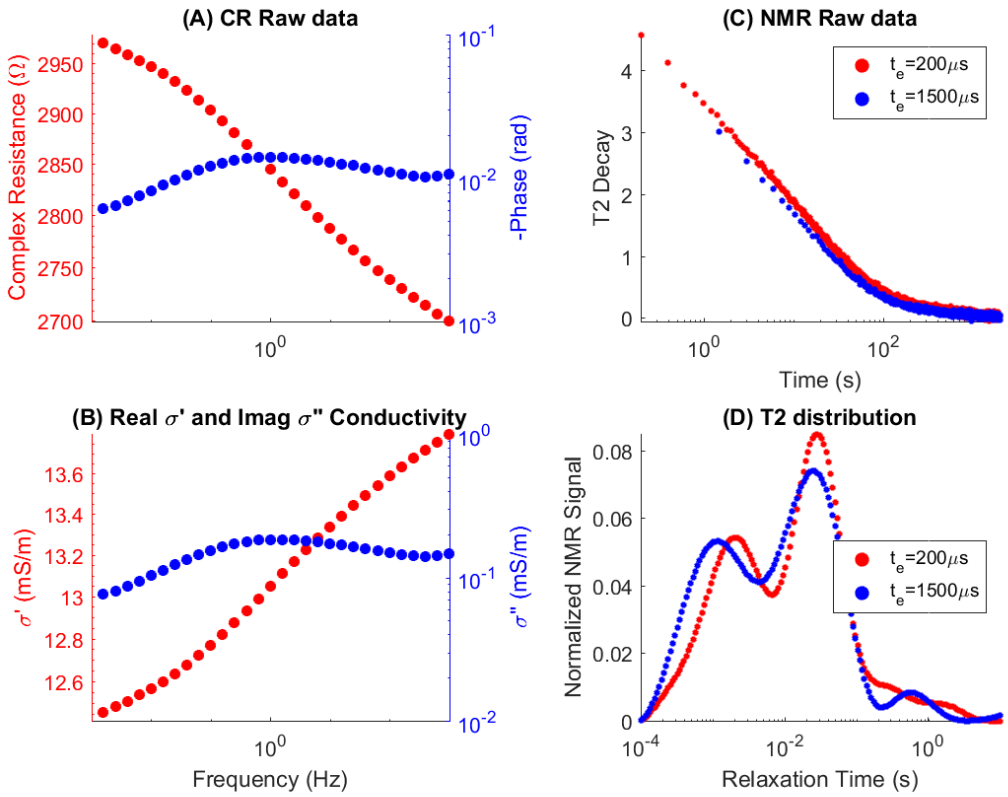

B.1 Table 34: SS-C3-P-038 Depth below ground surface=130.1 m

Physical properties

Permeability (mD): 0.873

Gravimetric Porosity (%): 12.5

Surface area normalized by pore volume (S_{por}) (μm^{-1}): 36.65

Electrical / CR measures

Electrical Formation Factor (F) (unitless): 59.59

Imaginary Conductivity at 1Hz (σ''_{1Hz}) (mS/m): 0.183

Peak relaxation time (τ_{peak}) (s): 0.126

NMR measures

Mean relaxation time echo time=200μs (T_{2ml}@t_e=200μs) (s): 1.07e-02

Peak relaxation time echo time=200μs (T_{2peak}@t_e=200μs) (s): 2.88e-02

Mean relaxation time echo time=1500μs (T_{2ml}@t_e=1500μs) (s): 7.46e-03

Peak relaxation time echo time=1500μs (T_{2peak}@t_e=1500μs) (s): 2.51e-02

B.1 Figure 35: SS-C3-P-040

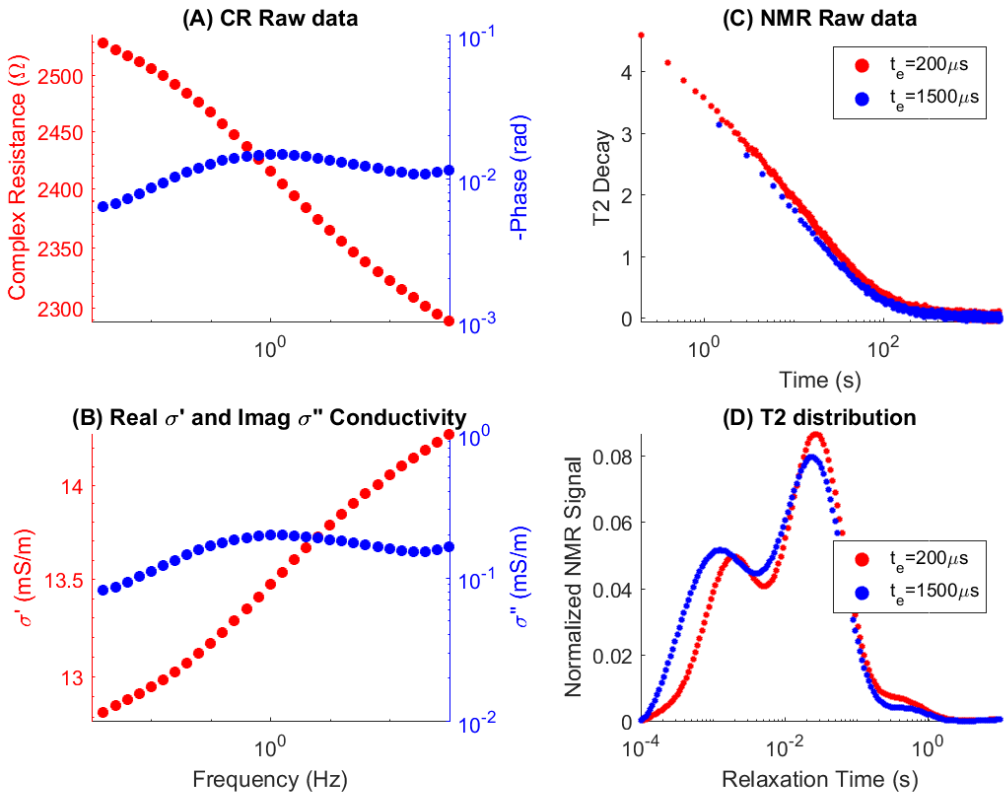

B.1 Table 35: SS-C3-P-040 Depth below ground surface=134.6 m

Physical properties

Permeability (mD): 1.87

Gravimetric Porosity (%): 14

Surface area normalized by pore volume (S_{por}) (μm^{-1}): 25.93

Electrical / CR measures

Electrical Formation Factor (F) (unitless): 47.63

Imaginary Conductivity at 1Hz (σ''_{1Hz}) (mS/m): 0.196

Peak relaxation time (τ_{peak}) (s): 0.126

NMR measures

Mean relaxation time echo time=200μs (T_{2ml}@t_e=200μs) (s): 1.16e-02

Peak relaxation time echo time=200μs (T_{2peak}@t_e=200μs) (s): 2.75e-02

Mean relaxation time echo time=1500μs (T_{2ml}@t_e=1500μs) (s): 7.35e-03

Peak relaxation time echo time=1500μs (T_{2peak}@t_e=1500μs) (s): 2.40e-02

B.1 Figure 36: SS-RD109-GEO-01

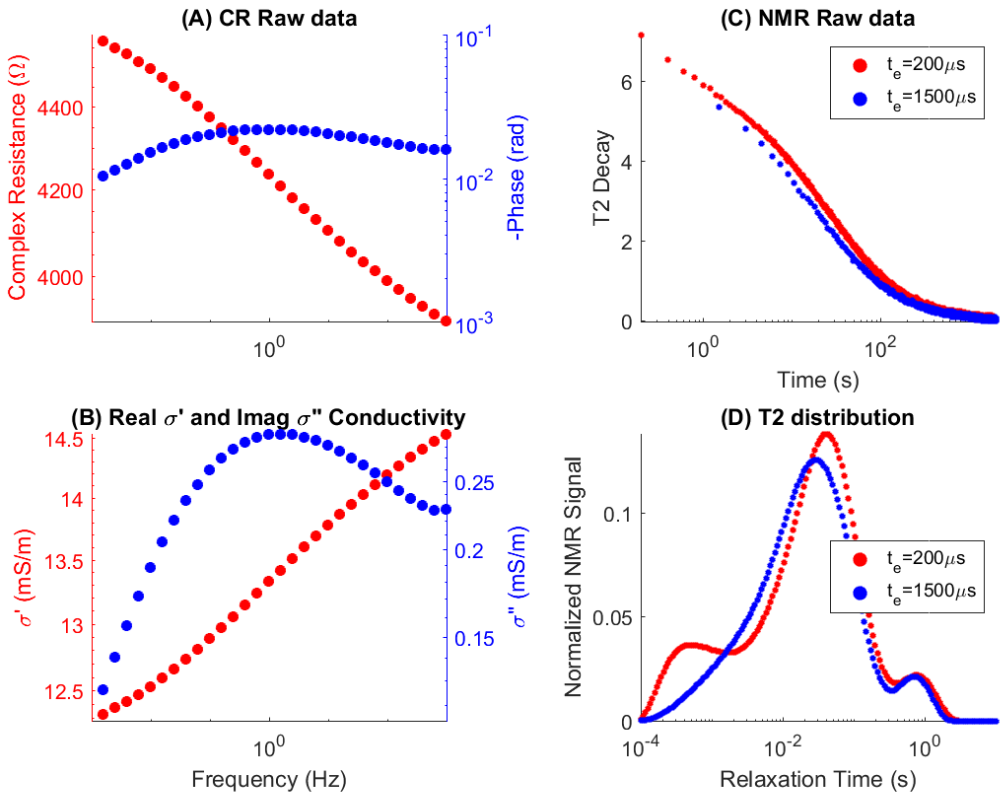

B.1 Table 36: SS-RD109-GEO-01 Depth below ground surface=4.961 m

Physical properties

Permeability (mD): 11.1

Gravimetric Porosity (%): 14.1

Surface area normalized by pore volume (S_{por}) (μm^{-1}): 29.6

Electrical / CR measures

Electrical Formation Factor (F) (unitless): 27.18

Imaginary Conductivity at 1Hz (σ''_{1Hz}) (mS/m): 0.291

Peak relaxation time (τ_{peak}) (s): 0.0784

NMR measures

Mean relaxation time echo time=200μs (T_{2ml}@t_e=200μs) (s): 1.85e-02

Peak relaxation time echo time=200μs (T_{2peak}@t_e=200μs) (s): 4.17e-02

Mean relaxation time echo time=1500μs (T_{2ml}@t_e=1500μs) (s): 2.07e-02

Peak relaxation time echo time=1500μs (T_{2peak}@t_e=1500μs) (s): 2.88e-02

B.1 Figure 37: SS-RD109-GEO-05

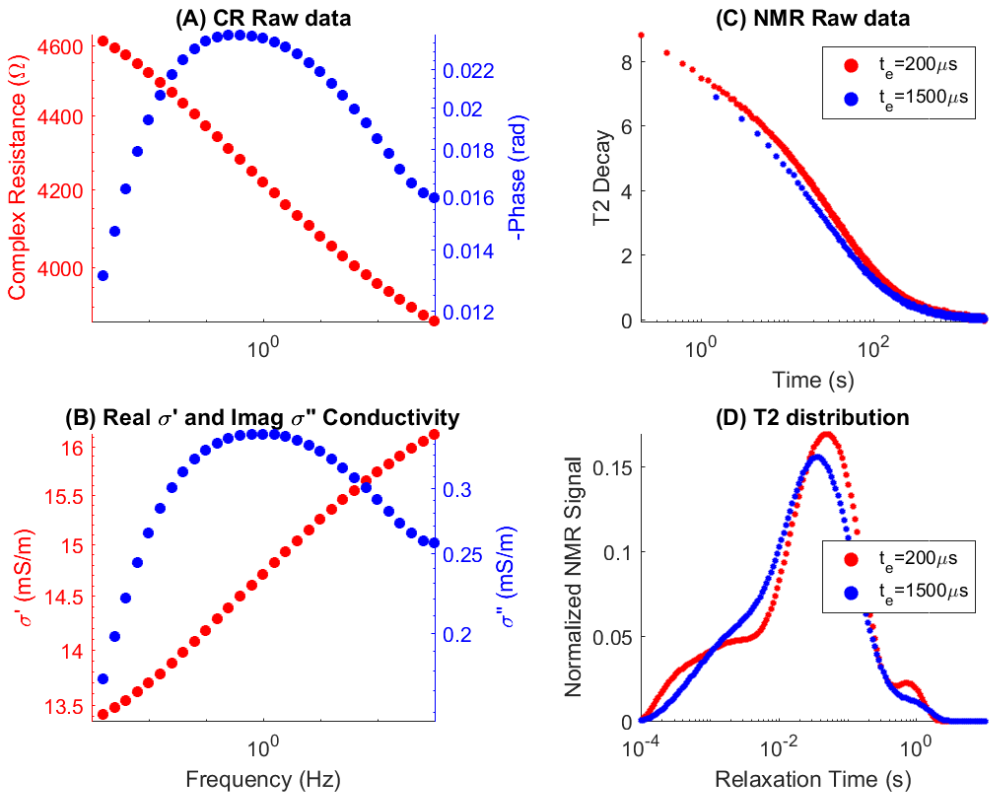

B.1 Table 37: SS-RD109-GEO-05 Depth below ground surface=15.45 m

Physical properties

Permeability (mD): 10.1

Gravimetric Porosity (%): 17.2

Surface area normalized by pore volume (S_{por}) (μm^{-1}): 32.13

Electrical / CR measures

Electrical Formation Factor (F) (unitless):

Imaginary Conductivity at 1Hz (σ''_{1Hz}) (mS/m): 0.35

Peak relaxation time (τ_{peak}) (s): 0.201

NMR measures

Mean relaxation time echo time=200μs (T_{2ml}@t_e=200μs) (s): 2.26e-02

Peak relaxation time echo time=200μs (T_{2peak}@t_e=200μs) (s): 5.01e-02

Mean relaxation time echo time=1500μs (T_{2ml}@t_e=1500μs) (s): 2.06e-02

Peak relaxation time echo time=1500μs (T_{2peak}@t_e=1500μs) (s): 3.63e-02

B.1 Figure 38: SS-RD109-GEO-06

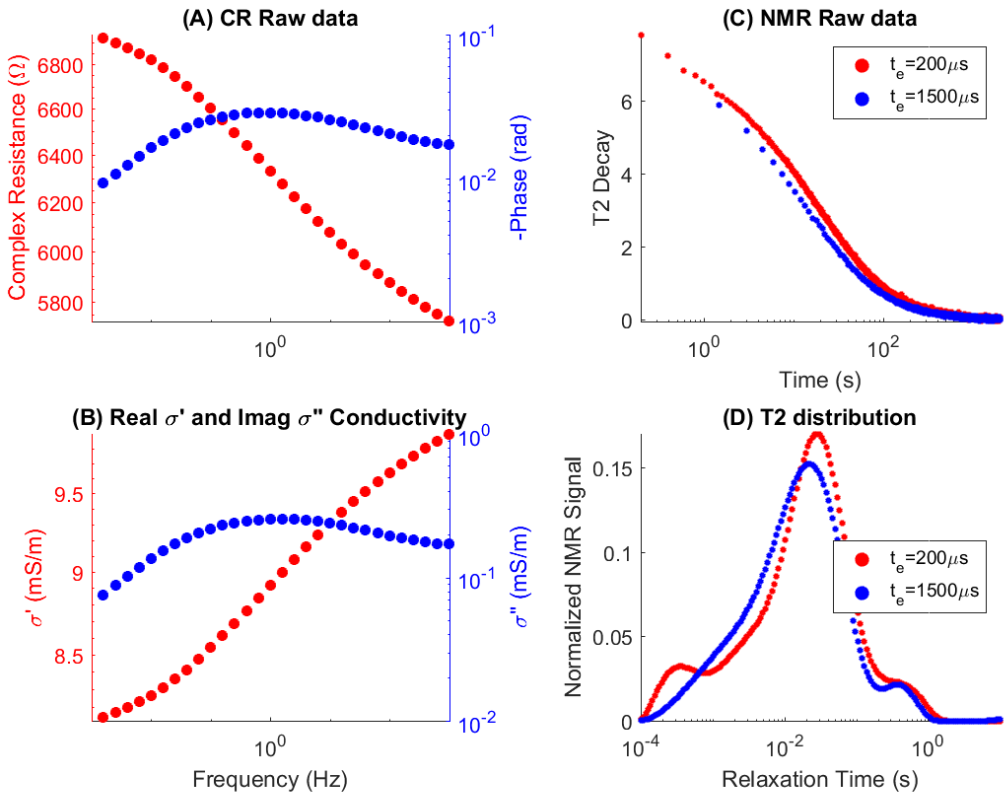

B.1 Table 38: SS-RD109-GEO-06 Depth below ground surface=18.88 m

Physical properties

Permeability (mD): 1.75

Gravimetric Porosity (%): 15.4

Surface area normalized by pore volume (S_{por}) (μm^{-1}): 40.71

Electrical / CR measures

Electrical Formation Factor (F) (unitless): 32.06

Imaginary Conductivity at 1Hz (σ''_{1Hz}) (mS/m): 0.255

Peak relaxation time (τ_{peak}) (s): 0.126

NMR measures

Mean relaxation time echo time=200μs (T_{2ml}@t_e=200μs) (s): 1.56e-02

Peak relaxation time echo time=200μs (T_{2peak}@t_e=200μs) (s): 2.88e-02

Mean relaxation time echo time=1500μs (T_{2ml}@t_e=1500μs) (s): 1.41e-02

Peak relaxation time echo time=1500μs (T_{2peak}@t_e=1500μs) (s): 2.19e-02

B.1 Figure 39: SS-RD109-GEO-14

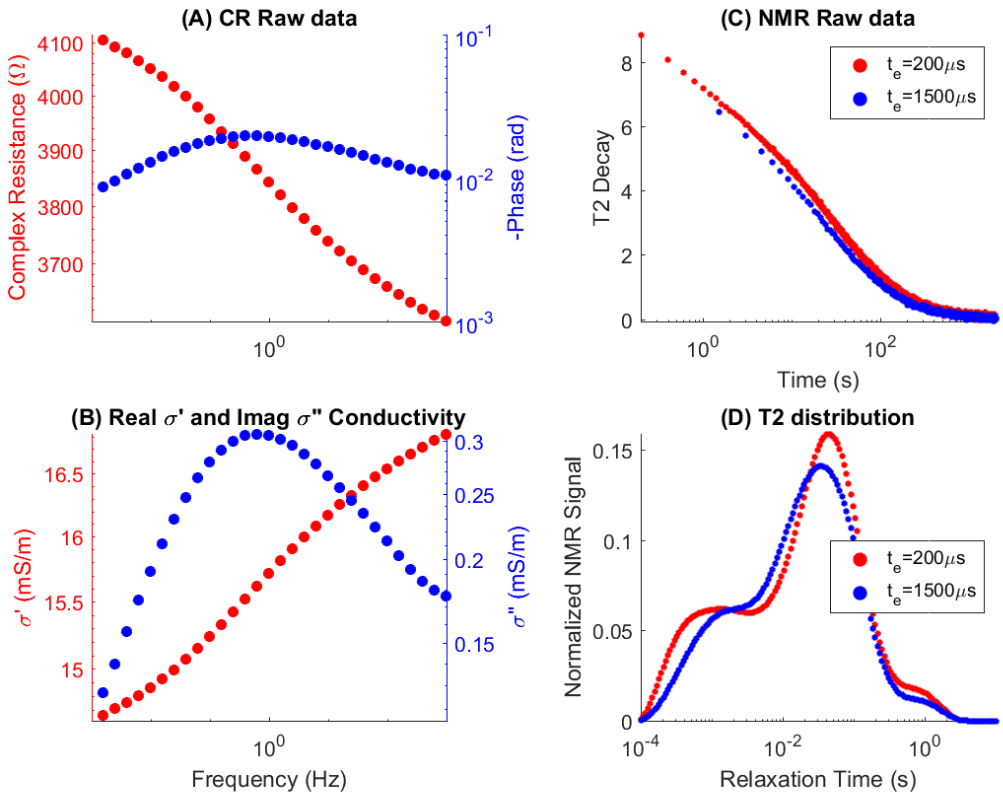

B.1 Table 39: SS-RD109-GEO-14 Depth below ground surface=27.04 m

Physical properties

Permeability (mD): 3.37

Gravimetric Porosity (%): 16

Surface area normalized by pore volume (S_{por}) (μm^{-1}): 25.48

Electrical / CR measures

Electrical Formation Factor (F) (unitless): 37.63

Imaginary Conductivity at 1Hz (σ''_{1Hz}) (mS/m): 0.306

Peak relaxation time (τ_{peak}) (s): 0.201

NMR measures

Mean relaxation time echo time=200μs (T_{2ml}@t_e=200μs) (s): 1.51e-02

Peak relaxation time echo time=200μs (T_{2peak}@t_e=200μs) (s): 4.37e-02

Mean relaxation time echo time=1500μs (T_{2ml}@t_e=1500μs) (s): 1.55e-02

Peak relaxation time echo time=1500μs (T_{2peak}@t_e=1500μs) (s): 3.47e-02

B.1 Figure 40: SS-RD109-GEO-16

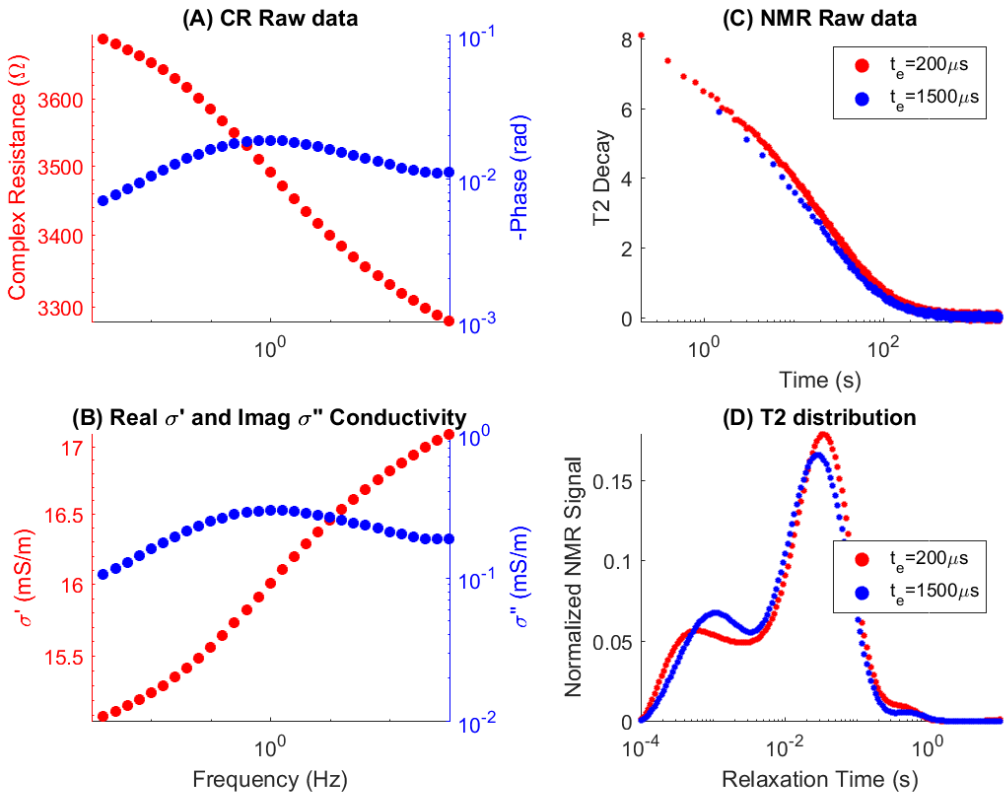

B.1 Table 40: SS-RD109-GEO-16 Depth below ground surface=29.55 m

Physical properties

Permeability (mD): 5.95

Gravimetric Porosity (%): 16.6

Surface area normalized by pore volume (S_{por}) (μm^{-1}): 24.28

Electrical / CR measures

Electrical Formation Factor (F) (unitless): 39.51

Imaginary Conductivity at 1Hz (σ''_{1Hz}) (mS/m): 0.294

Peak relaxation time (τ_{peak}) (s): 0.126

NMR measures

Mean relaxation time echo time=200μs (T_{2ml}@t_e=200μs) (s): 1.18e-02

Peak relaxation time echo time=200μs (T_{2peak}@t_e=200μs) (s): 3.47e-02

Mean relaxation time echo time=1500μs (T_{2ml}@t_e=1500μs) (s): 1.05e-02

Peak relaxation time echo time=1500μs (T_{2peak}@t_e=1500μs) (s): 2.88e-02

B.1 Figure 41: SS-RD109-P-01

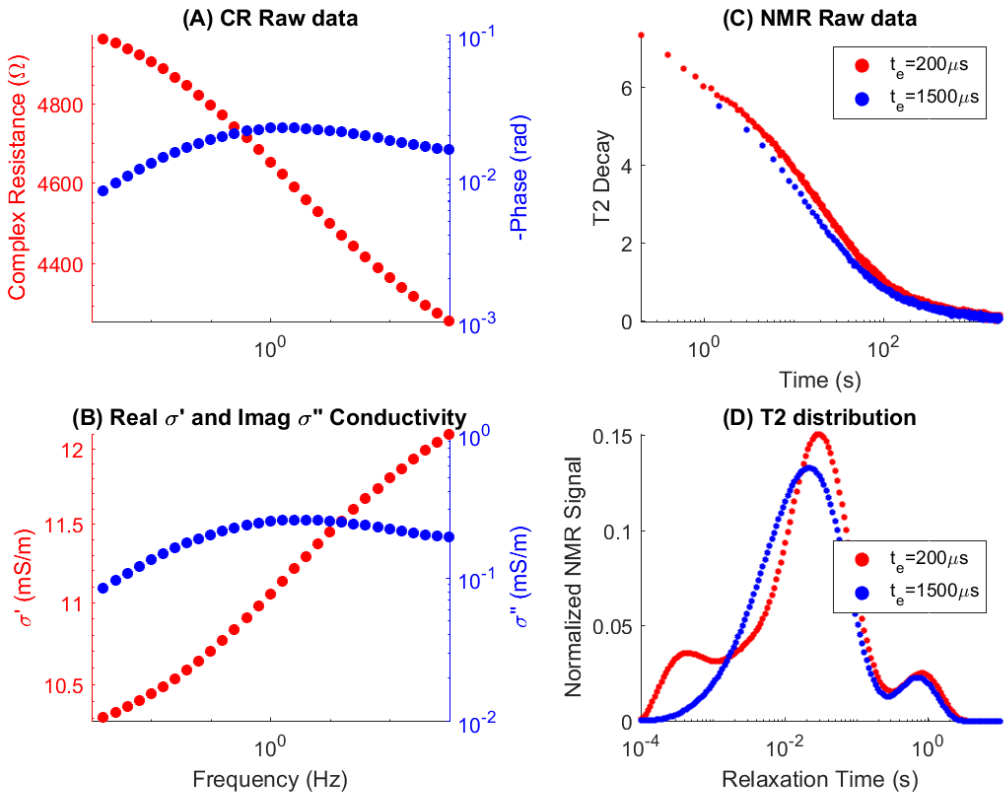

B.1 Table 41: SS-RD109-P-01 Depth below ground surface=6.858 m

Physical properties

Permeability (mD): 3.95

Gravimetric Porosity (%): 16.7

Surface area normalized by pore volume (S_{por}) (μm^{-1}): 21.5

Electrical / CR measures

Electrical Formation Factor (F) (unitless): 30.49

Imaginary Conductivity at 1Hz (σ''_{1Hz}) (mS/m): 0.246

Peak relaxation time (τ_{peak}) (s): 0.0489

NMR measures

Mean relaxation time echo time=200μs (T_{2ml}@t_e=200μs) (s): 1.73e-02

Peak relaxation time echo time=200μs (T_{2peak}@t_e=200μs) (s): 3.02e-02

Mean relaxation time echo time=1500μs (T_{2ml}@t_e=1500μs) (s): 1.99e-02

Peak relaxation time echo time=1500μs (T_{2peak}@t_e=1500μs) (s): 2.19e-02

B.1 Figure 42: SS-RD109-P-02

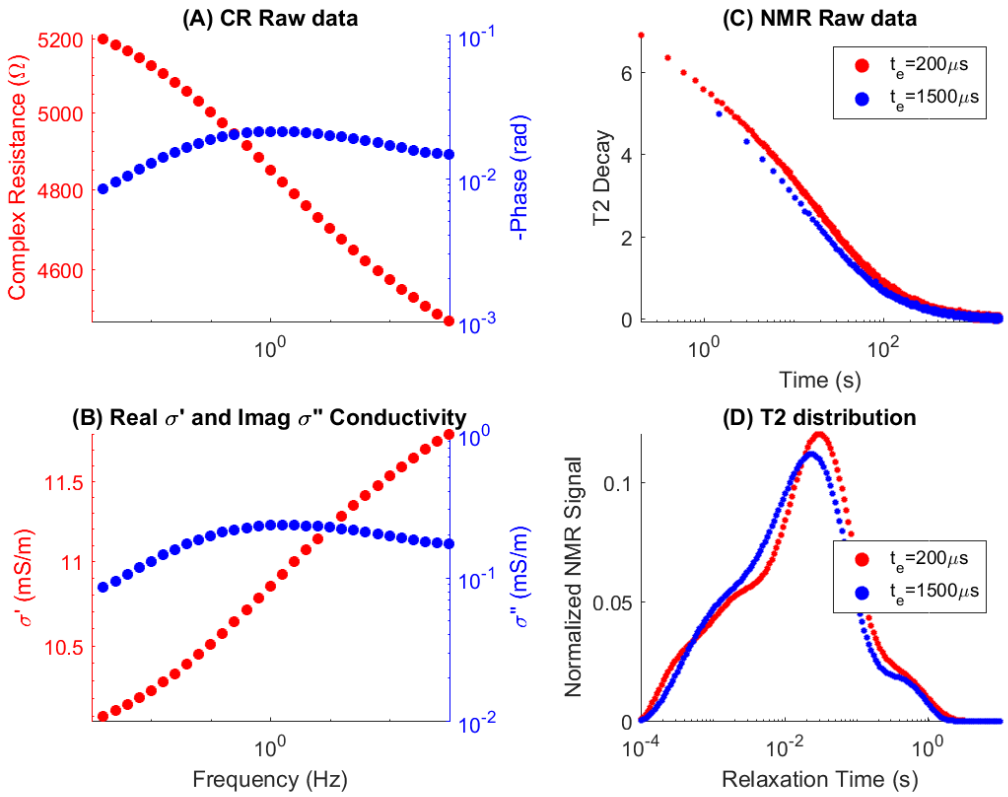

B.1 Table 42: SS-RD109-P-02 Depth below ground surface=20.54 m

Physical properties

Permeability (mD): 1.63

Gravimetric Porosity (%): 14.5

Surface area normalized by pore volume (S_{por}) (μm^{-1}): 25.41

Electrical / CR measures

Electrical Formation Factor (F) (unitless): 44.57

Imaginary Conductivity at 1Hz (σ''_{1Hz}) (mS/m): 0.23

Peak relaxation time (τ_{peak}) (s): 0.0784

NMR measures

Mean relaxation time echo time=200μs (T_{2ml}@t_e=200μs) (s): 1.45e-02

Peak relaxation time echo time=200μs (T_{2peak}@t_e=200μs) (s): 3.02e-02

Mean relaxation time echo time=1500μs (T_{2ml}@t_e=1500μs) (s): 1.24e-02

Peak relaxation time echo time=1500μs (T_{2peak}@t_e=1500μs) (s): 2.40e-02

B.1 Figure 43: SS-RD109-P-03

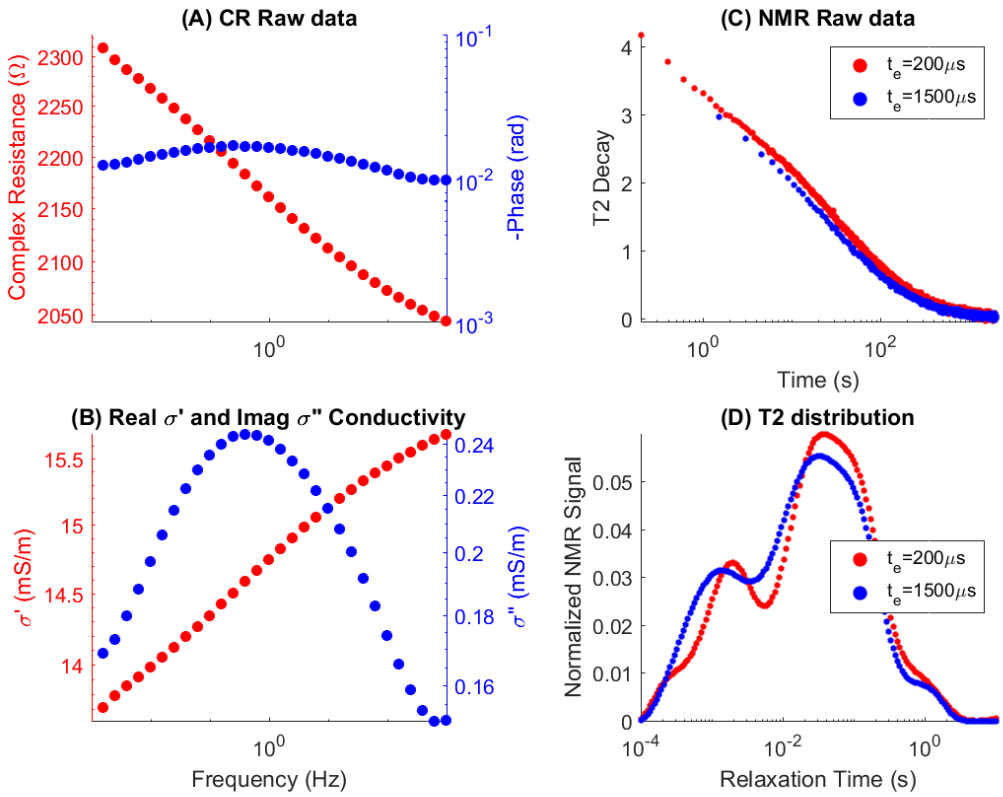

B.1 Table 43: SS-RD109-P-03 Depth below ground surface=23.88 m

Physical properties

Permeability (mD): 7.62

Gravimetric Porosity (%): 15.1

Surface area normalized by pore volume (S_{por}) (μm^{-1}): 25.6

Electrical / CR measures

Electrical Formation Factor (F) (unitless): 38.55

Imaginary Conductivity at 1Hz (σ''_{1Hz}) (mS/m): 0.241

Peak relaxation time (τ_{peak}) (s): 0.323

NMR measures

Mean relaxation time echo time=200μs (T_{2ml}@t_e=200μs) (s): 2.13e-02

Peak relaxation time echo time=200μs (T_{2peak}@t_e=200μs) (s): 3.80e-02

Mean relaxation time echo time=1500μs (T_{2ml}@t_e=1500μs) (s): 1.61e-02

Peak relaxation time echo time=1500μs (T_{2peak}@t_e=1500μs) (s): 3.16e-02

B.1 Figure 44: SS-RD109-P-04

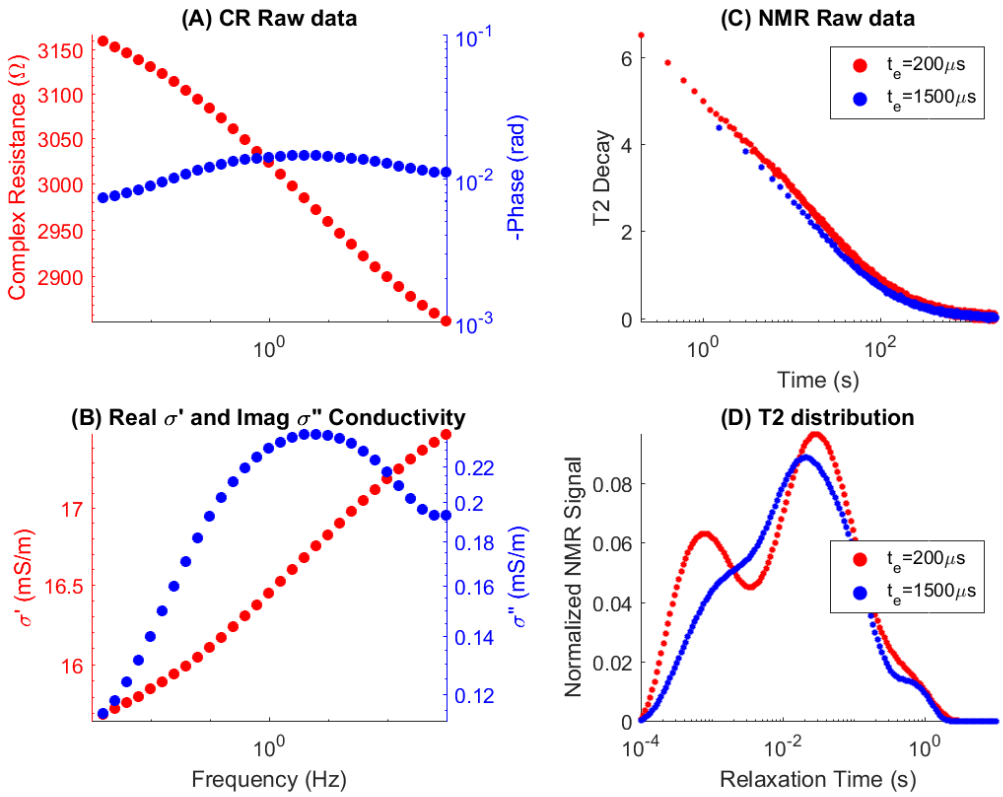

B.1 Table 44: SS-RD109-P-04 Depth below ground surface=25.66 m

Physical properties

Permeability (mD): 3.47

Gravimetric Porosity (%): 14.9

Surface area normalized by pore volume (S_{por}) (μm^{-1}): 28.38

Electrical / CR measures

Electrical Formation Factor (F) (unitless):

Imaginary Conductivity at 1Hz (σ''_{1Hz}) (mS/m): 0.231

Peak relaxation time (τ_{peak}) (s): 0.0305

NMR measures

Mean relaxation time echo time=200μs (T_{2ml}@t_e=200μs) (s): 1.07e-02

Peak relaxation time echo time=200μs (T_{2peak}@t_e=200μs) (s): 2.88e-02

Mean relaxation time echo time=1500μs (T_{2ml}@t_e=1500μs) (s): 1.30e-02

Peak relaxation time echo time=1500μs (T_{2peak}@t_e=1500μs) (s): 2.09e-02

B.1 Figure 45: SS-RD109-P-05

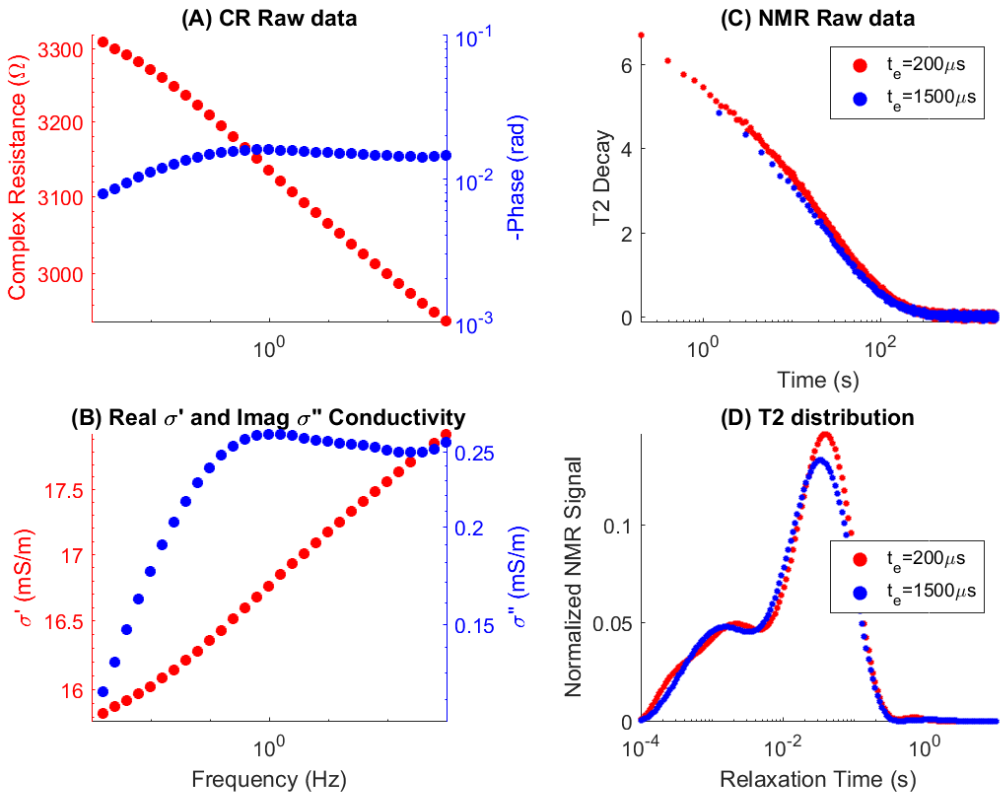

B.1 Table 45: SS-RD109-P-05 Depth below ground surface=40.81 m

Physical properties

Permeability (mD): 5.24

Gravimetric Porosity (%): 13.1

Surface area normalized by pore volume (S_{por}) (μm^{-1}): 27.87

Electrical / CR measures

Electrical Formation Factor (F) (unitless): 46.55

Imaginary Conductivity at 1Hz (σ''_{1Hz}) (mS/m): 0.264

Peak relaxation time (τ_{peak}) (s): 0.126

NMR measures

Mean relaxation time echo time=200μs (T_{2ml}@t_e=200μs) (s): 1.35e-02

Peak relaxation time echo time=200μs (T_{2peak}@t_e=200μs) (s): 3.98e-02

Mean relaxation time echo time=1500μs (T_{2ml}@t_e=1500μs) (s): 1.27e-02

Peak relaxation time echo time=1500μs (T_{2peak}@t_e=1500μs) (s): 3.47e-02

B.1 Figure 46: SS-RD109-P-06

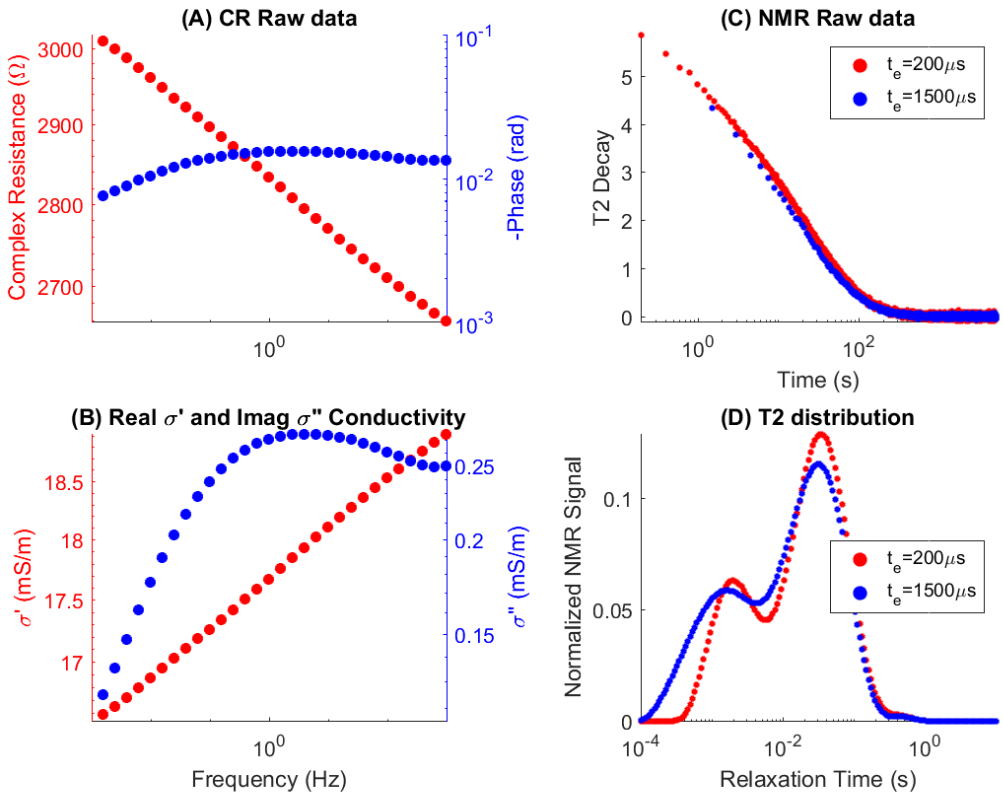

B.1 Table 46: SS-RD109-P-06 Depth below ground surface=42.52 m

Physical properties

Permeability (mD): 1.13

Gravimetric Porosity (%): 13.2

Surface area normalized by pore volume (S_{por}) (μm^{-1}): 22.11

Electrical / CR measures

Electrical Formation Factor (F) (unitless): 49.66

Imaginary Conductivity at 1Hz (σ''_{1Hz}) (mS/m): 0.271

Peak relaxation time (τ_{peak}) (s): 0.0305

NMR measures

Mean relaxation time echo time=200μs (T_{2ml}@t_e=200μs) (s): 1.48e-02

Peak relaxation time echo time=200μs (T_{2peak}@t_e=200μs) (s): 3.47e-02

Mean relaxation time echo time=1500μs (T_{2ml}@t_e=1500μs) (s): 9.66e-03

Peak relaxation time echo time=1500μs (T_{2peak}@t_e=1500μs) (s): 3.16e-02

B.1 Figure 47: NAWC-94BR-P-001

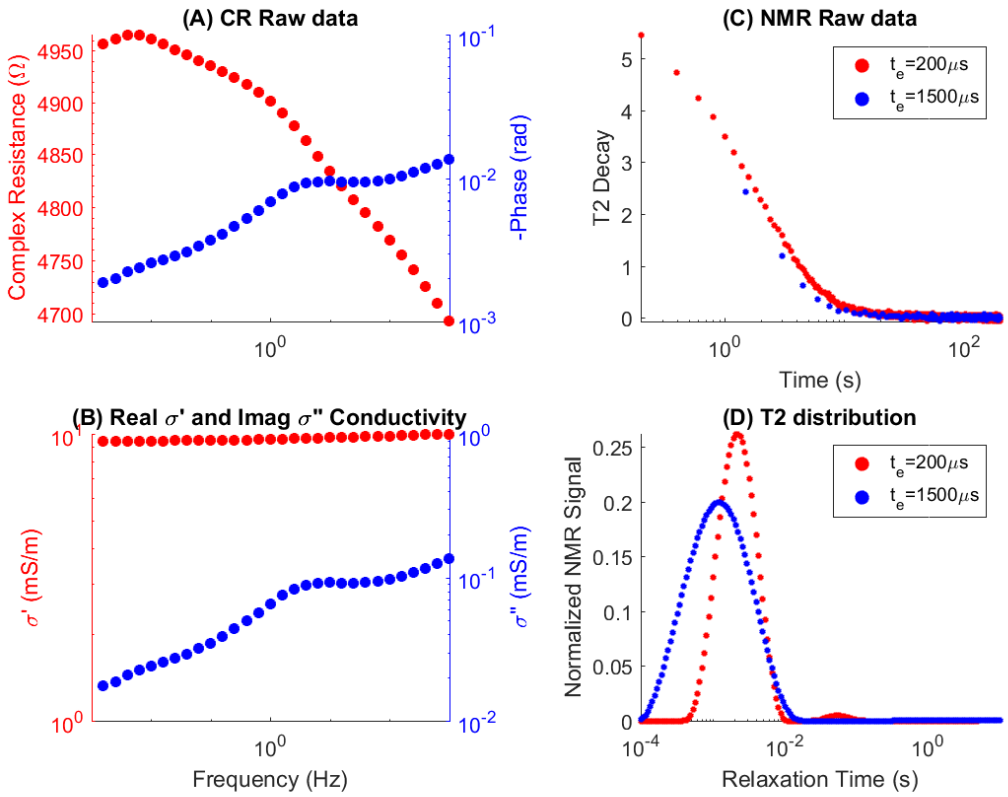

B.1 Table 47: NAWC-94BR-P-001 Depth below ground surface=12.95 m

Physical properties

Permeability (mD): 0.002

Gravimetric Porosity (%): 12.2

Surface area normalized by pore volume (S_{por}) (μm^{-1}): 130.4

Electrical / CR measures

Electrical Formation Factor (F) (unitless): 95.27

Imaginary Conductivity at 1Hz (σ''_{1Hz}) (mS/m): 0.0657

Peak relaxation time (τ_{peak}) (s): 0.0404

NMR measures

Mean relaxation time echo time=200μs (T_{2ml}@t_e=200μs) (s): 2.23e-03

Peak relaxation time echo time=200μs (T_{2peak}@t_e=200μs) (s): 2.19e-03

Mean relaxation time echo time=1500μs (T_{2ml}@t_e=1500μs) (s): 1.19e-03

Peak relaxation time echo time=1500μs (T_{2peak}@t_e=1500μs) (s): 1.20e-03

B.1 Figure 48: NAWC-94BR-P-003

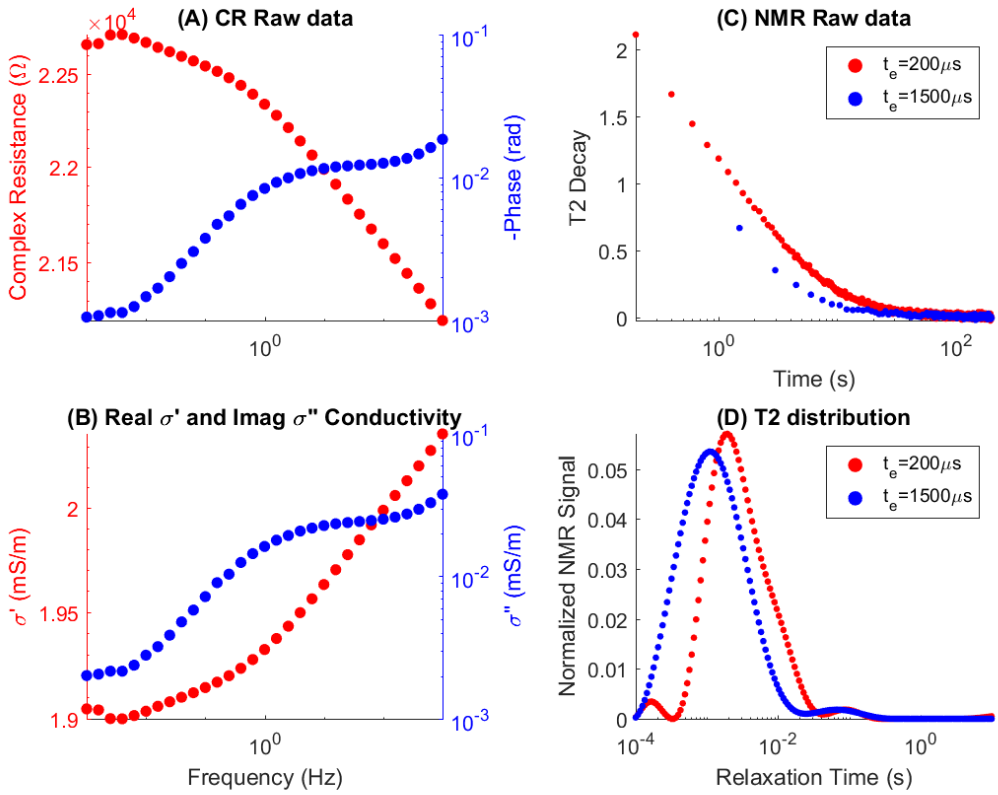

B.1 Table 48: NAWC-94BR-P-003 Depth below ground surface=15.76 m

Physical properties

Permeability (mD): 0.000911

Gravimetric Porosity (%): 4.36

Surface area normalized by pore volume (S_{por}) (μm^{-1}): 116.8

Electrical / CR measures

Electrical Formation Factor (F) (unitless): 306.7

Imaginary Conductivity at 1Hz (σ''_{1Hz}) (mS/m): 0.0162

Peak relaxation time (τ_{peak}) (s): 0.0682

NMR measures

Mean relaxation time echo time=200μs (T_{2ml}@t_e=200μs) (s): 2.81e-03

Peak relaxation time echo time=200μs (T_{2peak}@t_e=200μs) (s): 1.91e-03

Mean relaxation time echo time=1500μs (T_{2ml}@t_e=1500μs) (s): 1.29e-03

Peak relaxation time echo time=1500μs (T_{2peak}@t_e=1500μs) (s): 1.10e-03

B.1 Figure 49: NAWC-94BR-P-004

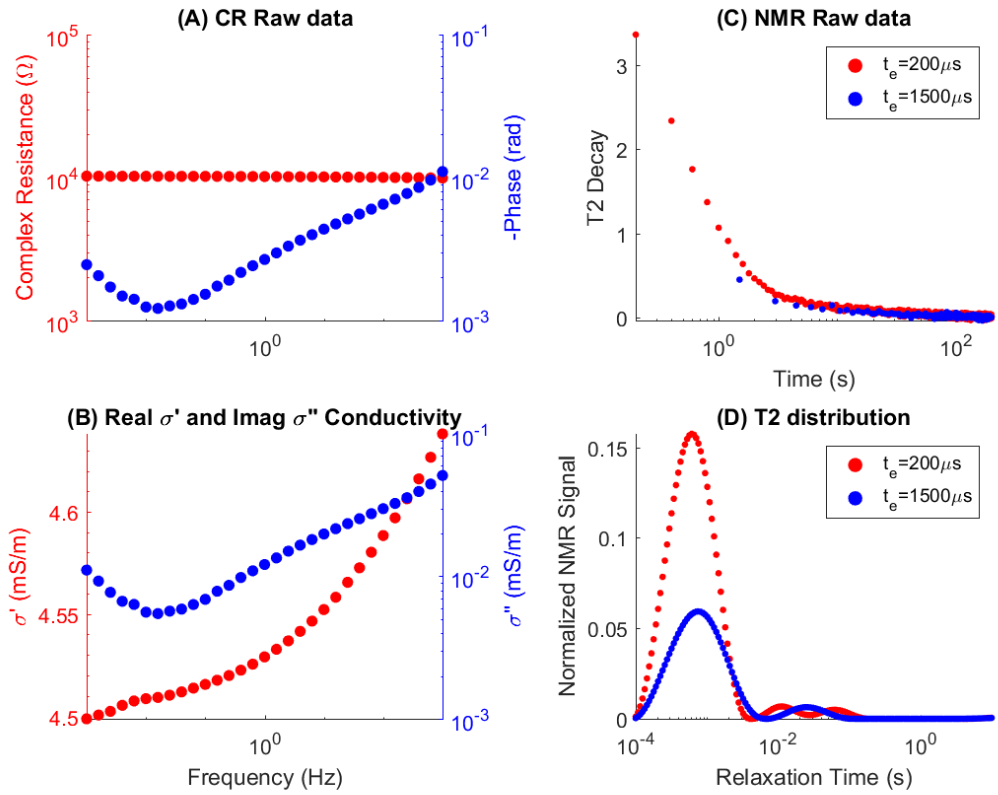

B.1 Table 49: NAWC-94BR-P-004 Depth below ground surface=16.55 m

Physical properties

Permeability (mD): 0.00187

Gravimetric Porosity (%): 7.76

Surface area normalized by pore volume (S_{por}) (μm^{-1}): 399.1

Electrical / CR measures

Electrical Formation Factor (F) (unitless): 328

Imaginary Conductivity at 1Hz (σ''_{1Hz}) (mS/m): 0.0121

Peak relaxation time (τ_{peak}) (s): NaN

NMR measures

Mean relaxation time echo time=200μs (T_{2ml}@t_e=200μs) (s): 6.95e-04

Peak relaxation time echo time=200μs (T_{2peak}@t_e=200μs) (s): 6.03e-04

Mean relaxation time echo time=1500μs (T_{2ml}@t_e=1500μs) (s): 9.34e-04

Peak relaxation time echo time=1500μs (T_{2peak}@t_e=1500μs) (s): 7.59e-04

B.1 Figure 50: NAWC-94BR-P-005

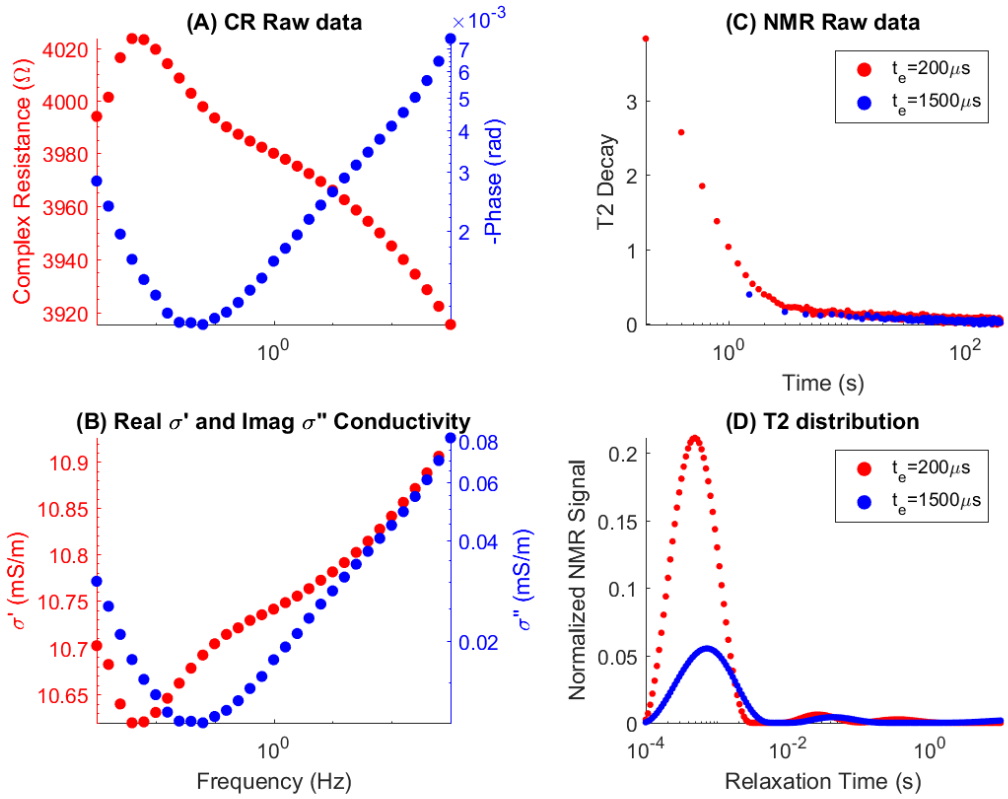

B.1 Table 50: NAWC-94BR-P-005 Depth below ground surface=17.61 m

Physical properties

Permeability (mD): NaN

Gravimetric Porosity (%): 10.2

Surface area normalized by pore volume (S_{por}) (μm^{-1}): 256.9

Electrical / CR measures

Electrical Formation Factor (F) (unitless):

Imaginary Conductivity at 1Hz (σ''_{1Hz}) (mS/m): 0.0175

Peak relaxation time (τ_{peak}) (s): NaN

NMR measures

Mean relaxation time echo time=200μs (T_{2ml}@t_e=200μs) (s): 5.65e-04

Peak relaxation time echo time=200μs (T_{2peak}@t_e=200μs) (s): 5.01e-04

Mean relaxation time echo time=1500μs (T_{2ml}@t_e=1500μs) (s): 9.51e-04

Peak relaxation time echo time=1500μs (T_{2peak}@t_e=1500μs) (s): 7.24e-04

B.1 Figure 51: NAWC-94BR-P-006

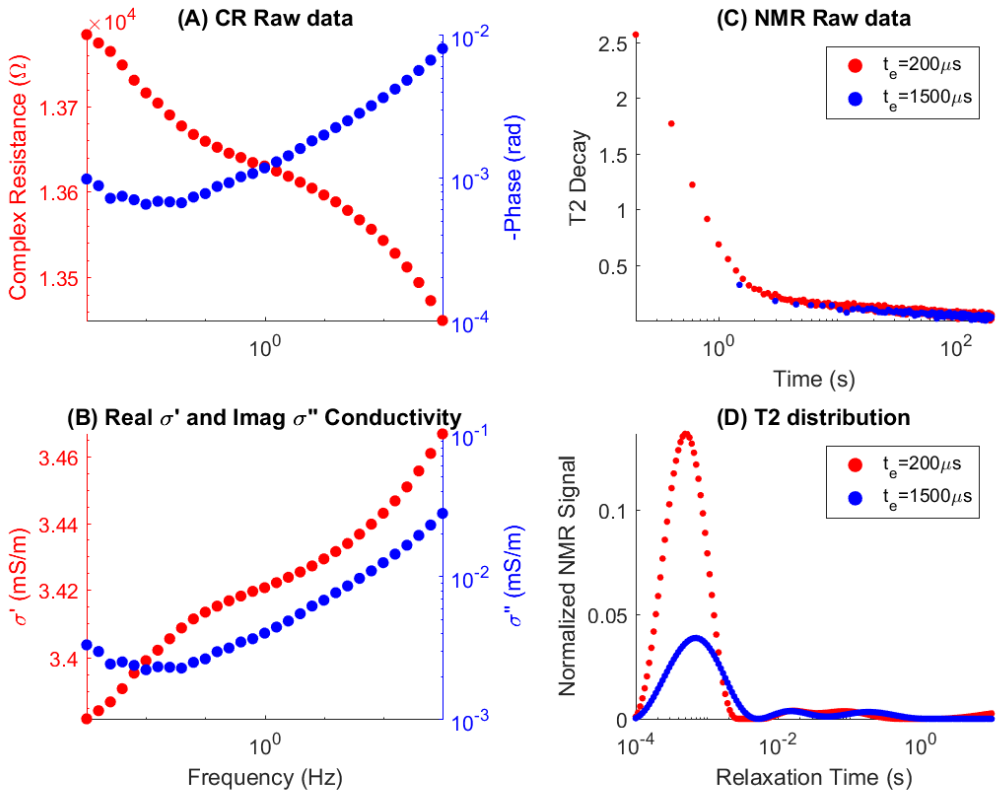

B.1 Table 51: NAWC-94BR-P-006 Depth below ground surface=18.85 m

Physical properties

Permeability (mD): 0.000608

Gravimetric Porosity (%): 5.94

Surface area normalized by pore volume (S_{por}) (μm^{-1}): 356.4

Electrical / CR measures

Electrical Formation Factor (F) (unitless): 643.2

Imaginary Conductivity at 1Hz (σ''_{1Hz}) (mS/m): 0.004

Peak relaxation time (τ_{peak}) (s): NaN

NMR measures

Mean relaxation time echo time=200μs (T_{2ml}@t_e=200μs) (s): 6.47e-04

Peak relaxation time echo time=200μs (T_{2peak}@t_e=200μs) (s): 5.01e-04

Mean relaxation time echo time=1500μs (T_{2ml}@t_e=1500μs) (s): 1.16e-03

Peak relaxation time echo time=1500μs (T_{2peak}@t_e=1500μs) (s): 6.92e-04

B.1 Figure 52: NAWC-94BR-P-007

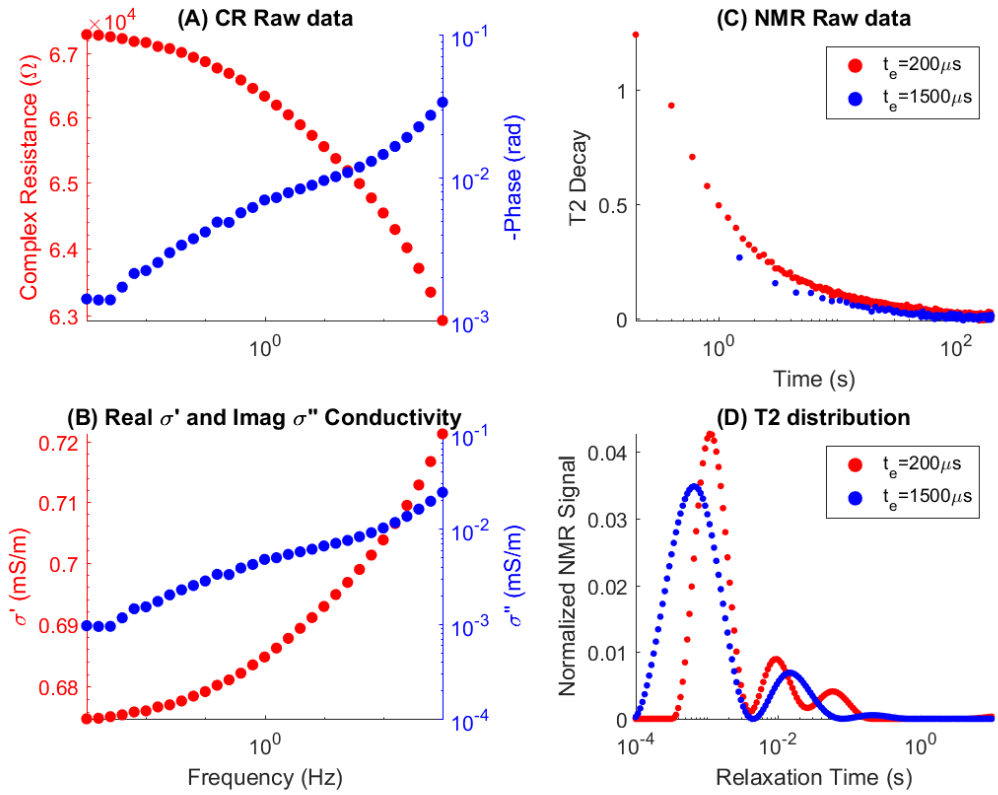

B.1 Table 52: NAWC-94BR-P-007 Depth below ground surface=19.43 m

Physical properties

Permeability (mD): 0.000267

Gravimetric Porosity (%): 2.19

Surface area normalized by pore volume (S_{por}) (μm^{-1}): 476.2

Electrical / CR measures

Electrical Formation Factor (F) (unitless): 1241

Imaginary Conductivity at 1Hz (σ''_{1Hz}) (mS/m): 0.00477

Peak relaxation time (τ_{peak}) (s): NaN

NMR measures

Mean relaxation time echo time=200μs (T_{2ml}@t_e=200μs) (s): 2.12e-03

Peak relaxation time echo time=200μs (T_{2peak}@t_e=200μs) (s): 1.10e-03

Mean relaxation time echo time=1500μs (T_{2ml}@t_e=1500μs) (s): 9.78e-04

Peak relaxation time echo time=1500μs (T_{2peak}@t_e=1500μs) (s): 6.61e-04

B.1 Figure 53: NAWC-94BR-P-008

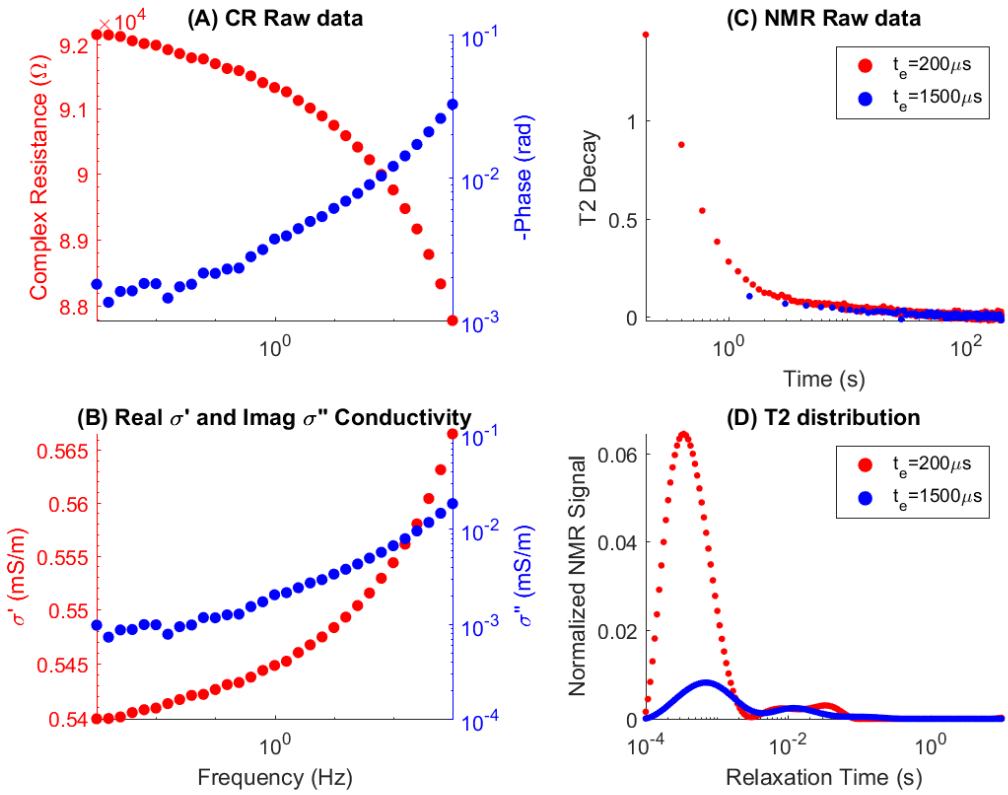

B.1 Table 53: NAWC-94BR-P-008 Depth below ground surface=20.69 m

Physical properties

Permeability (mD): 0.00048

Gravimetric Porosity (%): 4.18

Surface area normalized by pore volume (S_{por}) (μm^{-1}): 83.94

Electrical / CR measures

Electrical Formation Factor (F) (unitless): 2310

Imaginary Conductivity at 1Hz (σ''_{1Hz}) (mS/m): 0.00202

Peak relaxation time (τ_{peak}) (s): NaN

NMR measures

Mean relaxation time echo time=200μs (T_{2ml}@t_e=200μs) (s): 4.91e-04

Peak relaxation time echo time=200μs (T_{2peak}@t_e=200μs) (s): 3.47e-04

Mean relaxation time echo time=1500μs (T_{2ml}@t_e=1500μs) (s): 1.43e-03

Peak relaxation time echo time=1500μs (T_{2peak}@t_e=1500μs) (s): 6.92e-04

B.1 Figure 54: NAWC-94BR-P-009

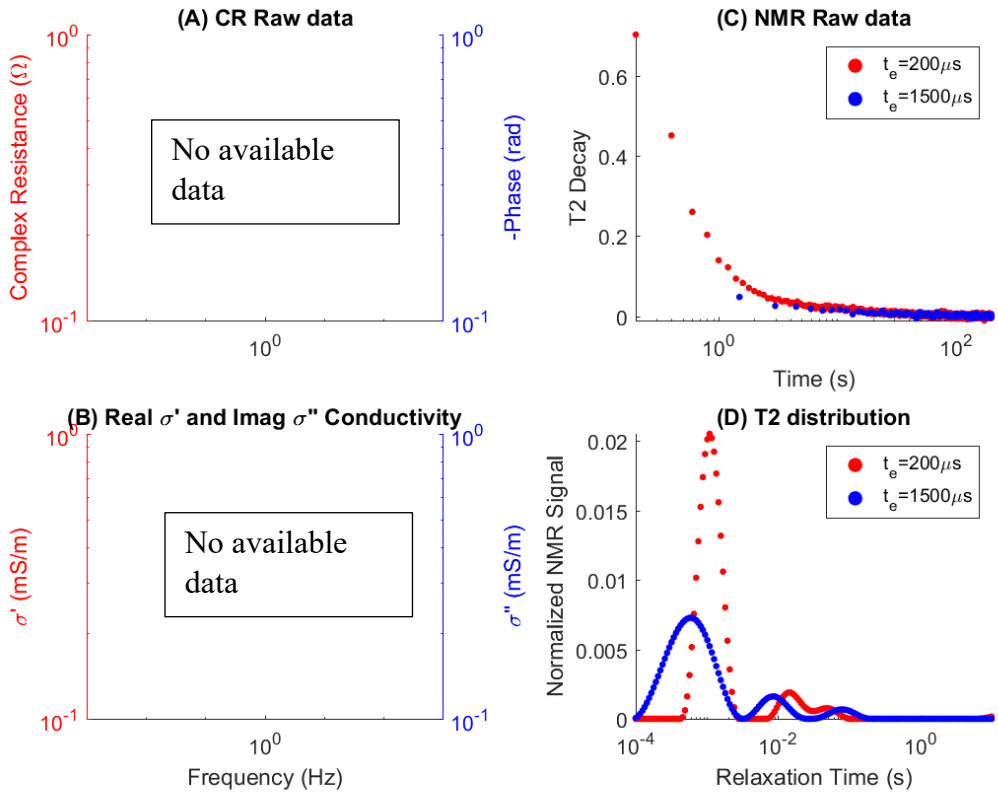

B.1 Table 54: NAWC-94BR-P-009 Depth below ground surface=22.61 m

Physical properties

Permeability (mD): 0.000245

Gravimetric Porosity (%): 0.698

Surface area normalized by pore volume (S_{por}) (μm^{-1}): NaN

Electrical / CR measures

Electrical Formation Factor (F) (unitless): 5502

Imaginary Conductivity at 1Hz (σ''_{1Hz}) (mS/m): 0

Peak relaxation time (τ_{peak}) (s):

NMR measures

Mean relaxation time echo time=200μs (T_{2ml}@t_e=200μs) (s): 1.53e-03

Peak relaxation time echo time=200μs (T_{2peak}@t_e=200μs) (s): 1.10e-03

Mean relaxation time echo time=1500μs (T_{2ml}@t_e=1500μs) (s): 9.05e-04

Peak relaxation time echo time=1500μs (T_{2peak}@t_e=1500μs) (s): 5.75e-04

B.1 Figure 55: NAWC-94BR-P-010

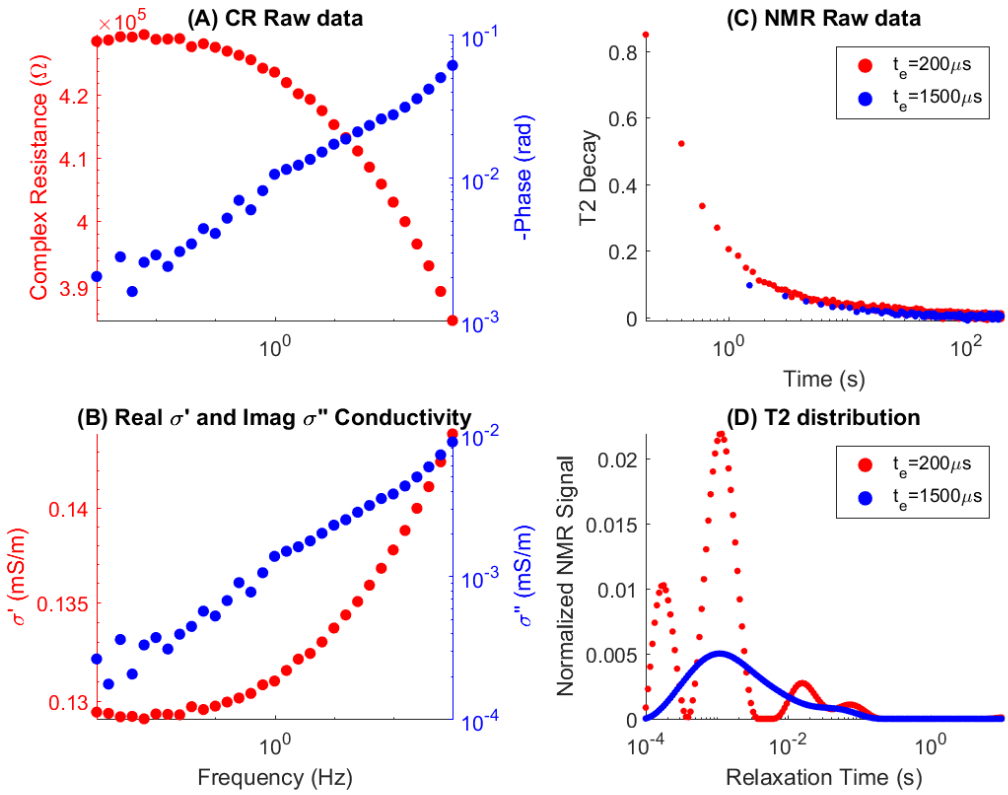

B.1 Table 55: NAWC-94BR-P-010 Depth below ground surface=23.12 m

Physical properties

Permeability (mD): 0

Gravimetric Porosity (%): 0.891

Surface area normalized by pore volume (S_{por}) (μm^{-1}): NaN

Electrical / CR measures

Electrical Formation Factor (F) (unitless): 7706

Imaginary Conductivity at 1Hz (σ''_{1Hz}) (mS/m): 0.00138

Peak relaxation time (τ_{peak}) (s): NaN

NMR measures

Mean relaxation time echo time=200μs (T_{2ml}@t_e=200μs) (s): 1.09e-03

Peak relaxation time echo time=200μs (T_{2peak}@t_e=200μs) (s): 1.15e-03

Mean relaxation time echo time=1500μs (T_{2ml}@t_e=1500μs) (s): 1.92e-03

Peak relaxation time echo time=1500μs (T_{2peak}@t_e=1500μs) (s): 1.10e-03

B.1 Figure 56: NAWC-94BR-P-011

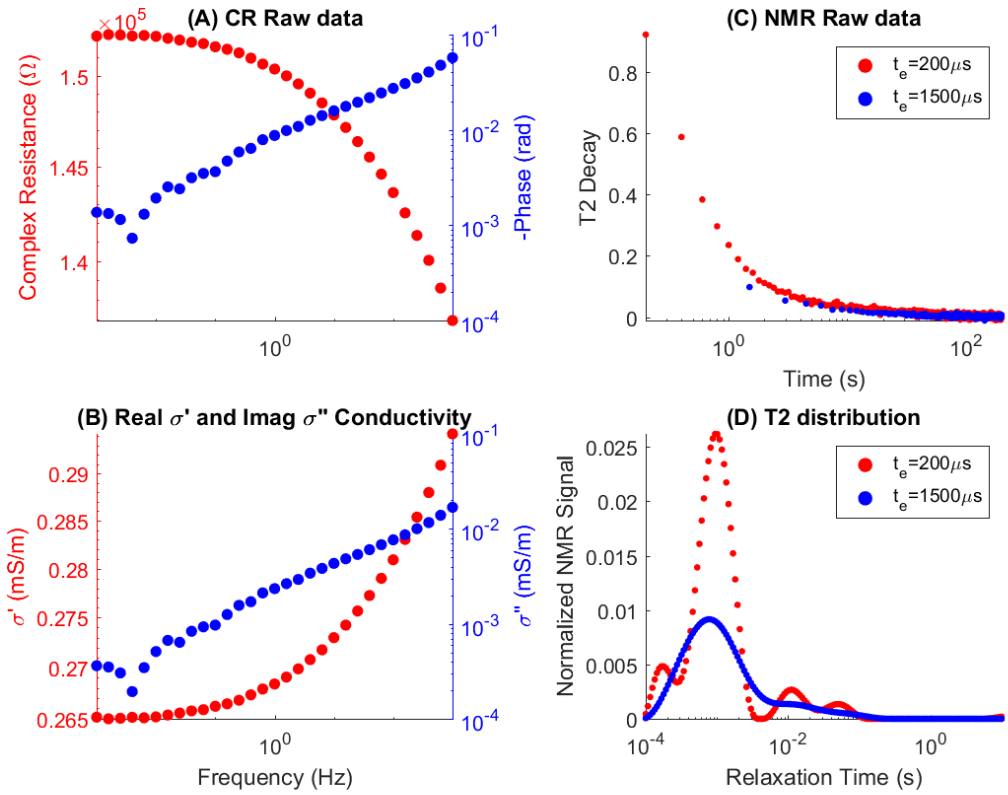

B.1 Table 56: NAWC-94BR-P-011 Depth below ground surface=23.8 m

Physical properties

Permeability (mD): 0.000291

Gravimetric Porosity (%): 1.53

Surface area normalized by pore volume (S_{por}) (μm^{-1}): NaN

Electrical / CR measures

Electrical Formation Factor (F) (unitless): 5744

Imaginary Conductivity at 1Hz (σ''_{1Hz}) (mS/m): 0.00235

Peak relaxation time (τ_{peak}) (s): NaN

NMR measures

Mean relaxation time echo time=200μs (T_{2ml}@t_e=200μs) (s): 1.09e-03

Peak relaxation time echo time=200μs (T_{2peak}@t_e=200μs) (s): 9.55e-04

Mean relaxation time echo time=1500μs (T_{2ml}@t_e=1500μs) (s): 1.19e-03

Peak relaxation time echo time=1500μs (T_{2peak}@t_e=1500μs) (s): 7.94e-04

B.1 Figure 57: NAWC-94BR-P-012

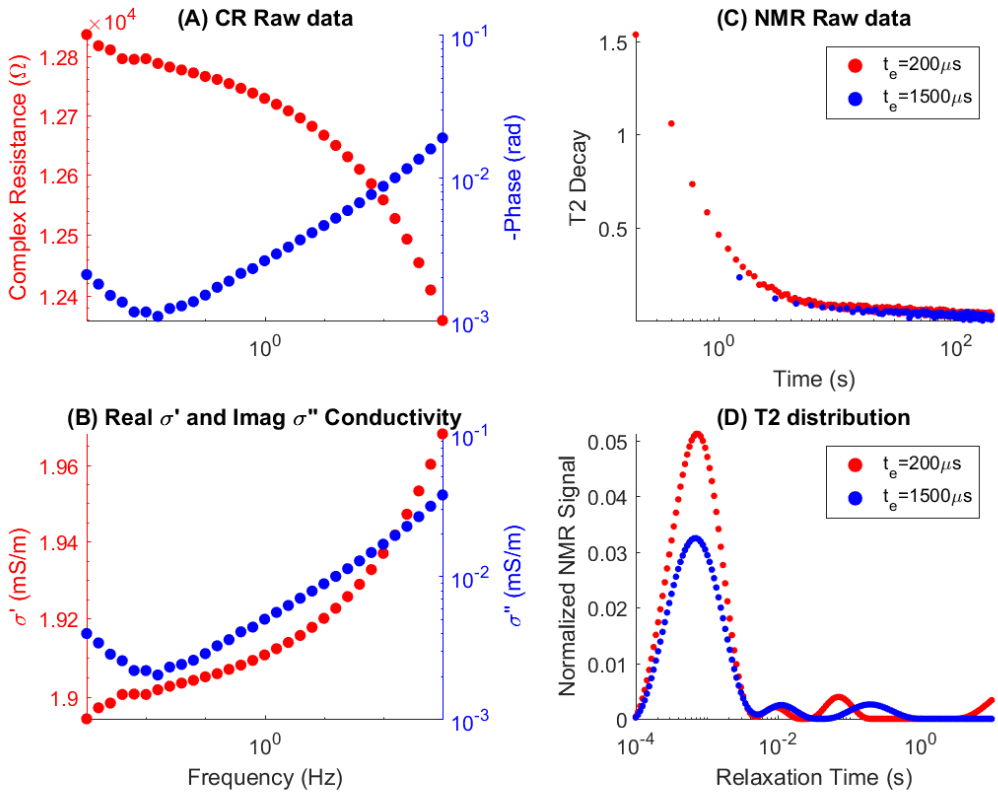

B.1 Table 57: NAWC-94BR-P-012 Depth below ground surface=24.69 m

Physical properties

Permeability (mD): 0.000248

Gravimetric Porosity (%): 6.06

Surface area normalized by pore volume (S_{por}) (μm^{-1}): 36.49

Electrical / CR measures

Electrical Formation Factor (F) (unitless): 1581

Imaginary Conductivity at 1Hz (σ''_{1Hz}) (mS/m): 0.005

Peak relaxation time (τ_{peak}) (s): NaN

NMR measures

Mean relaxation time echo time=200μs (T_{2ml}@t_e=200μs) (s): 9.40e-04

Peak relaxation time echo time=200μs (T_{2peak}@t_e=200μs) (s): 7.24e-04

Mean relaxation time echo time=1500μs (T_{2ml}@t_e=1500μs) (s): 1.01e-03

Peak relaxation time echo time=1500μs (T_{2peak}@t_e=1500μs) (s): 6.92e-04

B.1 Figure 58: NAWC-94BR-P-013

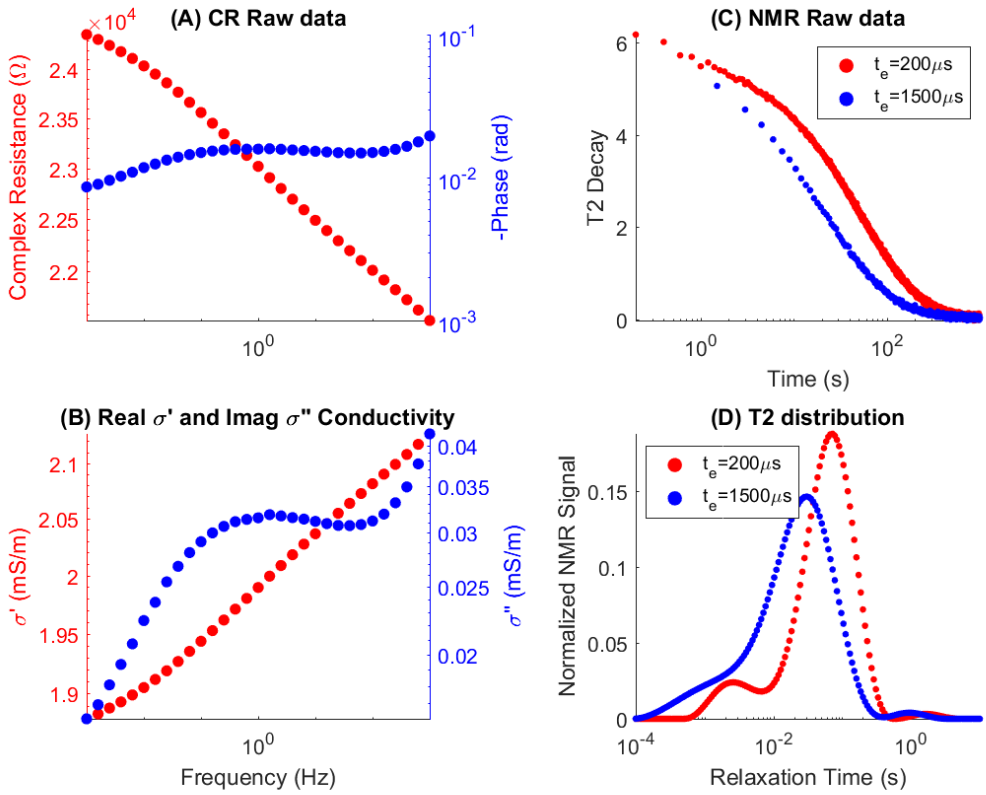

B.1 Table 58: NAWC-94BR-P-013 Depth below ground surface=26.81 m

Physical properties

Permeability (mD): 0.00339

Gravimetric Porosity (%): 14.1

Surface area normalized by pore volume (S_{por}) (μm^{-1}): 10.69

Electrical / CR measures

Electrical Formation Factor (F) (unitless):

Imaginary Conductivity at 1Hz (σ''_{1Hz}) (mS/m): 0.0315

Peak relaxation time (τ_{peak}) (s): 0.493

NMR measures

Mean relaxation time echo time=200μs (T_{2ml}@t_e=200μs) (s): 4.66e-02

Peak relaxation time echo time=200μs (T_{2peak}@t_e=200μs) (s): 7.24e-02

Mean relaxation time echo time=1500μs (T_{2ml}@t_e=1500μs) (s): 1.80e-02

Peak relaxation time echo time=1500μs (T_{2peak}@t_e=1500μs) (s): 3.02e-02

B.1 Figure 59: NAWC-94BR-P-014

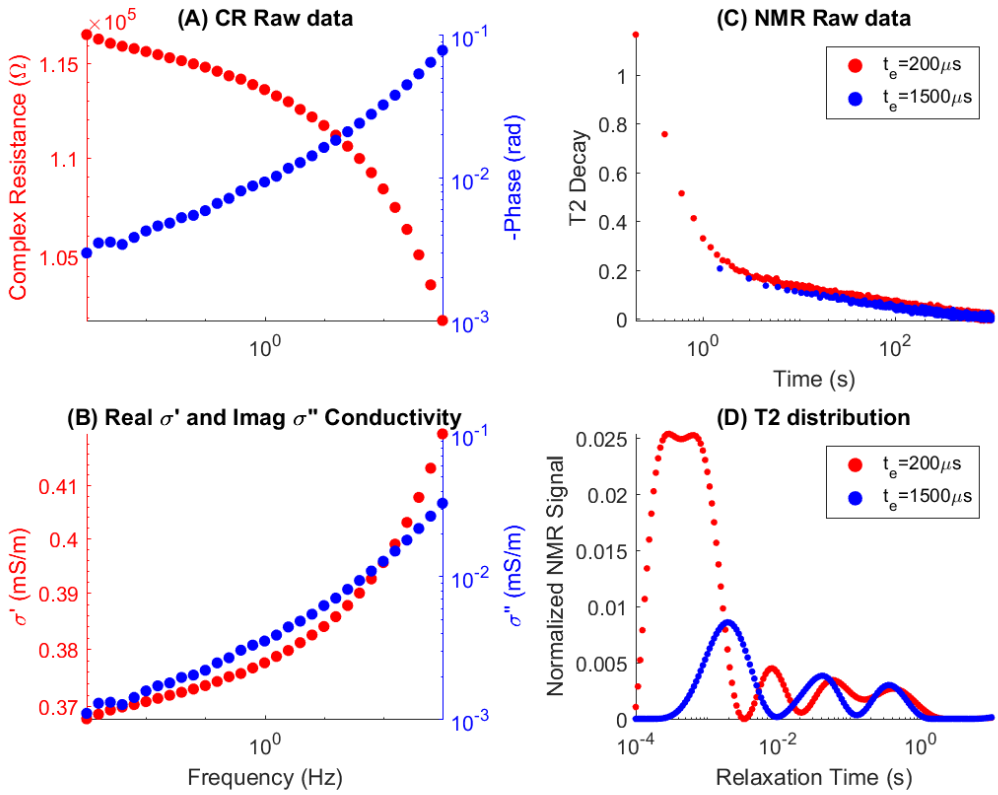

B.1 Table 59: NAWC-94BR-P-014 Depth below ground surface=28 m

Physical properties

Permeability (mD): 5.3e-05

Gravimetric Porosity (%): 3.06

Surface area normalized by pore volume (S_{por}) (μm^{-1}): 68.59

Electrical / CR measures

Electrical Formation Factor (F) (unitless):

Imaginary Conductivity at 1Hz (σ''_{1Hz}) (mS/m): 0.00352

Peak relaxation time (τ_{peak}) (s): NaN

NMR measures

Mean relaxation time echo time=200μs (T_{2ml}@t_e=200μs) (s): 1.14e-03

Peak relaxation time echo time=200μs (T_{2peak}@t_e=200μs) (s): 3.02e-04

Mean relaxation time echo time=1500μs (T_{2ml}@t_e=1500μs) (s): 8.17e-03

Peak relaxation time echo time=1500μs (T_{2peak}@t_e=1500μs) (s): 2.00e-03

B.1 Figure 60: NAWC-94BR-P-015

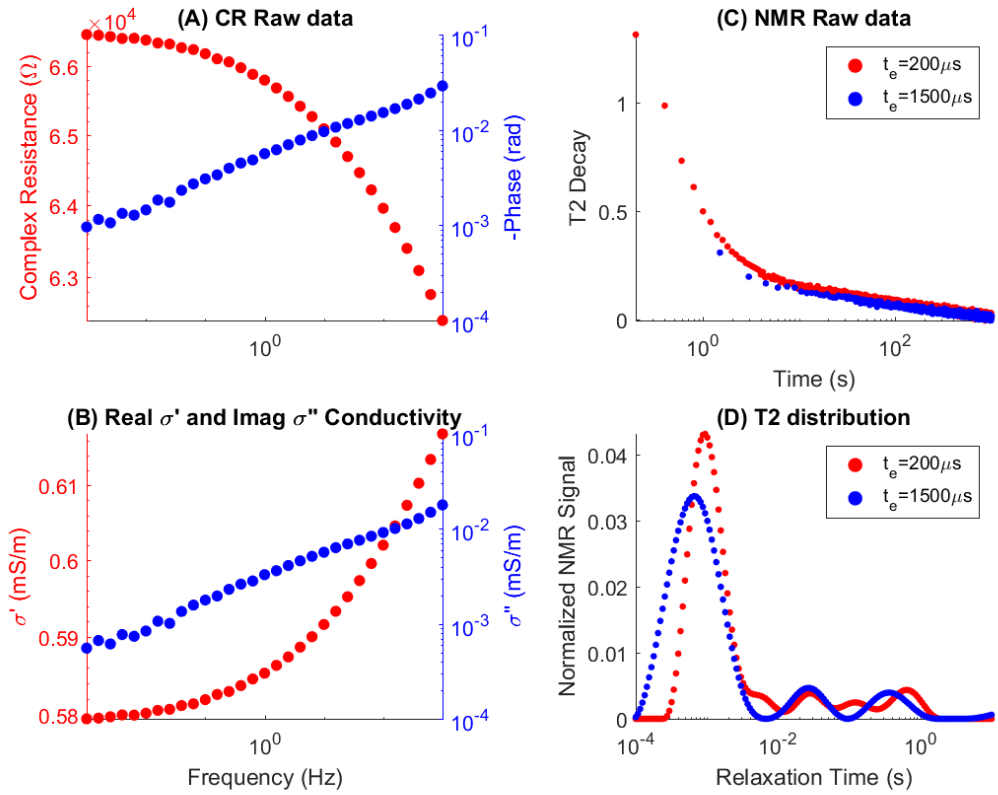

B.1 Table 60: NAWC-94BR-P-015 Depth below ground surface=29.34 m

Physical properties

Permeability (mD): 6.23e-05

Gravimetric Porosity (%): 2.64

Surface area normalized by pore volume (S_{por}) (μm^{-1}): 346.3

Electrical / CR measures

Electrical Formation Factor (F) (unitless): 1475

Imaginary Conductivity at 1Hz (σ''_{1Hz}) (mS/m): 0.00329

Peak relaxation time (τ_{peak}) (s): NaN

NMR measures

Mean relaxation time echo time=200μs (T_{2ml}@t_e=200μs) (s): 2.44e-03

Peak relaxation time echo time=200μs (T_{2peak}@t_e=200μs) (s): 9.12e-04

Mean relaxation time echo time=1500μs (T_{2ml}@t_e=1500μs) (s): 1.38e-03

Peak relaxation time echo time=1500μs (T_{2peak}@t_e=1500μs) (s): 6.61e-04

B.1 Figure 61: NAWC-94BR-P-016

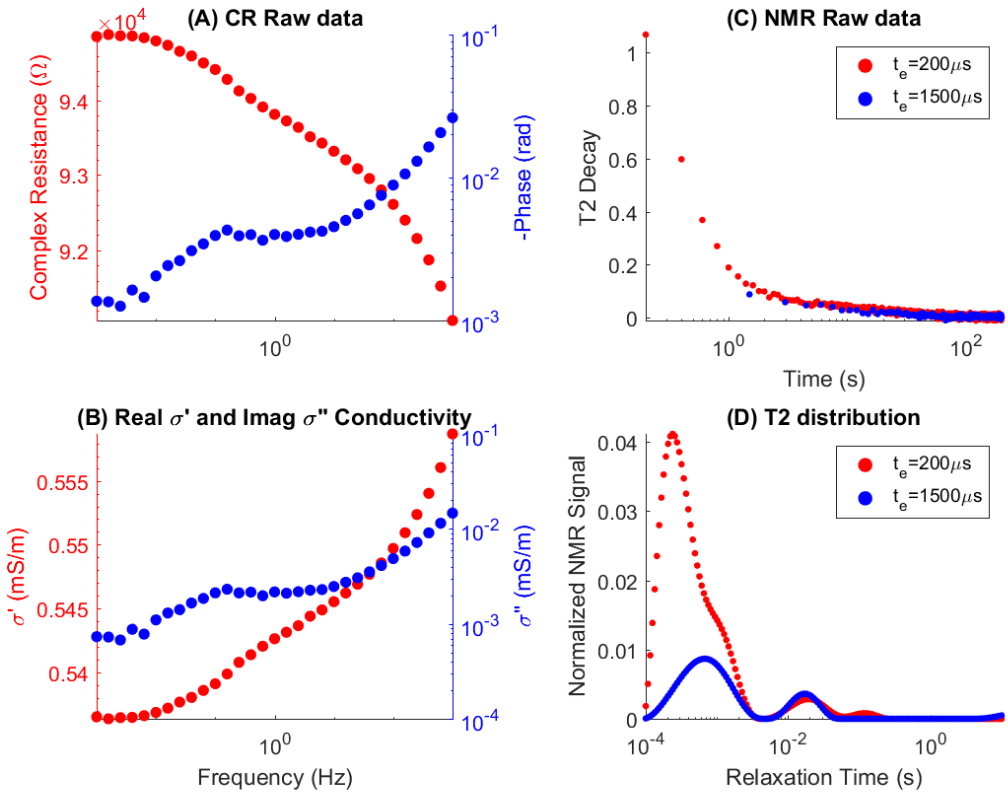

B.1 Table 61: NAWC-94BR-P-016 Depth below ground surface=31.42 m

Physical properties

Permeability (mD): 0.000154

Gravimetric Porosity (%): 1.52

Surface area normalized by pore volume (S_{por}) (μm^{-1}): 377.5

Electrical / CR measures

Electrical Formation Factor (F) (unitless):

Imaginary Conductivity at 1Hz (σ''_{1Hz}) (mS/m): 0.00217

Peak relaxation time (τ_{peak}) (s): NaN

NMR measures

Mean relaxation time echo time=200μs (T_{2ml}@t_e=200μs) (s): 4.81e-04

Peak relaxation time echo time=200μs (T_{2peak}@t_e=200μs) (s): 2.40e-04

Mean relaxation time echo time=1500μs (T_{2ml}@t_e=1500μs) (s): 1.27e-03

Peak relaxation time echo time=1500μs (T_{2peak}@t_e=1500μs) (s): 6.61e-04

B.1 Figure 62: NAWC-94BR-P-017

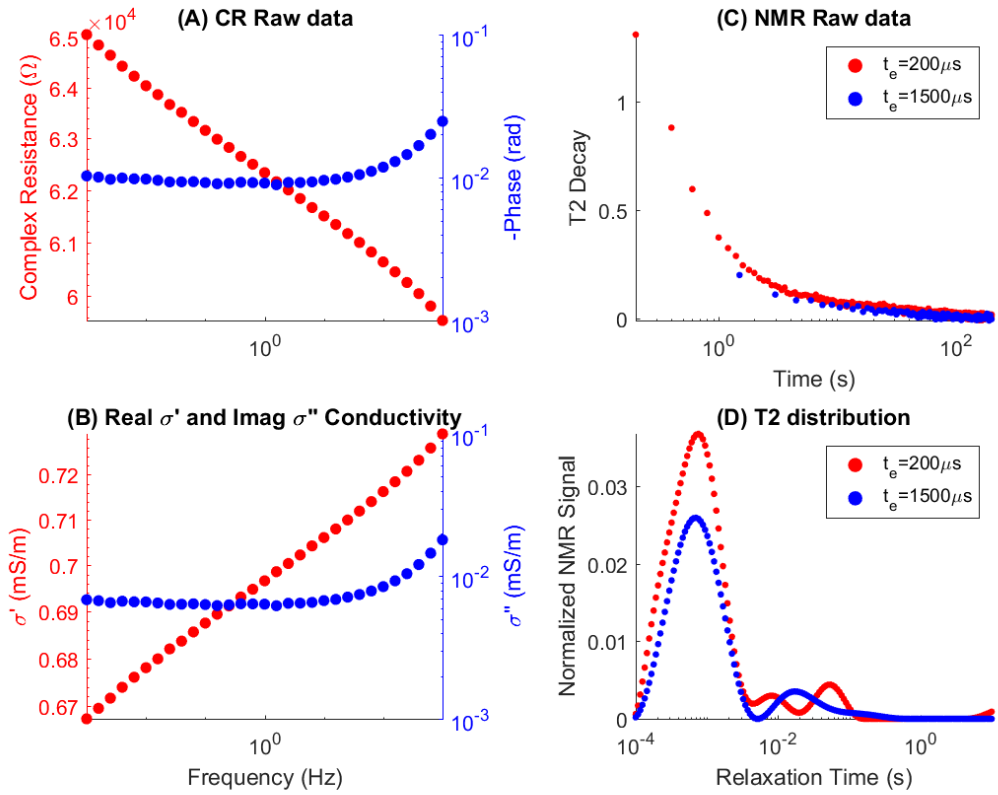

B.1 Table 62: NAWC-94BR-P-017 Depth below ground surface=32.72 m

Physical properties

Permeability (mD): 3.77e-05

Gravimetric Porosity (%): 2.43

Surface area normalized by pore volume (S_{por}) (μm^{-1}): 288.1

Electrical / CR measures

Electrical Formation Factor (F) (unitless): 1719

Imaginary Conductivity at 1Hz (σ''_{1Hz}) (mS/m): 0.00638

Peak relaxation time (τ_{peak}) (s): NaN

NMR measures

Mean relaxation time echo time=200μs (T_{2ml}@t_e=200μs) (s): 9.28e-04

Peak relaxation time echo time=200μs (T_{2peak}@t_e=200μs) (s): 7.59e-04

Mean relaxation time echo time=1500μs (T_{2ml}@t_e=1500μs) (s): 1.00e-03

Peak relaxation time echo time=1500μs (T_{2peak}@t_e=1500μs) (s): 6.92e-04

B.1 Figure 63: NAWC-94BR-P-018

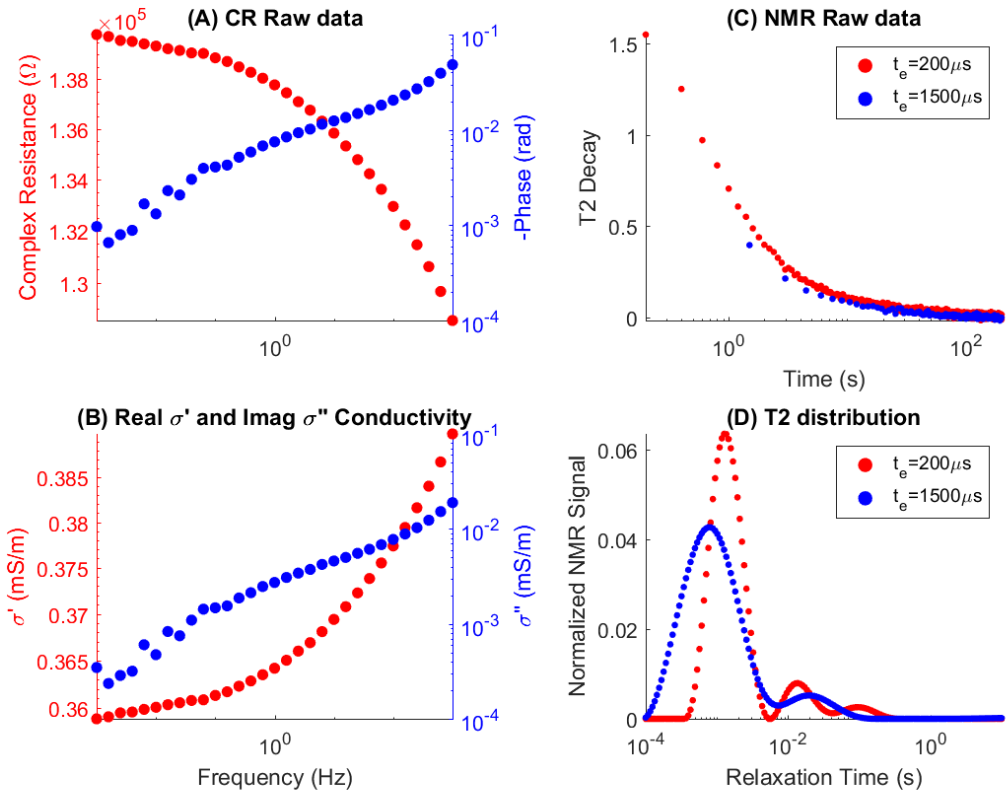

B.1 Table 63: NAWC-94BR-P-018 Depth below ground surface=33.14 m

Physical properties

Permeability (mD): 3.04e-05

Gravimetric Porosity (%): 2.73

Surface area normalized by pore volume (S_{por}) (μm^{-1}): 384.4

Electrical / CR measures

Electrical Formation Factor (F) (unitless): 1533

Imaginary Conductivity at 1Hz (σ''_{1Hz}) (mS/m): 0.00273

Peak relaxation time (τ_{peak}) (s): NaN

NMR measures

Mean relaxation time echo time=200μs (T_{2ml}@t_e=200μs) (s): 1.94e-03

Peak relaxation time echo time=200μs (T_{2peak}@t_e=200μs) (s): 1.32e-03

Mean relaxation time echo time=1500μs (T_{2ml}@t_e=1500μs) (s): 1.08e-03

Peak relaxation time echo time=1500μs (T_{2peak}@t_e=1500μs) (s): 7.94e-04

B.1 Figure 64: NAWC-94BR-P-020

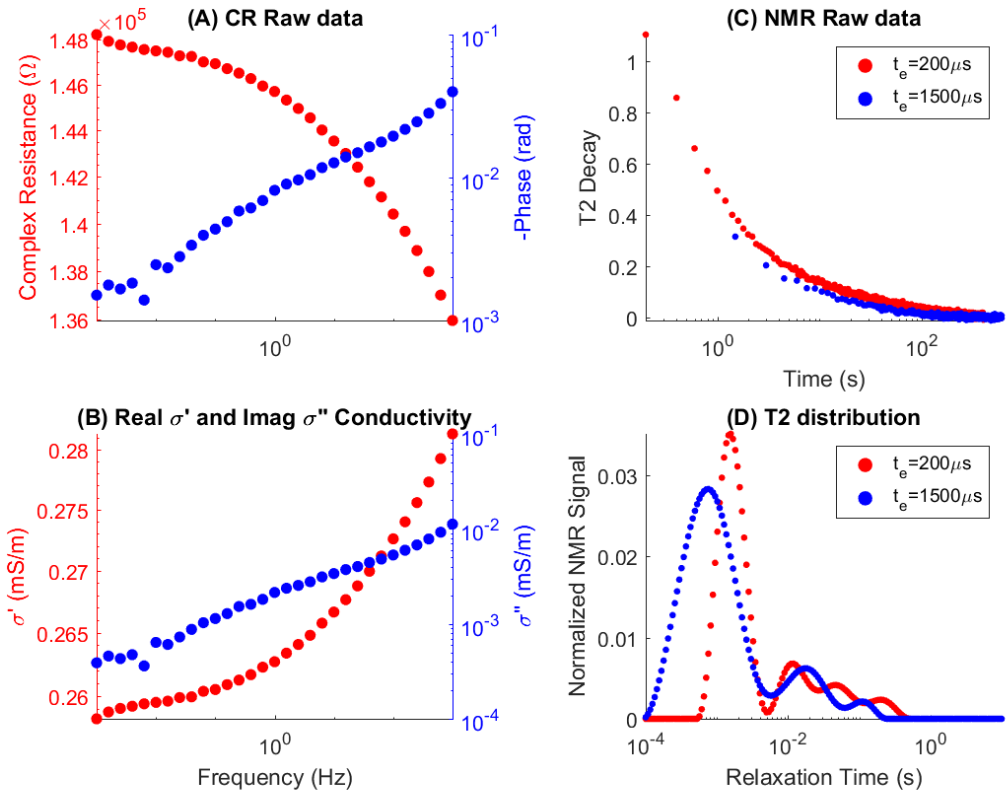

B.1 Table 64: NAWC-94BR-P-020 Depth below ground surface=35.46 m

Physical properties

Permeability (mD): 5.51e-05

Gravimetric Porosity (%): 2.23

Surface area normalized by pore volume (S_{por}) (μm^{-1}): 444.2

Electrical / CR measures

Electrical Formation Factor (F) (unitless): 1996

Imaginary Conductivity at 1Hz (σ''_{1Hz}) (mS/m): 0.00214

Peak relaxation time (τ_{peak}) (s): NaN

NMR measures

Mean relaxation time echo time=200μs (T_{2ml}@t_e=200μs) (s): 3.64e-03

Peak relaxation time echo time=200μs (T_{2peak}@t_e=200μs) (s): 1.51e-03

Mean relaxation time echo time=1500μs (T_{2ml}@t_e=1500μs) (s): 1.32e-03

Peak relaxation time echo time=1500μs (T_{2peak}@t_e=1500μs) (s): 7.59e-04

B.1 Figure 65: NAWC-94BR-P-021

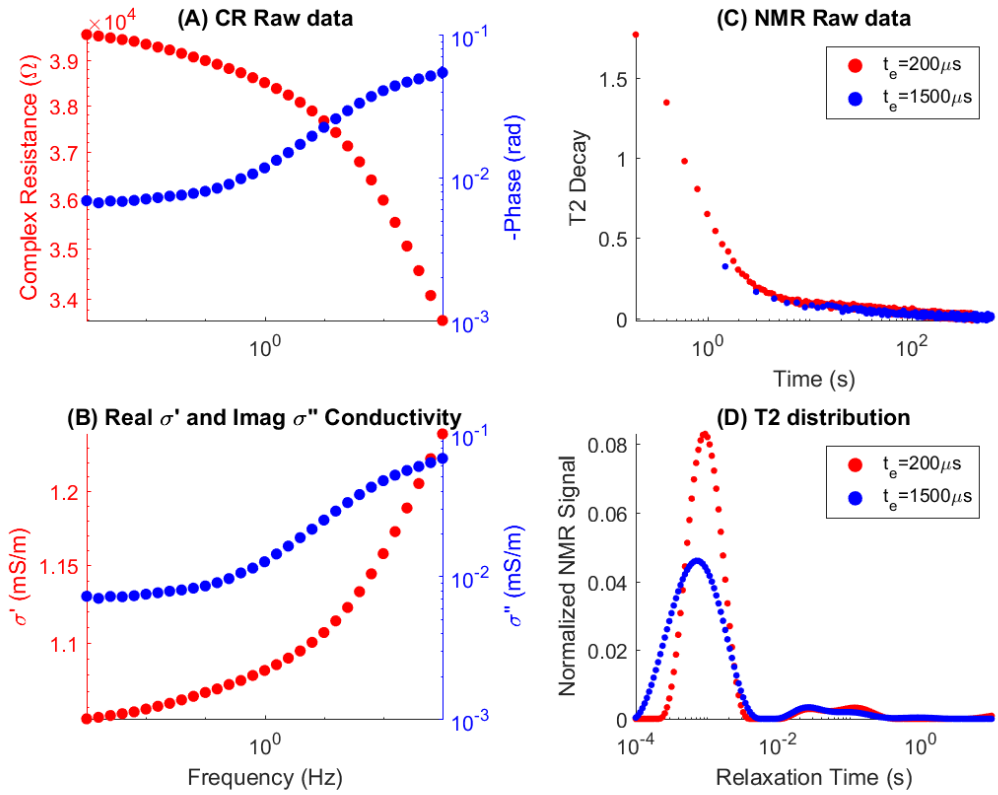

B.1 Table 65: NAWC-94BR-P-021 Depth below ground surface=36.97 m

Physical properties

Permeability (mD): 0.00469

Gravimetric Porosity (%): 4.12

Surface area normalized by pore volume (S_{por}) (μm^{-1}): 71.75

Electrical / CR measures

Electrical Formation Factor (F) (unitless):

Imaginary Conductivity at 1Hz (σ''_{1Hz}) (mS/m): 0.0127

Peak relaxation time (τ_{peak}) (s): NaN

NMR measures

Mean relaxation time echo time=200μs (T_{2ml}@t_e=200μs) (s): 1.23e-03

Peak relaxation time echo time=200μs (T_{2peak}@t_e=200μs) (s): 9.12e-04

Mean relaxation time echo time=1500μs (T_{2ml}@t_e=1500μs) (s): 9.44e-04

Peak relaxation time echo time=1500μs (T_{2peak}@t_e=1500μs) (s): 7.24e-04

B.1 Figure 66: NAWC-94BR-P-022

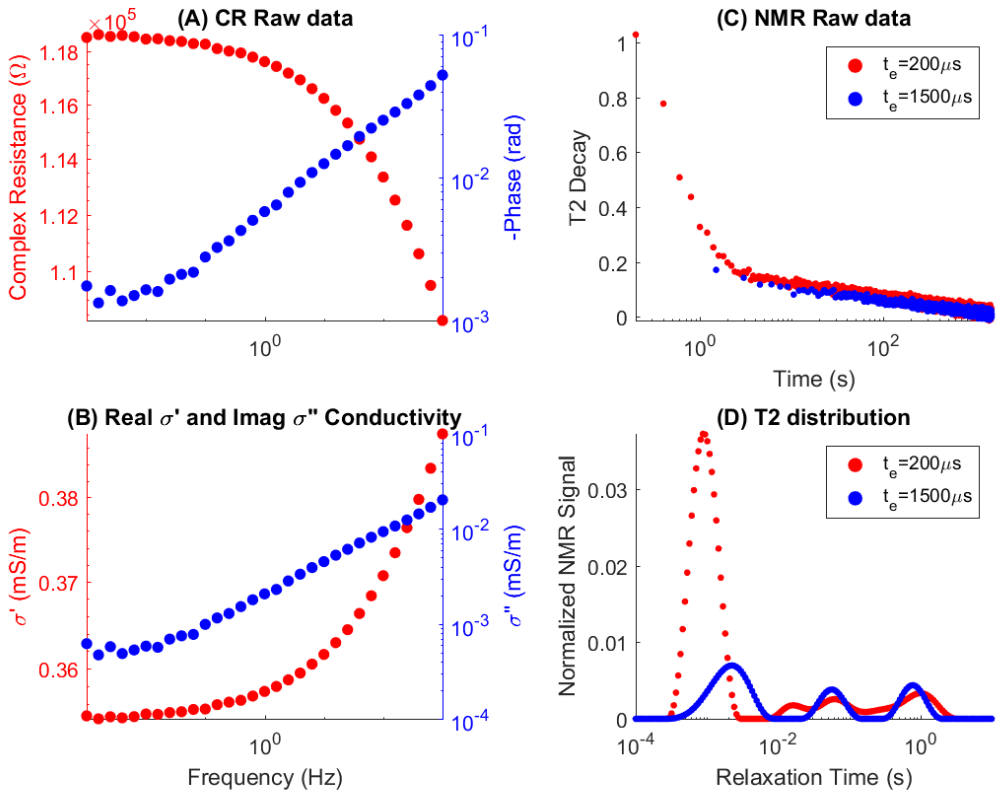

B.1 Table 66: NAWC-94BR-P-022 Depth below ground surface=37.6 m

Physical properties

Permeability (mD): 0

Gravimetric Porosity (%): 1.53

Surface area normalized by pore volume (S_{por}) (μm^{-1}): NaN

Electrical / CR measures

Electrical Formation Factor (F) (unitless):

Imaginary Conductivity at 1Hz (σ''_{1Hz}) (mS/m): 0.00207

Peak relaxation time (τ_{peak}) (s): NaN

NMR measures

Mean relaxation time echo time=200μs (T_{2ml}@t_e=200μs) (s): 2.58e-03

Peak relaxation time echo time=200μs (T_{2peak}@t_e=200μs) (s): 9.12e-04

Mean relaxation time echo time=1500μs (T_{2ml}@t_e=1500μs) (s): 1.45e-02

Peak relaxation time echo time=1500μs (T_{2peak}@t_e=1500μs) (s): 2.19e-03

B.1 Figure 67: NAWC-94BR-P-023

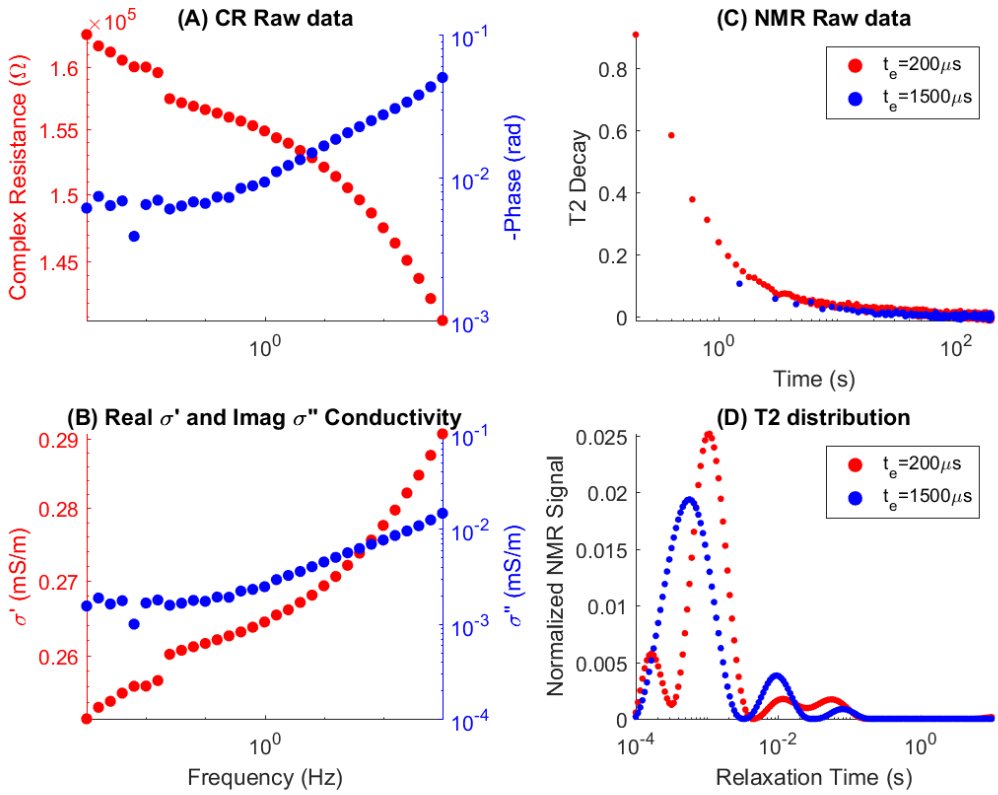

B.1 Table 67: NAWC-94BR-P-023 Depth below ground surface=38.88 m

Physical properties

Permeability (mD): 0

Gravimetric Porosity (%): 2.45

Surface area normalized by pore volume (S_{por}) (μm^{-1}): NaN

Electrical / CR measures

Electrical Formation Factor (F) (unitless): 4553

Imaginary Conductivity at 1Hz (σ''_{1Hz}) (mS/m): 0.00246

Peak relaxation time (τ_{peak}) (s): NaN

NMR measures

Mean relaxation time echo time=200μs (T_{2ml}@t_e=200μs) (s): 1.23e-03

Peak relaxation time echo time=200μs (T_{2peak}@t_e=200μs) (s): 1.05e-03

Mean relaxation time echo time=1500μs (T_{2ml}@t_e=1500μs) (s): 7.80e-04

Peak relaxation time echo time=1500μs (T_{2peak}@t_e=1500μs) (s): 5.75e-04

B.1 Figure 68: NAWC-94BR-P-024

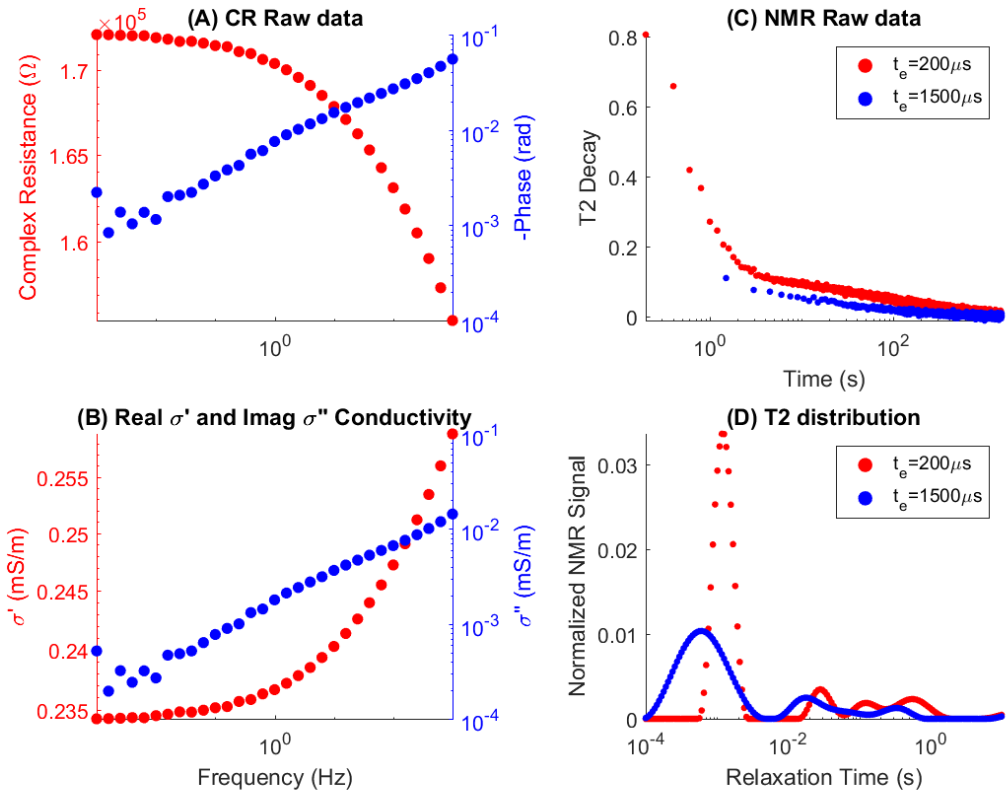

B.1 Table 68: NAWC-94BR-P-024 Depth below ground surface=40.02 m

Physical properties

Permeability (mD): 0

Gravimetric Porosity (%): 1.14

Surface area normalized by pore volume (S_{por}) (μm^{-1}): NaN

Electrical / CR measures

Electrical Formation Factor (F) (unitless): 4754

Imaginary Conductivity at 1Hz (σ''_{1Hz}) (mS/m): 0.00179

Peak relaxation time (τ_{peak}) (s): NaN

NMR measures

Mean relaxation time echo time=200μs (T_{2ml}@t_e=200μs) (s): 3.59e-03

Peak relaxation time echo time=200μs (T_{2peak}@t_e=200μs) (s): 1.20e-03

Mean relaxation time echo time=1500μs (T_{2ml}@t_e=1500μs) (s): 1.53e-03

Peak relaxation time echo time=1500μs (T_{2peak}@t_e=1500μs) (s): 6.03e-04

B.1 Figure 69: NAWC-94BR-P-025

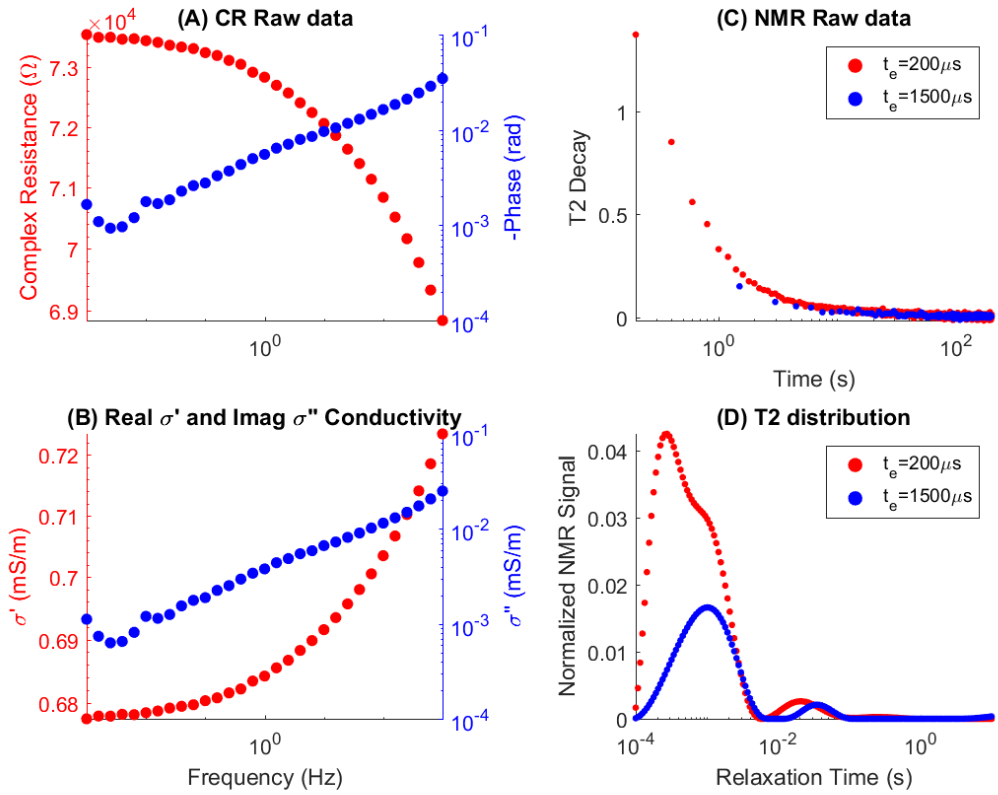

B.1 Table 69: NAWC-94BR-P-025 Depth below ground surface=40.36 m

Physical properties

Permeability (mD): 0

Gravimetric Porosity (%): 2.39

Surface area normalized by pore volume (S_{por}) (μm^{-1}): NaN

Electrical / CR measures

Electrical Formation Factor (F) (unitless): 2727

Imaginary Conductivity at 1Hz (σ''_{1Hz}) (mS/m): 0.00379

Peak relaxation time (τ_{peak}) (s): NaN

NMR measures

Mean relaxation time echo time=200μs (T_{2ml}@t_e=200μs) (s): 5.97e-04

Peak relaxation time echo time=200μs (T_{2peak}@t_e=200μs) (s): 2.75e-04

Mean relaxation time echo time=1500μs (T_{2ml}@t_e=1500μs) (s): 1.13e-03

Peak relaxation time echo time=1500μs (T_{2peak}@t_e=1500μs) (s): 1.00e-03

B.1 Figure 70: NAWC-94BR-P-026

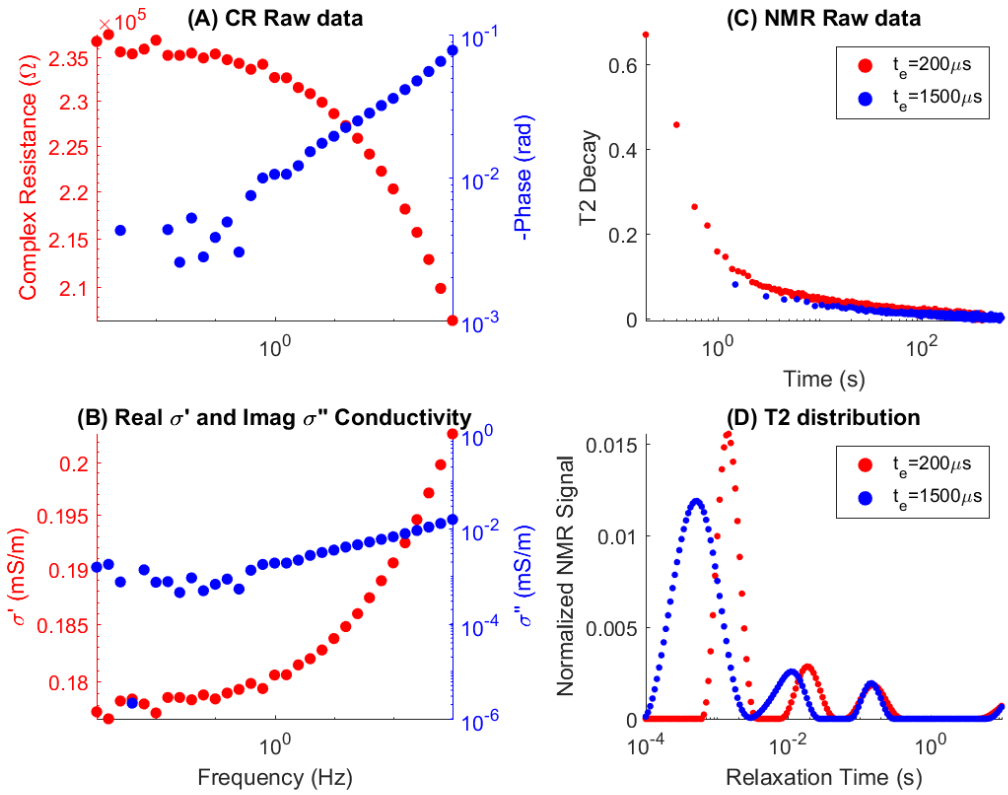

B.1 Table 70: NAWC-94BR-P-026 Depth below ground surface=41.59 m

Physical properties

Permeability (mD): 0

Gravimetric Porosity (%): 1.12

Surface area normalized by pore volume (S_{por}) (μm^{-1}): NaN

Electrical / CR measures

Electrical Formation Factor (F) (unitless): 6677

Imaginary Conductivity at 1Hz (σ''_{1Hz}) (mS/m): 0.0019

Peak relaxation time (τ_{peak}) (s): NaN

NMR measures

Mean relaxation time echo time=200μs (T_{2ml}@t_e=200μs) (s): 3.61e-03

Peak relaxation time echo time=200μs (T_{2peak}@t_e=200μs) (s): 1.45e-03

Mean relaxation time echo time=1500μs (T_{2ml}@t_e=1500μs) (s): 1.01e-03

Peak relaxation time echo time=1500μs (T_{2peak}@t_e=1500μs) (s): 5.25e-04

B.1 Figure 71: NAWC-94BR-P-027

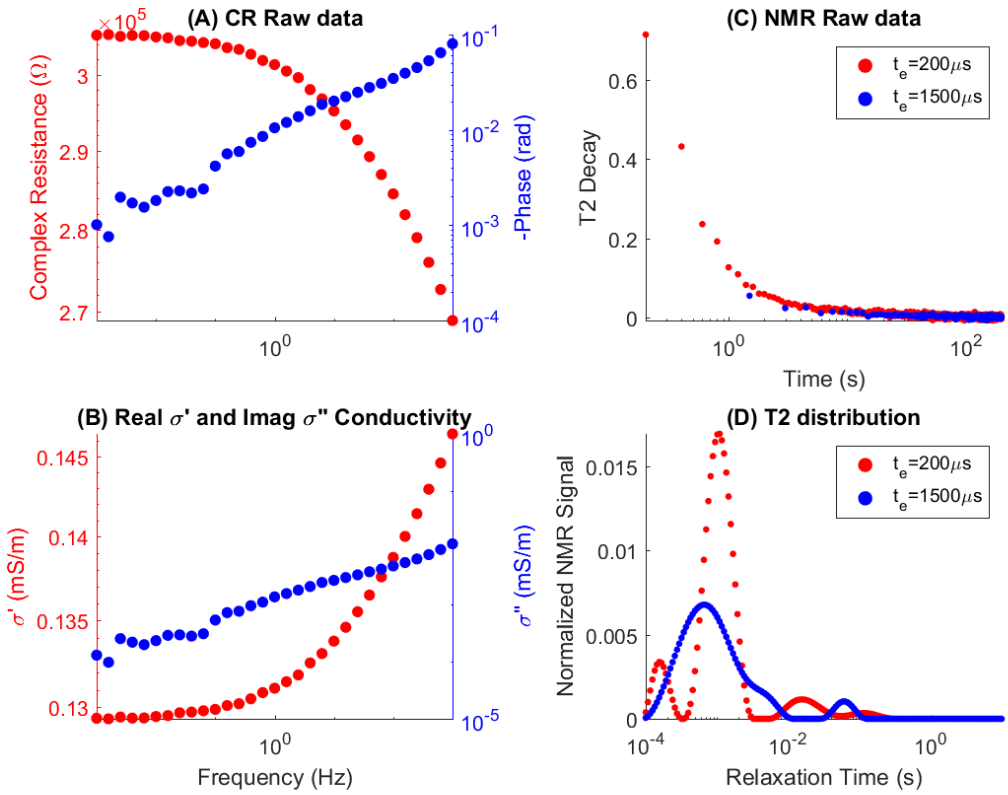

B.1 Table 71: NAWC-94BR-P-027 Depth below ground surface=43.37 m

Physical properties

Permeability (mD): 0.000191

Gravimetric Porosity (%): 0.965

Surface area normalized by pore volume (S_{por}) (μm^{-1}): NaN

Electrical / CR measures

Electrical Formation Factor (F) (unitless): 6766

Imaginary Conductivity at 1Hz (σ''_{1Hz}) (mS/m): 0.00138

Peak relaxation time (τ_{peak}) (s): NaN

NMR measures

Mean relaxation time echo time=200μs (T_{2ml}@t_e=200μs) (s): 1.14e-03

Peak relaxation time echo time=200μs (T_{2peak}@t_e=200μs) (s): 1.05e-03

Mean relaxation time echo time=1500μs (T_{2ml}@t_e=1500μs) (s): 9.75e-04

Peak relaxation time echo time=1500μs (T_{2peak}@t_e=1500μs) (s): 6.61e-04

B.1 Figure 72: NAWC-94BR-P-028

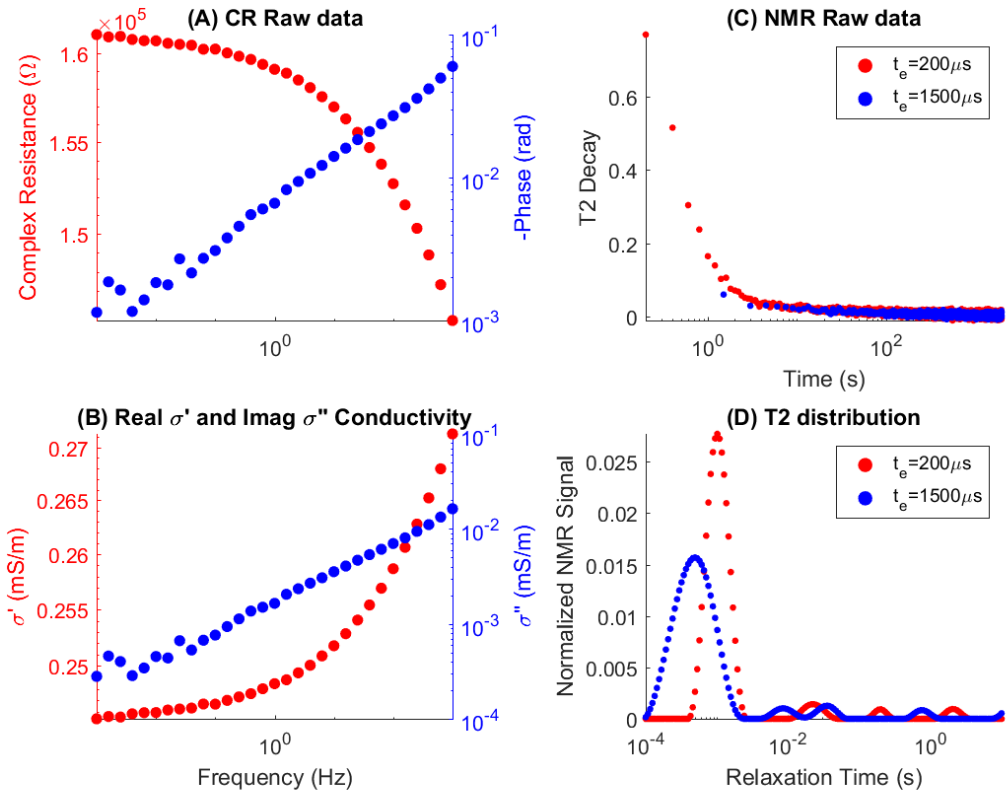

B.1 Table 72: NAWC-94BR-P-028 Depth below ground surface=45.89 m

Physical properties

Permeability (mD): 0.000156

Gravimetric Porosity (%): 1.1

Surface area normalized by pore volume (S_{por}) (μm^{-1}): NaN

Electrical / CR measures

Electrical Formation Factor (F) (unitless): 2460

Imaginary Conductivity at 1Hz (σ''_{1Hz}) (mS/m): 0.00164

Peak relaxation time (τ_{peak}) (s): NaN

NMR measures

Mean relaxation time echo time=200μs (T_{2ml}@t_e=200μs) (s): 1.46e-03

Peak relaxation time echo time=200μs (T_{2peak}@t_e=200μs) (s): 1.00e-03

Mean relaxation time echo time=1500μs (T_{2ml}@t_e=1500μs) (s): 6.86e-04

Peak relaxation time echo time=1500μs (T_{2peak}@t_e=1500μs) (s): 4.79e-04

B.1 Figure 73: NAWC-94BR-P-029

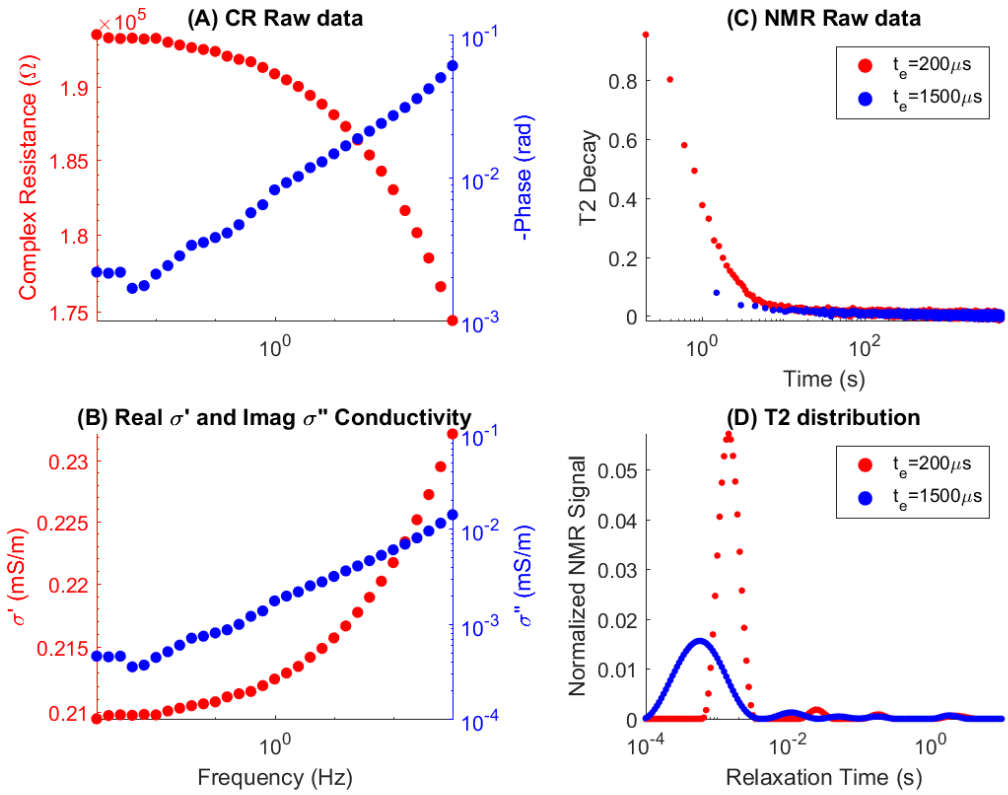

B.1 Table 73: NAWC-94BR-P-029 Depth below ground surface=44.42 m

Physical properties

Permeability (mD): 0

Gravimetric Porosity (%): 1.07

Surface area normalized by pore volume (S_{por}) (μm^{-1}): NaN

Electrical / CR measures

Electrical Formation Factor (F) (unitless): NaN

Imaginary Conductivity at 1Hz (σ''_{1Hz}) (mS/m): 0.00174

Peak relaxation time (τ_{peak}) (s): NaN

NMR measures

Mean relaxation time echo time=200μs (T_{2ml}@t_e=200μs) (s): 1.74e-03

Peak relaxation time echo time=200μs (T_{2peak}@t_e=200μs) (s): 1.45e-03

Mean relaxation time echo time=1500μs (T_{2ml}@t_e=1500μs) (s): 7.78e-04

Peak relaxation time echo time=1500μs (T_{2peak}@t_e=1500μs) (s): 5.75e-04

Appendix B.2: Nuclear magnetic resonance (NMR) T2 cutoff times

This relaxation time (T2) distribution has been used to distinguish regions of immobile fluids (associated with small pores) from mobile fluids (associated with large or well-connected pores) by assigning a time that represents the cutoff between the responses of immobile and mobile porosity (Equation 4.1.2).

Appendix B.2 displays the cumulative T2 distributions for a fully saturated sample (red) and a centrifuged sample (blue). Refer to section 6.4 for centrifuging details. The BFI is indicated by a horizontal cyan line and the T2 cutoff values by a vertical black line. Not all HC and SSFL samples remained intact during centrifuging. These samples are omitted from this Appendix. Centrifuging of several NAWC cores did not produce any free fluid; these are omitted from Appendix B.2. The omitted samples are shown in the following table.

Core Name	Reason for data gap
HC-MP25S-P-005-1V	Broke after low conductivity CR measurements
SSFL-C3-P-027	Missing data
SSFL-RD109-GEO-05	Crumbled during centrifuge
SSFL-RD109-P-04	Broke in half during disassembly
NAWC-94BR-P-004	Minimal fluid extracted during centrifuging
NAWC-94BR-P-009	Minimal fluid extracted during centrifuging
NAWC-94BR-P-010	Minimal fluid extracted during centrifuging
NAWC-94BR-P-020	Minimal fluid extracted during centrifuging
NAWC-94BR-P-021	Minimal fluid extracted during centrifuging
NAWC-94BR-P-022	Minimal fluid extracted during centrifuging
NAWC-94BR-P-023	Minimal fluid extracted during centrifuging
NAWC-94BR-P-024	Minimal fluid extracted during centrifuging
NAWC-94BR-P-025	Minimal fluid extracted during centrifuging
NAWC-94BR-P-026	Minimal fluid extracted during centrifuging
NAWC-94BR-P-027	Minimal fluid extracted during centrifuging
NAWC-94BR-P-028	Minimal fluid extracted during centrifuging
NAWC-94BR-P-029	Minimal fluid extracted during centrifuging

The statistics for the T2 cutoff times per site are as follows:

Site	Mean T2 cutoff (ms)	Standard deviation (ms)
Hydrite	87	161
Santa Susana	28	8
NAWC	9	20

B.2 Figure 1: NMR cumulative T_2 Distributions

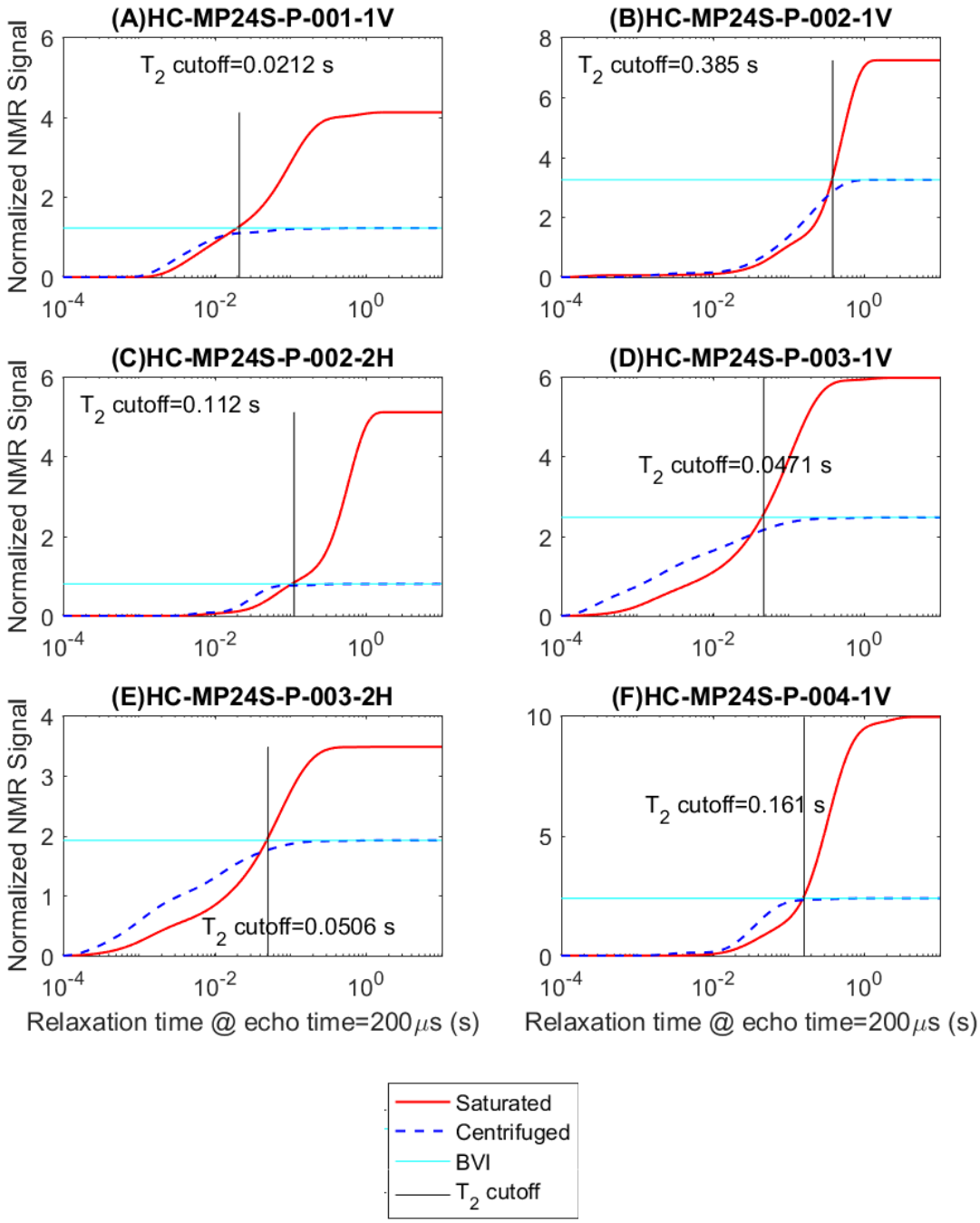

B.2 Figure 2: NMR cumulative T_2 Distributions

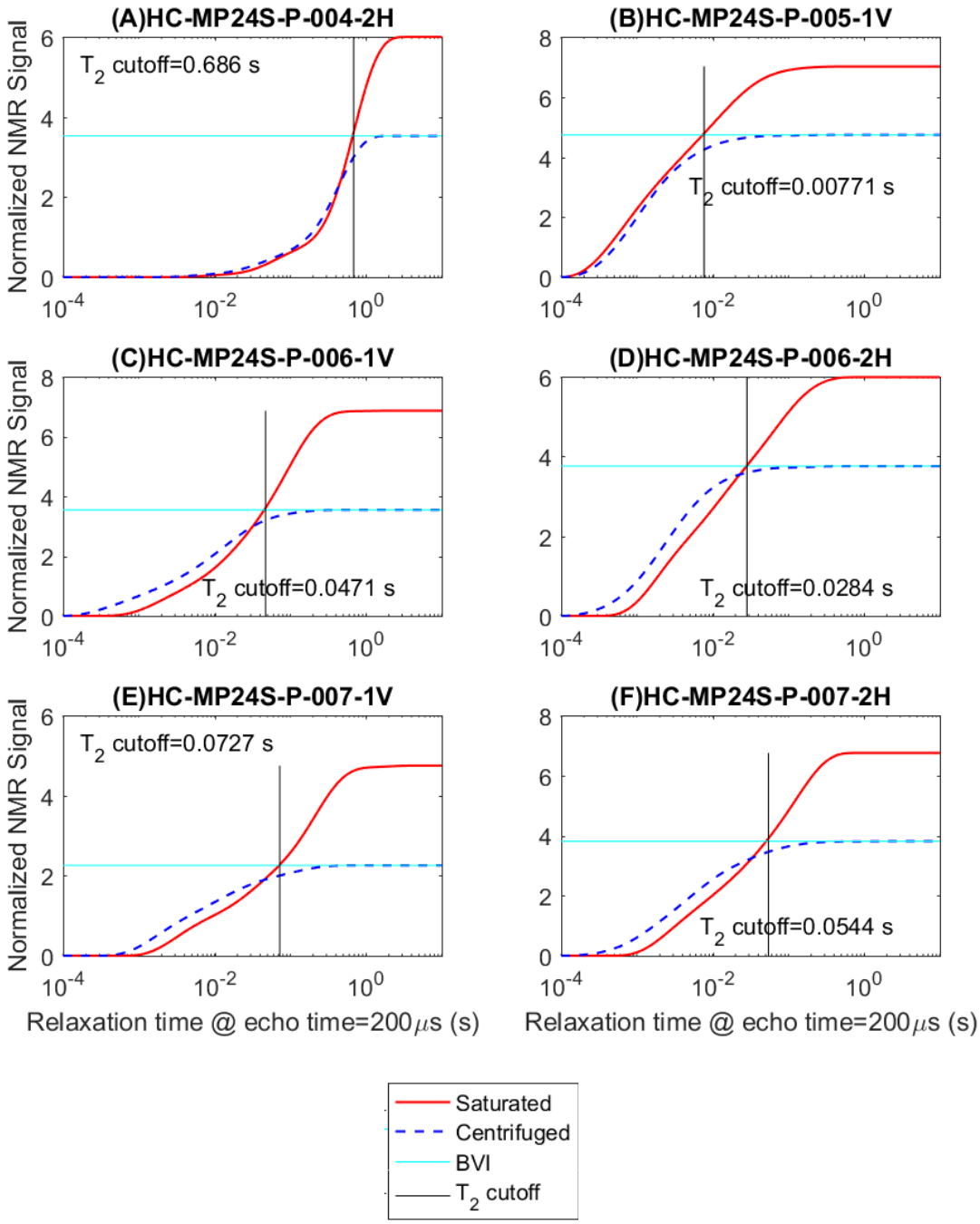

B.2 Figure 3: NMR cumulative T_2 Distributions

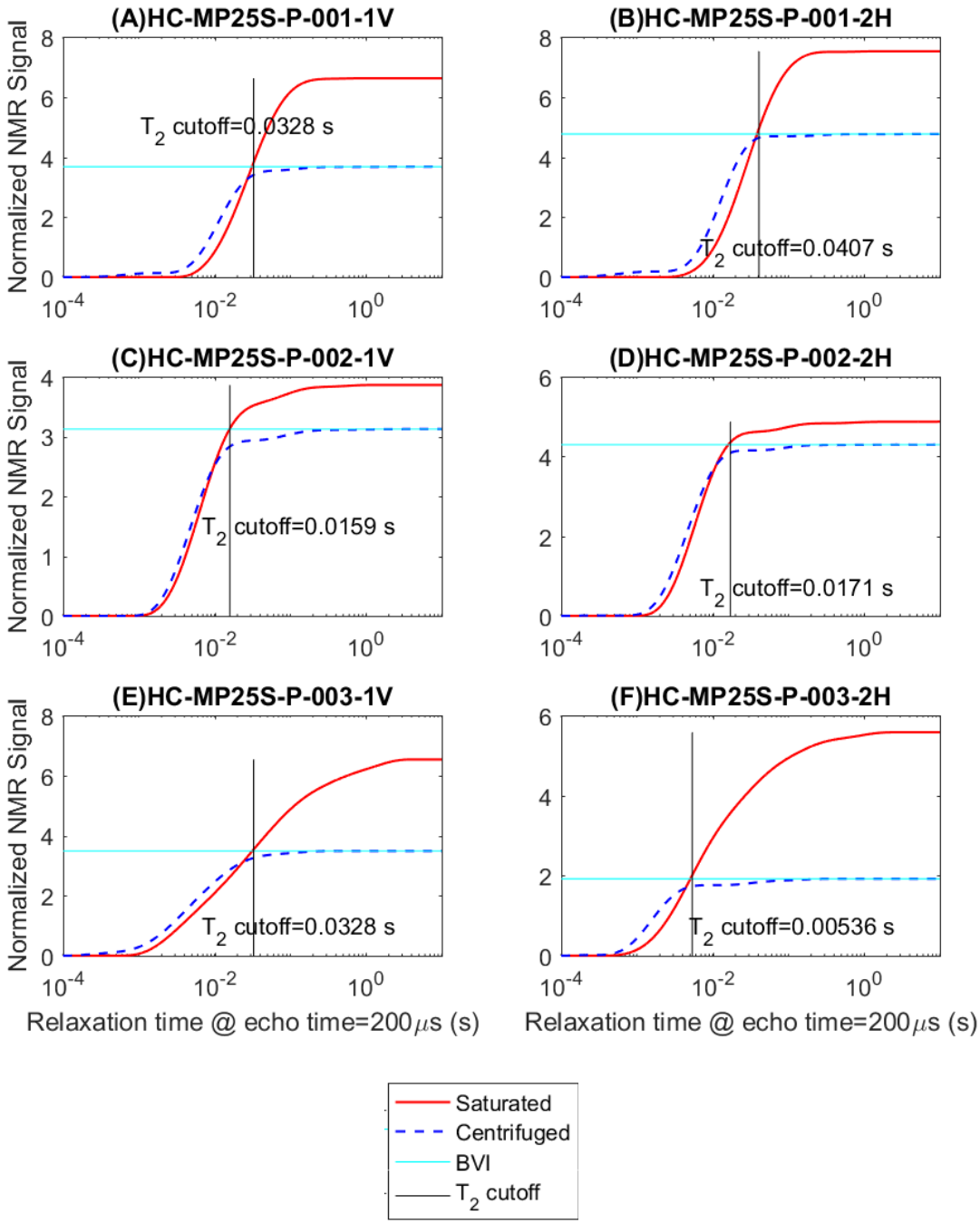

B.2 Figure 4: NMR cumulative T_2 Distributions

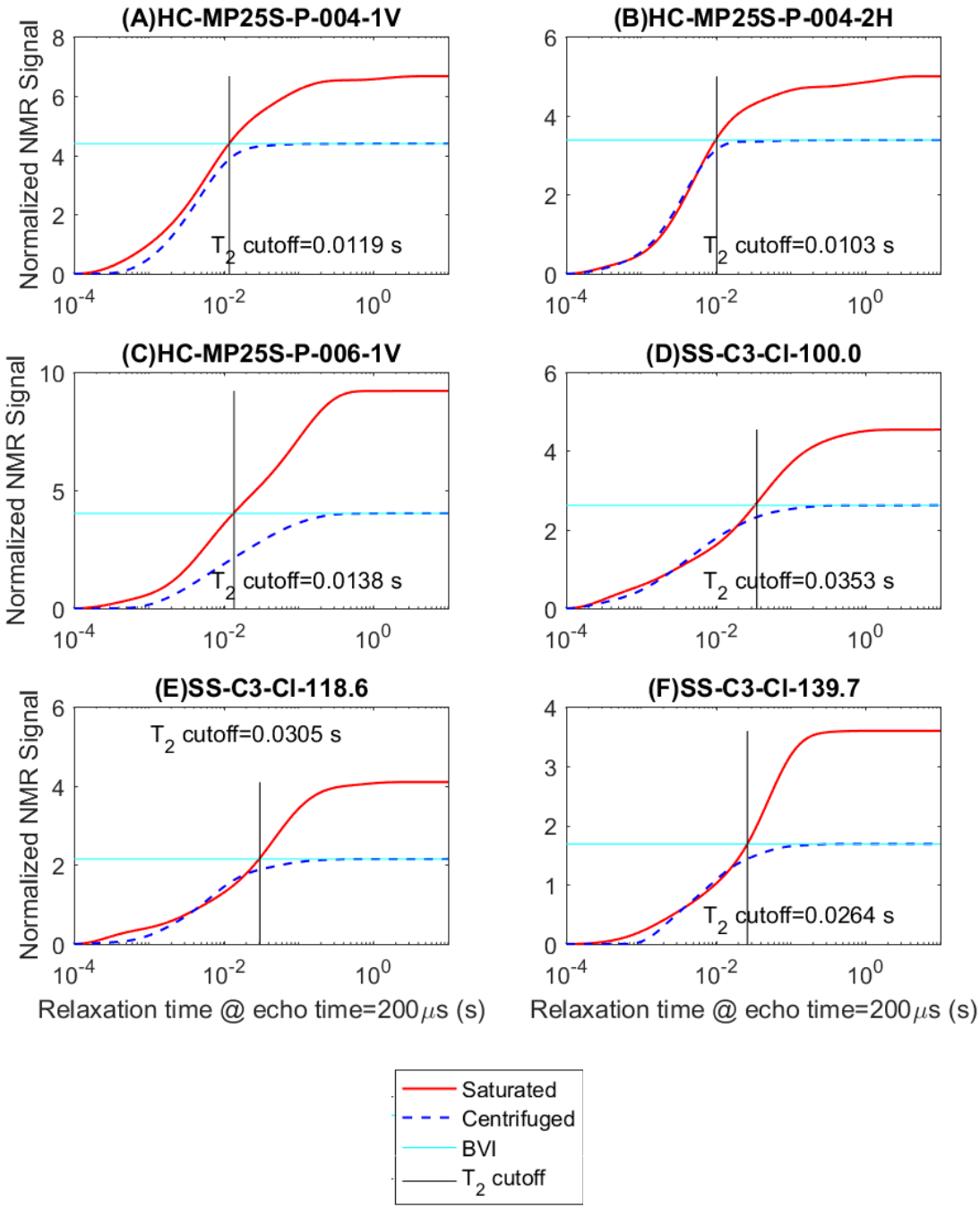

B.2 Figure 5: NMR cumulative T_2 Distributions

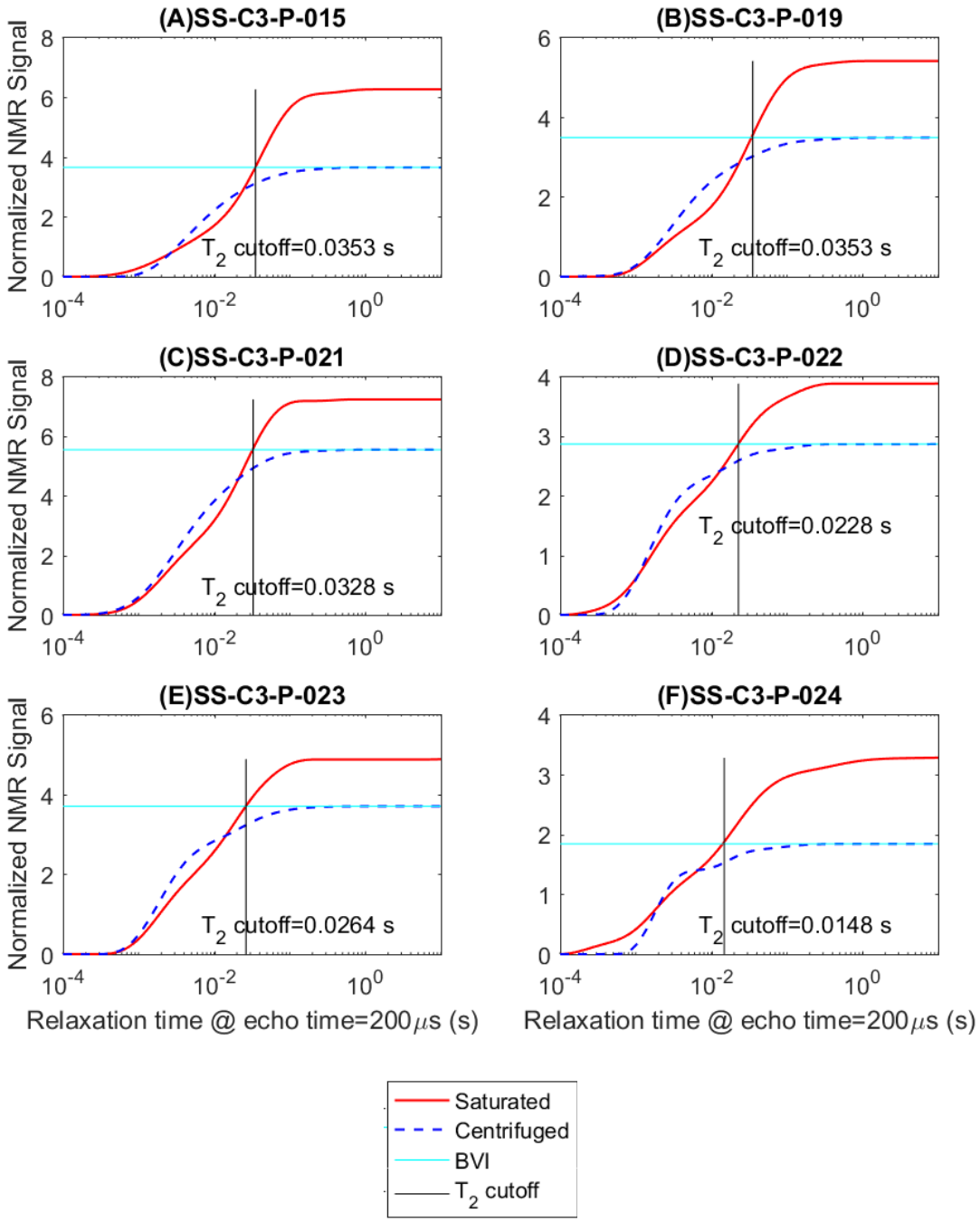

B.2 Figure 6: NMR cumulative T_2 Distributions

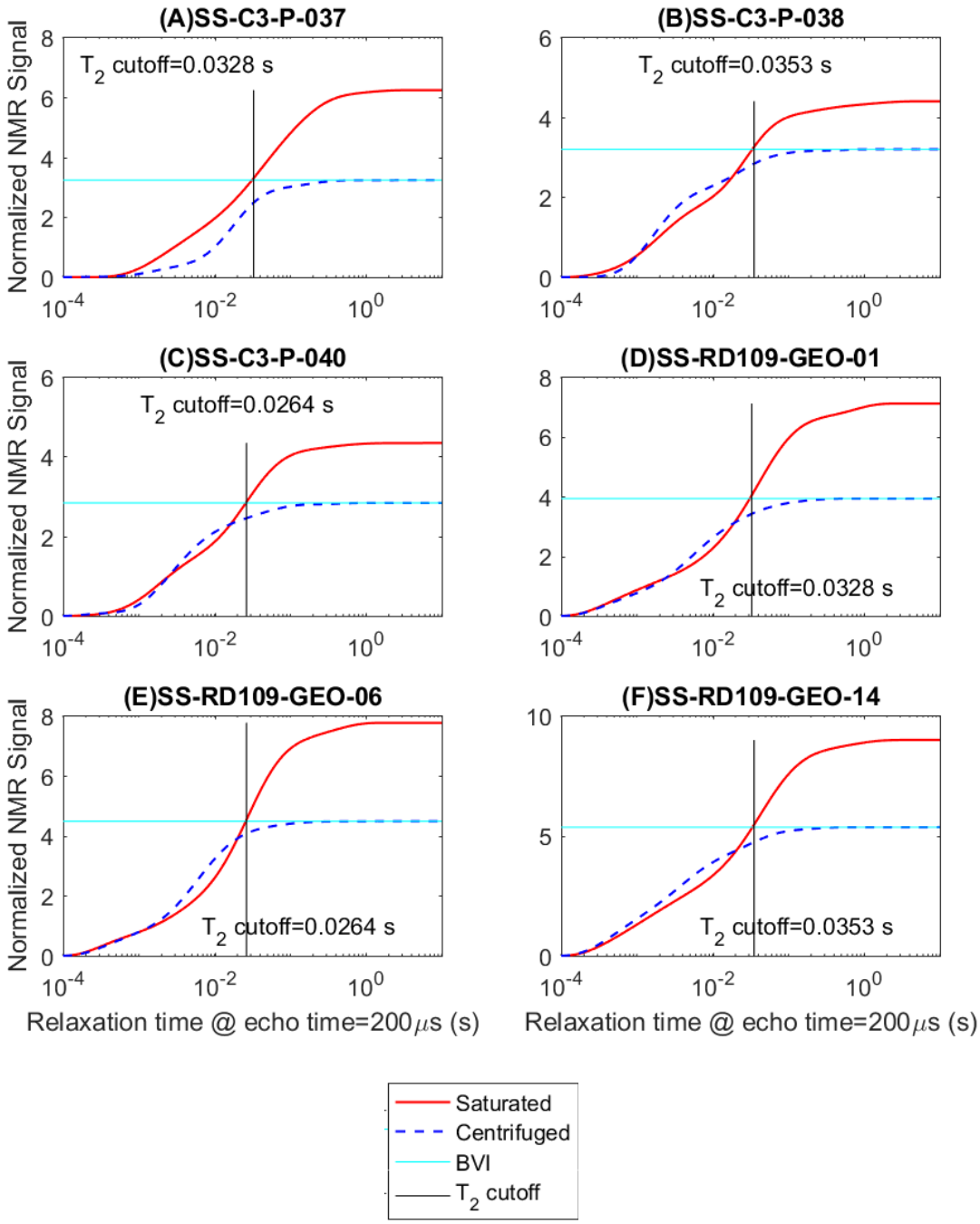

B.2 Figure 7: NMR cumulative T_2 Distributions

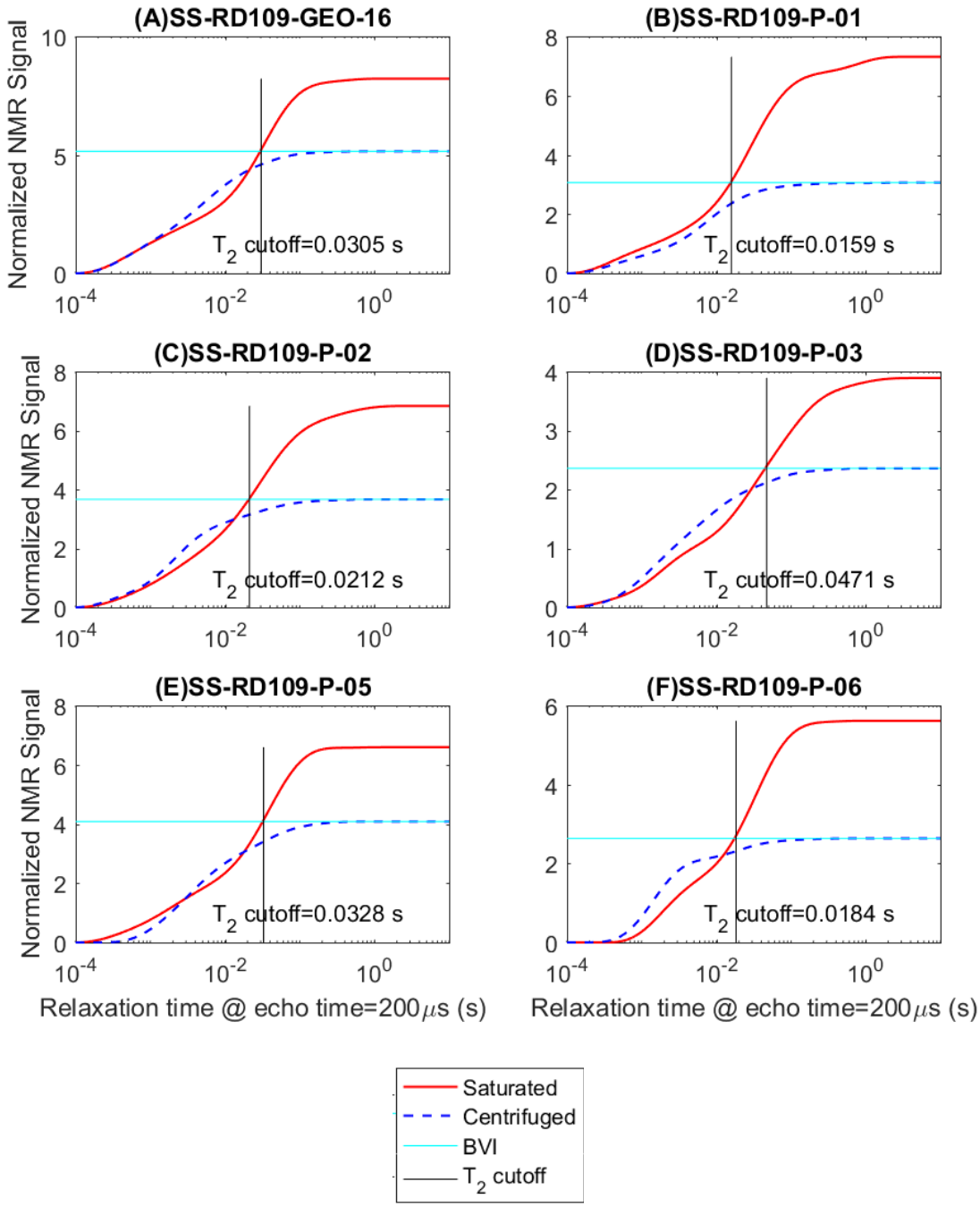

B.2 Figure 8: NMR cumulative T_2 Distributions

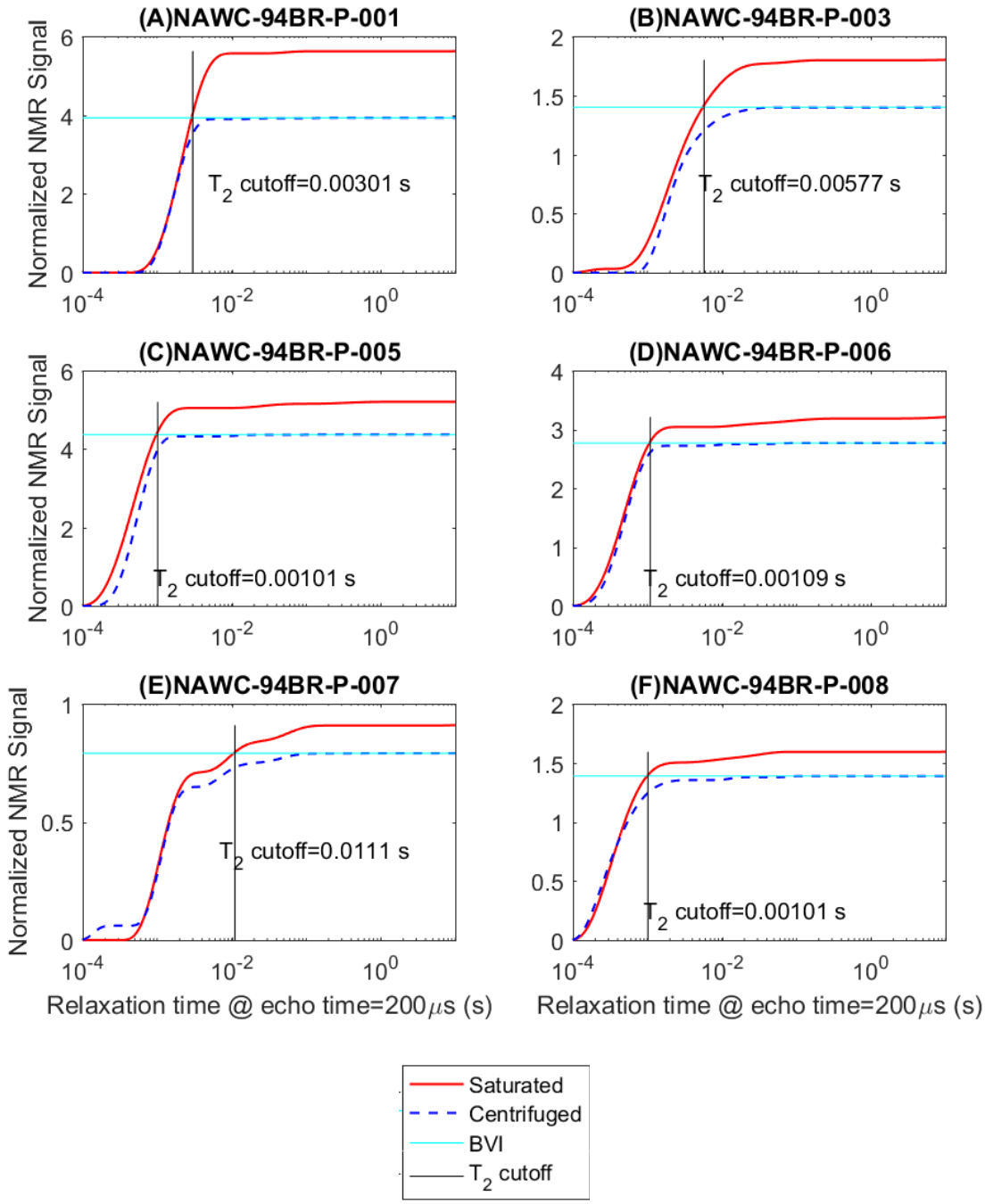

B.2 Figure 9: NMR cumulative T_2 Distributions

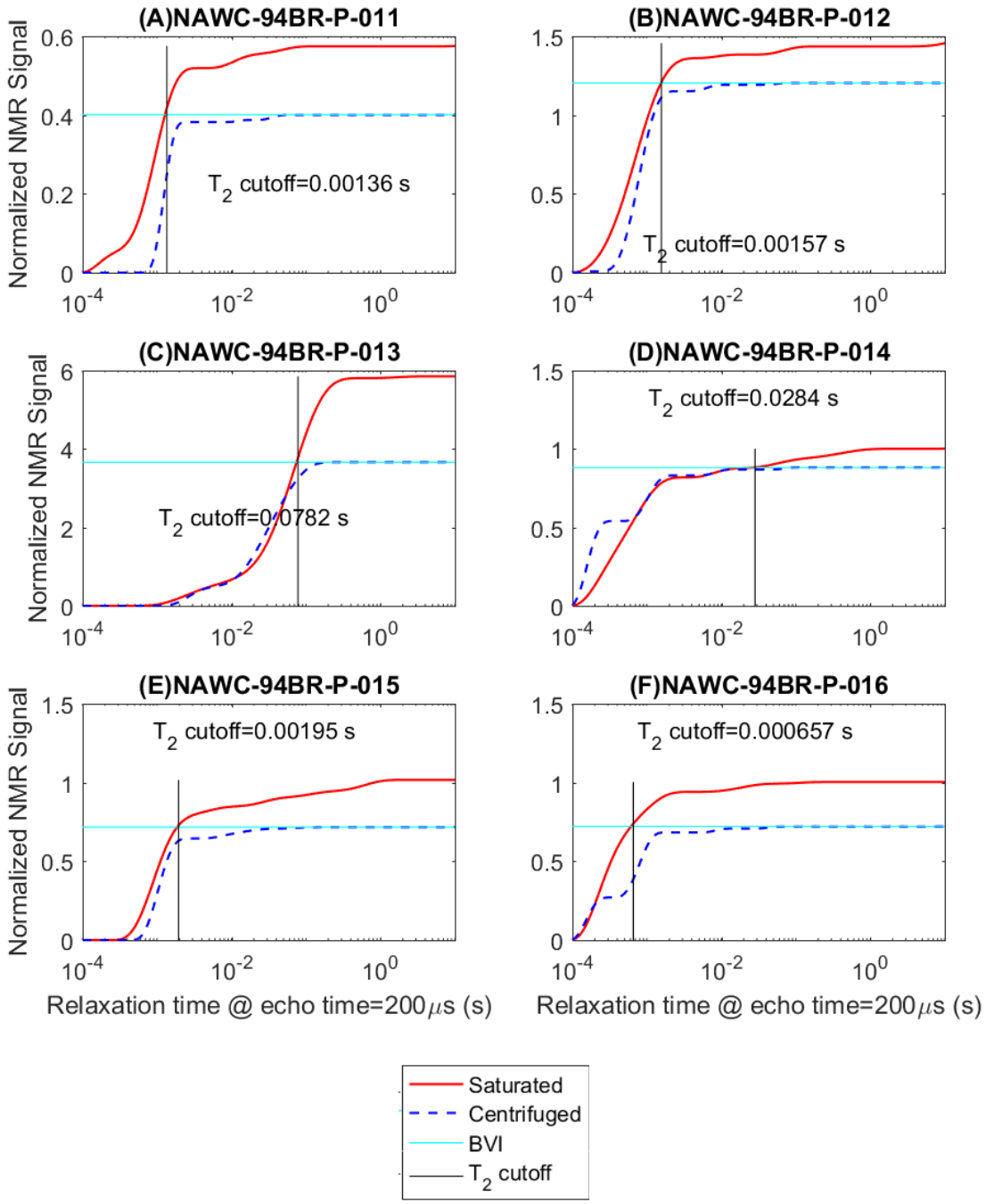

B.2 Figure 10: NMR cumulative T_2 Distributions

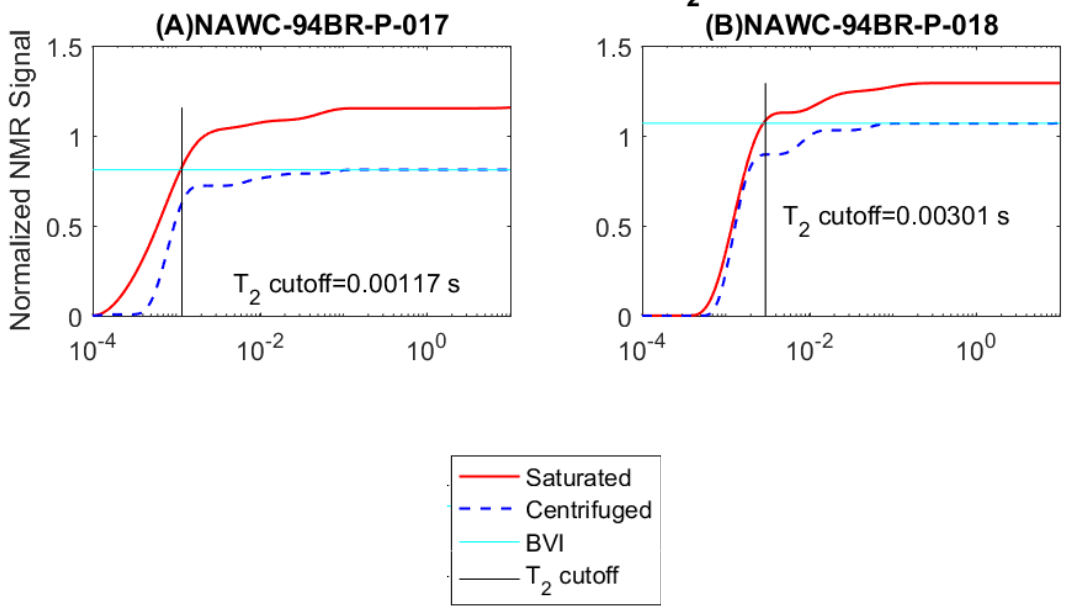

Appendix B.3: Mercury Injection Capillary Pressure (MICP) data

Mercury injection capillary pressure (MICP) data is presented in Appendix B.3 as cumulative intrusion (m^2/g) versus mean pore diameter (μm). For a given injection pressure P and assuming a circular pore opening, mean pore diameter is calculated using the Washburn equation (Washburn, 1921) injection pressure:

$$D = \frac{-4\gamma \cos\theta}{P} \quad \text{(B. 3.1)}$$

where D is the mean pore diameter, γ is the surface tension of mercury and θ is the contact angle of mercury. Given the inverse relationship between D and P in Equation B.3.1, the x-axis (i.e. mean pore diameter) is reversed to better demonstrate the mechanics of the measurement (e.g. cumulative intrusion increases with increasing injection pressures).

Other MICP measures are shown in each figure:

l_c (green filled circle)	The pressure associated with the maximum incremental intrusion. Hydraulically, this is defined as the pore throat diameter at which the entire pore space becomes hydraulically interconnected. Where l_c is not visible on the graph, l_c is equal to r_{50}.
r_{50} (red filled circle)	The pore radius calculated from the pressure at which 50% of the mercury intrusion occurred
r_{70} (blue circle)	The pore radius calculated from the pressure at which 70% of the mercury intrusion occurred

The Katz and Thompson (KT) permeability model (Banavar & Johnson, 1987; Katz & Thompson, 1987) uses l_c to predict permeability k,

$$k = \frac{l_c^2}{cF} \quad \text{(B. 3.2)}$$

where F is the electrical formation factor (unitless) and c is a unitless scaling constant set to 226 (Katz & Thompson, 1986) (refer to Section 4.2.1). Other measures such as r_{50} and r_{70} can also be calibrated in Equation B.3.2 and are shown here for completeness.

Katz and Thompson [1986] equated l_c to the inflection point on the MICP cumulative pore size distribution curve, considered to represent the threshold at which the pore space of a rock becomes hydraulically interconnected (i.e. sufficient fluid saturation for fluid flow). Johnson et al. [1986] reformulated this original model in terms of Λ (μm) and Banavar and Johnson (1987) related l_c to Λ by a scaling constant a. This reformulation results in,

$$k = \frac{\Lambda^2}{8F}. \quad \text{(B 3.3)}$$

Modeling the pore network as a distribution of cylindrical pores of differing radii, Banavar and Johnson (1987) derived two scaling constants a to represent different sizes of pores and multiplied l_c by a to calculate Λ (i.e. $\Lambda = al_c$). Revil et al (2014) equated Equations B.3.2 and B 3.3 with c=226 (Equation B.3.2) to derive a equal to 0.19.

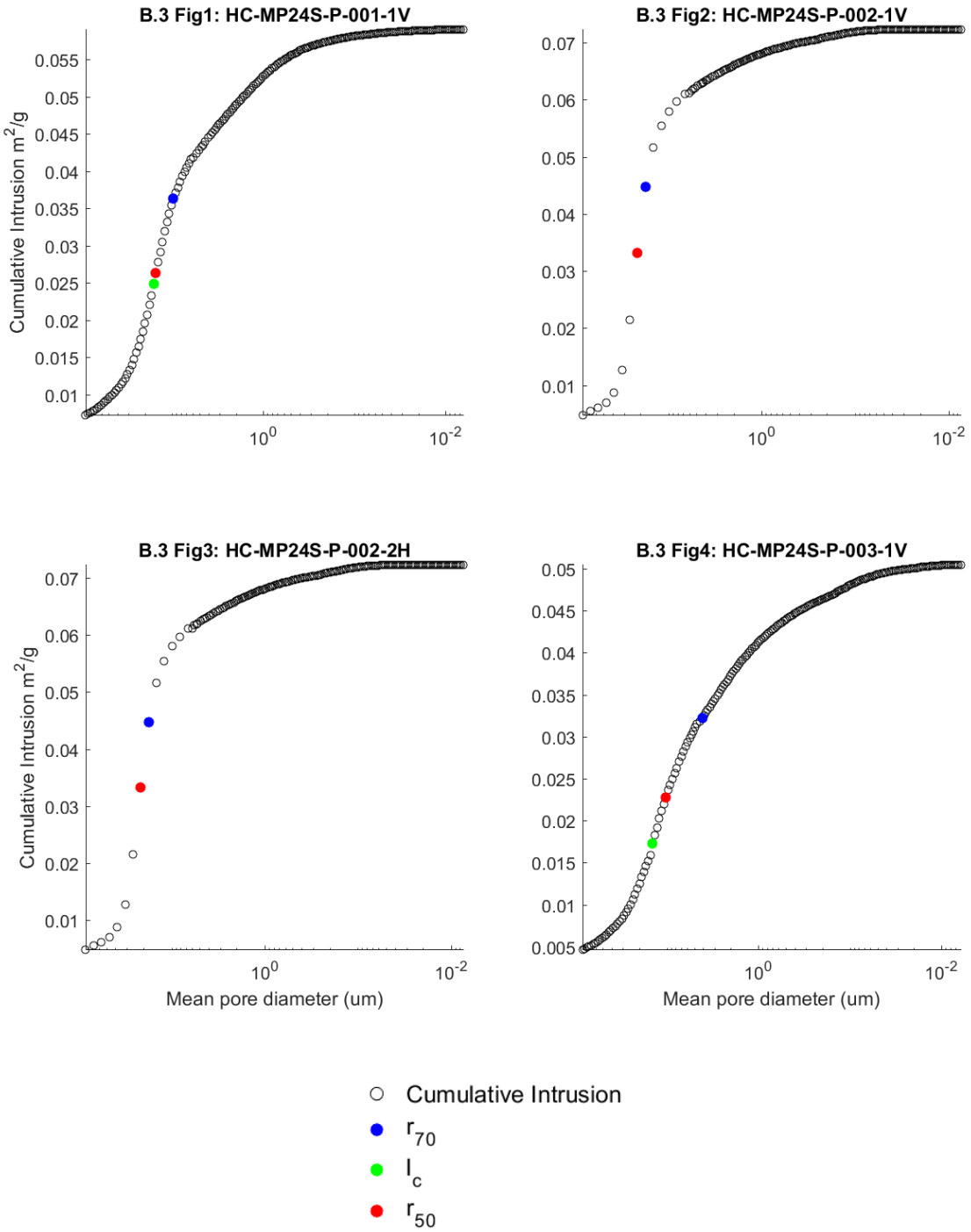
B.3 Fig1: HC-MP24S-P-001-1V
B.3 Fig2: HC-MP24S-P-002-1V
B.3 Fig3: HC-MP24S-P-002-2H
B.3 Fig4: HC-MP24S-P-003-1V
Cumulative Intrusion m2/g
Mean pore diameter (um)
Cumulative Intrusion
r70
lc
r50

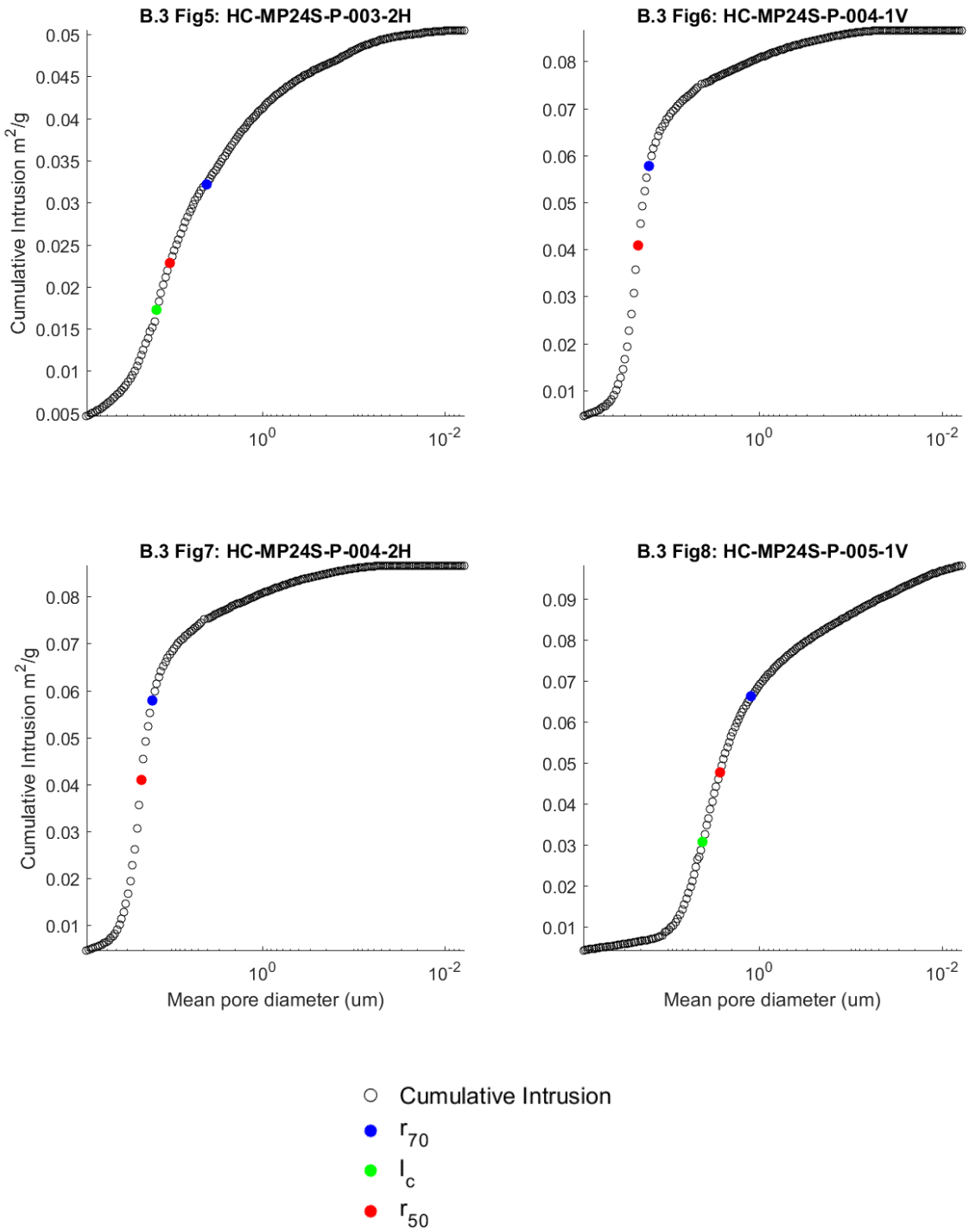
B.3 Fig5: HC-MP24S-P-003-2H
B.3 Fig6: HC-MP24S-P-004-1V
B.3 Fig7: HC-MP24S-P-004-2H
B.3 Fig8: HC-MP24S-P-005-1V
Cumulative Intrusion m2/g
Mean pore diameter (um)
Cumulative Intrusion
r70
lc
r50

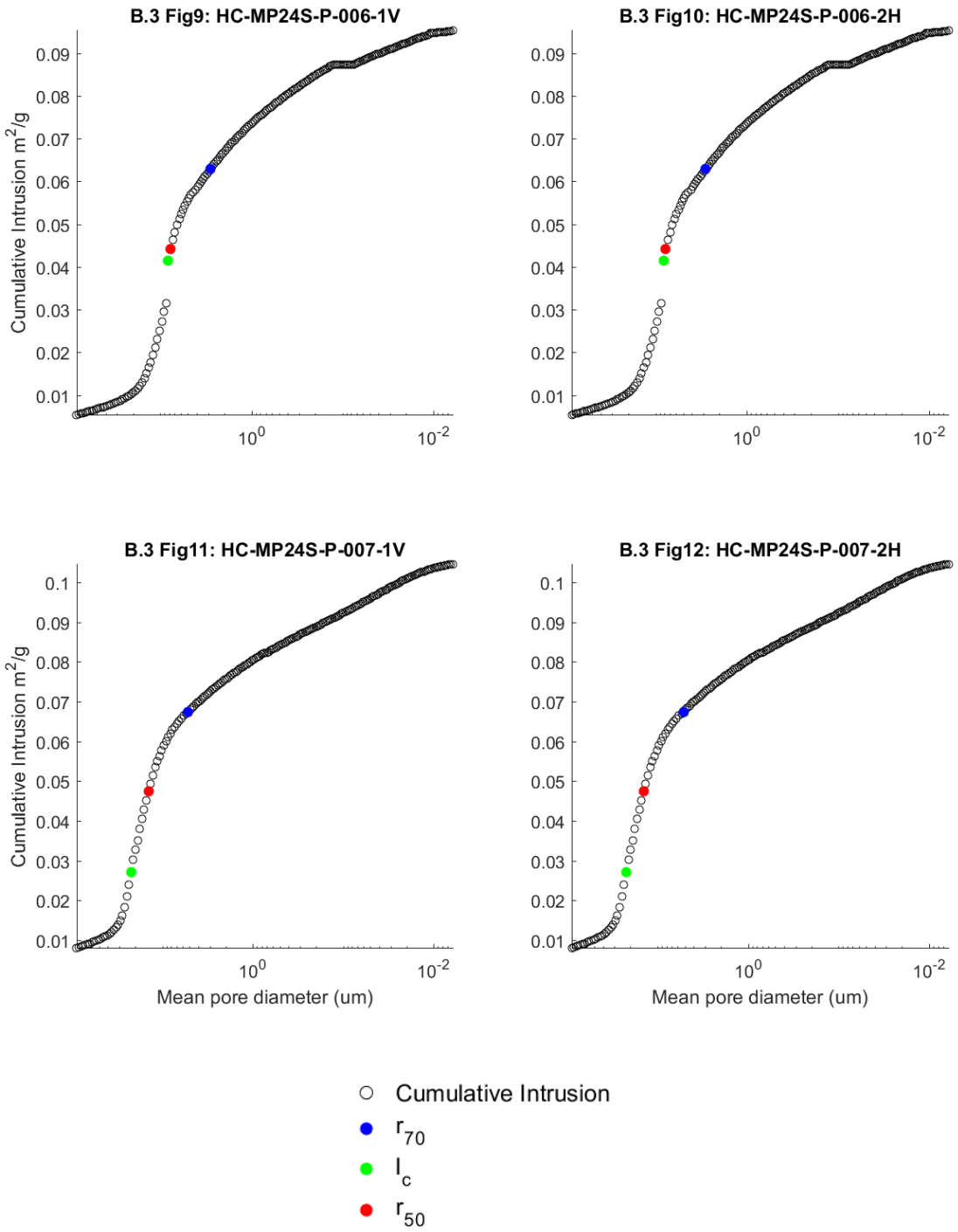
B.3 Fig9: HC-MP24S-P-006-1V
B.3 Fig10: HC-MP24S-P-006-2H
B.3 Fig11: HC-MP24S-P-007-1V
B.3 Fig12: HC-MP24S-P-007-2H
Cumulative Intrusion m2/g
Mean pore diameter (um)
Cumulative Intrusion
r70
lc
r50

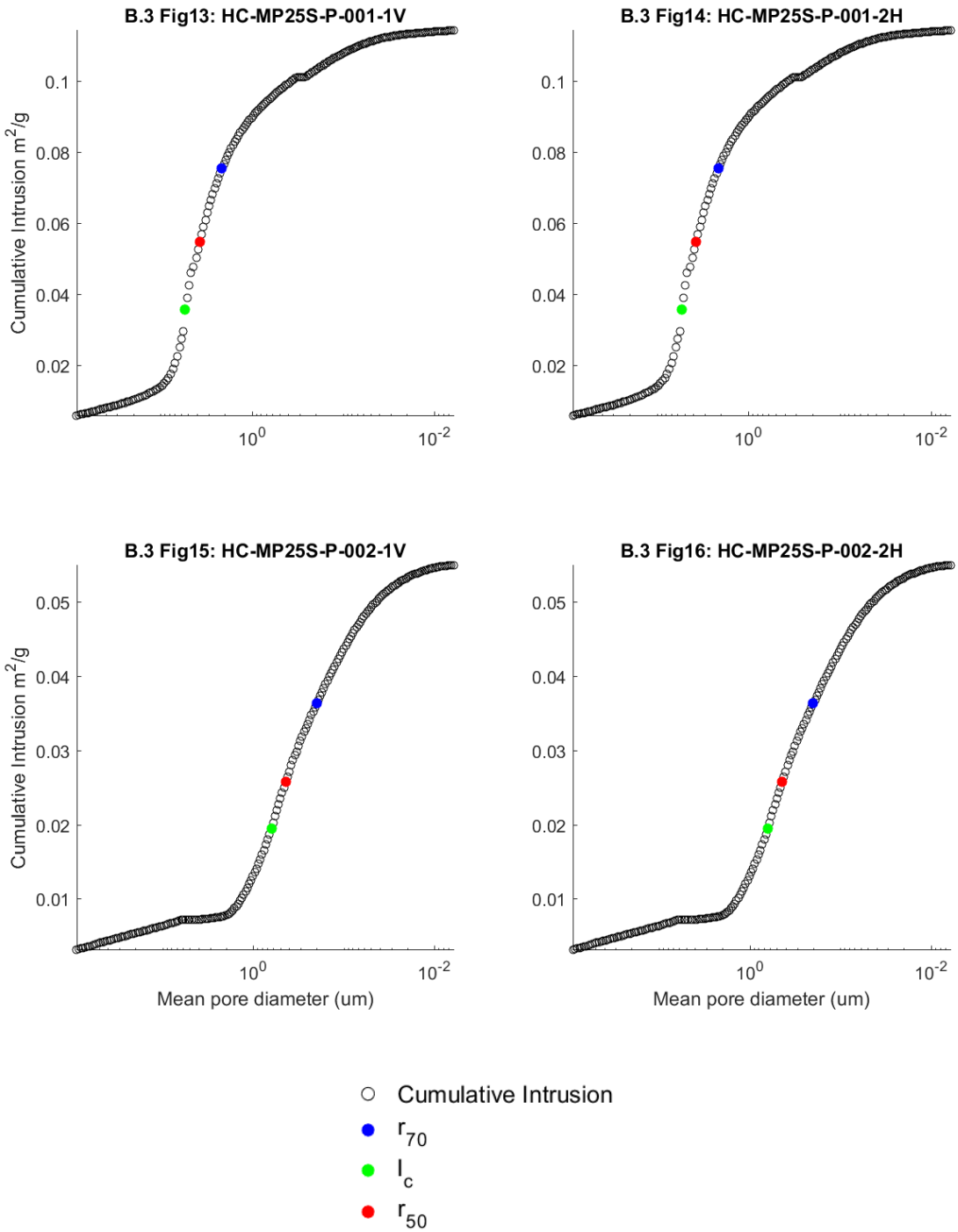
B.3 Fig13: HC-MP25S-P-001-1V
B.3 Fig14: HC-MP25S-P-001-2H
B.3 Fig15: HC-MP25S-P-002-1V
B.3 Fig16: HC-MP25S-P-002-2H
Cumulative Intrusion m2/g
Mean pore diameter (um)
Cumulative Intrusion
r70
lc
r50

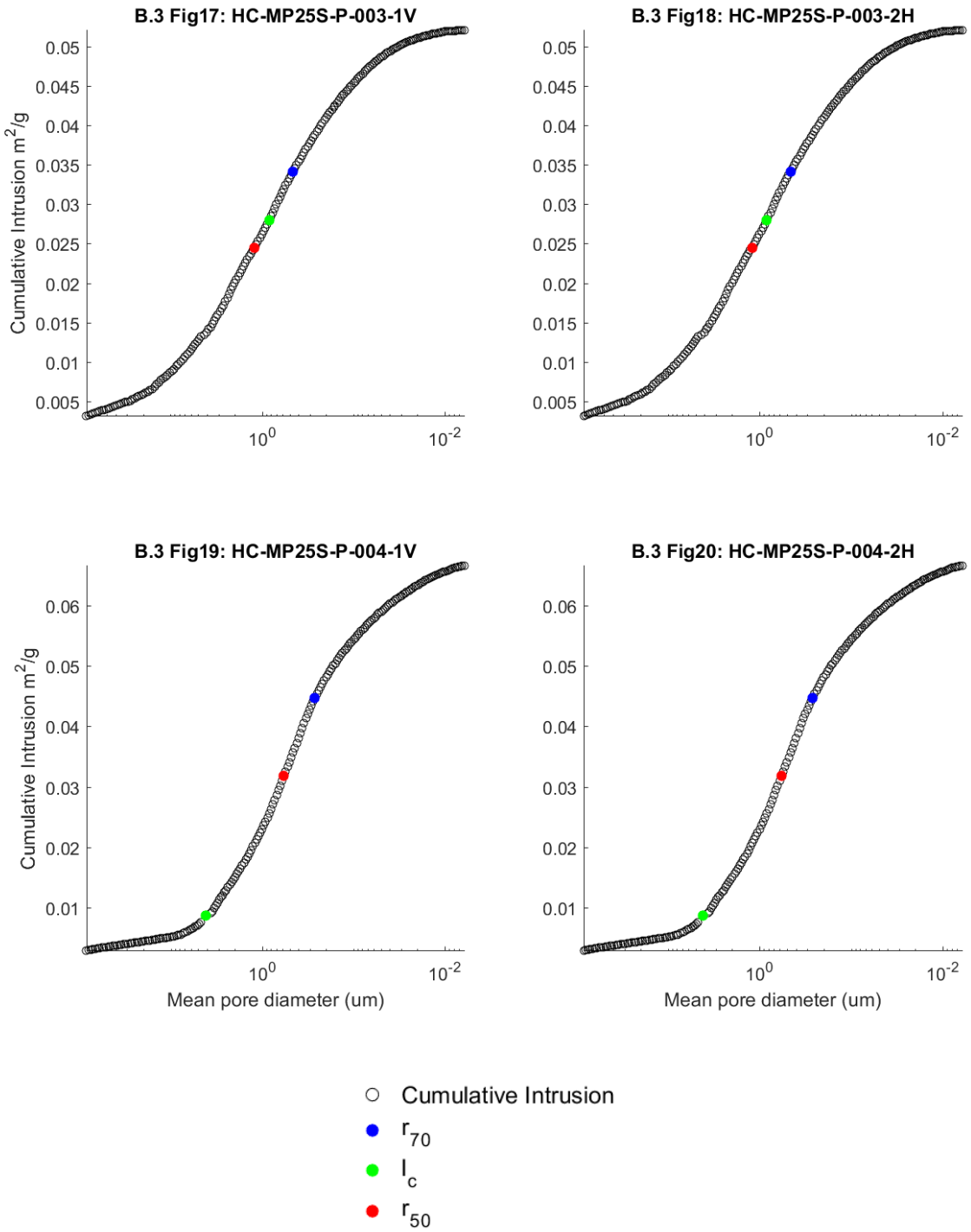
B.3 Fig17: HC-MP25S-P-003-1V
B.3 Fig18: HC-MP25S-P-003-2H
B.3 Fig19: HC-MP25S-P-004-1V
B.3 Fig20: HC-MP25S-P-004-2H
Cumulative Intrusion m2/g
Mean pore diameter (um)
Cumulative Intrusion
r70
lc
r50

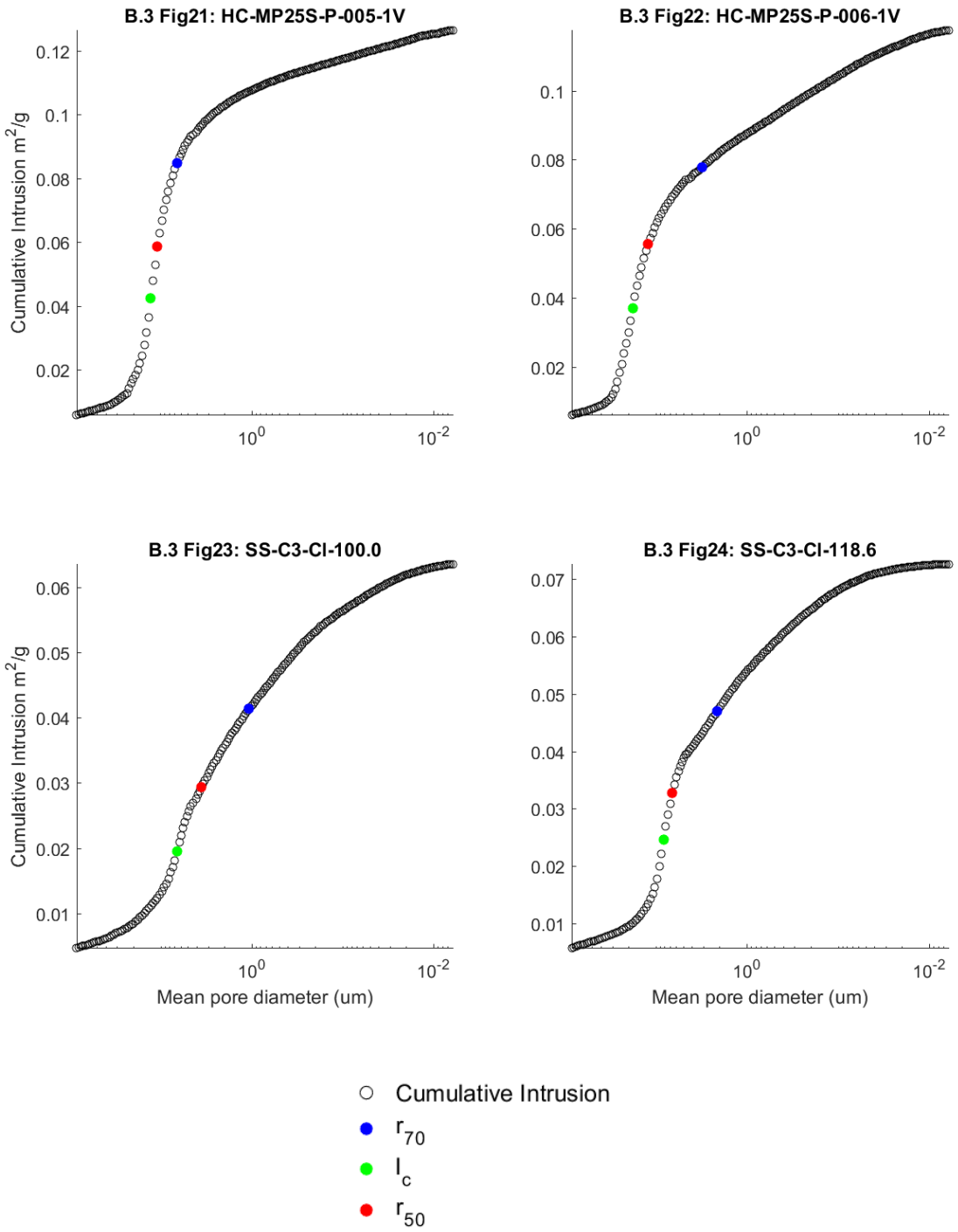
B.3 Fig21: HC-MP25S-P-005-1V
B.3 Fig22: HC-MP25S-P-006-1V
B.3 Fig23: SS-C3-Cl-100.0
B.3 Fig24: SS-C3-Cl-118.6
Cumulative Intrusion m2/g
Mean pore diameter (um)
Cumulative Intrusion
r70
lc
r50

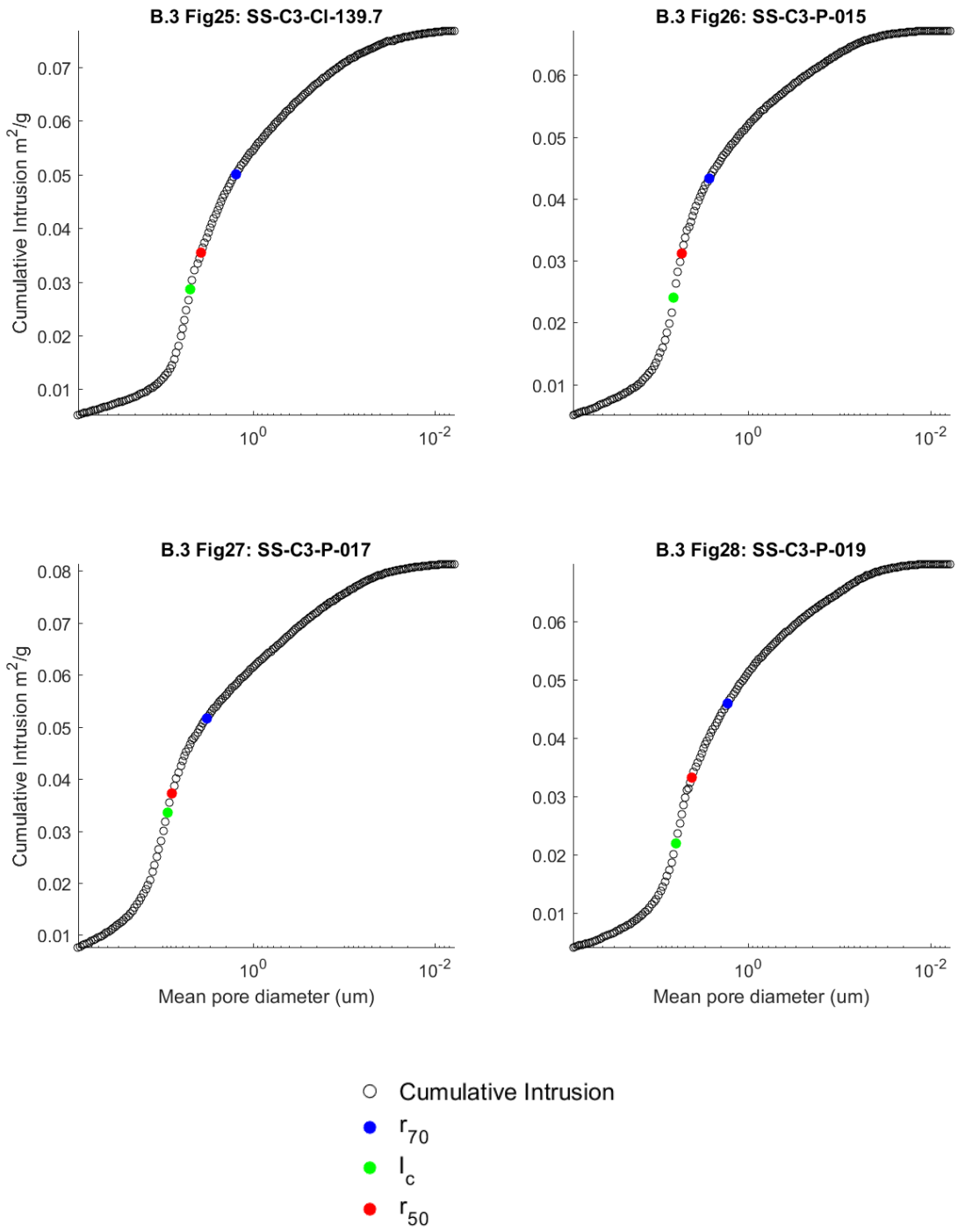
B.3 Fig25: SS-C3-Cl-139.7
B.3 Fig26: SS-C3-P-015
B.3 Fig27: SS-C3-P-017
B.3 Fig28: SS-C3-P-019
Cumulative Intrusion m2/g
Mean pore diameter (um)
Cumulative Intrusion
r70
lc
r50

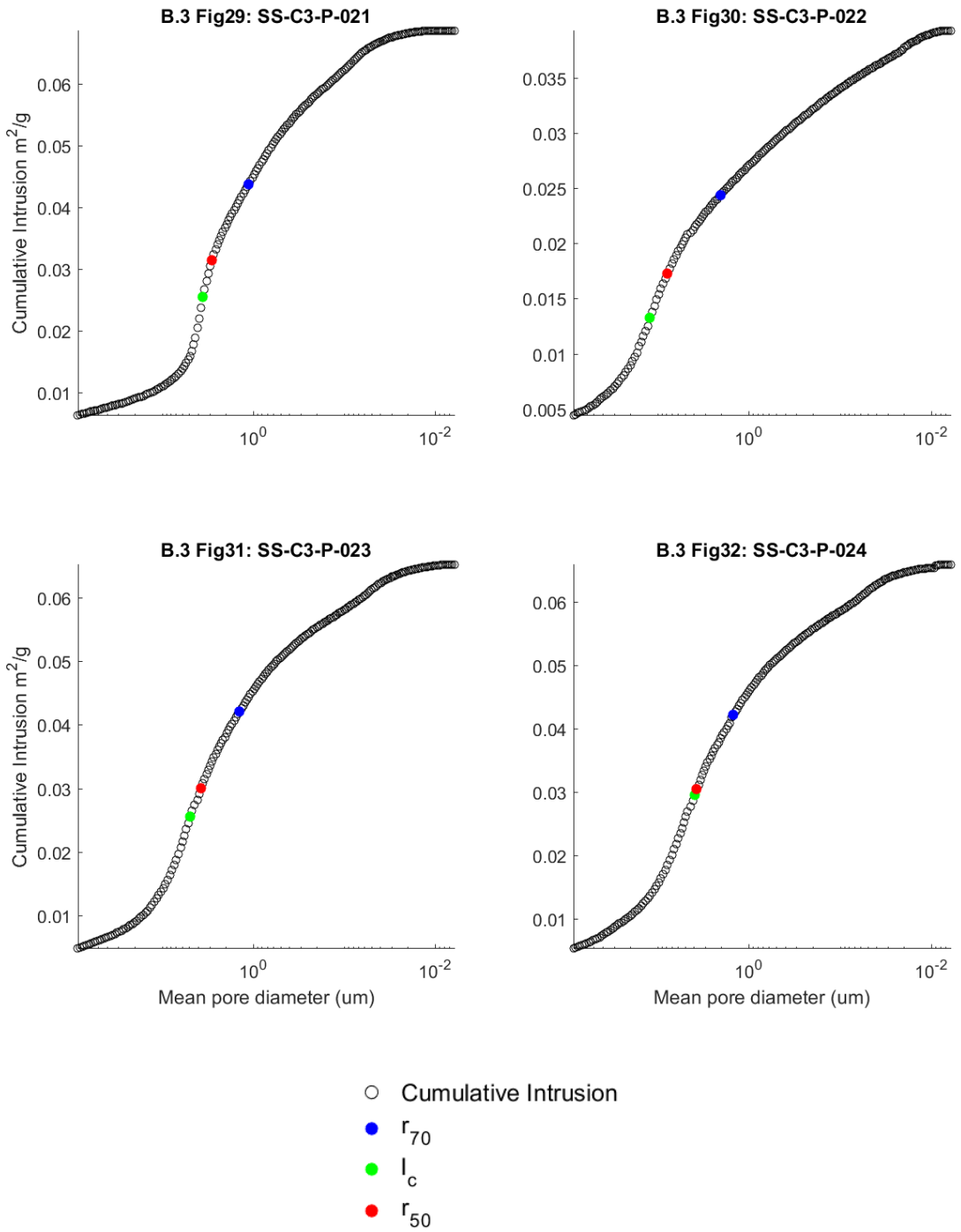
B.3 Fig29: SS-C3-P-021
B.3 Fig30: SS-C3-P-022
B.3 Fig31: SS-C3-P-023
B.3 Fig32: SS-C3-P-024
Cumulative Intrusion m2/g
Mean pore diameter (um)
Cumulative Intrusion
r70
lc
r50

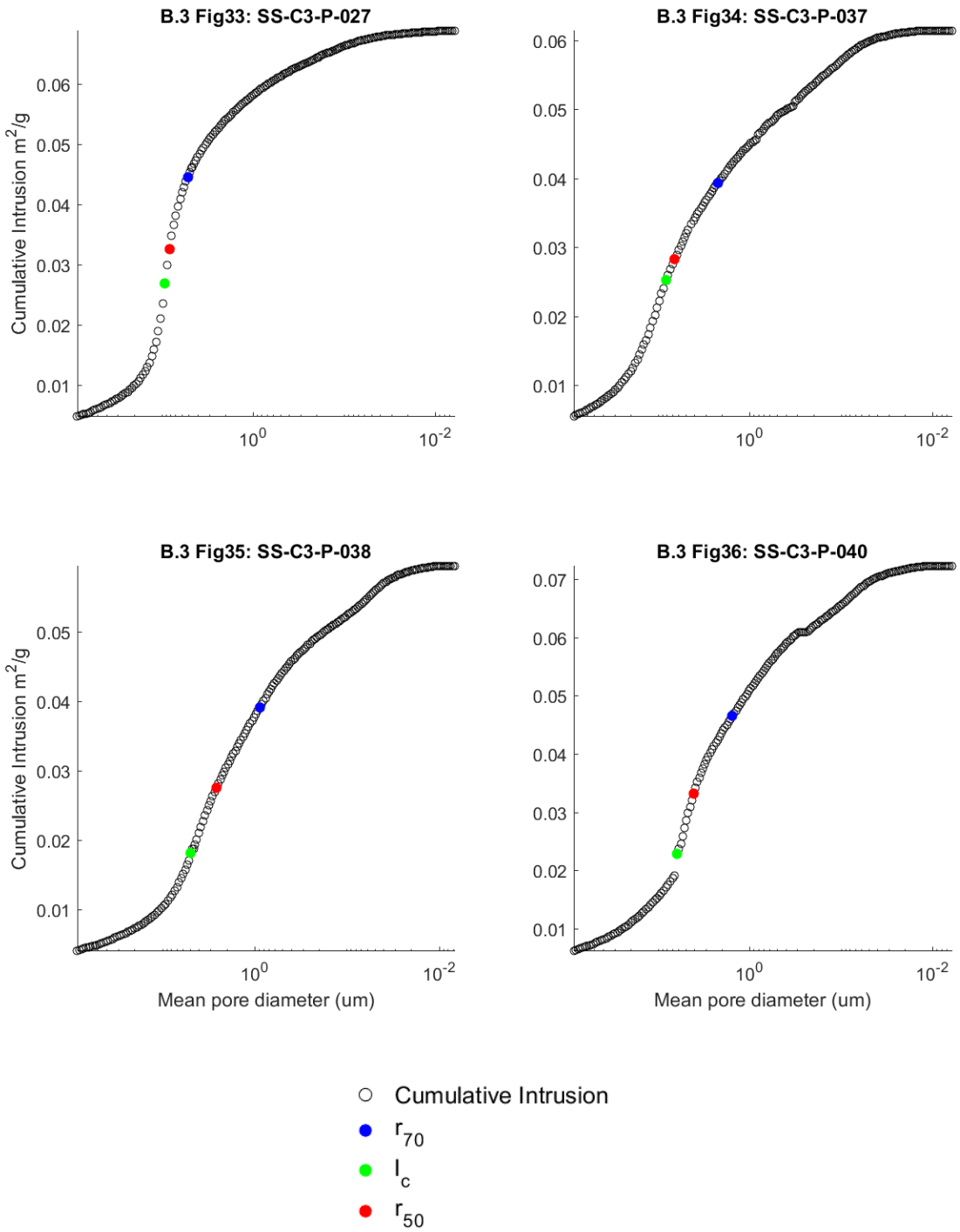
B.3 Fig33: SS-C3-P-027
B.3 Fig34: SS-C3-P-037
B.3 Fig35: SS-C3-P-038
B.3 Fig36: SS-C3-P-040
Cumulative Intrusion m2/g
Mean pore diameter (um)
Cumulative Intrusion
r70
lc
r50

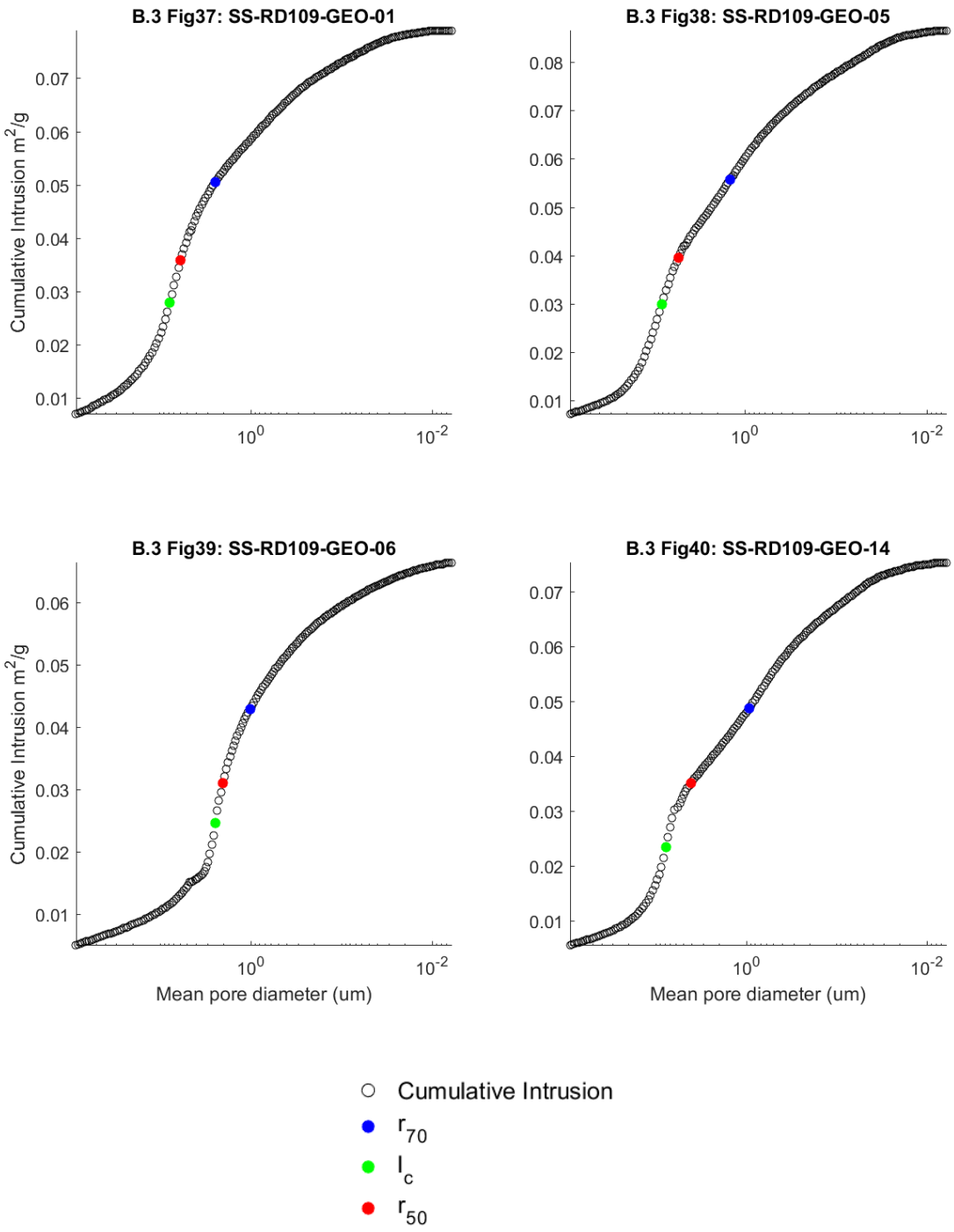
B.3 Fig37: SS-RD109-GEO-01
B.3 Fig38: SS-RD109-GEO-05
B.3 Fig39: SS-RD109-GEO-06
B.3 Fig40: SS-RD109-GEO-14
Cumulative Intrusion m2/g
Mean pore diameter (um)
Cumulative Intrusion
r70
lc
r50

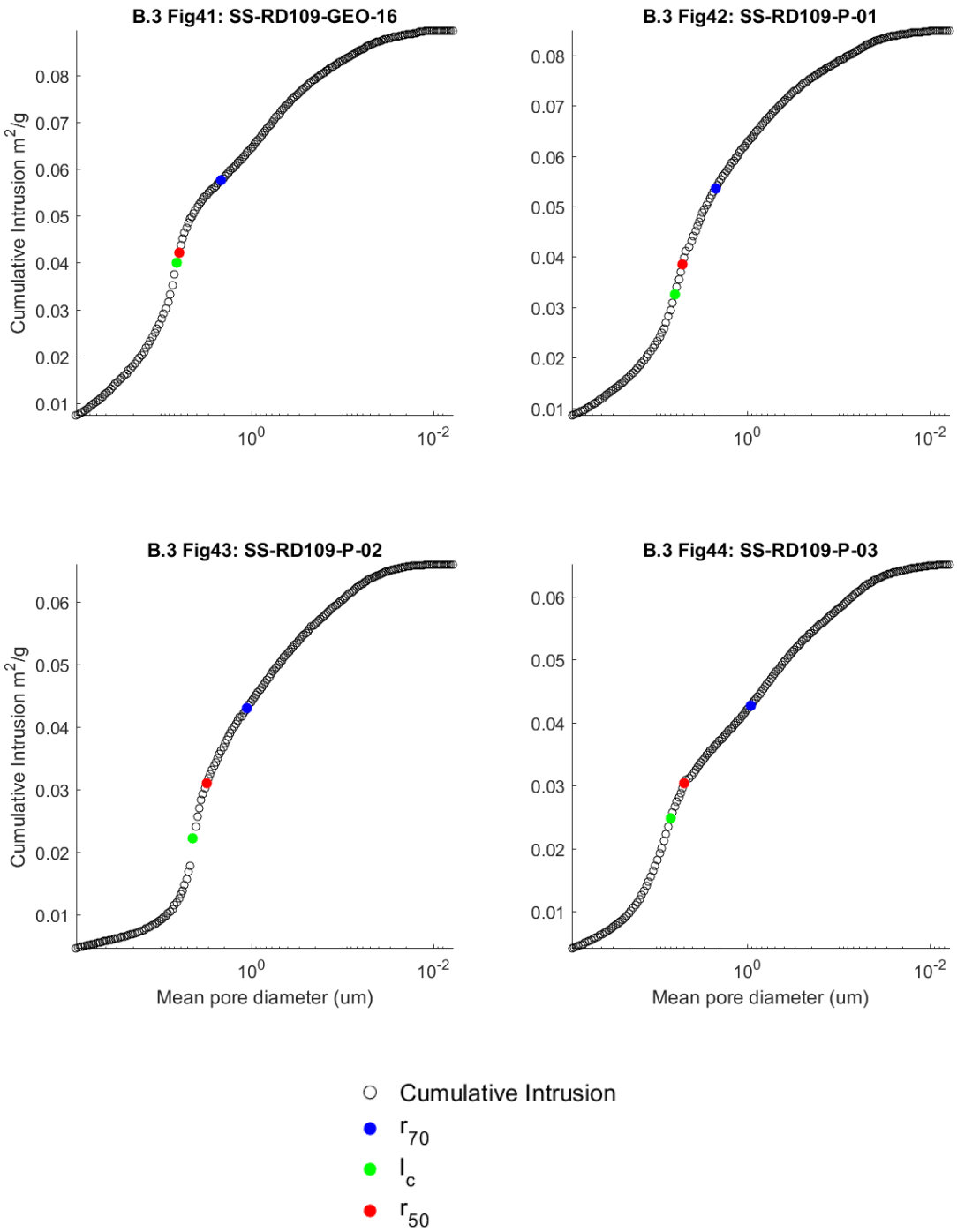
B.3 Fig41: SS-RD109-GEO-16
B.3 Fig42: SS-RD109-P-01
B.3 Fig43: SS-RD109-P-02
B.3 Fig44: SS-RD109-P-03
Cumulative Intrusion m2/g
Mean pore diameter (um)
Cumulative Intrusion
r70
lc
r50

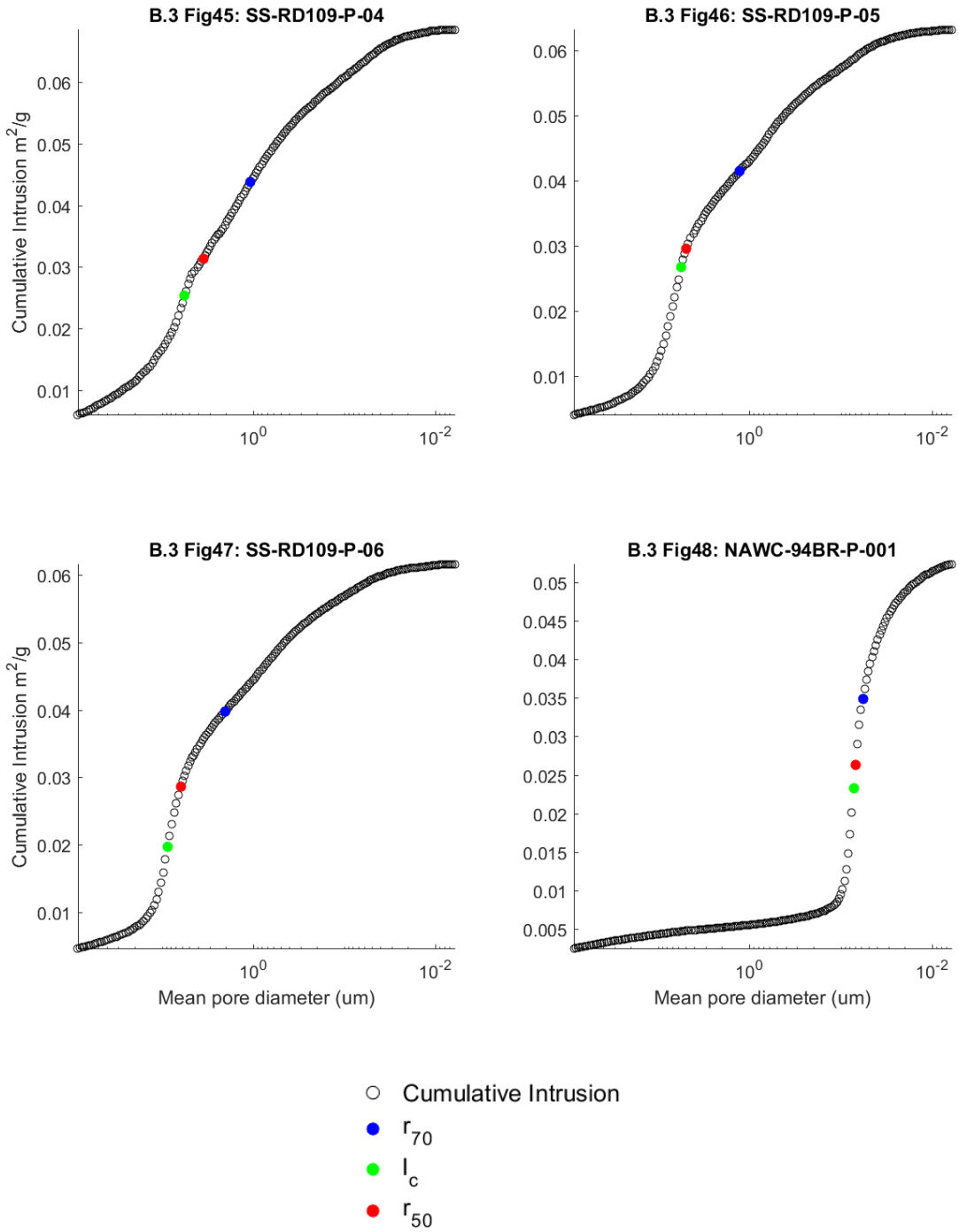
B.3 Fig45: SS-RD109-P-04
B.3 Fig46: SS-RD109-P-05
B.3 Fig47: SS-RD109-P-06
B.3 Fig48: NAWC-94BR-P-001
Cumulative Intrusion m2/g
Mean pore diameter (um)
Cumulative Intrusion
r70
lc
r50

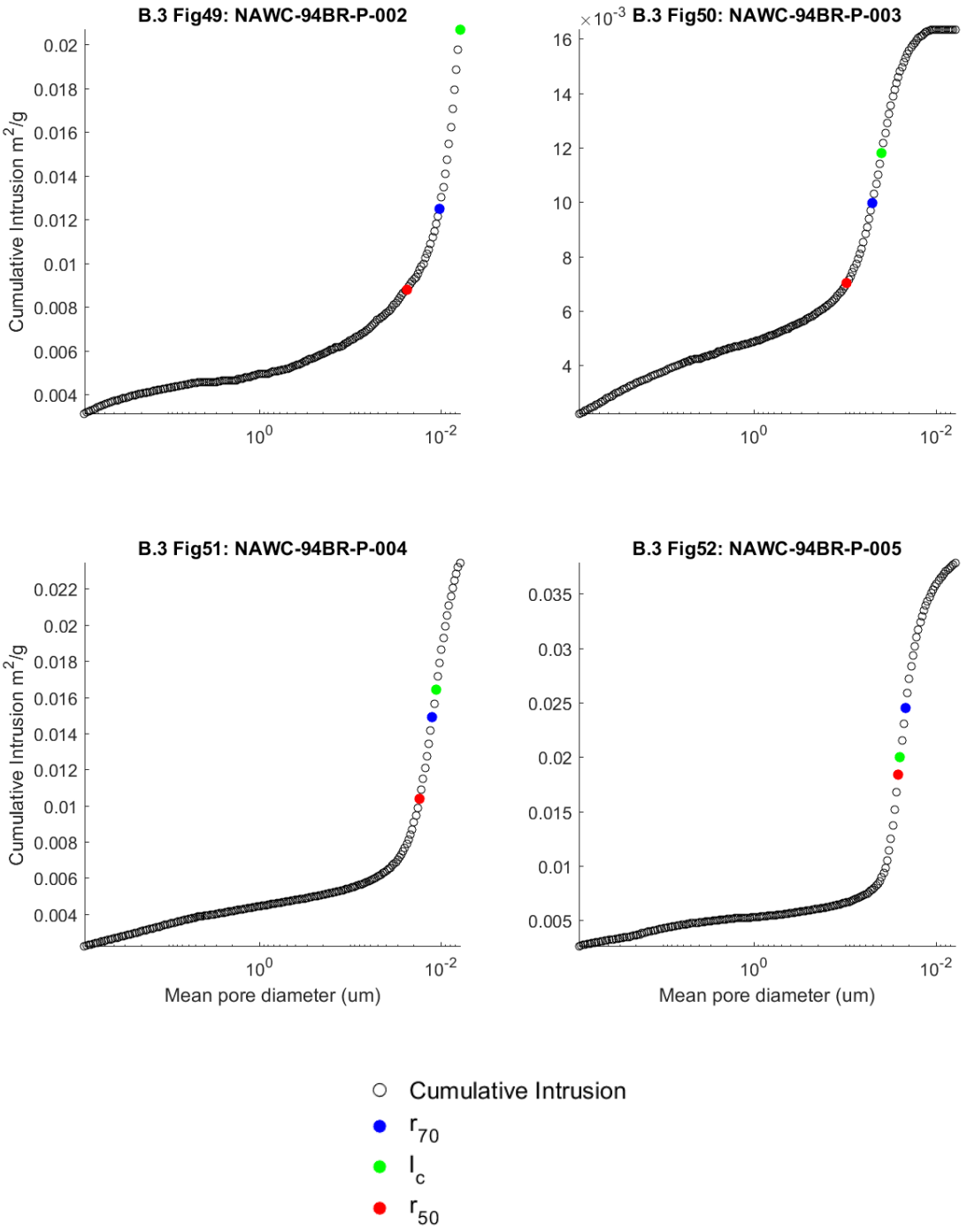
B.3 Fig49: NAWC-94BR-P-002
B.3 Fig50: NAWC-94BR-P-003
B.3 Fig51: NAWC-94BR-P-004
B.3 Fig52: NAWC-94BR-P-005
Cumulative Intrusion m2/g
Mean pore diameter (um)
×10-3
Cumulative Intrusion
r70
lc
r50

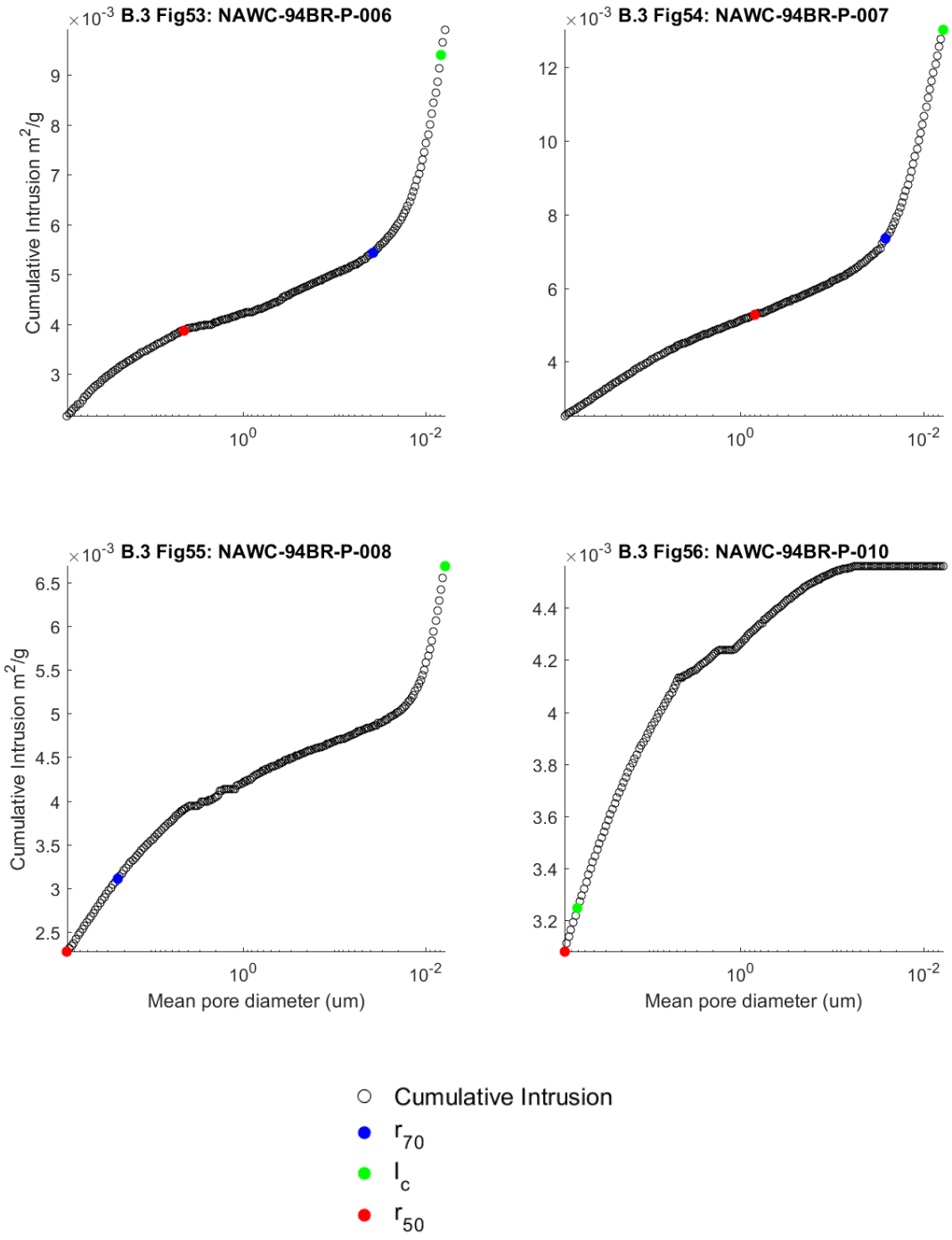
×10^-3 B.3 Fig53: NAWC-94BR-P-006
×10^-3 B.3 Fig54: NAWC-94BR-P-007
×10^-3 B.3 Fig55: NAWC-94BR-P-008
×10^-3 B.3 Fig56: NAWC-94BR-P-010
Cumulative Intrusion m^2/g
Mean pore diameter (um)
10^0
10^-2
Cumulative Intrusion
r70
lc
r50

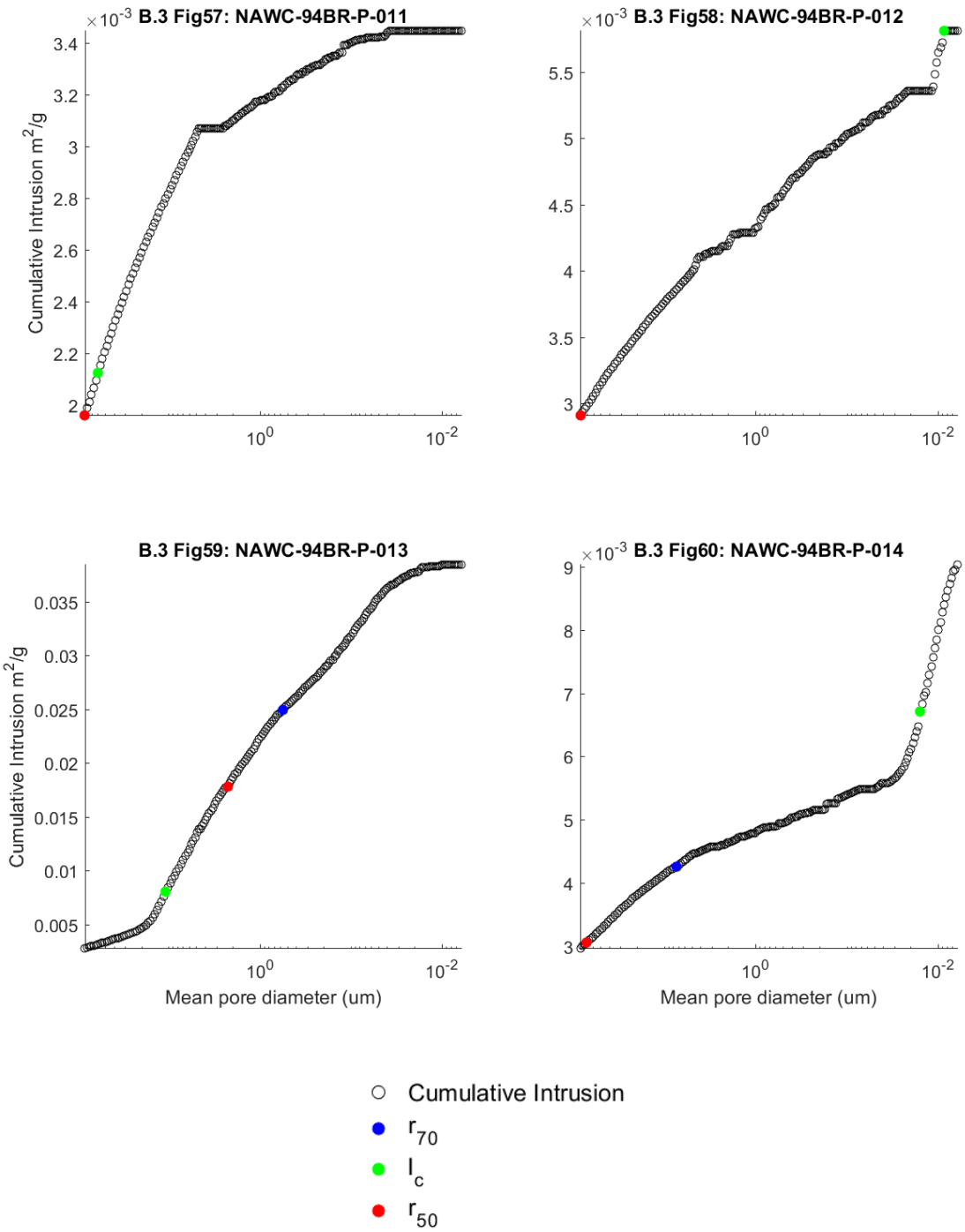
B.3 Fig57: NAWC-94BR-P-011
B.3 Fig58: NAWC-94BR-P-012
B.3 Fig59: NAWC-94BR-P-013
B.3 Fig60: NAWC-94BR-P-014
Cumulative Intrusion m2/g
Mean pore diameter (um)
Cumulative Intrusion
r70
lc
r50

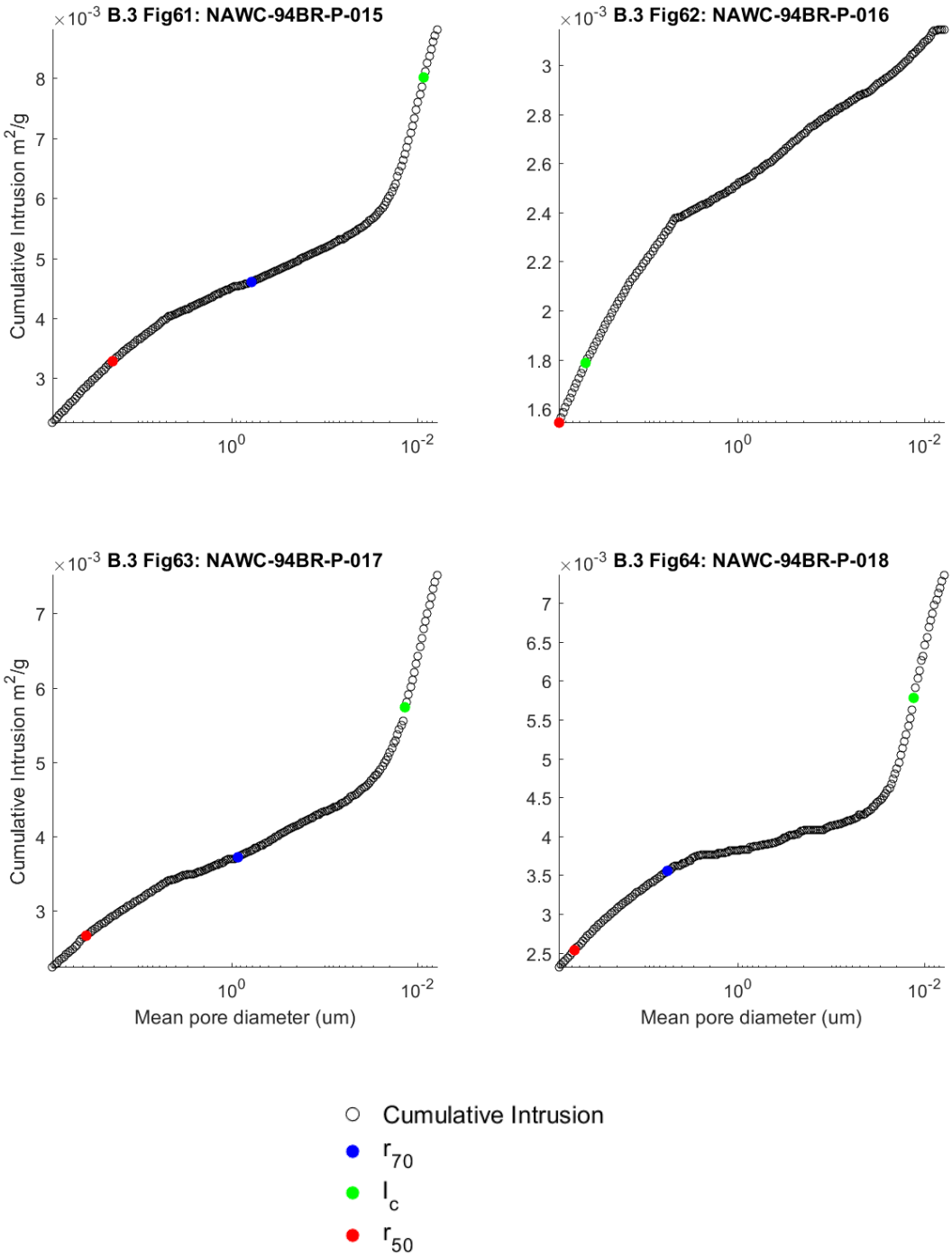
×10-3 B.3 Fig61: NAWC-94BR-P-015
×10-3 B.3 Fig62: NAWC-94BR-P-016
×10-3 B.3 Fig63: NAWC-94BR-P-017
×10-3 B.3 Fig64: NAWC-94BR-P-018
Cumulative Intrusion m2/g
Mean pore diameter (um)
Cumulative Intrusion
r70
lc
r50

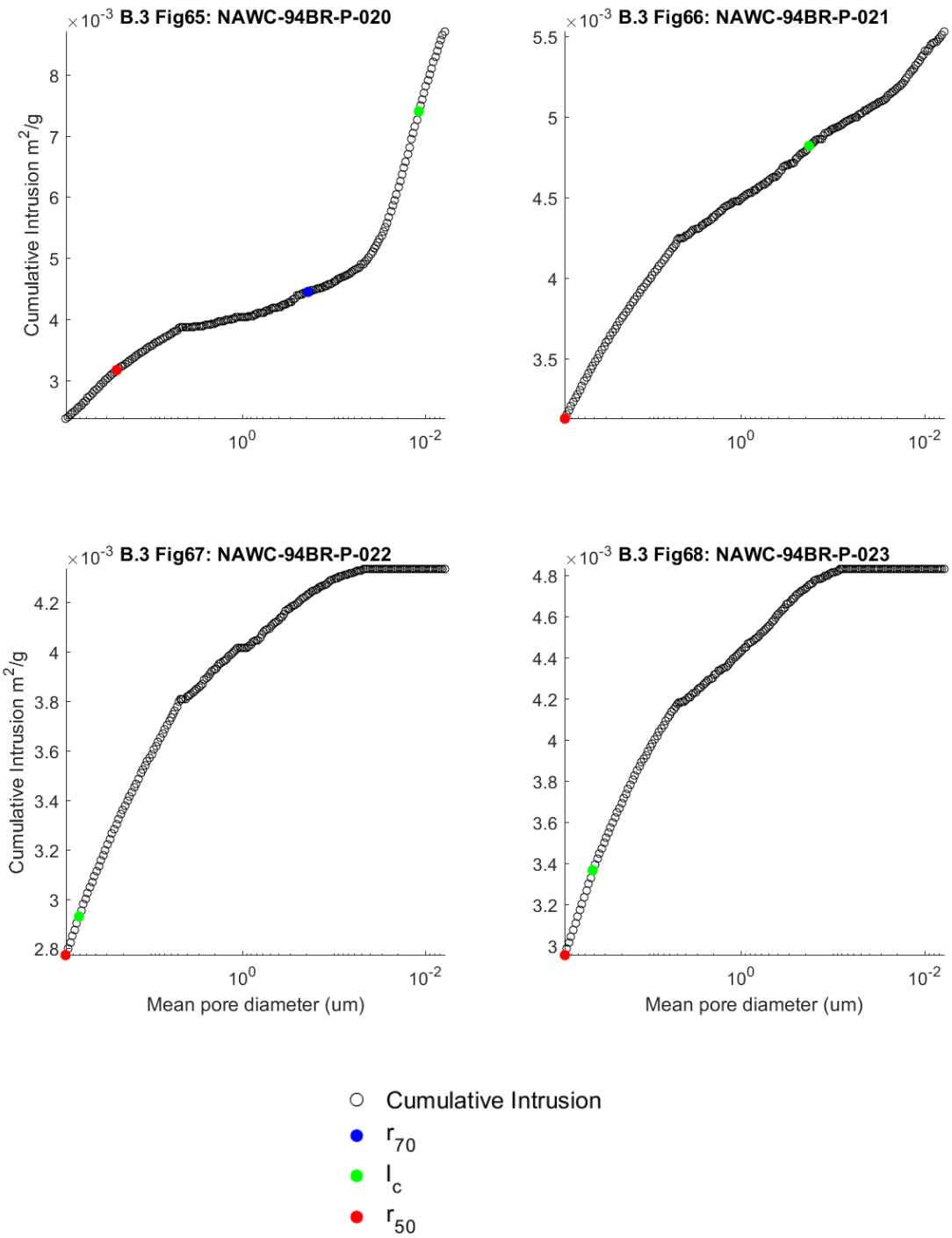
B.3 Fig65: NAWC-94BR-P-020
B.3 Fig66: NAWC-94BR-P-021
B.3 Fig67: NAWC-94BR-P-022
B.3 Fig68: NAWC-94BR-P-023
Cumulative Intrusion m2/g
Mean pore diameter (um)
Cumulative Intrusion
r70
lc
r50

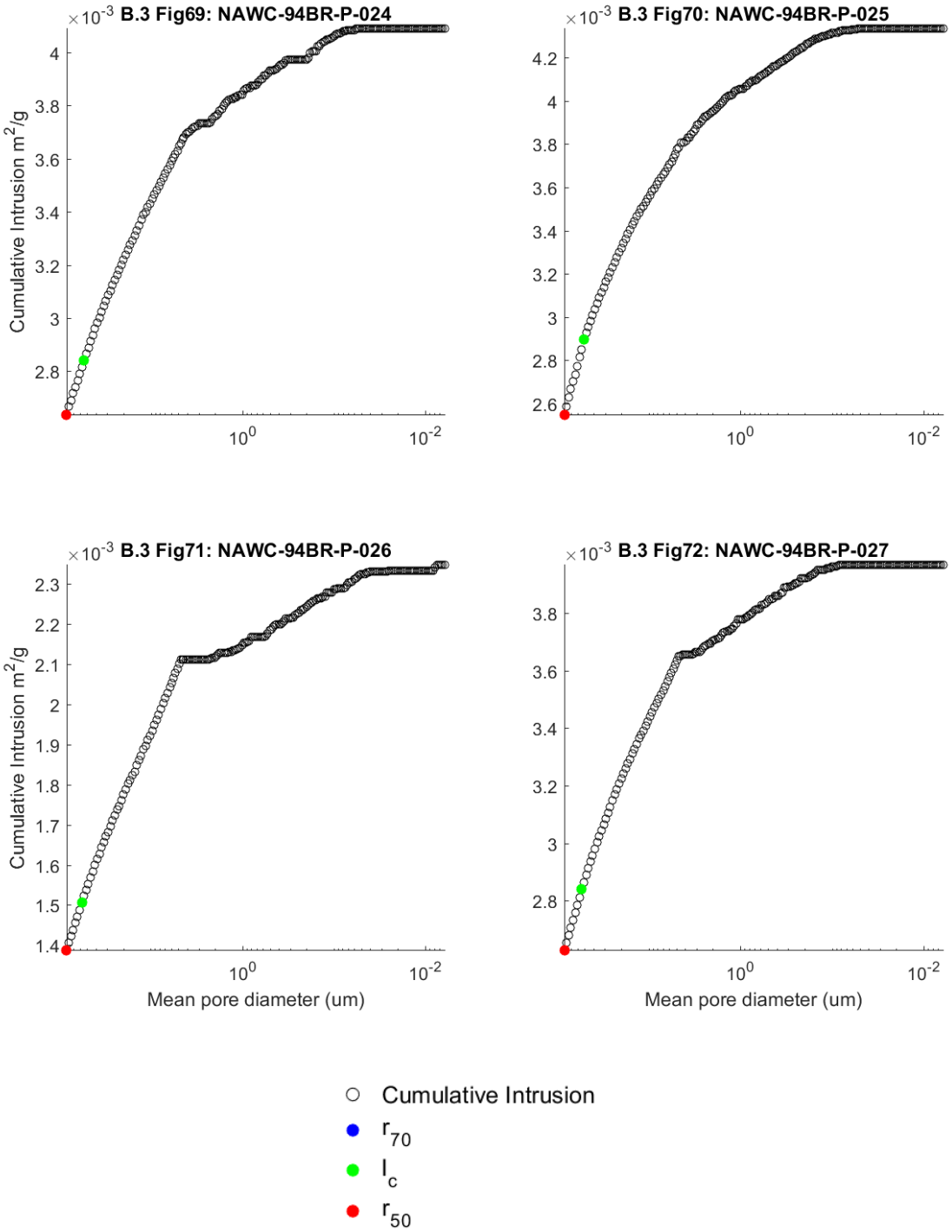
B.3 Fig69: NAWC-94BR-P-024
B.3 Fig70: NAWC-94BR-P-025
B.3 Fig71: NAWC-94BR-P-026
B.3 Fig72: NAWC-94BR-P-027
Cumulative Intrusion m²/g
Mean pore diameter (um)
Cumulative Intrusion
r70
lc
r50

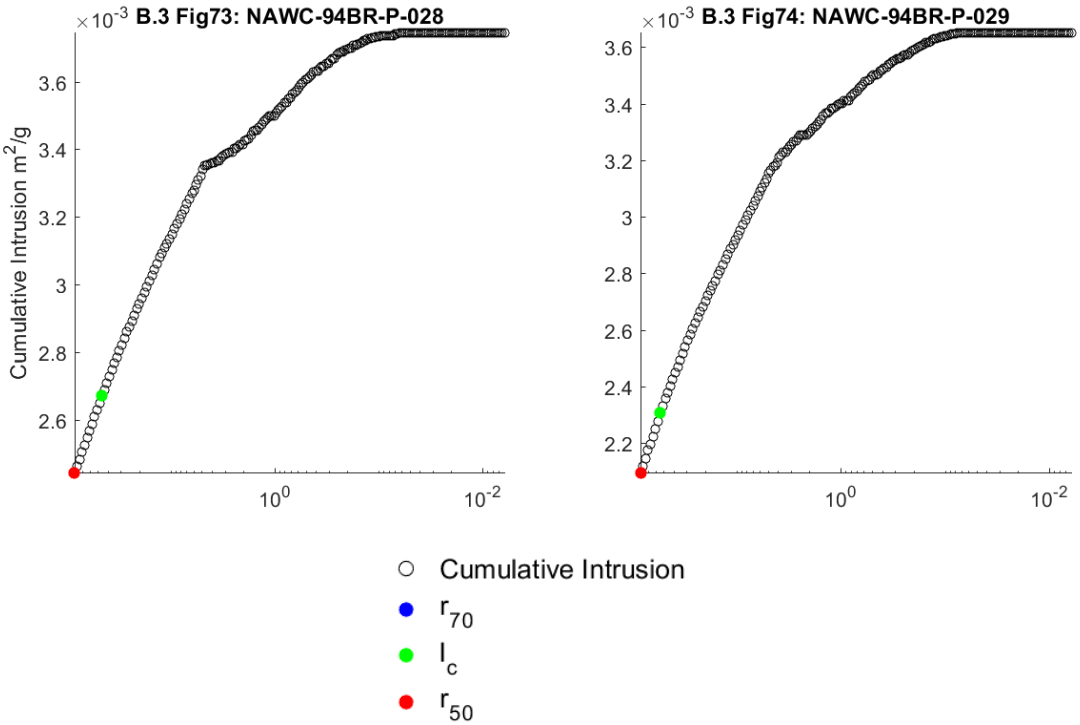
×10^-3 B.3 Fig73: NAWC-94BR-P-028
Cumulative Intrusion m^2/g
3.6
3.4
3.2
3
2.8
2.6
10^0
10^-2
×10^-3 B.3 Fig74: NAWC-94BR-P-029
3.6
3.4
3.2
3
2.8
2.6
2.4
2.2
10^0
10^-2
Cumulative Intrusion
r70
lc
r50

Appendix B.4: Laboratory data

To more concisely display laboratory data, Appendix B.4 summarizes key elements of data acquired on rock cores in a tabular format. Much of this information is duplicated from Appendices B.1-B.3, which presents laboratory data per sample and also in graphical format.

Tables 1 and 2 summarize physical property data. Portions of the physical data in this table can be found in Appendix B.1 for each sample**. Table 1** is an in-depth physical property summary. **Table 2** contains mercury injection capillary pressure (MICP) and BET data. MICP data can also be found in Appendix B.2.

Table 3 combines physical and geophysical data and lists iron content and magnetic susceptibility (MS) measurements. Where no data were acquired, the associated data cell are left empty.

Tables 4 and 5 summarize geophysical properties for each sample. **Table 4** lists nuclear magnetic resonance (NMR) data. Much of this information can also be found in Appendices B.1 and B.2. **Table 5** lists complex resistivity (CR) data. Where no data were acquired, the associated data cell are left empty. Much of the information in Table 5 can be found listed per sample in Appendix B.1.

B.4 Table 1: Physical property summary (page 1)

Sample Name	Depth (top) ft bgs	Depth (bottom) ft bgs	General Lithology	Diameter (cm)	Height (cm)	Submersible Volume (cm3)	Permeability (mD)	Gravimetric Porosity % Uguelph	Gravimetric Porosity % Rutgers
HC-MP24S-P-001-1V	111.480	111.880	Sandstone	3.790	4.370	47.621	5.44E+00	11.80	11.80
HC-MP24S-P-002-1V	137.600	138.600	Sandstone	3.810	5.930	66.068	6.20E+01	16.20	14.60
HC-MP24S-P-002-2H	137.600	138.600	Sandstone	3.800	4.600	51.793	2.49E+02	13.50	13.40
HC-MP24S-P-003-1V	146.860	147.570	Sandstone	3.840	6.090	68.324	7.93E+00	12.90	12.90
HC-MP24S-P-003-2H	146.860	147.570	Sandstone	3.790	4.650	51.925	1.79E+01	11.10	11.00
HC-MP24S-P-004-1V	153.450	154.050	Sandstone	3.800	6.090	67.310	3.30E+02	18.30	18.20
HC-MP24S-P-004-2H	153.450	154.050	Sandstone	3.800	4.550	50.564	3.67E+02	16.30	16.30
HC-MP24S-P-005-1V	156.700	157.600	Sandstone	3.810	4.970	56.287	1.74E-01	19.30	17.60
HC-MP24S-P-006-1V	172.520	173.270	shaley Sandstone	3.780	3.900	42.660	1.58E+00	22.40	22.20
HC-MP24S-P-006-2H	172.520	173.270	shaley Sandstone	3.800	4.190	46.042	6.51E+00	18.50	18.40
HC-MP24S-P-007-1V	177.400	178.200	Sandstone	3.780	3.090	33.758	3.41E-01	19.20	19.10
HC-MP24S-P-007-2H	177.400	178.200	Sandstone	3.750	4.170	45.689	6.31E+01	20.60	20.50
HC-MP25S-P-001-1V	131.550	132.600	Sandstone	3.800	3.610	39.628	5.79E+00	22.30	22.13
HC-MP25S-P-001-2H	131.550	132.600	Sandstone	3.780	4.500	49.583	5.95E+00	21.10	20.96
HC-MP25S-P-002-1V	137.200	138.300	Sandy Dolostone	3.800	3.680	40.943	9.33E-02	12.60	12.46
HC-MP25S-P-002-2H	137.200	138.300	Sandy Dolostone	3.760	4.210	46.637	1.80E-01	13.80	13.72
HC-MP25S-P-003-1V	155.500	156.000	Sandy Dolostone	3.800	4.960	55.153	1.39E+01	15.60	15.15
HC-MP25S-P-003-2H	155.500	156.000	Sandy Dolostone	3.790	4.590	51.329	4.07E+00	15.30	15.20
HC-MP25S-P-004-1V	168.850	169.500	Shaley Sandstone	3.760	4.980	54.849	1.03E+00	16.30	16.30
HC-MP25S-P-004-2H	168.850	169.500	Shaley Sandstone	3.740	3.740	41.204	7.93E-01	16.00	15.80

B.4 Table 1: Physical property summary (page 2)

Sample Name	Depth (top) ft bgs	Depth (bottom) ft bgs	General Lithology	Diameter (cm)	Height (cm)	Submersible Volume (cm3)	Permeability (mD)	Gravimetric Porosity % Uguelph	Gravimetric Porosity % Rutgers
HC-MP25S-P-005-1V	173.850	174.400	Sandstone	3.810	4.510	50.373	6.53E+00	24.30	25.40
HC-MP25S-P-006-1V	177.900	178.700	Sandstone	3.810	5.020	56.248	5.50E+00	21.60	22.20
SS-C3-Cl-100.0	100.000	100.350	Sandstone	3.794	3.641	40.566	1.91E+00	14.10	14.10
SS-C3-Cl-118.6	118.600	118.920	Sandstone	3.791	3.292	36.191	7.49E+00	14.90	15.40
SS-C3-Cl-139.7	139.700	140.000	Sandstone	3.781	2.782	30.880	1.33E+00	15.60	16.00
SS-C3-P-015	186.500	187.417	Sandstone	3.799	5.734	64.301	4.61E+00	13.10	13.20
SS-C3-P-017	206.667	207.583	Sandstone	3.761	5.194	57.359	6.56E+00	16.00	16.10
SS-C3-P-021	253.500	254.167	Sandstone	3.795	5.939	66.455	8.04E-01	14.20	14.00
SS-C3-P-022	257.000	257.667	Sandstone	3.799	4.513	49.927	2.75E+00	10.10	10.10
SS-C3-P-023	287.167	287.917	Sandstone	3.776	4.596	50.992	5.03E-01	12.90	12.70
SS-C3-P-024	296.667	297.167	Sandstone	3.759	2.742	29.648	1.83E+00	13.10	13.40
SS-C3-P-027	338.670	339.500	Sandstone	3.814	5.946	66.892	1.49E+01	13.30	13.40
SS-C3-P-037	415.000	415.417	Sandstone	3.809	5.348	59.865	7.64E+00	13.70	13.50
SS-C3-P-038	426.417	427.000	breccia	3.798	3.943	43.587	8.73E-01	12.50	12.60
SS-C3-P-040	441.083	441.833	Sandstone	3.799	3.419	38.286	1.87E+00	14.00	13.80
SS-RD109-GEO-01	15.800	16.750	Sandstone	3.644	5.645	54.910	1.11E+01	14.10	16.40
SS-RD109-GEO-05	50.300	51.100	Sandstone	3.628	6.145	59.829	1.01E+01	17.20	18.80
SS-RD109-GEO-06	61.500	62.400	Interbedded Sandstone/ Siltstone	3.760	6.091	67.427	1.75E+00	15.40	15.00
SS-RD109-GEO-14	88.300	89.100	Sandstone	3.773	6.435	71.562	3.37E+00	16.00	15.70
SS-RD109-GEO-16	96.500	97.400	Sandstone	3.772	5.922	65.925	5.95E+00	16.60	16.50
SS-RD109-P-01	22.000	23.000	Sandstone	3.746	5.445	58.271	3.95E+00	16.70	16.70
SS-RD109-P-02	67.000	67.800	Sandstone	3.786	5.706	63.773	1.63E+00	14.50	14.20

B.4 Table 1: Physical property summary (page 3)

Sample Name	Depth (top) ft bgs	Depth (bottom) ft bgs	General Lithology	Diameter (cm)	Height (cm)	Submersible Volume (cm3)	Permeability (mD)	Gravimetric Porosity % Uguelph	Gravimetric Porosity % Rutgers
SS-RD109-P-03	78.000	78.700	Sandstone	3.764	3.196	35.154	7.62E+00	15.10	14.90
SS-RD109-P-04	83.800	84.600	breccia	3.783	5.253	58.391	3.47E+00	14.90	14.50
SS-RD109-P-05	133.500	134.300	Sandstone	3.785	5.586	62.158	5.24E+00	13.10	13.90
SS-RD109-P-06	139.100	139.900	Sandstone	3.789	5.327	59.680	1.13E+00	13.20	13.30
NAWC-94BR-P-001	42.150	42.800	Mudstone	3.793	5.158	58.380	2.00E-03	N/A	12.18
NAWC-94BR-P-002	45.650	46.250	Mudstone	3.785	2.642	N/A	N/A	N/A	N/A
NAWC-94BR-P-003	51.500	51.900	Mudstone	3.798	4.862	55.198	9.11E-04	N/A	4.36
NAWC-94BR-P-004	53.900	54.700	Mudstone	3.790	5.122	57.772	1.87E-03	N/A	7.76
NAWC-94BR-P-005	57.500	58.050	Mudstone	3.787	4.619	52.564	N/A	N/A	10.25
NAWC-94BR-P-006	61.600	62.100	Mudstone	3.796	5.217	59.025	6.08E-04	N/A	5.94
NAWC-94BR-P-007	63.400	64.100	Mudstone	3.794	5.121	58.025	2.67E-04	N/A	2.19
NAWC-94BR-P-008	67.450	68.300	Mudstone	3.797	5.624	63.636	4.80E-04	N/A	4.18
NAWC-94BR-P-009	73.950	74.400	Mudstone	3.796	4.638	52.483	2.45E-04	N/A	0.70
NAWC-94BR-P-010	75.550	76.150	Mudstone	3.799	6.291	71.050	N/A	N/A	0.89
NAWC-94BR-P-011	77.750	78.450	Mudstone	3.795	4.559	51.373	2.91E-04	N/A	1.53
NAWC-94BR-P-012	80.650	81.350	Mudstone	3.790	2.708	30.484	2.48E-04	N/A	6.06
NAWC-94BR-P-013	87.700	88.250	Mudstone	3.798	5.152	58.346	3.39E-03	N/A	14.05
NAWC-94BR-P-014	91.400	92.350	Mudstone	3.791	4.834	54.695	5.30E-05	N/A	3.06
NAWC-94BR-P-015	95.950	96.550	Mudstone	3.793	4.341	49.129	6.23E-05	N/A	2.64
NAWC-94BR-P-016	102.800	103.400	Mudstone	3.796	5.750	65.134	1.54E-04	N/A	1.52
NAWC-94BR-P-017	107.100	107.600	Mudstone	3.798	4.907	55.572	3.77E-05	N/A	2.43
NAWC-94BR-P-018	108.400	109.050	Mudstone	3.799	5.681	64.234	3.04E-05	N/A	2.73

B.4 Table 1: Physical property summary (page 4)

Sample Name	Depth (top) ft bgs	Depth (bottom) ft bgs	General Lithology	Diameter (cm)	Height (cm)	Submersible Volume (cm3)	Permeability (mD)	Gravimetric Porosity % Uguelph	Gravimetric Porosity % Rutgers
NAWC-94BR-P-020	116.000	116.700	Mudstone	3.796	4.327	48.983	5.52E-05	N/A	2.23
NAWC-94BR-P-021	121.000	121.600	Mudstone	3.797	4.697	53.123	4.70E-03	N/A	4.12
NAWC-94BR-P-022	122.900	123.800	Mudstone	3.799	4.757	53.993	N/A	N/A	1.53
NAWC-94BR-P-023	127.050	128.050	Mudstone	3.793	4.623	52.361	N/A	N/A	2.45
NAWC-94BR-P-024	131.050	131.550	Mudstone	3.794	4.555	51.355	N/A	N/A	1.14
NAWC-94BR-P-025	132.100	132.700	Mudstone	3.792	5.615	63.500	N/A	N/A	2.39
NAWC-94BR-P-026	136.100	136.800	Mudstone	3.795	4.748	53.707	N/A	N/A	1.12
NAWC-94BR-P-027	141.700	142.900	Mudstone	3.797	5.017	57.608	1.91E-04	N/A	0.96
NAWC-94BR-P-028	150.300	150.800	Mudstone	3.799	4.475	50.570	1.56E-04	N/A	1.10
NAWC-94BR-P-029	145.400	146.100	Mudstone	3.828	4.666	53.058	N/A	N/A	1.07

B.4 Table 2: MICP and BET property summary (page 1)

Sample_Name	MICP porosity (%)	Maximum incremental intrusion radius l_c (μm)	r50 (μm)	BET Specific surface area (m^2/g)	S_{por} $(\mu m)^{-1}$
HC-MP24S-P-001-1V	11.32	7.959	7.53	0.708	14.048
HC-MP24S-P-002-1V	16.10	10.685	10.69	0.231	3.230
HC-MP24S-P-002-2H	16.10	10.685	10.69	0.231	3.923
HC-MP24S-P-003-1V	11.70	7.125	5.11	1.064	19.081
HC-MP24S-P-003-2H	11.70	7.125	5.11	1.064	22.672
HC-MP24S-P-004-1V	18.74	10.493	10.49	0.193	2.281
HC-MP24S-P-004-2H	18.74	10.493	10.49	0.193	2.627
HC-MP24S-P-005-1V	20.46	2.063	1.34	7.062	78.446
HC-MP24S-P-006-1V	20.06	4.096	3.87	7.290	67.208
HC-MP24S-P-006-2H	20.06	4.096	3.87	7.290	86.033
HC-MP24S-P-007-1V	21.87	11.089	7.13	6.127	69.078
HC-MP24S-P-007-2H	21.87	11.089	7.13	6.127	62.947
HC-MP25S-P-001-1V	22.60	2.688	1.86	2.239	20.552
HC-MP25S-P-001-2H	22.60	2.688	1.86	2.239	22.216
HC-MP25S-P-002-1V	13.27	0.315	0.22	4.157	81.583
HC-MP25S-P-002-2H	13.27	0.315	0.22	4.157	73.552
HC-MP25S-P-003-1V	12.82	0.418	0.60	3.310	50.835
HC-MP25S-P-003-2H	12.82	0.418	0.60	3.310	52.079
HC-MP25S-P-004-1V	15.31	2.082	0.29	5.559	78.750
HC-MP25S-P-004-2H	15.31	2.082	0.29	5.559	81.354
HC-MP25S-P-005-1V	24.18	6.375	5.40	5.694	46.670
HC-MP25S-P-006-1V	23.89	8.888	6.03	6.630	64.212
SS-C3-Cl-100.0	14.38	3.281	1.77	2.899	47.046
SS-C3-Cl-118.6	16.01	4.095	3.28	1.693	25.689
SS-C3-Cl-139.7	16.74	2.451	1.85	2.366	34.478
SS-C3-P-015	14.98	3.281	2.69	1.252	22.152
SS-C3-P-017	17.72	4.328	3.87	1.460	20.341
SS-C3-P-021	15.26	1.768	1.41	1.825	29.403
SS-C3-P-022	9.36	6.026	3.87	2.158	51.193
SS-C3-P-023	14.53	2.450	1.86	2.045	36.918
SS-C3-P-024	14.73	1.950	1.86	2.467	43.570
SS-C3-P-027	15.23	4.574	4.09	0.698	12.050

B.4 Table 2: MICP and BET property summary (page 2)

Sample_Name	MICP porosity (unitless)	Maximum incremental intrusion radius l_c (μm)	r50 (μm)	BET Specific surface area (m^2/g)	S_{por} $(\mu m)^{-1}$
SS-C3-P-037	13.71	4.094	3.28	1.115	18.698
SS-C3-P-038	13.55	2.451	1.29	1.969	36.651
SS-C3-P-040	16.03	3.105	2.03	1.584	25.933
SS-RD109-GEO-01	17.18	3.873	2.95	1.852	29.601
SS-RD109-GEO-05	18.63	4.094	2.69	2.536	32.133
SS-RD109-GEO-06	14.53	1.215	1.01	2.778	40.712
SS-RD109-GEO-14	16.52	3.875	2.04	1.822	25.476
SS-RD109-GEO-16	19.27	3.281	3.10	1.814	24.282
SS-RD109-P-01	18.13	3.105	2.57	1.621	21.504
SS-RD109-P-02	14.86	2.180	1.53	1.620	25.414
SS-RD109-P-03	14.59	3.467	2.45	1.713	25.601
SS-RD109-P-04	15.14	2.816	1.76	1.867	28.384
SS-RD109-P-05	14.26	2.816	2.45	1.580	27.868
SS-RD109-P-06	14.04	4.326	3.10	1.261	22.113
NAWC-94BR-P-001	12.20	0.036	0.03	6.684	130.416
NAWC-94BR-P-002	5.13	0.003	0.01	17.881	N/A
NAWC-94BR-P-003	4.28	0.020	0.05	1.946	116.839
NAWC-94BR-P-004	6.01	0.006	0.01	12.125	399.078
NAWC-94BR-P-005	9.31	0.012	0.01	10.679	256.885
NAWC-94BR-P-006	2.58	0.003	2.18	8.166	356.389
NAWC-94BR-P-007	3.41	0.003	0.35	3.899	476.190
NAWC-94BR-P-008	1.74	0.003	41.59	1.335	83.944
NAWC-94BR-P-010	1.20	29.948	41.63	0.000	N/A
NAWC-94BR-P-011	0.90	29.889	41.56	0.000	N/A
NAWC-94BR-P-012	1.49	0.004	41.62	0.868	N/A
NAWC-94BR-P-013	9.42	5.398	1.13	0.647	36.485
NAWC-94BR-P-014	2.40	0.008	35.25	0.793	10.695
NAWC-94BR-P-015	2.33	0.004	9.40	3.438	68.592
NAWC-94BR-P-016	0.85	21.565	41.67	2.123	346.312
NAWC-94BR-P-017	2.01	0.007	18.25	2.604	377.505
NAWC-94BR-P-018	1.93	0.006	28.31	3.999	288.128
NAWC-94BR-P-020	2.26	0.006	11.72	3.725	384.397

B.4 Table 2: MICP and BET property summary (page 3)

Sample_Name	MICP porosity (unitless)	Maximum incremental intrusion radius l_c (μm)	r50 (μm)	BET Specific surface area (m^2/g)	S_{por} $(\mu m)^{-1}$
NAWC-94BR-P-021	1.44	0.091	41.65	1.137	444.186
NAWC-94BR-P-022	1.12	29.962	41.64	0.000	71.748
NAWC-94BR-P-023	1.27	20.366	41.57	0.000	N/A
NAWC-94BR-P-024	1.06	26.848	41.66	0.000	N/A
NAWC-94BR-P-025	1.11	25.394	41.62	0.000	N/A
NAWC-94BR-P-026	0.61	28.336	41.61	0.000	N/A
NAWC-94BR-P-027	1.02	26.799	41.59	0.000	N/A
NAWC-94BR-P-028	0.96	22.784	41.66	0.000	N/A
NAWC-94BR-P-029	0.94	26.782	41.57	0.000	N/A

B.4 Table 3: Iron content and Magnetic Susceptibility (MS) Data Summary (page 1)

Sample_Name	IronII (%)	IronIII (%)	Iron Total (%)	MS dry (SI) 0.93 Hz	MS sat. (SI) 0.93 Hz	MS dry (SI) 10 kHz side	MS dry (SI) 10 kHz top	MS dry (SI) 100 kHz side	MS dry (SI) 100 kHz top
HC-MP24S-P-001-1V	0.076	0.020	0.096	4.00E-06	2.01E-06				
HC-MP24S-P-002-1V	0.014	0.007	0.021	-1.04E-06	-3.18E-06				
HC-MP24S-P-002-2H	0.014	0.007	0.021	5.50E-06	-1.36E-06	0.00E+00	0.00E+00	1.23E-03	1.24E-03
HC-MP24S-P-003-1V	0.086	0.243	0.329	1.00E-05	2.43E-05				
HC-MP24S-P-003-2H	0.086	0.243	0.329	2.13E-05	2.83E-05				
HC-MP24S-P-004-1V	0.025	0.005	0.031	-2.29E-06	-2.96E-06				
HC-MP24S-P-004-2H	0.025	0.005	0.031	2.31E-06	3.36E-06	0.00E+00		1.03E-03	1.02E-03
HC-MP24S-P-005-1V	0.016	1.023	1.039	1.22E-04	1.21E-04	8.90E-05	8.00E-05	1.47E-03	2.08E-03
HC-MP24S-P-006-1V	0.004	0.942	0.946	6.76E-05	6.72E-05				
HC-MP24S-P-006-2H	0.004	0.942	0.946	8.42E-05	8.33E-05				
HC-MP24S-P-007-1V	0.065	1.082	1.148	5.50E-05	5.89E-05				
HC-MP24S-P-007-2H	0.065	1.082	1.148	5.75E-05	5.69E-05				
HC-MP25S-P-001-1V	0.030	0.000	0.030	1.83E-06	1.36E-06				
HC-MP25S-P-001-2H	0.030	0.000	0.030	6.88E-06	2.61E-06				
HC-MP25S-P-002-1V	0.006	0.001	0.007	5.08E-05	0.00E+00				
HC-MP25S-P-002-2H	0.006	0.001	0.007	3.51E-05	3.16E-05				
HC-MP25S-P-003-1V	0.003	0.010	0.013	4.57E-05	3.60E-05				
HC-MP25S-P-003-2H	0.003	0.010	0.013	5.71E-05	4.88E-05				
HC-MP25S-P-004-1V	0.007	0.007	0.015	1.25E-04	1.23E-04	6.70E-05	6.00E-05	1.78E-03	1.82E-03
HC-MP25S-P-004-2H	0.007	0.007	0.015	1.12E-04	9.53E-05				
HC-MP25S-P-005-1V	0.009	0.400	0.409	8.49E-05	8.60E-05	6.70E-05	5.30E-05	1.36E-03	1.42E-03

B.4 Table 3: Iron content and Magnetic Susceptibility (MS) Data Summary (page 2)

Sample_Name	IronII (%)	IronIII (%)	Iron Total (%)	MS dry (SI)	MS saturated (SI)	MS dry (SI) 10 kHz side	MS dry (SI) 10 kHz top	MS dry (SI) 100 kHz side	MS dry (SI) 100 kHz top
HC-MP25S-P-006-1V	0.011	0.680	0.692	7.01E-05	6.15E-05	4.50E-05	4.00E-05	1.92E-03	1.80E-03
SS-C3-Cl-100.0	0.024	1.529	1.553	9.41E-05	9.13E-05	4.50E-05	6.00E-05	1.76E-03	2.16E-03
SS-C3-Cl-118.6	0.026	1.449	1.475	8.01E-05	8.57E-05	4.50E-05	4.00E-05	1.67E-03	1.82E-03
SS-C3-Cl-139.7	0.184	1.486	1.670	1.62E-04	1.59E-04	8.90E-05	1.00E-04	1.56E-03	1.96E-03
SS-C3-P-015	0.178	1.403	1.581	1.12E-04	1.13E-04	8.90E-05	8.00E-05	2.30E-03	2.18E-03
SS-C3-P-017	0.151	1.447	1.597	1.19E-04	8.91E-05				
SS-C3-P-021	0.135	1.633	1.768	1.36E-04	1.28E-04				
SS-C3-P-022	0.179	1.350	1.529	1.21E-04	1.17E-04				
SS-C3-P-023	0.099	1.356	1.456	1.81E-04	1.52E-04				
SS-C3-P-024	0.169	1.347	1.516	1.62E-04	1.56E-04				
SS-C3-P-027	0.083	1.154	1.237	9.93E-04	9.41E-05				
SS-C3-P-037	0.076	1.216	1.292	9.49E-05	1.01E-04				
SS-C3-P-038	0.075	1.503	1.578	1.88E-04	1.65E-04				
SS-C3-P-040	0.078	1.559	1.637	1.45E-04	1.39E-04				
SS-RD109-GEO-01	0.017	1.413	1.430	8.41E-05	7.55E-05	6.70E-05	6.00E-05	1.74E-03	2.12E-03
SS-RD109-GEO-05	0.020	1.498	1.517	7.25E-05	6.94E-05	6.70E-05	6.00E-05	1.92E-03	1.98E-03
SS-RD109-GEO-06	0.025	1.506	1.530	8.67E-05	1.85E-03				
SS-RD109-GEO-14	0.039	1.486	1.526	9.03E-05	8.61E-05				
SS-RD109-GEO-16	0.024	1.214	1.238	9.59E-05	8.98E-05				
SS-RD109-P-01	0.025	1.339	1.363	8.21E-05	7.90E-05				
SS-RD109-P-02	0.037	1.422	1.459	8.74E-05	8.49E-05				

B.4 Table 3: Iron content and Magnetic Susceptibility (MS) Data Summary (page 3)

Sample_Name	IronII (%)	IronIII (%)	Iron Total (%)	MS dry (SI)	MS saturated (SI)	MS dry (SI) 10 kHz side	MS dry (SI) 10 kHz top	MS dry (SI) 100 kHz side	MS dry (SI) 100 kHz top
SS-RD109-P-03	0.024	0.986	1.011	8.27E-05	7.97E-05				
SS-RD109-P-04	0.053	1.501	1.554	1.39E-04	1.37E-04				
SS-RD109-P-05	0.060	1.210	1.269	1.06E-04	1.03E-04	9.70E-05	8.00E-05	1.93E-03	2.08E-03
SS-RD109-P-06	0.053	1.350	1.403	1.09E-04	1.07E-04				
NAWC-94BR-P-001	0.024	0.495	0.519	1.96E-04	1.94E-04	1.56E-04	1.20E-04	1.40E-03	1.28E-03
NAWC-94BR-P-002	2.559	2.171	4.729	3.94E-04	0.00E+00	2.90E-04	2.80E-04	1.67E-03	1.84E-03
NAWC-94BR-P-003	0.021	0.735	0.757	4.00E-04	3.94E-04	3.12E-04	2.60E-04	1.34E-03	1.22E-03
NAWC-94BR-P-004	0.122	1.026	1.148	3.69E-04	3.37E-04	3.12E-04	2.80E-04	1.67E-03	1.72E-03
NAWC-94BR-P-005	3.250	1.257	4.508	5.64E-04	5.57E-04	4.68E-04	4.40E-04	2.07E-03	2.28E-03
NAWC-94BR-P-006	3.018	1.273	4.291	3.74E-04	3.71E-04	3.35E-04	3.00E-04	1.90E-03	1.84E-03
NAWC-94BR-P-007	3.233	2.020	5.253	5.63E-04	5.52E-04	3.57E-04	3.60E-04	1.49E-03	1.58E-03
NAWC-94BR-P-008	0.617	0.797	1.413	7.76E-04	7.73E-04	5.58E-04	4.60E-04	2.03E-03	1.90E-03
NAWC-94BR-P-009	2.610	1.860	4.470	1.41E-03	0.00E+00	1.05E-03	9.40E-04	2.07E-03	1.98E-03
NAWC-94BR-P-010	0.423	0.161	0.585	3.98E-04	3.97E-04	3.57E-04	2.40E-04	1.63E-03	1.46E-03
NAWC-94BR-P-011	0.599	0.143	0.743	5.07E-04	5.07E-04	4.24E-04	4.20E-04	1.74E-03	1.78E-03
NAWC-94BR-P-012	3.671	1.290	4.961	4.10E-04	4.07E-04	2.01E-04	2.80E-04	1.23E-03	1.68E-03
NAWC-94BR-P-013	0.164	1.198	1.363	1.77E-04	1.76E-04	1.49E-04	1.00E-04	1.12E-03	9.40E-04
NAWC-94BR-P-014	0.487	0.167	0.654	4.61E-04	4.61E-04	3.79E-04	3.60E-04	1.87E-03	1.76E-03
NAWC-94BR-P-015	2.453	1.955	4.407	3.91E-04	3.91E-04	3.35E-04	3.20E-04	1.56E-03	1.44E-03
NAWC-94BR-P-016	2.712	1.873	4.585	4.12E-04	4.07E-04	4.01E-04	3.40E-04	1.98E-03	1.66E-03
NAWC-94BR-P-017	0.454	0.356	0.810	3.52E-04	3.49E-04	3.12E-04	2.80E-04	1.63E-03	1.50E-03

B.4 Table 3: Iron content and Magnetic Susceptibility (MS) Data Summary (page 4)

Sample_Name	IronII (%)	IronIII (%)	Iron Total (%)	MS dry (SI)	MS saturated (SI)	MS dry (SI) 10 kHz side	MS dry (SI) 10 kHz top	MS dry (SI) 100 kHz side	MS dry (SI) 100 kHz top
NAWC-94BR-P-018	0.832	0.567	1.400	3.54E-04	3.55E-04	2.68E-04	3.00E-04	1.63E-03	1.44E-03
NAWC-94BR-P-020	1.833	1.708	3.541	3.28E-04	3.27E-04	2.90E-04	2.60E-04	1.32E-03	1.40E-03
NAWC-94BR-P-021	0.519	1.023	1.542	3.05E-04	3.00E-04	3.12E-04	2.60E-04	1.78E-03	1.80E-03
NAWC-94BR-P-022	3.728	0.637	4.365	6.32E-04	0.00E+00	5.35E-04	4.60E-04	2.03E-03	1.96E-03
NAWC-94BR-P-023	2.835	1.728	4.563	4.04E-04	4.05E-04	3.35E-04	3.00E-04	1.65E-03	1.68E-03
NAWC-94BR-P-024	3.305	0.949	4.255	8.87E-04	8.86E-04	6.69E-04	7.20E-04	2.01E-03	2.06E-03
NAWC-94BR-P-025	1.103	0.428	1.532	8.03E-04	7.94E-04	6.91E-04	5.80E-04	2.32E-03	2.06E-03
NAWC-94BR-P-026	2.756	2.602	5.359	2.16E-03	2.20E-03	1.78E-03	1.58E-03	2.97E-03	2.84E-03
NAWC-94BR-P-027	2.315	2.062	4.376	7.63E-04	7.63E-04	6.24E-04	5.60E-04	2.07E-03	1.98E-03
NAWC-94BR-P-028	2.917	2.408	5.326	5.44E-04	5.47E-04	4.46E-04	4.20E-04	1.72E-03	1.64E-03
NAWC-94BR-P-029	2.993	2.407	5.400	7.44E-04	7.44E-04	6.24E-04	5.80E-04	1.85E-03	1.82E-03

B.4 Table 4: NMR Data Summary (page 1)

Sample_Name	T2ml @te=200µs (s)	T2 peak @te=200µs (s)	NMR water content @ te200µs (mL)	T2ml @te=1500µs (s)	T2peak @te=1500µs (s)	T2cutoff (s)
HC-MP24S-P-001-1V	4.22E-02	1.00E-01	5.968	3.00E-02	8.32E-02	0.0212
HC-MP24S-P-002-1V	3.07E-01	5.25E-01	10.473	2.97E-01	5.01E-01	0.3845
HC-MP24S-P-002-2H	3.43E-01	6.03E-01	7.411	2.77E-01	5.50E-01	0.1123
HC-MP24S-P-003-1V	4.22E-02	1.10E-01	8.661	2.80E-02	8.71E-02	0.0471
HC-MP24S-P-003-2H	2.68E-02	7.24E-02	5.044	1.68E-02	5.75E-02	0.0506
HC-MP24S-P-004-1V	2.59E-01	3.47E-01	14.411	2.20E-01	3.16E-01	0.1613
HC-MP24S-P-004-2H	4.66E-01	6.92E-01	8.699	3.89E-01	6.92E-01	0.6862
HC-MP24S-P-005-1V	3.05E-03	7.24E-04	10.174	3.32E-03	1.32E-03	0.0077
HC-MP24S-P-006-1V	3.23E-02	9.55E-02	9.954	2.33E-02	7.59E-02	0.0471
HC-MP24S-P-006-2H	1.38E-02	2.09E-03	8.684	8.48E-03	2.19E-03	0.0284
HC-MP24S-P-007-1V	5.58E-02	2.19E-01	6.883	3.61E-02	1.91E-01	0.0727
HC-MP24S-P-007-2H	2.90E-02	1.26E-01	9.792	1.96E-02	1.00E-01	0.0544
HC-MP25S-P-001-1V	2.87E-02	2.88E-02	9.606	2.53E-02	2.75E-02	0.0328
HC-MP25S-P-001-2H	2.94E-02	2.88E-02	10.908	2.51E-02	2.88E-02	0.0407
HC-MP25S-P-002-1V	8.40E-03	6.61E-03	5.601	6.00E-03	6.03E-03	0.0159
HC-MP25S-P-002-2H	7.23E-03	6.03E-03	7.068	5.65E-03	5.25E-03	0.0171
HC-MP25S-P-003-1V	3.03E-02	3.31E-02	9.480	2.38E-02	3.63E-02	0.0328
HC-MP25S-P-003-2H	1.24E-02	5.25E-03	8.094	7.85E-03	4.57E-03	0.0054
HC-MP25S-P-004-1V	6.84E-03	6.31E-03	9.660	5.03E-03	3.80E-03	0.0119
HC-MP25S-P-004-2H	7.01E-03	5.25E-03	7.240	5.34E-03	3.80E-03	0.0103
HC-MP25S-P-005-1V	2.50E-02	1.10E-01	13.916	2.48E-02	9.12E-02	N/A
HC-MP25S-P-006-1V	1.92E-02	1.00E-01	13.352	1.77E-02	8.32E-02	0.0138

B.4 Table 4: NMR Data Summary (page 2)

Sample_Name	T2ml @te=200µs (s)	T2 peak @te=200µs (s)	NMR water content @ te200µs (mL)	T2ml @te=1500µs (s)	T2peak @te=1500µs (s)	T2cutoff (s)
SS-C3-Cl-100.0	1.71E-02	4.17E-02	6.588	2.05E-02	3.63E-02	0.0353
SS-C3-Cl-118.6	1.88E-02	4.79E-02	5.938	1.57E-02	4.37E-02	0.0305
SS-C3-Cl-139.7	2.06E-02	5.25E-02	5.210	1.79E-02	3.98E-02	0.0264
SS-C3-P-015	2.08E-02	4.17E-02	9.062	1.46E-02	3.16E-02	0.0353
SS-C3-P-017	2.32E-02	5.75E-02	10.107	2.51E-02	3.80E-02	N/A
SS-C3-P-021	1.04E-02	2.63E-02	10.473	6.45E-03	2.19E-02	0.0328
SS-C3-P-022	6.58E-03	1.66E-03	5.621	4.82E-03	1.15E-03	0.0228
SS-C3-P-023	8.35E-03	2.00E-02	7.074	5.81E-03	1.58E-02	0.0264
SS-C3-P-024	9.62E-03	2.09E-02	4.751	7.43E-03	1.91E-02	0.0138
SS-C3-P-027	5.68E-02	9.55E-02	9.799	4.44E-02	6.92E-02	N/A
SS-C3-P-037	2.46E-02	4.79E-02	9.032	1.62E-02	4.79E-02	0.0328
SS-C3-P-038	1.07E-02	2.88E-02	6.370	7.46E-03	2.51E-02	0.0353
SS-C3-P-040	1.16E-02	2.75E-02	6.293	7.35E-03	2.40E-02	0.0264
SS-RD109-GEO-01	1.85E-02	4.17E-02	10.302	2.07E-02	2.88E-02	0.0328
SS-RD109-GEO-05	2.26E-02	5.01E-02	12.685	2.06E-02	3.63E-02	N/A
SS-RD109-GEO-06	1.56E-02	2.88E-02	11.247	1.41E-02	2.19E-02	0.0264
SS-RD109-GEO-14	1.51E-02	4.37E-02	13.024	1.55E-02	3.47E-02	0.0353
SS-RD109-GEO-16	1.18E-02	3.47E-02	11.918	1.05E-02	2.88E-02	0.0305
SS-RD109-P-01	1.73E-02	3.02E-02	10.602	1.99E-02	2.19E-02	0.0159
SS-RD109-P-02	1.45E-02	3.02E-02	9.910	1.24E-02	2.40E-02	0.0212
SS-RD109-P-03	2.13E-02	3.80E-02	5.643	1.61E-02	3.16E-02	0.0471
SS-RD109-P-04	1.07E-02	2.88E-02	9.630	1.30E-02	2.09E-02	N/A

B.4 Table 4: NMR Data Summary (page 3)

Sample_Name	T2ml @te=200µs (s)	T2 peak @te=200µs (s)	NMR water content @ te200µs (mL)	T2ml @te=1500µs (s)	T2peak @te=1500µs (s)	T2cutoff (s)
SS-RD109-P-05	1.35E-02	3.98E-02	9.561	1.27E-02	3.47E-02	0.0328
SS-RD109-P-06	1.48E-02	3.47E-02	8.141	9.66E-03	3.16E-02	0.0184
NAWC-94BR-P-001	2.23E-03	2.19E-03	8.943	1.19E-03	1.20E-03	0.0030
NAWC-94BR-P-002	0.00E+00	0.00E+00	0.000	0.00E+00	0.00E+00	N/A
NAWC-94BR-P-003	2.81E-03	1.91E-03	2.865	1.29E-03	1.10E-03	0.0058
NAWC-94BR-P-004	6.95E-04	6.03E-04	6.623	9.34E-04	7.59E-04	N/A
NAWC-94BR-P-005	5.65E-04	5.01E-04	8.277	9.51E-04	7.24E-04	0.0010
NAWC-94BR-P-006	6.47E-04	5.01E-04	5.107	1.16E-03	6.92E-04	0.0011
NAWC-94BR-P-007	2.12E-03	1.10E-03	1.447	9.78E-04	6.61E-04	0.0111
NAWC-94BR-P-008	4.91E-04	3.47E-04	2.535	1.43E-03	6.92E-04	0.0010
NAWC-94BR-P-009	1.53E-03	1.10E-03	0.447	9.05E-04	5.75E-04	N/A
NAWC-94BR-P-010	1.09E-03	1.15E-03	0.787	1.92E-03	1.10E-03	N/A
NAWC-94BR-P-011	1.09E-03	9.55E-04	0.915	1.19E-03	7.94E-04	0.0014
NAWC-94BR-P-012	9.40E-04	7.24E-04	2.317	1.01E-03	6.92E-04	0.0016
NAWC-94BR-P-013	4.66E-02	7.24E-02	9.312	1.80E-02	3.02E-02	0.0782
NAWC-94BR-P-014	1.14E-03	3.02E-04	1.594	8.17E-03	2.00E-03	0.0284
NAWC-94BR-P-015	2.44E-03	9.12E-04	1.617	1.38E-03	6.61E-04	0.0019
NAWC-94BR-P-016	4.81E-04	2.40E-04	1.596	1.27E-03	6.61E-04	0.0007
NAWC-94BR-P-017	9.28E-04	7.59E-04	1.840	1.00E-03	6.92E-04	0.0012
NAWC-94BR-P-018	1.94E-03	1.32E-03	2.056	1.08E-03	7.94E-04	0.0030
NAWC-94BR-P-020	3.64E-03	1.51E-03	1.165	1.32E-03	7.59E-04	N/A
NAWC-94BR-P-021	1.23E-03	9.12E-04	2.610	9.44E-04	7.24E-04	N/A

B.4 Table 4: NMR Data Summary (page 4)

Sample_Name	T2ml @te=200µs (s)	T2 peak @te=200µs (s)	NMR water content @ te200µs (mL)	T2ml @te=1500µs (s)	T2peak @te=1500µs (s)	T2cutoff (s)
NAWC-94BR-P-022	2.58E-03	9.12E-04	1.124	1.45E-02	2.19E-03	N/A
NAWC-94BR-P-023	1.23E-03	1.05E-03	0.871	7.80E-04	5.75E-04	N/A
NAWC-94BR-P-024	3.59E-03	1.20E-03	0.731	1.53E-03	6.03E-04	N/A
NAWC-94BR-P-025	5.97E-04	2.75E-04	2.201	1.13E-03	1.00E-03	N/A
NAWC-94BR-P-026	3.61E-03	1.45E-03	0.384	1.01E-03	5.25E-04	N/A
NAWC-94BR-P-027	1.14E-03	1.05E-03	0.476	9.75E-04	6.61E-04	N/A
NAWC-94BR-P-028	1.46E-03	1.00E-03	0.591	6.86E-04	4.79E-04	N/A
NAWC-94BR-P-029	1.74E-03	1.45E-03	1.063	7.78E-04	5.75E-04	N/A

Appendix C: Publications

Journal Articles

Robinson, J., Slater, L., Weller, A., Keating, K., Robinson, T., Rose, C., et al. (2018). On permeability prediction from complex conductivity measurements using polarization magnitude and relaxation time. Water Resources Research, 54, 3436– 3452. https://doi.org/10.1002/2017WR022034

Day-Lewis, F.D., Slater, L.D., Robinson, J., Johnson, C.D., Terry, N. and Werkema, D. (2017). An overview of geophysical technologies appropriate for characterization and monitoring at fractured-rock sites. Journal of Environmental Management, 204, pp.709-720. https://doi.org/10.1016/j.jenvman.2017.04.033

Expanded Abstracts

Robinson, J., Slater, L., Keating, K., Robinson, T., Parker, B., Rose, C. and Prasad, M., (2018). On permeability estimation for mudstones using geophysical length scales. In SEG Technical Program Expanded Abstracts 2018 (pp. 4889-4893). Society of Exploration Geophysicists. https://doi.org/10.1190/segam2018-2985629.1

Published Abstracts

Slater, L., Day-Lewis, F., Falzone, S., Keating, K., Ntarlagiannis, D. and Parker, B., 2019, March. Complex Resistivity (CR) Monitoring of Tracer Tests for Assessing Mass Transfer and Sorption in Low Permeability Media. In SAGEEP 2019-32nd Annual Symposium on the Application of Geophysics to Engineering and Environmental Problems, Abstract http://www.earthdoc.org/publication/publicationdetails/?publication=95817

Falzone, S., Keating, K., Parker, B.L., Day-Lewis, F.D., Robinson, J. and Slater, L.D., 2018, December. Exploring the relationship between sorption, mass transfer, and flow rate in dual domain porosity media. AGU Fall Meeting Abstract #H41J-2202 http://adsabs.harvard.edu/abs/2018AGUFM.H41J2202F

Robinson, J., Slater, L.D., Keating, K., Parker, B.L. and Robinson, T., 2017, December. Relationship between pore geometric characteristics and SIP/NMR parameters observed for mudstones. AGU Fall Meeting Abstract #H21A-1430 http://adsabs.harvard.edu/abs/2017AGUFM.H21A1430R

Falzone, S., Slater, L.D., Day-Lewis, F.D., Parker, B.L., Keating, K. and Robinson, J., 2017, December. Characterizing Mobile/Less-Mobile Porosity and Solute Exchange in Dual-Domain Media Using Tracer Experiments and Electrical Measurements in a Hassler-Type Core Holder. AGU Fall Meeting Abstract #H21P-08

http://adsabs.harvard.edu/abs/2017AGUFM.H21P..08F

Robinson, T., Keating, K., Robinson, J., Slater, L.D. and Parker, B.L., 2016, December. Magnetic Susceptibility: Correlations with Clay Content and Apparent Diffusion Coefficients Controlling Electrical Double Layer Polarization. AGU Fall Meeting Abstract #ED31B-0876 http://adsabs.harvard.edu/abs/2016AGUFMED31B0876R

Robinson, J., Slater, L.D., Keating, K., Parker, B.L., Day-Lewis, F.D. and Robinson, T., 2016, December. Permeability prediction of high Spor samples from spectral induced polarization (SIP): limitations of existing models. AGU Fall Meeting Abstracts # H43L-04 http://adsabs.harvard.edu/abs/2016AGUFM.H43L..04R

Robinson, J., Slater, L.D., Keating, K., Parker, B.L., Rose, C., Meyer, J.R., Johnson, C.D., Robinson, T., Pehme, P., Chapman, S. and Day-Lewis, F.D., 2015, December. Evaluating petrophysical relationships in fractured rock using geophysical measurements. AGU Fall Meeting Abstract #H14A-07 http://adsabs.harvard.edu/abs/2015AGUFM.H14A..07R